Precision Glycomacromolecules with Hydrophobic Main Chain Motives

Inaugural-Dissertation

to obtain the academic degree
Doctor rerum naturalium (Dr. rer. nat)
of the Faculty of Mathematics and Natural Sciences
of Heinrich Heine University Düsseldorf

submitted by

Sophia Boden
from Düsseldorf

Düsseldorf, September 2019

From the Institute of Organic Chemistry and Macromolecular Chemistry at the Heinrich Heine University Düsseldorf

Published by permission of the
Faculty of Mathematics and Natural Sciences
Heinrich Heine University Düsseldorf

Supervisor: Prof. Dr. Laura Hartmann

Co-supervisor: PD Dr. Klaus Schaper

Date of oral examination: 22.11.2019

This thesis was accomplished in the period between October 2015 and March 2019 in the Institute of Organic Chemistry and Macromolecular Chemistry at Heinrich Heine University in Düsseldorf under supervision of Prof. Dr. Laura Hartmann.

I hereby declare that the thesis submitted is my own work without making use of impermissible aids, considering the "Rules on the Principles for Safeguarding Good Scientific Practice at Heinrich Heine University Düsseldorf". All direct or indirect sources used are acknowledged in the bibliography as references. I further declare that I have not submitted this nor a similar thesis at any other examination board in order to obtain a degree.

Düsseldorf, 08.09.2019

(Sophia Boden)

Acknowledgements

First of all, I would like to express my gratitude to my supervisor Prof. Dr. Laura Hartmann, for giving me the opportunity to obtain my Ph.D. degree in her working group. I want to thank her for the interesting projects and national as well as international collaborations during my Ph.D. thesis. I also want to thank her for giving me the opportunity to speak at international conferences and to do a three-month research stay at Davidson College, North Carolina, which both extended my personal and scientific skills. Prof. Dr. Hartmann always was enthusiastic, supportive and ready to give helpful advices which was a great motivation for me.

I would also like to thank PD Dr. Klaus Schaper for agreeing to be second supervisor of this thesis.

I want to thank Dr. Monir Tabatabai for always being helpful and a good advisor in both scientific and personal questions. I also want to thank her for spending endless hours proof reading my publications and this work as well as for her incomparable sense of humour.

Moreover, I want to thank Prof. Nicole L. Snyder for the time I could spend with her in Düsseldorf and in Davidson. I want to thank her for many helpful discussions, advices and her always having an open ear for me. I would also like to thank her for giving me the opportunity to do a three-month research stay in her work group at Davidson College in North Carolina and for her continuous work on this collaboration project. In this context I also want to thank Nika Fendler for her contributions and advices.

Furthermore, I would like to thank my collaboration partners, Dr. Franziska Reise, Prof. Dr. Thisbe K. Lindhorst, Dr. Kristina Wagner and Prof. Dr. Matthias Karg. Through these collaborations I not only had the chance to learn a lot in different scientific fields but also to produce interdisciplinary results contributing to this work.

I would also like to express my thanks to all current and former members of the Hartmann and the Schmidt group for the support, nice collaboration and the excellent working atmosphere during the time of my Ph.D. I really enjoyed working on my project, which in part can be attributed to you. I will never forget the great times we had during our after work barbecues, “Einstandspartys”, Christmas Parties and especially our group trips to the Netherlands and Malta. I am very thankful for the time we spent together and I am even more thankful for the friendships that developed during the time of my Ph.D.

I especially want to thank my lab partners Dr. Christoph Gerke, Markus Giesler, Peter Pasch and Theresa Seiler. Christoph was my lab partner for almost the whole time I spent in the Hartmann group and I want to express my gratitude for him being the best colleague one could wish for. I learned a lot

from him and never met someone so helpful and selfless as well as hard working in my life, before. I want to thank all lab partners for the great atmosphere in our lab. We could work together while sharing scientific as well as personal problems and we could always laugh together. This was very motivating and helped me through frustrating days.

Moreover, I want to thank the “Makro squad”, Dr. Monir Tabatabai, Mischa Baier, Markus Giesler and Philipp Reuther. I want to thank Dr. Monir Tabatabai for organizing the practical course and her unstoppable will to make every student understand Macromolecular Chemistry. I want to thank Mischa Baier, Markus Giesler and Philipp Reuther for every “Kuchenstrich” and for making the endless hours we spent in the practical course such a great time I will always keep in good memories.

I also want to thank the SPR team, Tanja Freichel and Markus Giesler. When we first started with the SPR measrurements we were complete beginners and had to learn everything about this instrument. But by great team work and lots and lots and lots of discussions and brain storming we finally succeeded in finding the right assay conditions. I really want to thank both of you for being great colleagues and friends who are so enthusiastic and cheering that even most frustrating SPR days still were fun.

Furthermore, I want to thank Tanja Paul for the great time we had during our trip to Boston and New York for attending the ACS conference. I gained countless new memories and first time experiences that I will always keep in my heart.

I would also like to thank Dana Itskalov who not only accompanied me throughout my Bachelor and Master studies but also during my Ph.D. in the Hartmann group. I want to thank her for not only being a good colleague but also for being such a good friend.

I also want to thank the lab technicians Stephanie Scheelen, Sonja Coors and Birgit Ohler for providing me with laboratory material and taking responsibility of the “Dest-Dienst”. I especially want to thank Stephanie Scheelen for the many little conversations we had and for every time we laughed together which always made my day and work much more pleasant. In addition, I want to thank the secretaries Michaela Kitza and Viola Schürmanns for always providing me with office material and help in all organizational questions while always being so friendly and understanding. Furthermore, I want to thank Maria Beuer and PD Dr. Klaus Schaper for performing NMR measurements and Dr. Peter Tommes for performong HRMS and MALDI-TOF-MS measurements.

Moreover, I want to thank my Bachelor students Jessica Kania and Christin Buchmann for the hard work and late hours they spent in the lab. I am especially grateful for their enthusiasm about their

projects and their high level of motivation so that they produced great results that in part also contributed to this work.

At the end, but most importantly, I want to thank my dear family and friends, for being understanding, supportive and encouraging throughout the whole time of my thesis. I especially want to thank my mother, Virginia Titz, the strongest person I know, for being the best role model one could wish for. I also want to thank my boyfriend, Max Düber, for his support, patience and belief in me, no matter what.

“No thief, however skillful, can rob one of knowledge, and that is why knowledge is the best and safest treasure to acquire”

- L. Frank Baum, The Lost Princess of Oz -

Parts of this thesis are already published or were presented on professional conferences:

Publications:

S. Boden, F. Reise, J. Kania, T. K. Lindhorst, L. Hartmann, "Sequence-defined Introduction of Hydrophobic Motifs and Effects in Lectin Binding of Precision Glycomacromolecules", *Macromolecular Bioscience,* **2019**, 1800425.

Contributions: Sophia Boden synthesized the glycomacromolecules after identifying an optimized coupling procedure. Sophia Boden characterized the obtained glycomacromolecules and performed and analyzed the ITC, SPR and NMR studies with ConA. Sophia Boden performed the DLS measurements with the glycomacromolecules. Sophia Boden also contributed in writing of the paper.

S. Boden, K. G. Wagner, M. Karg, L. Hartmann, "Presenting Precision Glycomacromolecules on Gold Nanoparticles for Increased Lectin Binding", *Polymers,* **2017***, 9,* 716.

Contributions: Sophia Boden synthesized and characterized the glycomacromolecules and glyco-AuNPs and performed and analyzed the UV-Vis absorbance and kinetic studies with ConA and SPR measurements. Sophia Boden also contributed in writing of the paper.

S. Igde, S. Röblitz, A. Müller, K. Kolbe, S. Boden, C. Fessele, T.K. Lindhorst, M. Weber, L. Hartmann, "Linear Precision Glycomacromolecules with Varying Interligand Spacing and Linker Functionalities Binding to Concanavalin A and the Bacterial Lectin FimH", *Macromolecular Bioscience*, **2017**, *12*, 1700198-n/a.

Contributions: Sophia Boden contributed to the analysis, interpretation and discussion of ITC measurements. Sophia Boden also contributed in writing of the paper.

Presentations on Professional Conferences:

S. Boden, F. Reise, T. K. Lindhorst, L. Hartmann, „Varying Hydrophobicity of Precision Glycomacromolecules and the Effect on Lectin Binding", German-Polish-Baltic Conference on Organic Chemistry, May 15-19, **2018**, Hamburg.

S. Boden, K. Wagner, M. Karg, L. Hartmann, „Functionalization of Gold Nanoparticles with Precision Glycomacromolecules for Enhanced Lectin Binding", American Chemical Society, National Meeting & Exposition: Nanoscience, Nanotechnology & Beyond, August 19-23, **2018**, Boston, MA.

Other Publications:

F. Jacobi, A. Camaleño de la Calle, S. Boden, A. Grafmüller, L. Hartmann, S. Schmidt, “Multivalent Binding of Precision Glycooligomers on Soft Glycocalyx Mimicking Hydrogels”, *Biomacromolecules*, **2018**, *19*, 3479.

C. Gerke, M.F. Ebbesen, D. Jansen, S. Boden, T. Freichel, L. Hartmann, “Sequence-Controlled Glycopolymers via Step-Growth Polymerization of Precision Glycomacromolecules for Lectin Receptor Clustering”, *Biomacromolecules,* **2017***, 18,* 787.

I. Joachim, S. Rikker, D. Hauck, D. Ponader, S. Boden, R. Sommer, L. Hartmann, A. Titz, “Development and Optimization of a Competitive Binding Assay for the Galactophilic Low Affinity Lectin LecA from Pseudomonas Aeruginosa, *Organic & Biomolecular Chemistry*, **2016**, *14*, 79.

Abstract

All cells in living organisms are surrounded by a sugar coat called the glycocalyx. This sugar coat represents the antennas of the cells and is involved in many important biological signal transduction processes such as cell cell communication and/or the adhesion of pathogens. The information is encoded in complex carbohydrate structures and then decoded by recognition of carbohydrate-recognizing proteins, termed lectins. An important concept underlying carbohydrate lectin recognition is multivalency, where only upon interactions of multiple carbohydrate and receptor sites, otherwise weak binding results in a strong signal.

Recently, Hartmann *et al.* demonstrated that so called precision glycomacromolecules are a promising tool for studying carbohydrate lectin interactions and can be used to obtain deeper insight into the underlying multivalent effects that govern these processes. Precision glycomacromolecules consist of an oligoamide backbone with pending carbohydrate side chains and are synthesized by solid phase polymer synthesis (SPPoS) based on protocols of peptide synthesis as introduced by Merrifield. In addition to natural amino acids, artificial building blocks are employed in SPPoS. By stepwise assembly of these building blocks on solid support a monodisperse, sequence-defined oligoamide scaffold with varying functional groups in the main and side chains can be synthesized. Subsequent sugar conjugation results in precision glycomacromolecules which provide a new class of multivalent glycomimetics suitable as ligands and inhibitors of bacterial and viral lectins.

In this thesis, three strategies to further develop the platform of precision glycomacromolecules are introduced: a) the introduction of hydrophobic motifs in the backbone to allow for secondary interactions in lectin binding, b) attaching glycomacromolecules onto gold nanoparticles (AuNPs) for further increase in multivalency and applications in cell targeting, c) first experiments towards dynamic combinatorial libraries of precision glycomacromolecule fragments (*Figure 1*).

In the first part of the thesis precision glycomacromolecules gradually changing in backbone hydrophobicity are synthesized by SPPoS. The change in backbone hydrophobicity is achieved by introducing a hydrophobic aliphatic (ODS) (octyl – diamine – succinic acid) as well as hydrophobic aromatic spacer building block (AR) (aromatic) in combination with the regularly employed hydrophilic EDS (ethylene glycol – diamine – succinic acid) spacer building block. As carbohydrate moiety an α-D-mannose azide derivative is employed to target the model lectin Concanavalin A (ConA) and the bacterial lectin receptor FimH. Binding affinity of the different precision glycomacromolecules to ConA is assessed by surface plasmon resonance (SPR) and isothermal titration calorimetry (ITC) measurements. Moreover, the inhibitory potency of the different glycomacromolecules is investigated

employing a bacterial adhesion inhibition assay with the *E. coli* (*Escherichia coli*) FimH receptor. NMR and dynamic light scattering (DLS) are also employed to gain further information about glycomacromolecule behavior in solution. Results show higher affinities as well as higher inhibitory potential for glycomacromolecules with hydrophobic and aromatic moieties in the backbone. This increase in affinity is rationalized by additional secondary interactions with hydrophobic amino acid side chains near the carbohydrate recognition domain. Additionally, glycomacromolecules seem to adapt their conformation in solution in dependence of the hydrophobicity of the backbone, where carbohydrate ligands of glycomacromolecules with higher hydrophobicity in the backbone are more exposed to the solution phase due to unfavorable interactions of hydrophobic moieties with the aqueous surrounding.

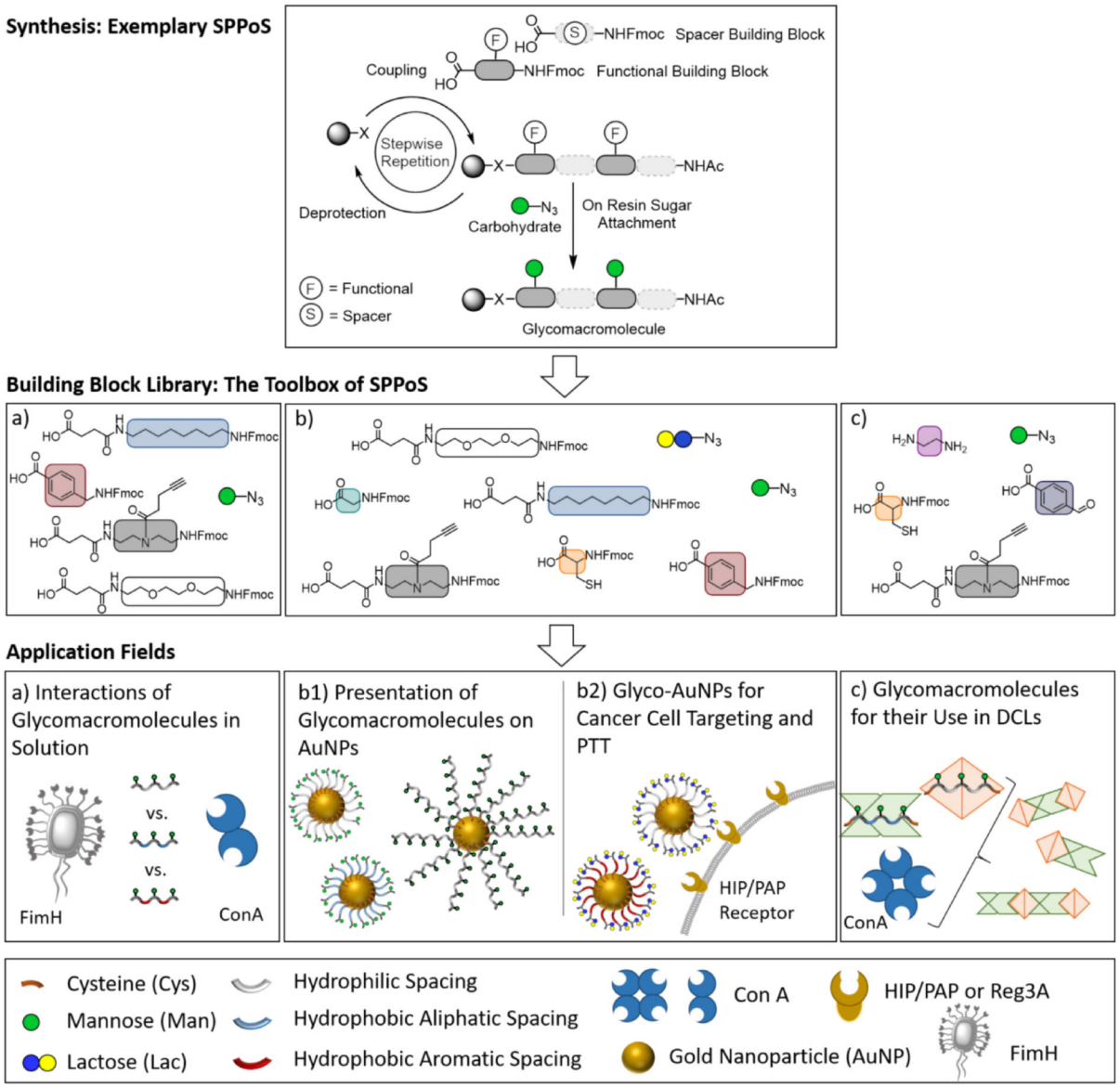

Figure 1: Schematic overview of the different parts of this thesis.

Based on the finding that hydrophobic backbone properties increase lectin binding, in the second part of this work, a first set of three glycomacromolecules varying in carbohydrate valency and backbone hydrophobicity are employed for their presentation on AuNPs. In SPPoS natural amino acids L-cysteine and L-glycine are used in addition to artificial building blocks, ODS, EDS and TDS, in order to introduce a thiol group for attachment to the gold surface as well as the introduction of an acid end group to increase the colloidal stability of obtained glyco-AuNPs. In this way glyco-AuNPs are obtained that exhibit a high degree of functionalization and good stability in buffer solution. The binding affinity of glyco-AuNPs towards model lectin ConA is evaluated by applying UV-Vis spectroscopy, DLS and SPR to understand the aggregation behavior or inhibitory potential of glyco-AuNPs together with ConA. Results show that in comparison to the binding affinity of free glycomacromolecule compounds towards ConA, glyco-AuNPs presenting glycomacromolecules with hydrophobic backbone properties demonstrated increased affinity. In addition, multivalent presentation on the gold surface leads to an enhancemenht in binding affinity in comparison to the free ligand.

In the next part of this thesis the glyco-nanoparticle concept is extended to the functionalization of gold nanoparticles with lactose bearing glycomacromolecules that again vary in carbohydrate number and backbone hydrophobicity. This time, their *in vitro* activity towards the HIP/PAP or Reg3A protein on cancer cells is evaluated by cellular uptake and subcellular localization studies. Again highly stable glyco-AuNPs with high degree of functionalization are obtained that additionally show no negative impact on cell viability. Results show that cell uptake determined by flow cytometry and inductively coupled plasma mass spectrometry (ICP-MS) in different cell lines is similar irrespective of the glycomacromolecule structure presented on the surface, with one exception, the presentation of a monovalent glycomacromolecule with aromatic spacer next to the carbohydrate carrying TDS building block. Different inhibition studies are carried out to gather insights into the reasons for this exceptional behavior but result in no clear indication.

The third part of the thesis presents a different approach for identifying high affinity glycomimetics. Instead of synthesizing a series of glycomacromolecules that vary in special design features in order to identify the glycomacromolecule with highest affinity, different glycomacromolecule components are presented to the lectin in a dynamic way so that the lectin itself can choose and help in the formation of the optimal glycomimetic species. This approach is based on a dynamic combinatorial library of glycomacromolecules. Different reversible dynamic bonds, namely the thiol-disulphide interchange and the formation of imines by the condensation reaction of aldehydes and amines, is tested. Even though small impacts of lectin presence on the constitution of the dynamic combinatorial library (DCL) can be observed the two systems still do not provide optimal DCL conditions requiring further optimization in future studies.

Kurzzusammenfassung

Jede Zelle in lebenden Organismen ist von einem Zucker-Mantel, der sogenannten Glykokalyx, umgeben. Dieser Zucker-Mantel fungiert als Antenne der Zellen und ist an vielen wichtigen biologischen Signalübertragungen, wie der Zell-Zell-Kommunikation und/oder der Adhäsion von Pathogenen, beteiligt. Informationen werden in den komplexen Kohlenhydratstrukturen kodiert und dann durch die Bindung von Kohlenhydrat-erkennenden Proteinen, den Lektinen, entschlüsselt. Ein wichtiges Konzept, das diesen Kohlenhydrat-Lektin-Wechselwirkungen zugrunde liegt, ist die Multivalenz, wobei durch die Wechselwirkung mehrerer Bindungseinheiten des Kohlenhydrat Liganden als auch des Rezeptors, die normalerweise schwache Wechselwirkung zwischen einzelen Kohlenhydraten und Bindungstaschen verstärkt wird.

Kürzlich haben Hartmann *et al.* gezeigt, dass sogenannte Präzisions-Glykomakromoleküle als vielversprechende Werkzeuge zur Untersuchung von Kohlenhydrat-Lektin-Wechselwirkungen dienen, um einen tieferen Einblick in die zugrundeliegenden multivalenten Effekte zu erlangen. Präzisionsglykomakromoleküle bestehen au einem Oligoamid Rückgrat mit angehängten Kohlenhydrat-Seitenketten und werden mithilfe der Festphasen Polymer Synthese (SPPoS), welche auf der klassischen Peptid Festphasessynthese von Merrifield basiert, dargestellt. Zusätzlich zu natürlichen Aminosäuren werden dabei synthetische Bausteine verwendet. Durch schrittweisen Aufbau dieser Bausteine auf der festen Phase wird ein monodisperses, sequenz-definiertes Oligoamid Rückgrat erhalten, welches Variationen in den funktionellen Gruppen der Haupt- und Seitenketten beinhaltet. Durch anschließende Konjugation eines Kohlenhydrat-Liganden an das Rückgrat, wird das Präzisionsglykomakromolekül erhalten, welches eine neue Klasse von multivalenten Glykomimetika repräsentiert, die als Liganden oder Inhibitoren von bakteriellen und viralen Lektinen fungieren.

In dieser Arbeit werden drei Strategien verfolgt, um die Plattform der Präzisionsglykomakromoleküle zu erweitern: a) die Verwendung eines hydrophoben Bausteins im Rückgrat für zusätzliche sekundäre Wechselwirkungen mit dem Lektin, b) Anbringung von Glykomakromolekülen auf Gold Nanopartikeln (AuNPs) für eine weitere Verstärkung der Multivalenz und Anwendung in der gezielten Ansteuerung von Zellen, c) erste Experimente für die Verwendung von Glykomakromolekül-Fragmenten in dynamischen kombinatorischen Bibliotheken (Abbildung 1).

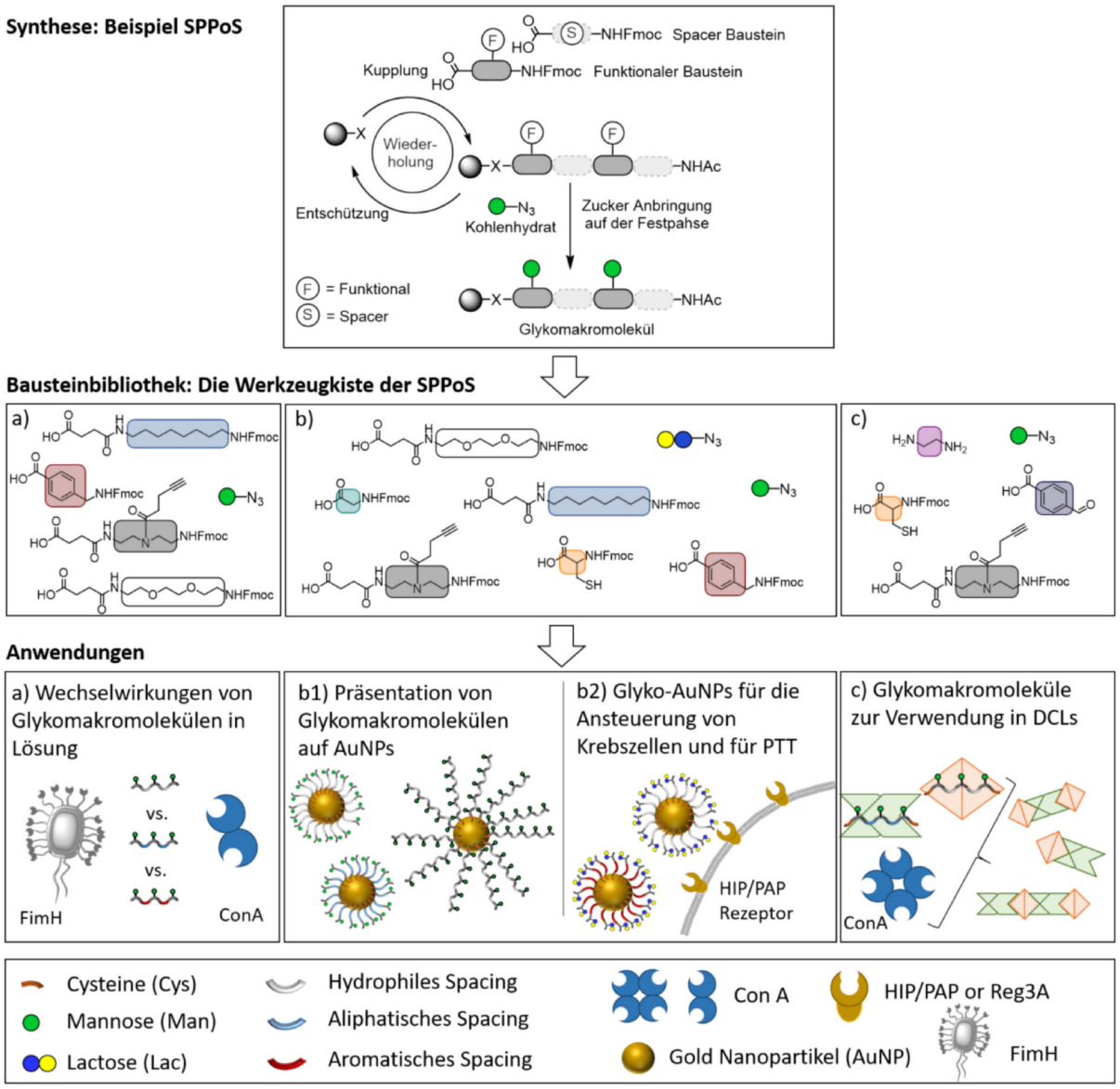

Abbildung 1: Schematische Übersicht der verschiedenen Abschnitte dieser Arbeit.

Im ersten Teil dieser Arbeit werden Präzisionsglykomakromoleküle mittels SPPoS synthetisiert, die in der Hydrophobizität des Rückgrats variieren. Die Änderung der Hydrophobizität des Rückgrats wird dadurch erreicht, dass ein hydrophober aliphatischer (ODS) (octyl – diamine – succinic acid) sowie ein hydrophober aromatischer Baustein (AR) (aromatisch) in Kombination mit dem standardmäßig verwendeten hydrophilen EDS (ethylene glycol – diamine – succinic acid) Spacer Baustein verwendet werden. Als Kohlenhydrat Einheit wird ein α-D-Mannose Azid Derivat gewählt, um das Modell Lektin Concanavalin A (ConA) und das bakterielle Lektin FimH anzusteuern. Die Bindungsaffinität zu den verschiedenen Glykomakromolekülen zu ConA wird mittels Oberflächenplasmonenresonanz (SPR) und Isothermer Titrations Kalorimetrie (ITC) Messungen bestimmt. Zudem wird das Inhibierungspotenzial der verschiedenen Glykomakromoleküle durch die Verwendung eines Bakterien Adhäsions-Inhibierungs Experiments mit *E. coli* (*Escherichia coli*) FimH Rezeptoren untersucht. Eine NMR Studie

und Dynamische Lichtstreuung (DLS) geben außerdem zusätzliche Einblicke in das Verhalten der Glykomakromoleküle in Lösung. Die Ergebnisse zeigen, dass höhere Bindungsaffinitäten sowie ein höheres Inhibitionspotenzial mit Glykomakromolekülen mit hydrophoben und aromatischen Eigenschaften im Rüchgrat erreicht werden. Die Zunahme in der Affinität kann vermutlich dadurch erklärt werden, dass zusätzliche sekundäre Wechslewirkungen mit hydrophoben Aminosäureseitenketten in der Nähe der Kohlenhydrat Bindungstasche sowie eine Änderung in der Konformation der Glykomakromoleküle in Lösung zum Tragen kommen. Die Änderung der Konformation wird dadurch erklärt, dass die Präsentation der Kohlenhydrate zur wässrigen polaren Ungebung, aufgrund der unvorteilhaften Exposition der hydrophoben Einheiten zur Lösung, bevorzugt wird.

Basierend auf dem Ergebnis, dass hydrophobe Rückgrat Eigenschaften die Lektin Bindungsaffinität erhöhen, werden im zweiten Teil dieser Arbeit drei Glykomakromoleküle, die in Kohlenhydrat Anzahl und Rückgrat Hydrophobizität variieren, synthetisiert, um sie auf der Oberfläche von AuNPs zu präsentieren. Zusätzlich zu den synthetischen Bausteinen, ODS, EDS und TDS, werden in SPPoS natürliche Aminosäuren, L-Cystein und L-Glycin, eingesetzt, um eine Thiol Funktionalität für die Anbringung an die Goldoberfäche sowie eine Säure Funktionalität für erhöhte kolloidale Stabilität der erhaltenen Glyko-Goldnanopartikel (Glyko-AuNPs) einzuführen. Auf diese Weise werden Glyko-AuNPs mit hohem Funktionalisierungsgrad und guter Stabilität in Puffer Lösungen erhalten. Die Bindungsaffinität der Glyko-AuNPs zu dem Modell Lektin ConA wird mittels UV-Vis Spektroskopie, DLS und SPR, basierend auf dem Aggregationsverhalten und des Inhibitionspotenzials in Gegenwart von ConA, untersucht. In Übereinstimmung mit den Ergebnissen, die für Glykomakromoleküle in Lösung erhalten wurden, zeigen auch Glyko-AuNPs mit hydrophoben Eigenschaften im Rückgrat der präsentierten Glykomakromoleküle eine erhöhte Bindungsaffinität. Zusätzlich kann durch die multivalente Präsentation auf der Goldoberfläche ein größeres inhibitionspotenzial beobachtet werden als für die gleichen Liganden in Lösung.

Im nächsten Teil dieser Arbeit wird das Glyko-Nanopartikel Konzept auf die Funktionalisierung von Gold-Nanopartikeln mit Lactose tragenden Glykomakromolekülen, die erneut in Kohlenhydrat Anzahl und Rückgrat Hydrophobizität variieren, erweitert. Diesmal werden die Glyko-AuNPs dazu verwendet, ihre *in vitro* Aktivität gegenüber des HIP/PAP oder Reg3A Proteins auf Krebszellen mittels Zellaufnahmestudien und Zelllokalisations Studien zu untersuchen. Erneut werden hoch stabile Glyko-AuNPs mit einem hohen Funktionalisierungsgrad, die zudem keinen negativen Einfluss auf die Zell Lebensfähigkeit haben, erhalten. Die Ergebnisse der Zellaufnahmestudien mittels Durchflusszytometrie und Massenspektrometrie mit induktiv gekoppeltem Plasma (ICP-MS) zeigen, dass alle Glyko-AuNPs, unabhängig von der Struktur des Glykomakromoleküls, welches auf der

Oberfläche präsentiert wird, in drei verschiedenen Zelllinien sehr ähnliche Aufnahmewerte aufweisen. Es gibt nur eine Ausnahme, die Präsentation des monovalenten Glykomakromoleküls mit hydrophoben aromatischen Spacing in direkter Nachbarschaft zu dem Kohlenhydrat tragenden TDS Baustein. Verschiedene Inhibitionsstudien werden durchgeführt, um Einblicke in die Gründe für dieses außergewöhnliche Verhalten zu erhalten, lassen allerdings keinen eindeutigen Schluss zu.

Der dritte Teil dieser Arbeit befasst sich mit einer unterschiedlichen Herangehensweise, um ein hoch affines Glykomimetikum zu identifizieren. Anstatt verschiedene Serien von Glykomakromolekülen, die in verschiedenen Design Merkmalen variieren, zu synthestisieren und anschließend die Glykomakromoleküle mit höchster Affinität zu identifizieren, werden verschiedene Glykomakromolekül Komponenten in einer dynamischen Weise präsentiert, so dass in Gegenwart des Lektins die optimale Glykomimetikum Spezies gebildet wird (Abbildung 1). Dieser Ansatz basiert auf einer dynamischen kombinatorischen Bibliothek (DCL) von Glykomakromolekülen. Verschiedene reversible dynamische kovalente Bindungen, nämlich der Thiol-Disulphid Austausch und die Bildung von Iminen durch die Kondensationsreaktion von Aldehyden und Aminen, werden untersucht. Obwohl kleine Einflüsse auf die Zusammensetzung der dynamisch kombinatorischen Bibliothek in Gegenwart des Lektins beobachtet werden können, zeigen die beiden untersuchten Systeme noch nicht die optimalen Bedingungen für eine DCL, so dass in zukünftigen Arbeiten weitere Optimierungen notwendig sind.

Table of Contents

Abstract XV

Kurzzusammenfassung XIX

1. General Introduction 1

1.1 Carbohydrates and Lectins 1

1.1.1 Carbohydrates and Lectins as Part of Biological Communication Processes 1

1.1.1.1 The Role of Carbohydrates and the Glycocalyx 1

1.1.1.2 The Role of Lectins 3

1.1.2 Carbohydrate Lectin Interactions 7

1.1.2.1 Monovalent Carbohydrate Lectin Interactions and Energetic Effects 8

1.1.2.2 Multivalency 12

1.1.2.3 Artificial Scaffolds for Multivalent Carbohydrate Presentation 15

1.2 Solid Phase Synthesis 18

1.2.1 Merrifield´s Vision 18

1.2.2 Solid Phase Polymer Synthesis (SPPoS) 22

2. Aims and Outline 25

3. Results and Discussion 28

3.1 The Effect of Hydrophobicity and Spacing of Glycomacromolecules on Lectin Binding 28

3.1.1 Structural Parameters Influencing Ligand Receptor Binding of Glycomimetics 28

3.1.2 Solid Phase Polymer Synthesis of Glycomacromolecules 32

3.1.2.1 Building Blocks for SPPoS 32

3.1.1.2 Synthesis of Glycomacromolecules Changing in Scaffold Characteristics 33

3.1.2 Lectin Binding Studies 43

3.1.2.1 Proton NMR Experiment for Investigating Hydrophobic Interactions in Solution 53

3.1.2.2 Bacterial Inhibition Study 56

3.2 Presentation of Glycomacromolecules on Gold Nanoparticles 61

3.2.1 Solid Phase Synthesis of Thiolated Glycomacromolecules 65

3.2.1.2 Capping of Thiolated Glycomacromolecules with N-Ethylmaleimide 69

3.2.2 Functionalization of Gold Nanoparticles with Thiol-Glycomacromolecules 71

3.2.3 Lectin Binding Studies 76

3.3 Glyco-Gold Nanoparticles for Cancer Treatment and Photothermal Therapy 84

3.3.1 Solid Phase Polymer Synthesis of Glycomacromolecules for HIP/PAP Targeting 87

3.3.2 Functionalization of Gold Nanoparticles 92
3.3.2.1 Towards the Functionalization of Gold Nanorods 96
3.3.3 Cell Studies 99
3.4 Towards Dynamic Combinatorial Libraries of Glycomacromolecules 116
3.4.1 Dynamers Based on Thiol-Disulphide Interchange 118
3.4.1.1 Dynamic Behavior of Dithiol-Glycomacromolecule Structures 119
3.4.2 Dynamers Based on Imine Bond Formation 123
3.4.2.1 Dynamic Behavior of Glycomacromolecule Structures Forming Imine Bonds 127
4. Conclusion and Outlook 131
5. Experimental Part 141
5.1 Materials 141
5.2 Instrumentation 143
5.3 General Methods 151
5.3.1 Cell Based Assays 160
5.4 Syntheses 167
5.4.1 Building Block Syntheses 167
5.4.2 Synthesis and Functionalization of Gold Nanoparticles 169
5.4.3 Solid Phase Polymer Synthesis (SPPoS) 170
5.4.3.1 SPPoS of Glycomacromolecules Varying in Backbone Characteristics 170
5.4.3.2 SPPoS of Thiolated Glycomacromolecules 181
5.4.3.3 Capping of Glycomacromolecule-Thiol Functionalities with N-ethylmaleimid 183
5.4.3.4 SPPoS of Glycomacromolecules for HIP/PAP Targeting 184
5.4.3.5 SPPoS of Glycomacromolecules for Dynamic Combinatorial Libraries 199
6. Appendix 204
6.1 List of Abbreviations 204
6.2 List of Figures 210
6.3 List of Schemes 218
6.4 List of Tables 219
6.5 Analytics 220
6.6 Additional Information 328
6.6.1 TFA Removal 328
6.6.2 Binding Studies with Glycomacromolecules by ITC 330
6.6.3 Binding Studies with Glycomacromolecules by SPR 338

6.6.4 NMR Study 347
6.6.5 Bacterial Inhibition-Adhesion Studies 349
6.6.6 Glyco-Gold Nanoparticles 355
6.6.7 Glyco-Gold Nanoparticles for HIP/PAP Targeting 358
6.6.8 Dynamic Combinatorial Libraries 362
7. References 363

1. General Introduction

1.1 Carbohydrates and Lectins

1.1.1 Carbohydrates and Lectins as Part of Biological Communication Processes

The human body is very complex with a tremendous number of biological processes taking place at the same time. The blueprint for these processes, including how individual constituents communicate with each other has occupied researchers' attention for decades. It is obvious that the complexity of the human body and the specificity of the processes taking place demand a language for communication and a possibility for information storage that is very versatile.

1.1.1.1 The Role of Carbohydrates and the Glycocalyx

In the machinery of the human body, three major classes of biopolymers are responsible for information storage and processing, namely nucleic acids, proteins, polysaccharides and combinations thereof. The chemical story of saccharides began with pioneering studies by Fischer in the late 19th century.[1] Fischer first revealed monosaccharide structure and stereochemistry and made the synthesis of glucose accessible. Thus, carbohydrate chemistry developed alongside the field of organic chemistry. Later the finding of complex oligosaccharides and polysaccharides from natural sources expanded the focus of carbohydrates from their synthesis to their biological roles.[1] However, carbohydrates were still not considered to play an important role in biological communication processes. In fact, up until fifty years ago, carbohydrates were still predominantly thought to only play significant roles in energy supply and structural components as, for example, cellulose in plants and chitin in insects and crabs.[2] Around the same time first studies revealed that cells display a dense carbohydrate coating. Bennett proposed the term glycocalyx to generally describe this sugar coat, and he wondered whether this coating is present on all cells and whether it is a common feature of cells.[3] Today, most of his questions have been answered and it is well understood that the glycocalyx is a common feature of all cells in living organisms and plays an important role in many important biological signal transduction processes like inflammatory and immune response, fertilization and the adhesion of pathogens.[4]

The carbohydrate structures of the glycocalyx include oligo- and polysaccharides attached to proteins and lipids to form glycoconjugates (Figure 2).[5] Glycoproteins are generated in the endoplasmic reticulum (ER) and Golgi apparatus by stepwise assembly of oligosaccharides to specific amino acid residues of asparagine (Asn), serine (Ser) or threonine (Thr).[6] Thereby, two different glycosylation pathways can be distinguished, N- and O-glycosylation.

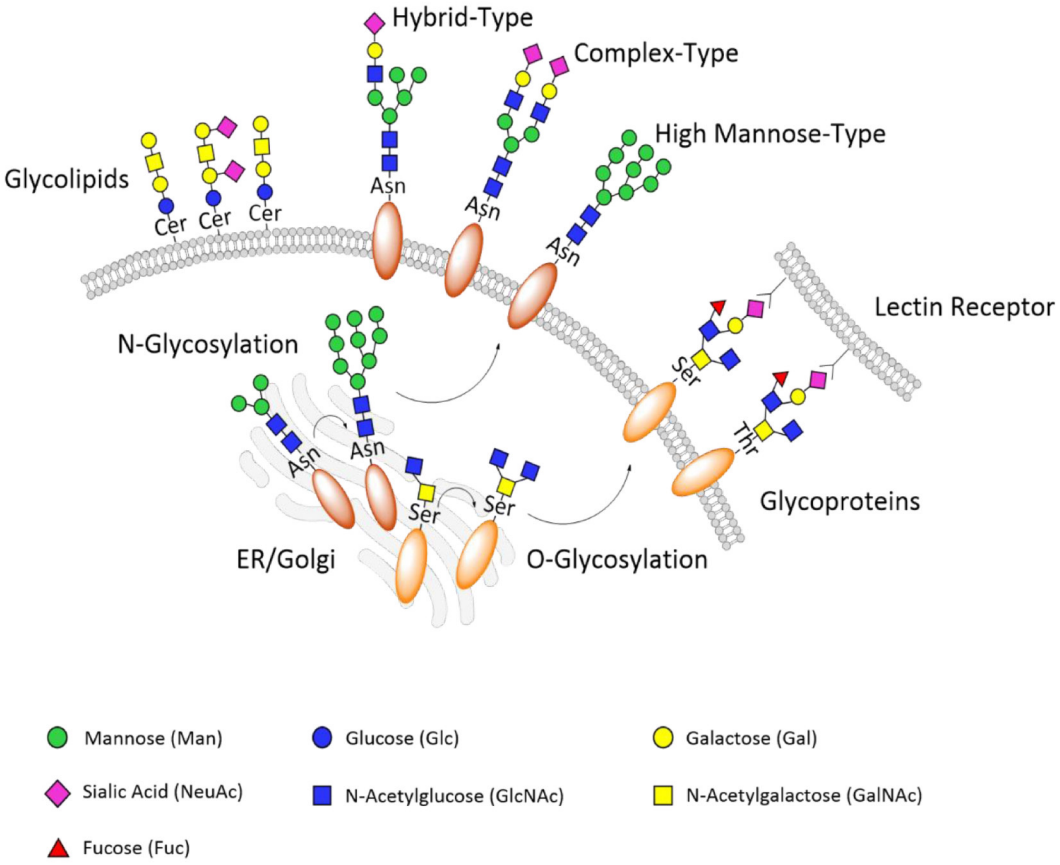

Figure 2: Schematic representation of the cell surface presented as cross-section through the membrane. The different glycosylation pathways within the cell are also schematically outlined (Adapted from [6]. Reprinted with permission from AAAS).

The *N*-linked glycosylation pathway is a co-translational process provoked by the amino acid sequence Asn-X-Ser/Thr. In this pathway, a trimannosyl core is attached to the amine group of the asparagine amino acid side chain.[7] This core structure is then modified by different glycosidases and glycosyl transferases.[7] Depending on the sugar residues added to the trimannosyl core and the final structure obtained, *N*-linked carbohydrate chains are classified into three groups, the complex-, high mannose- and hyprid-type .[8] The complex type constitutes the first group in which only non-mannose based carbohydrate ligands are added to the trimannosyl core. The high mannose type is the second group in which only α-mannose residues are added to the trimannosyl core. The hybrid type constitutes the third group and combines characteristics of both, complex- and high mannose type (Figure 2).[8] The O-linked glycosylation pathway is a posttranslational process. In this case, monosaccharides, typically starting with *N*-acetylgalactosamine, are enzymatically attached to the oxygen of the amino acid side chains of serine or threonine of the glycosylation sequon (Figure 2).[7] In the other component of the glycocalyx, the glycolipids, the monosaccharides galactose, glucose and N-acetylgalactoseamine are linked to ceramide (Figure 2).[9]

The role of glycosylation still is under debate. It is presumed that the major function of carbohydrate structures on the cell surface is to serve as recognition marker, e.g. for cell communication or pathogen adhesion, but it is also suggested that carbohydrates alter protein folding and stability.[6, 10] In order to be able to investigate their functions in detail, access to structurally defined oligosaccharides and glycoconjugates is mandatory. However, while technological breakthroughs in automation of sequencing and synthesis of oligonucleotides and proteins have accelerated progress in these two fields, structure determination and controlled synthesis remains a much more challenging task in the field of oligo- and polysaccharides.[2,11,12,13] Only recently, chemical and enzymatic methods as well as automated synthesis were developed to access pure oligosaccharides.[14,15,16] The slow technological progress in the field of glycobiology in comparison to the pace of development in nucleic acid and protein research is linked to the much higher complexity of carbohydrate structures.[6] Amino acids and nucleic acids can only be linked to one another in a linear form so that sequence defines the amount of information stored in proteins and DNA.[8] In carbohydrates, however, not only the sequence but also the linkage position, configuration and heterocyclic ring size can be varied.[17] For example, when two monomeric building blocks of amino or nucleic acids are combined, only one chemical structure can result from this linkage. For carbohydrates, the different linking positions at the hydroxyl groups of the monosaccharide building blocks can already give four isomeric structures. Taking into account also two different anomeric configurations and the potential for furanose and pyranose ring forms, a theoretical 16 isomers can be produced.[8] Three different monosaccharides could theoretically form more than 100 trisaccharides.[17] These two examples demonstrate the potential of a small number of monosaccharide building blocks to form many different carbohydrate structures.

On the one hand, this complexity has slowed down progress in carbohydrate research but on the other hand it can at the same time be seen as very diverse source of information.[47] In the beginning of this chapter the question was asked about which language could be versatile and eloquent enough to control the machineries of the human body. Of course, there are different communication pathways, but as Karlsson nicely describes the complexity of carbohydrate structures presents a rich language uncomparable in its potential range of expression.[17] This eloquent language makes specific communication possible. With carbohydrates presenting such a versatile language there must be a communication partner that can understand and transform it into action if necessary. These communication partners are called lectins.

1.1.1.2 The Role of Lectins

Lectins are defined as carbohydrate binding proteins other than immunoglobulins that do not show enzymatic activity against bound carbohydrates.[9] The history of lectins started in 1853 with the

discovery of the first mammalian lectin when Charcot and later Leyden discovered crystals in the sputum of asthma patients. The so-called Charcot-Leyden crystals were later identified as Galectin-10.[9,18] With this discovery they set the starting point of lectin history, but Charcot and Leyden were not aware of the fact that they paved the way to a whole new research area. Only a few years later Mitchell demonstrated the first example of lectin activity when he observed the agglutination of erythrocytes by rattlesnake venom.[19,20,21] The first identification of a plant protein demonstrating a similar agglutination behavior followed in 1888 by Stillmark.[19,22,23] These first indications of a new protein activity for the agglutination of red blood cells resulted in the first name for this new class of proteins which were referred to as hemagglutinins.[22]

In the following century, several major discoveries allowed for a new era of lectin research to develop. This era began with the isolation of the first pure plant lectin *Concanavalin A* (ConA) from the Jack Bean (*Canavalia ensiformis*) in crystalline form by Sumner in 1919. [24] A few years later he and Howell showed that ConA not only agglutinated erythrocytes and yeast but also formed insoluble complexes with glycogen. In addition, Sumner and Howell investigated the inhibition of this hemagglutination process using sucrose demonstrating the correlation of lectin activity and carbohydrates for the first time.[25] In the following years hemagglutinins played a major role in studies focused on blood group specificity which led Boyd and Shapleigh to rename this class of proteins with the term lectins originating from the Latin word legere which means “to choose”.[26,27] In the 1960s two discoveries by Nowell and Aub revealed the involvement of lectins in the mitogenic activity of lymphocytes and their preferred agglutination of malignant cells over healthy cells.[28,29,30] These findings led to the conclusion that lectins bind to carbohydrates on the lymphocyte cell surface transmitting the signal for mitosis and that cell surface carbohydrates can change depending on the different stages of disease. These two discoveries were the first evidence for the important roles lectins play in biological processes, and once again accelerated the pace of revelations in lectin research. In 1972 the last hurdle for a deeper insight into the molecular properties and activities of lectins was overcome by identifying the complete amino acid sequence and the first 3D structure of the plant lectin ConA by Edelmann *et al.* as well as Hardman and Ainsworth.[31,32] At this time many plant lectins were available, but the isolation of the first mammalian lectin by Stockert *et al.* paved the way for the purification and study of many animal lectins throughout the 1980s.[22,33] With the knowledge of the amino acid sequence of a multitude of lectins Drickamer succeeded in identifying a conserved carbohydrate recognition domain (CRD).[34] From then on it was possible to divide the lectins found in many different kinds of living organisms from bacteria through viruses and plants to animals and humans into families and superfamilies based on their sequence homologies.[16,36]

Plant Lectins

The major family in plant lectins is the legume lectin family with ConA as prime example (Figure 3).[19] ConA, which is found in high abundance in jack bean, was the first isolated and characterized lectin in sequence and 3D structure.[19,24,31,32] The finding that ConA preferentially agglutinated cancer cells over healthy cells further motivated researchers to study this lectin more intensively which made ConA a classical model lectin for today´s research.[35] The structural features of legume lectins can be described using ConA as an example. In dependence of pH conditions ConA exists as dimer (pH < 6) or as tetramer (neutral pH).[31] In legume lectins the polypeptide chain of the subunits is arranged in β-strands that in turn are connected by loops forming the so called "jellyroll" motif or legume lectin fold.[19,36] Each subunit is made up of about 250 amino acids with a total molecular weight of 26.5 kDa and typically contains one carbohydrate binding site. These carbohydrate binding sites are arranged in a tetrahedral orientation with a distance of 72 Å whereby a calcium^{2+} ion and a transition metal ion, manganese^{2+}, ensure the right conformation and orientation of the binding site amino acid side chains for effective carbohydrate binding.[37,38] This precise alignment of amino acid side chains in the carbohydrate binding site allows lectins to be specific for some carbohydrates while discriminating others. ConA, for example, binds specifically to α-D-mannose and with a lower binding affinity to α-D-glucose.[38] Even though the majority of plant lectins was identified before mammalian lectins, their physiological role is still basis for discussion. However, it is generally believed that they play a major role in plant defense and nitrogen fixing.[39,40]

Mammalian Lectins

Animal lectins can be divided into C-, S-, P- and I-type lectins and additional classes of pentraxines, calreticulin and calnexin as well as ERGIC-53 and VIP-36.[9] Besides these classes several proteins are known that show lectin function but are structurally assigned to other protein families, so called "orphan lectins".[9] Among all these groups, C-type lectins constitute the largest and most versatile class of animal lectins. The categorization of C-type lectins is based on their carbohydrate binding site with a common sequence of 120 amino acids whereby 31 are invariant.[41] C-type lectin polypeptide chains are arranged in a six-stranded antiparallel β-sheet sandwich enclosed by two α-helices.[37] Similar to the legume lectin family, calcium^{2+} ions are involved in binding. For C-type lectins calcium ions not only have structural functions but also are actively involved in carbohydrate binding which has been shown to be calcium^{2+} concentration dependent.[10,36]

HIP/PAP (hepatocarcinoma-intestine-pancreas/pancreatitis-associated protein), also known as Reg 3A, is one example of a mammalian protein expressed in animals and humans that contains a C-type lectin like domain (Figure 3). HIP/PAP is a secreted plasma protein of a molecular weight of 16 kDa.[42] It belongs to a special group of C-type lectins, group VII, characterizing a C-type lectin like

domain that is linked to a short *N*-terminal peptide, also called free CRD lectin group.[43,44] The CRD is specific to β-lactose so that the protein is also known as „lactose binding protein".[42] The biological role of HIP/PAP is linked to many different diseases. For example, HIP/PAP is overexpressed in many different types of carcinoma such as hepatocellular carcinoma, colorectal cancer or pancreatic ductal adenocarcinoma.[42] As a result HIP/PAP can be used as receptor for specifically targeting cancer cells or for detection of specific types of carcinoma.[42]

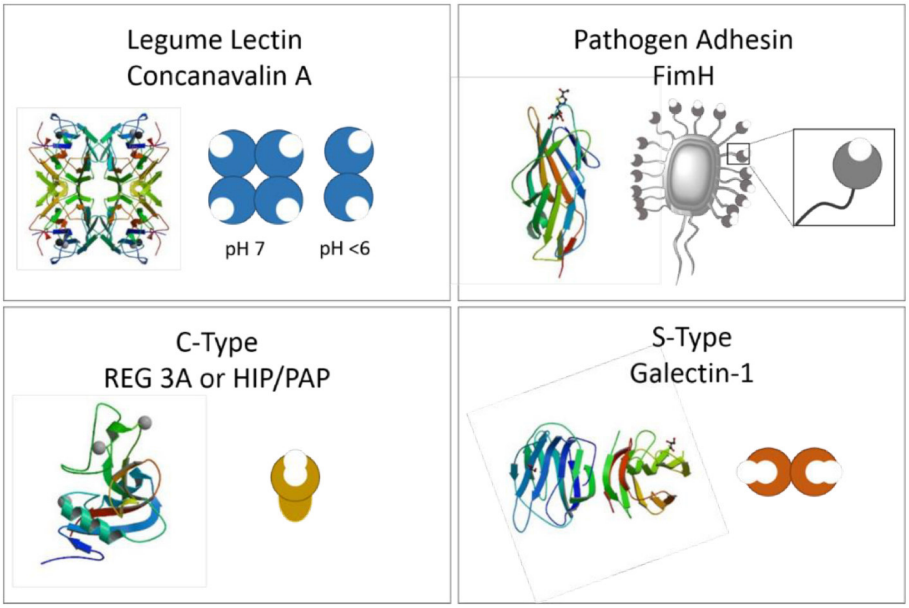

Figure 3: Examples of crystal structures and schematic representation of representatives of different legume lectin families (Protein Database codes: 1jbc, 3zl2, 4lbq, 4mth).

The second largest group of mammalian lectins is the S-type lectin family or Galectins. Galectins are also found in animals and humans. The name S-type lectins refers to the need for reducing conditions (S for thiol) to maintain their activity which was observed with the first identified S-type lectin, Galectin-1.[45] Later, however, it became clear that only a small number of S-type lectins shares this characteristic so that they are nowadays defined based on the criteria that they exhibit β-galactoside binding specificity as well as significant similarity in CRD sequence.[46] Their CRD is built up of 130 amino acids that determine carbohydrate binding specificity. Structurally, Galectins can be divided into three groups. Prototypical Galectins contain one CRD.[45] The second group, tandem-repeat-type Galectins, exhibit a single polypetide chain with two homologous CRDs. These two carbohydrate binding sites are connected by a linker of 70 amino acids. The third group, the Chimera-type, is represented by Galectin-3 whose CRD is linked to a nonlectin *N*-terminal region so that this Galectin is able to form pentamers by accumulation of the respective domains.[45] Galectin-1 belongs to the first group of prototypical Galectins (Figure 3). Even though this class of Galectins has only one CRD, Galectin-1 is bivalent in its carbohydrate binding activity because it is present as homodimer.[45] The same is true

for most other Galectins. They show either bivalent presentation because they exhibit two CRDs or form higher valent structures for carbohydrate recognition through other association processes. Galectins, are predominantly located in the intracellular cytoplasm or in the nucleus but can also be find as secreted membrane proteins.[9] Various biological roles have been assigned to the Galectin family. For example, they are involved in regulation of immune and inflammatory response and cancer progression.[46] Thus, this mammalian lectin family also displays a promising target in regard to cancer targeting or early cancer diagnosis.

Lectins from Pathogens

The adhesion of pathogens to the cell surface is a prerequisite for colonization and finally infection of the host cell. Thus, lectins from pathogens are characterized as adhesion molecules that are promoting the attachment to the host cell via carbohydrate lectin interactions.[47] One interesting example is the fimbrial adhesin FimH (Figure 3). This protein is involved in the infection of uropathogenic *Escherichia coli* (UPEC) by binding to carbohydrates on bladder cell surfaces leading to urinary tract infections.[48] FimH is located on the tip of type 1 fimbriae or pili, hair-like structures on the bacterial cell surface.[49] FimH contains one carbohydrate recognition domain specific for α-D-mannose.[50] The adhesion of bacteria to the cell surface via carbohydrate lectin interactions prior to infection provides an opportunity to develop new therapeutics blocking this interaction, especially against the background of increasing numbers of antibiotic resistance bacteria.[51,52] Therefore, carbohydrate based anti-adhesives that interfere with the adhesion of pathogens to the cell surface by completely blocking their binding sites is of increasing interest.[53] In order to be able to develop effective antiadhesives it is of great importance to understand mechanisms of carbohydrate lectin interactions in detail. In this way it should be possible to predict structure activity correlations and to design new therapeutics with optimized binding affinities.

1.1.2 Carbohydrate Lectin Interactions

The structural insights given by the amino acid sequencing and the solved 3D structures of lectins or carbohydrate lectin complexes has not only allowed for the classification of lectins into families, but has also aided in a better understanding of detailed binding events. As carbohydrate lectin interactions are involved in important biological communication processes, it was expected that their interaction would be strong and highly specific. However, it has become well known that the binding of individual monosaccharides to lectins is relatively weak with dissociation constants in the millimolar range. This low binding affinity is rationalized by the shape of the lectin binding sites, which are often shallow cavities and as such are solvent exposed and only make a few direct contacts to the ligand.[19]

1.1.2.1 Monovalent Carbohydrate Lectin Interactions and Energetic Effects

In monovalent carbohydrate lectin interactions, five distinct mechanisms play an important role which involve hydrogen bonding, hydrophobic interactions, metal ions, water and energetic effects.

Hydrogen Bonding

Carbohydrates display a high density of hydroxyl groups so that hydrogen bonding plays a major part in their recognition by lectins.[54] Hydrogen bonding can be divided into two classes: direct contacts to the protein and indirect hydrogen bonds that are mediated by water molecules.[55] Direct hydrogen bonding, especially cooperative binding where a carbohydrate hydroxyl group simultaneously acts as hydrogen-bond donor and –acceptor, is characteristic for carbohydrate lectin interactions (Figure 4).[56] Moreover, bidentate interactions of two neighbored hydroxyl groups with the same amino acid residue are favorable.[54] For example, one amino acidic side chain can function as hydrogen bond acceptor from two carbohydrate hydroxyl groups. Other amino acid functionalities that are involved in binding as hydrogen bond donor include main-chain or side-chain amide groups from asparagine or glutamine.[56]

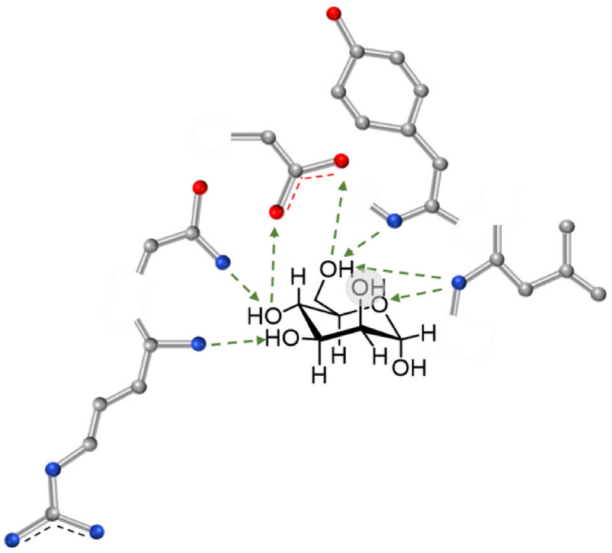

Figure 4: Schematic representation of mannose binding in the ConA binding site. Green arrows indicate hydrogen bonding. The hydroxyl group not involved in hydrogen bonding is highlighted with a grey circle (adapted from [57] with permission from Elsevier).

Carbohydrate functionalities that are involved in hydrogen bonding usually discriminate over specific recognition or discrimination of the respective carbohydrate while other functionalities that are not required as recognition element are solvent-exposed and form no direct contacts to the protein.[56] One perfect example confirming this observation is the carbohydrate binding specificity of ConA for both α-D-mannose and α-D-glucose. ConA forms hydrogen bonds with the 3-, 4- and 6-OH groups but

not with the 2-OH of the sugars in which mannose and glucose differ in their configuration (Figure 4).[19] In a similar manner lectins discriminate over anomeric specificity.[19]

Further contacts between the carbohydrate ligand and the protein are often mediated by water molecules. The advantage of water is that it is a small molecule that is able to act as both hydrogen bond donor and acceptor and as such can also function as a bridging molecule between the carbohydrate ligand and the protein binding site.[58] Comparison of structures of a free lectin and the corresponding lectin carbohydrate complex revealed that some water molecules remain in the binding site in the liganded as well as unliganded state.[56] These water molecules form hydrogen bonds to the carbohydrate that can be as strong as direct carbohydrate-protein contacts so that these water molecules are regarded as structural motifs of the protein binding site.[56]

Hydrophobic Interactions

Even though the majority of functional groups of a carbohydrate are hydrophilic in nature, the steric arrangement of these groups can create a local hydrophilic region on one side of the molecule (Figure 5).[59] As a result, a carbohydrate ligand usually displays a hydrophilic and a hydrophobic face, referred to as A- and B-face.[59]

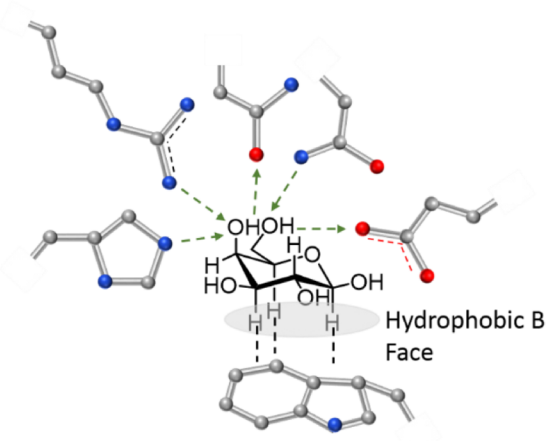

Figure 5: Schematic representation of galactose binding in the human Galectin-1 binding site. Green arrows indicate hydrogen bonding. The hydrophobic B face of galactose is highlighted with the grey oval. It is involved in C-H/π-interaction with the central tryptophan residue indicated by black dashed lines (adapted from [57] with permission from Elsevier).

The amphiphilic properties of some carbohydrate residues allow them to form nonpolar interactions with the protein. The arrangement of hydrogen bonds thereby supports the alignment of the hydrophobic face of the carbohydrate with hydrophobic amino acid side chains in or near the carbohydrate recognition domain (Figure 5).[54] The hydrophobic interactions involve van der Waals and π-π stacking interactions that both contribute to the stability and specificity of carbohydrate lectin complexes.[60] Aromatic amino acid side chains such as phenylalanine, tryptophan and tyrosine have

been observed to be involved in stacking interactions.[47] In case of hydrophobic interactions, binding affinity usually increases, but large aromatic residues can be used to partially discriminate for particular carbohydrate structures due to steric hindrance or by creating an unfavorable hydrophobic environment.[60] In accordance, it has been shown in literature that not only the carbohydrate but also additional aglycon units can influence lectin recognition activity.[19]

The Role of Metal Ions

As mentioned in Chapter 1.1.1.2, metal ions are crucial for the binding activity of some lectins whereby they can play an active or passive role in carbohydrate binding. In plant lectins, metal ions play a passive role but are nevertheless crucial for binding. The cations calcium^{2+} and manganese^{2+} or another divalent transition metal cation are coordinated near the binding site and support the right positioning of the amino acid residues interacting with the carbohydrate ligand.[61] The calcium^{2+} ion, for example, can be coordinated by a side-chain carbonyl oxygen of an asparagine residue that at the same time acts as hydrogen bond donor to the carbohydrate ligand via its side-chain -NH_2 functionality.[56] In a similar manner, one carboxylate oxygen of an acidic amino acid can be involved in hydrogen bonding to a bridging water molecule that is also coordinating a calcium^{2+} ion, while the second carboxylate oxygen is a hydrogen bond acceptor from the carbohydrate ligand.[56] On the other hand, the manganese^{2+} ion is not directly interacting with residues that are involved in carbohydrate binding but fixes the calcium^{2+} position.[56]

In bacterial and animal lectins many examples can be found where metal ions are directly involved in carbohydrate binding. The classical example are the C-type lectins that have gotten their name from their calcium ion dependent binding activity. In C-type lectins the calcium^{2+} ion forms direct coordination bonds with the carbohydrate ligand (Figure 6).[56] Two vicinal OH-groups thereby form a coordination bond with the divalent cation and simultaneously act as a hydrogen bond acceptor from a side-chain amide group and as hydrogen bond donor to an amino acid acidic oxygen (Figure 6).[56]

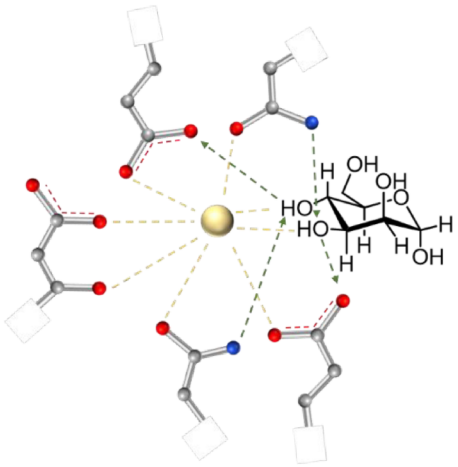

Figure 6: Schematic representation of mannose binding a C-type serum lectin and the involvement of the metal ion (yellow sphere) in carbohydrate binding. Green arrows represent hydrogen bonding and yellow dashed lines coordinative bonds (adapted from [57] with permission from Elsevier).

The Role of Water

Besides the role of water as mediator of hydrogen bond contacts, it also plays a crucial role in solvation. The release of solvation water to bulk water from both the carbohydrate ligand and the protein binding site is generally considered to have both entropic and enthalpic effects.[62] It has been argued that the solvation of the carbohydrate ligand and the protein binding site interferes with the low energy organization of bulk water.[62] Consequently the return of the higher energy solvation water to bulk should lead to a favorable enthalpy of binding.[63] When carbohydrate ligands of different hydrophobicity were tested for lectin binding in calorimetric studies, enthalpic-entropic compensation could be observed which is a common feature of lectin carbohydrate interactions.[54] This finding was rationalized by the increase of solvation water energy at hydrophobic surfaces whose release to bulk water is enthalpically favorable but entropically unfavorable due to water being disorderd at the surface but highly ordered in solution. In contrast, solvation water is highly ordered when interacting with the polar hydroxyl groups of a carbohydrate ligand so that the release to bulk water in this case is enthalpically unfavorable but entropically favorable.[54] As a result, the reorganization of water molecules upon carbohydrate lectin complexation plays a distinct role in the energetics of binding.

Energetic Effects

In addition to the role of water, also other effects contribute to the overall binding energetics of a carbohydrate lectin complex and the strong enthalpy-entropy compensatory behavior.[19] For a complete consideration of the energetic contributions, it is important to consider that the entropy of complexation is not only dependent on the entropy of solvation but also on other terms including the entropy of configuration, rotation and translation (Equation 1).

$$\Delta S = \Delta S_{solv} + \Delta S_{config} + \Delta S_{rot} + \Delta S_{trans} \quad (1)$$

When the carbohydrate ligand is approaching the lectin binding site, some amino acid side chains might move slightly in order to provide optimal orientation for hydrogen bonding and hydrophobic interactions. As a result, a flexible binding site would enhance hydrogen bonding and therefore the enthalpy of binding while simultaneously leading to entropic constraints based on the loss of degrees of freedom.[19] The same is true for the conformational flexibility of the carbohydrate ligand itself. To reduce loss in conformational entropy it has been suggested to use rigid carbohydrate analogs in order to obtain higher binding affinity.[54] At the same time this conformationally constrained compound must be able to perfectly fit into the binding site to prevent enthalpic costs due to a lower number of hydrogen bonds or hydrophobic interactions.[54] As a result, different energetic contributions can have a profound effect on carbohydrate lectin binding.

All in all, monovalent carbohydrate lectin interactions provide insight into how lectins can specifically bind to some carbohydrates while discriminating others. However, as mentioned above, the low affinity of these monovalent interactions would not meet the requirements for triggering many biological processes. Therefore, nature has installed multiple carbohydrate-lectin interactions leading to an overall increased avidity and specificity while maintaining reversibility of the binding process.

1.1.2.2 Multivalency

In multivalency, multiple ligands of one compound interact with multiple binding sites of one receptor. The advantage of multivalent binding is that the recognition event can be controlled by additional mechanisms other than the intrinsic affinity of a ligand to its receptor.[54] In case of tight binding, multiple copies of the ligand-receptor pair would also lead to tight binding causing a lack of specificity.[54] However, when monovalent binding is weak, a multivalent binding event helps to discriminate between structurally similar recognition elements leading to a highly selective binding process.[64] Moreover, multivalent interactions show unique kinetic characteristics. They show greater reversibility in the presence of competing ligands, and are more resistant to shear stress than single tight interactions.[54, 65] In addition, multivalent interactions provide the opportunity to adapt the nature of an interaction by varying the spacing or the orientation of the binding ligands without changing the recognition epitopes themselves.[66] Another interesting phenomenon in multivalent interactions, called the „cluster glycoside effect“, reveals that avidity is increased to a higher extent as would be expected for the sum of the individual monovalent interactions.[67] This increase in binding avidity is characterized by the enhancement factor β, the ratio of binding avidity constant for multivalent binding and the binding affinity constant for monovalent binding (Equation 2).

$$\beta = \frac{K_{multi}}{K_{mono}} \qquad (2)$$

This enhancement of affinity/avidity by multivalent interactions was first observed by Ashwell and coworkers.[68] They demonstrated that a 4-fold increase in carbohydrate presentation lead to a more than 10,000 fold increase in avidity to the corresponding lectin.[69] The question arises in which way this increase in avidity can be obtained. There are different mechanisms under discussion that show a potential for avidity enhancement involving chelation, receptor clustering, the „binding and sliding" mechanism, steric shielding and subsite association (Figure 7).

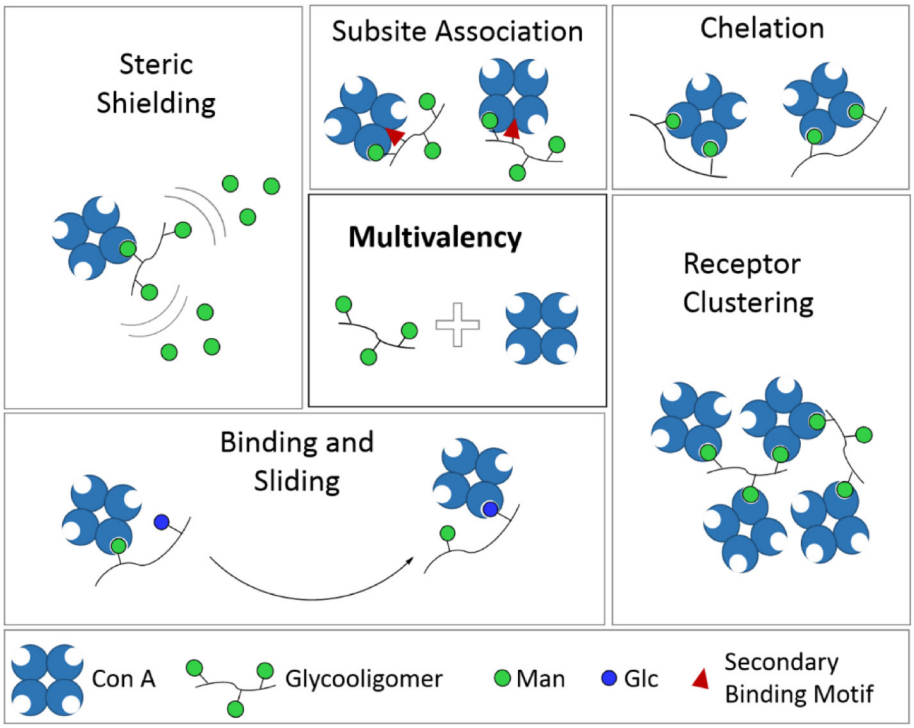

Figure 7: Multivalent binding modes discussed for enhancing multivalent binding avidity: chelation, receptor clustering, binding and sliding, steric shielding and subsite association.

Chelation

Chelation means that a multivalent ligand bridges at least two binding sites of a multivalent receptor (Figure 7). In inorganic chemistry chelation has long been known for increasing the affinity of a metal ligand complex.[70] The explanation for affinity enhancement was given as the gain in entropy which is based on the fact that complex formation in aqueous solution is accompanied by the substitution of water molecules of the hydration shell by the coordinating ligand.[70] When the ligand is monofunctional, the number of replaced water molecules and the number of new coordinating ligands is the same so that the number of freely movable particles in solution remains unchanged.[70] However, when the water molecules of the hydration shell are replaced by a multifunctional coordinating ligand, the number of water molecules that are then moving freely in solution is higher than the number of bound ligands which leads to an entropy gain.[70]

For a protein ligand complex the explanation for avidity gain in chelation is also based on the entropy of binding. When a ligand binds to a multivalent receptor with one binding epitope, binding of a second epitope to a second binding site of the receptor should be facilitated because translational entropy costs were already paid by the first binding event.[38,71] Thereby, the flexibility of the spacer linking the two binding epitopes and their orientation is of great importance because the gain in translational entropy is counterbalanced by the conformational entropy cost upon binding of the second binding epitope.[72] This counteracting effect of conformational entropy costs is, however, in some cases lower than expected.[67] This can be explained by the fact that the bound ligand might maintain parts of its flexibility or that the free ligand has access to less conformational states because it is partly restrained due to favorable intramolecular interactions or unfavorable interactions with the solvent.[67]

Receptor Clustering

In addition to chelation, multiple binding interactions by a multivalent ligand can also occur with several different receptors leading to the so called receptor clustering (Figure 7). This intermolecular binding event often leads to the formation of larger insoluble aggregates that precipitate from solution.[67]

"Binding and Sliding" Mechanism

The "binding and sliding" mechanism is based on statistical assumptions and is caused by the kinetic behavior of a multivalent ligand in comparison to a monovalent ligand.[38] For a multivalent ligand, the off-rate is much slower than for a monovalent ligand so that the close proximity of additional binding epitopes can easily lead to a replacement of binding epitopes within the binding site instead of complete detachment of the ligand (Figure 7).[38] The "binding and sliding" mechanism is also called a concentration effect because this replacement logically is more likely to happen when the local concentration of the binding epitopes is high which is true for a multivalent ligand.[54]

Steric Shielding

Steric shielding or steric stabilization is another mechanism by which multivalent ligands could show enhanced binding avidity. The idea behind avidity enhancement in this case is based on the fact that a multivalent ligand not only exhibits more than one binding epitope but is also often larger in size and volume than a monovalent ligand.[67] As a result, binding of this large sterically demanding species could prevent the approach of another potential binding partner to the binding site of the protein (Figure 7).[67] This mechanism of multivalent binding enhancement is specifically interesting in regard to inhibition of bacterial or viral approach to the cell surface.[73]

Subsite Association

In addition to the primary carbohydrate binding site lectins can bind multivalent ligands with increased avidity due to interactions of the ligand with further amino acid residues near or outside the recognition domain or with a secondary binding site (Figure 7).[54]

Although these mechanisms contribute to avidity enhancement in multivalent binding, it is still not completely understood which individual binding modes take place, and whether they occur at the same time or whether some binding mechanisms are preferred. As a result, multivalent synthetic carbohydrate analogs, so called glycomimetics, have been developed as a tool for unraveling the details of carbohydrate lectin interactions. Glycomimetics are further intended to be used as possible carbohydrate based antiadhesives in the design of therapeutics.

1.1.2.3 Artificial Scaffolds for Multivalent Carbohydrate Presentation

A glycomimetic is a simplified structure of the natural carbohydrate ligand. This means that in the design of a glycomimetic, complexity is reduced by focusing on the minimal carbohydrate structures required for binding.[74] These carbohydrate structures can be attached to a non-carbohydrate synthetic scaffold in an optimized fashion.[74] In order to find this optimized way of carbohydrate presentation, different aspects must be taken into consideration when designing a glycomimetic. In the case where a glycomimetic should be tested as competitive inhibitor against a pathogen, the design should be focused on combining high affinity/avidity together with good selectivity in order to provide specific blocking of the lectin binding site.[47] Moreover, the carbohydrate mimetic should be designed with the aim to make it more stable towards degradative enzymes, and to improve the bioavailability as well as reduce clearance rates from the body.[74]

In glycomimetic design, two different approaches can be followed, the ligand based approach and the receptor based approach (Figure 8). In the ligand based approach the natural ligand serves as the model so that the design is influenced by carbohydrate presentation in terms of valency, density and flexibility.[47] This approach is often difficult because detailed insights into the characteristics of the natural ligand are required. In the receptor based approach the lectin binding site serves as a model and is used to design a “best fit” glycomimetic structure.[47] For both approaches, similar synthetic concepts can be followed and the characteristics that can be adjusted are the number and type of carbohydrates, the arrangement of carbohydrate ligands, the linker between the synthetic scaffold and the carbohydrate moiety as well as the synthetic scaffold itself in order to find the best suited glycomimetic. One characteristic that is very important irrespective of the approach used, is that the glycomimetic system is precisely controlled in regard to sequence, size and carbohydrate functionalization. This is a prerequisite in order to be able to make detailed predictions about structure activity correlations.

With the knowledge about the interactions between carbohydrates and lectins, effects known to influence enthalpic or entropic contributions can additionally be taken into account for glycomimetic design. One strategy could be to introduce hydrophobic moieties in order to reduce the enthalpic costs for desolvation of polar groups or rather increase enthalpic gain by additional hydrophobic interactions with hydrophobic amino acid side chains at or near the binding site.[74] Another possibility could be to add an additional functional group. For example, when it is known that the carbohydrate ligand is coordinating a metal ion in the binding site, the respective hydroxyl group could be replaced by a better metal ligand in order to increase affinity.[74]

In designing a glycomimetic system, the starting point is always given by the synthetic scaffold employed. The scaffold determines the carbohydrate presentation and arrangement. So far, different synthetic scaffolds have been developed to present various carbohydrate valencies and topologies. A selection of examples is discussed in more detail in the following section.

Glycopolymers

Glycopolymers are a classical example of artificial scaffolds for multivalent carbohydrate presentation (Figure 8). There are two approaches for glycopolymer synthesis.[75] One is the polymerization of carbohydrate bearing monomers. The second is the post polymerization modification of the polymer backbone with carbohydrate moieties. For the first approach, classical radical polymerization was predominantly used for a long time. Radical polymerization has the advantage that it is very robust, that it does not always require high solvent and monomer purities, and that it is possible to use a variety of reaction conditions and monomer functionalities.[76] Moreover, initiators are commercial available at low cost. All in all, this makes radical polymerization a highly useful technique for glycopolymer synthesis.[67] However, disadvantages include the fact that heterogeneous compounds with high polydispersities and no control over terminal functionalities are obtained.[76] In addition, with the aimed application in aqueous systems or *in vivo*, the solubility and the toxicity of the polymer backbone must be also taken into consideration.[47]

In recent years also other polymerization techniques have been applied that allow for more control in regard to molecular weight and molecular weight distribution as well as sequence and end group functionality.[77] For example, controlled radical polymerization techniques like nitroxide-mediated radical polymerization (NMRP), atom transfer radical polymerization (ATRP) or reversible addition fragmentation chain transfer (RAFT) polymerization have been used for glycopolymer synthesis.[77] Another example is the ring-opening metathesis polymerization (ROMP) which is an attractive approach because it tolerates monomers with unprotected polar groups as well as water as solvent and allows for control over chain length and end group functionality.[75] Moreover, new approaches

for step-growth polymerizations, combined with specific protection strategies of the monomeric units, have been applied for sequence-controlled polymerizations.[78]

For the second approach of glycopolymer synthesis, the chemical conjugation of carbohydrate moieties to a preformed polymer scaffold, highly efficient organic click reactions like alkyne-azide, thiol-ene or active esters have been used.[77] This approach can be advantageous because it precludes complex multistep synthesis under special reaction conditions for carbohydrate monomers.[77] However, it is difficult to obtain full control over functionalization because some carbohydrates might not bind do the scaffold due to steric hindrance.

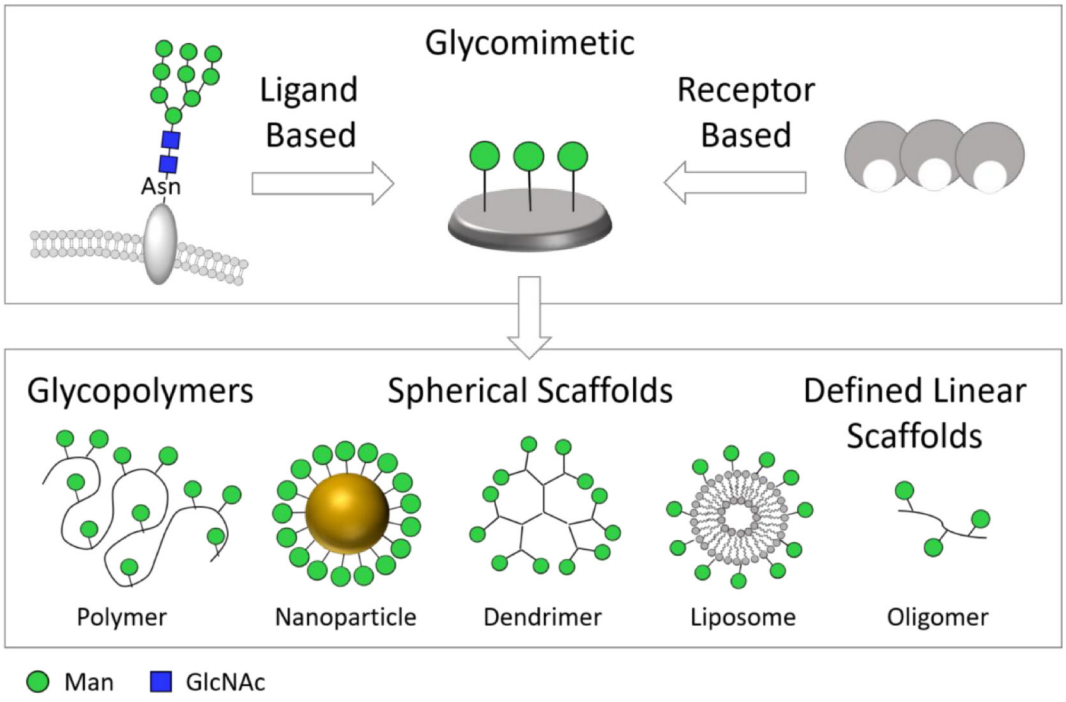

Figure 8: Ligand and receptor based approaches for glycomimetic design and schematic representatives for polymeric, spherical and defined glycomimetic scaffolds.

Spherical Scaffolds: Dendrimers, Nanoparticles and Liposomes

Natural oligosaccharides are often presented in a multiantennary fashion, which can be mimicked using spherical multivalent scaffolds such as dendrimers (Figure 8). Dendrimers are multibranched molecules with carbohydrate moieties displayed at the periphery of the dendritic arms in high symmetry.[67,75] Besides their tree-like structures, glycodendrimers have the advantage that they are monodisperse and very homogeneous while at the same time displaying a large number of binding epitopes.[67] The architectural features thereby can be customized by the choice of synthesis and scaffold used.[79] However, the rational design of a glycomimetic structure requires precise control of carbohydrate placement. This could be problematic for glycodendrimers of higher core size because then the exact spatial arrangement and flexibility of carbohydrate epitopes become difficult to

predict.[67] Moreover, the surface density might be a limiting factor in regard to size and generation level.[59]

Another example for spherically shaped synthetic scaffolds in the nanoscopic size range are nanoparticles (Figure 8). Nanoparticles also can display high numbers of carbohydrates on the nanoparticle surface.[47] Moreover, they display interesting electronic and spectrophotometric properties and have been shown to be very promising for displaying glycans against pathogen infection (for more details, see Chapter 3.2).[80]

Moreover, self-assembly systems provide a great opportunity for spherical and multivalent carbohydrate displays. One classical example are liposomes (Figure 8). They are noncovalent assemblies of lipids that form a hollow spherical shape of nearly homogeneous size.[79] Their aqueous core makes them very interesting as it gives them the potential as drug carrier agent.[54] The numbers of carbohydrates displayed on the liposome surface is controlled by using lipids that are carbohydrate functionalized and lipids that are non-functionalized. By varying the ratio of the two lipid forms carbohydrate presentation can be altered.[79] A disadvantage is that the single lipid components can diffuse two-dimensional within the liposome so that it is difficult to precisely predict the carbohydrate arrangement.[79]

Defined Linear Scaffolds

Another class of glycomimetics can be defined by structures that do not mimick the whole oligosaccharide composition, like glycopolymers, but are minimized structures only presenting a small number of carbohydrate epitopes.[54] Their shorter length often offers the advantage that they can be synthesized in a more controlled fashion to obtain homogenous structures.[59] Their synthesis is usually based on the conjugation of the carbohydrate moiety to a core scaffold and often involves combinatorial approaches that allow for easy customizing in regard to flexibility, valency, size and shape.[79]

One promising approach for the synthesis of an artificial defined scaffold for multivalent carbohydrate presentation is solid phase synthesis because it is a combinatorial approach that allows for high control over sequence, scaffold characteristics and positioning of functionalities.

1.2 Solid Phase Synthesis

1.2.1 Merrifield´s Vision

The idea of solid phase synthesis (SPS) evolved with Merrifield´s vision of finding a much more effective and faster way of peptide synthesis. The standard method for peptide synthesis at the time, as

introduced by Fischer and his students, was time consuming, difficult and limited in regard to the size and complexity of the peptide.[81,82,83] However, they had already established the general chemical requirements for peptide synthesis which also met the requirements for solid phase peptide synthesis (SPPS). These included the temporal blocking of the amine group as well as activation of the carboxy group for forming the peptide bond.[81,82] Based on this knowledge, Merrifield created his idea of SPPS in which the assembly of amino acids should proceed on a solid support in a stepwise manner.[84] This solid support is functionalized with a functional group X that enables the coupling of a first monomer by the formation of a stable covalent linkage (Figure 9,Figure 10).[83] To prevent side reactions, the monomer unit is blocked at one end and at possible reactive side chain motifs. After being anchored to solid support, the protecting group at the monomer end must be removed and the second monomer unit can be added using suitable reaction conditions involving an activation reagent (Figure 10). Subsequently, all further monomer units can be assembled on solid support in analogy to the first two. Only when the desired monomer sequence is completed, the covalent linkage between the oligomer or polymer chain and the solid support is selectively cleaved and the desired product can be isolated.[83]

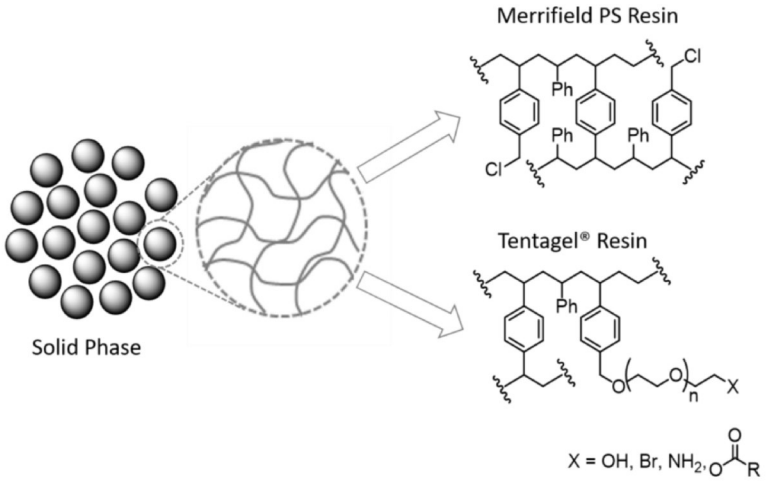

Figure 9: Schematic representation of the solid phase beads and different resin types, the Merrifield PS resin and the Tentagel® resin.

The Solid Support

In order to put his idea into action, Merrifield first needed to find a suitable solid support for the stepwise assembly of the amino acid monomeric units. The spherical beads that he obtained by crosslinking of styrene with 1% divinylbenzene in a suspension copolymerization were most promising (Figure 9).[83] This polystyrene (PS) resin showed good swelling behavior in suitable solvents like DCM assuring the accessibility of the functional groups on the resin as well as on the growing polypeptide chain.[85] However, when longer sequences or sequences of more hydrophobic amino acids were synthesized on the PS resin, these structures tended to aggregate on the hydrophobic solid support so that accessibility of functional groups was no longer guaranteed leading to deletion sequences.[83] In order to overcome this challenge, other solid supports have been tested. Among them Tentagel® resins

show interesting and promising properties (Figure 9). In addition to PS resins, polyethylene glycol (PEG) chains are grafted to the resin not only leading to more hydrophilic properties but also higher flexibility of the grafted chains on the resin.[85]

The Linker

In his original approach Merrifield used a chloromethyl group as linker to form a benzyl ester between the growing peptide chain and the solid support (Figure 9,Figure 10).[83] Cleavage was performed with hydrofluoric acid. Today many other linkages are employed that use different cleavage conditions that are more compatable to functional groups in the growing peptide chain. Moreover, they can be chosen in dependence of the functional end group desired after final cleavage.[85] One example is the chlorotrityl linker that allows for mild acidic cleavage conditions (about 1% trifluoracetic acid (TFA) in DCM) and produces an acid end group after cleavage (Figure 10). Another example is the rink-amide linker that also is acid labile and can be cleaved with 50 to 95% TFA in DCM resulting in an amide end group (Figure 10).

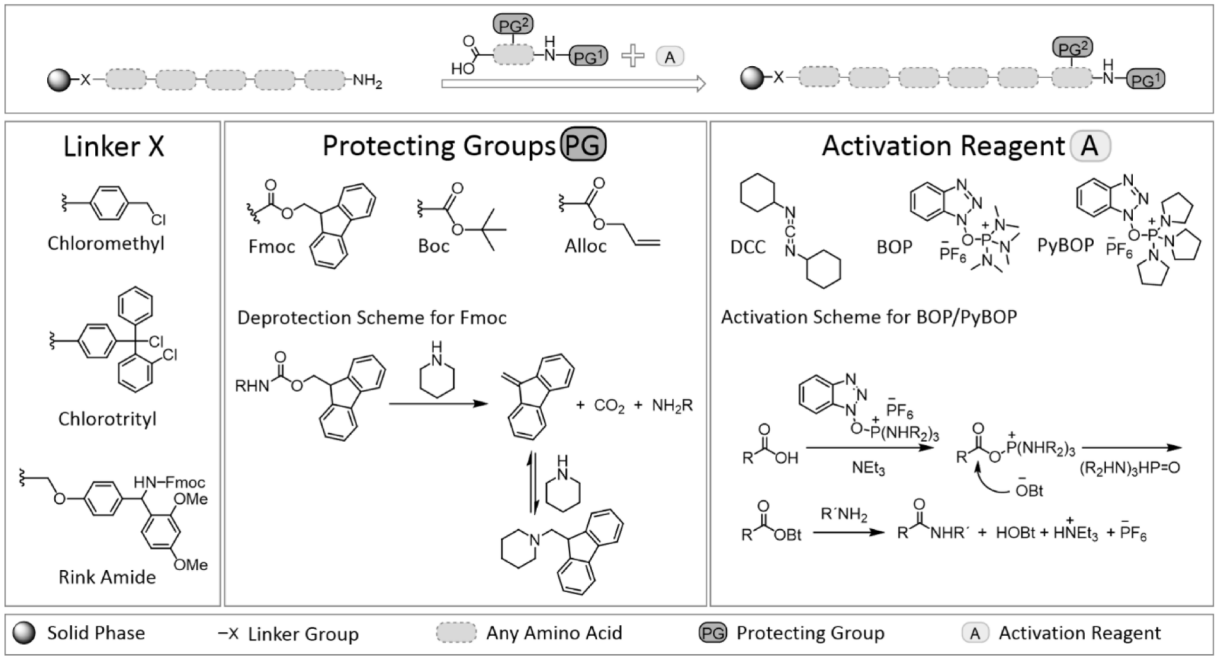

Figure 10: Schematic illustration of the principle of solid phase peptide synthesis (SPPS) together with exemplary illustrations of the linker group, protecting groups and activation reagents. The deprotection scheme for Fmoc and the activation scheme for BOP/PyBOP is also shown.

End- and Side-chain Protecting Groups

At the beginning of SPPS Merrifield employed a tert-butyloxycarbonyl (Boc) group to block amino acids at their amine end group. As side chain protecting groups mainly benzyl-based derivatives were used.[83] These two different protection strategies provided for the development of deprotection strategies to distinguish between deprotection of side chain and main chain functionalities.[83] This

orthogonality of protecting groups is a strategy still utilized today. The most commonly used protecting group for the terminal amine is the 9-fluorenylmethoxycarbonyl (Fmoc) protecting group used in so called standard Fmoc coupling protocols.[86] Advantages of this protecting group are that it is base labile and as such orthogonal to the acidic conditions used for most resin cleavages. Moreover, deprotection efficiency can be easily monitored using UV absorption or fluorescence spectroscopy to detect the dibenzofulvene chromophore formed after deprotection (Figure 10).[86] The piperidine used in a 25 vol% solution in DMF not only serves as base but also forms an adduct with dibenzofulvene (DBF) which prevents its polymerization (Figure 10).

For side chain protection Boc and allyloxycarbonyl (Alloc) groups are commonly used because these side chain groups remain inert throughout chain elongation and can easily be cleaved when desired (Figure 10). The Boc group can either be cleaved simultaneously with the final resin cleavage under strong acidic conditions or can be cleaved with milder conditions employing 4M HCl in dioxane which specifically cleaves the Boc group but leaves the bond to the resin linker untouched.[87] The Alloc group can only be cleaved individually employing a palladium(0) catalyst.[88,89]

The Activation Reagent

The last component needed for SPPS is the activation reagent which promotes amide bond formation. The activation reagent is crucial to activate the carboxyl functionality by introducing a leaving group to the acyl carbon facilitating the attack of the amine end group.[90] The carboxyl group thus is transformed into acyl halides, acyl azides, acyl imidazoles, anhydrides, esters and many more depending on the activation reagent used. Merrifield in his original approach used dicyclohexylcarbodiimide (DCC) which leads to the formation of an *O*-acylisourea mixed anhydride which can easily be attacked by the amine in the following step (Figure 10). The formation of an urea by-product is the driving force of the reaction.[90] However, disadvantages are that an unreactive *N*-acylurea can be formed by acetyl transfer and that racemisation can occur.[90] The acyl transfer can be suppressed by employing a nucleophile that reacts faster to this competing reaction but still leads to an intermediate active enough for amide bond formation.[90] Such a nucleophile was first employed in Castro´s reagent, the benzotriazol-1-yl-oxy-tris-(dimethylamino)-phosphonium hexafluorophosphate (BOP), an activated aromatic phosphonium ester of the nucleophilic hydroxyl benzotriazole (HOBt) component (Figure 10).[91] This oxonium salt reagent is used in combination with an additional base like triethyl-amine or Hünig´s base for activation in a one-pot coupling reaction. Thereby, the deprotonated carboxyl group reacts with BOP leading to the formation of an activated acyl-phosphonium species and HOBt. In the next step, HOBt attacks the activated carboxyl group to result in a reactive Bt ester. This Bt ester then reacts with the amine group to form the final amide bond (Figure 10). The driving force of the reaction is the formation of the phosphonium oxide species. However, in the case of Castro´s reagent,

hexamethylphosphoric triamide (HMPA) is extremely toxic. To reduce the toxicity of the reaction other phosphonium salt based activation reagents that form less problematic side-products have been introduced. One of the most employed examples is the benzotriazol-1-yl-oxy-tris-pyrrolidinophosphonium hexafluorophosphate (PyBOP®) (Figure 10).

In this way, small peptide chains can easily be generated by SPPS. However, the synthesis can be problematic for longer or more hydrophobic sequences with deletion sequences occurring more frequently. As mentioned above, incomplete conversions are typically caused by insufficient diffusion or swelling combined with aggregation phenomena leading to the reduced accessibility of functional groups on solid support. Besides these disadvantages, SPPS also combines many benefits. In comparison to multistep reactions in solution phase, in SPPS purification is not required after every step but it is instead replaced by simple, fast washing and filtration processes of the solid support in order to remove excess reagents. This, at the same time, increases the product yield by reducing loss due to purification and isolation of intermediate products.[83] Thus, SPPS not only simplifies and accelerates multistep processes but also makes them more efficient.[83] Another important advantage is the possibility to automate the SPPS process using commercially available peptide synthesizer.

After Merrifield´s pioneering work in SPS in the field of peptide synthesis, it quickly became clear that this advantageous method can be expanded to other multistep reactions with other monomeric units like nucleotides and saccharides.[92,93] The principle of SPS can even be expanded to more general monomeric units that are bifunctional and selectively blocked at one end while activated at the other. Hartmann *et al.* used the SPS principle to derive a new class of olgoamides establishing the so called solid phase polymer synthesis (SPPoS).[94]

1.2.2 Solid Phase Polymer Synthesis (SPPoS)

The idea of solid phase polymer synthesis (SPPoS) originated from the classical Merrifield SPPS method. The aim was to obtain sequence-defined and monodisperse poly(amidoamine) (PAA) segments. This was achieved by employing alternating condensation reactions of dicarboxylates and diamines on solid support instead of the repeatedly coupling of *N*-protected α-amino acids.[94] This method, developed by Hartmann *et al.*, was fast expanded to a second SPPoS method with artificial bifunctional building blocks as monomeric units allowing for more diverse PAA segments also enabling subsequent carbohydrate conjugation.[95] In this way the synthesis of sequence-defined and mono-disperse glyco-polymer segments, so-called precision glycomacromolecules, was accessible. These glycomimetic compounds could in turn be used to investigate different factors influencing multivalent binding avidity in a highly systematic manner.[95]

The artificial building blocks employed in SPPoS in general have to exhibit two important chemical functionalities for their use in standard Fmoc coupling protocols: A carboxyl functional group at one end and a protected amine functionality on the other end. To make their use in SPPoS feasible they need to be easily synthesized in an inexpensive fashion because of the large excess used in SPPoS to drive the single coupling steps to completion. In order to make the obtained precision glycomacromolecule exceptionally versatile, the Hartmann group has developed a library of different building blocks enabling precise positioning of the desired properties and functionalities by stepwise assembly on solid support.[95-103] This library can be divided into two groups of building blocks, functional building blocks and spacer building blocks (Figure 11). Functional building blocks have an additional functional group in their side chain that can, for example, be used for sugar attachment. Spacer building blocks are employed to adapt the positioning, number and spacing of the introduced sugar moieties.

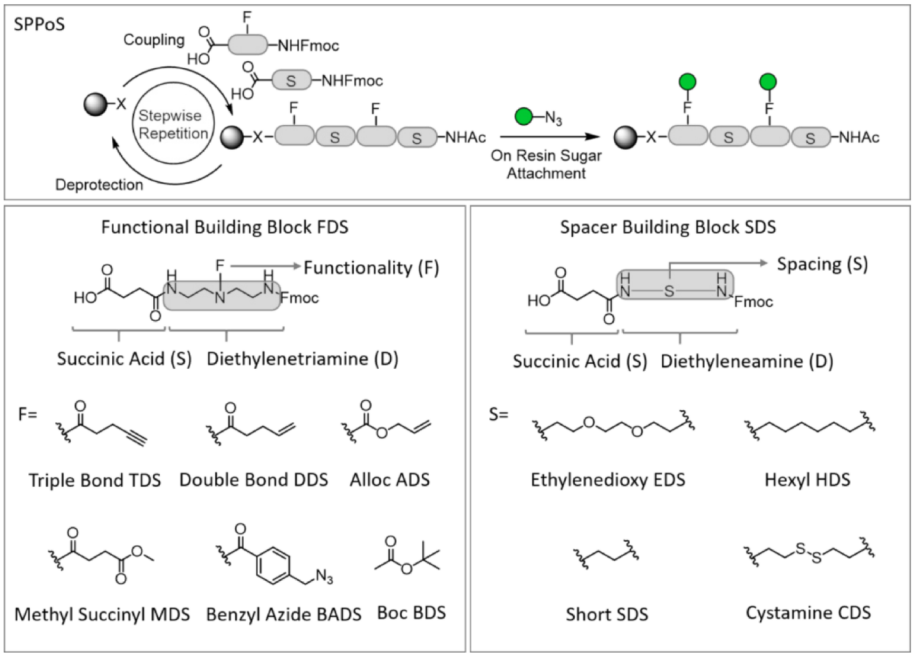

Figure 11: Overview of the solid phase polymer synthesis of precision glycomacromolecules. Exemplary structures for functional (left) and spacer (right) building blocks are listed below. For functional building blocks the structures for TDS[95], DDS[97], ADS[96], MDS[99], BADS[101] and BDS[96] are shown. For spacer building blocks the structures for EDS[95], HDS[104], SDS[104] and CDS[104] are shown.

One functional building block that is frequently employed in the Hartmann group is the TDS building block bearing an alkyne moiety in its functional side chain. This alkyne can be used for sugar attachment via a copper catalyzed azide alkyne cycloaddition (CuAAC) together with an azide-sugar derivative (Figure 11).[95] This reaction is a Cu(I)-catalyzed variant of the Huisgen´s [2+3]-cycloaddition and results in a 1,2,3-triazole as linking moiety between the sugar and the macromolecular backbone.[105,106] It is also often referred to as "click reaction". This term was first introduced by Sharpless *et al.* and defines reactions that only require mild conditions, simple workup and purification

steps with exceptionally high yield and selectivity.[107] Thus, this click reaction offers perfect conditions for its use on solid support.

Altogether SPPoS offers a versatile approach for the synthesis of glycomimetics. Due to high control over sequence and position of functionalities it gives the opportunity to systematically vary structural features of the precision glycomacromolecule obtained. Thus, synthesized precision glycomacromolecules are a great tool for investigating structure activity correlations of carbohydrate lectin binding.

2. Aims and Outline

Carbohydrates in form of glycoconjugates generate a sugar coat surrounding every cell surface. Together with special recognition proteins, termed lectins, they are involved in many important biological signal transduction processes such as fertilization and the immune response.[5] They also play an important role in the adhesion of pathogens to their host cell and in migration and developmental stages of cancer cells.[4] For these reasons, researchers consider carbohydrate lectin interactions as a possible starting point for the development of new carbohydrate based therapeutics. In order to be able to design suitable and effective therapeutics, it is of great importance to understand the underlying mechanisms of carbohydrate lectin interactions in more detail. It is known that while monovalent interactions are involved in carbohydrate lectin binding, multivalent interactions are especially important leading to increased avidity and specificity.[54] However, the fundamental mechanisms involved in multivalent binding are highly complex and many open questions remain. Therefore, glycomimetics have been developed as a tool for unraveling the details of carbohydrate lectin interactions and to serve as potential new carbohydrate based therapeutics.

Recently, Hartmann *et al.* developed a new approach, the so-called solid phase polymer synthesis (SPPoS), for the synthesis of highly defined glycomimetic structures.[94,95] Their approach is based on the classic solid phase peptide synthesis as introduced by Merrifield.[83] Instead of using natural amino acids, artificial building blocks are used to build up a macromolecular scaffold to which carbohydrate structures can be attached in the side chain.[95] This approach allows for straightforward and controlled variation of different structural parameters, such as the structure and composition of the scaffold as well as the positioning of different carbohydrate functionalities.

The motivation of this work is to gain further insights into the effect of scaffold properties of the macromolecular glycomimetic on lectin binding. This is achieved by controlled variation of different structural features of the scaffold and the investigation of lectin binding in solution as well as with lectins presented on pathogens or cancer cells. Literature studies have already indicated that different parameters in regard to the design of the glycomimetic structure have an influence on lectin binding affinity.[66, 108 - 119] For example, it has been demonstarted that the flexibility and length of the spacer[98,108,111,112,118], the distance, density and linker properties of the carbohydrate units[66,109,113,116,119-121], the molecular weight[109,110] and the geometry, as well as the composition of the scaffold[114,115,117] affect the interaction with the lectin. Researchers have also found that hydrophobic residues in the anomeric position of carbohydrates can impact their binding. For example, anomeric substituents on mannose enhance the affinity to the model lectin ConA.[122-126] Moreover, many lectin classes show specific interactions to hydrophobic aglycon structures.[127,128] With this information and

together with the opportunities provided by SPPoS, the main objective of this work is to investigate the effect of changes in backbone characteristics with special focus on hydrophobic in comparison to hydrophilic properties. This task is addressed by different approaches (Figure 12).

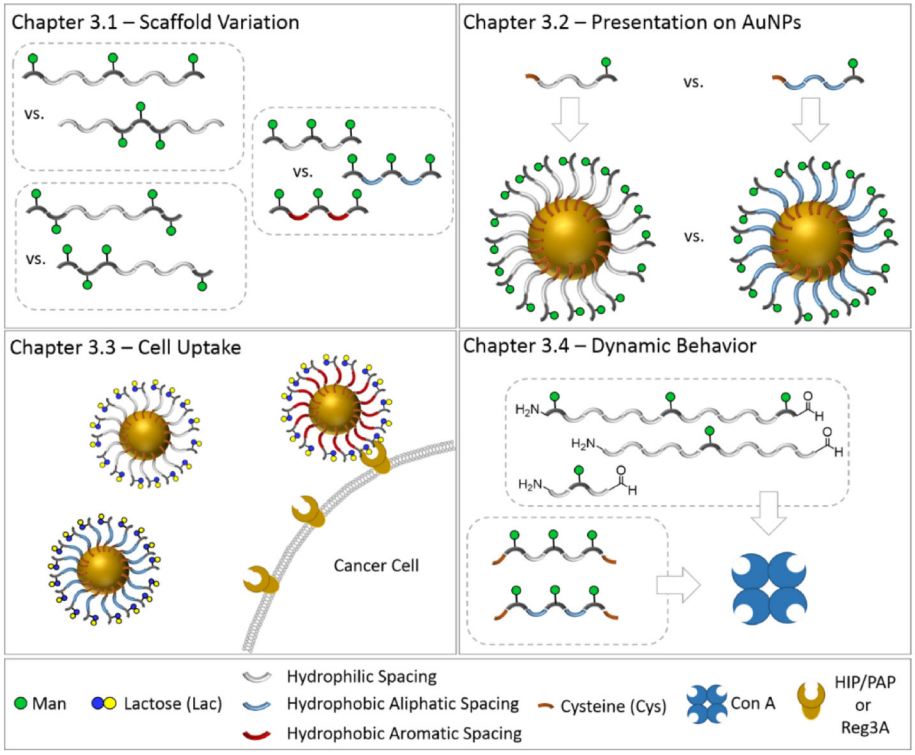

Figure 12: Overview of the four parts of the results and discussion section.

In the first part of this work a series of precision glycomacromolecules is synthesized by gradually changing backbone hydrophobicity as well as carbohydrate spacing, arrangement and number to provide a library of compounds for the systematic and comparative investigation of their ability to engage and bind the model lectin ConA. Binding studies using surface plasmon resonance (SPR) and isothermal titration calorimetry (ITC) are presented, in addition to an inhibition study with the bacterial lectin FimH. To further account for conformational properties of the glycomacromolecules, NMR and DLS measurements are carried out.

In the second part of this work the investigation of the effect of hydrophobic backbone characteristics is extended towards a higher level of multivalency by presenting precision glycomacromolecules on a macromolecular scaffold. This macromolecular scaffold is provided by gold nanoparticles (AuNPs) to which different thiol-functionalized precision glycomacromolecules are attached. Similarly, binding studies together with the model lectin ConA employing UV-Vis, DLS and SPR are carried out to quantify the effect of multivalent presentation as well as hydrophobic backbone characteristics.

This work provides proof of concept which is further extended to the synthesis of lactose-based analogues for targeting the HIP/PAP or Reg 3A protein on cancer cells in the third part of this work.

These compounds are studied using cell uptake and subcellular localization assays. This approach is particularly interesting because it provides insight into the applicability of the compounds *in vitro*.

In the final and fourth part of this work the approach for investigating the effect of backbone properties is reversed. In contrast to synthesizing various glycomacromolecules and subsequently testing for the best binder to the respective lectin, a dynamic selection of glycomacromolecule segments is used that in presence of Con A should under thermodynamic control result in the best binding ligand. Therefore, two different approaches for constructing dynamic covalent bonds are tested.

3. Results and Discussion

3.1 The Effect of Hydrophobicity and Spacing of Glycomacromolecules on Lectin Binding

3.1.1 Structural Parameters Influencing Ligand Receptor Binding of Glycomimetics

Carbohydrate lectin interactions are involved in central biological signal transduction processes, such as the adhesion and virulence of pathogens.[5,10] Various processes are believed to be involved in binding, but for the fundamental mechanisms underlying carbohydrate lectin interactions many questions remain unanswered.[47,79] This has motivated the development of multivalent synthetic glycomimetic systems as a tool for revealing the details of carbohydrate receptor interactions.[79] Thereby, different structural parameters of the glycomimetic compounds have been varied in order to provide detailed insights into the effects of these structural changes on lectin binding. The studies have the potential to provide fundamental insights that aid to design effective and high affinity compounds with the potential to serve as new therapeutics (Figure 13). Four parameters that have been identified to stongly influence lectin binding are: (i) the valency and (ii) architecture of the glycomimetic scaffold, as well as (iii) the spacing of carbohydrates along the scaffold, and (iv) the introduction of additional hydrophobic motifs.

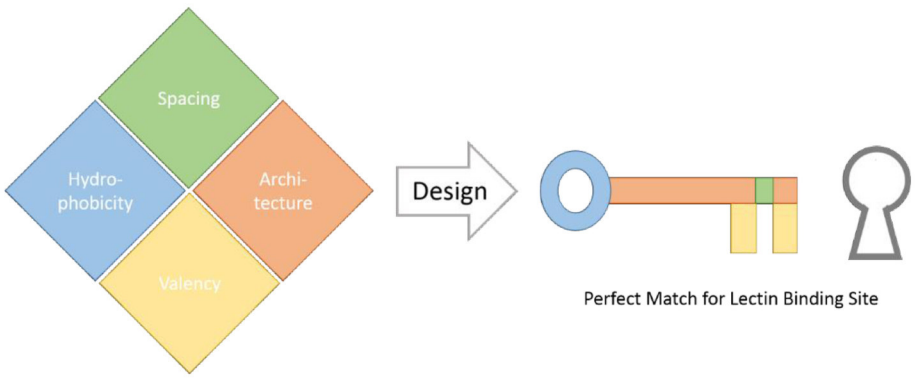

Figure 13: Schematic overview of glycomimetic design. By changing spacing, architecture, valency and hydrophobicity the perfect match for the lectin binding site is obtained.

Carbohydrate Valency

In the work group of Roy *et al.* it was shown that the sugar density of glycomimetics influences lectin binding.[129] In their study, multivalent dendrimers with increasing numbers of up to 16 mannopyranoside residues were synthesized. These structures were tested for their relative inhibitory potency in an enzyme-linked lectin assay (ELLA) with the model lectin ConA and methyl- and p-nitropheny α-D-

mannopyranosides as references. In accordance with known multivalency effect, it was found that the inhibitory potency of each compound tested increased with the number of carbohydrate ligands presented on the dendrimer structure, even when corrected for the number of mannopyranoside ligands.

Interestingly, in the work group of Kiessling *et al.* a contradictory effect was observed.[119] They synthesized neoglycopolymers by aqueous ring-opening metathesis polymerization (ROMP) and varied the carbohydrate density by employing repeating units with either one or two sugar ligands. In an inhibition assay for erythrocyte agglutination with ConA, they found that polymers with lower sugar density exhibited a higher inhibitory potency than polymers with higher density. They confirmed this finding in a second study using a series of synthetic polymers varying in their ligand binding epitope density.[66] Binding avidity was investigated by a clustering experiment with ConA. At first glance, polymers with a high binding epitope density resulted in faster clustering rates than polymers with lower binding epitope densities. However, the latter were more potent when compared on a binding epitope basis. These findings can be explained by the fact that with an increasing carbohydrate concentration, the amount of bound lectin together with the binding avidity increases in a similar fashion until a maximum point is reached. At this maximum the glycopolymer becomes saturated and no further lectin can be bound. Thus, a further increase in carbohydrate density only leads to excess ligands with no binding effect. The same trend was confirmed by systematic studies in the Hartmann group. When smaller glycomacromolecular structures varying in their carbohydrate valency are compared, a clear trend of higher binding affinity with increasing carbohydrate number can be observed.[95] If, however, structures of a much higher carbohydrate valency with up to 20 mannopyranoside units are employed, the multivalency effect clearly levels off when going to higher ligand numbers.[121]

Architecture

Another parameter influencing lectin binding was described by the work group of Kiessling *et al.* in 2002.[114] They synthesized 28 different compounds varying in their architecture. With these structures, the effect of architecture on the inhibition and clustering of ConA was investigated. They found that some architectures promoted inhibition while others mediated receptor clustering and concluded that the architecture of a glycomimetic structure is a key parameter determining its activity towards lectins. In the Hartmann group the important role of glycomimetic architecture in lectin binding was confirmed.[101] They investigated a small library of linear versus branched glycomacromolecules in a lectin binding assay towards ConA. A clear effect of branching on the binding kinetics of the compounds was observed.

Spacing and Molecular Weight

The character of spacing and the size of the glycomimetic compound has also been shown to influence lectin binding in literature. In a study of the working group of Fernández-García *et al.* the binding behavior of two different glycocopolymers towards ConA and *Ricinus communis* agglutinin was investigated.[117] They showed that the introduction of a flexible spacer enhances binding affinity. Another study by Kobayashi *et al.* confirmed this finding.[118] Again, flexible properties were advantageous for lectin binding leading to a highly specific interaction while rigid compounds showed little specificity.

In addition Stenzel *et al.* investigated ligand spacing in regard to the distance of carbohydrate ligands on star polymers.[109] They used different lectin binding assays with ConA and showed that longer spacing exhibited lower binding affinity than short spacing. They also found that the molecular weight of the glyco-starpolymers contributed to ConA binding. Similar observations were made by Fernández-García *et al.* who examined the binding behavior of different molecular weight glycopolymers towards ConA.[110] It was shown that the molecular weight has an influence on the aggregation behavior with ConA with the lower molecular weight polymer leading to less turbidity.

In the Hartmann group, the effect of systematic carbohydrate spacing was studied.[120] However, the effect of interligand distance on lectin binding could not clearly be determined so far. Changes in overall affinity with variations in carbohydrate spacing were observed, but these could not be assigned to a trend. One explanation might be that interligand distance was varied irrespective of changes in molecular weight. In order to complement these studies, in this work, SPPoS was employed as a tool to change interligand spacing while maintaining valency and overall molecular mass of the monodisperse and sequence defined precision glycomacromolecules. In this way, the influence of carbohydrate density independent of changes in molecular size can be systematically investigated. In addition, the overall carbohydrate arrangement can be changed from a symmetric to asymmetric orientation to determine in how far sugar distribution has an influence on carbohydrate receptor interactions (Figure 14).

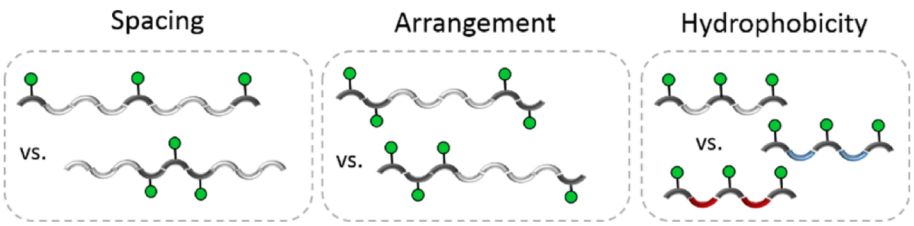

Figure 14: Overview of structural design features varied in the first part of this work: Carbohydrate Spacing with constant molecular weight (left), carbohydrate arrangement along the scaffold from symmetric to asymmetric (middle) and backbone hydrophobicity (right).

Hydrophobicity

In the early 1970s it was shown that hydrophobic residues at the anomeric position of α-D-mannopyranosides and even hydrophobic aglycon structures irrespective of a carbohydrate ligand led to an enhancement in binding affinity to ConA.[122,124,125] The same findings were subsequently made with other plant lectins.[123,128] It was further observed that the incorporation of hydrophobic moieties in the backbone and in linker position influence the binding of glycomimetic structures to lectins. In the work group of Fernández-García *et al.* the behavior of amphiphilic block glycopolymers with varying hydrophilic block length were investigated in their interaction with ConA.[117] The binding process was found to be favoured in the presence of the hydrophobic block, even when the glycopolymer with the smallest hydrophobic block was employed. In another study by Gibson *et al.* a secondary binding motif was introduced in the linker position of synthetic glycopolymers.[116] The gradual variation of this predominantly aromatic motif dramatically altered affinity as well as selectivity towards the two lectins CTx and PNA.

In the Hartmann group the change of the linker motif installed between the macromolecular backbone and the carbohydrate ligand was also systematically investigated.[120] It was shown that aglycon structures installed in the linker position lead to enhancement in lectin binding in dependence of their chemical composition with a preference for hydrophobic properties. However, variations in macromolecular backbone were not yet examined systematically. Therefore, in this work, special focus is directed to investigating the influence of hydrophobic backbone composition in carbohydrate lectin interactions in a systematic manner (Figure 14). As already mentioned in Chapter 1.1.2, a change in hydrophobicity is especially interesting because it addresses several phenomena of binding. On the one hand, hydrophobic moieties can be involved in monovalent carbohydrate lectin interactions when interacting with hydrophobic amino acid side chains near or inside the carbohydrate binding pocket, thereby leading to enhanced affinity by additional secondary interactions. On the other hand, hydrophobic moieties can also lead to favorable energetic effects due to the return of solvating water molecules to bulk water or due to a more rigid conformation in aqueous solution in order to reduce the contact of the hydrophobic components of the glycomimetic to the hydrophilic surrounding.

3.1.2 Solid Phase Polymer Synthesis of Glycomacromolecules

In this part of the thesis the influence of backbone hydrophobicity as well as scaffold composition in regard to carbohydrate spacing and arrangement on carbohydrate lectin interactions were systematically studied. Therefore, three series of precision glycomacromolecules were synthesized varying in (i) carbohydrate spacing while maintaining the overall molecular weight, (ii) carbohydrate arrangement and (iii) backbone hydrophobicity. In order to ensure complete control over these structural features, solid phase polymer synthesis (SPPoS) was employed as synthetic strategy. Thereby, changes in backbone hydrophobicity were achieved by the introduction of two different hydrophobic spacer building blocks. Subsequently, the three series of glycomacromolecules were tested in lectin binding studies with the model lectin ConA using isothermal titration calorimetry (ITC), surface plasmon resonance (SPR) and the bacterial lectin FimH in an inhibition experiment. In order to obtain additional information about the behaviour of the glycomacromolecules in solution NMR and DLS studies were performed.

3.1.2.1 Building Blocks for SPPoS

In SPPoS the monomeric units are comprised of artificial building blocks. For their application in solid phase synthesis and their use in standard Fmoc coupling protocols, these building blocks have to fulfill certain criteria. Most importantly, they have to be bifunctional with a carboxyl functionality at one end and an Fmoc protected amine on the other end of the molecule. Other prerequisites are solubility in DMF or NMP, which are used as standard solvents in SPS, and high purity to guarantee for similarly high purity of the final macromolecule after iterative couplings. Moreover, building blocks are employed in high excess in order to drive the coupling step to completion. Thus, their synthesis should be practicable and affordable on large scale. Based on these requirements, Hartmann *et al.* have developed a variety of building blocks suitable for SPPoS.[95-103] These building blocks can be divided into two groups, as was already discussed in Chapter 1.2.2.

In this part of the thesis, the functional building block TDS (triple bond - diethylenetriamine - succinic acid) was used for introduction of carbohydrate ligands.[95] This building block carries a triple bond in the side chain that can be used for on resin sugar attachment with an azide-sugar derivative in a Cu(I) catalyzed azide alkyne cycloaddition (CuAAC) (Figure 15). In order to address the carbohydrate binding sites on the model lectin ConA and the bacterial lectin FimH an α-D-mannose-azide derivative was employed.[130] Both lectins show high affinity to this carbohydrate. They do not bind β-D-galacto-pyranosides so that this azide-derivative was used for the synthesis of negative control structures (Figure 15). As spacer building block, the previously introduced EDS (ethylene glycol – diamine - succinic acid) spacer was used.[95] This spacer building block is based on an ethylene glycol unit and as

such comprises more hydrophilic properties (Figure 15). In addition, a more hydrophobic spacer building block based on *N*,*N*-diaminooctane, the so-called ODS (octyl – diamine - succinic acid) building block was employed to introduce more hydrophobic properties to the backbone. In comparison to EDS, the two oxygen atoms of the ethylene glycol unit are substituted by two methylene groups providing a higher hydrophobicity while maintaining the overall length of the spacer building block (Figure 15). In addition to aliphatic hydrophobic properties, hydrophobic aromatic properties were also desired. These were introduced to the macromolecular backbone via a commercially available spacer building block, 4-(Fmoc-aminomethyl)benzoic acid, termed AR for aromatic (Figure 15). Both building blocks, TDS and EDS, as well as the sugar azide were synthesized following established protocols.[95,100,131] The ODS building block was already established in the Hartmann group but final purification was optimized in this work.[100,132] All building blocks were obtained in moderate to high yields and purities of > 95% as confirmed by ^{1}H-NMR, ESI-MS and RP-HPLC analysis. With these building blocks in hand, hydrophobic backbone properties, as well as interligand spacing and arrangement could be easily varied by changing the number of EDS, ODS or AR spacers in between the sugar carrying TDS building blocks or by varying the number of TDS on each end of the macromolecule.

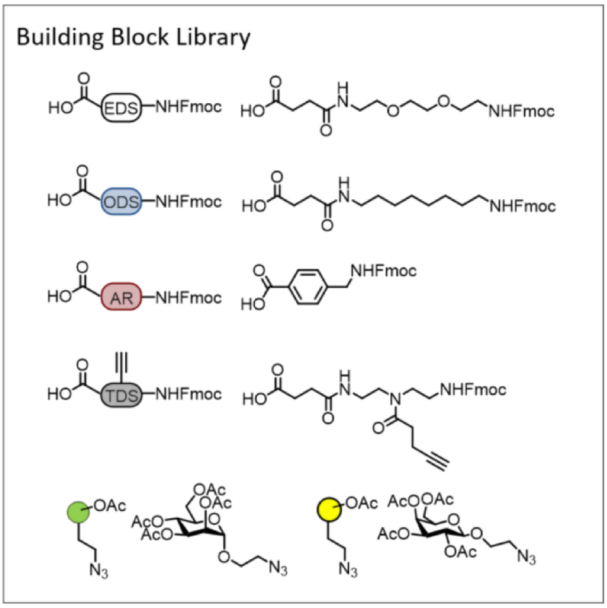

Figure 15: Overview of building blocks employed in SPPoS in this work.

3.1.1.2 Synthesis of Glycomacromolecules Changing in Scaffold Characteristics

The SPPoS of the three series of glycomacromolecules varying in (i) carbohydrate spacing while maintaining the overall molecular weight, (ii) carbohydrate arrangement and (iii) backbone hydrophobicity was based on the same overall solid phase procedure (Scheme 1). Differences in the final structures are introduced by a change in the number, sequence or type of building blocks employed. The SPPoS procedure thereby can be divided into two parts. First, the macromolecular

scaffold is build up on solid support in a stepwise manner. Second, the desired carbohydrate ligands are attached to the side chain of the scaffold via CuAAC reaction.

Here, commercially available Tentagel chlorotrityl resin was used after functionalization with an ethylenediamine (EDA) unit in linker position. This EDA-modification provides an amine end group after final cleavage of the macromolecular scaffold. The first step of the reaction involves swelling of the resin in DCM to expose all of the functional groups within the resin beads. After swelling, the first coupling step can be performed. Excess of the respective building block in the presence of diisopropylethylamine (DIPEA) as base and PyBOP as activation reagent were employed. The coupling step was followed by Fmoc deprotection, which was achieved by treating the resin with a solution of 25vol% piperidine in DMF (Scheme 1). These two steps were repeated until the desired sequence of building blocks was assembled on solid support. The stepwise construction of the macromolecular backbone was terminated by capping the free *N*-terminal site with acetic anhydride. Then, the second step of the procedure, the attachment of the carbohydrate to the side chain was performed. The triple bond of the TDS building block reacts with the azide group of the carbohydrate derivative in a CuAAC reaction forming a 1,2,3-triazole as connection between the carbohydrate and the backbone. This reaction was performed with protected carbohydrates that were subsequently deprotected on solid support using a solution of sodium methoxide in methanol (Scheme 1).

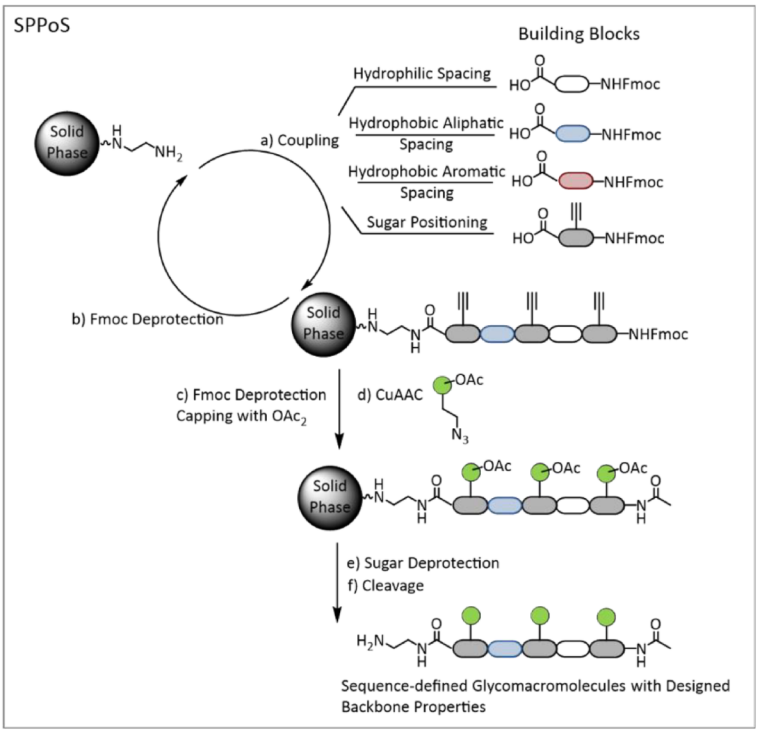

Scheme 1: SPPoS of precision glycomacromolecules varying in backbone composition and ligand distribution [adapted from [188] with permission from John Wiley and Sons].

In between coupling and deprotection steps, purification was achieved by washing the resin thoroughly with DMF. In case of the CuAAC reaction an additional washing solution of sodiumdiethydithiocarbamate in DMF/H_2O was used in order to completely remove copper from the reaction mixture. As last step, the product was cleaved from solid support employing a 30vol% solution of trifluoroacetic acid (TFA) in DCM. By precipitation in diethylether, subsequent centrifugation and lyophilization, the precision glycomacromolecule was isolated.

During cleavage glycomacromolecules were exposed to high TFA excess. This led to TFA residues that still could be found in isolated glycomacromolecules. Cationic structures could even be found as trifluoracetate salts. Before further studies with the glycomacromolecules could be performed, excess TFA was removed to prevent any influence of the acid on the behavior of the glycomacromolecules in lectin binding. For peptides it has been shown that TFA residues can be problematic leading to a change of the behavior of the peptide, modify its conformation or alter the accuracy of *in vivo* studies.[133-135] The excess of TFA in its acid form can be easily removed by classic freeze-drying evaporating the acid. However, the TF-acetate counter-ion is much more challenging to remove because it strongly interacts with the positive charges of the cationic glycomacromolecule. There are two alternative methods to remove the TF-acetate counter-ion. It can be removed by exposure to an excess of strong acid that reprotonates the TF-acetate into its free acid form. The free acid can subsequently be easily removed

by freeze drying. On the other hand, the TF-acetate anion can be replaced employing an anion exchange resin.

For the first method, which was inspired by the literature, the glycomacromolecule was dissolved in MilliQ water and 1M HCl was added to the solution to obtain a final concentration of 2-10 mM HCl.[136] This mixture was frozen with liquid nitrogen and freeze dried under continuous cooling and high vacuum. This procedure was repeated twice. Following the TFA signal by ^{19}F-NMR, the signal was significantly reduced when measured by NMR under the same conditions (Figure 16). This comparison in ^{19}F-NMR is not quantitative because no standard is added but the almost total disappearance of the signal can nevertheless be followed by this method (Figure 16).

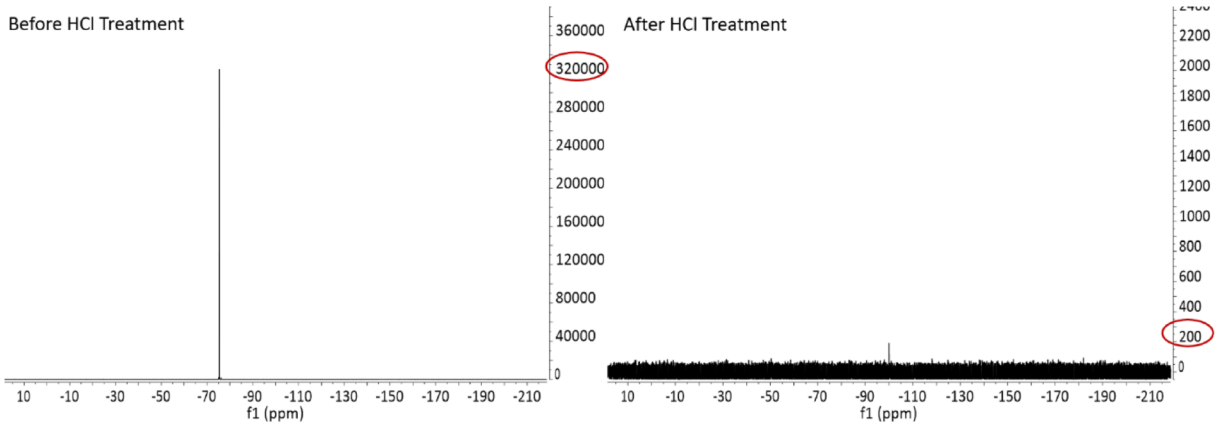

Figure 16: ^{19}F-NMR (300 MHz, D_2O) before (left) and after (right) HCl treatment and freeze drying in three cycles. The red circles highlight the signal reduction in the NMR spectrum.

As shown in Figure 16 removal of TF-acetate by HCl addition and thus exchange of the TF-acetate by chloride as counter ion worked. However, this method also has two major drawbacks: there is only a restrictive choice of counter ions (HCl, H_2SO_4, HF, HNO_3), and the very acidic solution can chemically damage the glycomacromolecule. Indeed, damage to the glycomacromolecule due to the strong acidic conditions could be followed by ^{1}H-NMR (Figure 17). The spectrum clearly shows the appearance of new signals after HCl treatment probably caused by impurities.

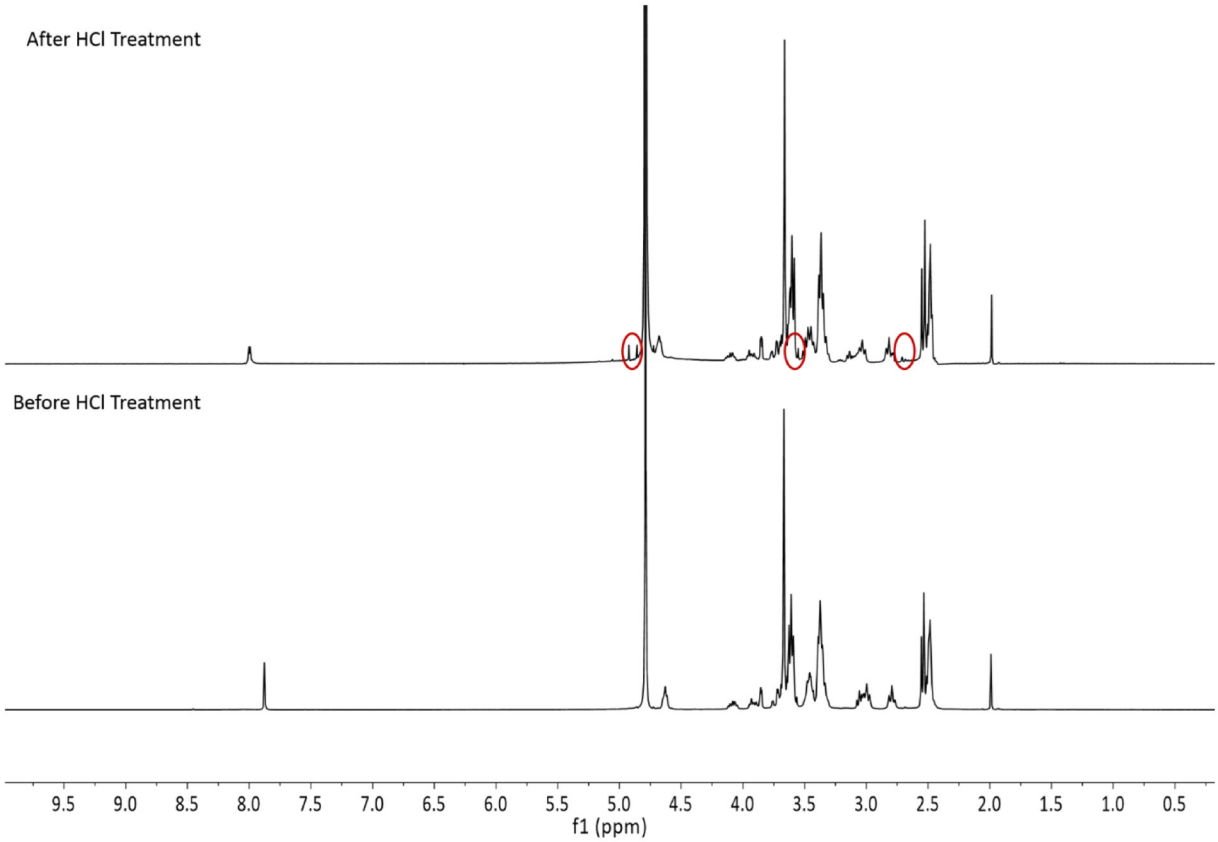

Figure 17: ^{1}H-NMR (300 MHz, D_2O) before (bottom) and after (top) HCl treatment. The red cycles highlight the impurities resulted from HCl treatment.

The feasibility of the second method was investigated following a procedure described in literature.[137] A strong anion exchange resin with acetate as counter ion was first activated with acetic acid, the glycomacromolecule was then dissolved in MilliQ water and added to the resin, and the mixture was shaken for 1 h. In this time TF-acetate counter ions were replaced by acetate ions loaded on the resin (Scheme 2). Then the procedure was repeated and the glycomacromolecule isolated by freeze drying.

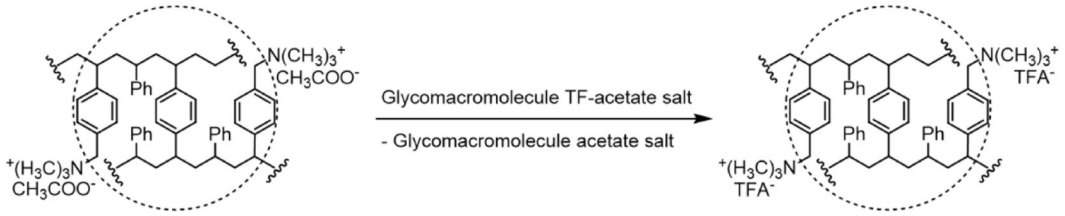

Scheme 2: Exchange of TF-acetate by acetate employing a strong anion exchange resin.

Following the ^{19}F-NMR signal of the TF-acetate gave similar results as for the first method with HCl treatment (Figure 16, Appendix 217). However, this method did not lead to the occurrence of impurities in ^{1}H-NMR analysis (Appendix 218). There was only one new peak at 1.92 ppm caused by the protons of the new acetate counter ion. As a result, the second procedure for TF-acetate removal with strong anion exchange resin was identified as the most suitable method for glycomacromolecule treatment.

Overall, three series of glycomacromolecules were synthesized (Figure 18). In the first series, four glycomacromolecules (**1**, **1a**, **1b**, **1c**) were synthesized having the same overall length of the backbone (nine building blocks) as well as valency (three mannopyranoside residues) but differed in the positioning of mannopyranoside ligands along the scaffold.

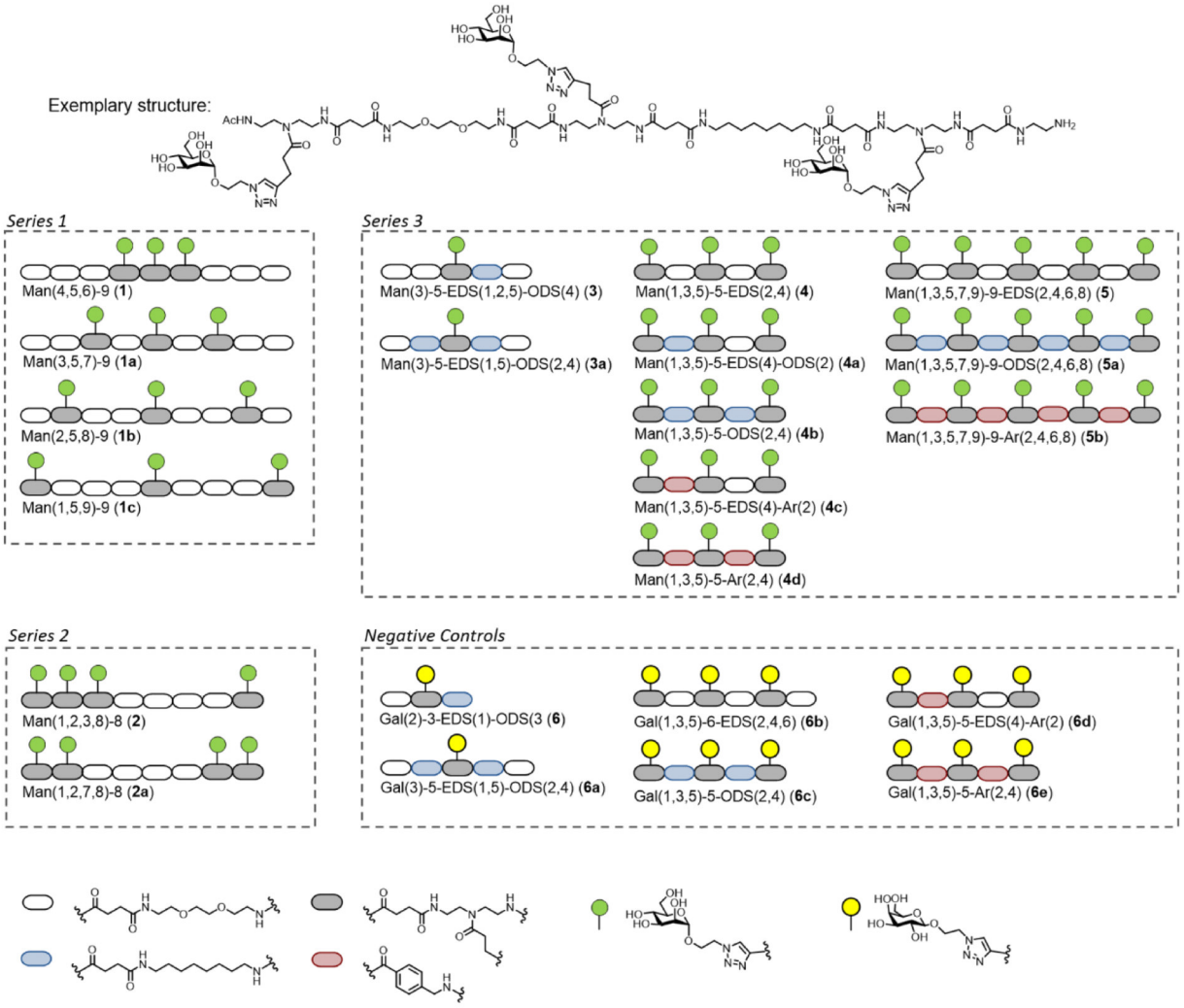

*Figure 18: Overview of glycomacromolecule structures of series 1 to 3. The glycomacromolecules presented, vary in different structural features. In series 1 the carbohydrate spacing is varied (**1**-**1c**). In series 2 the carbohydrate arrangement is varied (**2**-**2a**). For both series 1 and 2, carbohydrate valency and the molecular weight are kept constant. In series 3 the carbohydrate valency and backbone hydrophobicity are varied (**3**-**5b**). In addition, glycomacromolecules bearing β-D-galactopyranoside moieties are presented that function as negative controls. Glycomacromolecules **3a**, **4a** and **4b** were previously presented but no TFA removal was performed for these structures so that their synthesis was repeated in this work.[132] Glycomacromolecules **4** and **5** were also presented previously and were included in this work for comparability.[120] Glycomacromolecules **2**, **2a** and **6b** were provided by members of the Hartmann group[139,138] [adapted from [188] with permission from John Wiley and Sons].*

In the second series, the backbone length and valency were kept constant but ligands were presented either homogeneously distributed (**2a**) or non-homogenously distributed (**2**) along the scaffold (structures of the second series were provided by members of the Hartmann group).[139] In the third series, backbone hydrophobicity and carbohydrate valency were gradually changed. Backbone hydrophobicity was varied by using hydrophilic to aliphatic hydrophobic to aromatic hydrophobic

residues (**3**-**5b**). Carbohydrate valency was changed from one to three to five (**3**-**5b**). Moreover, six glycomacromolecules with β-D-galactopyranoside ligands were synthesized as negative controls for binding assays with the α-D-mannopyranoside binding lectins ConA and FimH (**6**-**6e**) (glycomacromolecule **6b** was provided by a member of the Hartmann group).[138] For monovalent hydrophobic glycomacromolecules (**3**), solubility in water was problematic in cases where more than two ODS building blocks were employed. As water solubility is a prerequisite for binding studies, the ODS/TDS ratio was kept ≤2. As the same behavior was expected for aromatic spacing no monovalent structures with AR spacer building block were synthesized.

After synthesis and TFA removal, the relative purity of the isolated compounds was determined by RP-HPLC. This analysis revealed that glycomacromolecules with more than two ODS building blocks exhibited much lower purities compared to glycomacromolecules with an EDS or AR spacer. It is known in literature that hydrophobic sequences are problematic in solid phase peptide synthesis, thus this could also be expected for coupling more hydrophobic building blocks in SPPoS.[140] In SPPS incomplete coupling as well as incomplete Fmoc deprotection have been observed. Factors influencing coupling and deprotection efficiency include the aggregation of the peptide on solid support, which reduces the accessibility of functional groups, as well as the low solubility of the growing hydrophobic peptide. It is reasonable that the same or a similar behavior can be expected for glycomacromolecules with a high number of ODS building blocks.

In order to prevent the occurrence of deletion sequences, the reaction parameters employed in SPPoS were optimized. The solvent is an important factor in solution phase reaction, the same is true for the choice of resin in solid phase. A Tentagel® resin was employed for all reactions because the incorporated polyethylene glycol (PEG) chains increase the solubilizing properties of the resin and also lead to more flexible and hydrophilic resin properties. In order to identify whether the deprotection or the coupling step is problematic in ODS coupling, both reactions were examined individually. It had already been previously demonstrated that the deprotection step after ODS coupling was not problematic.[132] However, sufficient coupling efficiency had not been studied in detail.[132] Thus, further conditions for ODS coupling efficiency were tested in this work. Coupling efficiency was monitored by comparing UV absorbance at 290 nm after the first deprotection step for a defined amount of resin to the initial resin loading.[141] Standard conditions for SPPoS employing 5 equivalents of building block, 4.9 equivalents of PyBOP and 10 equivalents of DIPEA for 1.5 h were first tested. These conditions were then varied in regard to amount of building block (10 equivalents), reaction time (double coupling for 2x45 min), coupling reagent (HATU) and coupling solvent (0.4 M LiCl in DCM/DMF).

Table 1 shows the results in comparison to the coupling efficiency of the amino acid valine determined under the same conditions and set to 100%. The results show that coupling efficiency for the ODS building block was around 70% for standard coupling conditions as well as coupling conditions with increased amount of building block, a different coupling reagent or double coupling for 2x45 min. However, coupling efficiency dramatically increased when a 0.4 M solution of LiCl in DCM/DMF (*v/v*, 50/50) was employed. This finding can be explained by the fact that the addition of the chaotropic salt LiCl together with increased resin swelling in DCM reduces chain aggregation and thus enables higher accessibility of reaction groups.[142,143] In contrast, the incorporation of the AR spacer building block led to high efficiency under standard as well as most other tested conditions. This explains the higher purities of glycomacromolecules containing this spacer building block. The same was true for glycomacromolecules with EDS spacer.

Table 1: Coupling efficiency determined by UV absorption at 290 nm for ODS and AR building block. Standard conditions for SPPoS are compared to conditions varied in regard to amount of building block, reaction time, coupling reagent and coupling solvent. Coupling efficiency is reported relative to the coupling efficiency determined for the amino acid valine under the same conditions set to 100% coupling efficiency [reprinted from [188] with permission from John Wiley and Sons].[100]

Coupling Solvent	Building Block	Coupling Reagent	Coupling Time	Coupling Efficiency ODS	Coupling Efficiency AR
DMF	5 eq	4.9 eq PyBOP	1.5 h	70±9%	107±7%
DMF	10 eq	4.9 eq PyBOP	1.5 h	74±1%	110±8%
DMF	5 eq	4.9 eq HATU	1.5 h	72±2%	97±26%
DMF	5 eq	4.9 eq PyBOP	2 x 45 min	64±9%	66±12%
0.4 M LiCl DCM/DMF	5 eq	4.9 eq PyBOP	1.5 h	91±8%	94±12%

All glycomacromolecules were synthesized employing the optimized coupling conditions. All compounds were purified by preparative HPLC to ensure high purities. Final glycomacromolecules were characterized using ^{1}H-NMR, MALDI-TOF-MS, RP-HPLC and HR-ESI. Relative purity was determined by RP-HPLC to be 90-99% for all structures.

Figure 19 shows an exemplary ^{1}H-NMR spectra of the trivalent compounds **4**, **4b** and **4d** with EDS, ODS or AR spacer, respectively. All spectra display typical resonances for the TDS functional building block, carbohydrate moiety, succinyl rest, end- and linker groups. Resonances of all mannopyranoside hydroxyl groups do not occur due to proton exchange with deuterated water. However, -NH protons can be assigned to a broad multiplet at 8.44 ppm. The ethylene units of the TDS building block show

broad multiplet resonances in the range of 3.52-3.30 ppm. These are partially overlapped by signals of the ethylenediamine (EDA) end group. In addition, the EDA group shows a triplet signal at 3.14 ppm. The linker group between TDS and the carbohydrate moiety also displays several distinct resonances shifted to low field due to the triazole ring and neighboured oxygen atoms. The proton of the triazole ring appears as multiplet in the aromatic region of the spectrum at 7.87 ppm. The ethylene bridge that belongs to the mannopyranoside azide derivative (protons d and e) shows three multiplet signals at 4.6, 4.1 and 3.9 ppm. The ethylene connection that belongs to the TDS building block (protons a and b) can be assigned to one multiplet signal in the range of 3.06-2.97 ppm, partially overlapping with the mannose proton j, and a triplet signal at 2.80 ppm. All other protons of the mannopyranoside moiety appear as multiplet signals in a range from 3.88 to 3.57 ppm. Protons for the acetyl group appear as two singlets at about 1.94 ppm with a ratio of 1:1 that can be assigned to two rotational isomers. A set of multiplet signals ranging from 2.56-2.44 ppm can be assigned to the succinyl rest of all building blocks. The EDS building block also shows distinct resonances in ^{1}H-NMR spectrum for compound **4**. The repetitive ethylene glycol unit can be found as two sets of signals at 3.70-3.57 and 3.39-3.31 ppm. These signals partially overlap with signals for the mannopyranoside unit and the TDS building block. The aliphatic protons of the ODS building block occur as three sets of multiplets at 3.17-3.09, 1.49-1.41 and 1.30-1.21 ppm in ^{1}H-NMR spectrum of compound **4b**. Signals for protons 8 and 9 in comparison to the protons 10 and 11 are shifted to low field caused by deshielding of the amide functionality. The assignment for the linker group and the carbohydrate moieties are a little bit different in case of glycomacromolecule **4d** with aromatic spacing. Here, linker protons split into several signals (e.g. see proton c) due to the higher rigidity of the aromatic scaffold (see Chapter 3.1.3.1). Moreover, typical resonances for the aromatic spacing can be found at 7.64-7.53 and 7.37-7.30 ppm. The protons of the methylene group are shifted to low field due to the neighboured aromatic ring and amide functionality and appear at 4.49-4.36 ppm. Only for aromatic spacing the anomeric proton f can be assigned to a multiplet at 4.77-4.70 ppm. For all other glycomacromolecules this signal is overlapped by the signal caused by the NMR solvent at 4.79 ppm. Integration of all proton signals is in accordance with the expected number of protons contributed to complete conversion in all reaction steps and successful synthesis of the glycomacromolecules **4**, **4b** and **4d**.

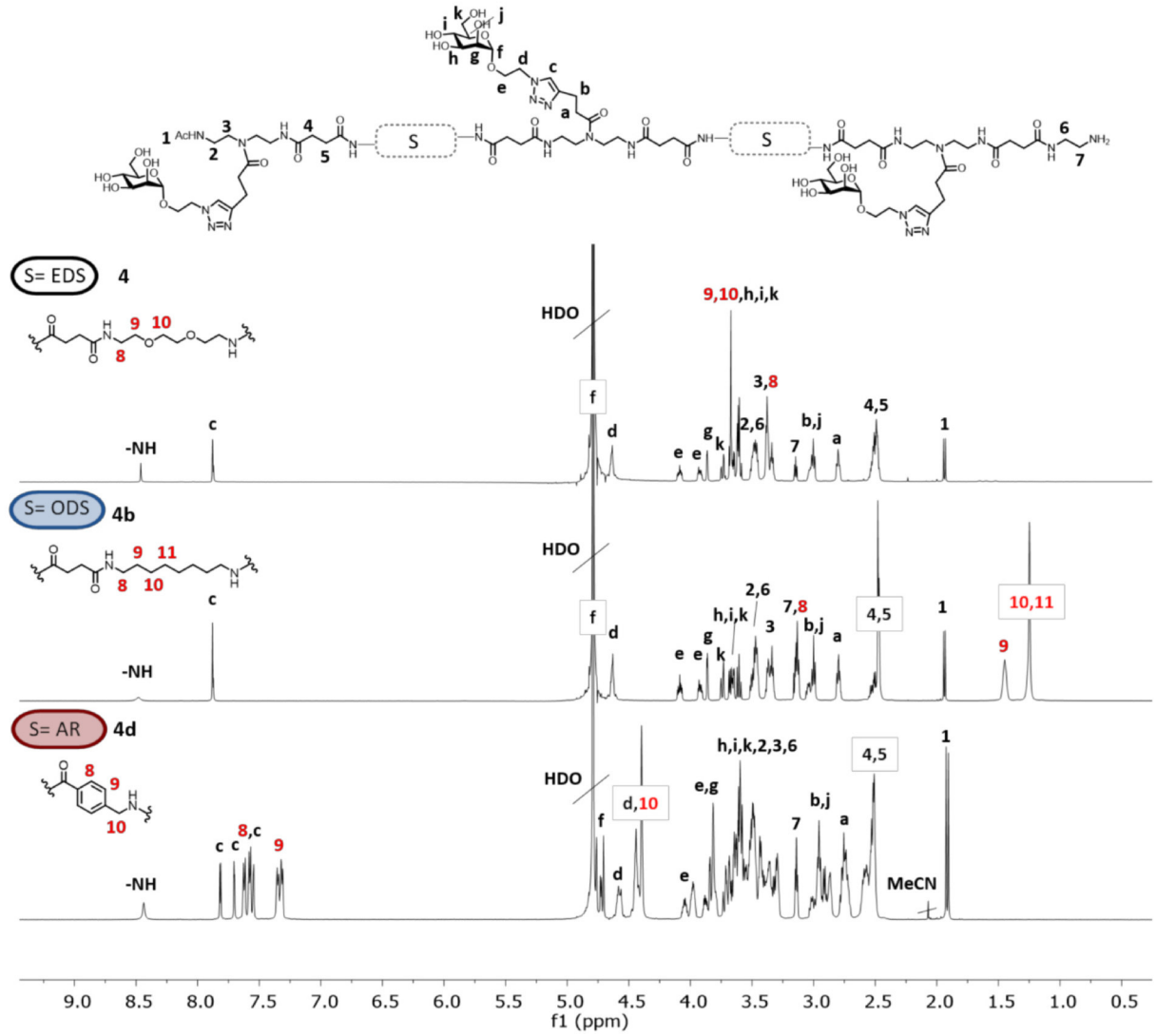

*Figure 19: Comparison of ^{1}H-NMR (600 MHz, D_2O) spectra of trivalent glycomacromolecules (**4**, **4b**, **4d**) with EDS, ODS or AR spacer. Spacer protons are highlighted in red.*

In order to further confirm the overall chemical composition of the synthesized glycomacromolecules, MALDI-TOF-MS and HR-ESI analyses were applied. The theoretically calculated mass-to-charge ratios thereby correspond to the observed values. Figure 20 shows an exemplary MALDI-TOF-MS and HR-ESI spectrum for glycomacromolecule **4**.

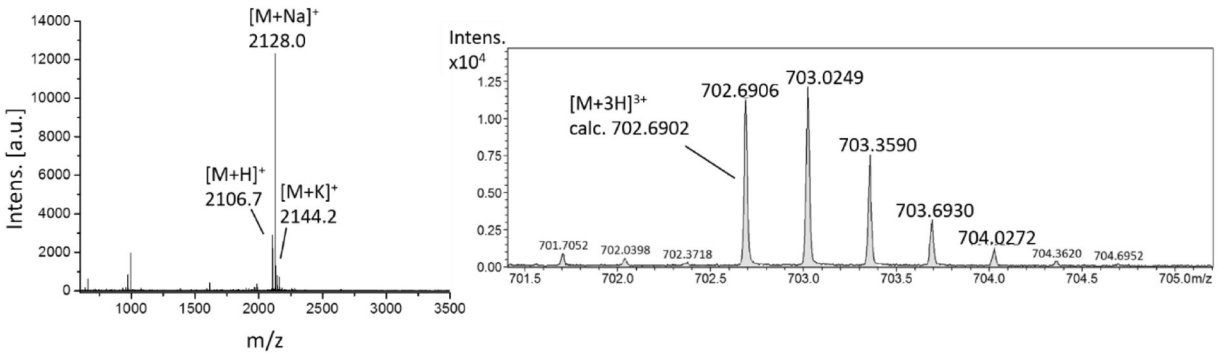

*Figure 20: Exemplary MALDI-TOF-MS (left) and HR-ESI (right) spectrum of glycomacromolecule **4**.*

Moreover, relative purity and monodispersity of the synthesized glycomacromolecules were confirmed by RP-HPLC analysis. Figure 21A shows exemplary RP-HPLC chromatograms for the trivalent compounds **4**, **4a, 4b, 4c** and **4d**. The retention time increases with the number of AR and ODS spacer building blocks within the backbone. This observation is expected based on the increased hydrophobicity of the glycomacromolecule when these hydrophobic spacer building blocks are employed in comparison to the hydrophilic EDS spacer. The same holds true for the monovalent compounds **3** and **3a** and the higher valent structures **5**, **5a** and **5b** (see Chapter 5.4.3.1, Chapter 6.4). In contrast, glycomacromolecules **1**, **1a**, **1b** and **1c** that only change in interligand spacing while maintaining the same overall length of the backbone show similar retention times in RP-HPLC analysis (Figure 21B). The same observation can be made for structures **2** and **2a**, which also show the same retention time irrespective of the change in carbohydrate arrangement (Chapter 5.4.3.1, Chapter 6.4).

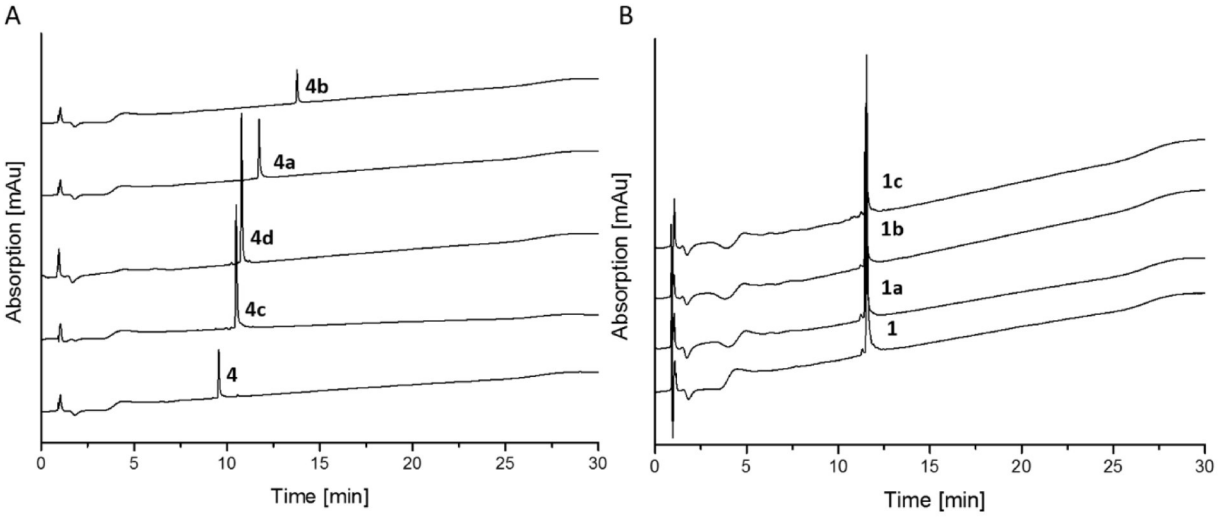

*Figure 21: RP-HPLC chromatogram (95/5 H_2O/MeCN with 0.1% formic acid (A) and 5/95 H_2O/MeCN with 0.1% formic acid (B); 100% A to 50% A in 30 min) determined at 214 nm for glycomacromolecules (A) **4**, **4a**, **4b**, **4c**, **4d** and (B) **1**, **1a**, **1b**, **1c** [adapted from [188] with permission from John Wiley and Sons].*

3.1.2 Lectin Binding Studies

After successful synthesis of glycomacromolecules varying in their scaffold composition, the next step was to investigate the effect of these structural features in lectin binding studies. First, the binding

affinity/avidity towards the model lectin ConA was measured. As discussed in Chapter 1.1.1.2 ConA belongs to the legume lectin family and has been extensively studied so that results with this lectin can be compared with a wide range of literature studies. ConA specifically binds α-D-mannopyranosides and α-D-glucopyranosides with a four times higher binding affinity for α-D-mannopyranosides.[37,144,145] It does not bind β-D-galactopyranosides; glycomacromolecules bearing a galactopyranoside entity (**6**-**6e**) serve as negative controls. Notably, ConA has different conformations in dependence of pH conditions. Under acidic conditions it forms dimers, and under neutral conditions it predominantly exists as tetramer.[146-148] In this work acidic conditions were used for binding experiments so that binding affinity to divalent ConA was investigated.

As first assay for investigating the binding behavior of glycomacromolecule series 1-3 towards ConA, isothermal titration calorimetry (ITC) was employed. In the experimental setup of ITC two identical, isolated cells are placed in an insulated compartment.[149] One cell is the reference cell, which is filled with pure solvent, and the other cell is the sample cell, which contains the lectin solution. A syringe, which delivers the carbohydrate ligand to the sample cell, is an important part of the experimental setup in ITC. At its lower part the syringe resembles a paddle to ensure rapid mixing of the sample solution by rotation of the syringe (Figure 22A). The carbohydrate ligand is added in small portions and in defined time intervals. As soon as the carbohydrate ligand is titrated into the sample cell containing the lectin, different events take place including association and dissociation of reversible inter- and intramolecular bonds as well as secondary interactions caused by hydrophobic effects but also the rearrangement of the solvation shell.[149] Each of these molecular processes is associated with a heat energy exchange with the environment. This heat effect is measured by ITC. It is determined by the temperature difference (ΔT) between the reference and the sample cell. The change in temperature triggers a regulator to maintain the same temperature in both cells. The change in electrical power needed to regulate the temperature produces a change in feedback current which produces the primary signal in ITC as a time-dependent heat pulse (Figure 22B).[150] Integration of the heat pulse over time and plotting the resulting energy values against the molar ratio of ligand to lectin results in a sigmoidal shaped titration curve (Figure 22B). Fitting of this curve with a least squares procedure and the *one-sets-of-independent-binding-sites* model using origin software, provides all thermodynamic parameters, the free Gibb´s energy (ΔG), the enthalpy of binding (ΔH), the entropy of binding (ΔS) and the equilibrium association constant (K_A), in a single experiment. The titration curve directly allows for the determination of ΔH and K_A. Further thermodynamic parameters such as ΔG and ΔS can be calculates using the *Gibbs-Helmholtz* and *van´t Hoff* equations. Moreover, provided that concentrations of lectin and ligand were precisely determined, ITC provides the stoichiometry n of the

carbohydrate lectin complex. Thus, ITC is a powerful tool to study carbohydrate lectin interactions, and has been widely employed in literature.[151-155]

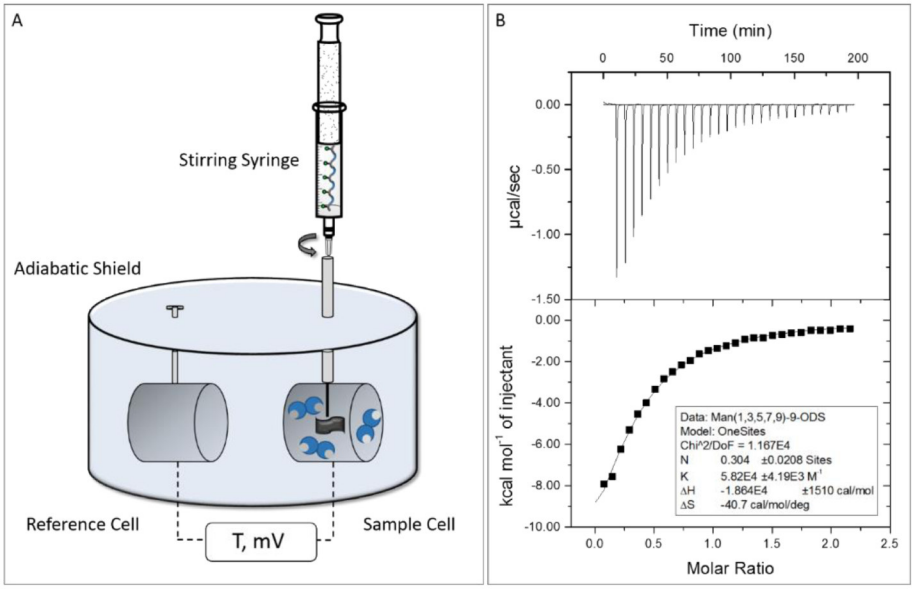

Figure 22: (A) Experimental setup of ITC ([156]), (B) ITC thermogram and binding isotherm of compound ***5a*** *binding to dimeric ConA at 25 °C.*

ITC measurements require different precautions because they are sensitive to a number of error sources.[157-168] Brewer *et al.* and Nguyen *et al.* for example observed that a lectin with a higher number of binding sites increases the possibility of precipitation which leads to an incorrect heat signal in ITC. In order to avoid this problem both working groups employed divalent ConA. The Hartmann group previously made the same observation that baseline noise increased with tetravalent ConA and higher valent glycomacromolecules.[120] For this reason, in this work, only divalent ConA was used in ITC experiments to prevent inaccurate results caused by precipitation of the carbohydrate lectin complex.

In addition, Toone *et al.* pointed out that one concern in ITC measurements is that different calorimetric values have been reported for ConA binding to methyl α-D-mannopyranoside.[159] Whereas Toone *et al.* suggest that differences in ITC values result from differences in the experimental conditions, such as ionic strength of the buffer, Brewer and co-workers suggested that the discrepancies could be a result of differences in ligand concentration determination.[147] In order to account for both aspects, the same buffer batch was used for all experiments in this work. Moreover, both lectin and carbohydrate ligand concentration were determined spectrophotometrically. For glycomacromolecules, concentration was determined based on the number of carbohydrates attached to the macromolecular scaffold using a modified phenol sulphuric acid method, first described by Dubois and coworkers.[169]

Another important factor in ITC measurements is the so-called *c*-value that was introduced by Wiseman and co-workers.[170] The *c*-value can be determined as the mathematical product of stoichi-

ometry n, K_A, and lectin concentration in the sample cell, and provides information about the quality of the fit. This *c*-value should be within a range of 1 to 500.[149] In case of a *c*-value <1 or >500, curve fitting is difficult and leads to inaccurate results. However, Turnbull *et al.* and Tellinghuisen argued that low affinity systems with c-values <0.1 still give reliable results when the n-value is set to a constant.[171,172]

Another phenomenon observed in ITC measurements is the enthalpy-entropy compensation, the linear relationship between ΔH and ΔS.[173-182] Pielak *et al.* describe this effect as small changes in overall ΔG that are accompanied by large and nearly compensatory changes in ΔH and ΔS.[173] Early studies describe this phenomenon as a property of reactions in water (see Chapter 1.1.2.1).[180] Moreover, it has been argued to be a general property of weak intermolecular interactions.[175] However, there is increasing concern about the real existence of the enthalpy-entropy compensation effect. Chodera and Mobley, for example, pointed out that enthalpy-entropy compensation might only be a mathematical artefact, and not a real experimental phenomenon.[183] They argue that thermodynamic values such as K_A and ΔH are both independently determined from the non-linear curve fit of the ITC experiment, whereas ΔG and ΔS are subsequently calculated from the obtained affinity and enthalpy values. Thereby an error in K_A only leads to a small error in ΔG because of the logarithmic dependence ($\Delta G = -RT \ln K_a$). In contrast, an error in ΔH leads to an accordingly high error in ΔS because of the linear dependency of these values ($\Delta G = \Delta H - T\Delta S$).

In order to gain more extensive insights about the effects of carbohydrate lectin binding, a second method, surface plasmon resonance (SPR), was employed in this work. In contrast to ITC, in SPR the lectin is not present in solution but immobilized on a sensor chip surface. The sensor chip exhibits a gold surface to which a linker layer with a linearized dextran matrix is attached (Figure 23A). The dextran matrix displays several carboxyl groups that can be used for lectin immobilization by *N*-hydroxysuccinimide (NHS)/ 1-ethyl-3-(3-dimethylaminopropyl)-carbodiimide (EDC) coupling via amine groups in lysine side chains of the lectin. Ethanolamine is used to react with the remaining active esters on the surface. The reference surface is only reacted with ethanolamine and lectin incubation is omitted. The obtained immobilization level sets the baseline for the SPR experiment.

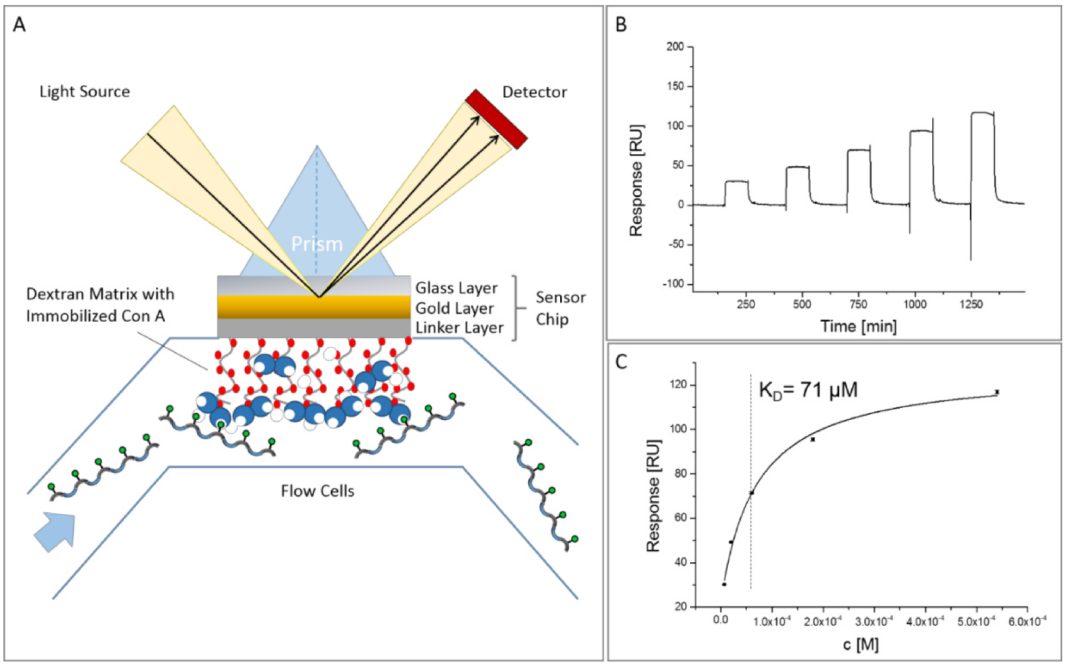

*Figure 23: (A) Experimental setup of SPR, (B) Exemplary SPR sensorgram of glycomacromolecule **5a** binding to immobilized ConA at various concentrations at 25 °C, (C) K_D evaluation where the equilibrium response values are plotted against glycomacromolecule concentration [adapted from [184] - Published by The Royal Society of Chemistry].*

The SPR detection system consists of a light source which is focalized on the chip surface by a prism resulting in stimulation of plasmon resonance in the gold surface. The emitted light is detected by a detection unit (Figure 23A). A change in refractive index of the surface leads to a detection angle shift which is translated into resonance units (RU) (1 RU= 0.0001°). The baseline level is set to zero RU. When glycomacromolecules are led over the surface resulting in a binding event, mass concentration on the surface changes. This leads to a proportional change in refractive index at the sensor chip surface and an increase in RU. When ligand injection is stopped, dissociation from the surface leads to decreasing RU values (Figure 23B). In order to ensure complete detachment from the surface, a regeneration step can be performed. In this work, regeneration with excess of methyl α-D-mannopyranoside was identified as best regeneration method after regeneration scouting employing different pH values and salt concentrations.

There are two different analysis methods available in SPR, multi-cycle kinetic (MCK) and single-cycle kinetic (SCK). In MCK, one glycomacromolecule concentration per measurement cycle directly followed by complete surface regeneration is employed. In SCK five concentrations per measurement cycle are used by sequential glycomacromolecule injection without regeneration in between the injection steps (Figure 23B). Only at the end of the experiment one regeneration step is performed. SCK is preferred when sensitive surfaces such as protein surfaces are employed. Thus, SCK was the method of choice in this work because ConA was immobilized on the surface.

When low molecular weight ligands are employed, binding kinetics are rapid leading to a square shape of the binding curve (Figure 23B). In this case it is not possible to determine binding kinetics. However, steady-state affinity analysis in form of a K_D value can be obtained by plotting the response at equilibrium against the concentration for the respective curve of the dilution series. This leads to a saturation curve. Fitting leads to the K_D value which corresponds to the concentration at half maximum (Figure 23C).

In combination, ITC and SPR assays offer great opportunities for the study of carbohydrate lectin interactions. For example, they allow for different perspectives because carbohydrate lectin binding can either be observed in solution or at solution surface interface. Thus, the information that can be drawn from both assays is much more versatile than from one assay alone. However, differences in experimental setup could also influence assay results as was shown in literature.[185-187] Thus, it is not surprising that absolute values of the dissociation equilibrium constant K_D derived by ITC and SPR differ from each other. However, the derived values show similar overall trends for the three series of glycomacromolecules evaluated (Table 2). The results are discussed in the following section.

Table 2: ITC-derived thermodynamic parameters of glycomacromolecules varying in carbohydrate spacing and arrangement or backbone hydrophobicity binding to dimeric ConA (acetate buffer pH 5.20±0.01, 25 °C). SPR derived K_D values of glycomacromolecules binding to immobilized dimeric ConA (acetate buffer pH 5.20±0.01, 25 °C) are also included [reprinted from [188] with permission from John Wiley and Sons].[188]

Ligand	FV[a]	ΔG[b]	ΔH[b]	-TΔS[b]	*c*[c]	K_D[d] (ITC)	K_D[d] (SPR)
Man(4,5,6)-9 **1**	1.9±0.03	-24.6±0.2	-52±3	27±3	2.1	49±4	150±3[e]
Man(3,5,7)-9 **1a**	2.0±0.03	-24.7±0.4	-51±2	26±2	2.3	48±7	138±2[e]
Man(2,5,8)-9 **1b**	2.0±0.03	-24.8±0.2	-51±4	26±4	2.0	45±4	127±2[e]
Man(1,5,9)-9 **1c**	2.2±0.05	-24.3±0.7	-56±7	32±6	1.7	58±17	128±2[e]
Man(1,2,3,8)-8 **2**	2.2±0.03	-25.8±0.3	-54±5	28±5	1.8	31±4	104±1[e]
Man(1,2,7,8)-8 **2a**	2.6±0.1	-25.8±0.3	-71±26	45±26	1.8	30±3	98±2[e]
Man(3)-5-EDS(1,2,5)-ODS(4) **3**	1.0*	-21.6±0.1	-27±1	5±1	0.8	166±7	279±10[e]
Man(3)-5-EDS(1,5)-ODS(2,4) **3a**	1.0*	-22.0±0.1	-26±1	4±1	0.9	140±4	207±79[e]
Man(1,3,5)-5-EDS(2,4) **4**	2.0±0.1	-25.1±0.2	-55±5	29±6	2.4	39±3	68±2
Man(1,3,5)-5-EDS(4)-ODS(2) **4a**	2.0±0.03	-25.4±0.1	-53±2	28±2	2.7	36±2	69±2
Man(1,3,5)-5-ODS(2,4) **4b**	2.1±0.03	-25.7±0.2	-55±3	29±4	3.1	32±2	67±2
Man(1,3,5)-5-EDS(4)-AR(2) **4c**	2.3±0.03	-25.5±0.2	-68±5	42±5	3.5	34±3	68±2

Man(1,3,5)-5-AR(2,4) **4d**	2.3±0.02	-26.0±0.2	-69±4	42±4	4.2	27±2	62±1
Man(1,3,5,7,9)-9-EDS **5**	2.8±0.03	-26.0±0.2	-79±7	52±7	2.1	24±2	79±2
Man(1,3,5,7,9)-9-ODS **5a**	3.3±0.02	-27.1±0.2	-71±7	44±7	2.9	18±1	71±2
Man(1,3,5,7,9)-9-AR **5b**	4.2±0.02	-28.6±0.1	-111±8	82±8	5.9	10±1	64±2

[a] FV is defined as FV=1/n and was experimentally determined from the binding stoichiometry n.
** For **3** and **3a** the binding stoichiometry was set to a fixed value due to c values <1.*
[b] Gibbs binding free energy ΔG, enthalpy of binding ΔH and entropy of binding ΔS are reported in kJ mol^{-1}.
[c] c values refer to the quality of the fit.
[d] Dissociation equilibrium constant K_D is reported in µM.
[e] SPR measurements for these compounds were performed on a CM5 sensor chip with an immobilization level of 2888.7 RU for ConA.
*All ITC data are the average of two independent titrations. SPR data are the average of two independent experiments (one for **3** and **3a**, triplicate determination per experiment). ITC control experiments performed by making identical injections of glycomacromolecules into a cell containing buffer without ConA showed insignificant heats of dilution which were subtracted from the obtained ITC data with ConA. Negative controls **6**-**6e** showed no binding.*

As mentioned above, enthalpy-entropy compensation is a typical phenomenon observed in ITC measurements when aqueous protein solutions are employed. The same holds true for the results obtained in this work. A change in binding enthalpy ΔH is always accompanied by an equally high change in -TΔS leading to overall similar ΔG values (see **1**-**1c, 2**-**2a**). Also for the third series, the lowest (most favorable) ΔH value (**5b**, -111 kJ mol^{-1}) is combined with the highest (most unfavorable) -TΔS value (**5b**, 82 kJ mol^{-1}). Due to the fact that it has not yet been determined whether this compensation is a real effect or a mathematical artefact, a detailed discussion is waived here.

The functional valency FV is defined as the reciprocal value of binding stoichiometry n. It defines the number of carbohydrates actually participating in lectin binding. It is generally not the same as the structural valency SV, the number of carbohydrate ligands attached to the macromolecular scaffold, but typically scales therewith. For monovalent compounds with low affinity towards ConA, FV was set to 1 because of low *c* values exceeding the allowed range 1< *c* <500. In order to guarantee for a high quality fit, fixing of this variable is necessary.[171,172] The value 1 was assigned based on the stoichiometry determined for glycomacromolecules of the same SV in previous studies.[120] All other compounds lie within the allowed *c* value range. For these compounds, FV increases in accordance

with SV. However, FV is smaller than SV throughout the three series indicating that only parts of the sugar ligands attached to the glycomacromolecular backbone simultaneously participate in lectin binding.

Even though FV mainly depends on SV, small trends correlating with sugar arrangement and backbone properties can be observed. In the first series, where different ligand spacing is investigated, the FV slightly decreases with increasing sugar density. Thus, the lowest FV value can be found for structure **1** (1.9) with densely packed mannopyranoside units, and the highest FV value can be assigned to glycomacromolecule **1c** (2.2) with three spacer units separating the mannopyranoside ligands. Glycomacromolecules of the second series, which exhibit a change in backbone symmetry, show similar results as glycomacromolecules changing in sugar spacing. Again, a higher density of the sugar moieties is accompanied by comparably low FV value (compare **2** and **2a**). In the third series of glycomacromolecules a higher FV can be observed with increasing hydrophobicity of the backbone. For the more hydrophobic pentavalent structures **5a** (3.3) and **5b** (4.2), higher FV are observed in comparison to the more hydrophilic structure **5** (2.8). The same observation can be made for trivalent structures **4**-**4d** (2.0-2.3) even though the effect is not as pronounced.

The binding free energy (ΔG) and K_D values determined by ITC both allow for the same conclusions due to their mathematical dependency. Thus, only K_D values are discussed in the following because they can be more easily compared to data obtained in SPR assay. For the first series of glycomacromolecules the variations in sugar spacing have little effect on K_D leading to very similar values within the margin of error in the ITC measurement (**1**, **1a**, **1b**, **1c,** Figure 24). Comparable results for K_D can also be found for the tetravalent structures with different backbone symmetry (**2**, **2a**). In SPR assays, glycomacromolecules of series one and two exhibit a different behavior. Here, the observed K_D values show a small correlation to the sugar density on the glycomacromolecular scaffold, and become more favorable with increasing spacing (e.g. compare **1** and **1c**, **2** and **2a**, Figure 24). For the first and second series of glycomacromolecules, two multivalent effects probably play a major role. On the one hand, narrow spacing associated with a high density of carbohydrate ligands could lead to avidity enhancement due to the statistical effect of the higher local concentration (sliding and binding mechanism).[185,189] On the other hand, the densely packed sugar units or the neighbouring free "spacer arms" could cause steric repulsion as indicated by decreasing FV values with increasing carbohydrate density. Another effect counterbalancing the positive impact of a higher local concentration of sugar ligands could be the entropic penalty associated with an alteration of conformation upon binding because the spacing is too short. However, the high degree of flexibility in spacing probably leads to a coiled conformation in solution which is in agreement with previous findings from fluorescence correlation spectroscopy. [190] Thus, differences in interligand spacing in the scaffold might not

necessarily lead to differences in spacing in the final attachment pattern of the carbohydrate ligands that is formed in solution. As a result, no big difference in affinity can be found for ITC results. The change of behaviour observed in the SPR experiments might be attributed to a change of the counterbalancing behavior of steric repulsion and statistical effects upon change of the assay used. With ConA immobilized on the sensor chip surface, steric restraints caused by neighbouring sugar ligands or dangling "spacer arms" might be enhanced due to the overall limited mobility of the complex leading to a more dominant influence of steric repulsion over statistical effects.

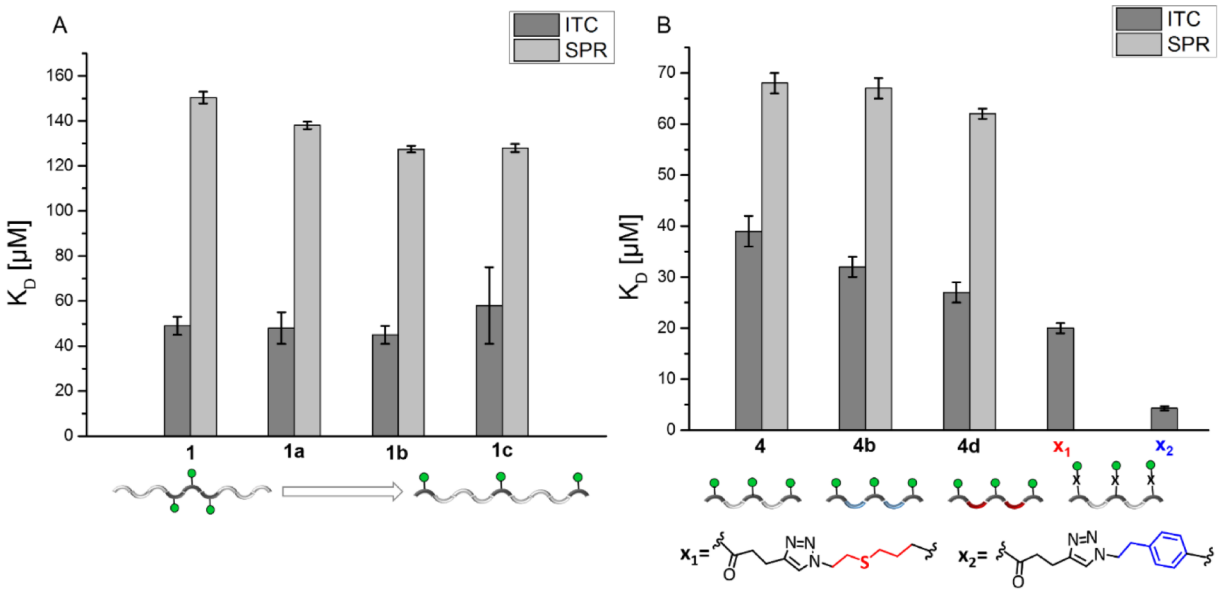

Figure 24: K_D values derived from ITC and SPR, A: Trivalent glycomacromolecules differing in carbohydrate spacing, B: Trivalent glycomacromolecules varying in backbone hydrophobicity. Structures ***x₁*** *and* ***x₂*** *with thiahexyl- and phenyl- linker were presented previously.[120] ITC results of these structures are included for comparison [adapted from [188] with permission from John Wiley and Sons].*

In the third series of glycomacromolecules, which varied in backbone hydrophobicity, a clear trend of more favorable K_D values with higher SV was observed in ITC (e. g. compare **3**, **4** and **5**). Comparing ITC to SPR results, it is striking that the correlation between SV and binding affinity/avidity towards ConA in SPR holds true only to a certain extent. There is a clear difference between monovalent and trivalent structures but the difference in K_D values clearly levels off for tetravalent and pentavalent structures (e.g. compare **3**, **4** and **5**). In regard to the effect of backbone hydrophobicity, both ITC and SPR results show that K_D values scale favorably with an increasing number of hydrophobic spacer building blocks incorporated in the macromolecular backbone. Thus, the lowest (most favorable) K_D value can be found for pentavalent structure **5b** (10±1 µM in ITC and 64±2 µM in SPR) with hydrophobic aromatic spacing. Structure **5**, where AR spacing is exchanged by EDS spacing, shows comparably lower affinity (24±2 µM in ITC and 79±2 µM in SPR). Trivalent (**4**, **4a**, **4b**, **4c**, **4d**) and monovalent (**3**, **3a**) structures show the same effect but less pronounced (Figure 24). Thus, the third series of glycomacromolecules demonstrates that there is a trend of enhanced ConA binding with rising backbone hydrophobicity.

This enhancement could be explained by additional interactions of the hydrophobic spacer with hydrophobic amino acid side chains near or inside the carbohydrate binding site of ConA.

Previous studies where hydrophobic moieties were included in the linker position allow for comparison and better classification of the results obtained in this work (Figure 24).[120] Previous results showed that an exchange of the regularly employed ethyl linker by a thiahexyl-linker $\mathbf{x_1}$ or by a phenyl-linker $\mathbf{x_2}$ led to an increase in binding affinity towards ConA as determined by ITC. The thiahexyl-linker $\mathbf{x_1}$ showed a decrease of 49% in K_D and the phenyl-linker $\mathbf{x_2}$ showed a decrease of 89% in comparison to glycomacromolecule **4**.[120] In contrast, the incorporation of hydrophobic aliphatic spacing with ODS (**4b**) only led to an increase of 18% in binding affinity. The aromatic hydrophobic spacing with AR spacer (**4d**) showed an increase of 31%. Thus, incorporation of hydrophobic moieties in backbone instead of linker seems to have a smaller effect on binding affinity. An explanation for this observation could be that the greater distance of the backbone to the carbohydrate moiety in comparison to the distance of the linker could minimize the involvement of secondary interactions with hydrophobic amino acid side chains near the carbohydrate binding site. This is also supported by the STD-NMR studies of Ponader *et al.* where it was found that the backbone shows weak or no proton saturation but medium to strong saturation was found for linker protons.[190]

When comparing all synthesized trivalent structures, it is striking that shorter structures exhibit more favorable K_D values than longer structures of the same valency and spacing (e.g. compare **1a** and **4**). Thus, the incorporation of a higher number of spacer building blocks seems to lower the binding affinity. This is probably due to the fact that the flexibility of the structures increases with the number of employed building blocks resulting in rising conformational entropic costs upon binding.[186, 191] Another explanation could be the higher local concentration of carbohydrate moieties in the smaller structures leading to a higher probability of binding (statistical effect).[38,54]

3.1.2.1 Proton NMR Experiment for Investigating Hydrophobic Interactions in Solution

SPR and ITC results for the three series of glycomacromolecules revealed some interesting trends. However, some questions could still not be definitely answered. For example, the difference in binding affinity between glycomacromolecules where the incorporation of hydrophobic moieties is in linker versus the backbone position is very interesting. Thus, a ^{1}H-NMR experiment was employed in order to further elucidate the potential effect of different spacer building blocks on the interaction of precision glycomacromolecules with hydrophobic amino acid side chains near the CRD of ConA.[192] For ConA it is known that the hydrophobic amino acid side chains of leucine and tyrosine are involved in additional hydrophobic interactions with aglycon structures.[193,194] Glycomacromolecules **5**, **5a** and **5b** were investigated at a concentration of 5 mM with increasing concentrations of phenol (4, 8, 12 and 16 mM) as a surrogate for tyrosine. The association of phenol with protons of the respective

glycomacromolecule was monitored by the upfield shift in ^{1}H-NMR spectrum in accordance to phenol concentration (Figure 25).

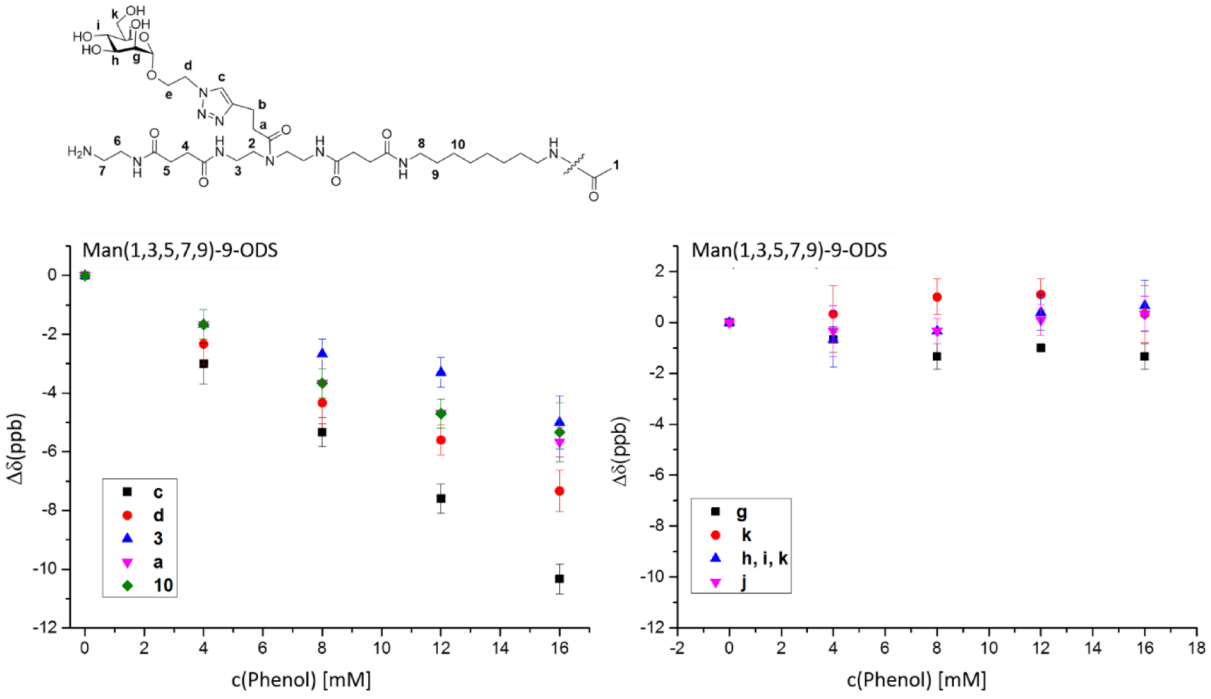

*Figure 25: Exemplary chemical shift changes of glycomacromolecule **5a** at varying phenol concentrations. Chemical shift changes for linker and spacer protons are significant (left) while chemical shift changes for the mannopyranoside unit are small or non-existent (right) [adapted from [188] with permission from John Wiley and Sons].*

Figure 26 shows the chemical structure of glycomacromolecules **5**, **5a** and **5b** with assignment of ^{1}H-NMR chemical shift changes at 16 mM phenol concentration relative to the phenol free solution. Circle size and color represent the magnitude of the chemical shift change. The first thing to be noticed when comparing the ^{1}H-NMR chemical shift changes of the three structures is that the mannopyranoside unit seems to be mostly unaffected by phenol present in solution. However, two other components, namely the linker and spacer, are significantly influenced by phenol based on the chemical shift of the respective protons. The highest ^{1}H-NMR chemical shift change for all structures can be assigned to the triazole proton c. When looking at the chemical shift changes of the other linker protons it is striking that they increase when combined with hydrophobic spacing. For glycomacromolecule **5** with hydrophilic EDS spacing, a chemical shift change of 3-6 ppb can be observed for the linker protons. In contrast, a chemical shift change of 5-10 ppb and 4-9 ppb can be found for glycomacromolecules **5a** and **5b** with hydrophobic ODS and AR spacing. A similar pattern can be observed for the chemical shift of spacer protons. While EDS protons only show insignificant chemical shift changes of 2-3 ppb, signals for ODS and AR protons shift by 4-5 ppb and 5-6 ppb, respectively.

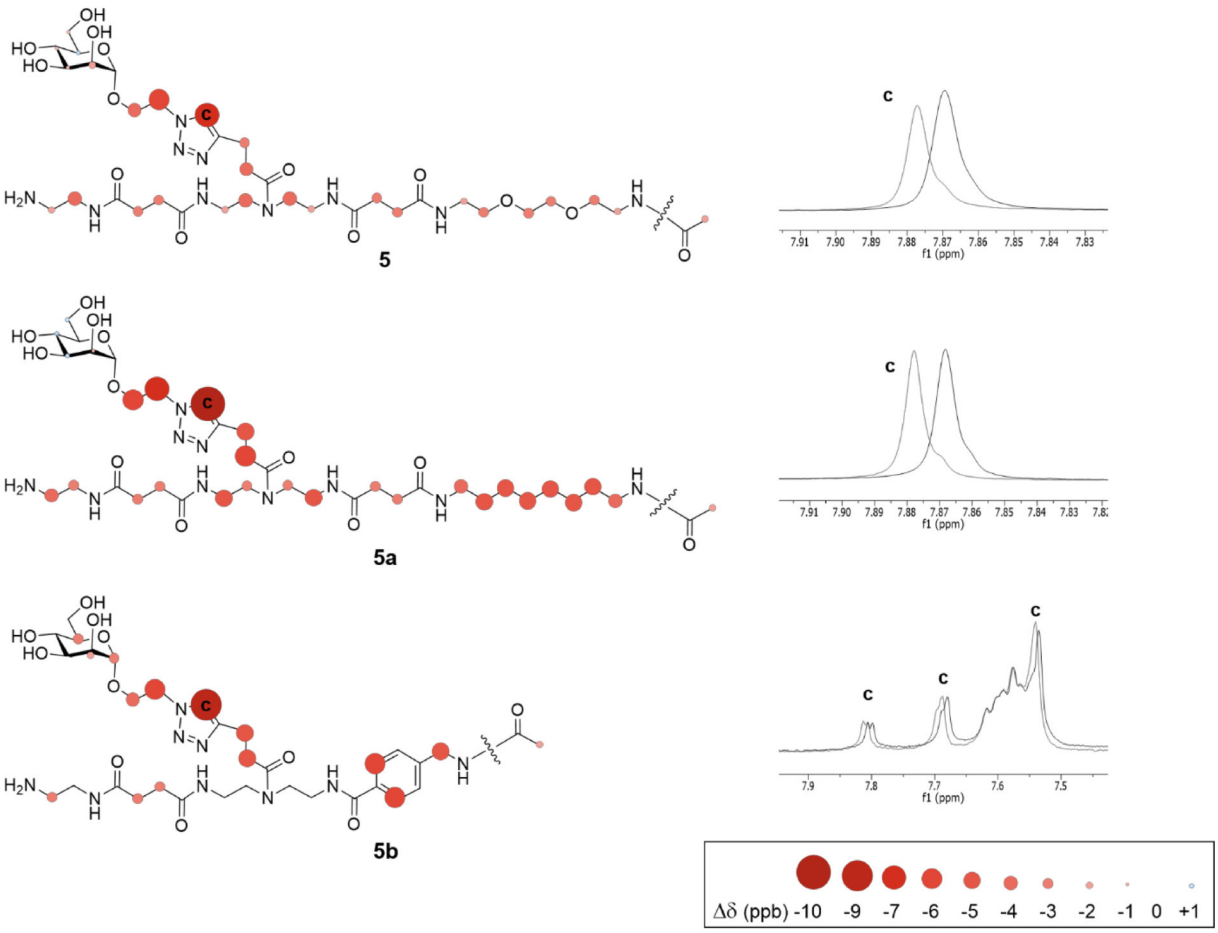

*Figure 26: ^{1}H-NMR chemical shift changes ($\Delta\delta$(ppb)= $\delta_{phenol} - \delta_{phenol\text{-}free}$) of glycomacromolecules **5**, **5a** and **5b** with 16 mM phenol in D_2O represented by circle size and color. The aromatic region of ^{1}H-NMR spectra for 5 mM glycomacromolecule solutions is exemplary shown for the triazole proton of the linker (c) without (black) and with (grey) phenol in D_2O [adapted from [188] with permission from John Wiley and Sons].*

In addition, Figure 26 shows the aromatic region of the ^{1}H-NMR spectrum for glycomacromolecules **5**, **5a** and **5b** showing the signal of proton c of the triazole ring. The black line shows the signal of phenol free solution, and the grey line the shifted signal in presence of 16 mM phenol. Here, it is particularly striking that the triazole protons for glycomacromolecule **5b** do not show one signal as for glycomacromolecules **5** and **5a**, but rather three partially overlapping signals. This indicates a difference in behavior of glycomacromolecules in solution caused by variation of the spacing. As this finding even holds true at higher temperatures, it points towards a higher rigidity of glycomacromolecule **5b** with aromatic spacing (Appendix 254).

As a result, this solution ^{1}H-NMR study shows that hydrophobic spacer building blocks in comparison to hydrophilic spacing clearly have the potential to interact with hydrophobic amino acid side chains, such as the phenol side chain of tyrosine. Moreover, hydrophobic spacing seems to promote increased interactions between the phenol and linker protons. This observation could be explained by a different spatial arrangement of the glycomacromolecular structure in solution due to the less favored exposure of hydrophobic spacer building blocks to the polar, aqueous solution phase. This could then further

lead to an increase in accessibility of the linker protons. At the same time, it is reasonable to assume that carbohydrate ligands become more accessible for binding when combined with hydrophobic spacing. As they are more hydrophilic, they are more likely to be exposed to the polar solution phase. This higher accessibility is also indicated by increasing FV values for hydrophobic structures **5a** and **5b** in ITC measurements (Table 2). This conclusion was confirmed by dynamic light scattering (DLS) studies of glycomacromolecules **5**, **5a** and **5b** at 2 mM concentration in acetate buffer. The hydrodynamic radius was determined to be 4.8 ± 0.6 nm for **5**, 3.4 ± 0.4 nm for **5a** and 3.6 ± 0.3 nm for **5b**. The smaller hydrodynamic radii found for the more hydrophobic structures **5a** and **5b** point towards a more compact conformation in comparison to hydrophilic structure **5**. All in all, this would mean that hydrophobic spacing only indirectly influences lectin binding explaining the comparably smaller increase of binding affinity observed in ITC and SPR measurements.

3.1.2.2 Bacterial Inhibition Study

While ITC and SPR studies with model lectin ConA were helpful for observing some general trends, these studies say little about the applicability of glycomacromolecular ligands as potential therapeutics. In order to gain further information about the effect of differences in structural features, glycomacromolecule series one and three (**1**-**1c** and **4**-**5b**) were examined in an inhibition experiment with *E. coli* targeting FimH receptors. These experiments were performed by a collaboration partner, Dr. Franziska Reise, in the Lindhorst group at Christiana Albertina University in Kiel.

The treatment of bacterial infections by overprescribing antibiotics has led to selection pressures resulting in an increasing number of drug resistant bacteria constituting a major global health problem.[195] *E. coli* is a key pathogen in many infectious diseases including bacteraemia, meningitis as well as respiratory and urinary tract infections.[196] Urinary tract infections caused by *uropathogenic Escherichia coli* (UPEC) is one of the most frequent infectious diseases in developed countries.[197] One prerequisite for infection is the adhesion of bacteria to the host cell. Infection is dependent on adhesive organelles expressed on the bacteria cell surface.[196] These organelles are hair-like proteins of 1-2 µm length and about 7 nm diameter called fimbriae or pili.[196] Fimbriae consist of different protein subunits with a lectin subunit at the fimbriae tip that mediates bacterial binding to the glycocalyx of the host cell.[198,199] Among them, type 1 fimbriae are one of the most characterized and most important virulence factors of *E. coli*.[199] The 32 kDa lectin subunit is called FimH which is specific to binding α-D-mannopyranosides (Chapter 1.1.1.2).[200,201] Thus, the adhesion of bacteria and the associated infection via FimH receptors could be prevented employing competitive α-D-mannopyranoside based inhibitors.[202]

In order to generate inhibitors effective and efficient enough to be applicable as new therapeutic they need to form strong interactions with the lectin receptor. Thus, a rational design of a glycomimetic structure is advisable. For FimH, three different X-ray analyses are available that reveal a single carbohydrate recognition domain in the monosaccharide size range.[202-205] The carbohydrate binding site predominantly consists of amino acids with hydrophilic side chains whereas the exterior portion of the binding pocket constitutes amino acids with more hydrophobic side chains forming the so-called "hydrophobic ridge" at the CRD entrance.[203,204] In addition, the entrance to the CRD is assembled with the "tyrosine gate" built by two aromatic amino acid side chains of Tyr48 and Tyr137 residues.[203,204] Taking this into account it is not surprising that mannopyranosides with an aromatic aglycon structure that can undergo favorable π-π stacking interactions with this tyrosine gate, such as p-nitrophenyl α-D-mannose (pNMan), show increased inhibitory potency of type 1 fimbriae when compared to methyl α-D-mannose (MeMan).[206] As a result, increasing hydrophobicity as in glycomacromolecule series three could also lead to an improved inhibitory potential. The variation in carbohydrate spacing, as introduced in series one, is an equally attractive parameter to investigate. Notably, even though the FimH receptor is monovalent, the manifold presentation of fimbriae of about 100 to 400 per bacterium could lead to multivalent binding when carbohydrates are arranged in a suitable distance.[207]

The assay employed was developed and carried out in the work group of Lindhorst and coworkers.[196] In their ELISA based assay they use a mannan coated microtiter plate. Bacterial adhesion or inhibition, respectively, is quantified by fluorescence intensity read out at 485 nm. Fluorescence is introduced by a GFP-tagged *E. coli* strain. The IC_{50} value of inhibition is determined based on a 50% reduction of fluorescence intensity; this reflects the inhibitor concentration that causes 50% inhibition of bacterial binding to the mannan surface.[196] Glycomacromolecules can act as inhibitors of *E. coli* binding because their carbohydrate ligands can block the FimH receptor (Figure 27). Thus, incubation of live bacteria with serial dilutions of glycomacromolecules allow for the determination of the IC_{50} value of the respective glycomimetic structures. However, absolute IC_{50} values for bacterial inhibition typically show variation from experiment to experiment. Relative inhibitory potency (RIP) values help in comparing the values obtained in these experiments. RIP values are determined by referencing the IC_{50} values of glycomacromolecules to the IC_{50} value obtained for MeMan always tested on the same plate.

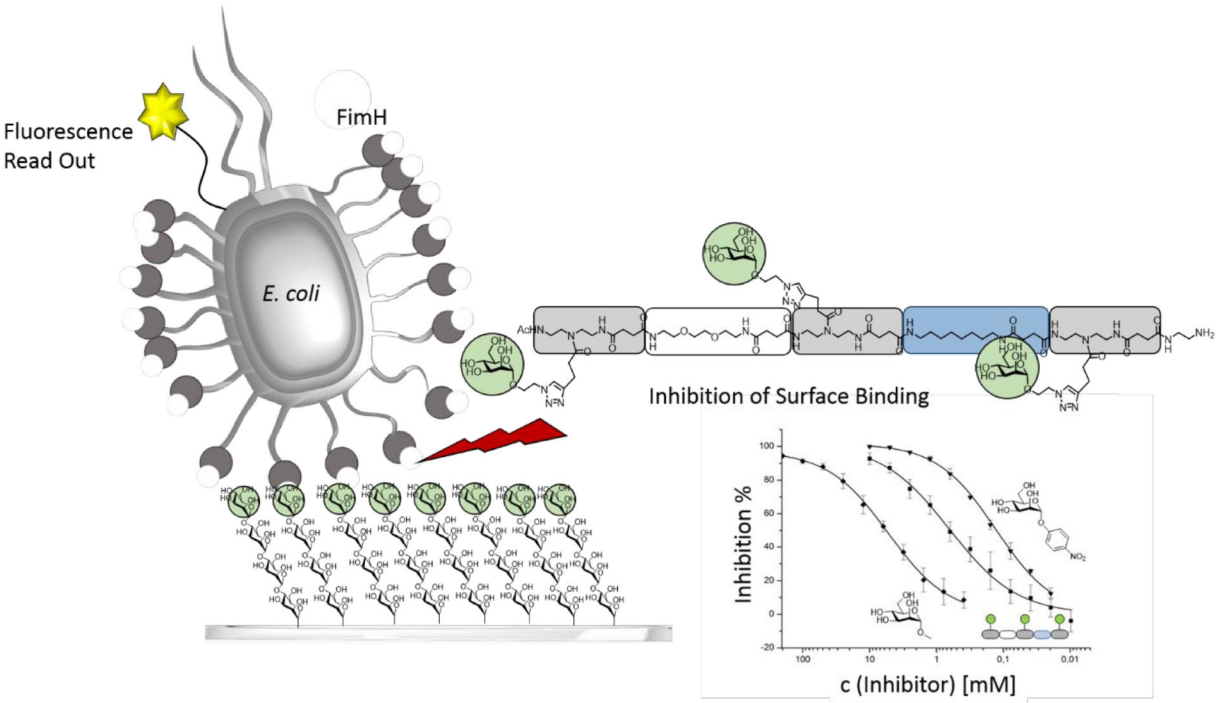

*Figure 27: Schematic presentation of the bacterial adhesion inhibition assay with E. coli FimH receptor and glycomacromolecule **4a** as inhibitor. Exemplary IC_{50} curves determined for **4a** in comparison to references methyl α-D-mannose and p-nitrophenyl α-D-mannose are also shown [adapted from [188] with permission from John Wiley and Sons].*

The results obtained for trivalent and pentavalent structures differing in backbone hydrophobicity, and trivalent structures differing in carbohydrate spacing are reported in Table 3. For comparison, the valency corrected RIP values were also calculated. The results show that inhibition of bacterial binding is possible by employing the investigated glycomacromolecules. When compared to the reference MeMan they show a higher inhibitory potency, but are less potent inhibitors than pNMan. The relative inhibitory potency thereby seems to be affected by similar design features as the binding affinity in ITC and SPR studies with ConA.

Previous studies with phenyl-linked carbohydrate ligands $\mathbf{x_2}$ on a glycomacromolecular scaffold showed that there is no correlation between the SV and the inhibitory potency of the glycomacromolecule.[120] This also holds true when comparing structures with hydrophilic EDS spacing (e.g. compare **4** and **5**). However, when comparing structures with hydrophobic ODS or AR spacing, an increase in inhibition potential can be observed with an increasing number of mannopyranoside ligands (e.g. compare **4b** and **5a** or **4d** and **5b**). Since the number of ODS or AR spacers, respectively, also increases for these structures from two to four building blocks effectively doubling the RIP value, it can be assumed that the increase in inhibitory potency is likely attributed to the increase of hydrophobic spacing rather than an increase in SV. This also correlates with the fact that hydrophobic

backbone properties enhance relative inhibitory potency when comparing hydrophilic and hydrophobic structures of the same valency (e.g. compare **4** and **4d** or **5** and **5b**).

Table 3: RIP and valency corrected RIP_{VC} values of glycomacromolecules varying in carbohydrate spacing and backbone hydrophobicity determined in bacterial-adhesion inhibition studies with the bacterial lectin FimH. MeMan was set as reference with RIP=1[adapted from [188] with permission from John Wiley and Sons].

Ligand	RIP	RIP_{VC}
MeMan	1	1
Man(4,5,6)-9 **1**	4.0±0.2	1.3
Man(3,5,7)-9 **1a**	3.0±0.5	0.9
Man(2,5,8)-9 **1b**	3.5±2.1	1.2
Man(1,5,9)-9 **1c**	3.8±2.3	1.3
Man(1,3,5)-5-EDS(2,4) **4**	7.2±0.5	2.4
Man(1,3,5)-5-EDS(4)-ODS(2) **4a**	9.3±0.1	3.1
Man(1,3,5)-5-ODS(2,4) **4b**	9.4±0.4	3.1
Man(1,3,5)-5-EDS(4)-AR(2) **4c**	8.0±0.9	2.7
Man(1,3,5)-5-AR(2,4) **4d**	10.4±0.9	3.5
Man(1,3,5,7,9)-9-EDS **5**	8.9±1.0	1.8
Man(1,3,5,7,9)-9-ODS **5a**	18.0±2.0	3.6
Man(1,3,5,7,9)-9-AR **5b**	21.0±1.9	4.2

*All data are the average of three (two for **2a**) independent experiments (triplicate determination per experiment). The negative control experiments with β-D-galactose bearing glycomacromolecules **6b**, **6c** and **6e** showed no inhibition of the bacterial adhesion to the mannosylated surface.*

However, as it was already observed in ITC and SPR measurements, changes in backbone hydrophobicity show a seven times weaker effect than the incorporation of a phenyl-linker $\mathbf{x_2}$ in

previous work.[120] The fact that the aforementioned glycomacromolecules are even less potent inhibitors than the pNMan control reaffirms the hypothesis of less pronounced secondary interactions with hydrophobic amino acid side chains near the carbohydrate binding site of lectins when hydrophobic properties are positioned in the backbone.

Moreover, it was previously demonstrated that the pentavalent structure Man(1,3,5,7,9)P-9 with phenyl-linker $\mathbf{x_2}$ to the carbohydrate moieties was the best inhibitor in a series of di- to decavalent phenyl linked glycomacromolecules.[120] The suspected reason for the outstanding inhibitory potency (twice to three times higher RIP value) was a one-sugar binding mode with an increased RIP due to optimal carbohydrate ligand density combined with the overall length of the molecule, leading to increased blocking of FimH receptor sites. To some extent this hypothesis is refuted by results in this work because glycomacromolecule Man(1,3,5,7,9)-9-EDS (**5**) should be very similar to compound Man(1,3,5,7,9)P-9 in regard to carbohydrate density and overall length. However, this molecule shows a 14 times lower RIP value. As a result, it is assumed that the density and number of hydrophobic moieties is a more decisive factor for the inhibition potential of glycomacromolecules than SV and spacing in this assay. This holds true when comparing the inhibitory potency of glycomacromolecules **1** to **1c** because variation in spacing shows no effect in interaction with the bacterial FimH receptor.

It is particularly striking that the backbone seems to have a significant negative impact on the ability to inhibit FimH binding. For structures comprising six (**1**-**1c**) compared to two spacer building blocks (**4**), the inhibitory potency is reduced by more than half leading to an inhibitory potency just as high as the monosaccharide control when normalized on the number of sugar units so that no multivalency effect can be observed for these structures (**1**-**1c**).

All in all, results with bacterial lectin FimH show very similar trends compared to the results obtained with model lectin ConA. It seems reasonable to suppose that the same overall effects that influence carbohydrate lectin interactions in SPR and ITC assays also influence the inhibitory potency of glycomacromolecules in the bacterial inhibition assay.

3.2 Presentation of Glycomacromolecules on Gold Nanoparticles

In the previous chapter, the concept of a glycomimetic system as tool for developing a better understanding of details of carbohydrate lectin interactions was introduced. It was shown that special design features, such as backbone hydrophobicity, can be varied in order to achieve an increase in overall binding avidity. Another factor that can be addressed is the multivalency. It was shown in Chapter 3.1 that changes in glycomacromolecule valency from one to five carbohydrate units increase affinity. In this chapter these two concepts are now combined and extended towards a higher level of multivalency (multivalency of multivalency) by the presentation of glycomacromolecules on gold nanoparticles (AuNPs).

Various macromolecular scaffolds have been successfully employed to create multivalent glycomimetics for studying carbohydrate lectin interactions (Chapter 1.1.2.3).[208-214] In recent years, AuNPs have received much attention in this research area because of their many advantageous properties (Figure 28). AuNPs are composed of an extremely inert and biocompatible material.[215] Due to its soft character, the noble metal gold (Au) can form stable bonds with sulphur-containing compounds via thiol or disulphide components.[216] This property makes AuNP synthesis simple and cost effective.

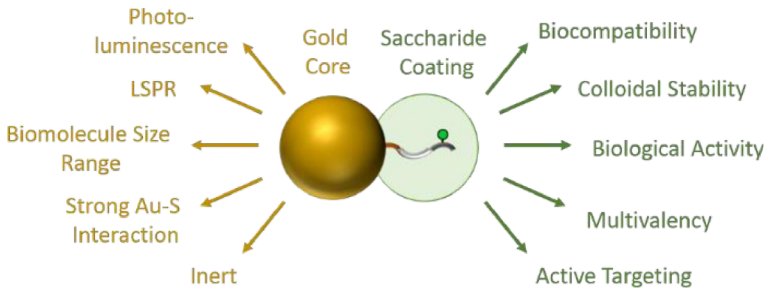

Figure 28: Advantageous properties of glyco-AuNPs resulting from metallic core and the glyco-coating [adapted from [216] with permission from Beilstein Journal of Organic Chemistry].

There are two different general strategies available for the synthesis of functionalized AuNPs (Figure 29).[217] The first strategy is based on a one-pot synthesis whereby Au^{3+} is reduced in the presence of thiol-carrying ligands.[216] This process was first described by Brust and co-workers.[218] They employed a two phase system of water and toluene in order to reduce gold tetrachloride ($AuCl_4^-$) with sodium borohydride ($NaBH_4$) in presence of dodecanthiol ($C_{12}H_{25}SH$). The phase transfer of $AuCl_4^-$ from water to toluene by the phase transfer agent tetraoctylammonium bromide (TOAB) allows for the attachment of self-assembled monolayers of thiol-ligands on the gold surface while the nuclei are growing.[218]

In the second strategy synthesis of gold nanoparticles stabilized with temporary compounds, like citrates, is followed by an exchange reaction with thiol-carrying ligands.[216] This synthetic strategy is

based on the Turkevich method.[219] The procedure described allows for the synthesis of citrate stabilized spherical nanoparticles in size ranges of 10 to 50 nanometres by addition of 1% sodium citrate solution to a boiling aqueous solution of chloroauric acid ($HAuCl_4$). The reaction can be followed by a color change to dark red.[216,218] Subsequently the temporary citrate ligand can be easily exchanged by the addition of a thiol-ligand because the S-Au-bond is preferred over citrate Au interaction.

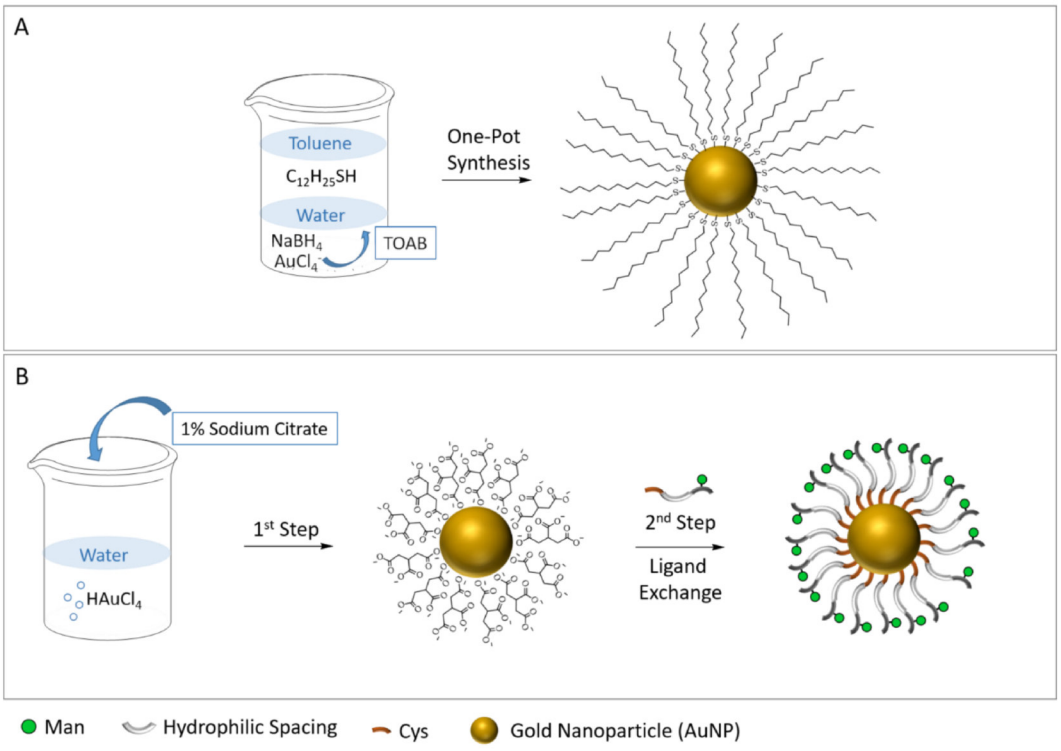

Figure 29: The two commonly employed approaches for AuNP synthesis. A: Brust method and B: Turkevich method.[218,219]

In this way a great variety of molecules can be easily installed on the AuNP forming a multivalent, dense surface of globular shape in similar size range as biomolecules.[220] When functionalized with ligands of sufficient stabilization properties, AuNPs exhibit a high degree of solubility as well as colloidal stability in buffer medium.[221] Without sufficient stabilization AuNPs tend to aggregate leading to a separation of liquid and particle phases. The DLVO theory (*Derjaguin*, *Landau*, *Verwey*, *Overbeek*) describes the stability of colloidally dispersed compounds, based on the interplay of attractive and repulsive forces between nanoparticles.[222] Attractive forces are van der Waals interactions and repulsive forces are electrostatic in nature resulting from the overlap of the electric double layer of nanoparticles whereby both forces are dependent on the interparticle distance. Stabilization of nanoparticles means a precise modification of the nanoparticle surface aiming either additional electrostatic or steric repulsive forces. Electrostatic stabilization can be achieved by installing charged compounds on the surface. Steric stabilization can be achieved by functionalization with higher molecular weight ligands or polymers forming a protective shield. With the introduction of

carbohydrate carrying ligands or other biomolecules functionalization can even lead to biological activity.

Moreover, AuNPs exhibit interesting and tuneable physical properties.[220] For example, they show unique optical properties highly dependent on the size and morphology of the gold core.[217] Small AuNPs with diameters between 0.5 and 2 nm lie in the range of the gold Fermi wavelength, and as such show photoluminescence properties.[223] When exceeding this size range, optical properties change. Instead of fluorescent emission, bigger AuNPs show a distinct absorption band, the so-called localized surface plasmon resonance (LSPR), with an absorption maximum around 520 nm resulting in the typical intensively red color.[216] This LSPR is evoked by a collective oscillation of free metal electrons stimulated by the impinging light. Thereby, AuNPs absorb light of the wavelength that corresponds to the oscillation frequency. The exact wavelength of LSPR on the AuNP surface is dependent on different structural parameters like size, shape, dispersion medium and degree of aggregation.[217] As soon as interparticle distance becomes smaller than nanoparticle diameter, the LSPR band broadens and shifts due to near-field resonance coupling leading to a macroscopic color change from red to blue/purple. Thus, these optical properties offer a great opportunity to monitor changes in the local environment of AuNPs which has led to the use of AuNPs in interesting applications such as colorimetric biosensors.

For example, Lin *et al.* employed different carbohydrate ligands for AuNP functionalization.[221] The corresponding glyco-gold nanoparticles (glyco-AuNPs) allowed for the reversible detection of the model lectin ConA and two other plant lectins in picomolar concentration using spectrophotometric monitoring of the LSPR. The induced color change from red to purple upon aggregation of glyco-AuNPs with lectin could even be detected by naked eye. A similar approach was described by Gibson *et al.* who created a library of glyco-AuNPs by immobilizing various monosaccharides on polymer-stabilized AuNPs.[224] This glyco-AuNP library was then tested for binding towards different lectins using a high-throughput assay. An advantage of their biosensing method was that only minimal analytical tools were required because no protein labelling or expensive infrastructure was needed. As a result, it was demonstrated that glyco-AuNPs give access to new analytical tools that in a simple and inexpensive way could help to easily detect low levels of lectins, and as such fight against the spread of infectious diseases caused by carbohydrate lectin interactions. In further studies the advantageous properties of glyco-AuNPs were demonstrated for other biological applications like HIV vaccines or X-ray contrast agents.[225,226]

As mentioned in Chapter 3.1 in order to use glycomacromolecule or glyco-AuNPs as therapeutic agents, in biosensing or other biological applications, it is important to employ a highly specific compound of high avidity. The question arises if similar changes in the design of the immobilized ligand,

that also influence glycomacromolecule lectin binding in solution, could have a positive impact on glyco-AuNP avidity to lectins. So far, most studies investigating variation in carbohydrate density or spacer type as well as length concentrate on preventing the undesirable aggregation of AuNPs in aqueous solutions of high ionic strength or buffer medium, respectively.[221,227,228] Only few studies have been performed that investigate the effect of structural features such as ligand architecture, carbohydrate valency, density or type on glyco-AuNP lectin binding. For example, Kikkeri *et al.* demonstrated the influence of nanoparticle shape on cellular uptake in different cancer cell lines.[229] They showed that rod shaped nanoparticles were taken up in highest portion, followed by star and then spherical shaped nanoparticles. In a second study they investigated the effect of multivalency and shape on bacterial binding employing heterogeneous glycodendrons immobilized on spherical and rod-shaped AuNPs. They identified the mannose multivalency and the nanoparticle shape as crucial factor for fine tuning the carbohydrate-protein interactions whereas the heterogeneity of the compounds only played a minor role.[230] In addition Russell *et al.* presented a colorimetric bioassay based on the aggregation of glyco-AuNPs for detection of ConA and a ricin surrogate, RCA_{120}.[231] Their focus was on determining the optimal surface coverage for maximal aggregation by investigating the effect of anchor chain length and carbohydrate density on aggregation behavior. Recently, Tsutsumi *et al.* demonstrated that AuNPs with monosaccharide-modified peptides showed preferred aggregation behavior with ConA when hydrophobic amino acids were installed next to the carbohydrate unit.[232] They explained the strong aggregation behavior by additional interactions of the hydrophobic amino acids with hydrophobic amino acid side chains near the CRD of ConA.

Based on these studies and the observations described for the work presented in Chapter 3.1, in this part of the thesis, the structural effect of the ligand installed on the AuNP surface was investigated in regards to lectin binding behavior with model lectin ConA. As only little effects of carbohydrate spacing and arrangement could be observed for glycomacromolecule lectin binding in solution (Chapter 3.1), the focus of this study lies on investigating the effects of backbone hydrophobicity and carbohydrate valency on the chemical, physical and binding properties of glycomacromolecule functionalized AuNP (Figure 30). Therefore, SPPoS was extended towards the synthesis and subsequent immobilization on AuNPs using a first set of glycomacromolecular compounds as a proof of concept approach.

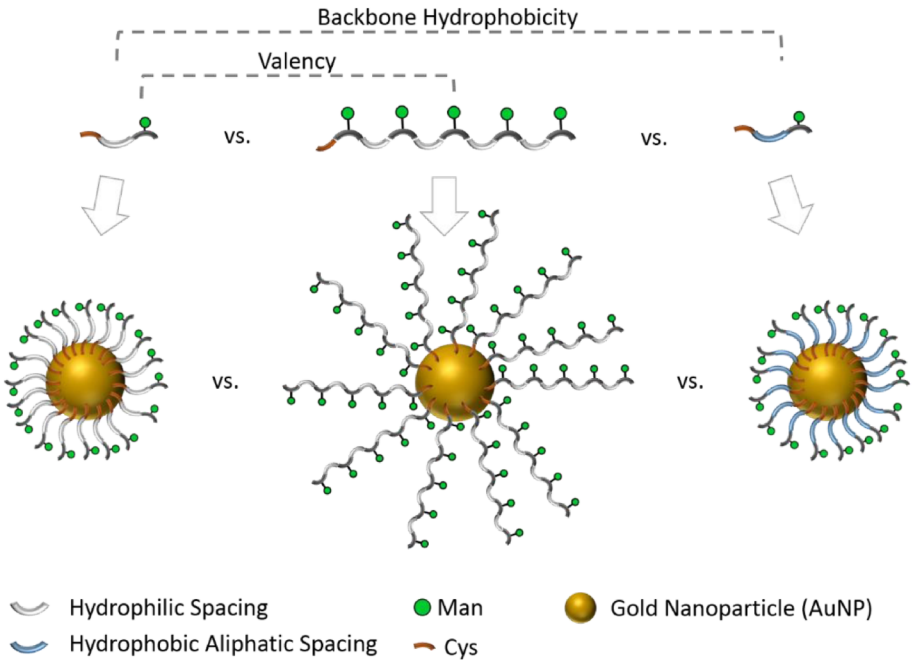

Figure 30: Overview of structural design features varied in the second part of this work. Glycomacromolecules are varied in backbone hydrophobicity and valency and installed on AuNP surface.

3.2.1 Solid Phase Synthesis of Thiolated Glycomacromolecules

In this part of the thesis the influence of backbone hydrophobicity and valency of glycomacromolecules when immobilized on AuNPs was investigated for a first series of structures. Therefore, three different glycomacromolecules were synthesized employing SPPoS in order to provide full control over building block sequence and characteristics. As already introduced in Chapter 3.1.1.1, a library of functional and spacer building blocks available for SPPoS were used for glycomacromolecule synthesis.[95-103] The functional building block TDS with a triple bond in the side chain enabled sugar attachment via CuAAC reaction (Figure 31). A α-D-mannose azide derivative was employed because the α-D-mannopyranoside specific model lectin ConA was targeted. EDS was used as a spacer building block to provide more hydrophilic backbone characteristics (Figure 31). In order to also test for hydrophobic backbone properties, the hydrophobic aliphatic ODS building block was employed (Figure 31). Building blocks were synthesized following well established protocols and were obtained in moderate to high yield as well as high purities.[95,100,131] Syntheses were confirmed by ^{1}H-NMR, ESI-MS and HPLC analysis.

As the resulting glycomacromolecules were to be installed on AuNP surfaces, characteristics other than spacing and carbohydrate positioning were important. For example, a thiol group had to be introduced to one end of the glycomacromolecule to enable Au-S-bond formation. Moreover, it was desirable to achieve high stabilization of the resulting AuNPs. Therefore, a carboxyl end group on the other end of the glycomacromolecule was incorporatedl to complement the steric stabilization provided by glycomacromolecule length with electrostatic stabilization. These two functionalities were introduced by combining artificial building blocks with natural amino acids. The thiol group was introduced by

coupling of L-cysteine as last building block on solid support (Figure 31). The carboxyl group was installed by resin choice. A resin with trityl linker was used which was preloaded with the amino acid L-glycine (Figure 31).

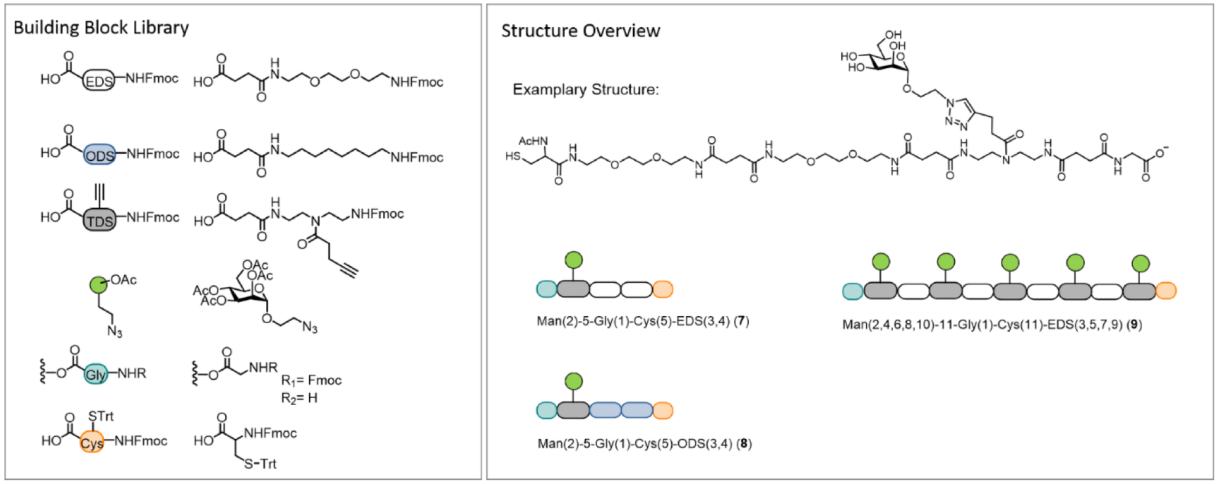

Figure 31: Overview of building blocks and natural amino acids employed in SPPoS (left) and overview of glycomacromolecule structures for AuNP functionalization (right).[100]

With these building blocks in hand SPPoS was employed to synthesize glycomacromolecules suitable for subsequent functionalization of AuNPs. SPPoS of hydrophilic glycomacromolecules was performed on a PS resin with trityl linker preloaded with glycine. After resin swelling in DCM, the first coupling step was performed employing 5 eq of building block, 4.9 eq of PyBOP and 10 eq of DIPEA. Due to high resin loading of 0.44 mmol/g capping of the remaining glycine amine groups was performed with acetic anhydride after the first coupling step resulting in approximately half of the initial resin loading. Afterwards Fmoc deprotection was accomplished with a 25% piperidine solution in DMF. By repeating coupling and deprotection steps, all further building blocks were assembled on solid support. The last building block, L-cysteine, was used in order to introduce the thiol functionality at the end of the glycomacromolecule. After capping of the *N*-terminal site with acetic anhydride, CuAAC reaction with protected 2-azidoethyl mannose was performed. With the trityl linker, carbohydrate deprotection could not be performed on solid support because the basicity of the 0.1 M solution of sodium methoxide in methanol was high enough to cleave the glycomacromolecule from solid support. Therefore, cleavage was performed directly after CuAAC reaction and carbohydrate deprotection followed in solution. Therefore, the glycomacromolecule was dissolved in methanol and the same amount of a 0.2 M methoxide in methanol solution was added to obtain a final methoxide concentration of 0.1 M. The reaction mixture was shaken for one hour before Amberlyte resin (hydrogen form) was added to neutralize the solution. The resin was filtered off and methanol was removed under reduced pressure. The final glycomacromolecule was isolated by lyophilisation. Subsequently TFA removal was performed to exchange TF-acetate counter ions by acetate. SPPoS of

the hydrophobic glycomacromolecule was performed on a Tentagel®-trityl-Gly-Fmoc resin because coupling of ODS building block on the hydrophobic PS resin was not possible leading to high impurities due to deletion sequences. The resin loading for the Tentagel® resin was much lower than for PS resin so that the capping step after the first building block coupling could be omitted. All other steps were proceeded as described for the PS resin.

In this way three different glycomacromolecules were synthesized (Figure 31). All structures **7**-**9** exhibit a thiol functionality on one end of the glycomacromolecule that can be used for AuNP functionalization. On the other end of the glycomacromolecule, a carboxyl group is installed for better stabilization of the resulting AuNPs. Both glycomacromolecules **7** and **8** are monovalent with one α-D-mannopyranoside unit, but differ in their backbone characteristics. Glycomacromolecule **7** with EDS spacer building block is rather hydrophilic while glycomacromolecule **8** with ODS building block is rather hydrophobic. The spacer building blocks for these two compounds are not only installed to vary backbone hydrophobicity, but also in order to increase the overall chain length leading to potentially enhanced steric stabilization of AuNPs after functionalization. Glycomacromolecule **9** shows the same spacer properties as compound **7** but exhibits a higher valency of five carbohydrate ligands. All glycomacromolecules were purified by preparative HPLC. Syntheses for the three glycomacromolecular structures was confirmed by ^{1}H-NMR, RP-HPLC, HRMS and MALDI-TOF.

The RP-HPLC and MALDI-TOF-MS analysis of hydrophobic compound **8** revealed the formation of a thioether side product as well as disulphide formation (Figure 32A and B). The formation of disulphides from thiols in solution is not surprising and cannot be completely prevented because oxidation occurs with atmospheric oxygen. However, the formation of a thioether side product was unexpected. Due to the fact that the L-cysteine thiol group is trityl-protected throughout solid phase synthesis the sugar deprotection step in solution was identified as critical reaction step for side product formation. An analogous thioether formation from disulphides was previously described in literature.[233] The mechanism starts with basic abstraction of the C_α proton of L-cysteine followed by sulphur extrusion. Subsequently, the resulting alkene moiety can be attacked by the thiolate anion resulting in a thioether (Figure 32C). This mechanism may also happen during sugar deprotection of the glycomacromolecules in solution as it also occurs under basic conditions. However, the described side product formation was only observed for glycomacromolecule **8** with hydrophobic ODS spacing. The reason might be that the hydrophobicity of the compound promoted the thioether formation. Thereby, hydrophobic intermolecular interactions of the compounds might be responsible for hydrophobic glycomacromolecules being in closer proximity to each other than hydrophilic compounds facilitating the intermolecular side reaction. Unfortunately, the thioether side product could not be removed by

preparative HPLC. Due to the fact that it should not interfere with AuNP functionalization that should only occur with free thiol groups, compound **8** was used without further purification.

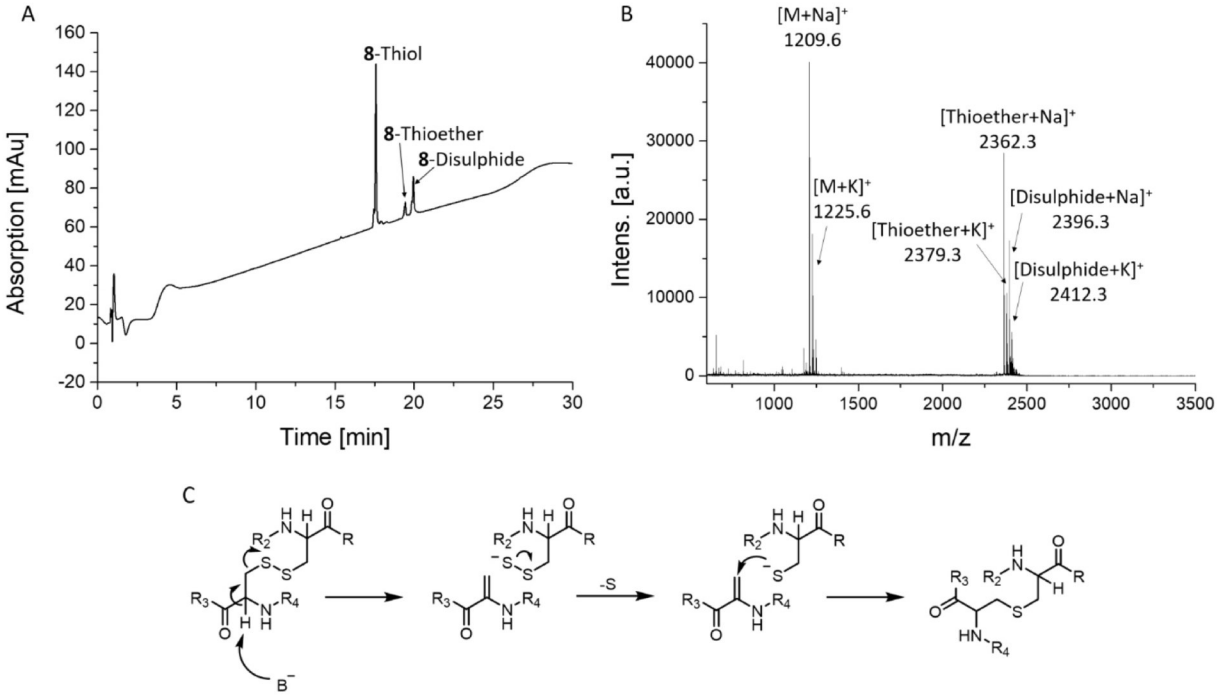

*Figure 32: A. RP-HPLC chromatogram of glycomacromolecule **8** displaying the product, thioether and disulphide peaks. B: MALDI-TOF-MS of glycomacromolecule **8** with m/z peaks for the product, thioether and disulphide. C: Mechanism of thioether formation suggested in literature.*[100,233]

Figure 33 shows an exemplary ^{1}H-NMR spectrum of glycomacromolecule **7**. Analogous to the ^{1}H-NMR spectra of glycomacromolecules in Chapter 3.1.1.2, typical resonances for TDS and EDS building blocks as well as the carbohydrate moiety and acetyl and group are displayed. Resonances of all mannopyranoside hydroxyl groups do not occur due to proton exchange with deuterated water. However, -NH protons can be assigned to a singlet at 8.27 ppm. The succinyl protons 7 and 8 of both building blocks EDS and TDS collapse into a multiplet in a range from 2.60 to 2.46 ppm. The ethylene protons of TDS can be further assigned to a multiplet signal from 3.51 to 3.32 ppm, partially overlapping with EDS protons 4. The two other EDS proton pairs 5 and 6 are shifted to low field due to deshielding of the neighboured oxygen atoms and form a multiplet from 3.70 to 3.58 ppm. The linker protons between TDS building block and carbohydrate moiety can be assigned to several multiplet signals at 4.66-4.62, 4.12-4.06, 3.95-3.90 and 3.06-2.98 ppm. The triazole proton gives a singlet at 7.88 ppm and the linker proton a gives a triplet at 2.80 ppm. Moreover, the mannopyranoside moiety can be assigned to typical resonances at 3.88-3.85, 3.77-3.72, 3.70-3.58 and 3.06-2.98 ppm. The signal for anomeric proton f is overlapped by the signal caused by the NMR solvent at 4.79 ppm. The acetyl protons 2 can be found as a singlet at 2.07 ppm. In addition to these artificial building blocks the protons that can be assigned to the natural amino acids L-cysteine and L-glycine are highlighted in red.

The L-glycine proton 11 gives a singlet that is partially overlapping with linker proton e and as such can be assigned to the multiplet signal from 3.95 to 3.90 ppm. Proton 3 of L-cysteine can be assigned to a triplet at 4.46 ppm. The C_β proton of L-cysteine with the neighboured thiol group can be found as doublet at 2.91 ppm with a corresponding coupling constant. All in all, integration of all proton signals is in accordance with the expected number of protons contributed to complete conversion in all reaction steps and successful synthesis of glycomacromolecule **7**. Similar spectra could be obtained for glycomacromolecules **8** and **9**.

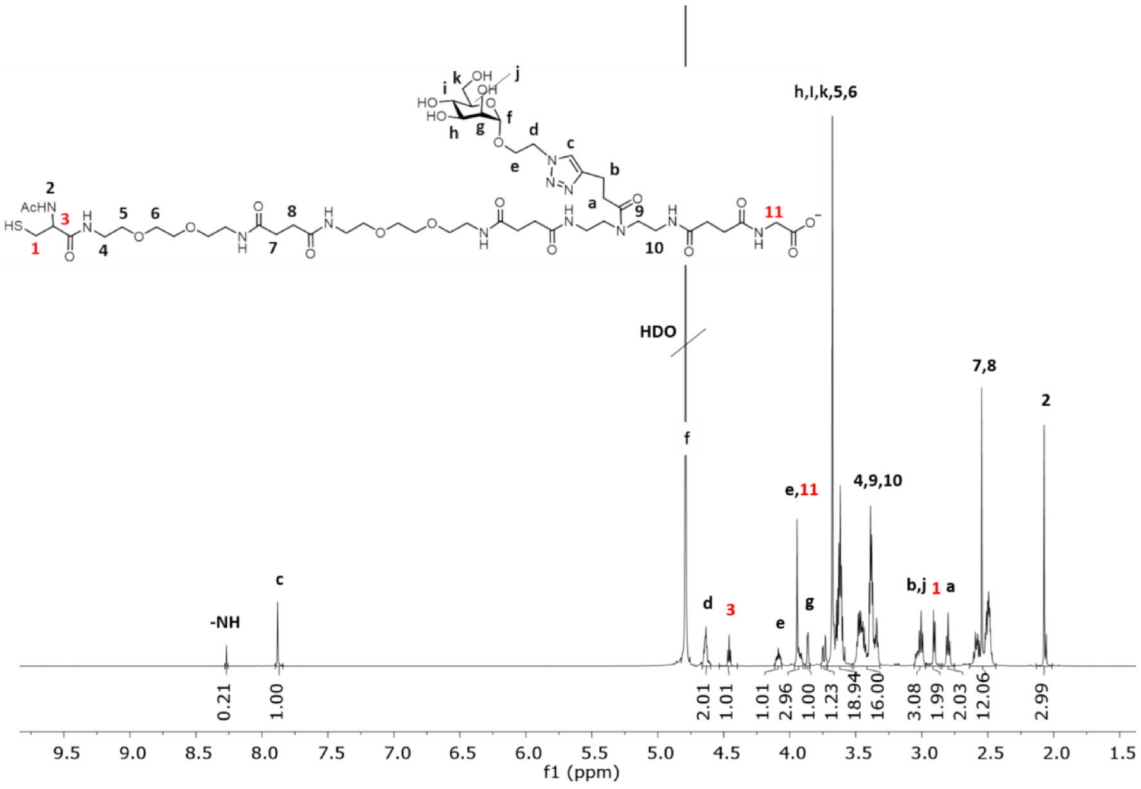

*Figure 33: Exemplary ^{1}H-NMR (600 MHz, D_2O) of glycomacromolecule **7**. Protons of natural amino acids L-cysteine and L-glycine are highlighted in red.*

3.2.1.2 Capping of Thiolated Glycomacromolecules with N-Ethylmaleimide

The analysis of glycomacromolecules **7**-**9** showed that full control over their structure is difficult due to unavoidable formation of disulphides. For glycomacromolecule **8** it was even more complicated due to additional thioether side product formation. Therefore, it was decided to react half of glycomacromolecules **7** and **9** with *N*-ethylmaleimide in order to cap the free thiol group and to obtain monodisperse precision glycomacromolecular structures. This should give the same glycomacromolecules in solution as presented on AuNPs to be compared in later binding studies with model lectin ConA.

Capping was performed by dissolving the respective glycomacromolecule together with excess of the reducing agent tris(2-carboxyethyl)phosphine (TCEP) in degassed Hepes buffer (pH 7). The reaction

mixture was flushed with nitrogen and shaken for 48 h before 15 equivalents of *N*-ethylmaleimide were added under nitrogen. After 8 h shaking the capped glycomacromolecule **7a** or **9a**, respectively, were isolated by preparative HPLC in moderate yields and high purity. The synthesis was confirmed by ^{1}H-NMR, RP-HPLC, HRMS and MALDI-TOF analysis.

Figure 34 shows an exemplary ^{1}H-NMR spectrum and MALDI-TOF-MS of capped glycomacromolecule **7a**. In the MALDI-TOF-MS it can clearly be seen that only product m/z signals and no disulphide signals occur in mass spectrometry.

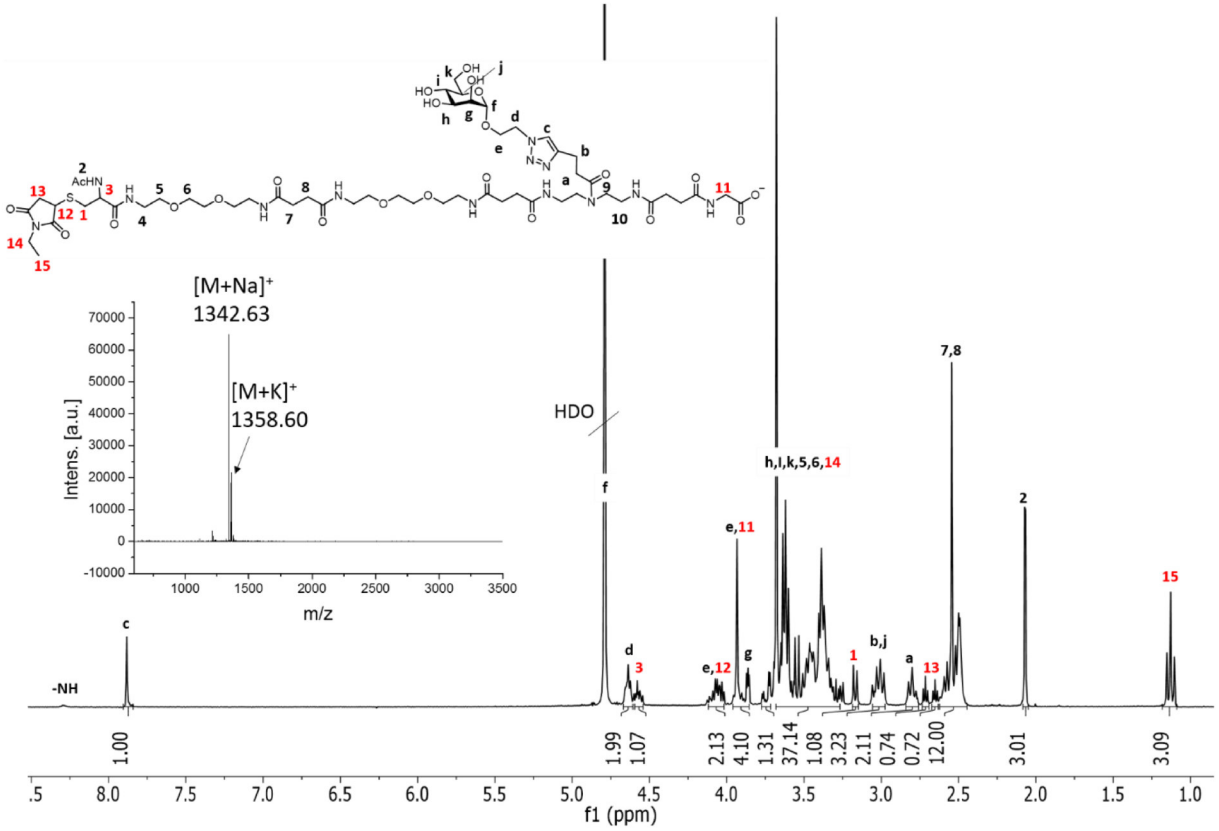

*Figure 34: Exemplary ^{1}H-NMR (600 MHz, D_2O) and MALDI-TOF spectra of glycomacromolecule **7a**. Protons of natural amino acids L-cysteine and L-glycine as well as protons of N-ethylmaleimide are highlighted in red.*

In addition, the ^{1}H-NMR shows that capping of the thiol group with *N*-ethylmaleimide was successful. First indications are the upfiled shifts of C_α and C_β protons of L-cysteine when compared to ^{1}H-NMR spectrum of glycomacromolecule **7** (Figure 33) due to changes in their chemical environment caused by the capping reaction. Moreover, the resonances for *N*-ethylmaleimide appear in the spectrum and are highlighted in red. The protons of the ethyl group can be assigned to a triplet at 1.13 ppm and a second signal in the range of 3.71-3.24 ppm that is overlapped by signals for EDS and mannopyranoside protons. Proton 12 can be assigned to a multiplet at 4.14-4.01 ppm again partly overlapping with linker protons. Neighbouring protons 13 can be found at lower field forming two triplet signals at 2.72 and 2.65 ppm. Integration of all proton signals is in accordance with the expected number of protons

contributed to complete conversion in all reaction steps and successful synthesis of glycomacromolecule **7a**.

3.2.2 Functionalization of Gold Nanoparticles with Thiol-Glycomacromolecules

After successful synthesis of thiolated glycomacromolecules varying in backbone hydrophobicity and valency, the next step was to functionalize AuNPs with these compounds. AuNPs were synthesized by a collaboration partner, Kristina Wagner, in the Karg group at Heinrich Heine University in Düsseldorf. AuNPs were synthesized employing the Turkevich-method to obtain spherical AuNPs with a diameter of about 14 nm.[219] Therefore, an aqueous solution of $HAuCl_4$ was brought to boil before a hot aqueous solution of sodium citrate dihydrate was added rapidly under vigorous stirring. Reduction of Au^{3+} to Au^0 and formation of citrate stabilized AuNPs (cAuNPs) could be followed by a color change to dark red. Purification was performed by several consecutive centrifugation steps and resuspension in MilliQ water. TEM-analysis showed that AuNPs were spherical and monodisperse with a diameter of 14.1±1.2 nm (Figure 35A and B).

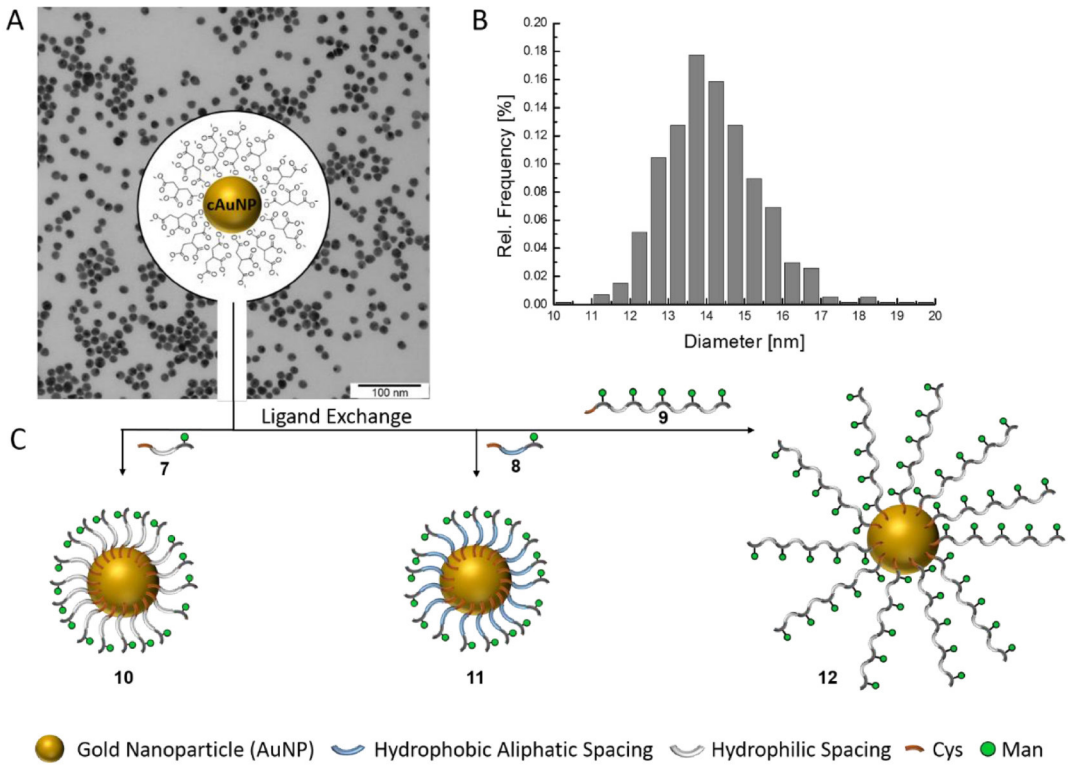

*Figure 35: A: TEM image of citrate stabilized AuNPs (cAuNPs). Inset: Sketch of citrate stabilized AuNP, B: TEM derived histogram of citrate stabilized AuNPs with derived diameter of 14.1±1.2 nm, C: Ligand exchange reaction of citrate stabilized cAuNPs with glacomacromolecules **7**-**9** resulting in glyco-AuNPs **10**-**12**.*[100]

Subsequent ligand exchange was performed as part of this work following established protocols (Figure 35C).[216] Citrate stabilized AuNPs (cAuNPs) dispersed in MilliQ water at about 5 nM concentration were stirred vigorously while excess of the thiolated glycomacromolecule ligand **7**, **8** or **9**, respectively, was added dropwise. The reaction mixture was stirred slowly for an additional 24 h in

the dark. During this time period the temporary citrate ligand was exchanged by the respective glycomacromolecules **7**-**9** resulting in glyco-AuNPs **10**-**12** (Figure 35C). Purification of glyco-AuNPs was performed by three consecutive centrifugation steps and resuspension in MilliQ water.

The obtained glyco-AuNPs were characterized by UV-Vis absorbance spectroscopy and DLS in comparison to cAuNPs. DLS measurements were performed by Kristina Wagner in the Karg group. The UV-Vis spectra display the typical LSPR band of spherical AuNPs with an absorption maximum around 520 nm (Figure 36A). The maximum for cAuNPs can be found at 517 nm whereby LSPR is redshifted for the obtained glyco-AuNPs. For compound **10** the maximum lies at 521 nm and the maximum for compounds **11** and **12** can be found at 522 nm. This redshift is caused by a change of local refractive index in close AuNP vicinity and as such is the first indication for successful ligand exchange. Moreover, the single peaks with small widths in the UV-Vis spectrum show the low dispersity of the systems. It is important to note that absorbance after LSPR maximum drops to zero and that LSPR width did not change significantly for glyco-AuNPs **10**-**12** in comparison to cAuNPs indicating good stabilization and dispersion of the compounds. The presence of aggregates would cause near-field resonance coupling between glyco-AuNPs in close proximity and thus could be determined by a significant broadening of LSPR peak width, a shift as well as decrease in intensity of LSPR maximum, and an increase of absorbance for higher wavelength approaching IR range.

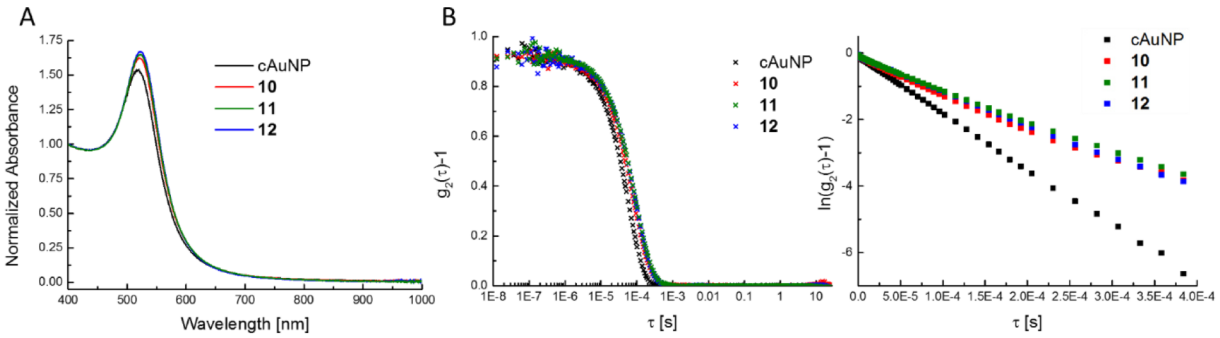

*Figure 36: A: UV-Vis spectra of cAuNPs in comparison to glyco-AuNPs **10**-**12**. B: Autocorrelation function and Cumulant plot determined by DLS of cAuNPs in comparison to glyco-AuNPs **10**-**12**.*[100]

DLS measurements resulted in the intensity-time autocorrelation function shown in Figure 36B. The monomodal exponential decay is characteristic for the Brownian motion of spherical, well stabilized colloids. The second-order Cumulant analysis of the autocorrelation functions resulted in hydrodynamic radii in MilliQ water for cAuNPs and glyco-AuNPs (Figure 36C, Table 4). The obtained hydrodynamic radii confirm a successful ligand exchange reaction. It can clearly be seen that hydrodynamic radii increase for glyco-AuNPs in comparison to cAuNPs which is consistent with the higher molecular weight and length of these glycomacromolecular ligands compared to the temporary citrate ligand. This also explains the higher hydrodynamic radius of **12** when compared to **10**, because

glycomacromolecule **9** is pentavalent and exhibits longer scaffold chain length than glycomacromolecule **7**. However, glyco-AuNP **11**, which is functionalized with glycomacromolecule **8** which has the same number of building blocks as **7** and as such is expected to show a similar chain length, also displays a larger hydrodynamic radius than **10**. This difference in behaviour can probably be rationalized by the difference in backbone characteristics from more hydrophilic to hydrophobic by the introduction of ODS building block in **8**. For example, the more hydrophobic glycomacromolecules covering the nanoparticle surface might display higher intermolecular interactions between the hydrophobic chains im comparison to their more hydrophilic counterparts. This could result in a more parallel alignment whereas the hydrophilic compounds might rather be present in a coiled conformation.

As a next characterization step the functionalization degree of glycomacromolecules per glyco-AuNP was determined. Two different colorimetric methods were employed. The first method determines the number of carbohydrates presented on the AuNP surface and is based on a modified phenol sulphuric acid (PSA) method originally introduced by Dubois and coworkers.[169,234] In this method, carbohydrates that are attached to the glycomacromolecule scaffold are hydrolysed by the rapid addition of sulphuric acid and the evolving heat. This further leads to the formation of a furfural intermediate, and in presence of phenol a yellow dye is obtained (Figure 37B). The absorbance at 490 nm was compared to a standard curve prepared with a series of dillutions consisting of known mannose concentrations to derive the unknown carbohydrate concentration. As a negative control, cAuNPs were tested in the same assay setup. Unfortunately, cAuNPs resulted in a wrong positive signal at 490 nm in UV-Vis spectroscopy (Figure 37A). Even though this background was subtracted from the obtained absorbance values at 490 nm, the method was highly prone to error (Table 4). This is why a second colorimetric method was employed to more precisely determine the functionalization degree of glyco-AuNPs. The so-called TBO-titration with the dye Toluidine Blue O (TBO) was adapted from an established protocol in the Hartmann group.[235] This method is based on the ionic interaction of the positively charged TBO dye with the negative charge of a carboxyl group in alkaline aqueous solution (Figure 37C). As glycomacromolecules were equipped with an acid end group in order to enhance colloidal stability TBO-titration was applicable for compounds **10**-**12**. Quantification was possible by measuring TBO absorbance at 633 nm. This wavelength was not impaired by absorbance of unfunctionalized AuNPs. However, this procedure is highly pH sensitive and as such could lead to unreliable results as glyco-AuNPs were dispersed in MilliQ water affecting the final pH value. When compared to previously reported literature values of PEG molecules of comparable size and hydrodynamic radius, PSA determined values seem to be in a more plausible range for AuNP surface loading.[236] Thus, it was decided to refer to PSA values in the following paragraphs. Nevertheless, TBO values confirm relative surface loading when comparing the glyco-AuNPs with one another. (Table 4).

Table 4: DLS derived hydrodynamic radii (R_H) in MilliQ water and degree of glycomacromolecule (GM) functionalization as determined by two methods: phenol sulfuric acid method (PSA) and Toluidine Blue O-titration (TBO). The degree of carbohydrate (C) functionalization and average of occupied surface area were calculated and are also listed.[100]

AuNP	R_H in Water [nm]	Degree of GM Functionalization per NP (PSA)	Degree of GM Functionalization per NP (TBO)	Average Degree of C Functionalization per NP	Average Occupied Surface Area per GM [nm²]
cAuNP	8.5±0.1	-	-	-	-
10	11.7±0.1	312±218	2210±553	~312	~2.0
11	13.3±0.3	231±98	1430±377	~231	~2.7
12	13.5±0.1	242±2	1620±206	~1210	~2.5

From the obtained values an average degree of carbohydrate functionalization and occupied surface area could be calculated (Table 4). An average occupied surface area of 2 nm^2 per glycomacromolecule lay within the expected range and showed that the ligand exchange reaction of temporary citrate ligands was effective. As a result, it was possible to obtain a densely packed glyco-AuNP surface which was desirable for the following binding studies with ConA.[231] Russell *et al.* investigated AuNPs coated with mannose ligands toward their aggregation behaviour with ConA. They systematically varied the amount of carbohydrate on the surface and found that a monolayer of 100% mannose led to maximal aggregation with ConA.

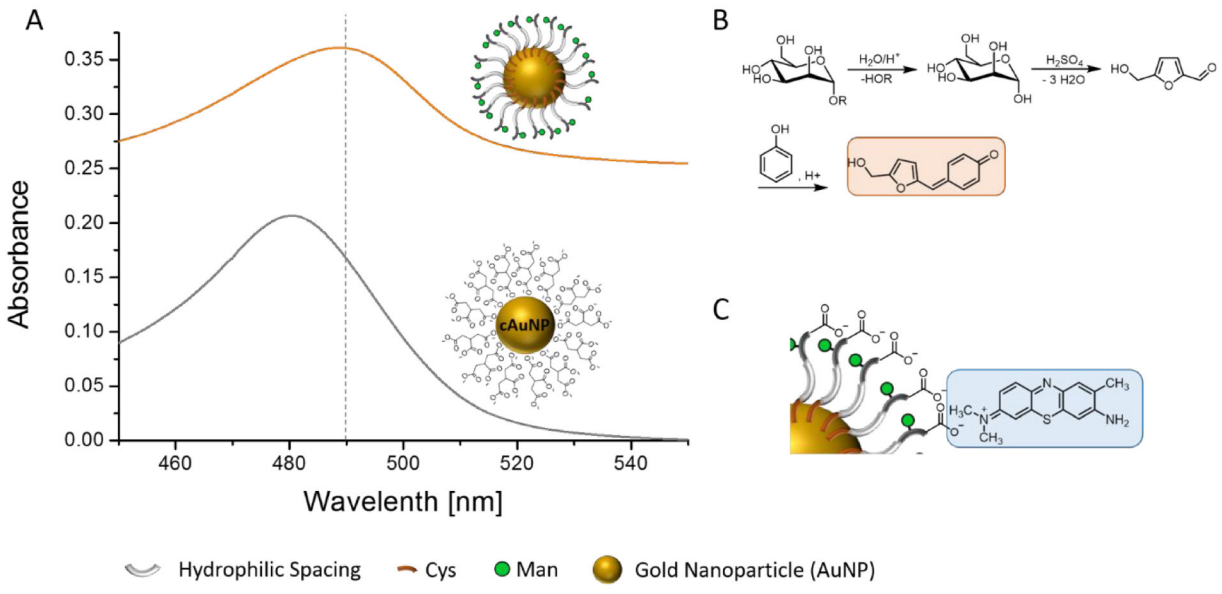

*Figure 37: A: UV-Vis spectrum recorded after PSA treatment of glyco-AuNP **10** and cAuNPs demonstrating the background signal at 490 nm. B: Reaction Scheme for PSA. C: Schematic illustration of TBO interaction.*

Besides the degree of functionalization introduced by glycomacromolecules, colloidal stability of glyco-AuNPs was also studied. This was especially important for ascertaining whether binding studies with

lectins in buffer media could be conducted. The first step towards buffer stability examination was a simplified test checking for stability in solution with increasing sodium chloride (NaCl) concentration over a 24 h time period. Therefore, glyco-AuNPs **10**-**12** were dispersed in MilliQ water in a 96-well microtiter plate. Subsequently, the same amount of a NaCl solution was added resulting in final concentrations of 5 nM glyco-AuNP and 0, 12.5, 25, 37.5, 50, 100, 125, 250, 500 and 1000 mM NaCl. Absorption spectra from 400-700 nm were recorded in defined time intervals over a 24 h time period (Figure 38). Comparing the spectra, special focus was given to the shape of LSPR band. Broadening or shifting indicated aggregation and thus less colloidal stability under the tested conditions. As shown in Figure 38, cAuNPs readily aggregated at low NaCl concentrations > 25 mM with complete disappearance of LSPR band. In contrast, all glyco-AuNPs **10**-**12** exhibited good stability even at high NaCl concentrations after 24 h. Only at very high NaCl concentrations > 250 mM small shifts in LSPR maximum could be observed for glyco-AuNPs **10** and **11** (that are functionalized with shorter glycomacromolecular structures **7** and **8**). However, for glyco-AuNP **12** even at NaCl concentrations of 1000 mM only insignificant shifts of LSPR maximum could be observed. This was consistent with higher steric stabilization given by higher molecular weight glycomacromolecule **9**.

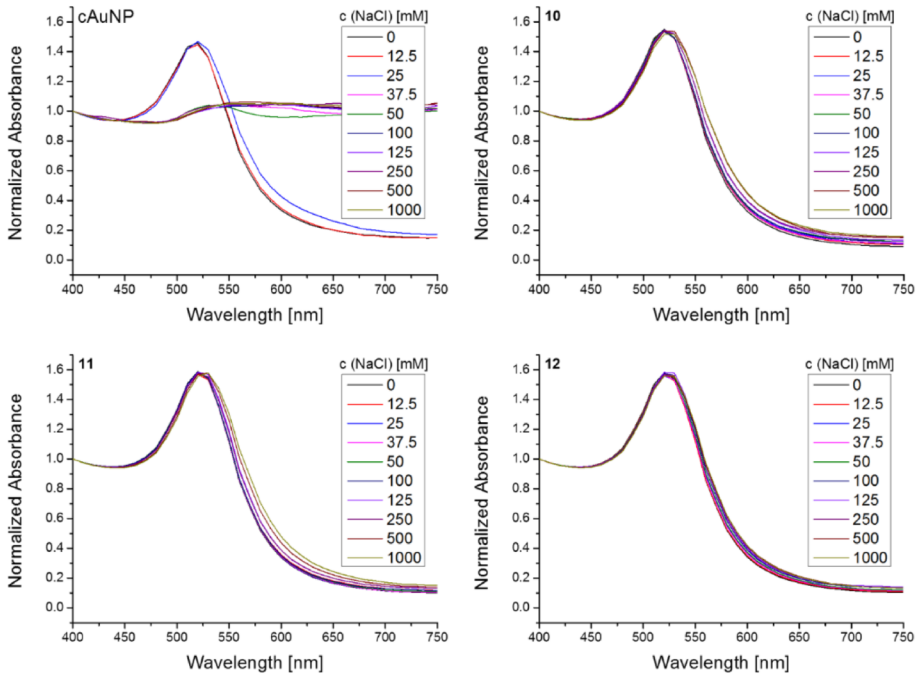

*Figure 38: UV-Vis absorbance spectra of cAuNP and glyco-AuNPs **10**-**12** testing for sodium chloride stability after 24 h incubation time.*[100]

The next step was to investigate buffer stability of glyco-AuNPs **10**-**12**. Due to the fact that tetravalent ConA was targeted in following binding studies, glyco-AuNPs were tested with Lectin Binding Buffer (LBB, pH 7.40 ± 0.01, 10 mM Hepes, 50 mM NaCl, 1 mM $CaCl_2$, 1 mM $MnCl_2$). In this buffer at pH 7.4 ConA should be predominantly present in its tetravalent conformation. The presence of sodium chloride ensured similar ionic strength as under physiological conditions and the addition of calcium

and manganese salts in LBB was necessary to maintain carbohydrate binding activity to ConA. While the NaCl concentration of 50 mM should not be problematic given the results of the colloidal stability tests, it was unclear how additional salts might influence glyco-AuNP stability. For LBB stability test glyco-AuNPs were centrifuged and redispersed in LBB at 5 nM concentration and their UV-Vis absorbance from 400-700 nm was followed over 24 h in comparison to the same dispersion in MilliQ water. This study revealed no change in LSPR band and thus no unwanted aggregation of glyco-AuNPs in LBB.

All in all, functionalization of AuNPs with precision glycomacromolecules by ligand exchange was successful leading to a high degree of functionalization accompanied by high colloidal stability even in solutions of high ionic strength which makes them valuable tools for studying lectin binding.

3.2.3 Lectin Binding Studies

For lectin binding studies ConA, was chosen as target molecule because it is a model lectin and well characterized in regard to its binding behavior toward different glycomimetic structures. Thus, the results obtained could easily be compared to literature values, as well as previous results in the Hartmann group. This was desirable because this part of the work specifically focused on the establishment of glycomacromolecules as ligands for AuNPs as proof of concept.

For the first lectin binding assay, the aggregation behavior of glyco-AuNPs **10**-**12** in presence of ConA was investigated. Glyco-AuNPs were dispersed at final concentrations of 5 nM in a 96-well plate. ConA was subsequently added in increasing concentrations ranging from 20 nM to 10,000 nM followed by a 30 min incubation time before the UV-Vis spectra from 400 to 750 nm were recorded. This assay was based on literature studies of glyco-AuNPs for biosensor applications.[231,237-239] Therein, aggregation of glyco-AuNPs in presence of lectins was monitored by naked eye due to a clearly visible color change from red to blue/purple. This color change could also be observed in this work when increasing concentrations of ConA were added to the glyco-AuNP dispersion (Figure 39B). In UV-Vis spectroscopy this color change could be followed by a shift of the LSPR maximum to a higher wavelength with a simultaneous increase of absorbance at 700 nm (Figure 39C, E, F). Corresponding dose-dependent binding isotherms for the aggregation behavior could be obtained by plotting the normalized absorbance at 700 nm (normalized to absorbance at 400 nm) in dependence of ConA concentration (Figure 39A). The obtained binding isotherms showed the same behavior for all glyco-AuNPs at low ConA concentrations (< 100 nM) with constant low absorbance at 700 nm. In this concentration range, glyco-AuNPs were individually dispersed and exhibited their usual optical behavior with no LSPR shift and intense red color. However, a steep ascent in normalized absorbance at 700 nm, reaching absorbance values approximately three times higher than the original value, could be observed when

ConA concentration increased further (150 nM < c(ConA) < 400 nM). This observation could be explained by the formation of aggregates whereby individual glyco-AuNPs were cross-linked by ConA binding sites. The decrease in interparticle distance upon binding led to near-field plasmon resonance coupling, which in turn resulted in the observed increase of absorbance at 700 nm. It was expected that further increases in ConA concentration would lead to stronger aggregation behavior with rising absorbance values at 700 nm. In contrast, further increase in ConA concentration resulted in the opposite outcome with decreasing absorbance at 700 nm after a maximum value has been reached. This observation can be rationalized by the fact that glyco-AuNPs at high lectin concentration became completely saturated by ConA so that crosslinking was diminished and glyco-AuNPs more and more behaved like individually dispersed particles resulting in a reduction in absorption at 700 nm.

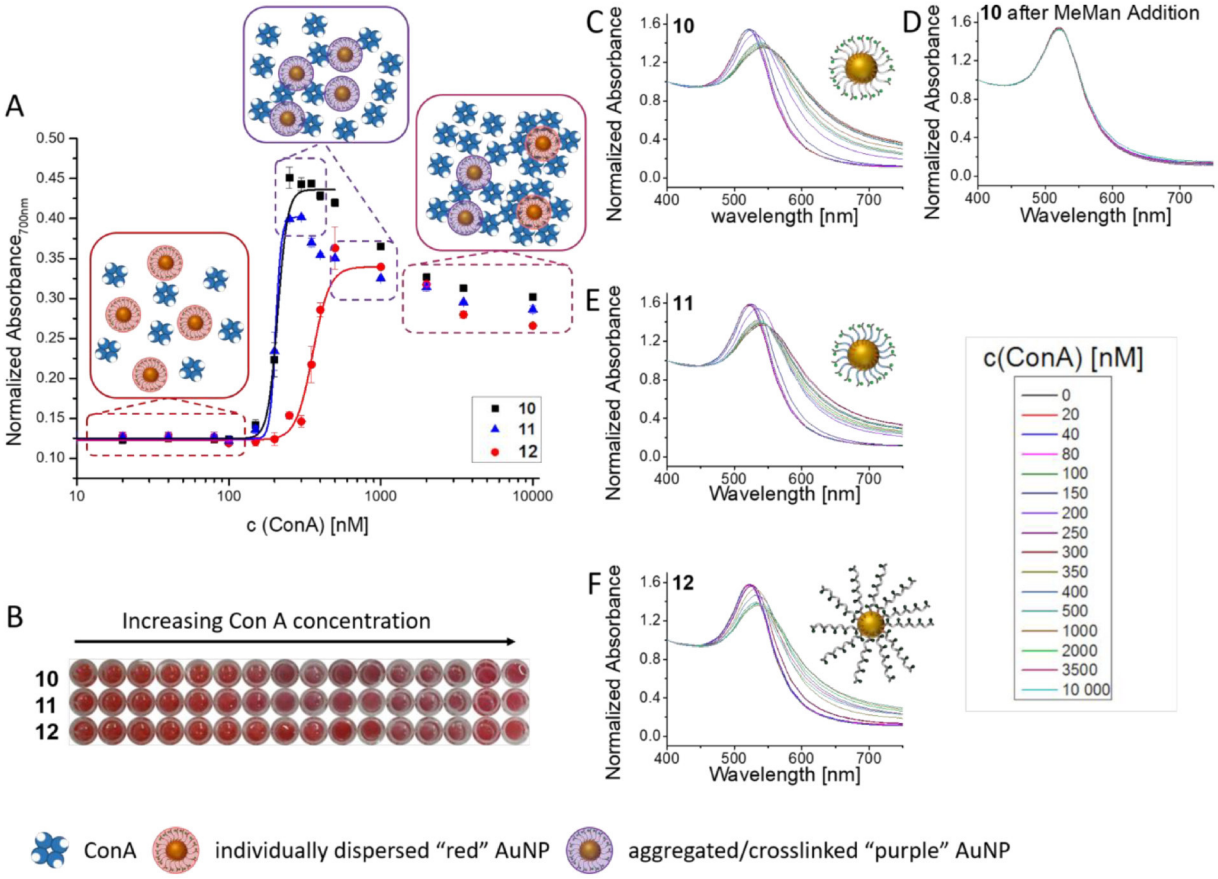

Figure 39: Aggregation behaviour of glyco-AuNPs in presence of increasing ConA concentration: A: Normalized absorbance (normalized to absorbance at 400 nm) at 700 nm plotted against ConA concentration, different scenarios of glyco-AuNP ConA binding are presented schematically; B: Photograph of 96-well plate (background removed); UV-Vis absorbance spectra in presence of increasing ConA concentration for glyco-AuNP C: ***10****, E:* ***11****, F:* ***12****; D: UV-Vis absorbance spectra in presence of increasing ConA concentration of glyco-AuNP* ***10*** *after addition of excess of MeMan.*[100]

When the evolution of absorbance at 700 nm were compared for glyco-AuNPs **10**-**12**, it could clearly be seen that the curve for glyco-AuNP **12** progressed much flatter than curves for glyco-AuNPs **10** and **11**. Thus, the shape of the binding isotherms already indicated some differences between glyco-AuNPs **10**, **11** and **12**. These differences could be quantified by fitting the Hill functions to plateau

concentrations (Figure 39A). In this way, the apparent dissociation constant $K_{D,app}$ (concentration of ConA where half maximum normalized absorbance at 700 nm is reached) could be obtained as measure of aggregation activity of glyco-AuNPs (Table 5). For better comparison $K_{D,app}$ values normalized on the number of glycomacromolecular (GM) and carbohydrate (C) ligands were calculated as well (Table 5). The obtained $K_{D,app}$ values allowed for quantitative comparison of the aggregation activity of glyco-AuNPs **10**-**12**, and the observed differences gave the first insights into optimal characteristics of glycomacromolecules for AuNP functionalization in order to obtain maximal aggregation activity or binding avidity, respectively. For example, glyco-AuNPs **10** and **11** could be used to probe differences caused by variation in backbone hydrophobicity of the installed glycomacromolecules **7** and **8**. In addition, a comparison of $K_{D,app}$ values obtained for glyco-AuNPs **10** and **12** gave first insights into the effect of carbohydrate valency and size when glycomacromolecules **7** and **9** are presented on AuNP surface.

Table 5 shows that absolute $K_{D,app}$ values of glyco-AuNPs **10** and **11** are very similar. However, when normalized on the number of glycomacromolecule or carbohydrate ligand, respectively, the aggregation activity differs with lower (more favourable) $K_{D,app}$ values for the more hydrophobic glycomacromolecule **8** presented on AuNP surface. This finding was consistent with a previous report by Tsutsumi and co-workers who found that AuNPs functionalized with monosaccharide carrying peptides showed a more than 10-fold increase in aggregation activity when hydrophobic amino acids were installed next to the carbohydrate moiety.[232] They proposed that this increase in aggregation activity is caused by additional secondary interactions of hydrophobic amino acids within the peptide with hydrophobic amino acid side chains near or inside the CRD of ConA. However, it was also previously reported in literature that carbohydrate density influences lectin binding.[111,113,232,240] As glyco-AuNPs **10** and **11** do not only differ in hydrophobicity but also surface loading, it was not clear which effect governed aggregation behaviour or if both effects overlap. Therefore, further studies need to be performed in the future to study both effects, hydrophobicity and surface loading, separately.

*Table 5: $K_{D,app}$ values obtained for glyco-AuNPs **10**-**12** and $K_{D,app}$ values normalized on the number of glycomacromolecules (GM) and carbohydrates (C) presented on one AuNP.[100]*

Glyco-Au-NP	$K_{D,app}$ [nM]	$K_{D,app}$ per GM Ligand [µM]	$K_{D,app}$ per C Ligand [µM]
10	209 ± 12	65	65
11	203 ± 4	47	47
12	357 ± 12	86	432

When comparing absolute $K_{D,app}$ values obtained for glyco-AuNPs **10** and **12**, the longer pentavalent structure **9** installed on glyco-AuNP **12** led to a comparably smaller aggregation activity as already indicated by flat curve progression in the binding-isotherm (Figure 39A). The difference between glyco-AuNPs **10** and **12** was even more pronounced when normalized on the number of carbohydrate ligands. This was again consistent with previous literature studies and results obtained in the Hartmann group.[95,121,240] Therein, it has been observed that glycomimetic avidity increases with increasing carbohydrate valency but levels off and reaches a plateau for high valencies and structures of high molecular weight. This can be explained by the saturation of lectins with carbohydrate ligands that sterically inhibits binding to neighbouring carbohydrates so that decreased accessibility results in an apparent decrease in lectin binding (compare Chapter 3.1.2). Moreover, it has been demonstrated in literature that the chain length of immobilized ligands has a profound effect on the aggregation behaviour of glyco-AuNPs with shorter structures resulting in faster aggregation than longer structures.[227,231] The chain length can also have an effect on the sensitivity of the aggregation assay because glyco-AuNPs with shorter surface functionalization can form denser aggregates, leading to stronger near-field resonance coupling and thus a more intense color change.[231] Thus, a comparison of $K_{D,app}$ values obtained for glyco-AuNPs **10** and **12** rather reflects differences in aggregation kinetics and aggregate density than differences in ConA avidity.

In order to gain deeper insight into the effect of glycomacromolecular structure on the aggregation behaviour of glyco-AuNPs **10**-**12** in presence of ConA, the kinetics of these three compounds were investigated. Therefore, several UV-Vis and DLS measurements were performed over a time period of 30 min after the addition of $K_{D,app}$ concentration of ConA (concentration of ConA where half maximum normalized absorbance at 700 nm is reached) to glyco-AuNP dispersions. Figure 40A shows the results obtained by UV-Vis measurement, where it can be seen that normalized absorbance at 700 nm (normalized to absorbance at 400 nm) steadily increased over time for all three glyco-AuNPs **10**-**12**. While glyco-AuNPs **11** and **12** show a strong increase in normalized absorbance at 700 nm in the first time interval (< 500s) the curves flatten out and seem to reach a maximum value at times > 1000 s (Table 6). In contrast, glyco-AuNP **10** showed a rather moderate increase in normalized absorbance at 700 nm in the initial period until a steep increase in the time interval between 300 and 800 s could be observed. Afterwards the curve also flattened in a similar manner as for glyco-AuNPs **11** and **12**. As a result, the kinetic of aggregation seemed to be very fast for all glyco-AuNPs with only small differences between the different glyco-AuNPs, and only minor changes in absorbance at 700 nm after approximately 1000 s. This is of course also important when considering the use of glyco-AuNPs as biosensors with fast color development.

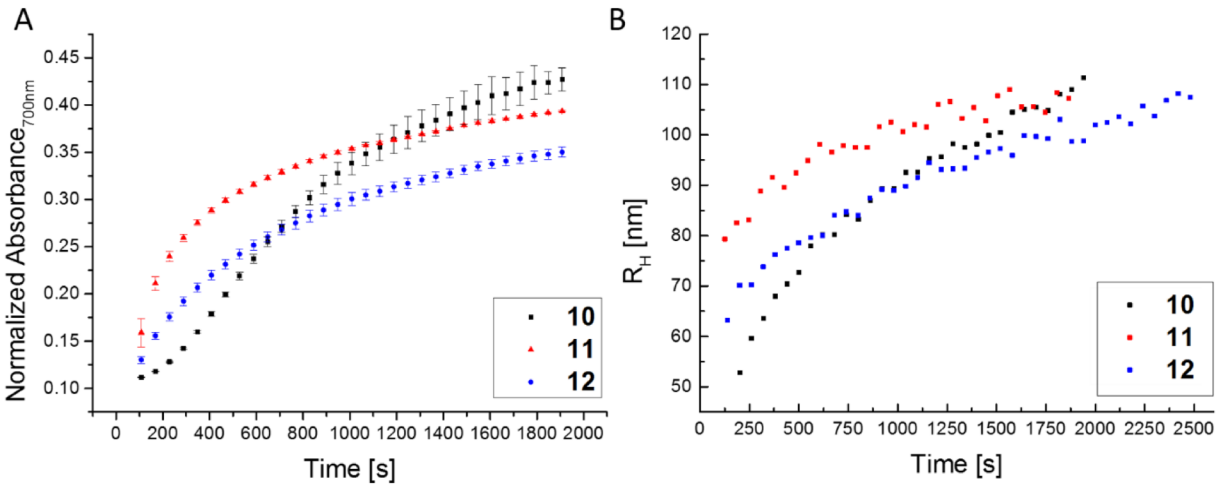

Figure 40: Kinetic analysis of glyco-AuNP interaction with ConA by A: UV-Vis absorbance at 700 nm and B: Representative evolutions of the hydrodynamic radii obtained from time-dependent DLS measurements at $K_{D,app}$ concentrations of ConA (for all curves see Appendix 269).[100]

Figure 40B shows the same kinetics followed by DLS. DLS measurements were performed together with Kristina Wagner in the Karg group. This graphic allows for the comparison of the kinetics of aggregation behaviour as followed by UV-Vis with the evolution of hydrodynamic radii in the DLS measurement. Results demonstrate that hydrodynamic radii for all three compounds **10**-**12** increased over time. In absence of ConA, hydrodynamic radii in LBB buffer were in a range between 10 to 12 nm but increased steadily over a time range of 30 minutes reaching values between 101 and 112 nm after ConA addition at $K_{D,app}$ concentration (Table 6). This confirmed that the increase of absorbance at 700 nm was caused by the formation of aggregates leading to near-field resonance coupling and a higher hydrodynamic radius. Moreover, the curve progression observed in the DLS measurement was similar to the progression curve observed in UV-Vis spectroscopy. Again, a steep increase in the beginning of the measurement that levelled off for higher time intervals was observed. The almost linear and very similar increase of hydrodynamic radii for times > 500 s for all glyco-AuNPs **10**-**12** could indicate that aggregation or growth, respectively, occurred independent of the glycomacromolecular structure and was only diffusion limited in this time interval.

Table 6: DLS derived hydrodynamic radii (R_H) for glyco-AuNPs in buffer medium as well as the determined R_H upon exposure to $K_{D,app}$ concentration of Con A after 30 min and after subsequent addition of αMeMan. The values for the absorbance at wavelengths of 700 nm (normalized to absorbance at 400 nm) are an indirect measure for the particle aggregation. Error values for kinetic measurements refer to the root mean square deviation from at least three repetitive experiments.[100]

Glyco-Au-NP	R_H in LBB [nm]	R_H at $K_{D,app}$ conc. of Con A [nm]	R_H after MeMan addition [nm]	Normalized $Abs_{700\,nm}$ at $K_{D,app}$ conc. of Con A
10	10.4 ± 0.2	106 ± 1	14.7 ± 0.7	0.43 ± 0.01
11	10.6 ± 0.1	112 ± 11	11.2 ± 0.2	0.39 ± 0.001
12	12.6 ± 0.1	101 ± 1	13.3 ± 0.2	0.35 ± 0.005

In order to test for the specificity of the interaction between glyco-AuNPs and ConA in both the aggregation study and DLS experiments, α-methyl-D-mannose (MeMan) was added as competitive inhibitor to the wells or cuvettes, respectively. After addition of MeMan, complete dispersion of the aggregates was immediately observed (Table 6,Figure 39D, Appendix 267). The color changed back to the intense red, and neither a shift or broadening of LSPR nor an increase in absorbance at 700 nm could be observed anymore (Figure 39D). The hydrodynamic radius after MeMan addition also returned to values in small decimal range (Table 6). This indicated that the observed aggregation behaviour resulted from specific interactions between the carbohydrates presented on the AuNP surface and ConA. Another experiment with a dilution series of the non-carbohydrate binding protein BSA in UV-Vis measurements with glyco-AuNPs **10**-**12** that showed no spectral changes confirmed this conclusion (Appendix 268).

As mentioned in Chapter 3.2, in addition to biosensing other interesting biological applications have been demonstrated for glyco-AuNPs. For example, it has been demonstrated that glyco-AuNPs can be used as inhibitors for lectin binding, leading to their potential use as therapeutic agents by blocking pathogen adhesion to host cell.[80,217,220] Thus, as second lectin binding assay, the inhibitory potential of glyco-AuNPs **10**-**12** was investigated in a SPR inhibition competition experiment. This examination was designed to help to identify differences in the inhibitory potential of glyco-AuNPs functionalized with glycomacromolecules varying in backbone hydrophobicity and carbohydrate valency.

In contrast to direct binding SPR setup in Chapter 3.1.2, in the inhibition experiment an α-D-mannose functionalized polyacrylamide fragment was immobilized on the sensor chip surface in the active flow cell while a β-D-galactose functionalized polymer was used for immobilization of the reference flow cell. Preincubation of ConA with increasing concentrations of the respective inhibitor, glyco-AuNPs **10**-**12**, or capped glycomacromolecules **7a** or **9a**, was performed. This mixture was subsequently led over the surface of the chip, and response levels in dependence of inhibitor concentration were recorded (Figure 41A and B).

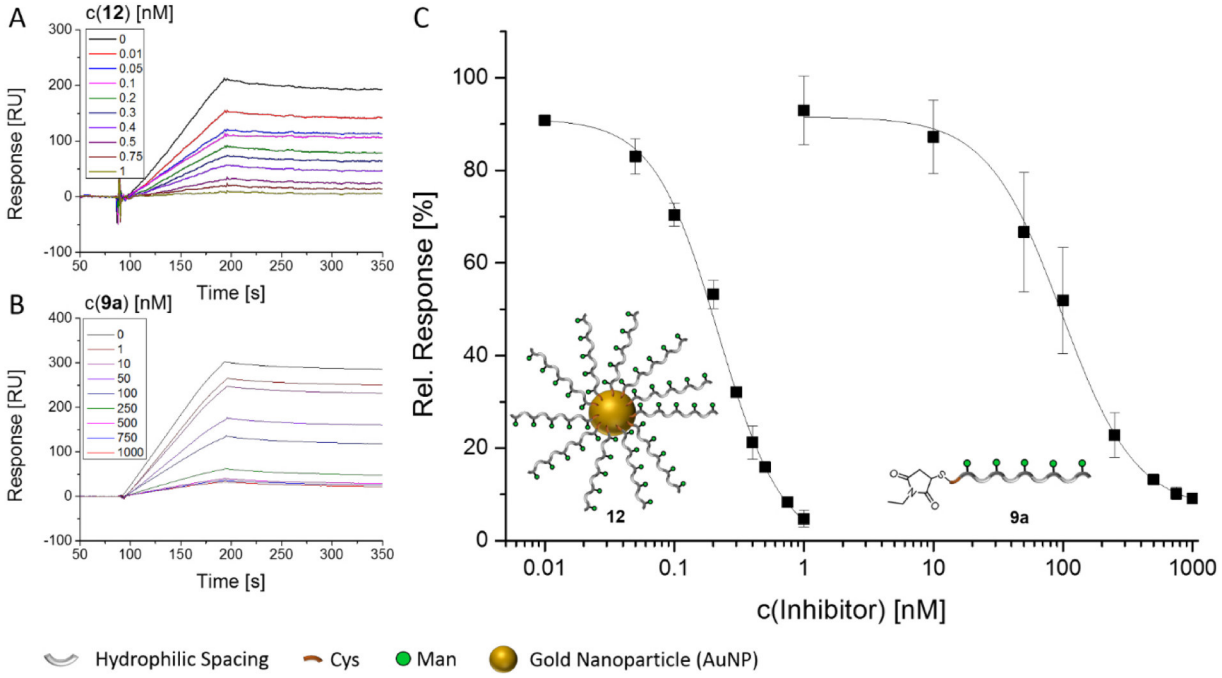

*Figure 41: Exemplary SPR sensorgram for solutions of 100 nM ConA incubated with serial dilutions of A: glyco-AuNP **12** and B: N-ethylmaleimide capped glycomacromolecule **9a**; C: resulting IC_{50} curve fitted to Hill1 function for glyco-AuNP **12** and N-ethylmaleimide capped glycomacromolecule **9a** (for all curves see Appendix 270-273).*[100]

Response of pure ConA solution in the absence of any inhibitor was set to 100% binding so that inhibition curves could be generated by referencing all further responses to this benchmark (Figure 41C). The inhibitor concentration that resulted in 50% inhibition represented the IC_{50} value of binding (Table 7). As IC_{50} values might differ in dependence on the sensor chip surface, MeMan was tested as reference inhibitor on the same chip which resulted in relative inhibitory potency (RIP) values.

The results are presented in Table 7. For better comparison, RIP values corrected for number of glycomacromolecule (GM) and carbohydrate (C) ligands were calculated and included for the array. Comparing results for free glycomacromolecules in solution it could be seen that the introduction of a macromolecular scaffold had a positive impact on the inhibitory potency. Monovalent glycomacromolecule **7a** in comparison to MeMan already showed a five-fold increase in inhibitory potency. This finding is consistent with previous studies and can be attributed to steric shielding of the carbohydrate moiety binding to the receptor by non-binding parts of the macromolecular scaffold, which helps to prevent binding of competing ligands to the receptor binding site.[95] This increase in inhibitory potency, however, was much more pronounced when going to higher valency and higher molecular weight structures as could be observed for glycomacromolecule **9a**. For this glycomacromolecule, steric shielding is dramatically enhanced and at the same time the increase in valency from one to five carbohydrate ligands led to a statistical effect which overall raised the RIP to a value that is about 400 times higher than for reference inhibitor MeMan.

*Table 7: IC_{50} and RIP values as measured for glyco-AuNPs **10–12** and N-ethylmaleimide capped glycomacromolecules **7a** and **9a** by SPR and derived RIP values corrected for glycomacromolecule (GM) and carbohydrate (C) number.*[100]

Glyco-Au-NP	IC_{50} [nM]	RIP	RIP per GM Ligand	RIP per C Ligand
αMeMan	$(5.17 \pm 0.84) \times 10^5$	1	1	1
7a[1]	$(0.7 \pm 0.5) \times 10^5$	5	5	5
9a[1]	155 ± 78	2096	2096	419
10	0.78 ± 0.09	$6.6 \cdot 10^5$	2115	2115
11	0.36 ± 0.10	$14.4 \cdot 10^5$	6234	6234
12	0.33 ± 0.09	$15.7 \cdot 10^5$	6487	1297

[1] Experiments were performed on a SA sensor chip with an IC_{50} of $(3.25 \pm 0.31) \times 10^5$ nM for αMeMan. D-(+)-galactose was measured as negative control for the assay setup at four representative concentrations and showed no inhibition.

When comparing the free glycomacromolecular ligands with the corresponding ligands presented on the AuNP surface, a strong increase of about 400 times in inhibitory potency could be observed for the monovalent compound **7a** on **10**, but only a comparably small increase of a factor of three could be observed for the pentavalent structure **9a** on **12**. In agreement with previous studies and the results discussed in Chapters 3.1.2 and 3.2.3, this finding can be attributed to a lower accessibility of the densely packed carbohydrate moieties on the surface of glyco-AuNP **12** which led to a seemingly lower increase in RIP values.[121] However, when compared without normalizing based on carbohydrate residues, glyco-AuNPs **12** showed the highest RIP value demonstrating the potential of higher molecular weight and pentavalent glycomacromolecules when installed on AuNP surface. It was especially striking that the RIP value of glyco-AuNP **11** presenting the monovalent hydrophobic glycomacromolecule **8** on its surface lay within the same scale although the number of carbohydrate ligands presented was much smaller. Moreover, the corresponding glyco-AuNP **10** with hydrophilic glycomacromolecule **7** exhibited only half of the observed inhibitory potential. This finding correlated with the observed aggregation behaviour of glyco-AuNP **11** and again indicated a positive impact of hydrophobic backbone properties on glyco-AuNP ConA binding. Overall, the results from this inhibition study nicely demonstrate the enhancement of glycomacromolecule lectin binding when presented on AuNPs as macromolecular scaffold. Moreover, it was shown that not only the multivalent presentation but also the macromolecular scaffold itself has an influence on the binding properties. Thus, these initial proof of concept studies clearly revealed the potential of glycomacromolecules presented on AuNPs towards studying carbohydrate lectin interactions and future applications in biosensing or as carbohydrate based antiadhesives.

3.3 Glyco-Gold Nanoparticles for Cancer Treatment and Photothermal Therapy

In the previous chapter, the functionalization of gold nanoparticles (AuNPs) with precision glycomacromolecules was introduced as a proof of concept study. It was demonstrated that AuNP functionalization with glycomacromolecules was effective, leading to high surface loading and good colloidal stability of the target glyco-AuNPs. Moreover, first studies regarding the aggregation behavior and inhibitory potency showed the potential use of the synthesized glyco-AuNPs for biological applications. In this chapter, this proof of concept is extended towards the synthesis of lactose carrying precision glycomacromolecules and their immobilization on AuNPs to test for their ability to target the overexpression of lactose binding proteins on tumor cells and serve as agents for photothermal therapy (PTT).

Cancer constitutes a major global health problem. In the United States alone 1,762,450 new cancer cases and 606,880 cancer deaths are estimated to occur in 2019, making cancer one of the number one killers in the US.[241] Today, standard cancer treatments are based on surgery, chemo-therapy and radiation.[242] Surgery, while invasive, can be very effective for the treatment of primary tumors provided that all tumor tissue is accessible and can be completely removed. Surgery is often combined with radiation whereby high energy ionization particles, like X-rays, gamma rays or electrons, are used to eradicate remaining cancer cells after surgery. However, healthy tissues in close proximity to the cancer cells or in the path of the irradiation beam can also be damaged by this treatment strategy.[242] Chemotherapy constitutes the third mainstream treatment for cancer. In this strategy, chemical drugs that kill cells that rapidly divide are administered to patients over a defined period of time. Unfortunately, these drugs are not only toxic to cancer cells, but also to healthy tissue so that patients often suffer from significant side effects.[242]

In recent years, photothermal therapy (PTT) has emerged as a new minimally-invasive therapeutic strategy for cancer treatment.[242] PTT is based on the absorption of photon energy and its transformation into heat leading to hyperthermia, a heat induced cell death. The process of PTT initially involves the absorption of light which leads to the transition of electrons from the ground state to an excited state. The increased energy of the system is subsequently released by nonradiative decay channels leading to an increase in kinetic energy and heat transfer to the local environment in close proximity to the photon absorbing compound.[243] This local heating leads to irreversible cell damage by protein denaturation as well as coagulation and destruction of the cell membrane. As absorption efficiency is very low for natural tissue absorbents, artificial additives, so called photothermal agents, are needed in order to reduce the power density of applied heat sources.[242,243] Common strategies use synthetic dye molecules like indocyanine green, naphthalocyanines or porphyrins that are

coordinated with transition metals.[244-246] The strong absorption of these compounds reduces the laser energy required to perform the work, which makes PTT much less invasive. However, one drawback of this approach is the rapid photobleaching of the photosensitizing dye molecules under laser irradiation.[243] AuNPs have emerged as a new tool for PTT that can overcome these limitations. AuNPs not only exhibit strong absorption efficiency and high photostability, but also combine these advantageous physical properties with biocompatibility.[242,243] As previously discussed in Chapter 3.2, spherical AuNPs show strong absorption in the visible region due to their local surface plasmon resonance (LSPR) which leads to their intense red color (Figure 42). The specific wavelength of LSPR maximum thereby is dependent on the size, shape, medium and colloidal stability of the AuNPs which makes AuNPs tunable photothermal agents. For example, when AuNPs increase in size or form aggregates, the LSPR maximum is redshifted; when AuNP shape changes from spheres to rods the LSPR splits into two bands (Figure 42).[243] This can be explained by two different oscillation pathways, the longitudinal and transversal oscillation. The transversal oscillation band can be found at similar wavelengths in the visible region as the LSPR for spherical AuNPs, but is rather weak compared to the strong wavelength band in NIR region provoked by longitudinal oscillation.[247,248] This strong absorption in NIR region is especially interesting in regard to the PTT treatments of tumors that are located in deep because in this wavelength range minimal absorption from tissue chromophores or water occurs.[249]

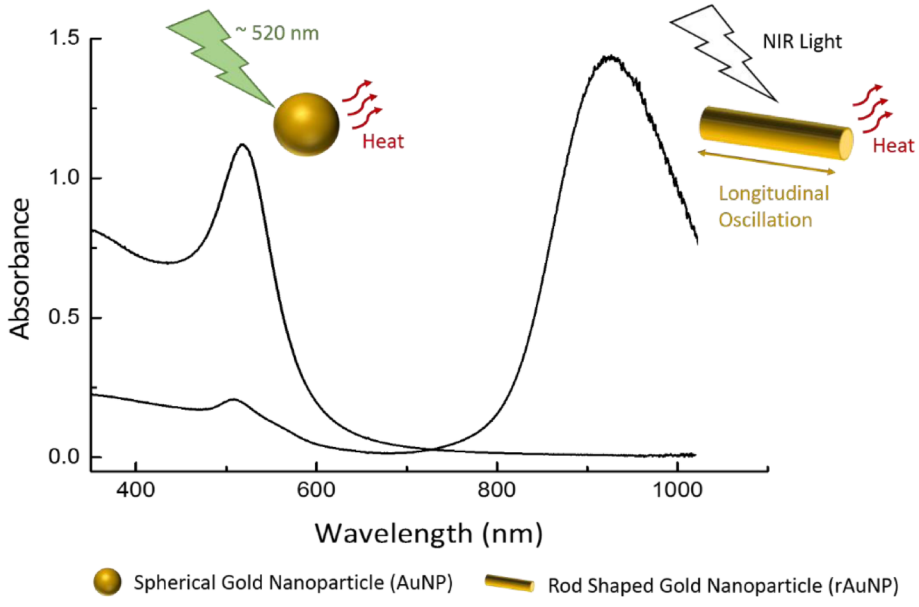

Figure 42: UV-Vis absorbance spectra of spherical and rod shaped AuNPs. The absorbance maximum for spherical AuNPs lies in the range of 520 nm so that green laser light can be used for PTT. The higher absorption cross section for rod shaped AuNPs lies in Near-IR (NIR) region so that laser light in this wavelength range can be used for effective PTT.

By nature, PTT has the potential to provide selective targeting of cancer cells to prevent the unintentional damage of healthy tissue by laser irradiation or hyperthermia. Many laser-based

therapeutic strategies are based on endoscopes and fiber optic catheters to specifically target the tumor region.[243] However, to make PTT even less invasive, immunotargeting strategies to specifically deliver the PTT agent to cancer cells were used previously and offer a promising approach to reduce nonspecific damage of healthy tissue.[243] The ease of AuNP functionalization thus presents another advantage because it allows for simple and straightforward biofunctionalization. One typically employed bioconjugation strategy uses polyethyleneglycol (PEG).[243] PEG improves the biocompatibility and stability of AuNPs, but only leads to "passive targeting" due to the enhanced permeability and retention (EPR) effect (Figure 43).[250] This effect is based on the characteristic of tumor tissue to have blood vessels of higher porosity so that macromolecular or polymeric compounds can enter cancer cells more easily. At the same time tumor tissue retains these molecules over a longer period of time due to decreased lymphatics.[243] Other bioconjugation strategies aimed at a more active and efficient targeting of cancer tissues involve the use of biomolecules such as antibodies or carbohydrates specific to receptors on the cancer cell.[251,252]

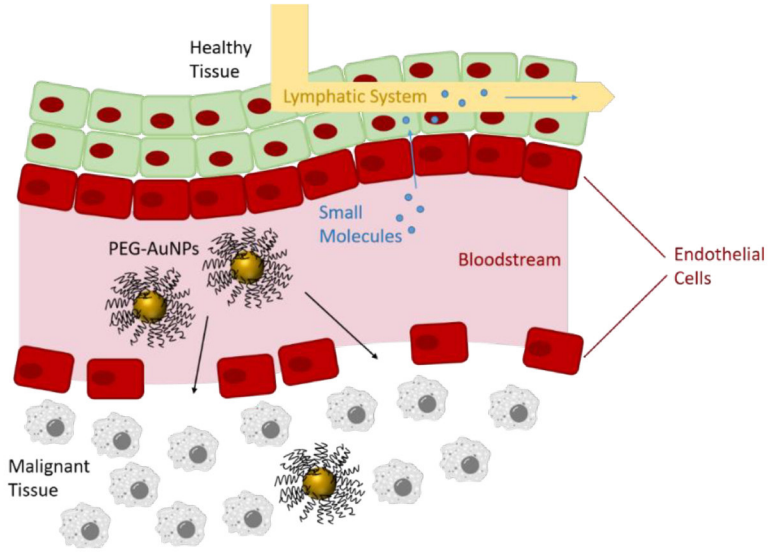

Figure 43: Illustration of the enhanced permeation and retention (EPR) effect of PEG functionalized AuNPs in malignant tissue (adapted from [253]).

Li and coworkers for example demonstrated specific targeting of a lactose specific receptor on cancer cells by using ^{18}F-labeled lactose as radio tracer.[254] Their target was the HIP/PAP (hepatocarcinoma intestine pancreas and pancreatitis associated protein) lectin also known as Reg3A. This lectin was already introduced in Chapter 1.1.1.2. It contains a C-type lectin like domain and is known as "lactose binding protein". Moreover, its overexpression is linked to many different types of carcinomas including hepatocellular carcinoma or colorectal cancer. In their study, Li *et al.* aimed to use HIP/PAP targeting in order to specifically detect these diseases. They then investigated two different cell lines, a breast cancer cell line, SK-BR-3, and a pancreatic carcinoma line, T3M4.[254] By western blot

experiments they confirmed the overexpression of HIP/PAP protein in T3M4 cells and showed that there is no expression of the protein in SK-BR-3 cells so that this cell line could be used as negative control. In a next step they used PET (positron emission tomography) imaging to show that the radiotracer only accumulated in T3M4 tumor and that no accumulation of radioactivity could be observed in the SK-BR-3 tumor region. As a result, specific targeting could be achieved.

The studies reported by Li *et al*. inspired the work described in this part of the thesis, which is aimed at synthesizing lactose carrying glycomacromolecules for immobilization on spherical and rod shaped AuNP surfaces. In this way specific HIP/PAP targeting should provide for enhanced glyco-AuNP uptake leading to selective and efficient PTT treatment for cells overexpressing this protein. In line with Chapter 3.1 and 3.2, a special emphasis is placed on investigating the effect of valency as well as hydrophobic motifs in the glycomacromolecule backbone on cancer cell uptake.

3.3.1 Solid Phase Polymer Synthesis of Glycomacromolecules for HIP/PAP Targeting

In this part of the thesis, the work of Chapter 3.2 on precision glycomacromolecule based gold nanospheres bearing mannose residues is extended to the synthesis of several lactose based analogs for targeting HIP/PAP protein. Therefore, the solid phase polymer synthesis (SPPoS) approach introduced in the Hartmann group was used to generate structures with full control over carbohydrate positioning and the introduction of specific backbone characteristics, as well as the introduction of functionalities required for AuNP functionalization, receptor targeting and monitoring in cellular uptake studies. This was accomplished by combining artificial building blocks with natural amino acids (Figure 44). Artificial building blocks were selected from the building block library introduced in the Hartmann group.[95-103] As a functional building block, TDS with a triple bond in the side chain was used to enable carbohydrate conjugation via CuAAC reaction.[95] The corresponding lactose-azide derivative for HIP/PAP targeting was kindly provided by Patrick Konietzny in the Hartmann group. As a spacer, three different building blocks were selected that differ in their hydrophobicity in order to allow for the adjustment of backbone characteristics. For the introduction of more hydrophilic properties, EDS was employed as spacer building block, whereas ODS was used when hydrophobic aliphatic properties were desired.[95,100] Moreover, aromatic hydrophobic properties were installed with the commercially available spacer building block AR.[132] With the combination of these artificial building blocks and the natural amino acid L-cysteine, the corresponding glycomacromolecules could be conjugated to AuNPs.

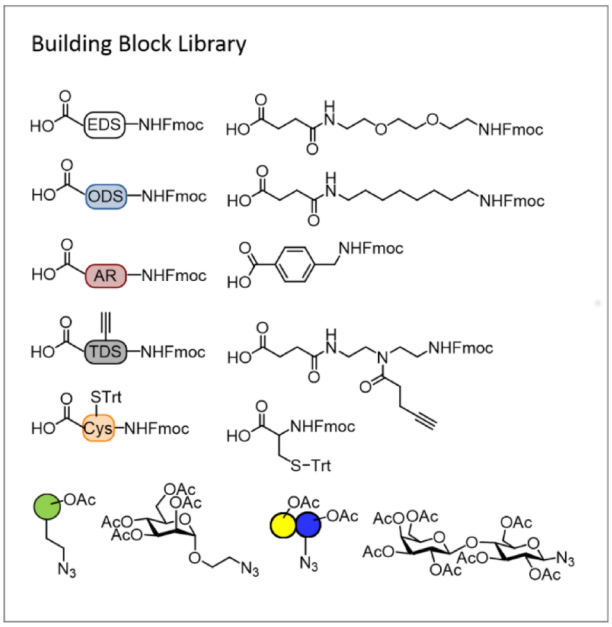

Figure 44: Overview of building blocks employed in SPPoS.

In contrast to the solid phase synthesis of the thiolated glycomacromolecules in Chapter 3.2.1, it was now desired to introduce not only a carboxylic endgroup, but also a variety of different functionalities on to the glycomacromolecule scaffold. Moreover, an effort was made to reduce the formation of the thioether side product as observed with the previous synthetic strategy. As a result, a different synthetic strategy was developed for the solid phase synthesis of thiloated glycomacromolecules in this part of the work. Instead of using a Tentagel® or PS-trityl resins preloaded with glycine, a Tentagel® resin with rink amide linker was employed, which after resin cleavage results in an amide end group. After swelling in DCM and Fmoc deprotection of the resin with a 25% piperidine solution in DMF, L-cysteine was always coupled as first building block followed by three consecutive coupling and deprotection steps employing the EDS building block. This fragment of -Cys-EDS-EDS-EDS- was designed to provide steric stabilization and add the same spacing between the AuNP core and each glycomacromolecular structure employed. After assembly of this "core" fragment on solid support, all further building blocks were selected on the basis of the desired design features, e.g. hydrophilic vs. hydrophobic or monovalent vs. trivalent. As last step of scaffold synthesis, the end group was installed. Here, three different end groups were provided for selection. First, coupling of succinic anhydride as the last building block resulted in an acid end group in analogy to Chapter 3.2.1 in order to provide electric stabilization. Second, coupling with the fluorescent dye fluoresceineisothiocyanate (FITC) enabled the monitoring of the glycomacromolecule in cellular uptake by fluorescence based methods. Third, standardly employed capping with acetic anhydride as a rather small and neutrally charged component enabled additional testing of the influence of end group characteristics. Coupling with succinic anhydride and acetic anhydride were proceeded directly after backbone synthesis on solid

support followed by CuAAC reaction with the β-lactose azide derivative and subsequent sugar deprotection and cleavage from solid support. This order was changed for glycomacromolecules with a FITC end-group. In this case, Fmoc deprotection of the last building block was not conducted before lactose conjugation via CuAAC reaction. Then Fmoc deprotection was performed followed by carbohydrate deprotection and FITC coupling. Finally, the glycomacromolecule was cleaved from solid support.

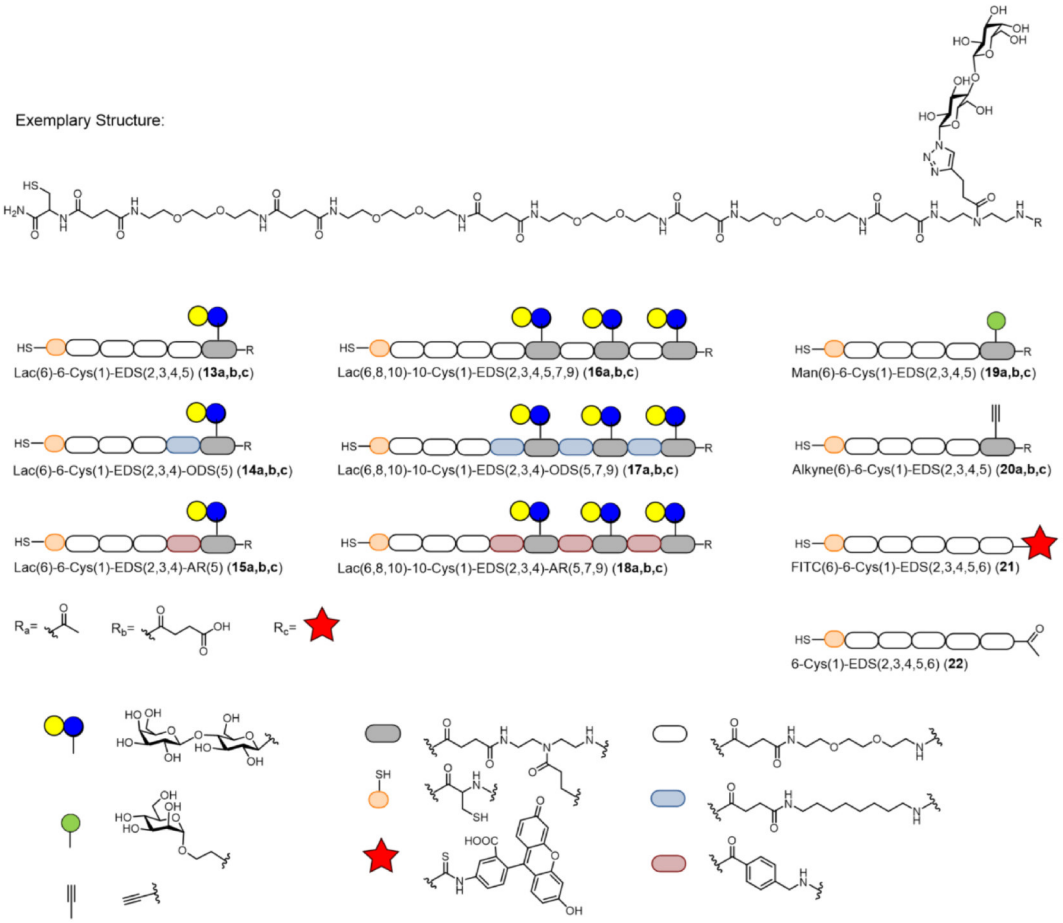

Figure 45: Overview of macromolecular structures obtained after SPPoS.

In this way six different glycomacromolecules were synthesized each exhibiting three different end groups **a** for acetyl, **b** for succinyl and **c** for FITC (Figure 45). Moreover, these six structures varied in their carbohydrate valency by either presenting one or three β-lactose moieties, as well as their backbone hydrophobicity from hydrophilic (EDS) to aliphatic (ODS) to aromatic (AR) properties. In addition to these lactose carrying compounds, two negative controls were obtained by clicking of a α-D-mannose azide derivative (**19**) or by completely omitting the CuAAC reaction step so that the alkyne group remained in the side chain of the glycomacromolecule (**20**) (Figure 45). In addition, two macromolecules without TDS building blocks consisting of only one Cys and four EDS building blocks with either an acetyl (**22**) or FITC (**21**) end group were synthesized in order to enable the introduction of fluorescent properties on AuNP surface while controlling the degree of functionalization. All

macromolecules were purified by preparative HPLC. Syntheses for the 26 macromolecular structures were confirmed by ^{1}H-NMR, RP-HPLC, HRMS and MALDI-TOF analyses.

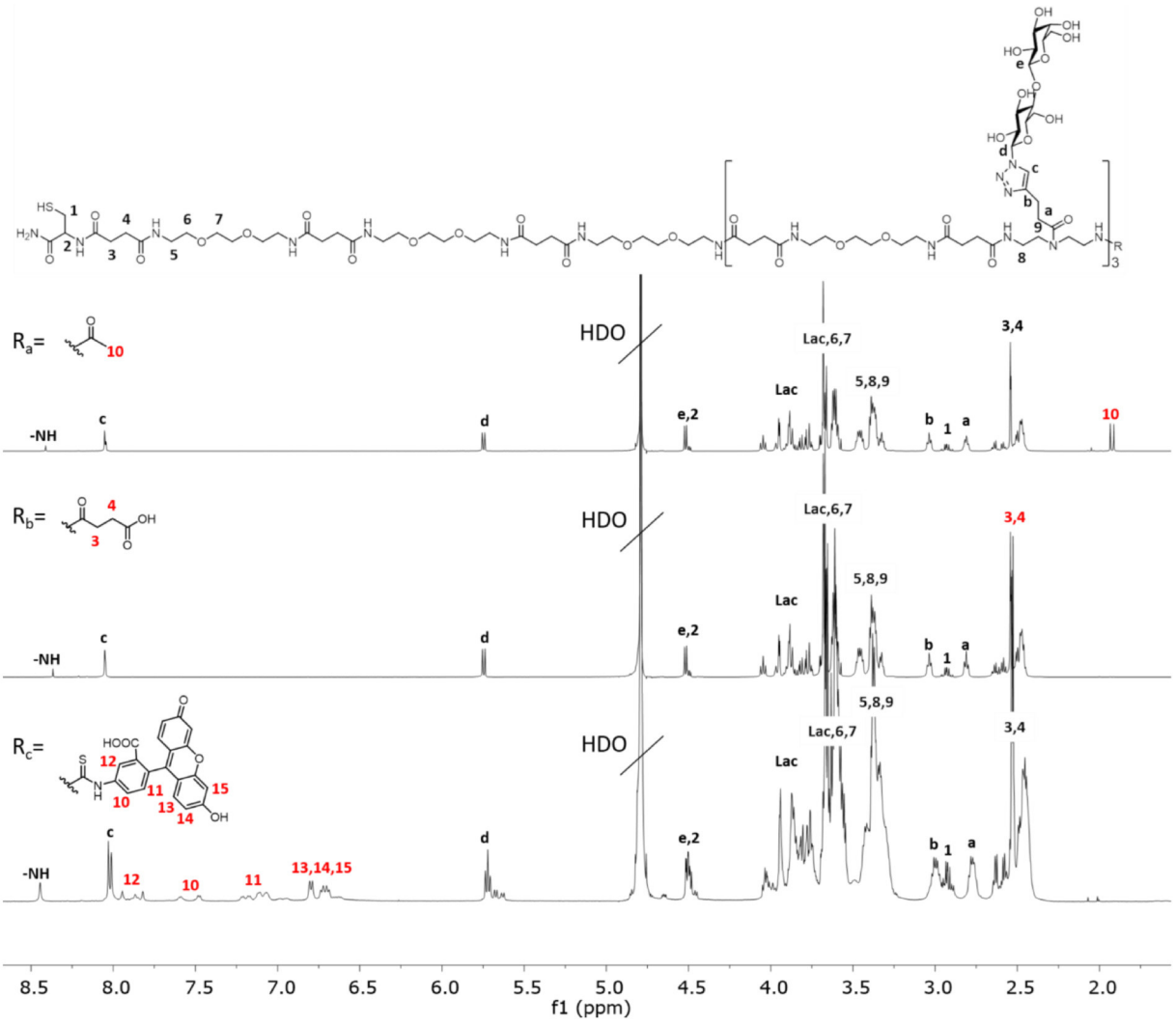

*Figure 46: Comparison of ^{1}H-NMR (600 MHz, D_2O) spectra of trivalent glycomacromolecule **16** with the three different end groups **a**, **b** and **c**. End group protons are highlighted in red.*

Figure 46 shows an exemplary ^{1}H-NMR spectra of the trivalent glycomacromolecule **16** with different end groups **a**, **b** and **c**. Resonances of all lactose hydroxyl groups do not occur due to proton exchange with deuterated water. However, -NH protons can be assigned to a broad singlet at 8.37 ppm. As already discussed in previous chapters, typical resonances for TDS and EDS building blocks can be found. EDS methylene groups in vicinity to oxygen atoms show a multiplet from 3.72 to 3.56 ppm. The third EDS moiety neighbouring the amide group is seen as multiplet at 3.50-3.30 ppm overlapping with the signals for TDS building block. Moreover, the TDS linker group can be identified as two triplet signals at 3.04 and 2.81 ppm. The triazole proton shows as singlet signal at 8.05 ppm. The natural amino acid L-cysteine shows one multiplet at higher field at 2.97-2.90 ppm for the C_β protons. The C_α proton gives a multiplet signal at lower field between 4.55-4.48 ppm. This multiplet signal overlaps

with the anomeric proton of the β-galactose moiety of lactose. The second anomeric proton of the β-glucose part of lactose can be found as doublet at 5.75 ppm. All other lactose protons are not specifically assigned but can be found between 4.05 to 3.74 ppm. These signals also overlap with the EDS multiplet signal from 3.72-3.56 ppm. For end group **a** with the acetyl group the three protons can be found as two singlets at 1.93 and 1.91 ppm with a 1:1 ratio that can be assigned to two rotational isomers. The succinyl building blocks as well as the succinyl end group of **16b** can be found as multiplet signal at 2.66-2.44 ppm. The FITC dye shows distinct resonances in the aromatic region of ^{1}H-NMR spectrum. The protons can be assigned to four multiplet signals at 7.97-7.80, 7.62-7.45, 7.24-7.03 and 6.83-6.59 ppm. Integration of all proton signals is in accordance with the expected number of protons contributed to complete conversion in all reaction steps and successful synthesis of the glycomacromolecules **16a**, **16b** and **16c**.

In order to further confirm successful synthesis of all macromolecules, RP-HPLC, MALDI-TOF-MS and HR-ESI analyses were employed. Exemplary spectra are shown in Figure 47. RP-HPLC spectra reveal the monodispersity and purity of the synthesized compounds. As already discussed in Chapter 3.2.1, disulphide formation in solution can not completely be prevented as air oxygen is sufficient to oxidize the L-cysteine thiol group. This could again be observed in RP-HPLC spectra for the current compounds (Figure 47A). However, the new synthetic strategy using a different resin linker with the introduction of the acid end group by coupling with succinic anhydride successfully prevented the formation of the thioether side product (Chapter 3.2.1). The retention time for the two different glycomacromolecules with acetyl **16a** or succinyl **16b** end groups are very similar. When the large and hydrophobic dye molecule FITC is introduced as end group in **16c**, the retention time increases in accordance with larger size and hydrophobicity of the compound.

MALDI-TOF and HR-ESI MS further confirmed successful synthesis of the macromolecular structures. The theoretically calculated mass-to-charge ratios correspond to the found values in mass spectrometry as exemplary shown for compound **16b** in Figure 47B and C.

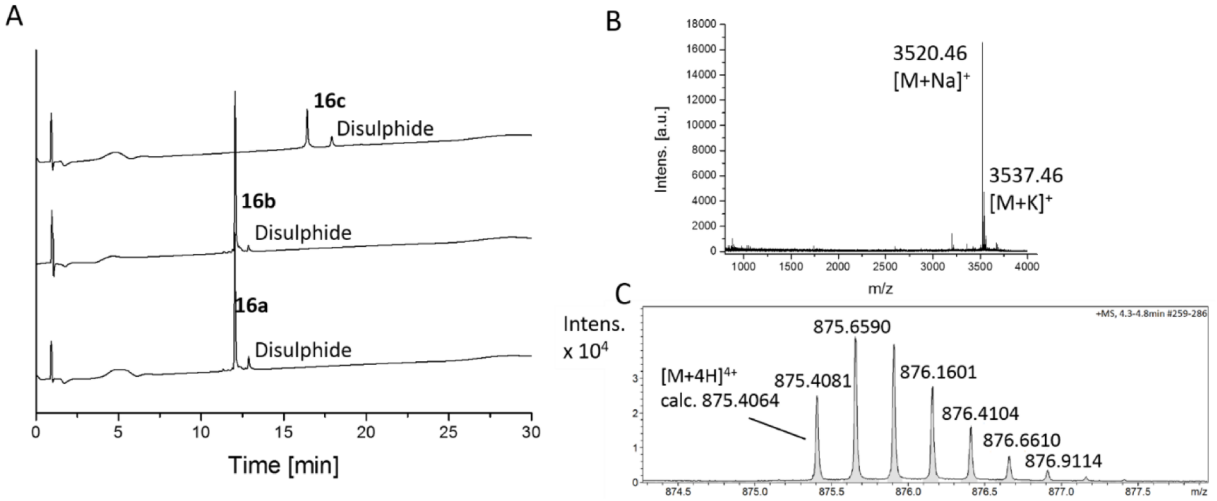

*Figure 47: A: RP-HPLC chromatogram (95/5 H_2O/MeCN with 0.1% formic acid (A) and 5/95 H_2O/MeCN with 0.1% formic acid (B); 100% A to 50% A in 30 min) determined at 214 nm for glycomacromolecules **16a**, **b** and **c**, B: Exemplary MALDI-TOF-MS of glycomacromolecule **16b**, C: Exemplary HR-ESI of glycomacromolecule **16b**.*

3.3.2 Functionalization of Gold Nanoparticles

After successful synthesis of glycomacromolecules and macromolecules **13**-**22** with different valency, backbone hydrophobicity and end groups, AuNP functionalization could be undertaken. AuNPs were synthesized by a collaboration partner, Kirsten Volk, in the Karg group at Heinrich Heine University in Düsseldorf. The synthesis followed the previously described Turkevich-method to obtain spherical AuNPs of a diameter of 13.7 ± 1.4 nm as derived from TEM analysis (Figure 48A and B).[219] In short, an aqueous solution of $HAuCl_4$ was brought to boil before a hot aqueous solution of sodium citrate dihydrate was added while stirring vigorously. The formation of citrate stabilized AuNPs could be observed by a color change to dark red. Purification was performed by several consecutive centrifugation and resuspension steps.

The following ligand exchange reaction was performed as part of this work. Besides the carbohydrate functionality it was also desired to introduce fluorescence properties to the glyco-AuNP for later fluorescence based cellular uptake studies. This is why in contrast to the ligand exchange in Chapter 3.2.2 a mixture of compounds was applied. When fluorescent properties were desired for the obtained glyco-AuNP, 10% of macromolecule **21** were mixed with 90% of the respective lactose carrying compound, preactivated with TCEP and then added drop wise to the cAuNP suspension under vigorous stirring. The reaction mixture was stirred for further 24h in the dark and was then purified by three consecutive centrifugation steps and resuspension in MilliQ water. This strategy was employed because of the concern that introducing fluorescence properties by ligand exchange with a glycomacromolecule with a FITC end group (e.g. **13c**) might shield the carbohydrate moieties from approaching receptors. An additional concern was that such glycomacromolecules might also lead to

reduced colloidal stability due to the high steric demands of the FITC dye and the resulting low surface loading. Another concern was the known toxicity of the FITC molecule, which could be problematic in following cell studies. As a result, the FITC free macromolecule **22** was applied in a similar ligand exchange reaction to obtain glyco-AuNPs that show no fluorescent properties but a similar carbohydrate surface density (Figure 48C).

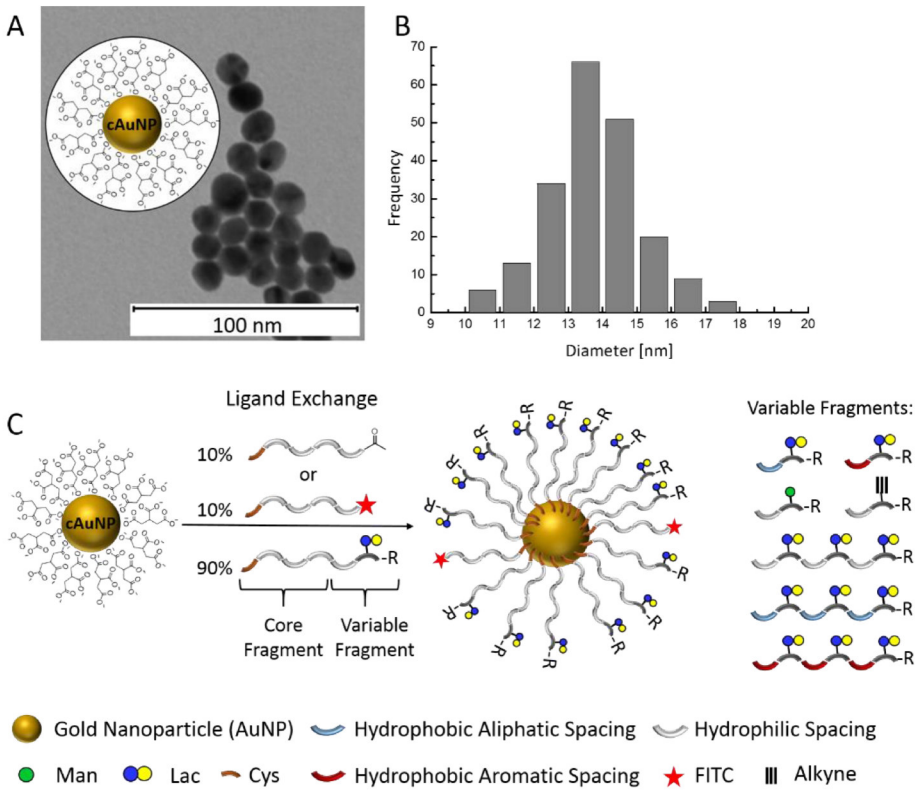

Figure 48: A: TEM image of citrate stabilized AuNPs (cAuNPs). The inset shows the sketch of a citrate stabilized AuNP. B: TEM derived histogram of citrate stabilized AuNPs with derived diameter of 13.7 ± 1.4 nm. C: Ligand exchange reaction of citrate stabilized AuNPs with a 1/9 ratio of dye functionalized macromolecule 21 or no dye carrying macromolecule 22 and a lactose carrying glycomacromolecule with varying backbone and end group fragments.

After ligand exchange reaction, the 32 obtained glyco-AuNPs were characterized by UV-Vis and DLS measurements in comparison to citrate stabilized cAuNPs. The UV-Vis spectra displayed the typical LSPR band with a maximum at 519 nm for citrate stabilized AuNPs (Figure 49A). The maximum was shifted to higher wavelengths from 524 to 526 nm for all glyco-AuNPs in accordance to glycomacromolecule size. The redshift results from a change of local refractive index in close vicinity to the AuNP surface, which is consistent with successful ligand exchange. The small width of the absorbance peak and rapid decay of the curve after LSPR maximum indicated low dispersity of the system and good colloidal stability after ligand exchange. In contrast, broadening of the LSPR band and an increase of absorbance at higher wavelengths would indicate low colloidal stability and the formation of aggregates.

The intensity-time autocorrelation function obtained by DLS was analyzed by a logarithmic fit provided by the instrument software in order to obtain the hydrodynamic radii of all glyco-AuNPs (Figure 49B, Table 8). The hydrodynamic radius for cAuNPs was determined to be 9.0 ± 0.1 nm and increased to approximately 13.5 to 14.0 nm for monovalent glycomacromolecules and 15.5 to 17 nm for trivalent glycomacromolecules immobilized on AuNP surface. This finding confirmed successful ligand exchange as the increase in hydrodynamic radius was consistent with glycomacromolecule size. Moreover, the change from acetyl end group **a** to succinyl end group **b** resulted in a small increase in hydrodynamic radius for most glyco-AuNPs. This could be explained by the fact that the succinyl group has a higher molecular weight than the acetyl group and as such results in higher hydrodynamic radii. However, it is more reasonable to assume that the repulsive forces between anionic end groups of the succinyl group overall led to increased AuNP size. When comparing glyco-AuNPs without and with fluorescent properties no distinct difference between hydrodynamic radii can be observed which is reasonable because only 10% of the AuNP surface functionalization changes between FITC free and FITC functionalized glyco-AuNPs.

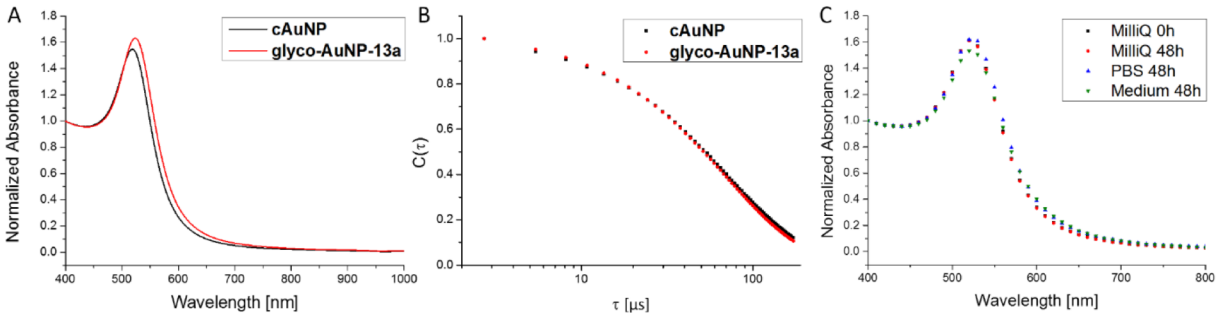

*Figure 49: A: Exemplary UV-Vis spectra of cAuNPs in comparison to glyco-AuNPs-**13a**. B: Exemplary autocorrelation function determined by DLS of cAuNPs in comparison to glyco-AuNPs-**13a**, C: Exemplary UV-Vis absorbance spectra of glyco-AuNP-**13a** in MilliQ water, PBS buffer and EMEM medium after 48 h in comparison to UV-Vis spectrum of the same glyco-AuNP in MilliQ water at time 0 (for all spectra see Appendix 274-281).*

The next characterization step was to determine the degree of glycomacromolecule functionalization per AuNP. Here, it was not desired to determine absolute functionalization levels but to determine whether functionalization of all glyco-AuNPs was in the same range. Therefore, TBO titration was used in an analogous manner to the method described in Chapter 3.2.2.[235] This method is based on the ionic interaction of the positively charged TBO dye and the negatively charged carboxylic end group in alkaline aqueous solution. Thus, this method was only applicable for glyco-AuNPs functionalized with glycomacromolecules that carry succinyl end group **b**. In this way, it could be shown that functionalization was similar for all investigated glyco-AuNPs (Table 8). In order to obtain a degree of functionalization for glyco-AuNPs with acetyl end group **a**, a modified phenol sulphuric acid protocol as originally introduced by Dubois and coworkers was employed.[169] However, this method led to unreliable values with very high errors. For example, for glyco-AuNP-**19a** the number of

glycomacromolecules per AuNP was determined to be 245 ± 225. As already discussed in Chapter 3.2.2 these high error values result from false positive signals due to absorbance of the gold core in the wavelength region of interest. Unfortunately, subtracting of this background signal did not lead to values with acceptable error.

Table 8: DLS derived hydrodynamic radii (R_H) in MilliQ water and relative degree of glycomacromolecule functionalization determined by TBO titration for glyco-AuNP with and without fluorescent properties.

AuNP	R_H [nm]	Degree of Functionali-zation	FITC-AuNP	R_H [nm]	Degree of Functionali-zation
cAuNP	9.0±0.1	-	-	-	-
Glyco-AuNP-**13a**	13.6±0.2	-	Glyco-AuNP-**13a-FITC**	13.7±0.2	-
Glyco-AuNP-**13b**	13.7±0.1	1335±87	Glyco-AuNP-**13b-FITC**	13.9±0.1	1547±159
Glyco-AuNP-**14a**	13.8±0.1	-	Glyco-AuNP-**14a-FITC**	13.2±0.3	-
Glyco-AuNP-**14b**	13.7±0.2	1646±132	Glyco-AuNP-**14b-FITC**	14.1±0.1	1173±95
Glyco-AuNP-**15a**	13.4±0.1	-	Glyco-AuNP-**15a-FITC**	13.0±0.3	-
Glyco-AuNP-**15b**	13.9±0.1	1185±97	Glyco-AuNP-**15b-FITC**	13.8±0.2	1343±57
Glyco-AuNP-**16a**	15.5±0.1	-	Glyco-AuNP-**16a-FITC**	15.4±0.1	-
Glyco-AuNP-**16b**	17.0±0.1	1165±21	Glyco-AuNP-**16b-FITC**	16.0±0.4	1270±62
Glyco-AuNP-**17a**	16.0±0.1	-	Glyco-AuNP-**17a-FITC**	16.3±0.2	-
Glyco-AuNP-**17b**	16.9±0.1	1183±47	Glyco-AuNP-**17b-FITC**	16.4±0.3	1197±60
Glyco-AuNP-**18a**	15.2±0.1	-	Glyco-AuNP-**18a-FITC**	15.2±0.2	-
Glyco-AuNP-**18b**	15.6±0.1	1437±65	Glyco-AuNP-**18b-FITC**	15.6±0.2	1393±15
Glyco-AuNP-**19a**	13.2±0.1	-	Glyco-AuNP-**19a-FITC**	13.7±0.1	-
Glyco-AuNP-**19b**	14.4±0.2	1470±127	Glyco-AuNP-**19b-FITC**	14.4±0.2	1270±133
AuNP-**20a**	15.1±0.1	-	AuNP-**20a-FITC**	14.7±0.4	-
AuNP-**20b**	14.2±0.1	1407±21	AuNP-**20b-FITC**	13.6±0.1	1580±71

In addition to absorption behavior and size another important characteristic of the synthesized glyco-AuNPs was their colloidal stability. For cellular uptake studies, stability in PBS buffer (0.01 M phosphate buffer, 0.0027 M KCl, 0.137 M NaCl, pH 7.2, 0.05% NaN3, 0.05% BSA (optionally)) and full growth medium (supplemented with 1% Penicillin/Streptomycin, 10% FBS) was of critical importance. Therefore, all glyco-AuNPs were concentrated by centrifugation and resuspended in the respective solvent at 10 nM concentration. The same glyco-AuNP concentration in MilliQ water served as reference. UV-Vis spectra recorded in a wavelength range from 400 to 800 nm in 10 nm steps helped to identify potential aggregation of glyco-AuNPs. However, no significant shift of LSPR maximum or

broadening of the absorbance band could be observed as exemplary shown for glyco-AuNP-**13a** in Figure 49C (for all spectra see Appendix 276-281).

As a result, functionalization of AuNPs with glycomacromolecular structures was successful and led to high colloidal stability of glyco-AuNPs perfectly suited for following cellular uptake studies. However, for PTT studies the LSPR maximum of spherical AuNPs in the visible region is not optimal for penetrating tissue in deeper body regions. More suitable are rod shaped AuNPs with high absorption in NIR region which lies outside the absorption range from tissue chromophores or water.[249]

3.3.2.1 Towards the Functionalization of Gold Nanorods

With regard to the potential application of glycomacromolecule functionalized AuNPs in PTT, it was equally desirable to use AuNP rods as scaffolds for glycomacromolecule presentation due to their high absorption in NIR region. AuNP rods were synthesized by a collaboration partner, Kristina Wagner, together with her Bachelor student, Christina Noffke, in the Karg group at Heinrich Heine University in Düsseldorf.

The synthesis of the rod shaped gold nanoparticles was based on a procedure previously described in literature.[255] In short, gold seeds were synthesized by rapidly adding an aqueous mixture of NaOH and $NaBH_4$ to an aqueous mixture of $HAuCl_4$ and cetyl trimethylammonium bromide (CTAB) under vigorous stirring. After addition, an immediate color change to rusty red could be observed. CTAB acts as a stabilizing agent in rod synthesis by forming micelles on AuNP surface. Rod synthesis was then proceeded by adding these gold seeds to an aqueous mixture of CTAB, $HAuCl_4$, silver nitrate ($AgNO_3$) and hydrochinon, followed rapid mixing of the reaction mixture and incubation in a water bath at 30 °C overnight. The obtained CTAB stabilized rods were purified by one centrifugation step at 32°C. Elevated temperature was used during centrifugation to prevent precipitation of CTAB from solution and to ensure better purification efficiency. Further centrifugation steps were omitted to guarantee high stability of the rod shaped AuNPs (rAuNPs) during long term storage.

CTAB stabilized rAuNPs were characterized by TEM and UV-Vis spectroscopy. From TEM analysis, a diameter of 16.6 ± 0.8 nm and a length of 73.3 ± 10.2 nm could be derived for the rod shape of the AuNPs (Figure 50A, C and D). A UV-Vis absorption spectrum revealed the typical LSPR resonances for transversal and longitudinal oscillation. The maximum for transversal oscillation lay at 508 nm and for longitudinal oscillation at 924 nm with a broad and intense peak in NIR region of the spectrum (Figure 50B).

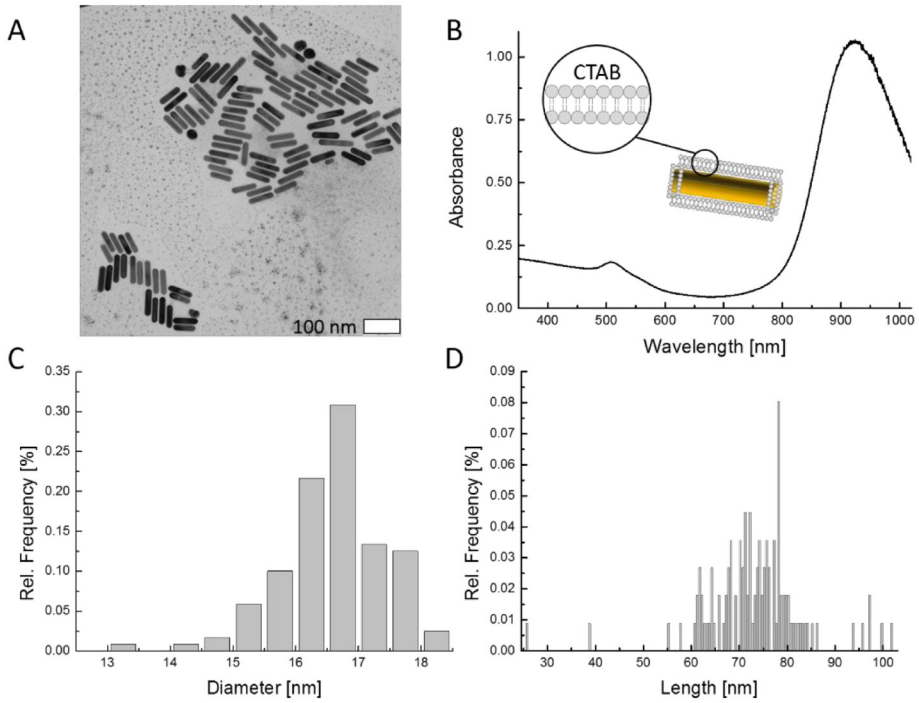

Figure 50: TEM image of CTAB stabilized rod shaped AuNPs (rAuNPs). B: UV-Vis absorbance spectrum of CTAB stabilized rAuNPs. The inset shows the sketch of a CTAB stabilized rAuNP. C: TEM derived histogram of CTAB stabilized rAuNPs with derived diameter of 16.6 ± 0.8 nm. D: TEM derived histogram of CTAB stabilized rAuNPs with derived length of 73.3 ± 10.2 nm.

The following ligand exchange reaction was performed as part of this work. As first approach, ligand exchange was proceeded in analogy to the standard procedure for the ligand exchange reaction of the spherical AuNPs described in Chapters 3.2.2 and 3.3.2. Therefore, rAuNPs were first centrifuged and resuspended in MilliQ water twice to remove excess of cytotoxic CTAB before ligand exchange. Then, a mixture consisting of a high excess of glycomacromolecule **13b** with TCEP was added drop wise under vigorous stirring. The reaction mixture was stirred slowly for an additional 48h in dark, and then centrifuged for purification. Irrespective of centrifugation speed (1000 to 7000 rcf) and time (5 to 60 min) aggregation of rods were immediately observed by decolorization and black accumulations within the solution. This observation by naked eye was confirmed by UV-Vis spectroscopy showing complete disappearance of LSPR peaks (Figure 51). This finding could probably be explained by the exchange of CTAB by glycomacromolecules, which led to insufficient colloidal stabilization of the nanorods.

In the next approach, higher steric stabilization was attempted by using either the higher molecular weight glycomacromolecule **16b** or through the addition of PEG-SH chains of a molecular weight of 3000 Da (50 to 70%) (Figure 51). This approach was inspired by the study of Semetey and coworkers.[256] They showed that colloidal stable gold nanorods could be obtained when ligand exchange was performed with PEG-SH with a molecular weight of 2000 Da. As both the glycomacromolecule **16b** and the additional PEG chain have a molecular weight above this threshold it was expected that colloidal stable rAuNPs could be obtained by ligand exchange with these

molecules. However, only one purification step by centrifugation could be performed before decolorization and accumulation of the rods could be observed. Even when purification was completely omitted, the functionalized rAuNPs were only stable for a time period of approximately 24 h in MilliQ water.

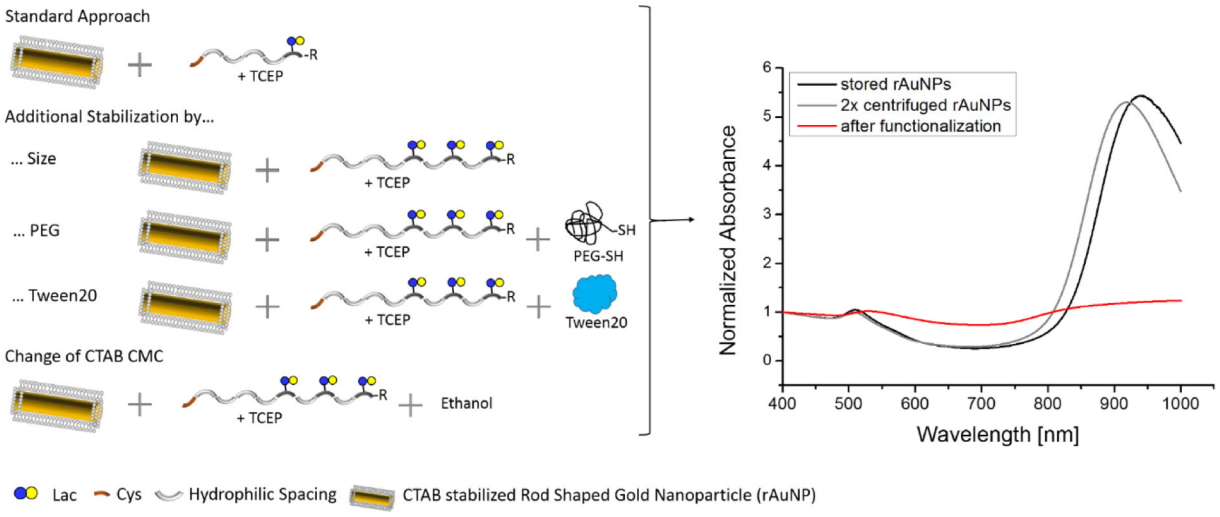

Figure 51: Schematic illustration of different approaches used for the ligand exchange reaction with all reactions resulting in insufficient stability and accumulation of rAuNPs observed by UV-Vis spectroscopy.

Yang *et al.* investigated ligand exchange of CTAB by PEG-SH in gold nanorods by using an additional stabiliser, Tween20.[257] They proposed that PEG-SH chains readily exchange CTAB as stabilizing agent due to the strong Au-S bond, and that remaining free spots can be covered by Tween20 weakly adsorbing to the gold surface. In this way they obtained gold nanorods that exhibited good colloidal stability even when dispersed in solutions of high ionic strength or extreme pH values. This approach seemed very promising so that an analogous CTAB exchange was conducted in this work with a mixture of glycomacromolecule **16b** and Tween20 (Figure 51). However, this strategy led to rAuNPs that began to decolorize during ligand exchange reaction and thus were even less stable than rAuNPs obtained in the previous approaches tested.

Another strategy described in literature by Fabris *et al.* makes use of the change of critical micelle concentration (CMC) of CTAB to destabilize the CTAB bilayer and thus facilitating ligand exchange.[258,259] The raise in CTAB CMC is achieved by going from a pure aqueous solution to an ethanolic aqueous solution in a two-step reaction. This strategy was also applied to the ligand exchange of CTAB with glycomacromolecule **16b**. However, addition of ethanol lead to immediate and complete decolorization of the rAuNP dispersion so that this approach was not feasible for the compounds used in this work (Figure 51). As a result, different strategies were tested for rAuNP functionalization but unfortunately no approach led to sufficiently stable glyco-rAuNPs.

3.3.3 Cell Studies

The cell studies described in this chapter took place as part of a collaboration project with the Snyder group at Davidson College, NC, USA, during a three-month research stay. As described in the previous chapter, functionalization of rod shaped glyco-rAuNPs with glycomacromolecular structures was not successful so that only the spherical shaped glyco-AuNPs could be used in cell studies. Inspired by the work of Li and coworkers who specifically targeted the HIP/PAP receptor in cancer cell lines with a ^{18}F-labeled lactose derivative, the same receptor was targeted in this work.[254] The major objective was to determine whether the selective uptake of lactose functionalized glyco-AuNPs in cancer cell lines overexpressing HIP/PAP protein in comparison to cancer cell lines with no HIP/PAP expression could be observed. Moreover, it was desired to investigate whether the introduction of hydrophobic backbone properties in glycomacromolecules immobilized on AuNPs has a positive effect on glyco-AuNP receptor interactions in *in vitro* studies as was observed for lectin binding studies in solution (Chapter 3.1 and 3.2). In addition, the investigation of the ability of AuNPs to target specific cancer cell lines could further help to identify suitable glyco-AuNP candidates for PTT. In analogy to the work of Li *et al.* the pancreatic carcinoma line T3M4 with high HIP/PAP expression was used as positive control and the breast cancer line SK-BR-3 with no HIP/PAP expression was used as negative control.[254] Moreover, the rectal carcinoma cell line RKO served as additional positive control as overexpression of HIP/PAP protein was also previously reported in literature for this cell line.[260]

The first step was to quantify cellular uptake of AuNPs functionalized with the different glycomacromolecules. Flow cytometry was used as a method of choice. For preparation of flow cytometry measurements, cell lines were seeded in 96 well plates overnight and then incubated with glyco-AuNP-FITC compounds. After the chosen incubation time, the medium was carefully aspirated and the content of the wells was transferred into polystyrene test tubes for washing after trypsin treatment. After three washes with PBS buffer (0.01 M phosphate buffer, 0.0027 M KCl, 0.137 M NaCl, pH 7.2, 0.05% NaN3, 0.05% BSA) by consecutive centrifugation steps, cells were resuspended in the same buffer and the resulting cell suspension was loaded into the flow cytometer. In flow cytometry, the flow rate of the suspension is carefully controlled in order to allow only one cell at a time to pass through a laser beam. The path of light through the cell and thus the scattering angle depends on the size and internal composition of the cell so that different cell lines as well as healthy and dead cells can be detected at different scattering angles. The degree of forward scattering is, for example, dependent on the cell surface area or size, and the degree of side scattering is proportional to the internal complexity of the cell. Besides the scattered light, different fluorescence colors can be detected depending on the dye that is used. For example, when FITC labeled glyco-AuNPs are taken up by the cell that passes through the laser beam, an increase in green fluorescence can be detected in

comparison to unstained cells. The increase in cell uptake can be quantified by measuring this fluorescence.

Before quantifying cell uptake of the synthesized glyco-AuNPs with the three cell lines, two test structures glyco-AuNP-**13a-FITC** and glyco-AuNP-**19a-FITC** were chosen to assess the right incubation time and concentration for flow cytometry measurements in RKO cells. These two test structures were selected on the basis that they are completely similar in regard to backbone characteristics but exhibit different carbohydrate moieties. The lactose functionalized glycomacromolecule immobilized on glyco-AuNP-**13a-FITC** was designed to serve as a positive control and the mannose functionalized glycomacromolecule immobilized on glyco-AuNP-**19a-FITC** was designed to serve as a negative control. In regard to incubation time, experiments revealed that a 3 h time range was not sufficient for glyco-AuNP incubation and only led to insignificant increase in fluorescence intensity compared to the unstained control as shown in Figure 52. In contrast, a 24 h incubation resulted in a significant increase in fluorescence intensity. Due to the fact that an incubation time of 48 h did not lead to a significant increase of fluorescent intensity in comparison to the 24 h incubation period, 24h was chosen for all further measurements. Figure 52 also displays the flow cytometry results obtained for different concentrations ranging from 2.5 to 10 nM for the two test glyco-AuNPs in RKO cells after 48 h incubation. The results nicely demonstrate that cellular uptake of the glyco-AuNPs was dose dependent for both test structures. The increase in fluorescence obtained for 2.5 and 5 nM was not significant so that it was decided to work at 10 nM concentration in all further tests.

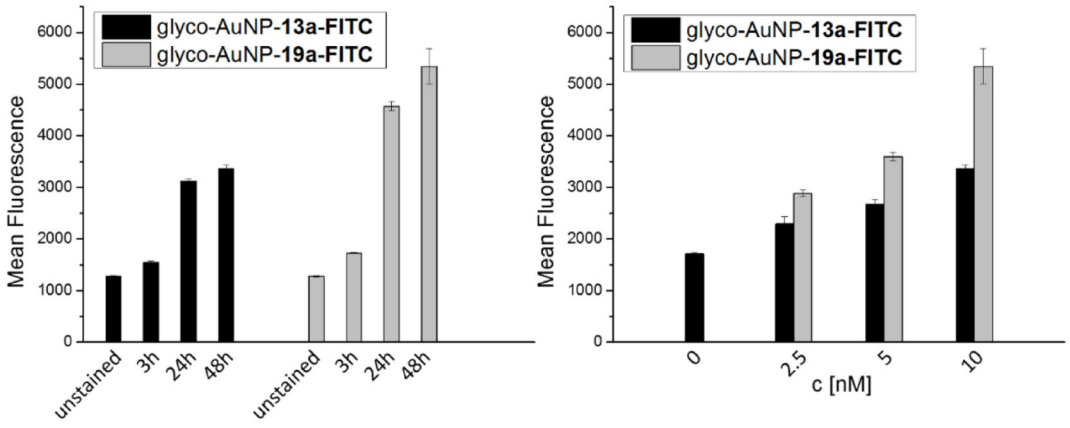

*Figure 52: Mean fluorescence obtained for different incubation times (10 nM concentration) (left) and different incubation concentrations (48 h incubation time) (right) for the two glyco-AuNPs **13a-FITC** and **19a-FITC** in RKO cell line in flow cytometry measurement.*

As next step it was important to test for cell viability in presence of the determined concentration of 10 nM for all glyco-AuNPs. Without irradiation in LSPR wavelength and thus without any PTT effect, cells should not be significantly impacted by the glyco-AuNPs. Cell viability was assessed by a XTT assay,

which is based on the reduction of the yellow XTT dye to a red formazan dye by a reductase system that is part of the respiratory chain of the mitochondria. Thus, reduction of XTT dye and formation of red color could only be observed for live cells so that the measured absorbance directly correlated to the number of viable cells. Cells of all three cell lines were seeded in a 96 well plate overnight before incubation with glyco-AuNPs at 10 nM for 48h at 37 °C and 5% CO_2. The yellow XTT dye was added to the wells, and after further 3 h incubation absorbance at 475 nm was recorded. Due to the fact that glyco-AuNPs show absorbance in the same region, background subtraction was performed. Notably, the XTT assay was only performed with glyco-AuNPs that were not fluorescence labeled because FITC is known to be cytotoxic. Figure 53 shows the cell viability on a percentage basis for the three cell lines T3M4, RKO and SK-BR-3 in the presence of all FITC free glyco-AuNPs at 10 nM concentration. Cell viability observed for unstained cells that were not treated with any additional substance was set to 100%. In comparison to unstained cells and to the vehicle control (MilliQ water), all glyco-AuNPs exhibited good cell viability with a minimum of 86% for glyco-AuNP-**18b** in T3M4 cell line.

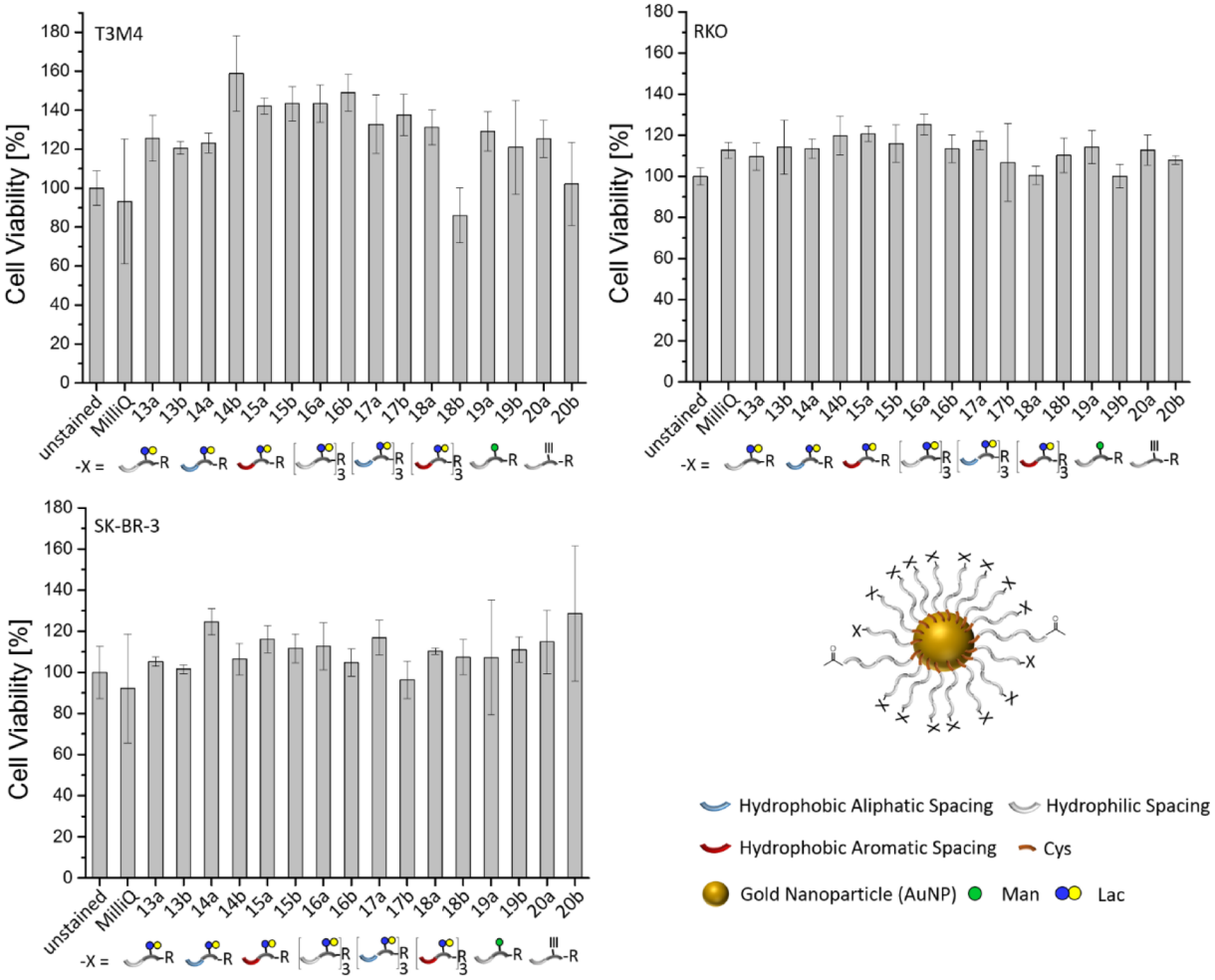

Figure 53: Percentual cell viability of T3M4, RKO and SK-BR-3 cell lines in presence of 10 nM glyco-AuNP after 48 h incubation at 37 °C and 5% CO_2. Cell viability of unstained cells was set to 100%. MilliQ water was used as vehicle control.

As a result, the concentration of 10 nM was determined to be suitable for further cellular uptake studies by flow cytometry. However, further questions needed to be answered before starting flow cytometry measurement with all compounds. In the first two preliminary tests with the lactose and mannose carrying glyco-AuNP test structures it was surprising that the mannose functionalized compound glyco-AuNP-**19a-FITC** which was intended to be the negative control exhibited higher uptake than the lactose carrying compound glyco-AuNP-**13a-FITC** which should specifically target the HIP/PAP receptor on RKO cells (Figure 52). One explanation for this finding could be that the difference in fluorescence intensity measured by flow cytometry is not caused by a difference in cell uptake, but rather a difference in the fluorescence labelling. Due to the fact that the ligand exchange reaction was proceeded by mixing 10% of FITC labelled glycomacromolecule **21** with 90% of the respective glycomacromolecule (**13**-**20**), there is no full control over actual surface labelling of the resulting glyco-AuNP-FITC compound. Thus, fluorescence intensity could vary for the different glyco-AuNPs (Figure 54C). In order to correct for this variation, the fluorescence of the glyco-AuNPs was measured in MilliQ water, PBS buffer and full growth medium and normalized. The obtained correction factor was used in all further fluorescence based measurements. Another explanation for the unexpected high uptake of the mannose carrying compound could be that besides the HIP/PAP receptor, mannose targeting receptors are also expressed on RKO cell lines. However, no information for this could be found in literature. Thus, it was decided to always include the non sugar carrying alkyne compound AuNP-**20-FITC** as negative control for all further assays. Another artefact which could lead to unspecific uptake, and which is widely discussed in literature, is the formation of a protein corona.[261] In theory, the proteins present in full growth medium during incubation could form a thin film over the AuNP surface. This protein corona would then determine the biological identity of the AuNP. If for example proteins are adsorbed to the AuNP surface that trigger cell surface receptors these proteins could be responsible for activating cell uptake of the AuNP irrespective of its original functionalization. This is why, in addition to full growth medium, PBS buffer (0.01 M phosphate buffer, 0.0027 M KCl, 0.137 M NaCl, pH 7.2) was used in the next FACS test in order to get insights into possible surface coating effects.

The above mentioned challenges were taken into account in the next flow cytometry study. As test structures, the lactose carrying glyco-AuNP-**13a-FITC** and the alkyne functionalized AuNP-**20a-FITC** were selected. The incubation time was set to 24 h and AuNPs were employed at 10 nM concentration. In order to assess surface coating effects both, full growth medium and PBS buffer were used as solvents during incubation. The obtained fluorescence values in flow cytometry measurements were corrected for fluorescence intensity measured for AuNPs in PBS buffer, which was used as solvent for flow cytometry measurements. Figure 54 shows the results obtained in flow cytometry measurements

as well as the fluorescence corrected values. The mathematical manipulation of the measured results led to values that can be used to compare uptake of glyco-AuNP-FITC compounds relative to each other. However, the corrected values are distorted in a way that would lead to false conclusions when compared to the control because then they seem too high. This is why both the original and corrected values will always be included in following graphs.

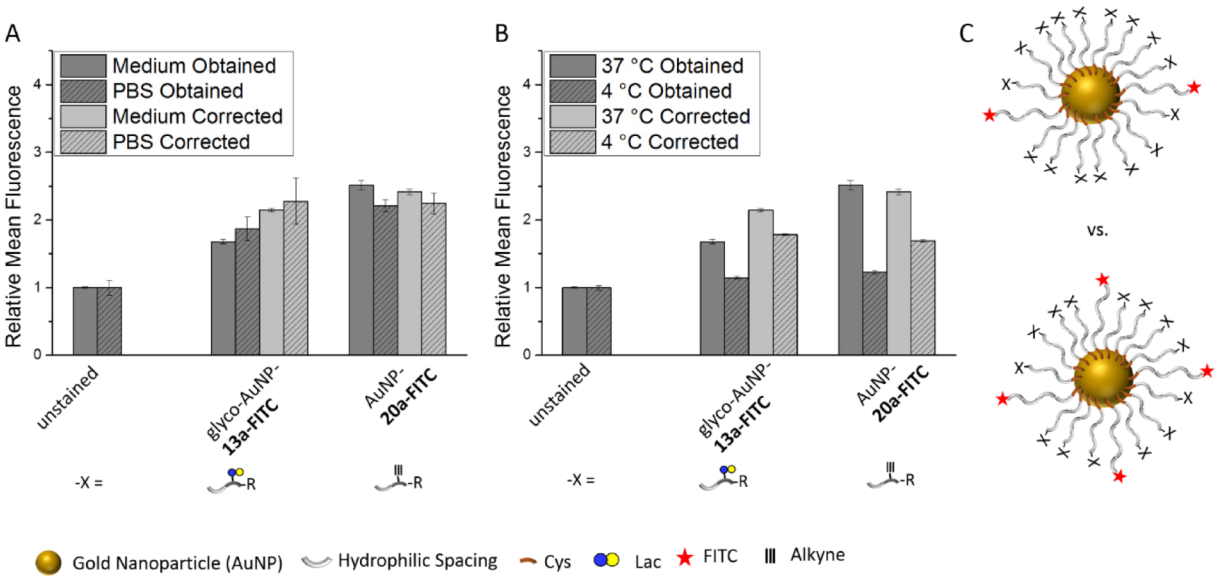

*Figure 54: A: Comparison of cell uptake in PBS buffer and full growth medium of glyco-AuNP-**13a-FITC** and -**19a-FITC** in RKO cancer cell line after 24 h incubation at 10 nM concentration. Fluorescence of the unstained control was set to 1, B: Comparison of cell uptake at 37 °C and 4 °C of glyco-AuNP-**13a-FITC** and -**19a-FITC** in RKO cancer cell line after 24 h incubation at 10 nM concentration. Relative and fluorescence corrected values are presented. Fluorescence of the unstained control was set to 1, C: Sketch of glyco-AuNP labelling demonstrating why fluorescence correction is necessary.*

In Figure 54A it can be seen that the results obtained in full growth medium do not significantly differ from the results obtained in PBS buffer, so that the formation of a protein corona did not seem to be the determining factor for uptake. However, uptake of the negative control, the alkyne functionalized AuNP-**20a-FITC**, was still unexpectedly high, lying in the same range as the values for lactose functionalized glyco-AuNP-**13a-FITC** even after correction for potential differences in fluorescence labeling. This finding challenged the specificity of the uptake and led to questions as to whether uptake occurred due to active receptor mediated endocytosis, or via passive diffusion through the cell membrane as previously observed for glycomacromolecular structures or both.[138] Thus, the same flow cytometry measurements with glyco-AuNP-**13a-FITC** and AuNP-**20a-FITC** were performed at 37 °C and at 4 °C (Figure 54B). The incubation at 4 °C was used to determine if the uptake is active because it is known that cellular endocytosis of nanoparticles is an energy-dependent process, while AuNPs entering cells by passive diffusion is independent of temperature. Experiments revealed that only an insignificant fluorescence signal could be obtained for both AuNP-FITC compounds at 4 °C when compared to the control and incubation at 37 °C (Figure 54B). These results suggested that the

pathway of AuNP-FITC entry into the cells was temperature dependent and thus proceeded via active receptor-mediated endocytosis.

Based on the preliminary results obtained with the three test structures glyco-AuNP-**13a-FITC,** glyco-AuNP-**19a-FITC** and AuNP-**20a-FITC**, the next step was to assess the uptake of all structures in the three different cell lines. Similar to the first test assays, cells were seeded overnight in a 96 well plate and then incubated with 10 nM concentration of glyco-AuNP-FITC compounds for 24 h at 37 °C and 5% CO_2. Afterwards the medium was carefully aspirated and the content of the wells was transferred into polystyrene test tubes for washing after trypsin treatment. After washing with PBS buffer (0.01 M phosphate buffer, 0.0027 M KCl, 0.137 M NaCl, pH 7.2, 0.05% NaN3, 0.05% BSA) by three consecutive centrifugation and resuspension steps the cell suspension was loaded into the flow cytometer and the mean FITC fluorescence intensity was recorded.

Figure 55 shows the results btained as well as the fluorescence corrected values for the uptake of all glyco-AuNP-FITC compounds in T3M4, RKO and SK-BR-3 cell lines. When comparing the unstained control with the relative mean fluorescence values for cells incubated with glyco-AuNP-FITC compounds, it can be seen that most values are small and lie within the range of the negative controls glyco-AuNP-**19-FITC** and AuNP-**20-FITC**. Only glyco-AuNP-**15b-FITC** showed uptake in RKO cells that was about twice as high as all of the other values obtained. This glyco-AuNP was labelled with monovalent glycomacromolecule **15b** with hydrophobic aromatic spacing in vicinity to the carbohydrate carrying building block and a succinyl end group. The same observation could be made for the fluorescence corrected results, albeit with slightly more variation between values observed for individual compounds. However, no clear trend in regard to carbohydrate valency, backbone hydrophobicity or end group could be assigned to these variations.

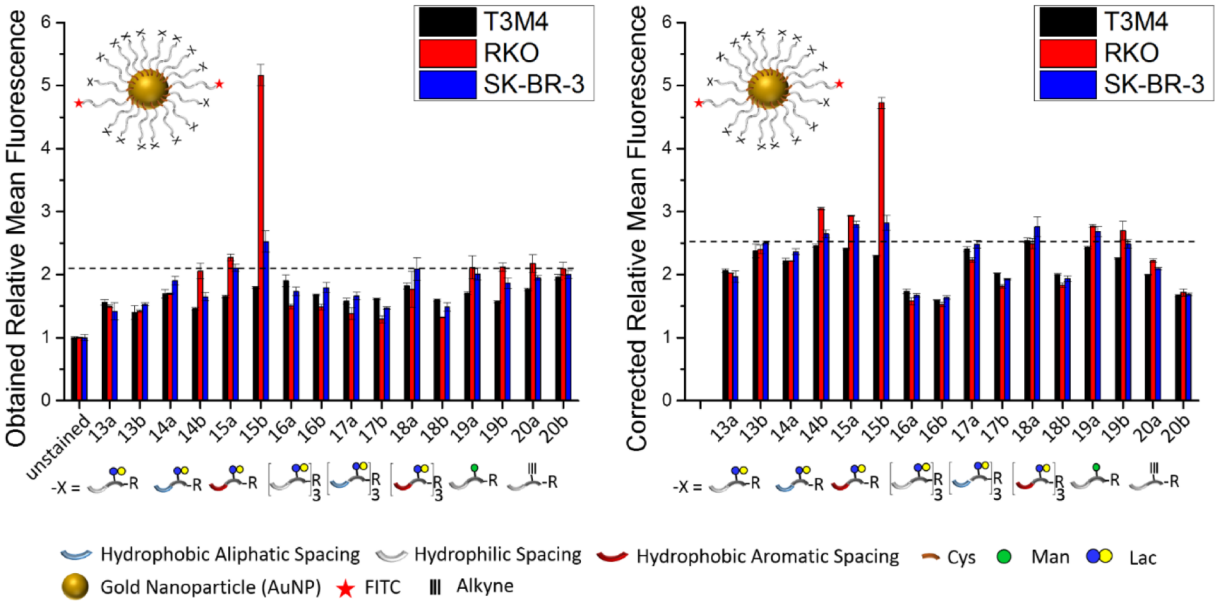

*Figure 55: Obtained (left) and corrected (right) mean fluorescence values in flow cytometry measurements of all glyco-AuNP-FITC in the three different cell lines after 24 h incubation at 37 °C and 5% CO_2 with 10 nM glyco-AuNP-FITC concentration. Fluorescence of the unstained control was set to 1. The dashed black line shows the threshold for the uptake of negative control structures glyco-AuNP-**19-FITC** and AuNP-**20-FITC**.*

It was especially striking that the change in valency of glycomacromolecules immobilized on the AuNP surface from monovalent to trivalent had no positive impact on cellular uptake and that the AuNP functionalized with the trivalent compound and hydrophobic aromatic spacing glyco-AuNP-**18b-FITC** did not exhibit the same increase in uptake as its monovalent counterpart glyco-AuNP-**15b-FITC**. In contrast, compounds functionalized with glycomacromolecules exhibiting three lactose moieties gave lower values than compounds with one lactose functionality. Moreover, it was unexpected that uptake was similar irrespective of the cell line employed. In general, there was no significant difference observed between positive T3M4 and RKO control cells and the negative SK-BR-3 control cell line for almost all compounds. Again only glyco-AuNP-**15b-FITC** showed strong uptake specific for the RKO cell line.

In order to confirm the results for glyco-AuNP-**15b-FITC**, the studies were repeated for all cell lines simultaneously. Figure 56 shows that the results were reproducible. Compound glyco-AuNP-**15b-FITC** was taken up about twice as high as all other values that lie in the range of the negative control AuNP-**20b-FITC**. Another explanation for the clear difference in uptake could be that different uptake mechanisms were involved. Therefore, incubation was either performed at 37 °C or at 4 °C to exclude passive diffusion of compound glyco-AuNP-**15b-FITC**. An insignificant increase in fluorescence intensity of cells incubated with glyco-AuNP-FITC compounds at 4 °C in comparison to the unstained control showed that uptake was active and proceeded via receptor mediated endocytosis for all investigated glyco-AuNP-FITC (Figure 56).

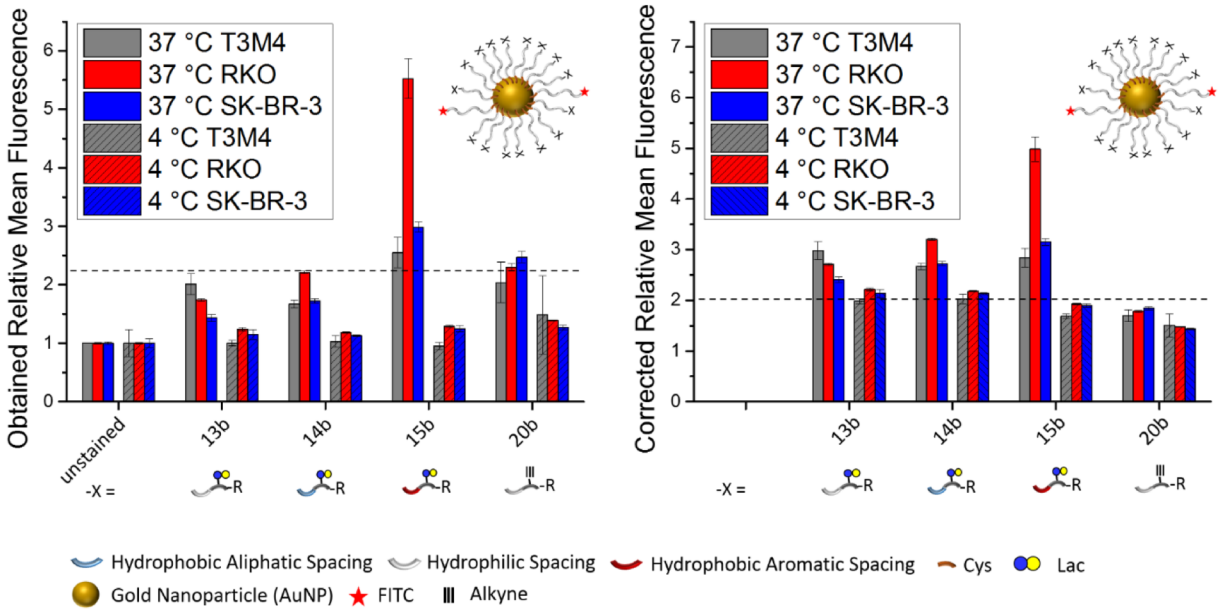

*Figure 56: Obtained (left) and corrected (right) mean fluorescence values in repeated flow cytometry measurements of monovalent glyco-AuNP-FITC compounds in the three different cell lines after 24 h incubation at 37 °C and 5% CO_2 with 10 nM glyco-AuNP-FITC concentration. The dashed black line shows the threshold for the uptake of negative control structure AuNP-**20b-FITC**.*

The next question was whether the same outstanding value in cellular uptake could be observed for glycomacromolecular structure **15** when not immobilized on AuNP surface but free in solution. For comparison, four further glycomacromolecules **13**, **16**, **18** and **20** were chosen to test for their uptake behaviour in RKO cell line. These glycomacromolecular structures were selected because they were determined to be good representatives to study the effects of carbohydrate valency and backbone hydrophobicity on receptor interactions. Quantification of cellular uptake by flow cytometry was performed as described for cellular uptake studies with glyco-AuNP-FITC compounds. RKO cells were seeded in 96 well plates overnight and were then incubated with glycomacromolecular structures with FITC end group **c** for later monitoring in flow cytometry measurements. After 24 h incubation at 37°C and 5% CO_2, the medium inside the wells was carefully aspirated and the content of the wells was transferred into polystyrene test tubes after trypsin treatment. Following three consecutive washing steps with PBS buffer (0.01 M phosphate buffer, 0.0027 M KCl, 0.137 M NaCl, pH 7.2, 0.05% NaN_3, 0.05% BSA) the cell suspension was used for flow cytometry measurement. In addition to a 24 h incubation time, a 3 h incubation was also employed based on a previous cellular uptake study with FITC labelled glycomacromolecular compounds.[138] Cells were directly seeded in polystyrene test tubes and incubated with the respective glycomacromolecules for 3 h at 37 °C and 5% CO_2. Afterwards three consecutive washing steps with PBS buffer (0.01 M phosphate buffer, 0.0027 M KCl, 0.137 M NaCl, pH 7.2, 0.05% NaN3, 0.05% BSA) were performed followed by flow cytometry measurements. For all glycomacromolecules, a concentration of 2 µM was employed based on the concentration used for

glyco-AuNP-FITC compounds of 10 nM and an estimated degree of functionalization of approximately 200 glycomacromolecules per AuNP (200 · 10 nM = 2 µM) (see Chapter 3.2.2).

As shown in Figure 57A, a significant increase in fluorescence intensity could be observed after 3 h and leveled off after 24 h of incubation, probably due to receptor cycling or the establishment of an equilibrium. Thus, the uptake of glycomacromolecular structures seemed to be much faster than uptake for the same structures when immobilized on the AuNP surface. Moreover, all structures showed very similar uptake lying in the same range as the negative control **20c**. Similar to glyco-AuNP-FITC compounds, no influence of carbohydrate valency or backbone hydrophobicity on cellular uptake could be observed. In contrast to glyco-AuNP-FITC uptake, structure **15c** did not show increased uptake in comparison to the other glycomacromolecules. One reason for this difference could be that the presentation on the AuNP surface makes the difference and that only passive diffusion governs cellular uptake for the small glycomacromolecular compounds as has been previously suggested.[138] Additional flow cytometry studies involving the incubation of RKO cells with glycomacromolecules at different concentrations and at different temperatures showed that uptake was not only dose dependent but also proceeded via energy-dependent receptor mediated endocytosis (Figure 57B and C).

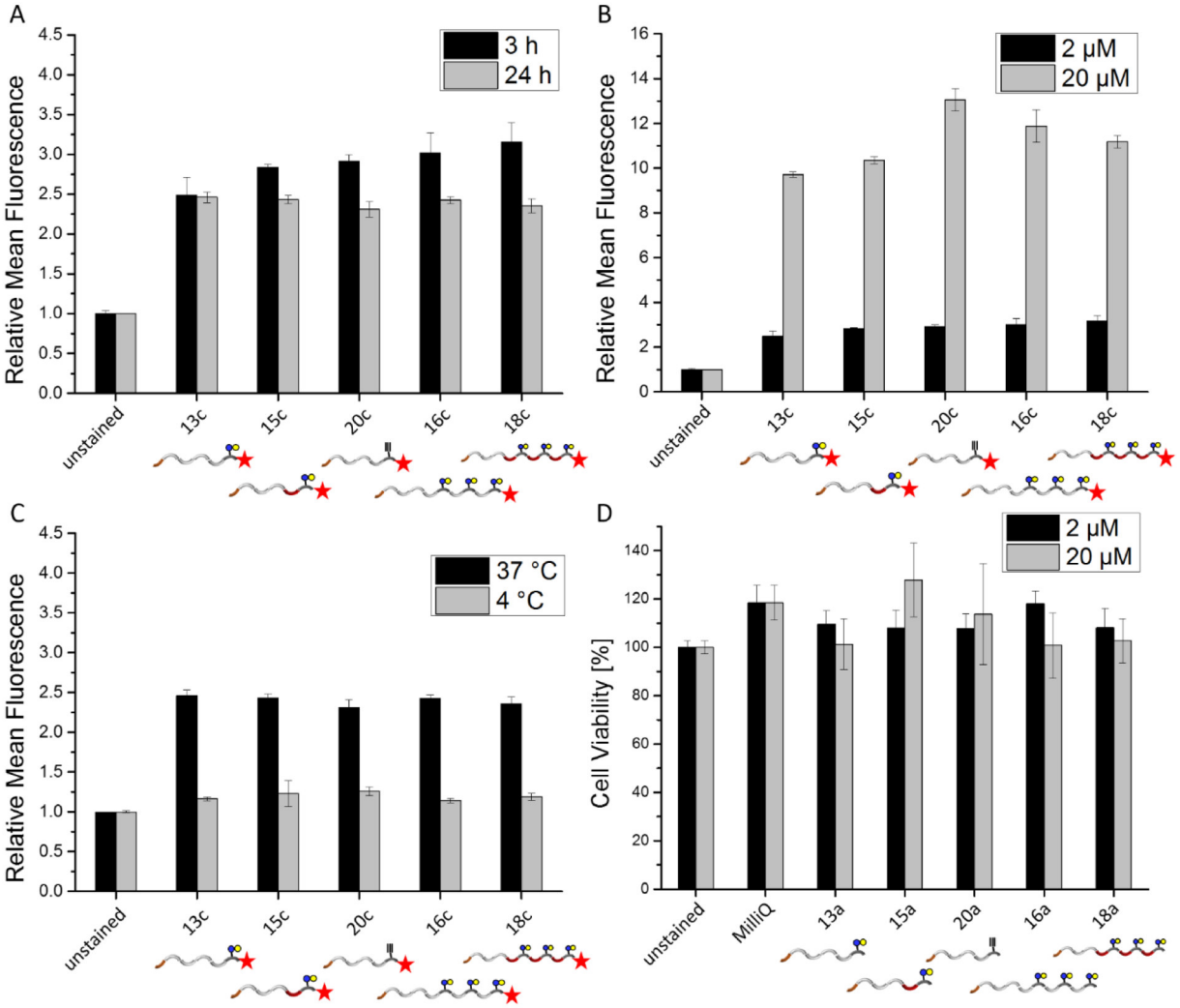

Figure 57: A: Comparison of cell uptake after 3 and 24 h incubation time, B: Comparison of cell uptake at 2 and 20 µM glycomacromolecule concentration, C: Comparison of cell uptake of 2 µM glycomacromolecule concentration after 24 h incubation time at 4 °C and 37 °C, D: Percentage of cell viability of RKO cell line in presence of 2 and 20 µM glycomacromolecule concentration after 48 h incubation at 37 °C and 5% CO_2. Cell viability of unstained cells was set to 100%. MilliQ water was used as vehicle control.

Another explanation for comparably low uptake of glycomacromolecule **15c** could be that the difference in end group functionality was a crucial factor. For flow cytometry measurements it was necessary to introduce a fluorescence label into glycomacromolecular structures so that the study was limited to glycomacromolecules with FITC end group **c**. This end group could have an influence on the binding behavior due to its steric demands and hydrophobicity. Moreover, the outstanding uptake of glyco-AuNP-**15b-FITC** functionalized with a glycomacromolecule with succinyl end group **b** could not be observed for the same compound with acetyl end group **a**. This finding suggested that the end group in combination with the aromatic hydrophobic spacer might have a significant effect on cellular uptake.

In addition to cellular uptake studies it was important to confirm cell viability in presence of glycomacromolecular structures in a XTT assay. Therefore, cells were seeded in a 96 well plate

overnight before glycomacromolecules were added in 2 and 20 µM concentration and incubated for 48 h at 37 °C and 5% CO_2. Then, XTT dye was added to the wells and after further 3 h incubation absorbance at 475 nm was recorded. XTT assay was performed with glycomacromolecular structures with non-fluorescent end group **a** because FITC is known to be cytotoxic. Figure 57D shows the cell viability on a percentage basis for RKO cell line in presence of glycomacromolecules **13a**, **15a**, **16a**, **18a** and **20a** at 2 and 20 µM concentration. In comparison to unstained cells that were not treated with any additional substance and the vehicle control, treated with MilliQ water, all tested glycomacromolecules showed good cell viability with values around 100% at both tested concentrations.

Unfortunately, overall glycomacromolecular uptake studies by flow cytometry could not confirm the same trend that was observed for the glyco-AuNP-FITC compounds with RKO cells. One concern in regard to flow cytometry studies was the reliability of the fluorescence read out that might be impaired by quenching effects of the fluorescence dye by the AuNP core, potentially leading to unreliable results. In order to exclude such quenching effects and to further confirm the results obtained in flow cytometry measurements, ICP-MS (Inductively Coupled Plasma – Mass Spectrometry) was employed to quantify the uptake of glyco-AuNP-FITC compounds irrespective of the fluorescence. ICP-MS allowed for the quantification of glyco-AuNPs based on the gold content of the sample. The high-temperature ICP source converts the atoms of the sample into ions that are then detected by the mass spectrometer in dependence of their mass-to-charge-ratio. After calibration with a reference substance the detected ion signal, which is proportional to the concentration, allows to determine the concentration of the investigated atom.

For ICP-MS the same procedure as for flow cytometry measurement was used for incubation. Cells were seeded in a 96 well plate overnight and were then incubated with glyco-AuNP-FITC compounds of 10 nM concentration for 24 h at 37 °C and 5% CO_2. Then, the wells were washed three times with PBS buffer. After trypsin treatment, the content of the wells was transferred into glass test tubes, centrifuged and the supernatant was poured out. The test tubes were left overnight at room temperature until they were completely dry. On the next day, the dry cell pellet was digested with aqua regia for 4 h at 85 °C. Subsequently, samples were cooled to room temperature and diluted with MilliQ water. Wells containing only cells as well as wells containing only AuNPs were included in the study as control. ICP-MS measurements were performed by a collaboration partner, Brandie M. Ehrmann, at the University of North Carolina at Chapel Hill, USA. Figure 58 shows the comparison of fluorescence corrected values obtained in FACS measurements and results obtained in ICP-MS for all glyco-AuNP-FITC compounds in RKO cell line. ICP-MS results exhibited higher error bars which can be explained by the high number of washing and transfer steps included in the assay procedure.

Nevertheless, ICP-MS results were in good agreement with the results obtained by flow cytometry. Again, small variations for the individual glyco-AuNP-FITC compounds could be observed but these variations could not be assigned to a trend in regard to carbohydrate valency or backbone hydrophobicity. More importantly, the increased uptake of glyco-AuNP-**15b-FITC** was observed, showing uptake that was about twice as high as uptake for all other glyco-AuNP-FITC compounds in ICP-MS measurement.

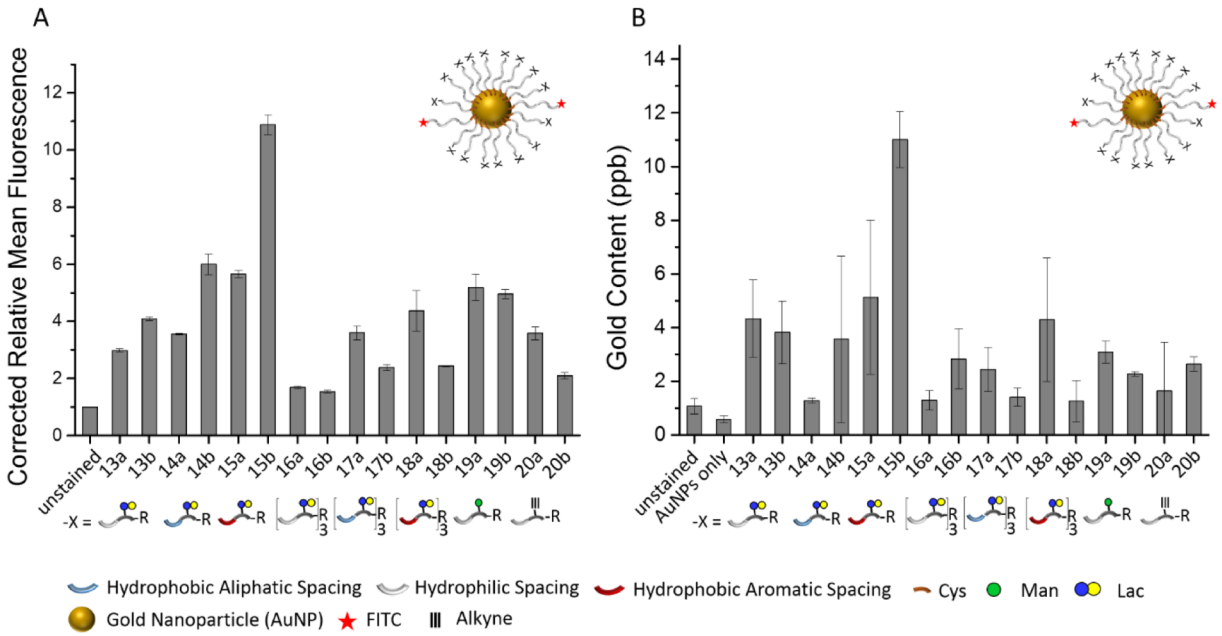

Figure 58: A: Corrected mean fluorescence values in flow cytometry measurement of all glyco-AuNP-FITC in RKO cell line after 24 h incubation at 37 °C and 5% CO_2 with 10 nM glyco-AuNP-FITC concentration. B: ICP-MS results obtained for all glyco-AuNP-FITC in RKO cell line after 24 h incubation at 37 °C and 5% CO_2 with 10 nM glyco-AuNP-FITC concentration. ICP-MS was performed in two different sets of experiments with triplicate determination per experiment.

With the confirmation of increased uptake for glyco-AuNP-**15b-FITC** in the RKO cell line, the next step was to assess the reason for this extraordinary behavior. The fact that high uptake was only observed in the RKO cell line and not in T3M4 cell line, both of which express the HIP/PAP receptor, suggested that uptake did not proceed via HIP/PAP receptor but that glyco-AuNP-**15b-FITC** potentially used a different pathway for entering the cell. One approach to assess whether AuNP uptake was promoted by HIP/PAP receptor or rather a different cellular uptake mechanism was to block the HIP/PAP or Reg3A receptor with competitive ligands like D-lactose and anti-Reg3A-antibody. For flow cytometry experiments, RKO and SK-BR-3 cells were seeded in a 96 well plate overnight. Then, preincubation with the respective competitor, 200 mM D-lactose, or 20 µg/mL anti-Reg3A-antibody was performed for 1 h before the AuNP-FITC compounds were added. Incubation continued for further 24 h at 37 °C and 5% CO_2. After incubation, the content of the wells was carefully aspirated, and remaining cells were transferred into polystyrene test tubes for washing after trypsin treatment. Washing was performed

with PBS buffer (0.01 M phosphate buffer, 0.0027 M KCl, 0.137 M NaCl, pH 7.2, 0.05% NaN3, 0.05% BSA) in three consecutive centrifugation and resuspension steps before the cell suspension was used in flow cytometry measurements. Figure 59A shows the results obtained in the flow cytometry experiment. Interestingly, no inhibition of cellular uptake in RKO cells could be observed by co-incubation of glyco-AuNP-**15b-FITC** with 200 mM D-lactose. The same was true for uptake in SK-BR-3 cells. Interestingly, for glyco-AuNP-**13b-FITC** and AuNP-**20b-FITC**, uptake increased in RKO cells in presence of 200 mM D-lactose. These results could be explained by the rapid uptake and digestion of D-lactose in the cells so that there is no remaining D-lactose blocking HIP/PAP receptors on the surface, though this is unlikely given the high concentration of D-lactose used in this study. For co-incubation with anti-Reg3A-antibody, a decrease of uptake in RKO cells could be observed for the two glyco-AuNP-FITC compounds that were functionalized with lactose carrying glycomacromolecules **15b** and **13b**. In contrast, the negative control AuNP-**20b-FITC** showed no decrease in cellular uptake when co-incubated with anti-Reg3A-antibody in RKO cells. Moreover, uptake of glyco-AuNP-**15b-FITC** in negative control cell line SK-BR-3 was not affected by presence of anti-Reg3A-antibody. These findings suggest that uptake of glyco-AuNP-FITC compounds in RKO cells was at least partially promoted by HIP/PAP receptors on the cell surface.

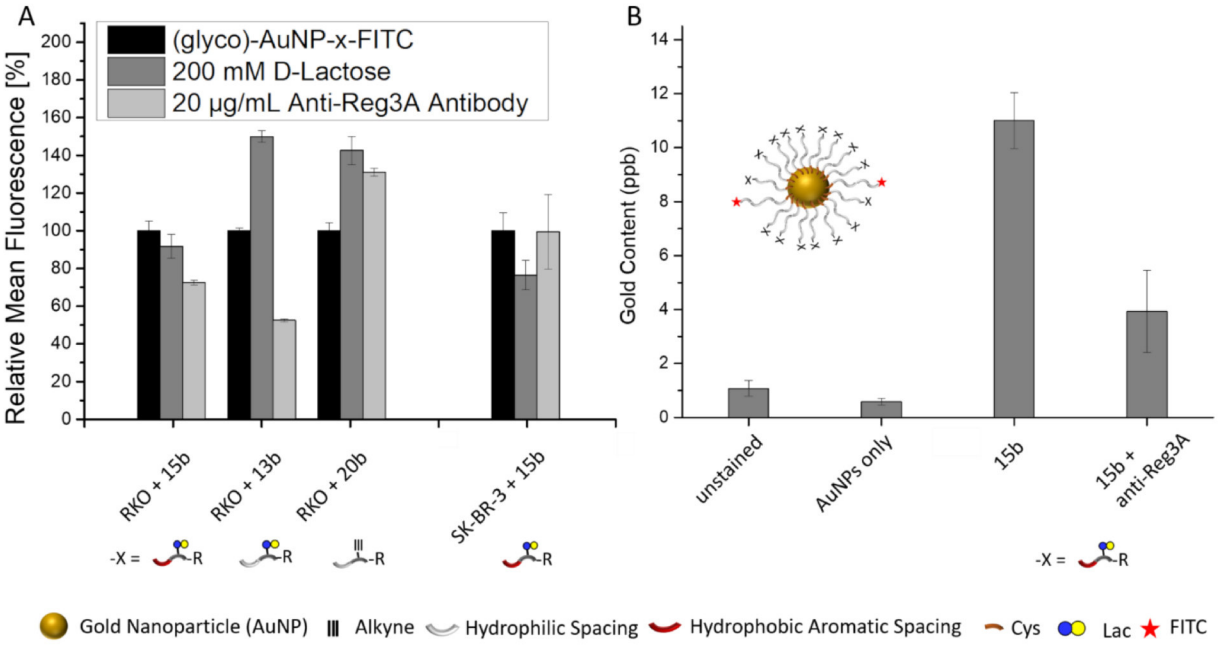

*Figure 59: A: Relative mean fluorescence obtained in flow cytometry measurements for the incubation of RKO and SK-BR-3 cells with 10 nM glyco-AuNP-**15b-FITC**, glyco-AuNP-**13b-FITC** and AuNP-**20b-FITC** alone and together with competitors D-lactose and anti-Reg3A-antibody after total incubation of 25 h. Fluorescence for cells treated with glyco-AuNP-**15b-FITC**, glyco-AuNP-**13b-FITC** and AuNP-**20b-FITC**, respectively, was set to 100%, B: ICP-MS results obtained for incubation of RKO cells with 10 nM glyco-AuNP-**15b-FITC** alone and together with anti-Reg3A-*

antibody as competitor after total incubation of 24 h at 37 °C and 5% CO_2. Wells that were only containing cells and AuNPs were included in the study as control.

In order to further confirm this finding, additional ICP-MS experiments were performed. Therefore, RKO cells were seeded in a 96 well plate overnight, and then incubated with glyco-AuNP-**15b-FITC** alone and together with anti-Reg3A-antibody for 24 h at 37 °C and 5% CO_2. Wells containing only cells and wells containing only AuNPs were included as control. After incubation, the content of the wells was carefully aspirated and wells were washed with PBS. The remaining cells were transferred into glass test tubes after trypsin treatment and centrifuged. The supernatant was poured out and the pellet was dried overnight. On the next day, the cell pellet was digested with aqua regia at 85 °C for 4 h before diluted with MilliQ water. ICP-MS experiment was performed by a collaboration partner, Brandie M. Ehrmann, at the University of North Carolina at Chapel Hill, USA. Figure 59B shows the results obtained in ICP-MS experiment. The results nicely demonstrate the decrease of about 65% of the original uptake of glyco-AuNP-**15b-FITC** in RKO cells when co-incubated with anti-Reg3A-antibody. The gold content obtained after co-incubation of glyco-AuNP-**15b-FITC** with this competitor lay in the same range as the uptake observed for all other glyco-AuNP-FITC compounds in the previous ICP-MS experiment (Figure 58B). These results also suggested that comparably high uptake of glyco-AuNP-**15b-FITC** could be promoted by specific interaction with HIP/PAP receptor on the cell surface.

In order to gain further information about which pathway is used by glyco-AuNP-**15b-FITC** for entering the cell, different endocytosis pathway mechanisms were taken into consideration. Endocytosis pathways can be divided into cellular uptake mechanisms following phagocytosis and mechanisms following pinocytosis.[262,263] In phagocytosis large solid particles are engulfed by the cell facilitated by actin filaments forming so called phagosomes. Pinocytosis involves the uptake of fluids and uptake of small molecules within vesicles, and it includes 112 icropinocytosis, clathrin-mediated endocytosis and caveolin-mediated endocytosis. In 112 icropinocytosis protusions are formed at the outer cell membrane. Similar to phagocytosis, forming of these protusions, called macropinosomes, is an actin-dependent process. Within these macropinosomes large volumes of extracellular fluid can be encapsulated and can enter the cell. Clathrin-mediated endocytosis is receptor-mediated. After its initiation, coated vesicles are formed by which uptake into the cell is mediated. These “coated pits” consist of transmembrane receptors and clathrin as a cytosolic protein forming a net like basket. In caveolin-mediated endocytosis coated vesicles are formed for cell uptake. The protein caveolin, in presence of increased levels of cholesterol, forms a flask-shaped invagination in the membrane which can be used for entering the cell. In order to investigate the pathway of cellular endocytosis used by glyco-AuNP-FITC compounds, specific pharmacological substances that specifically inhibit one of the described mechanisms can be used.[262,263] Cytochalasin D, for example, depolymerizes actin filaments

and acts as an inhibitor for phagocytosis and 112 icropinocytosis. Chlorpromazine hydrochloride can be used to inhibit clathrin-dependent endocytosis because it induces the loss of clathrin from the cell surface. Moreover, methyl-β-cyclodextrin inhibits caveolin-mediated endocytosis by depletion of cholesterol from the cell membrane.

Due to the fact that these pharmacological substances inhibit important cellular uptake mechanism they are highly toxic to the cells. This is why as a first step cell viability of RKO cells in presence of chlorpromazine hydrochloride (ChlorH), methyl-β-cyclodextrin (MβCD) and cytochalasin D (CytoD) was tested in a time-dependent fashion. Therefore, 90 µL of RKO cells were mixed with 10 µL of the respective inhibitor stock solution (1000 µM ChlorH, 100 mM MβCD, 40 µM CytoD) to obtain final inhibitor concentrations that were previously reported in literature.[263] This mixture was incubated at 37 °C and 5% CO_2 until 10 µL aliquots were removed after 0, 1 and 4 h, mixed with 10 µL trypan blue and loaded in a hemocytometer to count the number of live and dead cells. Trypan blue is an azo dye that stains dead cells blue, but cannot penetrate intact cell membranes of live cells so that live cells remain unstained.

Figure 60A shows the results obtained in the trypan blue assay. At time zero, about 90% of the cells were viable independent of the treatment employed. However, after 1 h the ratio of live cells decreased to about 70% for cells treated with ChlorH in comparison to untreated cells that still showed about 90% of viable cells. For the other endocytosis pathway inhibitors, MβCD and CytoD, the amount of live cells decreased less drastically to values of about 80 to 85%. After 4 h, only 80% of the untreated cells remained viable under the tested conditions. For ChlorH treatment cell viability was similar to the result obtained after 1 h with about 70% viable cells. The treatment with CytoD also lead to about 80% live cells after 4 h treatment. However, MβCD treatment drastically decreased the amount of live cells to only 60%, so that an incubation time of 4 h should not be exceeded for the tested concentration for MβCD.

Flow cytometry measurements were performed based on this cell viability test. RKO cells were seeded in polystyrene test tubes and were preincubated with the three endocytosis pathway inhibitors ChlorH, MβCD and CytoD for 1h at 37°C and 5% CO_2. Then, glyco-AuNP-**15b-FITC** and AuNP-**20b-FITC** were added at 20 nM concentration in order to counteract the short incubation time of 3 h. These two AuNP structures were selected because glyco-AuNP-**15b-FITC** showed highest uptake in previous tests and AuNP-**20b-FITC** served as negative control. A total incubation time of 4 h was not exceeded to maintain highest-possible cell viability. As a control, untreated cells and cells only treated with the respective AuNP compound were included in the study. After washing with PBS buffer (0.01 M phosphate buffer, 0.0027 M KCl, 0.137 M NaCl, pH 7.2, 0.05% NaN3, 0.05% BSA) cell suspensions were used for flow cytometry measurements. Figure 60B shows the relative mean fluorescence values obtained where

fluorescence was set to 100% for cells that were only treated with the respective AuNP compound. For RKO cells treated with glyco-AuNP-**15b-FITC**, no inhibition of cellular uptake could be observed when treated with ChlorH or CytoD, respectively. Only for treatment with MβCD a small decrease in fluorescence intensity to about 90% could be observed. For cells treated with AuNP-**20b-FITC,** no statistical significant effect of ChlorH and CytoD treatment on RKO cellular uptake could be observed. However, MβCD treatment reduced cellular uptake of AuNP-**20b-FITC** to about 65% of uptake without inhibitors. These results suggest that uptake in RKO cells was facilitated by a caveolin-dependent process. However, cell viability was also strongly affected by MβCD so that the reduced number of live cells could have an impact on AuNP uptake. Moreover, inhibitor concentration of ChlorH and CytoD might be too low to completely block the respective uptake pathways leading to false negative results. Thus, more tests would be necessary in order to identify the maximum inhibitor concentration that completely blocks the uptake mechanism but is at the same time minimally harmful to the cells.

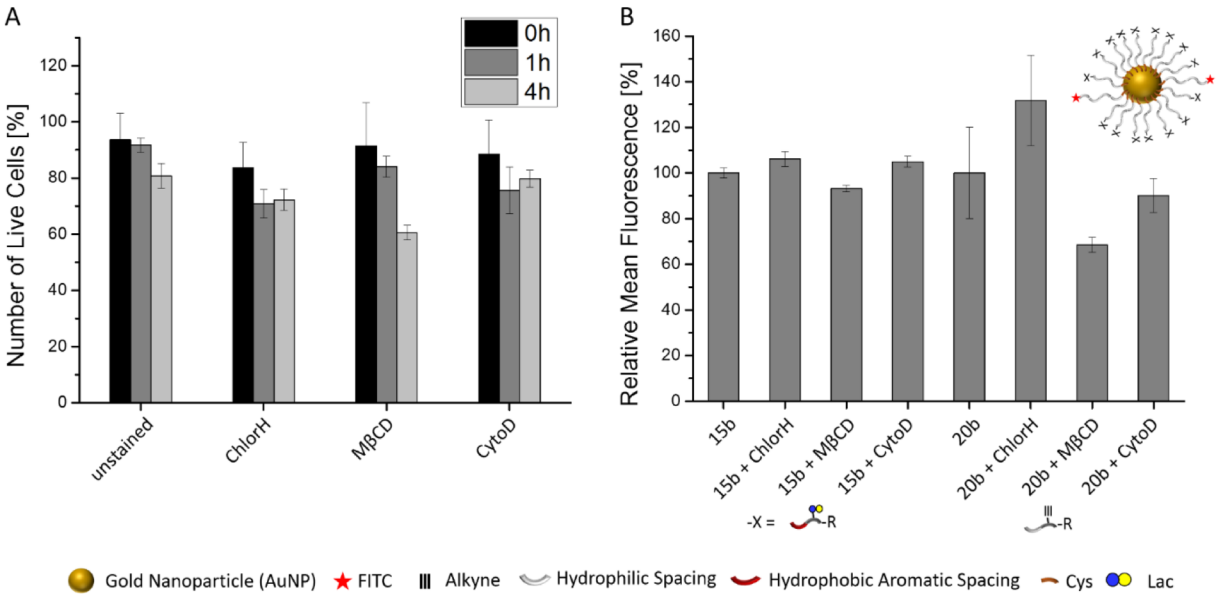

*Figure 60: A: RKO cell viability test with trypan blue for unstained cells and in prescence of endocytosis pathway inhibitors chlorpromazine hydrochloride (ChlorH), methyl-β-cyclodextrin (MβCD) and cytochalasin D (CytoD) after 0, 1 and 4 h, B: Relative mean fluorescence values obtained in flow cytometry measurements for incubation of RKO cells with 20 nM glyco-AuNP-**15b-FITC** and AuNP-**20b-FITC** alone and together with the endocytosis pathway inhibitors chlorpromazine hydrochloride (ChlorH), methyl-β-cyclodextrin (MβCD) and cytochalasin D (CytoD) after total incubation of 4 h. Fluorescence for cells treated with glyco-AuNP-**15b-FITC** and AuNP-**20b-FITC**, respectively, was set to 100%.*

In order to further investigate the cellular fate of glyco-AuNP-FITC compounds after entering the cells, fluorescence microscopy was employed. Therefore, cover slips were prepared by poly-lysine coating and washing with MIlliQ water before they were used for cell culturing. RKO and SK-BR-3 cells were seeded on the cover slips in petri dishes until confluence was reached. Then, cells were incubated with hit-structure glyco-AuNP-**15b-FITC**, lactose carrying glyco-AuNP-**13b-FITC** and negative control AuNP-**20b-FITC** at 10 nM and 20 nM concentration for 24 h at 37 °C and 5% CO_2. As a negative control,

unstained cells were included to correct for autofluorescence. Cells were washed with PBS buffer and nuclear and actin staining were performed. The cover slip was washed with PBS buffer and finally mounted on a glass slide for microscopy. Unfortunately, the fluorescence intensity was too weak to draw any firm conclusions. This experiment will be repeated in future studies in the Hartmann group to obtain higher fluorescence intensities with the goal of being able to draw conclusions about where glyco-AuNPs accumulate in the cell.

3.4 Towards Dynamic Combinatorial Libraries of Glycomacromolecules

Dynamic combinatorial libraries (DCL) or dynamic combinatorial chemistry (DCC) were first employed in the early 1980s. Since then, they have become important tools in today's chemical and biological research, especially drug discovery.[264] The idea behind DCC is that instead of using synthetic approaches for the design of discrete and stable molecules that are individually tested for their target effects in a screening processes, the target itself selects the best ligand from a library.[264] In DCC this library does not have a fixed number of constituents, but instead is able to undergo changes in order to adapt to the target requirements. Thereby, a virtual dynamic library is formed by the reversible reaction of the library constituents under thermodynamic control and it is expected that only in presence of the target molecule the best binder is preferentially formed and amplified (Figure 61).[265]

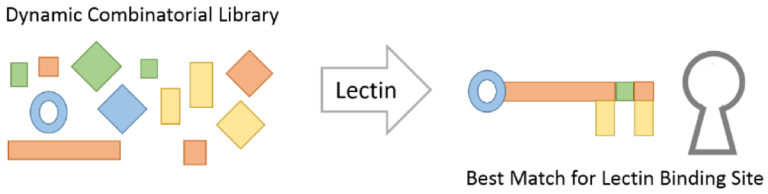

Figure 61: Schematic illustration of the concept of a dynamic combinatorial library.

Different prerequisites have to be met to produce such flexible and adaptive libraries. First, the library components, so called dynamers, have to be able to reversibly interact with each other to form interchanging "keys". Second, the conditions for library generation need to be established. Third, the selection pressure in form of a molecular "lock" has to be subjected to the DCL.[264] In order to meet the first requirement, library components have to exhibit functional groups that can undergo reversible exchange. In particular, the formation of reversible covalent bonds has been shown to be efficient for the use in DCLs. Another desirable feature is the opportunity of fixation which means that once the DCL has been formed, the exchange process is no longer accessible.[265] Possible fixation methods involve a change in pH, temperature or quenching reagents.[264]

When biological molecules are targeted, even more precautions have to be taken in selecting best suitable functional groups for reversible exchange because they have to be compatable with mild and aqueous conditions.[264] Imine formation and their exchange (transamination) as well as thiol-disulphide interchange have been identified as attractive reactions when proteins are targeted as the receptor.[264] Imine formation can be characterized by rapid formation equilibria and exchange rates and thus is suitable for DCL formation. In addition, cyanoborhydride can be added to freeze out the interchanging bonds. However, the C=N bond in imines is not stable under aqueous conditions so that the equilibrium lies towards the starting amines and aldehydes. Moreover, the presence of free amine groups at the protein surface can interfere with the reaction.[264] Thiol-disulphide interchange is well

suited for use in aqueous medium. Library generation can be performed under neutral to slightly alkaline conditions, and the equilibrium should be stopped or at least drastically reduced under acidic conditions. This approach is especially advantageous when proteins that do not exhibit free thiol groups or disulphide linkages are employed.[264]

For example, Lehn *et al.* introduced a virtual DCL by self-assembly based on the condensation reaction of several aldehydes and amines.[266] They employed their library to identify suitable inhibitors of carbonic anhydrase (CA) and found that the presence of CA led to preferred formation of those library constituents expected to be strong binders for the CA active site.[266] Moreover, Stoddart *et al.* used the DCL principle for the template driven synthesis of rotaxanes by imine bond formation.[267] Furthermore, they highlighted the advantageous properties of this approach, such as simplicity, effectiveness and high yields. The principle of such dynamers can be further extended to DCLs that contain components with biorelevant residues, so called biodynamers.[268] These structures combine the advantageous properties of biofunctionality and the adaptive feature of dynamers. One example is the use of saccharides as biofunctionality leading to glycodynamers.[268] Lehn *et al.* for example used the DCL approach of imine bond formation to target the binding site of ConA.[269] The dynamic carbohydrate library was generated by mild disulphide interchange of a set of four to six initial carbohydrate dimers. Virtual DCLs contained up to 21 compounds in equal amounts. When ConA was added to the mixture only one disulphide component presenting two α-D-mannose functionalities was preferentially bound.[269]

In this work strategies towards a dynamic combinatorial library of glycomacromolecules using previously introduced building blocks should be explored. As library, sets of glycomacromolecules with different backbone units and different linker lengths carrying α-D-mannose were incubated in the presence of ConA and evaluated for the formation of a preferred DCL component (Figure 62). Two different DCL approaches based on thiol-disulphide interchange and imine bond formation were employed, each presenting its own advantages and disadvantages.

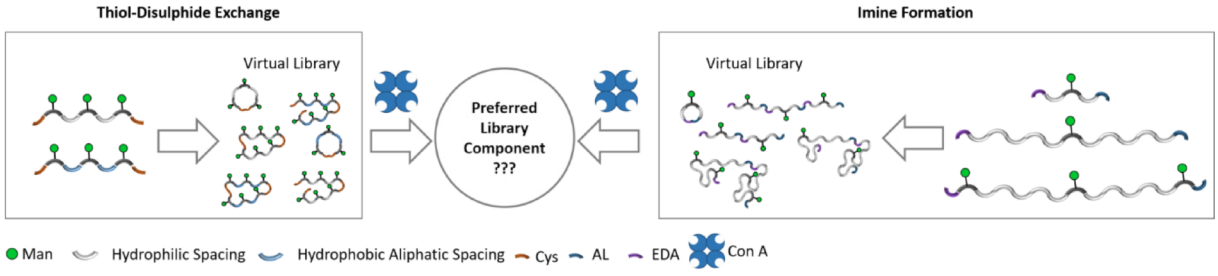

Figure 62: Overview of structural design features varied in the two different DCL approaches: Backbone hydrophobicity in thiol-disulphide exchange (left) and carbohydrate spacing in imine formation approach (right).

3.4.1 Dynamers Based on Thiol-Disulphide Interchange

As a first approach, the thiol-disulphide interchange approach was selected for DCL formation because of previous experience with the SPPoS of thiol-functionalized precision glycomacromolecules (Chapter 3.2 and 3.3). The glycomacromolecules in the library thus were designed to have two thiol endgroups and three carbohydrate moieties with the same overall scaffold length. They differ in backbone characteristics as the determining factor for DCL amplification in presence of ConA based on the previous results that the lectin interacts more strongly with scaffolds containing hydrophobic moieties (Figure 63).

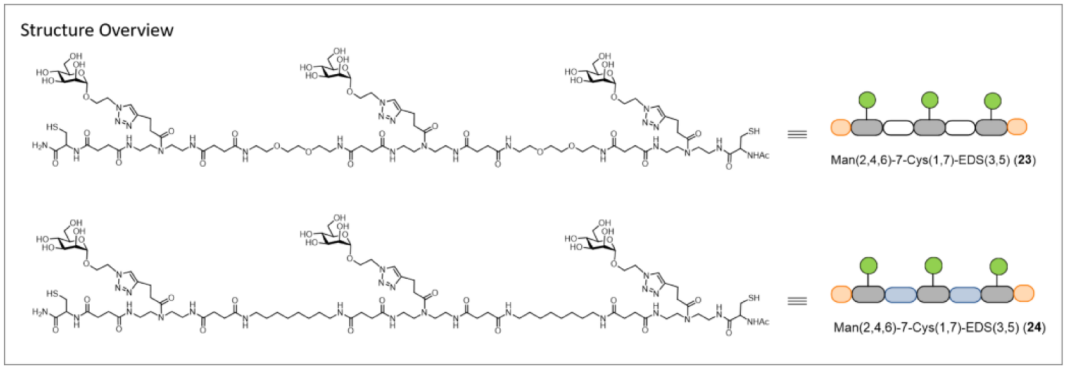

Figure 63: Overview of chemical and schematic glycomacromolecule structures for use in DCL.

SPPoS and purification of products was proceeded as described in Chapter 3.3. to give glycomacromolecules decorated with two thiol groups, one on each end of the backbone. This structural feature should enable the formation of longer chains or rings with glycomacromolecule segments when combined in a DCL. Synthesis was confirmed by ^{1}H-NMR, MALDI-TOF-MS and HPLC analysis.

Figure 64 shows an exemplary ^{1}H-NMR spectrum of glycomacromolecule **23**. In analogy to proton NMR spectra described in previous chapters typical resonances for TDS and EDS building blocks, L-cysteine as well as carbohydrate moiety are displayed. Moreover, a strong signal for the acetate group present as counter ion after ligand exchange can be found at a chemical shift of 1.93 ppm. For detailed information please refer to the description of proton NMR in Chapter 3.2 and 3.3 as well as in the experimental part and appendix.

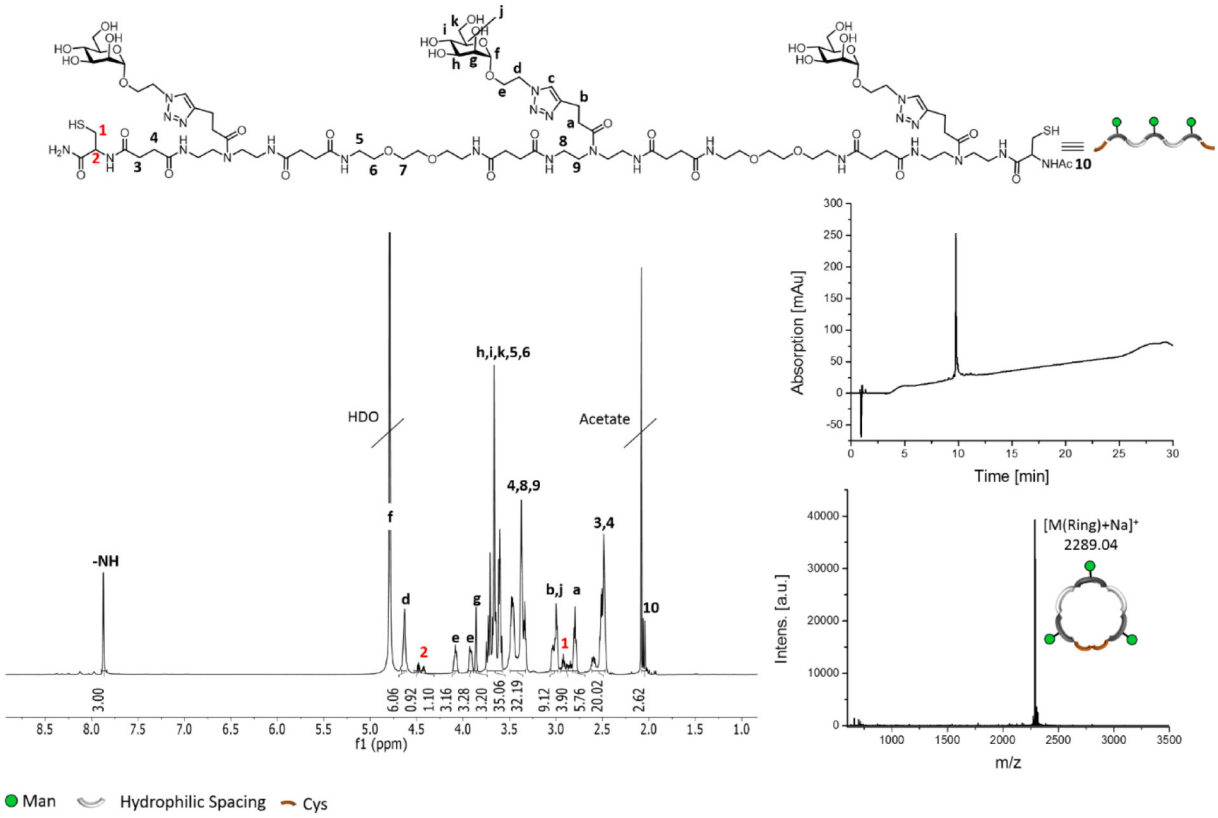

*Figure 64: Exemplary ^{1}H-NMR (600 MHz, D2O), RP-HPLC chromatogram (95/5 H_2O/MeCN with 0.1% formic acid (A) and 5/95 H_2O/MeCN with 0.1% formic acid (B); 100% A to 50% A in 30 min) and MALDI-TOF-MS spectrum of glycomacromolecule **23**. Protons of natural amino acid L-cysteine are highlighted in red.*

In order to further confirm the overall chemical composition of the synthesized glycomacromolecules, MALDI-TOF-MS and RP-HPLC analyses were applied as exemplary shown in Figure 64. The theoretically calculated mass-to-charge ratios correspond to the observed values in MALDI-TOF mass spectrometry for the cyclized monomer form. Here, only the ring form could be found due to delayed MALDI-TOS measurement and the prior storage in solution. The RP-HPLC chromatogram nicely demonstrates the monodispersity and high relative purity of the synthesized compound (Figure 64).

3.4.1.1 Dynamic Behavior of Dithiol-Glycomacromolecule Structures

After synthesizing the two dithiol-glycomacromolecule test structures, the first step was to assess time-related and pH conditions for disulphide formation. Literature protocols for DCLs based on thiol-disulphide interchange suggests an equilibration time of 3 days and up to two weeks at neutral (pH 7.4) to basic (pH 9) pH conditions in presence of atmospheric oxygen.[269,270,271] Under these conditions, the disulphides should readily form thiol-groups and interchange in presence of catalytic amounts of thiol. Thereby, the thiol is deprotonated and the corresponding thiolate nucleophilic attacks the disulphide leading to the formation of a new disulphide and thiol group.[272,273] This inter-change should be prevented at acidic conditions due to the fact that thiol deprotonation does not occur anymore.

In analogy to these literature studies, glycomacromolecules **23** and **24** were dissolved at 10 mM concentration under different pH conditions. Acetate buffer was used to prepare solutions at pH 4.75. Hepes buffer was used for slightly basic pH conditions of pH 7.4, and phosphate buffer was employed to introduce basic pH values of 8. These solutions were exposed to atmospheric oxygen under shaking. Oxidation was followed by quantifying the amount of remaining thiol groups with Ellman´s reagent after defined time intervals over a two week period.[274] Elman´s reagent or 5,5´-dithiobis-(2-nitrobenzoic acid) is a compound that can be used for the determination of the amount of free thiol groups in solution. Together with Elman´s reagent, thiols react under release of 2-nitro-5-thiobenzoate, which under neutral to basic conditions functions as yellow dye which can be followed spectrophotometrically (Figure 65A).[275]

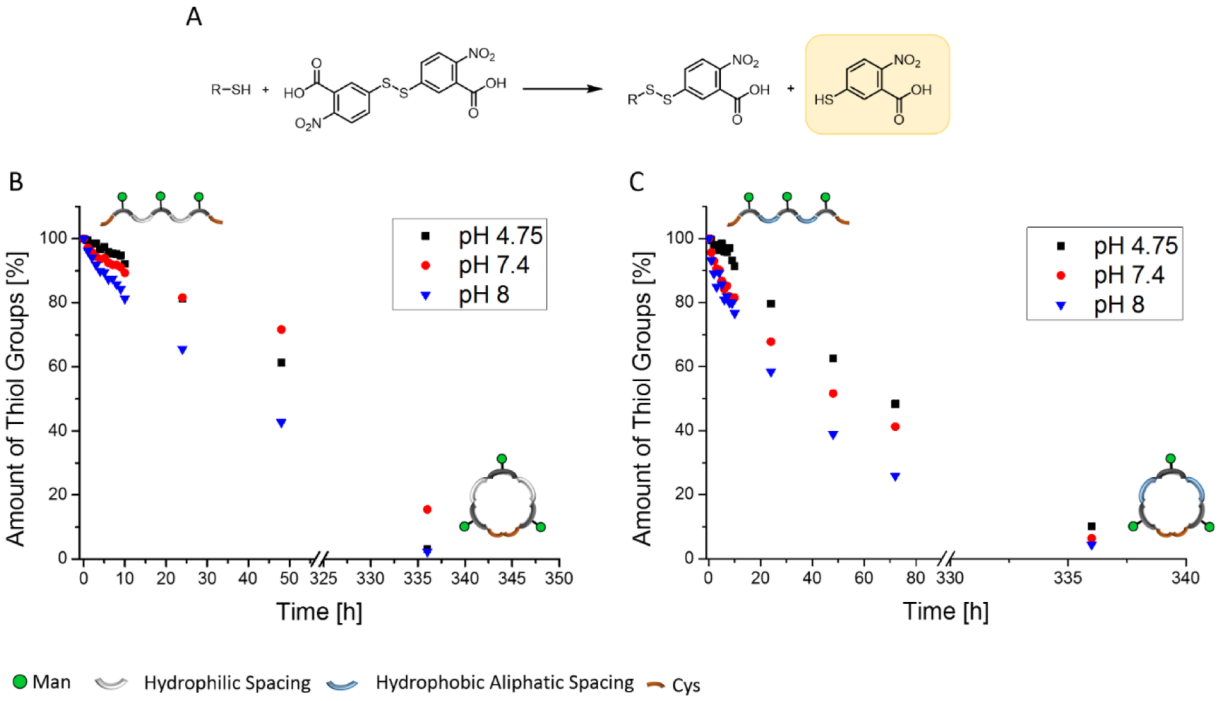

*Figure 65: A: Color development in the reaction of thiol groups with Elman´s reagent. Development of the amount of thiol groups in solution under atmospheric oxygen over a time period of two weeks for B: glycomacromolecule **23** and C: glycomacromolecule **24**.*

The results obtained for the two glycomacromolecules **23** and **24** are presented in Figure 65B and C. The UV absorption at time zero was set to 100% and from there all further measurements were related to this starting point. For all tested pH conditions (4.75, 7.4 and 8), the amount of thiol groups steadily decreased over time reaching zero to approximately 10% after two weeks of exposure to atmospheric oxygen. In the case that predominantly linear structures were formed, it would be expected that the amount of thiol groups would not drop below 50%. However, the low value obtained in this experiment suggests that circular structures were dominant. As it was stated in literature, thiol oxidation by atmospheric oxygen could be avoided at pH values around 5. It was striking that the decrease of thiol

groups under acidic conditions was similarly fast as under basic conditions.[276] This observation led to questions about the freezing ability of the dynamic system under acidic conditions, as the thiolate anion is the reactive group in both oxidation and disulphide exchange.

In order to further examine disulphide formation and the components formed during DCL equilibration in the different experimental setups, RP-HPLC analysis coupled with an ESI mass spectrometer was employed. An exemplary chromatogram is shown in Figure 66. As already expected from the change of thiol content in solution, as determined by UV-Vis, RP-HPLC-MS analysis confirmed that ring structures were predominantly formed. Ring structures of monomeric and dimeric structures could be confirmed by RP-HPLC-MS analysis. Only small peaks could be found for monomeric and dimeric linear structures. It is important to note that the magnitude of the peak integrals is dependent on the extinction coefficient of the compound analyzed. However, it can be expected that the extinction coefficient does not significantly change when going from the linear to cyclic form. When going from monomeric to dimeric structures, the extinction coefficient probably increases such that integral size might comparably seem too large and that the amount of higher molecular weight structures lies below the value expected from integration.

The preference for the formation of smaller linear or ring structures over higher order structures was also previously observed in literature.[265,271] Even though libraries containing a small number of bifunctional components could in theory lead to an infinite number of higher molecular weight structures in linear or ring form, in practice the evolution of the library stopped at the stage of pentamers or hexamers.[265] This could be due to very low concentrations of higher order structures that lie below the detection limit. However, it is more likely that the formation of these larger structures does not occur because of entropic constraints that need to be overcome by favourable enthalpic contributions.[265] These favourable enthalpic contributions could, for example, be introduced by high affinity interactions of the formed structure with the binding site of a receptor.

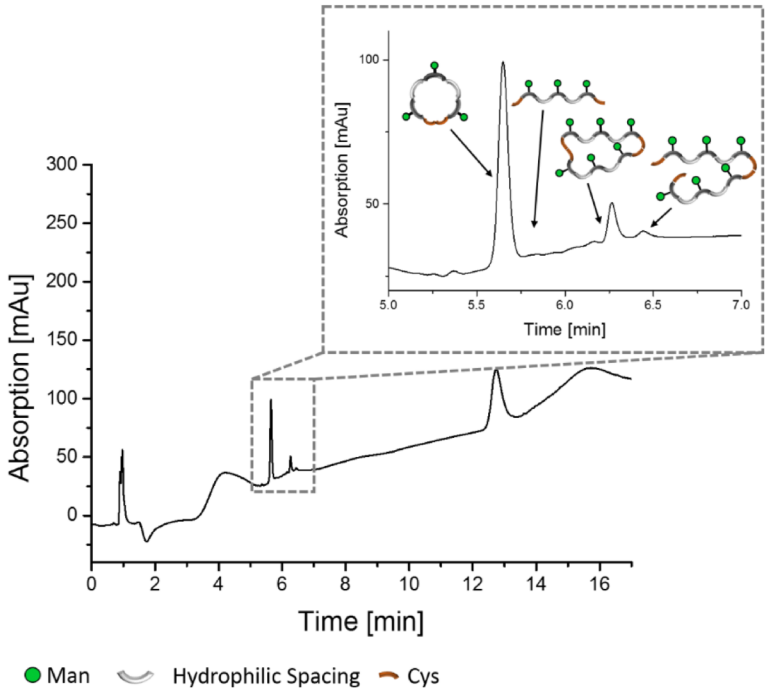

*Figure 66: Exemplary RP-HPLC chromatogram (95/5 H_2O/MeCN with 0.1% formic acid (A) and 5/95 H_2O/MeCN with 0.1% formic acid (B); 100% A to 5% A in 17 min)of compound **23** at 10 mM concentration and pH 8 after two weeks of equilibration under atmospheric oxygen. Broad peaks at time ranges from 4 to 5 and 12 to 13 minutes belong to the blank. The inset shows the magnification of the chromatogram area of interest.*

As a next step, the evolution of DCL components was monitored in presence of the model lectin ConA in order to test for the potential amplification of one of the library components due to favourable interactions with the carbohydrate binding site of the lectin. Therefore, two approaches were applied. In the first approach, ConA was added to a pre-equilibrated DCL of glycomacromolecules **23** and **24**. In the second approach, the two dithiol structures were equilibrated together with ConA. Due to the fact that solutions had to be very dilute in order to prevent precipitation of the lectin ligand complex, 20 µM solutions of ConA and glycomacromolecules, respectively, were mixed in a 1:1 ratio and equilibrated. Unfortunately, these solutions were too dilute to be analysed by RP-HPLC-MS. Therefore, an approach used by Lehn *et al.* who use immobilized ConA and then used a subsequent filtration step for DCL formation was employed.[269] ConA-sepharose was loaded into a 5 mL syringe reactor and equilibrated with LBB buffer. Then, the ConA-sepharose slurry was either added to the pre-equilibrated library of compounds **23** and **24** or was equilibrated together with these glycomacromolecules. In addition, a mixture of both glycomacromolecules was subjected to ConA treatment. For comparison, samples containing no ConA were prepared under similar conditions. In order to promote fast thiol-disulphide exchange, catalytic amounts of dithiothreitol (DTT) were added. DTT can function as an initiating reagent by reducing the disulphide bonds to the required thiol groups.[269] After two weeks under atmospheric oxygen, the reaction mixture was transferred into a centrifuge filter and washed with MilliQ water. The bound species were then released by addition of hydrochloric acid and a second

filtration step. Analysis of DCL composition was performed by RP-HPLC-MS analysis. The results obtained are displayed in Figure 67. DCL composition was different when glycomacromolecules were incubated together with the model lectin ConA. Thus, the presence of the receptor and binding of the glycomacromolecules to the lectin binding sites seem to have an effect on compound formation in DCL. Instead of monomeric and dimeric ring forms, only monovalent ring form could be observed in presence of ConA (Figure 67A and B). This result was found for both pre-equilibrated and co-equilibrated libraries. Even when DCL opportunities were expanded due to the presence of two different glycomacromolecular structures **23** and **24** interacting with ConA molecule simultaneously, no change in this behaviour could be observed (Figure 67C). This finding suggested that ConA preferentially bound to smaller monomeric rings so that formation of bigger ring sizes was omitted in the dynamic library setting.

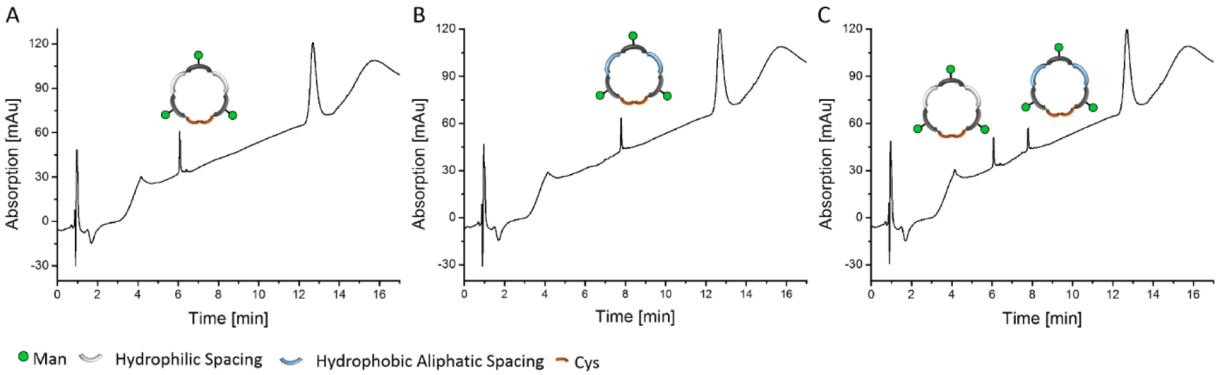

*Figure 67: RP-HPLC chromatograms (95/5 H_2O/MeCN with 0.1% formic acid (A) and 5/95 H_2O/MeCN with 0.1% formic acid (B); 100% A to 5% A in 17 min) of A: **23**, B: 24 and C: 23 and 24. Broad peaks at time ranges from 4 to 5 and 12 to 13 minutes belong to the blank.*

It seems that there is a template effect of ConA in DCLs of glycomacromolecule dithiol compounds, however, it does not lead to higher molecular weight structures but rather favoured the formation of cyclic glycomacromolecules through intramolecular ring formation. Furthermore, no difference for glycomacromolecules with more hydrophilic (EDS based) or hydrophobic (ODS based) scaffolds was observed. Most critically, disulphide formation was not stopped at low pH values which makes a full control over the library by freezing out the thiol-disulphide exchange questionable. This is why a second approach based on the formation of imine bonds by the condensation reaction of amines and aldehydes was assessed for DCL formation of precision glycomacromolecules.

3.4.2 Dynamers Based on Imine Bond Formation

As alternative approach, a dynamic combinatorial library based on imine bond formation by the condensation reaction of aldehydes and amines positioned on the end of a glycomacromolecular backbone was investigated. Imine bond formation and exchange was expected to be more rapid in aqueous media in comparison to the disulphides. Moreover, in theory the reaction mixture can be

equilibrated at neutral conditions, and efficiently frozen out by the addition of sodium cyanoborohydride ($NaBH_3CN$). The addition of the reducing agent should lead to the reduction of imine bonds to amines prohibiting further the dynamic exchange in DCL. Similar to work described in the previous chapter, the addition of the targeted receptor ConA should lead to the preferred formation of one component out of the theoretical possible number of structures in the DCL. In order to introduce the amine group for imine bond formation at one end of the glycomacromolecule no building block was used. Instead a Tentagel® resin with trityl linker was prefunctionalized with ethylenediamine (EDA), which after cleavage resulted in a primary amine end group.[95] However, no approach for the introduction of aldehydes into the glycomacromolecular backbone was previously investigated in the Hartmann group. Based on literature studies that showed that aromatic aldehydes together with aliphatic amines show efficient imine bond formation under aqueous conditions commercially available 4-formylbenzoic acid (here termed AL for aldehyde) was chosen for the introduction of the aldehyde functionality at the other end of the glycomacromolecule (Figure 68).[277]

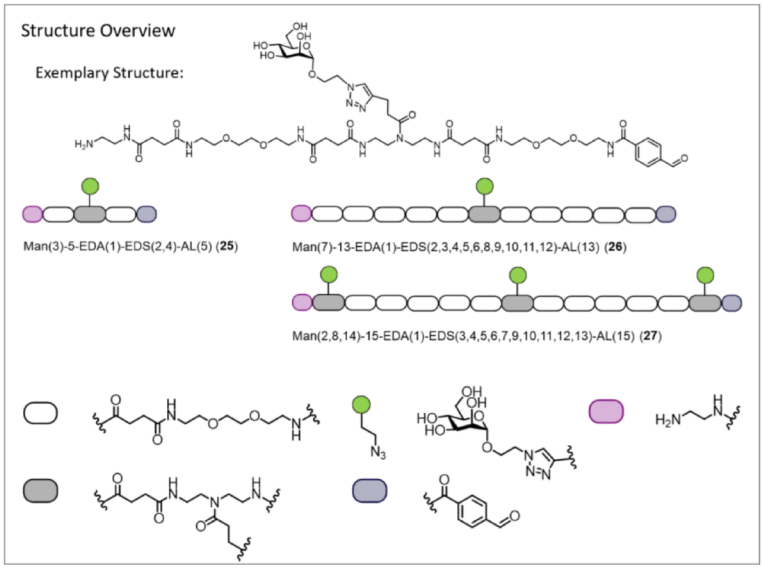

Figure 68: Overview of glycomacromolecule structures for use in DCL.

Glycomacromolecules were assembled on solid support as described in previous chapters. For introduction of AL building block, different reaction conditions were tested (Figure 69A). The first route followed the standardly employed procedure used for all other building blocks. Thus, the last building block assembled on solid support was deprotected with 25% piperidine in DMF and then coupling of 5 eq. of AL building block was undertaken with PyBOP as coupling reagent in presence of DIPEA as base. Subsequently CuAAC reaction, sugar deprotection and cleavage from solid support were performed. However, the basic conditions used for sugar deprotection and strong acidic conditions used for final cleavage from solid support led to the formation of side products as shown in Figure 69B.

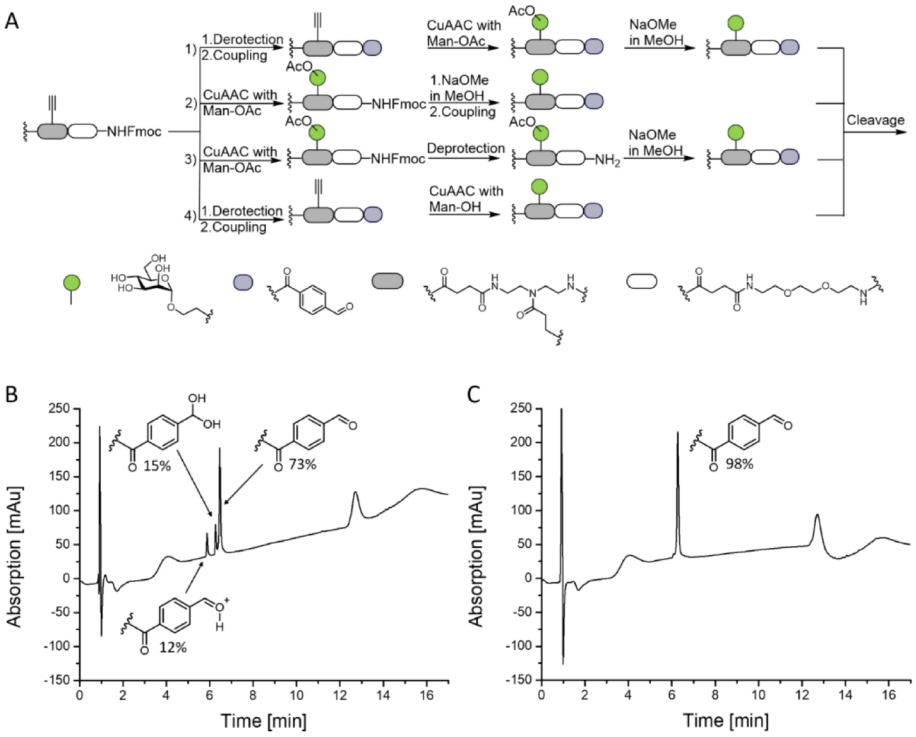

Figure 69: A: Schematic Overview of synthetic routes employed to test for optimal coupling of AL building block, B: RP-HPLC chromatogram (95/5 H_2O/MeCN with 0.1% formic acid (A) and 5/95 H_2O/MeCN with 0.1% formic acid(B); 100% A to 5% A in 17 min) of the product obtained by the first route, C: RP-HPLC chromatogram (95/5 H_2O/MeCN with 0.1% formic acid (A) and 5/95 H_2O/MeCN with 0.1% formic acid(B); 100% A to 5% A in 17 min) of the product obtained by route 4. Broad peaks at time ranges from 4 to 5 and 12 to 13 minutes belong to the blank.

As a consequence, the sequence of the reaction steps was inverted. Therefore, the Fmoc group of the last building block was not directly removed, but CuAAC reaction was performed and then sodium methoxide in methanol was employed to remove both carbohydrate and Fmoc protecting group simultaneously. Alternatively, the CuAAC reaction was followed by first Fmoc removal and then carbohydrate deprotection. Both strategies showed the formation of impurities that could not be assigned to a specific side product. In order to further reduce the exposure of AL building block to harsh basic or acidic conditions, instead of using a protected sugar for CuAAC reaction the α-D-mannose azide derivative was deprotected in solution before use in solid phase synthesis so that resin treatment with sodium methoxide could be omitted. Moreover, the amount of TFA that was used for final cleavage from solid support was reduced from 30% to 10%. In this way high purity of the final glycomacromolecule could be obtained as shown by RP-HPLC chromatogram in Figure 69C.

Overall, three different glycomacromolecules were synthesized following this procedure: a short monovalent glycomacromolecule with only one EDS spacer next to the carbohydrate carrying TDS building block (**25**), and two longer glycomacromolecular structures, monovalent compound **26** and trivalent compound **27** (Figure 68). All three compounds exhibited a primary amine group on the one end of the glycomacromolecule and an aldehyde functionality on the other end of the

glycomacromolecule which makes them suitable candidates for DCL based on imine formation. Synthesis of the three compounds was confirmed by ^{1}H-NMR, MALDI-TOF-MS and HPLC analysis.

Figure 70 shows an exemplary ^{1}H-NMR spectrum of glycomacromolecule **25**. In analogy to proton NMR spectra described in Chapter 3.4.1 typical resonances for TDS and EDS building blocks as well as carbohydrate moiety are displayed. Moreover, a strong signal for the acetate group, which is present as a counter ion after ligand exchange, can be found at a chemical shift of 1.93 ppm. For detailed information please refer to the description of proton NMR in previous capters or the experimental part as well as the appendix. Signals that were not discussed before are highlighted in red and belong to functional groups involved in DCL. The aldehyde proton can be found as multiplet at low field with a chemical shift of 10.04 to 9.94 ppm. Other aromatic protons that can be assigned to AL building block can be found as multiplet signals in a range from 8.09 to 7.73 ppm partially overlapping with the proton of the triazole ring. Protons of the EDA linker group can be found at a higher field with multiplet signals at 3.53-3.09 ppm, partiallly overlapping with TDS protons. The NMR spectrum also reveals imine formation of the sample, by the signal of the imine proton as a multiplet signal at 7.64 to 7.50 ppm.

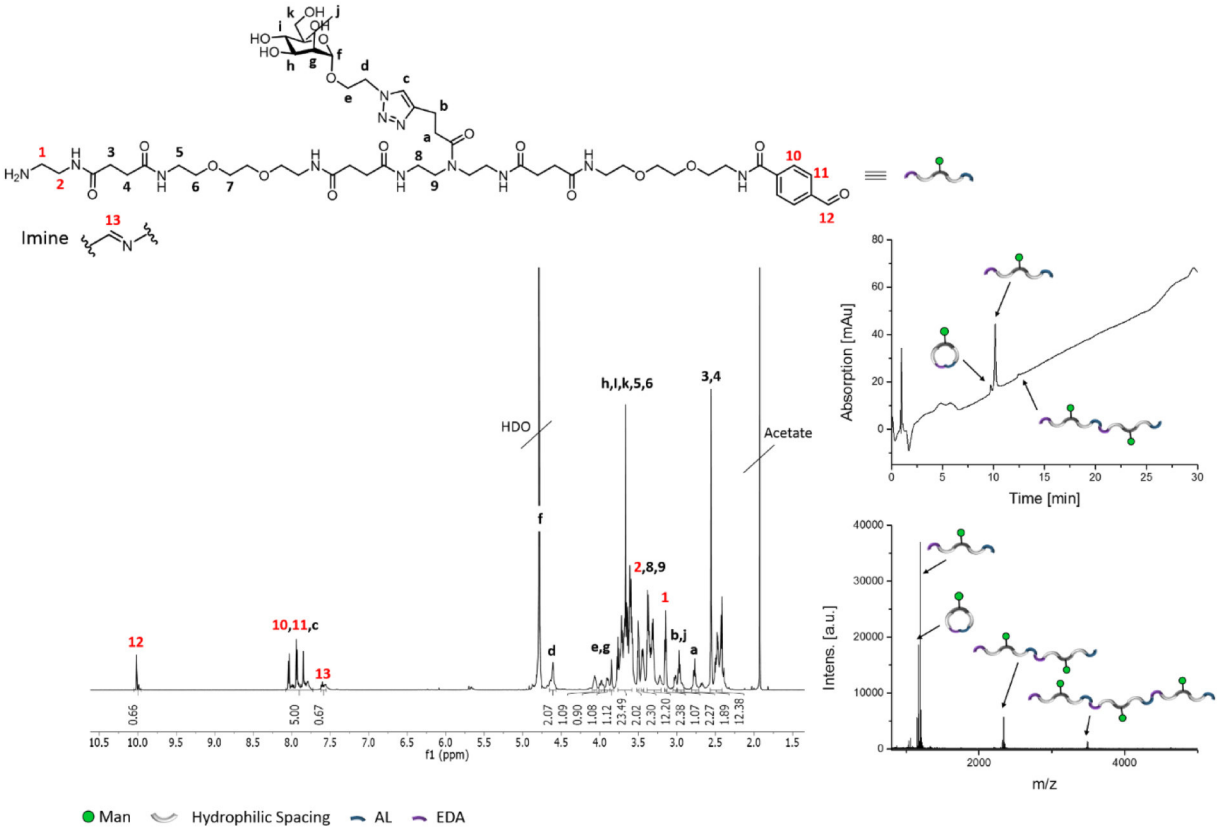

*Figure 70: Exemplary ^{1}H-NMR (600 MHz, D_2O), RP-HPLC chromatogram (95/5 H_2O/MeCN with 0.1% formic acid (A) and 5/95 H_2O/MeCN with 0.1% formic acid (B); 100% A to 50% A in 30 min) and MALDI-TOF-MS spectrum of glycomacromolecule **25**. Protons of EDA and AL moiety as well as of the formed imine bond are highlighted in red.*

Further proof for imine bond formation in aqueous solution was provided by RP-HPLC-MS chromatogramm and MALDI-TOF mass spectrometry (*Figure 70*). In the RP-HPLC-MS chromatogram, formation of the ring structure and the linear compound **25** as well as the linear dimer form could be verified. In addition, MALDI-TOF-MS also showed the formation of the linear trimer form of **25** (*Figure 70*). As a result, the different analytic methods not only provided proof for the synthesis of the compounds but also that imine formation occurred.

3.4.2.1 Dynamic Behavior of Glycomacromolecule Structures Forming Imine Bonds

After successful synthesis of the three glycomacromolecular compounds with amine and aldehyde end groups, the next step was to assess the time dependent evolution of imine formation in aqueous solution. Therefore, the smallest compound **25** was chosen as a test structure that at 20 mM concentration was exposed to different pH conditions and freezing agent $NaBH_3CN$. Library composition was then analysed by RP-HPLC-MS after defined time intervals over a four week period (Figure 71A).

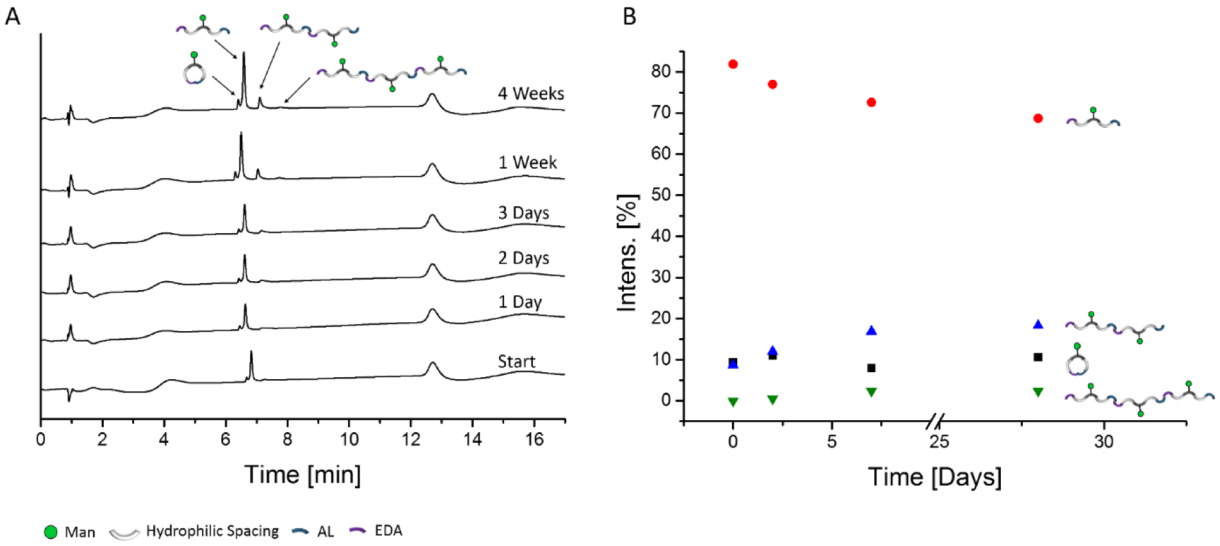

*Figure 71: A: Exemplary RP-HPLC chromatogram (95/5 H_2O/MeCN with 0.1% formic acid (A) and 5/95 H_2O/MeCN with 0.1% formic acid (B); 100% A to 5% A in 17 min) of compound **25** at 20 mM concentration and pH 7.4 after 0, 1, 2, 3, 7 and 28 days of equilibration. Broad peaks at time ranges from 4 to 5 and 12 to 13 minutes belong to the blank. B: Evolution of the signal intensity of the respective DCL compounds as determined by integration of RP-HPLC chromatogram peaks after 0, 1, 2, 3, 7 and 28 days of equilibration.*

Irrespective of acidic (acetate buffer, pH 5.2) or neutral (LBB, pH 7.4) pH conditions, library evolution followed a very similar behaviour. As a result, it was decided to work at pH 7.4 because at this pH condition the target receptor ConA is predominantly present in tetrameric form and as such provides more binding pockets in close proximity to each other. As shown in Figure 71A and B for pH 7.4, the amount of the linear compound **25** slightly decreased while the amount of linear dimer and trimer structures slightly increased over time. The amount of the ring structure of **25** remained mainly constant. After one week, the composition of the library seemed to reach equilibrium and did not

significantly change after 4 weeks in comparison to the one-week time interval. Thus, one week was chosen as time interval for all further equilibration experiments.

When analysing the ratio of different DCL species by integration of the peaks in RP-HPLC-MS chromatogram, it is again important to note that extinction coefficient of the compounds might be different not allowing for quantitative comparison of integrals. This is why only the evolution of the percentage of each integral over time can be used to make a statement on formation of different DCL products. Similar to results presented in Chapter 3.4.1.1 on DCL formation using disulphide structures, it was observed that the evolution of the library stopped at the stage of trimers, even though in theory the formation of higher molecular weight structures would be possible. This could either be explained by the fact that high molecular weight structures are entropically unfavourable or that the amount of higher molecular weight compounds formed lies below the detection limit.

As a next step, the evolution of DCL components was monitored in presence of the model lectin ConA in order to test for the potential amplification of one of the library components due to favourable interactions with the carbohydrate binding site of the lectin. At first, the same approach as for disulphide structures in Chapter 3.4.1.1 was employed for test compound **25**. Therefore, the glycomacromolecule was dissolved in LBB at 20 mM concentration and equilibrated together with ConA (0.4 mM) that was immobilized on sepharose. After the equilibration period of one week, a change of integrals could be observed but was very similar to samples without ConA. Potentially, ConA concentration was too low so that equilibrium was not significantly influenced by the target but mainly by high sample concentration. As loading of ConA on sepharose was 10-16 mg ConA/mL, higher ConA concentration was not feasible. Therefore, in a next experiment, immobilized as well as free ConA was used. Moreover, the glycomacromolecule **25** was checked for imine formation at lower concentration in absence and presence of ConA. For convenience a concentration of 1 mg/mL (0.9 mM), which can directly be used for RP-HPLC measurements was chosen. One of the samples was equilibrated with equimolar concentration of free ConA in solution. After one day this sample showed the formation of a colorless precipitate which could also be observed for a control sample containing only ConA. This suggested that ConA concentration was too high leading to aggregation of the lectin in solution. A second sample of 1 mg/mL glycomacromolecule was equilibrated with ConA on sepharose leading to a 2 to 1 ratio of glycomacromolecule to ConA. After one week both samples were transferred into a centrifuge filter and washed with MilliQ water. The bound species were then released by addition of hydrochloric acid in MilliQ water and a second filtration step. Analysis of DCL composition was performed by RP-HPLC-MS analysis. In both samples, the monomeric linear species seemed to be favoured in presence of ConA. One reason could be that glycomacromolecules occupy binding sites of ConA but distances of end groups are too large to effectively allow crosslinking of multiple

glycomacromolecules attached to one receptor. Alternatively, not enough neighboring binding sites were occupied simultaneously.

Therefore, larger glycomacromolecules **26** and **27** were used in order to investigate if crosslinking can occur with larger structures and ratio of glycomacromolecules to ConA was increased to 1 to 10. Results obtained are displayed in Figure 72.

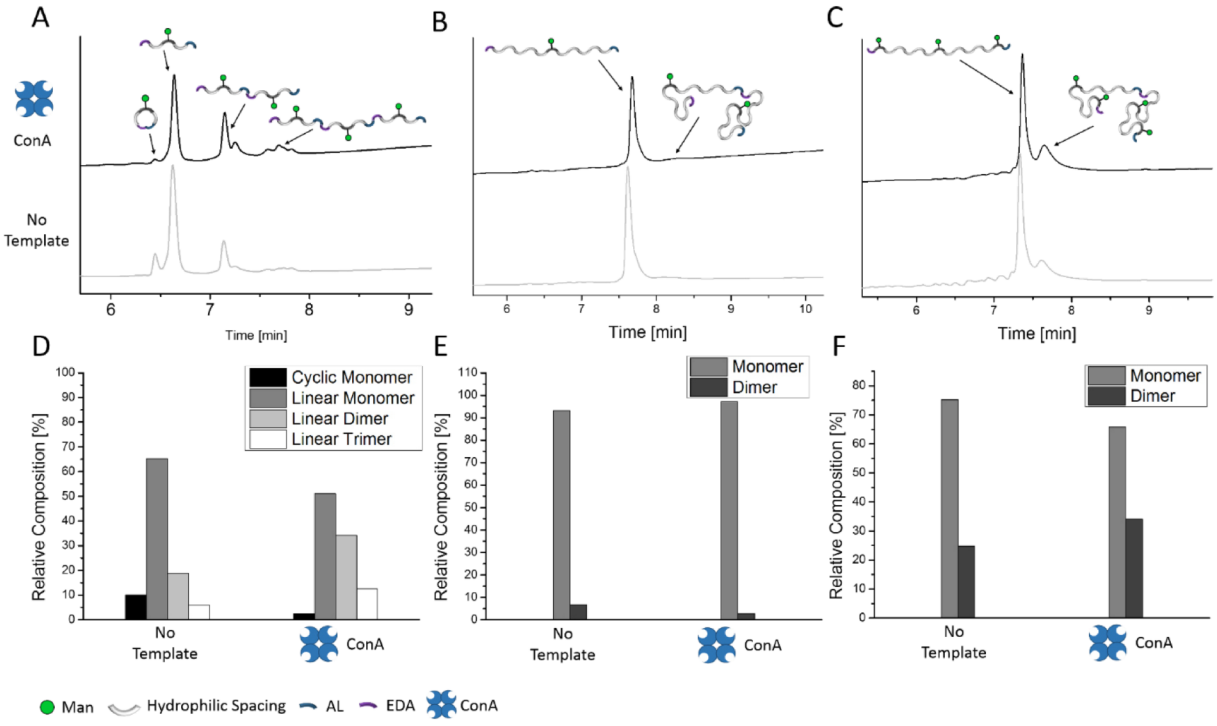

*Figure 72: RP-HPLC chromatogram (95/5 H_2O/MeCN with 0.1% formic acid (A) and 5/95 H_2O/MeCN with 0.1% formic acid (B); 100% A to 5% A in 17 min) of compound A: **25**, B: **26**, C: **27** at 0.9 mM concentration and pH 7.4 after one week of equilibration in absence (grey line) and presence (black line) of ConA. Evolution of the signal intensity of the respective DCL compounds as determined by integration of RP-HPLC chromatogram peaks of compound D: **25**, E: **26**, F: **27**.*

Interestingly, formation of dimers and trimers is only favoured for the shorter glycomacromolecule **25** now in higher concentration, while the longer structures show no or only minimal increase in formation of dimers. Potentially, the longer scaffold structures sterically hinder binding of glycomacromolecules to neighboring binding sites and thus formation of dimers and trimers.

Next, all three synthesized glycomacromolecules were simultaneously used in a DCL library in the presence and absence of ConA in order to further test for the discrimination of smaller DCL compounds over larger structures. The results obtained after one week of equilibration are shown in Figure 73. The results confirmed the results obtained when glycomacromolecular structures were equilibrated with ConA alone. In absence of ConA all DCL components that could be observed for individual compounds could also be observed for the mixed library. For compound **25** the monomer ring and linear structure as well as the dimer form could be observed in RP-HPLC-MS chromatogram. The trimer

structure could not be found, but might be overlapping with the peaks of the higher molecular weight structures **26** and **27** for which the monomer structure could be found in RP-HPLC-MS chromatogram. When the mixture was equilibrated in presence of ConA, the amount of the small structure **25** was drastically reduced while the amount of larger structures increased.

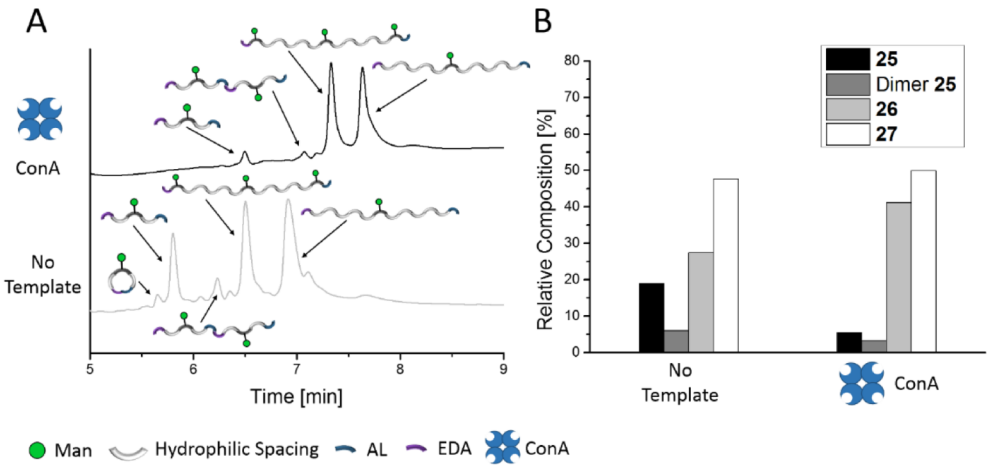

*Figure 73: A: RP-HPLC chromatogram (95/5 H_2O/MeCN with 0.1% formic acid (A) and 5/95 H_2O/MeCN with 0.1% formic acid (B); 100% A to 5% A in 17 min) of compounds **25**, **26**, **27** at 0.9 mM concentration and pH 7.4 after one week of equilibration in absence (grey line) and presence (black line) of ConA. B: Evolution of the signal intensity of the respective DCL compounds as determined by integration of RP-HPLC chromatogram peaks.*

In summary, these results demonstrate a template effect of ConA in DCLs of glycomacromolecules forming reversible imine bonds. However, this approach, similar to the disulphide approach, was also accompanied by some drawbacks. A general problem was to find the right protein concentration to work with. It has been stated in literature that in the case of high target concentration, the amplification factor does not necessarily correlate with the binding affinity of the compounds such that it was recommended to work with relatively low concentrations of target or at least conditions where library components were the dominant species in solution.[278] Indeed, employing different glycomacromolecule ConA ratios clearly affected the DCL products. Another drawback was that for both DCL approaches no “perfect DCL” was obtained. In a perfect DCL, each species would be present in almost identical amounts at equilibrium.[278] If one of the compounds, however, was already present in much larger proportions than all other compounds, the detection of template-induced amplification of this species would be difficult.[278] Another drawback that was observed for both approaches was the rather slow equilibrium of the DCL. Thus, for future experiments it would be interesting to investigate the feasibility of a different DCL approaches. For example, the formation of acylhydrazones generated from aldehydes and acylhydrazine reaction sites has been shown to be a very efficient approach in the literature.[279-281]

4. Conclusion and Outlook

The synthesis of precision glycomacromolecules varying in backbone hydrophobicity, carbohydrate number, spacing and arrangement as well as their presentation on gold nanoparticles has been demonstrated for the systematic investigation of the effect of these structural design features on lectin binding. SPPoS, as introduced by Hartmann *et al.*, was employed in order to guarantee high structural definition to allow for the investigation of structure activity correlations in carbohydrate lectin binding.[95]

In the first part of this thesis, SPPoS was employed in order to synthesize three series of glycomacromolecules presenting differences in carbohydrate number, spacing and arrangement as well as backbone hydrophobicity. The difference in spacing and arrangement of carbohydrate ligands was achieved by a variation in the number and sequence of functional building block TDS and spacer building block EDS during their assembly on solid support. The change in backbone hydrophobicity was obtained by the introduction of a hydrophobic aliphatic spacer building block (ODS) and a commercially available hydrophobic aromatic building block (AR) in addition to hydrophilic EDS spacing. As carbohydrate moiety, an α-D-mannose azide derivative was employed that was attached to the triple bond of the functional TDS building block via CuAAC. This carbohydrate unit was chosen due to its specific binding to the targeted model lectin ConA and the bacterial lectin FimH. In addition to the α-D-mannopyranoside carrying glycomacromolecules, negative control structures with β-D-galactopyranoside moieties were synthesized because the two target lectins show no affinity to this carbohydrate.

Even though SPPoS and the employed standard Fmoc coupling protocols were already developed in the Hartmann group some further optimizations were introduced in this work. Due to the fact that glycomacromolecule cleavage from solid support was generally performed with high levels of TFA ranging from 30 to 95% in DCM, TF acetate could be found as counter ion in the final glycomacromolecular structures. Since TFA can potentially affect the outcome of protein binding studies, the removal of TF acetate after SPPoS was introduced in this work.[133-135] Therefore, two different approaches were investigated. The first employed HCl treatment, and the second employed a strong anion exchange resin.[136,137] Both approaches showed efficient TF acetate removal but due to the fact that HCl treatment also led to the formation of impurities, the second approach using a strong anion exchange resin was employed as the method of choice.

In addition, a new hydrophobic spacer builing block, ODS, was introduced. However, the incorporation of this building block in SPPoS initially proved problematic. With an increasing number of ODS building

blocks, impurities due to deletion sequences could be observed in obtained glycoamacromolecular structures. This can probably be explained by the aggregation of the hydrophobic moieties on the solid support partially blocking the reaction site for chain elongation.[140] In accordance, coupling efficiency tests employing standard coupling conditions showed only low efficiency of 70 ± 9%. By investigating different coupling conditions, a solution of 0.4 M LiCl in a one to one mixture of DCM and DMF was identified as best coupling solvent leading to the highest coupling efficiency of 91 ± 8% for ODS building block. In contrast, the use of hydrophobic, aromatic, AR building block was unproblematic in SPPoS exhibiting high coupling efficiency of 107±7% under standard coupling conditions (in comparison to coupling of the amino acid L-valine, which was set to 100%).

After successful synthesis of the three series of glycomacromolecules, ITC and SPR measurements were employed to investigate the binding affinity/avidity towards the model lectin ConA. The two different assays were designed to give different insights into the binding behaviour of glycomacromolecules in solution. In ITC, the ConA receptor is present in the solution phase while in SPR, the ConA receptor is immobilized on a sensor chip surface. For glycomacromolecules of series one and two, differing in carbohydrate spacing and arrangement, no effect on binding avidity could be observed in ITC measurements. However, in SPR, binding became more favourable with increasing spacing of the carbohydrate ligands. With regards to the multivalent effects involved in binding, this finding can probably be explained by two effects. On the one hand, the arrangement of carbohydrate ligands in close proximity could lead to enhanced binding due to statistical effects. On the other hand, high carbohydrate density could lead to steric repulsion that might diminish lectin affinity. While in ITC both effects seem to be of similar magnitude, in SPR steric repulsion might be increased due to the limited movement of the immobilized receptor, so that binding gets more favourable with increased spacing.

For the third series of glycomacromolecules, which varied in carbohydrate valency while gradually changing in backbone hydrophobicity, a clear trend of more favourable K_D values with a higher valency could be observed. Moreover, binding avidity became more favourable with an increasing number of hydrophobic spacer building blocks (Figure 74). This finding can probably be explained by additional secondary interactions of the hydrophobic moieties in the backbone with hydrophobic amino acid side chains near the carbohydrate binding site. However, when the effect of hydrophobic backbone properties on lectin binding was compared to the effect of hydrophobic moieties that were previously introduced in linker position, a much lower effect on binding avidity was found for the hydrophobic backbone.[120] This can be rationalized by the greater distance of the backbone moieties to the CRD region which likely minimized their involvement in secondary binding interactions when compared to hydrophobic motifs in the linker position.

In order to gain a deeper insight into the potential involvement of glycomacromolecules containing hydrophobic backbone components with protein derived hydrophobic amino acid side chains, a NMR study with phenol as tyrosine surrogate was performed. The involvement in secondary interactions with phenol was followed by an upfield shift of proton signals in NMR spectrum. The results showed that hydrophobic spacing not only enabled stronger interactions to spacer moieties when compared to the hydrophilic spacer building block EDS, but it also promoted increased interactions with linker protons. This pointed towards a different spatial arrangement of hydrophobic glycomacromolecules in solution. This can be rationalized by more favourable exposure of hydrophilic carbohydrate moieties to the polar, aqueous solution phase and a less favoured exposure of the hydrophobic backbone moieties. This, in turn, would lead to higher accessibility of the carbohydrate ligands for binding. This explanation was supported by DLS measurements showing larger hydrodynamic radii for hydrophilic structures in comparison to hydrophobic structures, and higher FV values for hydrophobic compounds in ITC measurements.

In order to test for the potential applicability of glycomacromolecules as future therapeutics, an additional lectin binding study was performed by a collaboration partner, Franziska Reise, in the working group of Thisbe K. Lindhorst from the Christiana Albertina University in Kiel. She employed a bacterial adhesion inhibition assay of the bacterial lectin FimH to a mannosylated surface using different glycomacromolecules as inhibitors. The assay showed that inhibition of the bacterial adhesion to the mannosylated surface by the synthesized glycoamcromoelcules was possible and that the inhibitory potential was affected by similar design features as observed with ConA binding in ITC and SPR measurements.

In the second part of the thesis, the findings from the first part were extended to a higher level of multivalency by presenting glycomacromolecules on an AuNP surface. AuNPs are promising scaffolds for the manifold presentation of carbohydrate ligands because they comprise an inert and biocompatible material, are in the same size range as biomolecules, and exhibit interesting physical properties. In addition, the strong thiol gold interaction allows for easy immobilization of compounds with a thiol functionality. Based on the finding that backbone hydrophobicity as well as higher carbohydrate valency promoted the higher binding avidity of free glycomacromolecules with lectins in the first part of this thesis, the effect of hydrophobic backbone properties and different valencies of glycomacromolecules when immobilized on AuNP surface were tested in lectin binding.

Precision glycomacromolecules were synthesized employing SPPoS and standard Fmoc coupling protocols. Hydrophobicity in the backbone was introduced by the use of the hydrophobic aliphatic ODS spacer building block, whereas hydrophilic properties were introduced by employing the hydrophilic EDS building block. Differences in carbohydrate valency were achieved by increasing the number of

carbohydrate carrying TDS building blocks. In addition to these artificial builing blocks, the natural amino acid L-cysteine was employed as building block in SPPoS in order to introduce the thiol functionality for attachment to the gold surface. A carboxylic end group was introduced at the other end of the glycomacromolecule in order to increase colloidal stability of obtained glyco-AuNPs by electrostatic stabilization. This carboxylic end group was obtained after resin cleavage and was introduced by resin and linker choice. A polystyrene resin for hydrophilic compounds and a Tentagel® resin for more hydrophobic compounds, both with a trityl linker prefunctionalized with the natural amino acid L-glycine, were employed. Due to the fact that these resins were much more sensitive to strong acidic and basic conditions, carbohydrate deprotection was proceeded in solution after cleavage of the glycomacromolecule from the resin. In the case of the hydrophobic glycomacromolecule, this deprotection step led to the formation of a thioether side product. However, this side product should not interfere with AuNP functionalization so that further purification was omitted. Another side product that was inevitable observed was the disulphide formed by the oxidation reaction of thiol functionalities in presence of air oxygen. This led to the idea of capping the free thiol group of half of the glycomacromolecule batches with *N*-ethylmaleimide in order to obtain defined structures for later studies comparing glycomacromolecules immobilized on AuNP surface and the free ligand in solution. Overall, three thiol-functionalized glycomacromolecules were synthesized. Two of these structures were monovalent and varied in their backbone hydrophobicity, one exhibiting EDS and the other ODS spacing. Thus, the comparison of these two structures allowed for the investigation of backbone effects. In addition to the monovalent structure with EDS spacing, a higher valent counterpart with five carbohydrate ligands was synthesized in order to allow for the investigation of valency effects. These two EDS spaced compounds were also capped with *N*-ethylmaleimide for later comparability studies.

After successful synthesis of thiolated glycomacromolecules, they were used for AuNP functionalization. AuNPs were synthesized by a collaboration partner, Kristina Wagner, from the Karg group at Heinrich Heine University in Düsseldorf. The functionalization proceeded via ligand exchange reaction of the temporary citrate ligand by the different glycomacromolecules. UV-Vis and DLS analysis showed successful ligand exchange by a shift in the LSPR wavelength and an increase in hydrodynamic radius in accordance with the molecular weigth of the immobilized glycomacromolecule. Moreover, obtained glyco-functionalized AuNPs (glyco-AuNPs) exhibited a high degree of functionalization as determined by phenol sulphuric acid method (PSA). This high degree of functionalization was accompanied by good stability in solutions of high ionic strength and buffer solutions which is a prerequisite for following binding studies with lectins.

In lectin binding studies the model lectin ConA was targeted. As first assay, the aggregation behaviour of glyco-AuNPs was monitored by UV-Vis in the presence of increasing ConA concentrations. A shift of the LSPR maximum to higher wavelength with a simultaneous increase of absorbance at 700 nm indicated aggregation of the glyco-AuNPs induced by crosslinking over ConA binding sites. This change in absorbance maximum could even be observed by naked eye, pointing towards a possible application of these compounds in biosensors. By plotting the absorbance at 700 nm against ConA concentration, a binding isotherm could be obtained for the different functionalized glyco-AuNP compounds. Fitting of this binding isotherm with Hill1 function could be used to determine apparent dissociation constants $K_{D,app}$.

The results showed that the glyco-AuNPs functionalized with the glycomacromolecule with hydrophobic backbone properties exhibited strongest aggregation behaviour. This finding might be explained by additional secondary interactions of the hydrophobic backbone with hydrophobic amino acid side chains near the carbohydrate binding site as also previously discussed in literature.[232] However, there was also a difference in the degree of functionalization for the hydrophilic and hydrophobic compounds, and it is not yet clear which influence this change in carbohydrate density could have on the aggregation behaviour. It was particularly striking that a lower aggregation activity could be found for the pentavalent hydrophilic compound in comparison to the monovalent hydrophilic compound when immobilized on AuNP surface. On the one hand, this could be explained by the fact that the high glycomacromolecule and therewith carbohydrate density presented on AuNP surface led to partially blocked carbohydrate ligands that were no longer accessible for binding. On the other hand, the longer chain length could lead to higher steric stabilization, and as such higher interparticle distance in the aggregates. Thus, the chain length could have an influence on the sensitivity of the aggregation assay leading to an apparent decrease of aggregation potency. To augment the results obtained in the aggregation study, the kinetics of the aggregation process were monitored both by UV-Vis and DLS measurement. An increase of absorbance at 700 nm correlated with an increase in hydrodynamic radius, confirming that the increase of absorbance was caused by the formation of aggregates leading to near-field resonance coupling and a higher hydrodynamic radius. Moreover, the specificity of the aggregation process was tested by the addition of MeMan as a competitive inhibitor in high excess which led to complete redispersion of glyco-AuNPs. Moreover, the same study with the non-carbohydrate binding protein BSA showed no spectral changes at all.

In a next step the inhibitory potential of glyco-AuNPs was assessed by SPR measurement. Therefore, carbohydrate carrying polymers were immobilized on the sensor chip surface and ConA binding to the surface was measured in dependence of glyco-AuNP concentration co-incubated with ConA as inhibitor. The free glycomacromolecules that were capped with *N*-ethylmaleimide were tested in the

same assay setup. The results confirmed the observations of the aggregation study. Again, a positive impact of the hydrophobic backobone properties of the glycomacromolecule immobilized on AuNP surface could be found on the inhibitory potential of glyco-AuNPs. In addition, a strong enhancement of inhibitory potency could be found for glycomacromolecules presented on AuNP surface in comparison to free ligands validating the multivalency effect (Figure 74).

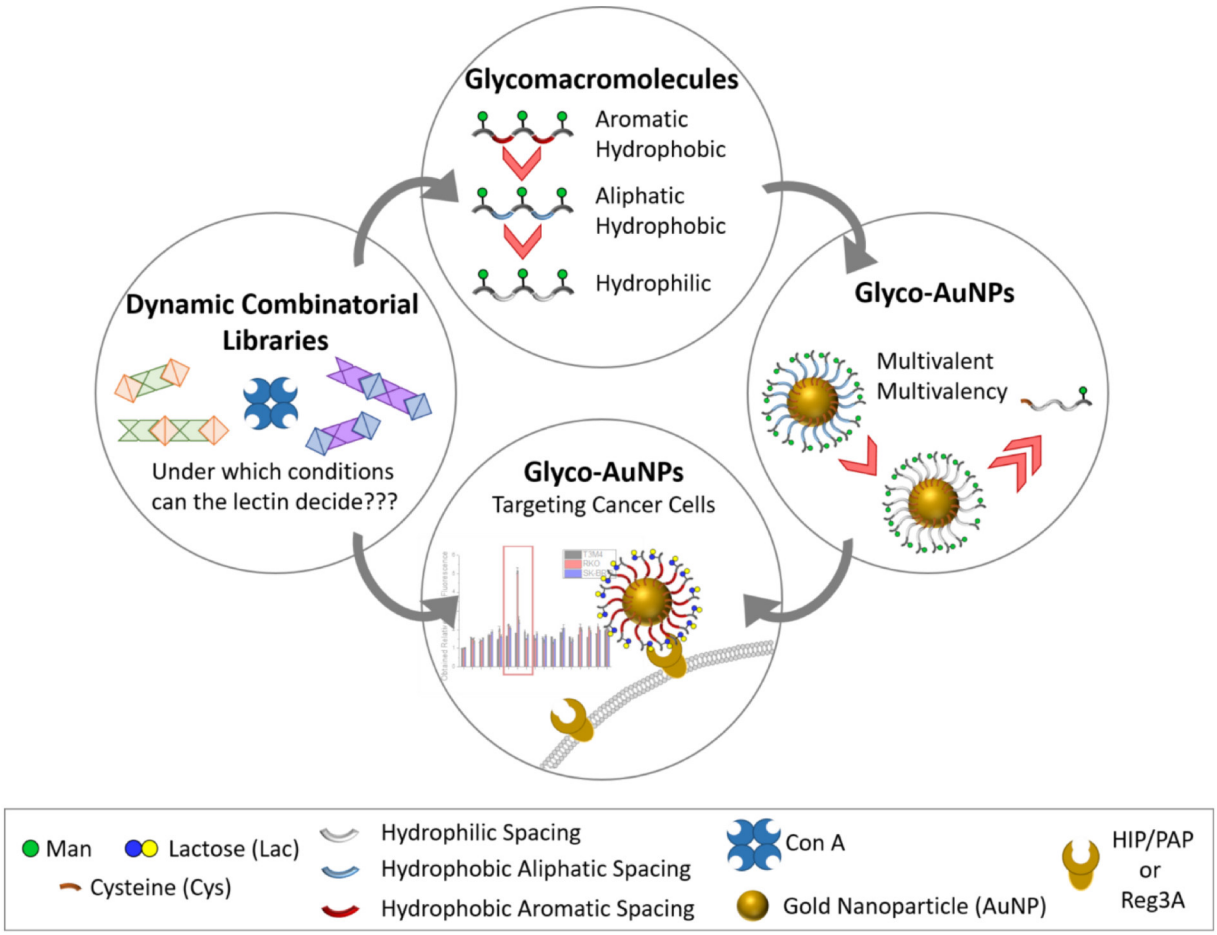

Figure 74: Schematic overview of the results obtained in the different part of this thesis.

In the next part of this thesis, this glyco-AuNP concept was extended towards AuNPs functionalized with lactose bearing glycomacromolecules. This project aimed to target a specific receptor, the HIP/PAP or Reg3A receptor, which is overexpressed in colorectal and pancreatic cancer cell lines, for PTT. PTT is a novel minimally invasive approach for cancer treatment based on the absorption of photon energy and its transformation into heat leading to hyperthermia, a heat induced cell death. Although, AuNPs are effective photothermal agents due to their high absorption efficiency and high photostability, spherical AuNPs are only partially suitable due to their LSPR in the visible region whereas, rod shaped AuNPs are very promising PTT agents due to their longitudinal absorbance band in NIR region which lies outside the so called water window and as such are also applicable for malignant tissue in deep.

Synthesis of lactose bearing glycomacromolecules was performed similar to the previous part of the thesis with some adaptions. In order to prevent thioether side product formation, a different resin, a Tentagel® SRam resin with rink amide linker was chosen allowing for sugar deprotection on solid support. Moreover, the sequence of building blocks during assembly on solid support was adapted. L-cysteine was always coupled as the first building block followed by three EDS building blocks forming the "core fragment" with sufficient spacing to the AuNP surface. Subsequently, different variations were introduced to the glycomacromolecule. A difference in backbone hydrophobicity was introduced by the different spacer building blocks EDS, ODS or AR, respectively. Moreover, monovalent and trivalent structures were synthesized by adapting the number of TDS building blocks, accordingly. Another variation was introduced at the end group by either coupling succinic anhydride as last building block to obtain a carboxylic end group or by capping the N-terminus with acetic anhydride in order to obtain a neutral end group. In addition, the fluorescent dye fluorescein isothiocyanate (FITC) was employed to make later monitoring in fluorescence-based methods possible. In this way, 18 lactose bearing glycomacromolecules were synthesized by SPPoS. In addition, negative controls with an α-D-mannose residue and without carbohydrate functionalities were produced. Furthermore, two macromolecular structures with and without FITC end group were synthesized for specific AuNP labelling.

After successful synthesis of these glycomacromolecules they could be used for AuNP functionalization. Spherical AuNPs were synthesized by a collaboration partner, Kirsten Volk from the Karg group at Heinrich Heine University in Düsseldorf. Glycomacromolecules were attached to the gold surface by a ligand exchange reaction by replacing temporary citrate ligands. As previously described, successful functionalization was determined by a shift of LSPR maximum in UV-Vis spectrum and an increase in hydrodynamic radius in DLS. In addition, the relative degree of functionalization was determined by TBO titration indicating a similar degree of functionalization for glyco-AuNP surfaces. The obtained glyco-AuNPs show good colloidal stability in PBS buffer and full growth medium employed in following cell studies. In addition to spherical AuNPs, rod shaped AuNps were synthesized by a collaboration partner, Kristina Wagner together with her Bachelor student Christina Noffke from the Karg group at Heinrich Heine University in Düsseldorf. However, functionalization of these nanorods with glycomacromolecules was not successful leading to aggregated particles irrespective of functionalization approach employed.

All cell studies and cell culturing methods were performed as part of a three-month research stay at Davidson College in North Carolina, USA, in collaboration with Prof. Nicole L. Snyder. As cell lines, rectal carcinoma cell line RKO as well as pancreatic carcinoma cell line T3M4 were employed as positive controls with high HIP/PAP expression. The breast cancer cell line SK-BR-3 with no HIP/PAP expression

was used as negative control. The uptake of glyco-AuNPs was assessed by flow cytometry and ICP-MS. Both methods independently and reproducibly show that uptake for all glyco-AuNPs was very similar with only one exception in RKO cell line: The glyco-AuNP that was functionalized with a monovalent lactose bearing glycomacromolecule with hydrophobic aromatic spacing showed uptake that was about twice as high as uptake for all other glyco-AuNPs including the negative controls (Figure 74). In order to find an explanation for this exceptional uptake, different inhibition studies were performed. First, co-incubation with different cell uptake inhibitors provided some insight into the endocytosis pathway of glyco-AuNP. However, these studies were unreliable. In a second inhibition experiment, glyco-AuNPs were co-incubated with lactose and Reg3A antibody as competitive inhibitors. This co-incubation led to a decrease in cell uptake indicating that uptake at least partially proceeded via the targeted Reg3A receptor. However, further experiments are necessary to gain a deeper insight into the mechanisms involved in binding.

In the future different investigations could be performed to obtain a deeper insight into the potential of glyco-AuNPs and their different areas of application. First, an important factor that needs to be investigated systematically is the influence of the degree of functionalization or rather the carbohydrate density on the AuNP surface on lectin binding. The approach introduced in this thesis provides a basis for further investigations. With regards to the second glyco-AuNP project in cell uptake studies, it would be particularly interesting to determine the specific uptake pathway in RKO cells. Therefore, further inhibition tests with uptake pathway inhibitors or receptor binding competitors should be used. Fluorescence microscopy with a higher concentration of glyco-AuNPs might also be used in order to obtain better resolution and to find out more about the subcellular localization of glyco-AuNPs. Moreover, in a next step it would be important to also investigate the effects of these compounds as PTT agents to determine whether there is a correlation between the high uptake and heat evolution.

In the last part of the thesis the opportunity to apply a dynamic library approach was evaluated to allow the lectin itself to choose the best binding constituent from a library of glycomacromolecule fragments. Thiol-disulphide exchange and imine formation were explored as reversible covalent bonds during the templating process. For the formation of DCLs the latter was chosen as first approach based on the previous experience with thiolated glycomacromolecules. Thus, two test glycomacromolecules, one hydrophilic and the other hydrophobic, both displaying three α-D-mannopyranoside ligands for ConA binding, were equipped with two thiol functionalities at both ends of the glycomacromolecules. The disulphide formation was monitored by UV-Vis spectroscopy in dependence of different pH conditions over a time range of two weeks. This test indicated complete conversion of thiols to disulphides and thus, the formation of ring structures. RP-HPLC analysis under the same conditions

confirmed this assumption showing the monomer and dimer ring structures and only small amounts of the respective linear compounds. However, no library constituents of higher molecular weight could be identified, even though a library of bifunctional components in theory could lead to an infinite number of structures. This could be due to very low concentrations of higher order structures that lie below the detection limit. However, it is more likely that the formation of these larger structures does not occur because of entropic constraints that need to be overcome by favourable enthalpic contributions.[265]

In the second approach, the formation of imines based on the condensation reaction between aldehydes and amines was chosen due to the feasibility of this approach in SPPoS. The amine was introduced by employing a Tentagel® trityl resin prefunctionalized with ethylene diamine. The aldehyde functionality was introduced on the other end of the glycomacromolecule by employing the commercially available 4-formylbenzoic acid. In order to install the aldehyde functionality, the standard SPPoS protocol was adapted to account for the reactivity of the formyl group to strong acidic and basic conditions. Therefore, side product formation was circumvented by the use of previously deprotected α-D-mannopyranoside azide derivatives and lower amounts of TFA in the cleavage solution. In this way, three different glycomacromolecules with different overall lengths and carbohydrate spacings were synthesized.

In a next step, it was assessed whether library constitution could be influenced by ConA presence during equilibration. An increase of one of the library components or the formation of a completely new structure in DCL would indicate preferred binding of the respective compound to ConA. However, for dithiol glycomacromolecules, only a small influence of ConA presence on DCL constitution could be observed. In presence of ConA, the monomer ring structure was predominantly observed in RP-HPLC ananlysis pointing towards a preferred binding of this compound. No influence with regards to the hydrophobicity of the glycomacromolecules could be observed when both structures were tested with ConA at the same time. For glycomacromolecules of the second library following the imine approach, RP-HPLC analysis showed that larger structures of about five spacer building blocks between the carbohydrate carrying TDS building blocks were preferred in DCL. Thus, also for this DCL approach, a small influence of ConA could be observed on library constitution (Figure 74).

Despite the aforementioned results, both approaches have distinctive drawbacks. Most importantly, both DCL approaches were no “perfect DCL”. In a “perfect DCL” each species would be presented in almost identical amounts at equilibrium.[278] If one of the compounds, however, was already present in much larger proportions than all other compounds, the detection of the template-induced amplification of this species would be difficult.[278] Another drawback that was observed for both approaches was the rather slow equilibrium of the DCL. In addition, for the thiol-disulphide approach

it was striking that disulphide formation was not stopped at low pH values which makes a full control over the library by freezing out the thiol-disulphide exchange questionable.

Thus, for future experiments it would be interesting to investigate the feasibility of different DCL approaches. For example, the formation of acylhydrazones generated from initial aldehydes and acylhydrazine reaction sites has been shown to be a very efficient approach in literature.[282-284] This DCL approach is not only reversible and rapid at a wide range of pH values (pH 3-7), but it can also be readily controlled by adjusting the pH to values pH > 7. In addition, reaction conditions are mild and the acylhydrazones formed in the reaction are sufficiently stable in aqueous media. The approach is also fesible for its combination with SPPoS. By the reaction of succinic anhydride with tert-butyl hydrazinecarboxylate a new building block for the introduction of an acylhydrazide could be easily prepared.[285]

Overall, this work enabled the systematic investigation of the effect of different design features in developing glycomimetics. Special focus was devoted to the effects of hydrophobic backbone properties on lectin binding. Introduction of hydrophobic moieties in glycomacromolecules showed the potential to fine tune lectin binding properties in different binding studies, both in solution and *in vitro*. Especially in using glycomacromolecules of different backbone characteristics to target cancer cells, it could be shown that the specific incorporation of hydrophobic moieties has the potential to create specific and selective glycomimetics with high affinity, a key prerequisite for potential future applications in therapeutics, and possibly in cancer therapy.

5. Experimental Part

5.1 Materials

Diethyl ether (with BHT as inhibitor, ≥99.8%), triisopropylsilane (TIPS) (98%), (+)-sodium-L-ascorbate (≥ 99%), acetic acid (99.8%), triethylsilane (99%), conc. hydrochloric acid (p.a.), Amberlite® IR 120 resin (hydrogen form), toluidine blue O (TBO), Bovine serum albumin (BSA) (≥96%), sodium citrate dihydrate (≥99%), gold(III)chloride trihydrate (≥99%), *N*-ethylmaleimide (≥98%), α-D-mannose (99%), phosphate buffered saline tablet (1 tablet in 200 mL water gives 137 mM NaCl, 2.7 mM KCl, 10 mM phosphate buffer solution, pH 7.4), chlorpromazine hydrochloride (ChlorH) (≥98%), methyl-β-cyclodextrin (MβCD) (≥98%), cytochalasin D (CytoD) (≥98%), sodium cyanoborohydride ($NaBH_3CN$) (95%), 5,5´-dithiobis(2-nitrobenzoic acid) (Elman´s reagent) (≥98%) and manganese chloride tetrahydrate (≥99%) were all purchased from Sigma-Aldrich. *N, N*-Diisopropylethylamine (DIPEA) (≥99%), lithium chloride (LiCl) (≥99%) and tris(2-carboxyethyl)phosphine hydrochloride (TCEP) (≥98%) were purchased from Carl Roth. Lactose (anhydrous) was purchased from Carbosynth. Methanol (p.a.), concentrated sulphuric acid (95%), sodium hydroxide (1 M) and acetic anhydride (99.7%) were purchased from VWR BDH Prolabo Chemicals. Dimethylformamide (DMF) (99.8%, for peptide synthesis), piperidine (99%), 1,8-diaminooctane (98%), triphenylmethyl chloride (Trt-Cl) (98%), succinic anhydride (99%), methyl-α-D-mannopyranoside (MeMan), sodium azide (biochemistry, 99+%) and copper(II) sulphate (98%) were purchased from Acros Organics. Dichloromethane (DCM) (99.99%), sodium chloride (99.98%), tetrahydrofuran (THF) (analytical reagent grade), ethyl acetate (analytical reagent grade), sodium hydrogen carbonate (analytical reagent grade), toluene (analytical reagent grade), nitric acid (65%), dithiothreitol (DTT) and 4-(2-hydroxyethyl)-1-piperazineethanesulfonic acid (HEPES) (99%) were purchased from Fisher Scientific. Concanavalin A (ConA) was purchased from LKT Laboratories. Calcium chloride (≥ 97%), phenol (crystalline for analysis), potassium carbonate (for analysis), citric acid (for analysis), triethylamine (pure) and D-(+)-galactose (pure) were purchased from AppliChem. Trifluoroacetic acid (TFA) (99%), trichloroacetonitrile, (Benzotriazol-1-yloxy)tripyrrolidino-phosphonium hexafluorophosphate (PyBOP) and 1,8-diazabicyclo[5.4.0]undec-7-ene (DBU) were purchased from Fluorochem. O-(7-Azabenzotriazol-1-yl)-*N*,*N*,*N*′,*N*′-tetramethyluronium hexafluorophosphate (HATU) (99%) was purchased from Abcr. 9-Fluorenylmethoxycarbonyl chloride (Fmoc-Cl) (98%) was purchased from ChemPur. Hydrazine acetate (99%) was purchased from JK Chemical. Sodium sulphate (anhydrous) was purchased from Caelo. Boron trifluoride diethyl etherate (98%), sodium methoxide (98%), fluoresceine isothiocyanate (FITC) (95%) and β-D-galactose pentaacetate (98%) were purchased from Alfa Aesar. 4-(Fmoc-aminomethyl)benzoic acid (>98%) and 4-formylbenzoic acid (>98%) were purchased from TCI. Acetate buffer (10 mM sodium acetate, pH 4.5),

ethanolamine hydrochloride (1 M solution, pH 8.5), *N*-hydroxysuccinimide (NHS), 1-ethyl-3-(3-dimethylaminopropyl)carbodiimide (EDC), sodium hydroxide (2 M solution), sodium hydroxide (0.2 M solution), sodium chloride solution (5.0 M), HBS-P+ buffer (0.1 M Hepes, 1.5 M NaCl, 0.5% v/v surfactant P20, pH 7.4), ConA sepharose™ 4B (10-16 mg ConA/mL) and HyClone RPMI-1640 medium (+ 2.05 mM L-glutamine) were purchased from GE Healthcare. α-D-Galactose-PAA-biotin and α-D-mannose-PAA-biotin were purchased from Glyco Tech. Fmoc-Gly-Trt Tentagel® resin (0.22 mmol/g), H-Gly-2-chlorotrityl PS resin (0.44 mmol/g) and *N*-α-(9-fluorenylmethyloxycarbonyl)-S-trityl-L-cysteine (Fmoc-L-Cys(Trt)-OH) (99.9%) were purchased from Iris Biotech. Tentagel® chlorotrityl resin and Tentagel® SRam resin were purchased from Rapp Polymere. The strong anion exchange resin AG1-X8 (550 mg, quarternary ammonium, 100-200 mesh, acetate form) was purchased from BioRad. Trypsin-EDTA solution (0.05% trypsin), Eagle's Minimum Essential Medium (EMEM), McCoy's 5A Medium, RKO and SK-BR-3 cell line were purchased from ATCC. Anti-hReg3A mouse monoclonal IgG antibody was purchased from R&D chemicals. Trypan blue solution (2% in PBS buffer) was purchased from VWR. XTT cell viability assay kit was purchased from Biotium. Water was purified with a Milli-Q system (Millipore) obtaining a final resistivity of 18 MΩcm.

Buffers

Lectin binding buffer (LBB): 10 mM Hepes, 50 mM NaCl, 1 mM $CaCl_2$, 1 mM $MnCl_2$, pH 7.40; acetate buffer: 100 mM sodium acetate, 100 mM NaCl, 5 mM $MnCl_2$ and $CaCl_2$, pH= 5.20); pH was adjusted with 0.1 M NaOH and 0.1 M HCl.

Buffers for Bacterial Adhesion Inhibition Study

PBS buffer: PBS tablets were obtained from GIBCO containing phosphate (as sodium phosphates), 10 mM, potassium chloride (KCl), 2.68 mM, sodium chloride (NaCl), 140 mM, pH = 7.45; PBST buffer: PBS buffer + 0.05% v/v Tween®20; carbonate buffer solution (pH 9.6): sodium carbonate (10.6 g) and sodium hydrogen carbonate (8.40 g) were dissolved in bidest. water (1.0 L), pH values were adjusted by using 0.1 M HCl or 0.1 M NaOH.

Buffers Used in Cell Studies/Cell Culturing

PBS buffer: PBS tablets from Sigma Aldrich, 137 mM NaCl, 2.7 mM KCl, 10 mM phosphate buffer solution, pH= 7.2; PBS+ buffer: 137 mM NaCl, 2.7 mM KCl, 10 mM phosphate buffer solution, 0.05% NaN_3, 0.05% BSA, pH= 7.2; pH was adjusted with 0.1 M NaOH and 0.1 M HCl.

5.2 Instrumentation

Nuclear Magnetic Resonance Spectroscopy (NMR) (performed by Maria Beuer, Heinrich Heine University Düsseldorf)

^{1}H-NMR and ^{13}C-NMR spectroscopy was performed on a Bruker AVANCE III 300 (300 MHz) and 600 (600 MHz) at room temperature unless stated otherwise. Chemical shifts are referenced relative to the residual ^{1}H peaks of the used solvent as internal standards ($CDCl_3$: ^{1}H 7.26, DMSO-d_6: ^{1}H 2.50, D_2O: ^{1}H 4.79). Chemical shifts are reported in delta (δ) expressed in parts per million (ppm). Chemical shift changes are reported in Δδ expressed in parts per billion (ppb). Multiplicities are abbreviated as follows: s = singlet, d = doublet, t = triplet, q = quartet and m = multiplet.

Mass Spectrometry (ESI, MALDI-TOF-MS, HR-MS) (performed by Dr. Peter Tommes, Heinrich Heine University Düsseldorf)

Electrospray ionization (ESI) mass spectra were recorded with a mass spectrometer type Ion-Trap-API Finningan LCQ Deca.

Matrix-assisted laser desorption-ionization time-of-flight (MALDI-TOF) measurements were performed on a MALDI-TOF Ultraflex I (Bruker Daltonics) with 2,5-dihydroxybenzoic acid (DHB) and α-cyano-4-hydroxycinnamic acid (CHCA) as matrix. The ratio of compound to matrix was 10:1.

High resolution mass spectrometry was performed on a Bruker UHR-QTOF maXis 4G instrument with a direct inlet via syringe pump, an ESI source and a quadrupole followed by a Time Of Flight (QTOF) mass analyzer.

Reversed-Phase-High Pressure Liquid Chromatography – Mass Spectrometry (RP-HPLC-MS)

RP-HPLC-MS analysis was performed on an Agilent 1260 Infinity instrument coupled to a variable wavelength detector (VWD) (set to 214 nm) and a 6120 Agilent Quadrupole LC/MS containing an Electrospray Ionisation (ESI) source operating in positive ionization mode in a m/z range of 200 to 2000. As HPLC column a Poroshell 120 EC-C18 1.8 µm (3.0x50 mm, 2.5 µm) RP column from Agilent was used. The mobile phases A and B were 95/5 H_2O/MeCN, 0.1% formic acid (A) and 5/95 H_2O/MeCN, 0.1% formic acid (B). Samples were analyzed at a flow rate of 0.4 mL/min using a linear gradient from 100% A to 50% B in a time range of 30 min at 25°C. For the analysis of dynamic combinatorial libraries samples were measured at a flow rate of 0.4 mL/min using a linear gradient from 100% A to 100% B in a time range of 17 min at 25°C. UV and MS spectral analysis were performed within the OpenLab ChemStation software for LC/MS from Agilent Technologies.

Preparative Reversed-Phase-High Pressure Liquid Chromatography (Prep-RP-HPLC)

Prep-RP-HPLC analysis was performed on an Agilent Technologies1260 Infinity instrument coupled to a variable wavelength detector (VWD) (set to 214 nm). As HPLC column a CAPCELL PAK C18 (20 mml.D. x 250 mm, 5 µM) RP column was used. The mobile phases A and B were H_2O, 0.1 % formic acid (A) and MeCN, 0.1 % formic acid (B); the mobile phases A1 and B1 were H_2O (A1) and MeCN (B1). Samples were purified at a flow rate of 20 mL/min at 25°C using a linear gradient from 95% A to 95% B in a time range of 20 min for compounds **3a**, **4**, **4a, 4b**, **5b**; 95% A to 95% B in 10 min for compound **1a**, **4c**, **6d**, **7a**, **9a**, **20a**, **22**; 80% A to 60% B in 6 min for compounds **3**, **5**, **5a**; 95% A to 60% B in 10 min for compounds **1b**, **6**, **13a, 13b**, **14b**, **15a**, **15b**; 95% A to 50% B in 10 min for compounds **14a**, **19a**, **19b**, **20b**; 95% A to 60% B in 6 min for compounds **1**, **1c**; 95% A to 50% B in 30 min for compound **6a**; 88% A1 to 8% B1 in 8 min for compound **6b**; 100% A to 60% B in 15 min for compound **6c**, 90% A to 50% B in 10 min for compound **4d**, **6e**; 90% A to 35% B in 12 min for compounds **16a**, **16b**; 75% A to 35% B in 10 min for compound **7**; 80% A to 26% B in 10 min for compound **9**; 80% A to 80% B in 10 min for compound **8**; 80% A to 50% B in 12 min for compounds **16c**, **18c**; 65% A to 55% B in 12 min for compound **13a**, **20c**, **21**; 70% A to 100% B in 10 min for compound **14c**; 70% A to 80% B in 10 min for compound **15c**, **19c**; 70% A to 50% B in 12 min for compounds **17a**, **17c**; 80% A to 45% B in 12 min for compound **17b**; 85% A to 40% B in 12 min for compounds **18a**, **18b**. The eluent fractions with the desired product were collected by an automated fraction collector and were then combined, concentrated and lyophilized.

UV-Vis Photometer

UV-Vis spectroscopic measurements were performed using a dual-trace spectrometer Specord® 210 Plus from Analytik Jena AG. The instrument was operated using Win Aspect Plus software. For ConA concentration determination, a spectral scan from 270-290 nm was used. The concentration of ConA expressed in terms of the monomer (M= 26 500 g/mol) was then determined at 280 nm by applying the Beer-Lambert law with ε_{280}= 26380 $M^{-1}cm^{-1}$ for divalent ConA and with ε_{280}= 30150 $M^{-1}cm^{-1}$ for tetravalent ConA. The coupling efficiency was determined at 290 nm in a spectral scan from 280-320 nm. For glyco-AuNP concentration determination, a spectral scan from 390-410 nm was used. Based on the assumption that the nanoparticles are spheres with a radius of 7 nm and that an absorbance of A = 0.3 at a wavelength of 400 nm corresponds to a gold concentration of $c(Au^0)$= $1.25 \cdot 10^{-4}$ M, the concentration of the nanoparticles was determined using the equation described by X. Liu and coworkers. [286] Thiol content in solution was determined by employing Ellman´s reagent and measuring in a wavelength range from 390 to 430 nm at alkaline pH. All solutions were measured in a 3.5 mL precision quartz glass cuvette (d = 1 cm) from Carl Roth GmbH + Co. KG or disposable polystyrene cuvettes.

At Davidson College UV-Vis spectroscopic measurements were performed using a Varian Cary® 100 Bio UV-Vis spectrophotometer. For glyco-AuNP concentration determination at a wavelength of 400 nm was measured. Based on the assumption that the nanoparticles are spheres with a radius of 7 nm and that an absorbance of A = 0.3 at a wavelength of 400 nm corresponds to a gold concentration of $c(Au^0)= 1.25 \cdot 10^{-4}$ M, the concentration of the nanoparticles was determined using the equation described by X. Liu and coworkers.[286] Measurements were performed in disposable polystyrene cuvettes.

Fluorescence Spectrofluorometer

At Davidson College a FluoroMax-3 from HORIBA Scientific was employed for fluorescence measurements. As excitation wavelength of FITC 495 nm was selected. The emission spectrum from 480 to 680 nm with a maximum at 519 nm was recorded. Measurements were performed in disposable polystyrene cuvettes.

Microtiter Plate Spectrophotometer

UV-Vis spectroscopic measurements in 96-well microplate-format were performed on a Thermo Scientific™ Multiscan™ GO spectrophotometer at 22 °C. The measurement was either performed in a wavelength range from 400 to 750 nm in 1 to 10 nm steps or in multiple wavelength mode measuring at 400 and 700 nm. For all experiments, Corning® 96-well clear flat bottom polystyrene not treated microplates were used.

At Davidson College UV-Vis spectroscopic measurements in 96-well microplate-format were performed on a BioTek™ Synergy H1 at 25 °C. The measurement was either performed in a wavelength range from 400 to 800 nm in 10 nm steps for stability measurement of glyco-AuNPs or at single wavelengths of 475 or 660 nm for XTT assay. For all experiments, Corning® 96-well clear flat bottom polystyrene sterile microplates were used.

Freeze Dryer

Lyophilization of final glycomacromolecules was performed on an Alpha 1-4 LD plus instrument from *Martin Christ Freeze Dryers GmbH*. The main drying method was set to -54°C and 0.1 mbar.

Dynamic Light Scattering (DLS)

Dynamic light scattering experiments were conducted at a PSS Nicomp ZLS Z3000 instrument from *Soliton Laser- und Messtechnik GmbH* with a laser wavelength of 660 nm. The measurements were performed at a scattering angle of 90° and at a constant temperature of 20 °C. The resulting intensity-time autocorrelation functions were analyzed by a logarithmic fit as provided by the instrument software to obtain the hydrodynamic diameter. For all measurements dust-free disposable culture

tubes made of borosilicate glass from *Kimble* were used. All measurements were performed three times using acquisition times of 2 min for glyco-AuNPs and of 30 min for glycoamcromolecules.

In the Karg group dynamic light scattering experiments (performed by Kristina Wagner) were conducted at a standard goniometer setup (LS Instruments, 2D-DLS) using a HeNe-laser (632.8 nm) with a maximum constant output power of 35 mW as light source. The measurements were performed at a scattering angle of 90° and at a constant temperature of 20 °C which was achieved by a heat-controlled decalin bath connected to a circulating water bath (Julabo CF31). The light scattered by the sample was detected by two avalanche photodectors operating in pseudo-cross-correlation mode. The resulting intensity-time autocorrelation functions were analyzed by second-order Cumulant analysis as provided by the instrument software to obtain the hydrodynamic radius. For all measurements dust-free disposable culture tubes made of borosilicate glass (Fisher Scientific) were used. All measurements were performed three times using acquisition times of 30 s.

Transmission Electron Microscopy (performed by Marion Nissen, Heinrich Heine University Düsseldorf)

Transmission electron microscopy (TEM) was performed with a Zeiss E902 transmission electron microscope with an accelerating voltage of 80 kV in bright-field mode. The sample was prepared by drop-casting of the dispersion on a carbon-coated copper grid (200 mesh, Electron Microscopy Sciences).

Isothermal Titration Calorimetry (ITC)

ITC experiments were performed using a MicroCal^{TM} VP-ITC instrument. A total number of 29 injections of 10 µL of glycomacromolecule solution were added from a computer controlled mycrosyringe (syringe volume= 281 µL) at an interval of 400 sec into the sample solution of ConA dissolved in the same buffer as the ligand (cell volume = 1.4288 mL). The microsyringe was stirred at 416 rpm. The initial injection of 1 µL was discarded from the data sheet in order to remove the effect of titrant diffusion across the syringe tip during the equilibration process. A fresh solution of the protein was prepared by dissolving the required amount of the model lectin ConA in acetate buffer at pH 5.20 at a concentration around 3 mg/mL and shaking for 1 h. The exact protein concentration was obtained by absorption spectroscopy after filtration using an Acrodisc® 32 mm syringe filter with a 0.1 µm Supor® membrane from *Pall Corporation*. ConA concentrations for the ITC experiments were maintained between 51 and 110 µM. A fresh and highly concentrated solution of the respective glycomacromolecule was prepared in MilliQ water at concentrations of 50 mM. This solution was then used for concentration determination by phenol sulphuric acid method because buffer ions might interfere with the colorimetric test. This stock solution was then used to prepare two independent

solutions of the glycomacromolecule in acetate buffer at pH 5.20. The concentration of the glycomacromolecule buffer solutions ranged between 1.1 and 5.4 mM, depending on the glycomacromolecule affinity for ConA. Both protein and ligand solutions were degassed at 25°C for 10 min before starting an ITC measurement.

To eliminate any unspecific enthalpic contributions (heat of dilution, ligand dilution) control experiments were performed by titration of the glycomacromolecule ligand into the corresponding buffer solution. The data obtained for ligand dilution were subtracted from the data obtained for ligand-protein titration experiments. The remaining experimental data were fitted to a theoretical titration curve using Origin 7.0 software supplied by Microcal. Thereby, a least-squares procedure and the one sets of independent binding sites model were applied with ΔH, K_A and n as adjustable parameters if not otherwise stated. The binding free energy ΔG and binding entropy ΔS were computed using the Gibbs-Helmholtz equation. The K_D and FV value were obtained as reciprocal of K_A and n, respectively. Experiments were performed with *c* values in a range of $\sim 0.8 < c < 5.9$

Surface Plasmon Resonance (SPR)

SPR measurements were performed on a Biacore X100 instrument from GE Healthcare Life Sciences. Sensorgrams were recorded with the Biacore X100 Control Software and evaluated with the Biacore X100 Evaluation Software.

For measurements presented in Chapter 3.1.2, a CM5 sensor chip from GE Healthcare Life Sciences was used. ConA was immobilized on the sensor chip surface on flow cell 2 using the standard amine coupling procedure provided by the wizard template for immobilization while a blank amine immobilization was used for flow cell 1. Therefore, a 1 mg/mL stock solution of ConA in acetate buffer (pH 4.5, GE Healthcare) was prepared and was shaken for 1 h. Then the solution was diluted in acetate buffer (pH 4.5, GE Healthcare) to a final ConA concentration of 50 µg/mL. As running buffer HBS-P+ buffer (pH 7.4, GE Healthcare) in a flow rate of 10 µL/min was used. 3000 RU were set as target level for immobilization. EDC, NHS, ethanolamine and sodium hydroxide solution were prepared as specified by the manufacturer. For flow cell 1 an immobilization level of 160.0 RU (196.6 RU on second sensor chip) and for flow cell 2 an immobilization level of 2888.7 RU (3035.1 RU on second sensor chip) were obtained.

After immobilization, the sensor chip was not directly used for binding studies but was first subjected to three consecutive injections of glycomacromolecule solution (100 µM solution of compound **4** in acetate buffer, contact time 105 sec, 30 µL/min) followed by two regeneration steps, first 0.8 M methy-α-D-mannopyranoside in acetate buffer and second acetate buffer for a contact time of 60 sec and a flow rate of 30 µL/min to make sure that all loose protein is washed out in order to obtain a stable baseline for following measurements.

SPR binding studies were performed using the wizard template kinetics/affinity with contact times of 105 sec and dissociation times of 180 sec. Before the run, the system was primed with acetate buffer which was used as running buffer and two startup cycles were performed. Because of the sensitive protein surface, the single cycle mode was used. For monovalent glycomacromolecules **3** and **3a** concentrations of 62.5-1000 µM with a dilution factor of 2, for trivalent glycomacromolecules **1a**-**1c**, **4c**, **4d**, **6c**, **6d**, **6e** concentrations of 6.67-540 µM with a dilution factor of 3, for trivalent glycomacromolecules **4a** and **4b** concentrations of 4.98-402 µM with a dilution factor of 3, for trivalent glycomacromolecule **4** concentrations of 5.8-470 and 7.8-630 µM with a dilution factor of 3, for tetravalent and pentavalent glycomacromolecules concentrations of 6.67- 540 µM with a dilution factor of 3 were used. The glycomacromolecule solutions were prepared in the same way as for ITC measurements: A fresh and highly concentrated solution of the respective glycomacromolecule was prepared in MilliQ water at concentrations of 50 mM. This solution was then used for concentration determination by phenol sulphuric acid method because buffer ions might interfere with the colorimetric test. This stock solution was then used to prepare the dilution series in acetate buffer.
As regeneration solutions a 0.8 M solution of methy-α-D-mannopyranoside in acetate buffer followed by acetate buffer with a contact time of 60 sec for both regeneration steps were used. All measurements were performed in triplicates that were each performed twice.

For measurements presented in Chapter 3.2.3 a SA sensor chip from GE Healthcare Life Sciences was used. The positive (α-D-Mannose-PAA-biotin, flow cell 2) and negative (α-D-Galactose-PAA-biotin, flow cell 1) control for ConA binding were immobilized on the sensor chip surface using the standard biotin streptavidin capture method as adapted from previously established protocols.[95,98] Therefore, a 4.2 µg/mL solution of both polymers was prepared in HBS-P+ buffer (pH 7.4, GE Healthcare). The same buffer was used as running buffer in a flow rate of 10 µL/min. For immobilization, the immobilization wizard was used with a specified contact time of 420 sec. Sodium chloride, sodium hydroxide and isopropanol solutions were prepared as specified by the manufacturer. For flow cell 1 an immobilization level of 1168.5 RU and for flow cell 2 an immobilization level of 842.8 RU was obtained. After approximately 500 measurement cycles, a new SA chip was used for further measurements. For immobilization the same procedure was used as described above. For flow cell 1 an immobilization level of 1153.4 RU and for flow cell 2 an immobilization level of 794.4 RU was obtained. In order to make all experiments comparable, MeMan was used as a reference inhibitor on both SA sensor chips before and after the measurement series.
SPR inhibition competition studies were performed using the wizard template kinetics/affinity with contact times of 105 sec and dissociation times of 180 sec. Before the run, the system was primed with LBB which was used as running buffer and two startup cycles were performed. The experiment was

performed in multi cycle mode. For all experiments a 1 mg/mL stock solution of ConA was prepared in LBB and was shaken for 1 h. Then it was filtrated (Acrodisc® 32 mm syringe filter with a 0.1 µm Supor® membrane from Pall Corporation) and the concentration was determined spectrophotometrically. The stock solution was diluted to give a 200 nM solution of ConA. Glyco-AuNP solutions were concentrated by centrifugation (Beckman Coulter Allegra™ 25R Centrifuge, 12h, 4500 rcf, 20 °C) and were resuspended in LBB to give a 20 nM stock solution. The concentration was verified by UV measurement. This glyco-AuNP stock solution was then used to prepare the dilution series in LBB. For glyco-AuNP **10** a dilution series with concentrations of 0, 0.02, 0.1, 0.2, 0.6, 0.8, 1, 1.5, 2 nM, for **11** 0, 0.02, 0.1, 0.2, 0.4, 0.6, 0.8, 1, 1.5, 2 nM and for **12** 0, 0.02, 0.1, 0.2, 0.4, 0.6, 0.8, 1, 1.5, 2 nM were prepared. For *N*-ethylmaleimide capped glycomacromolecule **7a** a dilution series with concentrations of 0, 1, 10, 20, 50, 100, 200, 500, 1000 µM and **9a** a dilution series with concentrations of 0, 2, 20, 100, 200, 500, 1000, 1500, 2000 nM was prepared. For αMeMan a dilution series with concentrations of 0, 10, 100, 500, 1000, 1500, 2000, 5000 µM was prepared. As negative control four representative concentrations of 0, 10, 1500 and 5000 µM were prepared for D-(+)-galactose.

For the experiment ConA and sample solutions were mixed in a 1:1 ratio to give half of the prepared concentrations. Each mixture was injected over both flow cells whereas the binding signal on flow cell 1 was subtracted from the response on flow cell 2. As regeneration procedure three consecutive injections of a 0.8 M solution of methy-α-D-mannose in LBB with a contact time of 30 sec was used. The relative response value at the beginning of the dissociation phase (20 sec after the end of sample injection) for the 100 nM ConA solution with zero sample concentration was set to 100% binding. The relative response values of the ConA solutions incubated with the respective sample in serial dilutions were referred to ConA and calculated for relative binding in %. IC_{50} values were calculated as concentration of the sample that result in 50% inhibition of ConA binding to the mannosylated sensor chip surface. RIP (relative inhibitory potencies) values are based on the IC_{50} value for MeMan (IP ≡ 1), which was tested on the same sensor chip surface. All glyco-AuNPs, glycomacromolecules and MeMan have been tested in three independent experiments (triplicate determination per experiment for MeMan and glyco-AuNPs, dublicate determination per experiment for glycomacromolecules **7a** and **9a**).

Flow Cytometry

For flow cytometry analysis at Davidson College an Accuri™ C6 flow cytometer was employed. For flow cytometry measurements, cells were suspended in 50 to 100 µL PBS+ buffer and filtered using a Nylon 6/6 woven mesh sheet (12” x 12”, 50 micron mesh size, purchased from amazon). A minimum of 5,000 cells was collected with a medium flow rate of 35 uL/min leading to approximately 1000 events/sec with a threshold of 800,000 on FSC-H. In between each sample, a one minute wash with MilliQ water

at a flow rate of 66 µL/min were performed. After every sixth sample two washing steps with first a deconatmination solution containing 4% of hypochlolrite followed by a five minutes wash with MilliQ water. The washing steps were employed to avoid clogging or partly clogging the system.

ICP-MS (performed by Dr. Brandie M. Ehrmann, University of North Carolina at Chapel Hill)
ICP-MS analysis was performed on a Thermo Element XR – Optional laser ablation source. The two different sets of triplicate samples were examined independently with different calibration curves. For each measurement series, a calibration curve at the beginning and at the end of the queue was collected (6 to 7 hours apart). From these two calibration curves, an average calibration curve was obtained for each data set. ^{115}In was used as internal standard and all data were reported as a ratio of response of Au to response of ^{115}In. Samples were prepared by mixing 250 µL of ^{115}In standard at 10 ppb with 500 µL of the respective sample and 4.25 mL of 2% nitric acid in water. This dilution factor was chosen to reduce the acid concentration in the samples which ideally lies below 5% during ICP-MS analysis.

5.3 General Methods

TFA Removal

The removal of TF acetate counter ions was first performed by employing a strong acid such as hydrochloric acid (HCl) following a procedure described in literature.[136] The glycomacromolecule was dissolved in MilliQ water at a concentration of 1 mg/mL and HCl was added to a final HCl concentration of 2 to 10 mM. The mixture was shaken for 10 min and then frozen by liquid nitrogen. Lyophilization was performed under high vacuum and continuous cooling. The HCl treatment was repeated two times by redissolving the obtained solid in HCl solution (2 to 10 mM) followed by a lyophilisation step under high vacuum.

A second, milder method for removal of TF acetate counter ions followed a literature procedure.[137] This procedure is based on the exchange of TF acetate counter ions by acetate counter ions employing a strong anion exchange resin (AG1-X8, quarternary ammonium, 100-200 mesh, acetate form, from BioRad). In order to ensure a total counter ion exchange, a high excess of 500 mg of this resin was prepared by successively washing the resin three times with 1.6 N acetic acid (20 mL) and three times with 0.16 N acetic acid (20 mL). Therefore, a 20 mL syringe reactor (polypropylene reactor with a polyethylene frit, closed at the bottom with a luer stopper from Multisyntech) was used which was also used for the following anion exchange reaction. The glycomacromolecule solution (75 mg, 0.035 mmol, in 9 mL of MilliQ water) was loaded in the syringe reactor and was shaken for 1 h. Then the resin suspension was filtered and the liquid phase recovered. The resin was washed 5 times with 2 mL of water. The solutions were pooled and the glycomacromolecule was isolated by removind the water under reduced pressure and lyophilization.

Coupling Efficiency Test

The coupling efficiency test followed a procedure adapted from literature.[141] Different coupling conditions were tested for the hydrophobic aliphatic building block ODS and the hydrophobic aromatic building block AR in comparison to coupling of the amino acid valine which was set to 100% coupling efficiency. As conditions (1) standard coupling in DMF with 5 eq of building block, 4.9 eq PyBOP with a coupling time of 1.5 h, (2) coupling in DMF with 10 eq of building block, 4.9 eq PyBOP with a coupling time of 1.5 h, (3) coupling in DMF with 5 eq of building block, 4.9 eq HATU with a coupling time of 1.5 h, (4) coupling in DMF with 5 eq of building block, 4.9 eq PyBOP with a coupling time of 2 x 45 min and (5) coupling in 0.4 M LiCl in a one to one mixture of DCM and DMF with 5 eq of building block, 4.9 eq PyBOP with a coupling time of 1.5 h were tested. For each reaction condition approximately 20 mg of trityl-Tentagel® resin (loading 0.195 mmol/g, 0.004 mmol) modified with EDA linker were used. The resin was loaded in a 5 mL syringe reactor (polypropylene reactors with a polyethylene frit, closed at

the bottom with a luer stopper from Multisyntech) standardly used for solid phase polymer synthesis. The resin was preswollen in DCM for 30 minutes and then washed with DMF 3 times. For coupling conditions where 5 eq. of building block were employed, the respective amount of AR (7.5 mg), ODS building block (9.4 mg) or valine (6.8 mg) was used together with 10.8 mg PyBOP or 7.6 mg HATU and 0.02 mL DIPEA in 0.25 mL coupling solvent. For coupling of 10 eq. of building block the amounts were doubled accordingly. Coupling was proceeded for the depicted coupling time and then the resin was washed 10 times with DMF and 5 times with DCM. The resin was dried for 1.5 h under high vacuum and subsequently 5 mg of each resin batch were transferred into 1.5 mL Eppendorf tubes for the UV test. 1 mL of a solution of 25% piperidine in DMF was added to each sample and left for 15 min under shaking and left for additional 5 min without shaking. Subsequently, 100 µL from the top liquid (without resin) were diluted to 2 mL with 25% piperidine in DMF in a UV cuvette. A reference was created by filling 2 mL of the 25% piperidine solution in DMF in a UV cuvette. Absorbance was recorded at 290 nm in a spectral scan from 280-320 nm.

NMR Study

The NMR study with phenol as tyrosine mimic was oriented towards a procedure described in the literature.[192] For the NMR study a stock solution of the respective glycomacromolecule (55.15 mg of **5** in 1535 µL D_2O, 58.87 mg of **5a** in 1645 µL D_2O, 55.41mg of **5b** in 1720 µL D_2O) in D_2O was prepared to obtain a final concentration of 10 mM. In addition, 13.55 mg of phenol were dissolved in 4520 µL D_2O to give a 32 mM solution of phenol. As zero sample 300 µL of the glycomacromolecule stock solution were mixed with 300 µL D_2O to give 5 mM glycomacromolecule in absence of phenol. Further samples were prepared by mixing (1) 300 µL of the glycomacromolecule stock solution with 75 µL of 32 mM phenol stock solution and 225 µL of D_2O to give 5 mM of the glycomacromolecule and 4 mM of phenol, (2) 300 µL of the glycomacromolecule stock solution with 150 µL of 32 mM phenol stock solution and 150 µL of D_2O to give 5 mM of glycomacromolecule and 8 mM of phenol, (3) 300 µL of the glycomacromolecule stock solution with 225 µL of 32 mM phenol stock solution and 75 µL of D_2O to give 5 mM of glycomacromolecule and 12 mM of phenol and (4) 300 µL of the glycomacromolecule stock solution with 300 µL of 32 mM phenol stock solution to give 5 mM of glycomacromolecule and 16 mM of phenol. The ^{1}H-NMR spectrum was recorded for all samples in triplicates.

Phenol-Sulphuric Acid Method

The phenol-sulphuric acid method used for glycomacromolecule concentration determination with small modifications follows the procedure described by *Dubois* and coworkers.[139,169] The standard curve was generated using α-D-mannose in concentrations of 30, 55, 80, 110, 140, 220, 350 and 420 µM in Milli-Q water. Three 250 µL aliquots of each concentration were transferred in three test series

A, B and C in a 5 mL Eppendorf vessel. To series A, 250 µL of 5 *wt.*% aqueous phenol solution and 1250 µL concentrated sulphuric acid, to series B, 250 µL water and 1250 µL concentrated sulphuric acid and to series C, 250 µL of 5 *wt.*% aqueous phenol solution and 1250 µL water were added consecutively. After vigorous mixing of the vessels they were incubated at 30 °C for 30 min. Then sugar concentration was determined at 490 nm in a spectral scan from 450-550 nm at 25 °C using the dual-trace spectrometer Specord® 210 Plus from Analytik Jena AG. Milli-Q water was used as a reference and the absorption at 490 nm of the control series B, C and the zero sample (250 µL water, 250 µL 5 *wt.*% aqueous phenol solution, 1250 µL concentrated sulphuric acid) were subtracted from absorption at 490 nm of series A.

Glycomacromolecule concentration was determined by diluting a stock solution of 50 mM of the respective glycomacromolecule in Milli-Q water to a corresponding mannose concentration in the range of 80 to 220 µM. Subsequently, it was proceeded in an analogous fashion to series A, B and C of the standard curve. All measurements were performed in triplicates. Through the comparison to the standard curve, glycomacromolecule concentration was calculated. All solutions were placed in a disposable polystyrene cuvette (10x4x45 mm) from Sarstedt.

The phenol-sulphuric acid method used for degree of functionalization determination of the glyco-AuNPs followed the procedures described previously.[169,234] The standard curve was generated using α-D-mannose in concentrations of 20, 40, 80, 160 and 320 µM in Milli-Q water. For detachment of the α-D-mannopyranoside moieties from the glyco-AuNPs, 200 µL of the respective nanoparticle solution were treated with 40 µL of concentrated hydrochloric acid. The mixture was stored at 80 °C for 24 h. After HCl treatment, the solutions were centrifuged (Wisespin® CF-10, 90 min, 13500 rpm) and 100 µL of the supernatant were treated with 100 µL of 5 wt.% phenol in MilliQ water and 500 µL concentrated sulphuric acid. After vigorous mixing of the vessels they were incubated at room temperature for 30 min. Then sugar concentration was determined at 490 nm in a spectral scan from 450-550 nm at 25°C using the dual-trace spectrometer Specord® 210 Plus from Analytik Jena AG. Milli-Q water was used as a reference. The absorption at 490 nm of a control series of the zero sample (100 µL citrate stabilized nanoparticles after HCl treatment, 100 µL 5 wt.% aqueous phenol solution, 500 µL concentrated sulphuric acid) were subtracted from absorption at 490 nm. All measurements were performed in triplicates. Through the comparison to the standard curve, glycomacromolecule concentration was calculated and compared with nanoparticle concentration resulting in the degree of functionalization. All solutions were placed in a disposable polystyrene cuvette (10x4x45 mm) from Sarstedt.

TBO Titration

The colorimetric titration with the dye toluidine blue O (TBO) followed a procedure adapted from a previously published general method for quantification of carboxylic end groups.[235] For TBO titration, an aqueous solution with pH 10.4 was prepared. In addition, a previously prepared 12.5 mM TBO solution (prepared at least one day in advance and stored in the dark) was diluted by factor 40. The glyco-AuNP solutions were concentrated by centrifugation (Beckman Coulter Allegra™ 25R Centrifuge, 6 h, 15000 rpm, 20 °C) and the supernatant was removed to give 300 µL of glyco-AuNP solutions in the concentration range of 129 to 154 nM. The concentrated solution was then distributed by transferring 50 µL of the glyco-AuNP solution into three 1.5 mL Eppendorf tubes. At the same time three blank Eppendorf tubes were prepared that contained 50 µL of MilliQ water. To each of these six Eppendorf tubes, 283 µL of the diluted TBO solution were added. The Eppendorf tubes were covered with aluminum foil and were shaken overnight. The next day, all Eppendorf tubes were centrifuged (Beckman Coulter Allegra™ 25R Centrifuge, 6 h, 15000 rpm, 20 °C). Then, 100 µL of the supernatant were diluted with 567 µL of the alkaline aqueous solution. The solutions were placed into a 600 µL Hellma Analytics quartz glass cuvettes and the UV absorbance of the diluted solution was measured at 633 nm. By comparing blank and glyco-AuNP absorbance intensity, the concentration of carboxylic groups and thus the degree of functionalization of glyco-AuNP was determined.

Stability of Glyco-AuNPs in Dependence of Sodium Chloride Concentration or (Buffer) Medium

The stability of glyco-AuNPs in dependence of sodium chloride concentration was studied following a procedure described in literature with some modifications.[221] The colorimetric assay was performed by dividing a 10 nM solution of the glyco-AuNP solution in MilliQ water into 96-well microtiter plates (100 µL/well). 100 µL of sodium chloride solutions in MilliQ water were added to each well to obtain final concentrations of 5 nM glyco-AuNPs and serial dilutions of 0, 12.5, 25, 37.5, 50, 100, 125, 250, 500 and 1000 mM sodium chloride. After 24 h the absorption spectrum (wavelength range 400 to 750 nm, 10 nm step) was recorded.

The stability of glyco-AuNPs in lectin binding buffer was investigated similarly to sodium chloride stability. A 5 nM solution of the glyco-AuNPs in lectin binding buffer (LBB) was prepared by concentrating an aqueous solution of the glyco-AuNPs by centrifugation (Beckman Coulter Allegra™ 25R Centrifuge, 12 h, 4500 rcf, 25 °C) and resuspension in LBB. The 5 nM solution was divided into 96-well microtiter plates (200 µL/well). After 24 h the absorption spectrum (wavelength range 400 to 750 nm, 10 nm step) was recorded.

At Davidson College stability of glyco-AuNPs in EMEM full growth medium (supplemented with 1% streptomycin/penicillin, 10% FBS) and PBS buffer was tested in comparison to their stability in MilliQ

water. Therefore, glyco-AuNPs were concentrated by centrifugation (Beckmann Coulter Avanti® J-E, 4000 rpm, 6h, 20 °C) and redispersed in MilliQ water at 100 nM concentration as verified by UV measurement. This dispersion was then used for the stability test by mixing 10 µL with 90 µL of the respective medium or buffer solution or MilliQ water, respectively, to obtain a final concentration of 10 nM in a 96 well plate format. Stability was monitored by recording the UV-Vis spectra in a wavelength range from 400 to 800 nm in 10 nm steps after specific time intervals (0 h, 24 h, 48 h).

Plate-Based Colorimetric Aggregation Study with ConA

The colorimetric aggregation study with Con A followed a procedure adapted from a previously published method for lectin induced aggregation studies by absorbance.[287] A 10 nM solution of the glyco-AuNP in lectin binding buffer (LBB) was prepared by concentrating an aqueous solution of the glyco-AuNP by centrifugation (Beckman Coulter Allegra™ 25R Centrifuge, 12 h, 4500 rcf, 25 °C) and resuspension in LBB. The 10 nM solution was divided into 96-well microtiter plates (100 µL/well). 100 µL of ConA serial dilutions in LBB were added to each well to obtain final concentrations of 5 nM glyco-AuNP and 0, 20, 40, 80, 100, 150, 200, 300, 500, 1000, 2000, 3500 and 10000 nM of ConA. After 30 min the absorption spectrum (wavelength range 400 to 750 nm, 1 nm step) was recorded. Then 50 µL of MeMan in LBB were added to give a concentration of 60 mM MeMan in each well. After 5 min the absorption spectrum (wavelength range 400 to 750 nm, 1 nm step) was recorded.

To test for unspecific protein adsorption, the same procedure was repeated for BSA. The 10 nM glyco-AuNP solution was divided into 96-well microtiter plates (100 µL/well). 100 µL of BSA serial dilutions in LBB were added to each well to obtain final concentrations of 5 nM glyco-AuNP and 0, 20, 200, 2000, and 10000 nM of BSA. After 30 min the absorption spectrum (wavelength range 400 to 750 nm, 1 nm step) was recorded.

Kinetic Study of Aggregation Behavior with ConA by DLS and UV-Vis Spectroscopy

For the kinetic study of aggregation behavior with ConA performed by DLS and UV-Vis spectroscopy, a similar procedure as described by the group of Gibson was performed.[217,227] For both studies, a 10 nM solution of glyco-AuNPs in LBB was mixed in a 1:1 ratio with ConA to obtain K_D concentration of ConA (209 nM for **10**, 203 nM for **11**, 357 nM for **12**) and 5 nM glyco-AuNP concentration.

For the kinetic studies using absorbance spectroscopy, the stock solutions were mixed in wells of a 96-well microtiter-plate (100 µL of each solution per well). The absorbance at 400 and 700 nm was measured every minute for 30 min.

For the kinetic studies using DLS (performed together with Kristina Wagner in the Karg group), the stock solutions were filtrated twice (Roth, Rotilabo® syringe filter, PTFE, 5.0 µm) and were pre-tempered to 20 °C. Then 750 µL of each stock solution were filled into the culture tubes and mixed.

DLS measurements were performed at 20 °C and a scattering angle of 90°. Every minute an intensity-time autocorrelation function was recorded with an acquisition time of 30 s during a period of 30 min.

UV-Vis Thiol Monitoring in Solution

For monitoring the amount of thiol groups in solution Ellman´s reagent was employed. The measurement was proceeded as recommended by the manufacturer Thermo Fisher Scientific. First, three standard curves were produced using cysteine ethyl ester hydrochloride at different concentrations under different pH conditions (acetate buffer pH 5.2, Hepes buffer pH 7.4, phosphate buffer pH 8.0) in order to test for the impact of the pH on the outcome of the reaction with Ellman´s reagent. For each buffer a stock solution of L-cysteine ethyl ester hydrochloride (6.94 mg in 25 mL buffer) was prepared in a volumetric flask. From this stock solution a dilution series was prepared by mixing (1) 2.5 mL of the stock with 0.5 mL of buffer, (2) 2.0 mL of the stock with 1.0 mL of buffer, (3) 1.5 mL of the stock with 1.5 mL of buffer, (4) 1.0 mL of the stock with 2.0 mL of buffer, (5) 0.5 mL of the stock with 2.5 mL of buffer, (6) 0 mL of the stock with 3 mL of buffer. A stock solution of Ellman´s reagent was prepared by dissolving 20.29 mg in 5 mL of the phosphate buffer. 50 µL of this Ellman´s reagent solution were transferred into a 15 mL falcobn tube and mixed with 2.5 mL phosphate buffer. Then 250 µL of each dilution (with changing pH value of the buffer) was added, the mixture shaken and incubated for 15 min. Absorbance was recorded at 412 nm in a wavelength range from 390 to 430 nm.

After preparation of the standard curves, thiolated glycomacromolecules **23** and **24** were tested using three different pH conditions. Therfore, a 10 mM solution of the glycomacromolecule was prepared in the different buffer solutions (acetate buffer pH 5.2, Hepes buffer pH 7.4, phosphate buffer pH 8.0) in a 15 mL centrifuge tube. To ensure oxygen circulation, the cap of the tube was punctured with a short cannula. The falcon tubes were shaken at RT and each hour on the first day, then after 24 h, 48 h, 72 h, 1 week and 2 weeks a 250 µL sample was removed and diluted as reported for samples of the standard curve (50 µL Ellman´s reagent solution and 2.5 mL reaction buffer). The mixture was shaken, incubated for 15 min and absorbance was recorded at 412 nm in a wavelength range from 390 to 430 nm.

DCL Based on Thiol Disulphide Exchange

The investigation of DCL formation based on thiol disulphide exchange of dithiol-glycomacromolecules followed a procedure described in literature.[269] The lectin component was prepared by using 20 mL of the ConA-sepharose slurry (ConA Sepharose™ 4B, GE Healthcare, 10 to 16 mg ConA/mL) that was washed 10 times with LBB in a syringe reactor (polypropylene reactors with a polyethylene frit, closed at the bottom with a luer stopper from Multisyntech). About 9 mL of the remaining medium were resuspended in 10 mL LBB to obtain a concentration of approximately 0.5 mM ConA.

Glycomacromolecule stock solutions were prepared by dissolving 34.92 mg of **23** in 794 µL LBB buffer and 39.44 mg of **24** in 870 µL LBB buffer to obtain a concentration of 20 mM. DTT solution was prepared by dissolving 3.15 mg (0.02 mmol) in 1021 µL buffer to give a 20 mM solution. Based on these stock solutions six different reaction mixtures were prepared for equilibration, (1) 450 µL of glycomacromolecule stock **23** were mixed with 450 µL of the ConA slurry, (2) 450 µL of glycomacromolecule stock **24** were mixed with 450 µL of the ConA slurry, (3) 150 µL of glycomacromolecule stock **23** and **24** were mixed with 300 µL of the ConA slurry, (4) 150 µL of glycomacromolecule stock **23** were mixed with 150 µL LBB, (5) 150 µL of glycomacromolecule stock **24** were mixed with 150 µL LBB, (6) 150 µL of glycomacromolecule stock **23** and **24** were mixed with 300 µL of LBB. To each mixture 50 µL of DTT stock were added. The prepared mixtures were shaken for two weeks in 2 mL Eppendorf tubes that were punctured with a short cannula to ensure oxygen exposure of the samples. After two weeks the mixtures containing ConA-sepharose were transferred into a centrifuge filter (Amicon Ultra-50, PLQK Ultracel-PL membrane, 50 kDa from Merck) and centrifuged at 4400 rpm for 30 min (Eppendorf centrifuge 572). The centrifuge vessel was washed with MilliQ water twice. Then the sepharose particles were resuspended in 400 µL MilliQ water and 100 µL HCl were added. The mixture was centrifuged at 4400 rpm for 30 min (Eppendorf centrifuge 572). The filtrate was used for RP-HPLC-MS analysis.

DCL Based on Imine Formation

For investigation of DCL formation based on imine formation of glycomacromolecules equipped with aldehyde and primary amine functionality, compound **25** was employed as test structure. First, different stock solutions were prepared: 47.06 mg of **25** were dissolved in acetate buffer and 46.02 mg of **25** were dissolved in LBB buffer to obtain 20 mM concentration of glycomacromolecule, 7.64 mg of $NaBH_3CN$ were dissolved in 1013 µL acetate buffer and 5.42 mg $NaBH_3CN$ were dissolved in 719 µL LBB buffer to obtain 120 mM concentration of the reducing agent, 816 µL (1/50 eq, 0.2 µmol, 0.4 mM in 500 µL) of ConA-sepharose in LBB or acetate buffer. With these stock solutions the following mixtures were prepared by combining 250 µL of glycomacromole stock with 250 µL of respective additive or buffer or ConA sephaose: (1) 10 mM **25** in LBB, (2) 10 mM **25** in acetate buffer, (3) 10 mM **25** with 0.4 mM ConA in LBB, (4) 10 mM **25** with 0.4 mM ConA in acetate buffer, (5) 10 mM **25** with 60 mM $NaBH_3CN$ in LBB, (6) 10 mM **25** with 60 mM $NaBH_3CN$ in acetate buffer, (7) 10 mM **25** with 0.4 mM ConA and 60 mM $NaBH_3CN$ in LBB, (8) 10 mM **25** with 0.4 mM ConA and 60 mM $NaBH_3CN$. The prepared mixtures were shaken for four weeks in 2 mL Eppendorf tubes. After specified time intervals of 0 h, 1 day, 2 days, 3 days, 1 week and four weeks 21 µL of the sample were removed and diluted with 479 µL MilliQ water for analysis. The mixtures containing ConA-sepharose were transferred into a centrifuge filter (Amicon Ultra-50, PLQK Ultracel-PL membrane, 50 kDa from Merck) and centrifuged

at 4400 rpm for 30 min (Eppendorf centrifuge 572). The centrifuge vessel was washed with MilliQ water twice. Then the sepharose particles were resuspended in 400 µL MilliQ water and 100 µL HCl were added. The mixture was centrifuged at 4400 rpm for 30 min (Eppendorf centrifuge 572). The filtrate was used for RP-HPLC-MS analysis.

In a second test with compound **25** imine formation was investigated at lower concentrations. Therefore, glycomacromolecule **25** was dissolved in LBB at 1 mg/mL (0.89 mM) concentration (1.5 mg **25** in 1.5 mL LBB). A ConA-sepharose stock solution was prepared by washing 816 µL ConA-sepharose (0.4 mM in 500 µL) 3 times with LBB in a syringe reactor (polypropylene reactors with a polyethylene frit, closed at the bottom with a luer stopper from Multisyntech) and resuspension in 500 µL LBB. In addition, a stock solution of free ConA in solution was prepared by dissolving 11 mg of ConA in 500 µL LBB buffer (0.86 mM). With these stock solutions different samples were prepared for DCL formation: (1) 1 mg/mL **25** in LBB, (2) 1 mg/mL **25** with 1 eq. ConA in LBB, (3) 500 µL of 1 mg/mL stock of glycomacromolecule **25** was loaded in syringe reactor with ConA sepharose to give glycomacromolecule/ConA ratio of 2/1, (4) 1 mg/mL 25 with 289 µL ConA-sepharose (0.086 mM in 1000 µL) to give glycomacromolecule/ConA ratio of 10/1 in 825 µL, (5) 0.86 mM ConA in LBB. The prepared mixtures were shaken for one week in 2 mL Eppendorf tubes. For analysis mixtures containing ConA were transferred into a centrifuge filter (Amicon Ultra-50, PLQK Ultracel-PL membrane, 50 kDa from Merck) and centrifuged at 4400 rpm for 30 min (Eppendorf centrifuge 572). The centrifuge vessel was washed with MilliQ water twice. Then the sepharose particles were resuspended in 400 µL MilliQ water and 100 µL HCl were added. The mixture was centrifuged at 4400 rpm for 30 min (Eppendorf centrifuge 572). The filtrate was used for RP-HPLC-MS analysis.

Based on DCL tests with compound **25** a final investigation of DCL formation based on imine formation of all three glycomacromolecules **25**, **26** and **27** was performed. Therefore, different stock solutions of glycomacromolecules and ConA were prepared. 2.37 mg (1 µmol) of **25**, 6.05 mg (1 µmol) of **26** and 8.22 mg (1 µmol) of **27** were dissolved in 1000 µL LBB for glycomacromolecule stock solutions. In regard to the mass of the monomer unit, a ratio of 1/10 of ConA/glycomacromolecule was desired so that 10.59 mg ConA were dissolved in 2000 µL LBB to prepare the ConA stock solution. 500 µL of each glycomacromolecule stock solution were either combined with 500 µL LBB or 500 µL ConA stock solution. The prepared mixtures were shaken for one week in 2 mL Eppendorf tubes. For analysis mixtures containing ConA were transferred into a centrifuge filter (Amicon Ultra-50, PLQK Ultracel-PL membrane, 50 kDa from Merck) and centrifuged at 4400 rpm for 30 min (Eppendorf centrifuge 572). The centrifuge vessel was washed with MilliQ water twice. Then 400 µL MilliQ water and 100 µL HCl were added. The mixture was centrifuged at 4400 rpm for 30 min (Eppendorf centrifuge 572). The filtrate was used for RP-HPLC-MS analysis.

As last experiment, DCL formation based on imine formation of a mixture of all three glycomacromolecules **25**, **26** and **27** was performed. Therefore, different stock solutions of glycomacromolecules and ConA were prepared. 2.24 mg of **25**, 8.35 mg of **26** and 8.46 mg of **27** were dissolved in 1000 µL LBB in one vial. With regards to the mass of the monomer unit a ratio of 1/10 of ConA/glycomacromolecule was desired so that 7.30 mg ConA were dissolved in 1379 µL LBB to prepare the ConA stock solution. 400 µL of the glycomacromolecule mixture was combined with 400 µL ConA stock solution. 200 µL of the glycomacromolecule mixture was combined with 200 µL LBB. 500 µL of ConA stock solution were combined with 500 µL LBB as a reference probe. The prepared mixtures were shaken for one week in 2 mL Eppendorf tubes. For analysis mixtures containing ConA were transferred into a centrifuge filter (Amicon Ultra-50, PLQK Ultracel-PL membrane, 50 kDa from Merck) and centrifuged at 4400 rpm for 30 min (Eppendorf centrifuge 572). The centrifuge vessel was washed with MilliQ water twice. Then 400 µL MilliQ water and 100 µL HCl were added. The mixture was centrifuged at 4400 rpm for 30 min (Eppendorf centrifuge 572). The filtrate was used for RP-HPLC-MS analysis.

Bacterial Adhesion-Inhibition Assay (performed by Dr. Franziska Reise, Christiana Albertina Universität Kiel)

The bacterial *E. coli* strain PKL1162[288] was cultured from a frozen stock in LB media (+ampicillin 100 mg/mL and chloramphenicol 50 mg/mL) overnight at 37°C. The bacterial pellet resulting after centrifugation and decantation of media was washed twice with PBS (2 mL) and suspended in PBS buffer afterwards. The bacterial suspension was adjusted to OD_{600} = 0.4 with PBS.

The inhibition assay was performed according to literature.[289] Black 96-well microtiter plates (Nunc; MaxiSorp) were prepared for the assay by incubating with mannan from *Saccharomyces cerevisiae* (1.2 mg mL^{-1} in carbonate buffer, 120 µL per well) for 12 h at 37 °C at 100 rpm to evaporate the buffer. The plates were washed with PBST three times and afterwards blocked with PVA (poly vinyl alcohol) solution (1% in PBS, 120 µL per well). The PVA blocking was performed with 100 rpm at room temperature for 2 h. The plates were washed with PBST twice and once with PBS. Finally, a serial dilution of the particular glycomacromolecules (**1**-**1c**, **4**-**4d**, **5**-**5b** and **6b**-**c**, **6e**) in PBS was prepared (50 µL per well) on the mannan-coated microtiter plates. The bacterial suspension was added (50 µL per well). After incubation for 1 h at 37 °C and 100 rpm, the microtiter plates were washed 3 times with PBS and filled with PBS (100 µL per well) for terminal fluorescence intensity readout (excitation wavelength 485 nm, emission wavelength 535 nm).

5.3.1 Cell Based Assays (performed at Davidson College)

Cell Lines and Tissue Culturing

Tissue culturing was performed in a SterilGARD® III Advance SG 603 laminar flow hood from Baker Company. Cell cultures were monitored with a Zeiss Axiovert 25 inverted microscope. RKO and SK-BR-3 cell lines were purchased from ATCC. T3M4 cell line was kindly provided by Mitchell Ho from the NIH (National Institute of Health). The RKO cell line was grown in Eagle's Minimum Essential Medium (EMEM). The SK-BR-3 cell line was grown in McCoy´s 5A medium. The T3M4 cell line was grown in HyClone RPMI-1640 medium supplemented with 2.05 mM L-glutamine. All media were filtered with a Thermo Fisher Scientific Nalgene filter (0.2 µm aPES membrane, 75 mm diameter) and supplemented with 10% of FBS and 1% penicillin/streptomycin (pen/strep). Cell lines were cultured in tissue culture flask from TPP at 37 °C and 5% CO_2 in a CO_2 water jacketed incubator 3110 from Scientific Inc. The medium was exchanged twice per week and splitting of confluent cells was performed employing trypsin-EDTA solution (0.05% trypsin) for subculturing as recommended by the supplier. For cell counting a 2% trypan blue solution in PBS and disposable hemacytometers from Incyto C-chip™ were used. Counting was performed on a Micromaster® microscope from Fisher Scientific.

Uptake Studies – Flow Cytometry

Time and Concentration Dependent Glyco-AuNP Uptake

The entire procedure was performed while avoiding light exposure to the samples. RKO cells were trypsinized for 3 minutes, centrifuged (Beckmann Coulter™, Allegra 6R, 1000 rpm, 10 min, 4 °C) and resuspended in 7 mL full growth medium for counting. Cells were seeded with 500,000 cells per well in a 96 well plate. Therefore, 200 µL of a 6 mL cell suspension of a density of $4 \cdot 10^6$ cells/mL were used for each well. Cells were incubated for 24 h at 37 °C and 5% CO_2. The medium was carefully aspirated and 90 µL of fresh full growth medium were added to each well. 10 µL of the respective FITC labeled glyco-AuNP compound (100 nM (50 nM; 25 nM for 48 h incubation) in MilliQ water, concentrated by centrifugation Beckmann Coulter, Avanti® J-E, 4000 rpm, 6 h, 20 °C) was added to the well in order to obtain final glyco-AuNP concentration of 10 nM (5 nM; 2.5 nM). Unstained control cells that remained untreated were included in the study. Incubation was performed for either 3 h, 24 h or 48 h at 37 °C and 5% CO_2 in the dark. The medium was carefully aspirated and 200 µL of a 0.05% trypsin-EDTA solution was added to each well and incubated for 3 min at RT. The content of each well was transferred into a polystyrene test tube (5 mL polystyrene round bottom tube, 12 x 75 mm from Falcon®). Wells were washed with 200 µL PBS+ and transferred into the same respective test tube. 1 mL PBS+ was added to the test tubes for centrifugation (Beckmann Coulter™, Allegra 6R, 1000 rpm, 10 min, 4°C). Supernatant was poured out and 1 mL fresh PBS+ was added for washing. Washing was

performed by three consecutive centrifugation and resuspension steps in PBS+ buffer. After the last washing step, cells were resuspended in 100 µL PBS+ buffer for flow cytometry measurement. Flow cytometry was performed at a medium flow rate (35 µL/min) and minimum 10,000 events were collected. Measurements were performed in triplicates.

24 h Glyco-AuNP Uptake

The entire procedure was performed while avoiding light exposure to the samples. Cells were trypsinized for 3 minutes, centrifuged (Beckmann Coulter™, Allegra 6R, 1000 rpm, 10 min, 4 °C) and resuspended in 5.5 mL full growth medium for counting. Cells were seeded in a 96 well plate. Therefore, 90 µL of a 2.5 mL cell suspension of a density of $2.5 \cdot 10^6$ ($0.7 \cdot 10^6$ for SK-BR-3) cells/mL were used for each well. Cells were incubated for 24 h at 37 °C and 5% CO_2. The medium was carefully aspirated and 90 µL of fresh full growth medium (PBS buffer for PBS uptake test) were added to each well. 10 µL of the respective FITC labeled glyco-AuNP compound (100 nM in MilliQ water, concentrated by centrifugation Beckmann Coulter, Avanti® J-E, 4000 rpm, 6 h, 20 °C) were added to the well in order to obtain final glyco-AuNP concentration of 10 nM. Unstained control cells were also included in the study. Incubation was performed for 24 h at 37 °C (4 °C for 4 °C incubation test) and 5% CO_2 in the dark. The medium was carefully aspirated and 200 µL of a 0.05% trypsin-EDTA solution was added to each well and incubated for 3 min at RT. The content of each well was transferred into a polystyrene test tube (5 mL polystyrene round bottom tube, 12 x 75 mm from Falcon®). Wells were washed with 200 µL PBS+ and transferred into the same respective test tube. 1 mL PBS+ was added to the test tubes for centrifugation (Beckmann Coulter™, Allegra 6R, 1000 rpm, 10 min, 4°C). Supernatant was poured out and 1 mL fresh PBS+ was added for washing. Washing was performed by three consecutive centrifugation and resuspension steps in PBS+ buffer. After the last washing step, cells were resuspended in 50 µL PBS+ buffer for flow cytometry measurement. Flow cytometry was performed at a medium flow rate (35 µL/min) and minimum 30,000 (13,000 for SK-BR-3 cells; 20,000 at 4 °C incubation; 500 with PBS buffer incubation) events were collected. Measurements were performed in triplicates.

24 h Glyco-AuNP Uptake with Competitor

The entire procedure was performed while avoiding light exposure to the samples. Cells were trypsinized for 3 minutes, centrifuged (Beckmann Coulter™, Allegra 6R, 1000 rpm, 10 min, 4 °C) and resuspended in 3 mL full growth medium for counting. Cells were seeded in a 96 well plate. Therefore, 90 µL of a cell suspension of a density of $6 \cdot 10^6$ cells/mL ($0.24 \cdot 10^6$ for SK-BR-3) were used for each well. Cells were incubated for 24 h at 37 °C and 5% CO_2. The medium was carefully aspirated. 90 µL of fresh full growth medium containing either 200 mM D-lactose or 20 µg/mL anti-hReg3A-antibody as competitive inhibitor of Reg3A receptor were added to each well and preincubated for 1 h. Unstained

control cells were also included in the study. 10 µL of the respective FITC labelled glyco-AuNP compound (100 nM in MilliQ water, concentrated by centrifugation Beckmann Coulter, Avanti® J-E, 4000 rpm, 6 h, 20 °C) was added to the well in order to obtain final glyco-AuNP concentration of 10 nM. Co-incubation was performed for further 24 h at 37 °C and 5% CO_2 in the dark. The medium was carefully aspirated and 200 µL of a 0.05% trypsin-EDTA solution was added to each well and incubated for 3 min at RT. The content of each well was transferred into a polystyrene test tube (5 mL polystyrene round bottom tube, 12 x 75 mm from Falcon®). Wells were washed with 200 µL PBS+ and transferred into the same respective test tube. 1 mL PBS+ was added to the test tubes for centrifugation (Beckmann Coulter™, Allegra 6R, 1000 rpm, 10 min, 4°C). Supernatant was poured out and 1 mL fresh PBS+ was added for washing. Washing was performed by three consecutive centrifugation and resuspension steps in PBS+ buffer. After the last washing step, cells were resuspended in 50 µL PBS+ buffer for flow cytometry measurement. Flow cytometry was performed at a medium flow rate (35 µL/min) and minimum 30,000 (2,000 for SK-BR-3) events were collected. Measurements were performed in triplicates.

24 h Glyco-AuNP Uptake with Cell Uptake Pathway Inhibitors

Before FACS measurement could be performed, cell viability was tested in presence of the respective inhibitor by trypan blue staining. Inhibitor stock solutions in full growth medium were prepared by dissolving 3.2 mg of ChlorH in 9 mL medium (1000 µM), 13 mg MβCD in 99 µL medium (100 mM) and mixing 25 µL CytoD (1 mg in 1 mL DMSO) with 975 µL medium (40 µM). RKO cells were trypsinized for 3 minutes, centrifuged (Beckmann Coulter™, Allegra 6R, 1000 rpm, 10 min, 4 °C) and resuspended in 5 mL full growth medium for counting. 150 µL of the cell suspension of a density of $3 \cdot 10^6$ cells/mL were diluted with 300 µL medium. 90 µL of this dilution were mixed with 10 µL of the respective inhibitor stock solution. 10 µL of the mixture were added to 10 µL trypan blue solution and the amount of dead and live cells was counted after 0 h, 1 h and 4 h.

The entire procedure for flow cytometry was performed while avoiding light exposure to the samples. RKO cells were trypsinized for 3 minutes, centrifuged (Beckmann Coulter™, Allegra 6R, 1000 rpm, 10 min, 4 °C) and resuspended in 4.5 mL full growth medium for counting. 90 µL of the cell suspension of a density of $3 \cdot 10^6$ cells/mL were seeded in a polystyrene test tube (5 mL polystyrene round bottom tube, 12 x 75 mm from Falcon®). 10 µL of the respective inhibitor stock solution was added and the cells were preincubated for 1 h. Unstained control cells were also included in the study. Subsequently, 10 µL of the respective FITC labelled glyco-AuNP compound (200 nM in MilliQ water, concentrated by centrifugation Beckmann Coulter, Avanti® J-E, 4000 rpm, 6 h, 20 °C) was added. Co-incubation was performed for further 3 h at 37 °C and 5% CO_2 in the dark. 1 mL PBS+ was added to the test tubes for centrifugation (Beckmann Coulter™, Allegra 6R, 1000 rpm, 10 min, 4°C). Supernatant was poured out

and 1 mL fresh PBS+ was added for washing. Washing was performed by three consecutive centrifugation and resuspension steps in PBS+ buffer. After the last washing step, cells were resuspended in 50 µL PBS+ buffer for flow cytometry measurement. Flow cytometry was performed at a medium flow rate (35 µL/min) and minimum 5,000 events were collected. Measurements were performed in triplicates.

3 h Glycomacromolecule Uptake

The entire procedure was performed while avoiding light exposure to the samples. RKO cells were trypsinized for 3 minutes, centrifuged (Beckmann Coulter™, Allegra 6R, 1000 rpm, 10 min, 4 °C) and resuspended in 4 mL full growth medium for counting. 90 µL of the cell suspension of a density of $6 \cdot 10^6$ ($1 \cdot 10^6$ cells/mL) were seeded in a polystyrene test tube (5 mL polystyrene round bottom tube, 12 x 75 mm from Falcon®). 10 µL of the respective FITC labelled glycomacromolecule compound (20 µM (200 µM) in MilliQ water) was added in order to obtain final glycomacromolecule concentration of 2 µM (20 µM). Unstained control cells were also included in the study. Incubation was performed for 3 h at 37 °C and 5% CO_2 in the dark. 1 mL PBS+ was added to the test tubes for centrifugation (Beckmann Coulter™, Allegra 6R, 1000 rpm, 10 min, 4°C). Supernatant was poured out and 1 mL fresh PBS+ was added for washing. Washing was performed by three consecutive centrifugation and resuspension steps in PBS+ buffer. After the last washing step, cells were resuspended in 50 µL PBS+ buffer for flow cytometry measurement. Flow cytometry was performed at a medium flow rate (35 µL/min) and minimum 20,000 (3,000) events were collected. Measurements were performed in triplicates.

24 h Glycomacromolecule Uptake

The entire procedure was performed while avoiding light exposure to the samples. Cells were trypsinized for 3 minutes, centrifuged (Beckmann Coulter™, Allegra 6R, 1000 rpm, 10 min, 4 °C) and resuspended in 4 mL full growth medium for counting. RKO cells were seeded in a 96 well plate. Therefore, 90 µL of a cell suspension of a density of $6 \cdot 10^6$ cells/mL were used for each well. Cells were incubated for 24 h at 37 °C and 5% CO_2. The medium was carefully aspirated and 90 µL of fresh full growth medium were added to each well. 10 µL of the respective FITC labelled glycomacromolecule compound (20 µM in MilliQ water) was added to the well in order to obtain final glycomacromolecule concentration of 2 µM. Unstained control cells were also included in the study. Incubation was performed for 24 h at 37 °C (4 °C for 4 °C uptake test) and 5% CO_2 in the dark. The medium was carefully aspirated and 200 µL of a 0.05% trypsin-EDTA solution was added to each well and incubated for 3 min at RT. The content of each well was transferred into a polystyrene test tube (5 mL polystyrene round bottom tube, 12 x 75 mm from Falcon®). Wells were washed with 200 µL PBS+ and transferred into the same respective test tube. 1 mL PBS+ was added to the test tubes for centrifugation (Beckmann

Coulter™, Allegra 6R, 1000 rpm, 10 min, 4°C). Supernatant was poured out and 1 mL fresh PBS+ was added for washing. Washing was performed by three consecutive centrifugation and resuspension steps in PBS+ buffer. After the last washing step, cells were resuspended in 50 µL PBS+ buffer for flow cytometry measurement. Flow cytometry was performed at a medium flow rate (35 µL/min) and minimum 20,000 events were collected. Measurements were performed in triplicates. Measurements were performed in triplicates.

Uptake Studies – ICP-MS

The entire procedure was performed while avoiding light exposure to the samples. Cells were trypsinized for 3 minutes, centrifuged (Beckmann Coulter™, Allegra 6R, 1000 rpm, 10 min, 4 °C) and resuspended in 5.5 mL full growth medium for counting. RKO cells were seeded in a 96 well plate. Therefore, 90 µL of a cell suspension of a density of $3 \cdot 10^6$ cells/mL were used for each well. Cells were incubated for 24 h at 37 °C and 5% CO_2. On the next day, the medium was carefully aspirated and replaced with 90 µL of fresh full growth medium. Then 10 µL of a 100 nM glyco-AuNP solution in MilliQ water (concentrated by centrifugation Beckmann Coulter, Avanti® J-E, 4000 rpm, 6 h, 20 °C) was added to yield a final concentration of 10 nM glyco-AuNP in the wells. For the control wells with cells only, 10 µL of medium were added. For the control wells with glyco-AuNPs only, no cells were seeded in the respective wells and 90 µL of fresh medium were used for diluting 10 µL of the 100 nM glyco-AuNP solution. For the Reg3A inhibition wells a 10 µg/mL solution of anti-hReg3A antibody in full growth medium was used and 10 µL of a 100 nM glyco-AuNP solution were added (10 nM final concentration). All wells were incubated for 24h at 37 °C, 5% CO_2. After the 24h incubation period, the medium was carefully aspirated and the wells were washed 3 times with PBS+ buffer. Therefore, 200 µL PBS+ buffer were added to the wells, they were centrifuged (Beckmann Coulter™, Allegra 6R , 1000 rpm, 10 min, 4 °C) and the PBS+ buffer was carefully removed. Then 200 µL of the 0.05% trypsin-EDTA solution were added to the wells and they were incubated for 3 minutes at RT. After incubation the content of each well was transferred into a glass test tube (PYREX®, 12x75 mm, beaded rim). The wells were washed with 200 µL PBS+ and the PBS+ buffer was transferred into the same respective test tube. Test tubes were centrifuged (Beckmann Coulter™, Allegra 6R , 1000 rpm, 10 min, 4 °C), the supernatant was poured out and the test tube tapped on a tissue and dried to complete dryness at RT. On the next day, the pellet was digested with 0.5 mL of fresh aqua regia, test tubes were covered with parafilm and heated for 4h at 85 °C in a heat block (VWR Scientific products, Standard Heatblock). After 4h, test tubes were cooled to room temperature and the content was transferred into 1 mL of MilliQ water. Test tubes were rinsed 2x with 1 mL of MilliQ water to yield a total volume of 3.5 mL in the samples. Samples were stored in the fridge until analysis was performed at University of North Carolina at

Chapel Hill by Brandie Ehrmann. Measurements were performed in two sets of experiments with triplicate determination per experiment.

XTT Assay

The entire procedure was performed while avoiding light exposure to the samples. For XTT cell viability assay a XTT kit from Biotium was used. Cells were seeded in 96 well plates at a density of 5,000 cells/mL in 90 µL full growth medium. 10 µL of the respective glyco-AuNP solution (100 nM in MilliQ water, concentrated by centrifugation Beckmann Coulter, Avanti® J-E, 4000 rpm, 6 h, 20 °C) was added to reach final concentrations of 10 nM in a final volume of 100 µL per well. As unstained control cells only treated with 10 µL full growth medium and as vehicle control cells treated with 10 µL MilliQ water were included in XTT assay. Incubation was performed for 48 h at 37 °C and 5% CO_2. For background subtraction wells only containing 100 µL full growth medium and 10 nM solutions of glyco-AuNPs in MilliQ water were prepared.

XTT working solution was prepared immediately before use by heating XTT solution to 37 °C and gently swirling the solution until a clear solution was obtained. For one 96 well plate to be tested, 5 mL of XTT solution were mixed with 25 µL activation reagent. 50 µL of this activated XTT solution were added to each well to obtain total volumes of 150 µL. After 3 h further incubation at 37 °C and 5% CO_2 absorbance at 475 nm and background absorbance at 660 nm was recorded for all wells.

Fluorescence Microscopy

The whole procedure was performed in Falcon® tissue culture dishes (polystyrene, 35x10mm, sterile, non-pyrogenic). The cover slips (15 mm round cover glass from Celltreat) were placed in the petri dish and coated with 1 mL of a 0.01% poly-L-lysine solution from Sigma Aldrich for 5 min at RT. After coating, the poly-L-lysine solution was removed and the cover slips were washed three times with 2.5 mL of MilliQ water and dried at RT for 2h. The cell lines were trypsinized, counted and diluted in full growth medium to minimum 80,000 cells/mL. 2 mL of this cell suspension were added to the cover slips and the cover slips were incubated at 37°C, 5% CO_2 until confluence was reached (24 to 48h). After incubation, the medium was aspirated and the cover slip transferred into a new clean petri dish. 900 µL of medium and 100 µL of a 100 nM FITC labeled glyco-AuNP solution in MilliQ water were premixed to reach a final glyco-AuNP concentration of 10 nM and then added to the cover slip. Glyco-AuNP incubation was performed for 24 h at 37°C, 5% CO_2. The medium was aspirated and the cover slips were transferred into a new clean petri dish for fixing and permeabilization. The cover slips were washed two times with 2 mL of prewarmed PBS and then the cells were fixed with 1 mL of a 37% formaldehyde solution in PBS for 10 min at RT. After washing two times with 2 mL of prewarmed PBS, cells were permeablized with 1 mL 0.1% tween 20 in PBS for 5 min at RT. The cover slips were washed two times with 2 mL of prewarmed PBS, freed from buffer by tapping the cover slips on a sterile tissue

and transferred into a new clean petri dish for staining. For reference staining Alexa Fluor™ 647 Phalloidin for actin and Hoechst 33342 staining for the nucleus were used, both purchased from Invitrogen. The dilutions were performed as recommended by the manufacturer: 100 mg of Hoechst were dissolved in 10 mL of deionized water and 5 µL of this stock solution were further diluted in 10 mL PBS buffer for staining of the cover slip. Alexa Fluor™ 647 Phalloidin was dissolved in 1.5 mL methanol and 5 µL of this stock solution were further diluted in 200 µL PBS for staining. 200 µL of both staining solutions were added to the cover slips simultaneously and incubated for 40 min at RT in the dark. The supernatant was removed, and the cover slips were washed three times with PBS buffer. TrueBlack® Lipofuscin autofluorescence quencher from Biotium was prepared as recommended by the manufacturer by mixing 50 µL of the 20x stock solution with 1 mL 70vol% ethanol in MilliQ water right before use. The cover slips were incubated with this solution for 30 s and then washed three times with PBS. One drop of ProLong™ Gold as antifade mountant from Invitrogen was put on a clean slide (VWR™ VistaVision, 3”x1”x 1.2 mm) and the cover slip was carefully lowered onto the antifade reagent to avoid trapping air bubbles. The cover slip was dried for 48 h at RT before fluorescence microscopy was performed with an Olympus DP80 coupled with a Prior Scientific Launches L200S fluorescence illumination system.

5.4 Syntheses

5.4.1 Building Block Syntheses

The method employed for the syntheses of the TDS functional building block and the EDS as well as ODS spacer building block followed that reported by Hartmann and coworkers.[95,100,131,132]

1-(Fluorenyl)-3,11-dioxo-7-(pent-4-ynoyl)-2-oxa-4,7,10-triazatetradecan-14-oic acid, TDS

The overall yield of the synthesis was 23%.

^{1}H-NMR (600 MHz, DMSO-d_6): δ(ppm) = 11.84 (br s, -O-H), 8.03 (t, ^3J= 5.75 Hz, -N-H), 7.87 (d, ^3J= 7.55 Hz, 2H, Ar-H), 7.67 (dd, ^3J= 7.36, ^4J= 2.47 Hz, 2H, Ar-H), 7.43 (t, ^3J= 7.44 Hz, 3H, Ar-H),7.39 (t, ^3J= 5.93 Hz, -N-H), 7.37 – 7.30 (m, 2H, Ar-H), 4.30 (d , ^3J= 6.82 Hz, 1H, -C(O)OC**H**$_2$CH-), 4.27 (d, ^3J= 6.94 Hz, 1H, -C(O)OC**H**$_2$CH-), 4.21 (t, ^3J= 6.79 Hz, 1H, -C(O)OCH$_2$C**H-**), 3.34 – 3.22 (m, 4H, -NC**H**$_2$CH$_2$NH-), 3.21 – 3.06 (m, 4H, -NCH$_2$C**H**$_2$NH-), 2.78 – 2.70 (m, 1H, -C(O)CH$_2$CH$_2$CC**H**), 2.54 – 2.47 (m, 2H, -C(O)C**H**$_2$CH$_2$CCH, overlapped by DMSO-d_5), 2.46 – 2.38 (m, 2H, -C(O)CH$_2$C**H**$_2$CCH), 2.37 – 2.25 (m, 4H, -C(O)C**H**$_2$C**H**$_2$COOH).

ESI-MS**:** m/z calcd. for $C_{28}H_{31}N_3O_6$ $[M+H]^+$ 506.2; found 506.2.

1-(9H-Fluoren-9-yl)-3,14-dioxo-2,7,10-trioxa-4,13-diazaheptadecan-17-oic acid, EDS

The overall yield of the synthesis was 59%.

^{1}H-NMR (600 MHz, DMSO-d_6): δ(ppm) = 11.86 (br s, -O-H), 7.94 – 7.85 (m, 3H, -N-H, Ar-H), 7.69 (d, ^3J= 7.46 Hz, 2H, Ar-H), 7.41 (t, ^3J= 7.46 Hz, 2H, Ar-H), 7.33 (t, ^3J= 7.50 Hz, 2H, Ar-H), 4.30 (d, ^3J= 6.97 Hz, 2H, -C(O)OC**H**$_2$CH-), 4.21 (t, ^3J= 6.92 Hz, 1H, -C(O)OCH$_2$C**H-**), 3.50 (s, 4H, -OC**H**$_2$C**H**$_2$O-), 3.44 – 3.35 (m, 4H, -NHCH$_2$C**H**$_2$O-), 3.19 (q, ^3J= 5.82 Hz, 2H, -NHC**H**$_2$CH$_2$O-), 3.14 (q, ^3J= 5.87 Hz, 2H, -NHC**H**$_2$CH$_2$O-), 2.42 (t, ^3J= 6.72 Hz, 2H, -C(O)CH$_2$C**H**$_2$COOH), 2.32 (t, ^3J= 7.22 Hz, 2H, -C(O)C**H**$_2$CH$_2$COOH).

ESI-MS: m/z calcd. for $C_{25}H_{30}N_2O_7$ $[M+H]^+$ 471.2; found 471.2, $[M+Na]^+$ 493.2, found 493.2.

4-((8-((((9H-fluoren-9-yl)methoxy)carbonyl)amino)octyl)amino)-4-oxobutanoic acid, ODS

The synthesis of ODS building block was already established in the Hartmann group but the final purification step was optimized as part of this work.[132] In the last synthesis step 12.5 g (27 mmol) of the TFA salt precursor were dissolved in 300 mL DCM after the addition of 11 mL (81 mmol) triethylamine. 2.7 g (27 mmol) succinic anhydride were added to the colorless solution. The reaction mixture was stirred at room temperature. Some of the colorless product precipitates after 1 h. After 2 h the mixture was poured into 1 L of 5% aqueous solution of citric acid. Vigorous stirring led to precipitation of a colorless fluffy solid. The solid was filtered and washed with 5% aqueous solution of

citric acid and water. After drying the precipitate under vacuum, it was redissolved in a DCM/MeOH/AcOH (100/10/1, *v/v*) mixture and was extracted with water. In the second washing step a fluffy colorless precipitate was formed that was filtered and dried under high vacuum to yield 11.5 g (25 mmol, 92 %) of the pure product ODS.[100]

The overall yield of the synthesis was 85 %.

^{1}H-NMR (600 MHz, DMSO-d_6): δ(ppm) = 11.60 (br s, 1H, -O-H), 7.88 (d, ^3J= 7.40 Hz, 2H, Ar-H), 7.79 (t, ^3J= 5.35 Hz, 1H, -N-H), 7.68 (d, ^3J= 7.37 Hz, Ar-H), 7.41 (t, ^3J= 7.37 Hz, 2H, Ar-H), 7.32 (t, ^3J= 7.37 Hz, Ar-H), 7.25 (t, ^3J= 5.64 Hz, 1H, -N-H), 4.29 (d, ^3J= 6.84 Hz, 2H, -C(O)OC**H**$_2$CH-), 4.20 (t, ^3J= 6.65 Hz, 1H, -C(O)OCH$_2$C**H-**), 3.00 (q, ^3J= 6.32 Hz, 2H, -NHC**H**$_2$-), 2.96(q, ^3J= 6.32 Hz, 2H, -NHC**H**$_2$-), 2.41 (t, ^3J= 6.18 Hz, 2H, -C(O)C**H**$_2$CH$_2$COOH), 2.29 (t, ^3J= 6.46 Hz, 2H, -C(O)CH$_2$C**H**$_2$COOH), 1.45 – 1.30 (m, 4H, -NHCH$_2$C**H**$_2$-), 1.29 – 1.19 (br s, 8H, -NH(CH$_2$)(C**H**$_2$)$_6$(CH$_2$)NH$_2$-).

ESI-MS m/z calcd. for $C_{27}H_{34}N_2O_5$ $[M+H]^+$ 467.3; found 467.3.

(2-azidoethyl)-2,3,4,6-tetra-O-acetyl-α-D-mannopyranoside

The synthesis proceeded according to literature.[290]

The overall yield of the synthesis was 17%.

^{1}H-NMR (300 MHz, $CDCl_3$): δ(ppm) = 5.34 (dd, ^3J= 10.01, 3.44 Hz, 1H, H3), 5.29 (d, ^3J= 9.99 Hz, 1H, H4), 5.26 (dd, ^3J= 3.33, 1.72 Hz, 1H, H2), 4.86 (d, ^3J= 1.45 Hz, 1H, H1), 4.27 (dd, ^3J= 5.32 Hz, ^2J= 12.26 Hz, 1H, H6), 4.11 (dd, ^3J= 2.35 Hz, ^2J= 12.27 Hz, 1H, H6), 4.06 – 4.01 (m, 1H, H5), 3.89 – 3.83 (m, 1H, -OC**H**$_2$CH$_2$N$_3$), 3.69 – 3.63 (m, 1H, -OC**H**$_2$CH$_2$N$_3$), 3.52 – 3.40 (m, 2H, -OCH$_2$C**H**$_2$N$_3$), 2.15 (s, 3H, -OCH$_3$), 2.09 (s, 3H, -OCH$_3$), 2.04 (s, 3H, -OCH$_3$), 1.99 (s, 3H, -OCH$_3$).

ESI-MS: m/z calcd. for $C_{16}H_{23}N_3O_{10}$ $[M+NH_4]^+$ 435.2; found 435.3.

(2-azidoethyl)-2,3,4,6-tetra-O-acetyl-β-D-galactopyranoside

The synthesis proceeded according to literature.[291]

The overall yield of the synthesis was 29%.

^{1}H-NMR (300 MHz, $CDCl_3$): δ(ppm) = 5.39 (dd, ^4J= 3.4, 1.0 Hz, 1H, H4), 5.24 (dd, ^3J= 10.5, 7.9 Hz, 1H, H2), 5.02 (dd, ^3J= 10.5, 3.4, Hz, 1H, H3), 4.56 (d, ^3J= 7.9 Hz, 1H, H1), 4.23-4.0 (m, 3H, H5, H6), 3.92 (td, ^3J= 6.7, 1.2, 1H, -OC**H**$_2$CH$_2$N$_3$) 3.74-3.64 (m, 1H, -OC**H**$_2$CH$_2$N$_3$), 3.57 – 3.46 (m, 1H, -OCH$_2$C**H**$_2$N$_3$), 3.30 (ddd, ^3J= 13.4, 4.7, 3.3 Hz, 1H, -OCH$_2$CH$_2$N$_3$), 2.16 (s, 3H, -OCH$_3$), 2.05 (2s, 6H, -OCH$_3$), 1.99 (s, 3H, -OCH$_3$).

All solution-phase reactions were monitored by thin-layer chromatography (TLC) using MACHERY-NAGEL silica gel 60 F_{254} (0.20 mm thickness). The TLC plates were visualized with UV light and by ninhydrine or sugar staining followed by heating.

5.4.2 Synthesis and Functionalization of Gold Nanoparticles

Synthesis of Citrate Stabilized AuNPs (performed by Kristina Wagner, Kirsten Volk, working group Karg, Heinrich Heine University Düsseldorf)

Spherical citrate stabilized AuNPs were synthesized according to the well-known Turkevich-method.[219] 545 mL of water and 5.46 mL of $HAuCl_4$ (0.05 M in water) were brought to the boil. 27.5 mL of a hot aqueous solution of sodium citrate dihydrate (1wt%) were added rapidly under vigorous stirring. After the reduction was completed the dark red nanoparticle dispersion was allowed to cool to room temperature. According to TEM-analysis the AuNPs are spherical and monodisperse.

Synthesis of Rod Shaped AuNPs (performed by Kristina Wagner, Christina Noffke, working group Karg, Heinrich Heine University Düsseldorf)

The synthesis for rod shaped gold nanoparticles was oriented towards a procedure described in literature.[255] The gold seed was prepared by adding 3.078 mL of a mixture of 10 mL NaOH (0.01 M in H_2O) and 3.8 mg $NaBH_4$ rapidly to a aqueous solution of 0.6627 mL $HAuCl_4$ (0.0528 M in H_2O) and 66.37 g CTAB (0.1 M in H_2O) under vigorous stirring. An immediate color change to rust red could be observed.

The rod synthesis was performed by well mixing 4160 mL of CTAB (0.1 M in H_2O), 39.078 mL $HAuCl_4$ (0.0528 M in H_2O), 29.4 mL $AgNO_3$ (0.521 g in 29.4 mL H_2O) and 209.7 mL of a hydrochinone solution (2.221 g in 210 mL H_2O). To this mixture 67.1 mL of the gold seeds were added and the obtained growth solution was mixed thoroughly and allowed to age overnight at 30 °C. Purification was performed by centrifugation (Beckman Coulter Allegra™ 25R Centrifuge, 30 min, 7000 rpm, 32 °C) and redispersion in MilliQ water.

Functionalization of AuNPs by Ligand Exchange

All glassware that was used for the ligand exchange experiments was washed with aqua regia and MilliQ water. 100 mL of citrate stabilized AuNPs ($5.5 \cdot 10^{-10}$ mol) were transferred into a 250 mL round bottom flask. With the assumption that one glycomacromolecule occupies 1 nm² of the AuNP surface, 200% excess of glycomacromolecule ($6.85 \cdot 10^{-7}$ mol) was used. The glycomacromolecule was dissolved in MilliQ water (1 mg/mL) and preactivated with 2 eq. of TCEP. The AuNP solution was stirred vigorously while preactivated glycomacromolecule solution was added dropwise. The stirring speed was reduced, and the reaction mixture was stirred at room temperature in the dark for 48 h. Then, the

reaction mixture was transferred into 50 mL falcon tubes and purified by three centrifugation steps (Beckman Coulter Allegra™ 25R Centrifuge, 2000x*g,* 20 °C, 2x12 h) and each time redispersed in MilliQ water. After centrifugation, glyco-AuNP concentration was determined spectrophotometrically.

5.4.3 Solid Phase Polymer Synthesis (SPPoS)

All solid phase reactions were performed in 10 mL polypropylene reactors with a polyethylene frit, closed at the bottom with a luer stopper from Multisyntech.

5.4.3.1 SPPoS of Glycomacromolecules Varying in Backbone Characteristics

All listed precision glycomacromolecules were synthesized on solid support by stepwise assembly of different building blocks according to general coupling protocol and Fmoc cleavage protocol.[121] As building blocks, functional building block bearing an alkyne group, termed TDS, and spacer building blocks with either hydrophilic ethylene glycol units (EDS) or hydrophobic aliphatic (ODS) or aromatic (AR) properties were employed. In case of the hydrophobic spacer building block, ODS, a 0.4 M solution of LiCl in DCM/DMF (1/1, *v/v*) was used as coupling solution instead of pure DMF. All other steps were proceeded as described previously.

After successful assembly of the desired number of building blocks, capping of the N-terminal primary amine group was performed employing acetic anhydride.[121] The subsequent conjugation of the azide functionalized carbohydrates proceeded by general CuAAC protocol.[121] Then, the sugar moieties were deprotected by the use of a 0.1 M solution of sodium methoxide in methanol and as last step the product was cleaved from solid support with 30% TFA and 1% TIPS in DCM. After cleavage trifluoracetic acid (TFA) residues were removed by the use of a strong anion exchange resin AG1-X8 (550 mg, quarternary ammonium, 100-200 mesh, acetate form, BioRad) as described by Roux and coworkers.[137] The procedure was repeated to ensure complete anion exchange from TF-acetate to acetate. As a last step the glycomacromolecule was isolated by freeze-drying.

All glycomacromolecules were purified by preparative RP-HPLC.

For all structures commercially available Tentagel® chlorotrityl resin modified with ethylene diamine was used as resin for solid phase synthesis.[95] The batch sizes for synthesizing the glycomacromolecules varied between 0.05 mmol for structures **1**-**1c**, **3**, **3a**, **4**, **5**, **5a**, **5b**, **6**, **6a**, **6c** and 0.1 mmol for structures **2**, **2a**, **4a**, **4b**, **4c**, **4d**, **6b**, **6d**, **6e**.

Man(4,5,6)-9-EDS, **1**

Compound **1** was obtained in a yield of 53% after purification by preparative RP-HPLC. The anomeric proton of mannose could not be examined in ^{1}H-NMR due to the overlaying signal of the residual solvent.

^{1}H-NMR (600 MHz, D_2O): δ(ppm) = 8.51 (br. s, -N-H), 7.87 (s, 3H, Ar-H), 4.65–4.60 (m, 6H, -OCH$_2$C**H**$_2$N- (side chain)), 4.11–4.05 (m, 3H, -OC**H**$_2$CH$_2$N- (side chain)), 3.94–3.89 (m, 3H, -OC**H**$_2$CH$_2$N- (side chain)), 3.87–3.85 (m, 3H, Man-H), 3.79–3.56 (m, 60H, -OC**H**$_2$C**H**$_2$O- (EDS), -NHCH$_2$C**H**$_2$O- (EDS), Man-H), 3.53–3.43 (m, 14H, -NH$_2$CH$_2$C**H**$_2$NH- (EDA), -C(O)NHCH$_2$C**H**$_2$N- (TDS)), 3.41–3.29 (m, 36H,- NHC**H**$_2$CH$_2$O- (EDS), -C(O)NHC**H**$_2$CH$_2$N- (TDS)), 3.15 (t, ^3J= 5.9 Hz, 2H, -NH$_2$C**H**$_2$CH$_2$NH- (EDA)), 3.05–2.95 (m, 9H, Man-H, -NC(O)CH$_2$C**H**$_2$- (side chain)), 2.81-2.75 (m, 6H, -NC(O)C**H**$_2$CH$_2$- (side chain)), 2.58–2.39 (m, 36H, -C(O)C**H**$_2$C**H**$_2$C(O)-), 2.00 (2s, 3H, -C(O)CH$_3$).

MALDI-TOF-MS for $C_{127}H_{220}N_{32}O_{52}$: $[M+H]^+$ calcd. 3026.6, found 3026.7, $[M+Na]^+$ calcd. 3048.6, found 3048.8, $[M+K]^+$ calcd. 3064.6, found 3064.8.

HR-ESI-MS for $C_{127}H_{220}N_{32}O_{52}$ (exact monoisotopic mass 3025.5554): $[M+5H]^{5+}$ calcd. 606.1184, found 606.1182, mass accuracy +0.3 ppm.

RP-HPLC (linear gradient from 0-50% eluent B in 30 min at 25 °C): t_r= 11.5 min. Determined purity: 95%.

Man(3,5,7)-9-EDS, **1a**

Compound **1a** was obtained in a yield of 38% after purification by preparative RP-HPLC. The anomeric proton of mannose could not be examined in ^{1}H-NMR due to the overlaying signal of the residual solvent.

^{1}H-NMR (600 MHz, D_2O): δ(ppm) = 8.45 (br. s, -N-H), 7.88 (s, 3H, Ar-H), 4.66–4.61 (m, 6H, -OCH$_2$C**H**$_2$N- (side chain)), 4.11–4.06 (m, 3H, -OC**H**$_2$CH$_2$N- (side chain)), 3.95–3.90 (m, 3H, -OC**H**$_2$CH$_2$N- (side chain)), 3.88–3.85 (m, 3H, Man-H), 3.78–3.56 (m, 60H, -OC**H**$_2$C**H**$_2$O- (EDS), -NHCH$_2$C**H**$_2$O- (EDS), Man-H), 3.52–3.42 (m, 14H, -NH$_2$CH$_2$C**H**$_2$NH- (EDA), -C(O)NHCH$_2$C**H**$_2$N- (TDS)), 3.42–3.30 (m, 36H, -NHC**H**$_2$CH$_2$O- (EDS), -C(O)NHC**H**$_2$CH$_2$N- (TDS)), 3.15 (t, ^3J= 5.8 Hz, 2H, -NH$_2$C**H**$_2$CH$_2$NH- (EDA)), 3.05–2.97 (m, 9H, Man-H, -NC(O)CH$_2$C**H**$_2$- (side chain)), 2.80 (t, ^3J= 7.3 Hz, 6H, -NC(O)C**H**$_2$CH$_2$- (side chain)), 2.58–2.44 (m, 36H, -C(O)C**H**$_2$C**H**$_2$C(O)-), 2.00 (2s, 3H, C(O)CH$_3$).

MALDI-TOF-MS for $C_{127}H_{220}N_{32}O_{52}$: $[M+H]^+$ calcd. 3026.6, found 3026.1, $[M+Na]^+$ calcd. 3048.6, found 3048.7, $[M+K]^+$ calcd. 3064.6, found 3064.7.

HR-ESI-MS for $C_{127}H_{220}N_{32}O_{52}$ (exact monoisotopic mass 3025.5554): $[M+4H]^{4+}$ calcd. 757.3961, found 757.3967, mass accuracy -0.8 ppm.

RP-HPLC (linear gradient from 0-50% eluent B in 30 min at 25 °C): t_r= 11.5 min. Determined purity: 97%.

Man(2,5,8)-9-EDS, **1b**

Compound **1b** was obtained in a yield of 40% after purification by preparative RP-HPLC. The anomeric proton of mannose could not be examined in ^{1}H-NMR due to the overlaying signal of the residual solvent.

^{1}H-NMR (600 MHz, D_2O): δ(ppm) = 8.65 (br. s, -N-H), 7.88 (s, 3H, Ar-H), 4.67–4.62 (m, 6H, -OCH$_2$C**H**$_2$N- (side chain)), 4.12–4.04 (m, 3H, -OC**H**$_2$CH$_2$N- (side chain)), 3.96–3.89 (m, 3H, -OC**H**$_2$CH$_2$N- (side chain)), 3.87–3.85 (m, 3H, Man-H), 3.75–3.56 (m, 60H, -OC**H**$_2$C**H**$_2$O- (EDS), -NHCH$_2$C**H**$_2$O- (EDS), Man-H), 3.53–3.43 (m, 14H, -NH$_2$CH$_2$C**H**$_2$NH- (EDA), -C(O)NHCH$_2$C**H**$_2$N- (TDS)), 3.43–3.30 (m, 36H, -NHC**H**$_2$CH$_2$O- (EDS), -C(O)NHC**H**$_2$CH$_2$N- (TDS)), 3.15 (t, ^3J= 5.8 Hz, 2H, -NH$_2$C**H**$_2$CH$_2$NH- (EDA)), 3.05–2.97 (m, 9H, Man-H, -NC(O)CH$_2$C**H**$_2$- (side chain)), 2.80 (t, ^3J= 7.2 Hz, 6H, -NC(O)C**H**$_2$CH$_2$- (side chain)), 2.58–2.44 (m, 36H, -C(O)C**H**$_2$C**H**$_2$C(O)-), 2.00 (2s, 3H, -C(O)CH$_3$).

MALDI-TOF-MS for $C_{127}H_{220}N_{32}O_{52}$: $[M+H]^+$ calcd. 3026.6, found 3026.9, $[M+Na]^+$ calcd. 3048.6, found 3048.8, $[M+K]^+$ calcd. 3064.6, found 3064.7.

HR-ESI-MS for $C_{127}H_{220}N_{32}O_{52}$ (exact monoisotopic mass 3025.5554): $[M+4H]^{4+}$ calcd. 757.3961, found 757.3961, mass accuracy ±0.0 ppm.

RP-HPLC (linear gradient from 0-50% eluent B in 30 min at 25 °C): t_r= 11.5 min. Determined purity: 97%.

Man(1,5,9)-9-EDS, **1c**

Compound **1c** was obtained in a yield of 39% after purification by preparative RP-HPLC. The anomeric proton of mannose could not be examined in ^{1}H-NMR due to the overlaying signal of the residual solvent. For the acetyl group on the N-terminal end two singlets with a 1:1 ratio were observed that we assign to two rotational isomers in equal amounts.

^{1}H-NMR (600 MHz, D_2O): δ(ppm) = 8.61 (br. s, -N-H), 7.90-7.86 (m, 3H, Ar-H), 4.66–4.61 (m, 6H, -OCH$_2$C**H**$_2$N- (side chain)), 4.11–4.04 (m, 3H, -OC**H**$_2$CH$_2$N- (side chain)), 3.95–3.89 (m, 3H, -OC**H**$_2$CH$_2$N- (side chain)), 3.87–3.83 (m, 3H, Man-H), 3.77–3.56 (m, 60H, -OC**H**$_2$C**H**$_2$O- (EDS), -NHCH$_2$C**H**$_2$O- (EDS), Man-H), 3.53–3.42 (m, 14H, -NH$_2$CH$_2$C**H**$_2$NH- (EDA), -C(O)NHCH$_2$C**H**$_2$N- (TDS)), 3.40–3.28 (m, 36H, -NHC**H**$_2$CH$_2$O- (EDS), -C(O)NHC**H**$_2$CH$_2$N- (TDS)), 3.14 (t, ^3J= 5.9 Hz, 2H, -NH$_2$C**H**$_2$CH$_2$NH- (EDA)), 3.05–2.96 (m, 9H, Man-H, -NC(O)CH$_2$C**H**$_2$- (side chain)), 2.83-2.75 (m, 6H, -NC(O)C**H**$_2$CH$_2$- (side chain)), 2.57–2.44 (m, 36H, -C(O)C**H**$_2$C**H**$_2$C(O)-), 1.94+1.92 (2s, 3H, -C(O)CH$_3$).

MALDI-TOF-MS for $C_{127}H_{220}N_{32}O_{52}$: $[M+H]^+$ calcd. 3026.6, found 3026.7, $[M+Na]^+$ calcd. 3048.6, found 3048.8, $[M+K]^+$ calcd. 3064.6, found 3064.9.

HR-ESI-MS for $C_{127}H_{220}N_{32}O_{52}$ (exact monoisotopic mass 3025.5554): $[M+4H]^{4+}$ calcd. 757.3961, found 757.3965, mass accuracy -0.5 ppm.

RP-HPLC (linear gradient from 0-50% eluent B in 30 min at 25 °C): t_r= 11.5 min. Determined purity: 95%.

Man(3)-5-EDS(1,2,5)-ODS(4), **3**

Compound **3** was obtained in a yield of 18% after purification by preparative RP-HPLC. The anomeric proton of mannose could not be examined in ^{1}H-NMR due to the overlaying signal of the residual solvent.

^{1}H-NMR (600 MHz, D_2O): δ(ppm) = 8.46 (s, -N-H), 7.88 (s, 1H, Ar-H), 4.66–4.59 (m, 2H, -OCH$_2$C**H**$_2$N- (side chain)), 4.12–4.06 (m, 1H, -OC**H**$_2$CH$_2$N- (side chain)), 3.95–3.90 (m, 1H, -OC**H**$_2$CH$_2$N- (side chain)), 3.88–3.85 (m, 1H, Man-H), 3.76–3.58 (m, 28H, -OC**H**$_2$C**H**$_2$O- (EDS), -NHCH$_2$C**H**$_2$O- (EDS), Man-H), 3.52–3.32 (m, 22H, -NH$_2$CH$_2$C**H**$_2$NH- (EDA), -C(O)NHC**H**$_2$C**H**$_2$N- (TDS), -NHC**H**$_2$CH$_2$O- (EDS)), 3.18–2.98 (m, 9H, -NH$_2$C**H**$_2$CH$_2$NH- (EDA), -NHC**H**$_2$(CH$_2$)$_6$C**H**$_2$NH- (ODS), -NC(O)CH$_2$C**H**$_2$- (side chain), Man-H), 2.80 (t, ^3J= 7 Hz, 2H, -NC(O)C**H**$_2$CH$_2$- (side chain)), 2.60–2.44 (m, 20H, -C(O)C**H**$_2$C**H**$_2$C(O)-), 2.00 (s, 3H, -C(O)CH$_3$), 1.52–1.42 (m, 4H, -NHCH$_2$C**H**$_2$(CH$_2$)$_4$C**H**$_2$CH$_2$NH- (ODS)), 1.33–1.24 (m, 6H, -NH(CH$_2$)$_2$(C**H**$_2$)$_4$(CH$_2$) $_2$NH- (ODS)).

MALDI-TOF-MS for $C_{67}H_{120}N_{16}O_{24}$: $[M+H]^+$ calcd. 1533.9, found 1534.0, $[M+Na]^+$ calcd. 1555.9, found 1556.0, $[M+K]^+$ calcd. 1571.9, found 1571.7.

HR-ESI-MS for $C_{67}H_{120}N_{16}O_{24}$ (exact monoisotopic mass 1532.8661): $[M+3H]^{3+}$ calcd. 511.9627, found 511.9631, mass accuracy -0.9 ppm.

RP-HPLC (linear gradient from 0-50% eluent B in 30 min at 25 °C): t_r= 13.1 min. Determined purity: 95%.

Man(3)-5-EDS(1,5)-ODS(2,4), **3a**

Compound **3a** was obtained in a yield of 53% after purification by preparative RP-HPLC. The anomeric proton of mannose could not be examined in ^{1}H-NMR due to the overlaying signal of the residual solvent.

^{1}H-NMR (600 MHz, D_2O): δ(ppm) = 8.46 (s, -N-H), 7.88 (s, 1H, Ar-H), 4.67–4.60 (m, 2H, -OCH$_2$C**H**$_2$N- (side chain)), 4.11–4.06 (m, 1H, -OC**H**$_2$CH$_2$N- (side chain)), 3.95–3.89 (m, 1H, -OC**H**$_2$CH$_2$N- (side chain)), 3.87–3.85 (m, 1H, Man-H), 3.77–3.58 (m, 20H, -OC**H**$_2$C**H**$_2$O- (EDS), -NHCH$_2$C**H**$_2$O- (EDS), Man-H), 3.53–3.44 (m, 6H, -NH$_2$CH$_2$C**H**$_2$NH- (EDA), -C(O)NHCH$_2$C**H**$_2$N- (TDS)), 3.42–3.31 (m, 12H, -NHC**H**$_2$CH$_2$O- (EDS), -C(O)NHC**H**$_2$CH$_2$N- (TDS)), 3.20– 3.11 (m, 10H, -NH$_2$C**H**$_2$CH$_2$NH- (EDA), -NHC**H**$_2$(CH$_2$)$_6$C**H**$_2$NH- (ODS)), 3.26–2.97 (m, 3H, Man-H, -NC(O)CH$_2$C**H**$_2$- (side chain)), 2.80 (t, ^3J= 7.3 Hz, 2H, -NC(O)C**H**$_2$CH$_2$- (side chain)), 2.60–2.43 (m, 20H, -C(O)C**H**$_2$C**H**$_2$C(O)-), 2.00 (s, 3H, -C(O)CH$_3$), 1.51–1.42 (m, 8H, -NHCH$_2$C**H**$_2$(CH$_2$)$_4$C**H**$_2$CH$_2$NH- (ODS)), 1.32–1.23 (m, 16H, -NH(CH$_2$)$_2$(C**H**$_2$)$_4$(CH$_2$) $_2$NH- (ODS)).

MALDI-TOF-MS for $C_{69}H_{124}N_{16}O_{22}$: $[M+H]^+$ calcd. 1529.9, found 1529.9, $[M+Na]^+$ calcd. 1551.9, found 1551.9, $[M+K]^+$ calcd. 1567.9, found 1567.9.

HR-ESI-MS for $C_{69}H_{124}N_{16}O_{22}$ (exact monoisotopic mass 1528.9076): $[M+3H]^{3+}$ calcd. 510.6431, found 510.6436, mass accuracy -0.8 ppm.

RP-HPLC (linear gradient from 0-50% eluent B in 30 min at 25 °C): t_r= 15.0 min. Determined purity: 98%.

Man(1,3,5)-5-EDS(2,4), **4**

Compound **4** was obtained in a yield of 27% after purification by preparative RP-HPLC. The anomeric proton of mannose could not be examined in ^{1}H-NMR due to the overlaying signal of the residual solvent. For the acetyl group on the N-terminal end two singlets with a 1:1 ratio were observed that were assigned to two rotational isomers in equal amounts.

^{1}H-NMR (600 MHz, D_2O): δ(ppm) = 8.46 (s, -N-H), 7.89-7.86 (s, 3H, Ar-H), 4.66–4.61 (m, 6H, -OCH$_2$C**H**$_2$N- (side chain)), 4.12–4.05 (m, 3H, -OC**H**$_2$CH$_2$N- (side chain)), 3.95–3.89 (m, 3H, -OC**H**$_2$CH$_2$N- (side chain)), 3.88–3.85 (m, 3H, Man-H), 3.76–3.71 (m, 3H, Man-H), 3.70–3.57 (m, 25H, -OC**H**$_2$C**H**$_2$O- (EDS), -NHCH$_2$C**H**$_2$O- (EDS), Man-H), 3.52–3.43 (m, 14H, -NH$_2$CH$_2$C**H**$_2$NH- (EDA), -C(O)NHCH$_2$C**H**$_2$N- (TDS)), 3.39–3.31 (m, 20H, -NHC**H**$_2$CH$_2$O- (EDS), -C(O)NHC**H**$_2$CH$_2$N- (TDS)), 3.14 (t, ^3J=5.8 Hz, 2H, -NH$_2$C**H**$_2$CH$_2$NH- (EDA)), 3.06–2.97 (m, 9H, Man-H, -NC(O)CH$_2$C**H**$_2$- (side chain)), 2.80 (t, ^3J= 7.3 Hz, 6H, -NC(O)C**H**$_2$CH$_2$- (side chain)), 2.56–2.44 (m, 20H, -C(O)C**H**$_2$C**H**$_2$C(O)-), 1.95+1.93 (2s, 3H, -C(O)CH$_3$).

MALDI-TOF-MS for $C_{87}H_{148}N_{24}O_{36}$: $[M+H]^+$ calcd. 2106.0, found 2106.7, $[M+Na]^+$ calcd. 2128.1, found 2128.0, $[M+K]^+$ calcd. 2144.1, found 2144.2.

HR-ESI-MS for $C_{87}H_{148}N_{24}O_{36}$ (exact monoisotopic mass 2105.0488): $[M+3H]^{3+}$ calcd. 702.6902, found 702.6906, mass accuracy -0.6 ppm.

RP-HPLC (linear gradient from 0-50% eluent B in 30 min at 25 °C): t_r= 9.6 min. Determined purity: 95%.

Man(1,3,5)-5-EDS(4)-ODS(2), **4a**

Compound **4a** was obtained in a yield of 56% after purification by preparative RP-HPLC. The anomeric proton of mannose could not be examined in ^{1}H-NMR due to the overlaying signal of the residual solvent. For the acetyl group on the N-terminal end two singlets with a 1:1 ratio were observed that we assign to two rotational isomers in equal amounts.

^{1}H-NMR (600 MHz, D_2O): δ(ppm) = 8.46 (s, -N-H), 7.89–7.87 (m, 3H, Ar-H), 4.68–4.60 (m, 6H, -OCH$_2$C**H**$_2$N- (side chain)), 4.12–4.06 (m, 3H, -OC**H**$_2$CH$_2$N- (side chain)), 3.95–3.90 (m, 3H, -OC**H**$_2$CH$_2$N- (side chain)), 3.88–3.85 (m, 3H, Man-H), 3.76–3.72 (m, 3H, Man-H), 3.70–3.58 (m, 17H, -OC**H**$_2$C**H**$_2$O- (EDS), -NHCH$_2$C**H**$_2$O- (EDS), Man-H), 3.52–3.44 (m, 14H, -NH$_2$CH$_2$C**H**$_2$NH- (EDA), -C(O)NHCH$_2$C**H**$_2$N- (TDS)), 3.40–3.31 (m, 16H, -NHC**H**$_2$CH$_2$O- (EDS), -C(O)NHC**H**$_2$CH$_2$N- (TDS)),

3.17–3.11 (m, 6H, -$NH_2C\mathbf{H}_2CH_2NH$- (EDA), -$NHC\mathbf{H_2}(CH_2)_6C\mathbf{H}_2NH$- (ODS)), 3.06–2.98 (m, 9H, Man-H, -$NC(O)CH_2C\mathbf{H}_2$- (side chain)), 2.83–2.76 (m, 6H, -$NC(O)C\mathbf{H}_2CH_2$- (side chain)), 2.55–2.45 (m, 20H, -$C(O)C\mathbf{H}_2C\mathbf{H}_2C(O)$-), 1.94+1.93 (2s, 3H, -$C(O)CH_3$), 1.48–1.41 (m, 4H, -$NHCH_2C\mathbf{H_2}(CH_2)_4C\mathbf{H}_2CH_2NH$- (ODS)), 1.28–1.22 (m, 8H, -$NH(CH_2)_2(C\mathbf{H}_2)_4(CH_2)_2NH$- (ODS)).

MALDI-TOF-MS for $C_{89}H_{152}N_{24}O_{34}$: $[M+H]^+$ calcd. 2102.1, found 2101.7, $[M+Na]^+$ calcd. 2124.1, found 2124.5, $[M+K]^+$ calcd. 2140.1, found 2140.2.

HR-ESI-MS for $C_{89}H_{153}N_{24}O_{34}$ (exact monoisotopic mass 2101.0903): $[M+3H]^{3+}$ calcd. 701.3707, found 701.3707, mass accuracy ±0.0 ppm.

RP-HPLC (linear gradient from 0-50% eluent B in 30 min at 25 °C): t_r= 11.7 min. Determined purity: 99%.

Man(1,3,5)-5-ODS, **4b**

Compound **4b** was obtained in a yield of 34% after purification by preparative RP-HPLC. The anomeric proton of mannose could not be examined in ^{1}H-NMR due to the overlaying signal of the residual solvent. For the acetyl group on the N-terminal end two singlets with a 1:1 ratio were observed that we assign to two rotational isomers in equal amounts.

^{1}H-NMR (600 MHz, D_2O): δ(ppm) = 8.48 (s, -N-H), 7.89–7.86 (m, 3H, Ar-H), 4.66–4.61 (m, 6H, -$OCH_2\mathbf{C}H_2N$- (side chain)), 4.12–4.06 (m, 3H, -$O\mathbf{C}H_2CH_2N$- (side chain)), 3.95–3.90 (m, 3H, -$O\mathbf{C}H_2CH_2N$- (side chain)), 3.87–3.85 (m, 3H, Man-H), 3.77–3.72 (m, 3H, Man-H), 3.70–3.58 (m, 9H, Man-H), 3.53–3.43 (m, 14H, -$NH_2CH_2C\mathbf{H}_2NH$- (EDA), -$C(O)NHCH_2C\mathbf{H}_2N$- (TDS)), 3.40–3.31 (m, 12H, -$C(O)NHC\mathbf{H}_2CH_2N$- (TDS)), 3.17–3.09 (m, 10H, -$NH_2C\mathbf{H}_2CH_2NH$- (EDA), -$NHC\mathbf{H_2}(CH_2)_6C\mathbf{H}_2NH$- (ODS)), 3.07–2.97 (m, 9H, Man-H, -$NC(O)CH_2C\mathbf{H}_2$- (side chain)), 2.83–2.76 (m, 6H, -$NC(O)C\mathbf{H}_2CH_2$- (side chain)), 2.56–2.44 (m, 20H, -$C(O)C\mathbf{H}_2C\mathbf{H}_2C(O)$-), 1.95+1.93 (2s, 3H, -$C(O)CH_3$), 1.49–1.41 (m, 4H, -$NHCH_2C\mathbf{H_2}(CH_2)_4C\mathbf{H}_2CH_2NH$- (ODS)), 1.30–1.21 (m, 8H, -$NH(CH_2)_2(C\mathbf{H}_2)_4(CH_2)_2NH$- (ODS)).

MALDI-TOF-MS for $C_{91}H_{156}N_{24}O_{32}$: $[M+H]^+$ calcd. 2098.1, found 2098.1, $[M+Na]^+$ calcd. 2120.1, found 2120.1, $[M+K]^+$ calcd. 2136.1, found 2136.1.

HR-ESI-MS for $C_{91}H_{156}N_{24}O_{32}$ (exact monoisotopic mass 2097.1317): $[M+3H]^{3+}$ calcd. 700.0512, found 700.0503, mass accuracy +1.3 ppm.

RP-HPLC(linear gradient from 0-50% eluent B in 30 min at 25 °C): t_r= 13.8 min. Determined purity: 99%.

Man(1,3,5)-5-EDS(4)-AR(2), **4c**

Compound **4c** was obtained in a yield of 55% after purification by preparative RP-HPLC. For the acetyl group on the N-terminal end two singlets with a 1:1 ratio were observed that we assign to two rotational isomers in equal amounts.

^{1}H-NMR (600 MHz, D_2O): δ(ppm) = 8.35 (s, -N-H), 7.90–7.80 (m, 2H, Ar-H (triazole)), 7.75-7.54 (m, 3H, Ar-H (triazole)), 7.53-7.27 (m, 2H, Ar-H, (AR)), 4.74-4.70 (m, 3H, Man-H), 4.66-4.54 (m, 4H, -OCH**$_2$**C**H**$_2$N- (side chain)), 4.49-4.40 (m, 4H, -OCH**$_2$**C**H**$_2$N- (side chain), -NHCH_2- (AR)), 4.10–3.96 (m, 3H, -OC**H$_2$**CH_2N- (side chain)), 3.94–3.79 (m, 6H, -OC**H$_2$**CH_2N- (side chain), Man-H), 3.77–3.26 (m, 50H, -OC**H**$_2$C**H**$_2$O- (EDS), -NHC**H**$_2$C**H**$_2$O- (EDS), Man-H, -NH$_2$CH$_2$C**H**$_2$NH- (EDA), -C(O)NHC**H**$_2$C**H**$_2$N- (TDS)), 3.14 (t, ^3J= 5.7 Hz, 2H, -NH$_2$C**H**$_2$CH$_2$NH- (EDA)), 3.05–2.86 (m, 9H, Man-H, -NC(O)CH$_2$C**H**$_2$- (side chain)), 2.83–2.73 (m, 6H, -NC(O)C**H**$_2$CH$_2$- (side chain)), 2.61–2.43 (m, 16H, -C(O)C**H**$_2$C**H**$_2$C(O)-), 1.94+1.92 (2s, 3H, -C(O)CH_3).

MALDI-TOF-MS for $C_{85}H_{137}N_{23}O_{33}$: $[M+Na]^+$ calcd. 2031.0, found 2031.0, $[M+K]^+$ calcd. 2047.0, found 2047.0.

HR-ESI-MS for $C_{85}H_{137}N_{23}O_{33}$ (exact monoisotopic mass 2007.9749): $[M+3H]^{3+}$ calcd. 670.3322, found 670.3320, mass accuracy -0.4 ppm.

RP-HPLC (linear gradient from 0-50% eluent B in 30 min at 25 °C): t_r= 10.5 min. Determined purity: 98%.

Man(1,3,5)-5-AR, **4d**

Compound **4d** was obtained in a yield of 71% after purification by preparative RP-HPLC. For the acetyl group on the N-terminal end two singlets with a 1:1 ratio were observed that we assign to two rotational isomers in equal amounts.

^{1}H-NMR (600 MHz, D_2O): δ(ppm) = 8.44 (s, -N-H), 7.82 (d, 1H, $^3J_{H-H}$= 4.8 Hz, Ar-H (triazole)), 7.71-7.69 (m, 1H, Ar-H (triazole)), 7.64-7.53 (m, 5H, Ar-H (AR), Ar-H (triazole)), 7.37-7.30 (m, 4H, Ar-H, (AR)), 4.77–4.70 (m, 3H, Man-H), 4.61-4.55 (m, 2H, -OCH**$_2$**C**H**$_2$N- (side chain)), 4.49-4.36 (m, 8H, -OCH**$_2$**C**H**$_2$N- (side chain), -NHCH_2- (AR)), 4.08–4.01 (m, 1H, -OC**H$_2$**CH_2N- (side chain)), 4.01–3.95 (m, 2H, -OC**H$_2$**CH_2N- (side chain)), 3.91–3.78 (m, 6H, -OC**H$_2$**CH_2N- (side chain), Man-H), 3.75–3.27 (m, 38H, Man-H, -NH$_2$CH$_2$C**H**$_2$NH- (EDA), -C(O)NHC**H**$_2$C**H**$_2$N- (TDS)), 3.14 (t, ^3J= 5.8 Hz, 2H, -NH$_2$C**H**$_2$CH$_2$NH- (EDA)), 3.04–2.84 (m, 9H, Man-H, -NC(O)CH$_2$C**H**$_2$- (side chain)), 2.80–2.69 (m, 6H, -NC(O)C**H**$_2$CH$_2$- (side chain)), 2.63–2.48 (m, 12H, -C(O)C**H**$_2$C**H**$_2$C(O)-), 1.92+1.91 (2s, 3H, -C(O)CH_3).

MALDI-TOF-MS for $C_{83}H_{126}N_{22}O_{30}$: $[M+Na]^+$ calcd. 1933.9, found 1934.0, $[M+K]^+$ calcd. 1949.9, found 1949.9.

HR-ESI-MS for $C_{83}H_{126}N_{22}O_{30}$ (exact monoisotopic mass 1910.9010): $[M+3H]^{3+}$ calcd. 637.9743, found 637.9742, mass accuracy -0.1 ppm.

RP-HPLC(linear gradient from 0-50% eluent B in 30 min at 25 °C): t_r= 10.8 min. Determined purity: 95%.

Man(1,3,5,7,9)-9-EDS, **5**

Compound **5** was obtained in a yield of 64% after purification by preparative RP-HPLC. The anomeric proton of mannose could not be examined in ^{1}H-NMR due to the overlaying signal of the residual solvent. For the acetyl group on the N-terminal end two singlets with a 1:1 ratio were observed that we assign to two rotational isomers in equal amounts.

^{1}H-NMR (600 MHz, D_2O): δ(ppm) = 7.89–7.87 (m, 5H, Ar-H), 4.66–4.62 (m, 10H, -OCH$_2$C**H**$_2$N- (side chain)), 4.12–4.06 (m, 5H, -OC**H**$_2$CH$_2$N- (side chain)), 3.94–3.90 (m, 5H, -OC**H**$_2$CH$_2$N- (side chain)), 3.87–3.85 (m, 5H, Man-H), 3.76–3.71 (m, 5H, Man-H), 3.69–3.58 (m, 47H, -OC**H**$_2$C**H**$_2$O- (EDS), -NHCH$_2$C**H**$_2$O- (EDS), Man-H), 3.52–3.44 (m, 22H, -NH$_2$CH$_2$C**H**$_2$NH- (EDA), -C(O)NHCH$_2$C**H**$_2$N- (TDS)), 3.41–3.31 (m, 36H, -NHC**H**$_2$CH$_2$O- (EDS), -C(O)NHC**H**$_2$CH$_2$N- (TDS)), 3.15 (t, ^3J= 5.9 Hz, 2H, -NH$_2$C**H**$_2$CH$_2$NH- (EDA)), 3.05–2.97 (m, 15H, Man-H, -NC(O)CH$_2$C**H**$_2$- (side chain)), 2.80 (m, ^3J= 7.2 Hz, 10H, -NC(O)C**H**$_2$CH$_2$- (side chain)), 2.55–2.45 (m, 36H, -C(O)C**H**$_2$C**H**$_2$C(O)-), 1.94+1.93 (2s, 3H, -C(O)CH$_3$).

MALDI-TOF-MS for $C_{149}H_{252}N_{40}O_{62}$: $[M+H]^+$ calcd. 3594.8, found 3593.2, $[M+Na]^+$ calcd. 3616.8, found 3616.8, $[M+K]^+$ calcd. 3632.8, found 3632.8.

HR-ESI-MS for $C_{149}H_{252}N_{40}O_{62}$ (exact monoisotopic mass 3593.7796): $[M+4H]^{4+}$ calcd. 899.4522, found 899.4527, mass accuracy -0.5 ppm.

RP-HPLC (linear gradient from 0-50% eluent B in 30 min at 25 °C): t_r= 11.1 min. Determined purity: 98%.

Man(1,3,5,7,9)-9-ODS, **5a**

Compound **5a** was obtained in a yield of 40% after purification by preparative RP-HPLC. The anomeric proton of mannose could not be examined in ^{1}H-NMR due to the overlaying signal of the residual solvent. For the acetyl group on the N-terminal end two singlets with a 1:1 ratio were observed that we assign to two rotational isomers in equal amounts.

^{1}H-NMR (600 MHz, D_2O): δ(ppm) = 8.62 (br.s, -N-H), 7.89–7.86 (m, 5H, Ar-H), 4.66–4.61 (m, 10H, -OCH$_2$C**H**$_2$N- (side chain)), 4.12–4.06 (m, 5H, -OC**H**$_2$CH$_2$N- (side chain)), 3.95–3.89 (m, 5H, -OC**H**$_2$CH$_2$N- (side chain)), 3.87–3.85 (m, 5H, Man-H), 3.76–3.72 (m, 5H, Man-H), 3.69–3.58 (m, 15H, Man-H), 3.52–3.44 (m, 22H, -NH$_2$CH$_2$C**H**$_2$NH- (EDA), -C(O)NHCH$_2$C**H**$_2$N- (TDS)), 3.40–3.31 (m, 20H, -C(O)NHC**H**$_2$CH$_2$N- (TDS)), 3.17–3.10 (m, 18H, -NH$_2$C**H**$_2$CH$_2$NH- (EDA), -NHC**H**$_2$(CH$_2$)$_6$C**H**$_2$NH- (ODS)), 3.08–2.97 (m, 15H, Man-H, -NC(O)CH$_2$C**H**$_2$- (side chain)), 2.82–2.77 (m, 10H, -NC(O)C**H**$_2$CH$_2$- (side chain)), 2.56–2.44 (m, 36H, -C(O)C**H**$_2$C**H**$_2$C(O)-), 1.94+1.93 (2s, 3H, -C(O)CH$_3$), 1.49–1.40 (m, 16H, -NHCH$_2$C**H**$_2$(CH$_2$)$_4$C**H**$_2$CH$_2$NH- (ODS)), 1.28–1.20 (m, 32H, -NH(CH$_2$)$_2$(C**H**$_2$)$_4$(CH$_2$)$_2$NH- (ODS)).

MALDI-TOF-MS for $C_{157}H_{268}N_{40}O_{54}$: $[M+Na]^+$ calcd. 3601.0, found 3601.0, $[M+K]^+$ calcd. 3616.9, found 3616.9.

HR-ESI-MS for $C_{157}H_{268}N_{40}O_{54}$ (exact monoisotopic mass 3577.9455): $[M+5H]^{5+}$ calcd. 716.5964, found 716.5966, mass accuracy -0.4 ppm.

RP-HPLC(linear gradient from 0-50% eluent B in 30 min at 25 °C): t_r= 16.1 min. Determined purity: 95%.

Man(1,3,5,7,9)-9-AR, **5b**

Compound **5b** was obtained in a yield of 62% after purification by preparative RP-HPLC. For the acetyl group on the N-terminal end two singlets with a 1:1 ratio were observed that we assign to two rotational isomers in equal amounts.

^{1}H-NMR (600 MHz, D_2O): δ(ppm) = 8.29 (s, -N-H), 7.81 (d, 1H, ^3J= 4.8 Hz, Ar-H (triazole)), 7.71-7.67 (m, 2H, Ar-H (triazole)), 7.62-7.51 (m, 10H, Ar-H (AR), Ar-H (triazole)), 7.35-7.24 (m, 8H, Ar-H, (AR)), 4.76–4.67 (m, 5H, Man-H), 4.60-4.53 (m, 2H, -OCH$_2$C**H**$_2$N- (side chain)), 4.46-4.31 (m, 16H, -OCH$_2$C**H**$_2$N- (side chain), -NHCH$_2$- (AR)), 4.07–3.94 (m, 5H, -OC**H**$_2$CH$_2$N- (side chain)), 3.90-3.76–3.95 (m, 10H, -OC**H**$_2$CH$_2$N- (side chain), Man-H), 3.74–3.26 (m, 62H, Man-H, -NH$_2$CH$_2$C**H**$_2$NH- (EDA), -C(O)NHC**H**$_2$C**H**$_2$N- (TDS)), 3.13 (t, ^3J= 5.8 Hz, 2H, -NH$_2$C**H**$_2$CH$_2$NH- (EDA)), 3.03–2.81 (m, 15H, Man-H, -NC(O)CH$_2$C**H**$_2$- (side chain)), 2.78–2.67 (m, 10H, -NC(O)C**H**$_2$CH$_2$- (side chain)), 2.61–2.47 (m, 20H, -C(O)C**H**$_2$C**H**$_2$C(O)-), 1.91+1.90 (2s, 3H, -C(O)CH$_3$).

MALDI-TOF-MS for $C_{141}H_{208}N_{36}O_{50}$: $[M+H]^+$ calcd. 3206.5, found 3206.4, $[M+Na]^+$ calcd. 3228.5, found 3229.4.

HR-ESI-MS for $C_{141}H_{208}N_{36}O_{50}$ (exact monoisotopic mass 3205.4840): $[M+4H]^{4+}$ calcd. 802.3783, found 802.3783, mass accuracy ±0.0 ppm.

RP-HPLC(linear gradient from 0-50% eluent B in 30 min at 25 °C): t_r= 12.5 min. Determined purity: 94%.

Gal(2)-3-EDS(1)-ODS(3), **6**

Compound **6** was obtained in a yield of 24% after purification by preparative RP-HPLC.

^{1}H-NMR (600 MHz, D_2O): δ(ppm) = 8.46 (s, -N-H), 7.90 (s, 1H, Ar-H), 4.65 (t, ^3J= 5.2 Hz 2H, -OCH$_2$C**H**$_2$N- (side chain)), 4.37 (d, ^3J= 7.9 Hz, 1H, Gal-H), 4.31–4.27 (m, 1H, -OC**H**$_2$CH$_2$N- (side chain)), 4.12–4.07 (m, 1H, -OC**H**$_2$CH$_2$N- (side chain)), 3.92–3.90 (m, 3H, Gal-H), 3.78–3.59 (m, 12H, -OC**H**$_2$C**H**$_2$O- (EDS), -NHCH$_2$C**H**$_2$O- (EDS), Gal-H), 3.52–3.43 (m, 7H, -NH$_2$CH$_2$C**H**$_2$NH- (EDA), -C(O)NHCH$_2$C**H**$_2$N- (TDS), Gal-H), 3.41-3.31 (m, 8H, -C(O)NHC**H**$_2$CH$_2$N- (TDS), -NHC**H**$_2$CH$_2$O- (EDS)), 3.17-3.09 (m, 6H, -NH$_2$C**H**$_2$CH$_2$NH- (EDA), -NHC**H**$_2$(CH$_2$)$_6$C**H**$_2$NH- (ODS)), 3.01 (t, ^3J= 7.2 Hz, 2H, -NC(O)CH$_2$C**H**$_2$- (side chain)), 2.80 (t, ^3J= 6.4 Hz, 2H, -NC(O)C**H**$_2$CH$_2$- (side chain)), 2.58–2.45 (m, 12H, -C(O)C**H**$_2$C**H**$_2$C(O)-), 1.97 (s, 3H, -C(O)CH$_3$), 1.51–1.44 (m, 4H, -NHCH$_2$C**H**$_2$(CH$_2$)$_4$C**H**$_2$CH$_2$NH- (ODS)), 1.32–1.23 (m, 8H, -NH(CH$_2$)$_2$(C**H**$_2$)$_4$(CH$_2$)$_2$NH- (ODS)).

MALDI-TOF-MS for $C_{47}H_{84}N_{12}O_{16}$: $[M+H]^+$ calcd. 1073.6, found 1073.7, $[M+Na]^+$ calcd. 1095.6, found 1095.7, $[M+K]^+$ calcd. 1111.6, found 1111.6.

HR-ESI-MS for $C_{47}H_{84}N_{12}O_{16}$ (exact monoisotopic mass 1072.6128): $[M+4H]^{4+}$ calcd. 537.3137, found 537.3138, mass accuracy -0.3 ppm.

RP-HPLC (linear gradient from 0-50% eluent B in 30 min at 25 °C): t_r= 11.7 min. Determined purity: 92%.

Gal(3)-5-EDS(1,5)-ODS(2,4), **6a**

Compound **6a** was obtained in a yield of 35% after purification by preparative RP-HPLC.

^{1}H-NMR (600 MHz, D_2O): δ(ppm) = 7.93-7.87 (m, 1H, Ar-H), 4.65 (t, ^3J= 5.1 Hz 2H, -OCH**$_2$**C**H**$_2$N- (side chain)), 4.37 (dd, $^{3,4}J$= 7.8, 1.6 Hz, 1H, Gal-H), 4.33–4.24 (m, 1H, -OC**H$_2$**CH$_2$N- (side chain)), 4.14–4.04 (m, 1H, -OC**H$_2$**CH$_2$N- (side chain)), 3.92 (d, ^3J= 3.3 Hz, 1H, Gal-H), 3.78–3.58 (m, 20H, -OC**H**$_2$C**H**$_2$O- (EDS), -NHCH$_2$C**H**$_2$O- (EDS), Gal-H), 3.54–3.29 (m, 17H, -C(O)NHC**H**$_2$C**H**$_2$N- (TDS), Gal-H, -NHC**H**$_2$CH$_2$O- (EDS)), 3.15 (td, ^3J= 6.8, 2.4 Hz, 8H, -NHC**H$_2$**(CH$_2$)$_6$C**H**$_2$NH- (ODS)), 3.05-2.96 (m, 2H, -NC(O)CH$_2$C**H**$_2$- (side chain)), 2.80 (t, ^3J= 7.4 Hz, 2H, -NC(O)C**H**$_2$CH$_2$- (side chain)), 2.57–2.45 (m, 20H, -C(O)C**H**$_2$C**H**$_2$C(O)-), 2.00 (s, 3H, -C(O)CH$_3$), 1.55-1.40 (m, 8H, -NHCH$_2$C**H$_2$**(CH$_2$)$_4$C**H**$_2$CH$_2$NH- (ODS)), 1.31–1.23 (m, 16H, -NH(CH$_2$)$_2$(C**H**$_2$)$_4$(CH$_2$)$_2$NH- (ODS)).

MALDI-TOF-MS for $C_{67}H_{119}N_{15}O_{22}$: $[M+Na]^+$ calcd. 1508.9, found 1508.9, $[M+K]^+$ calcd. 1524.9, found 1524.8.

HR-ESI-MS for $C_{67}H_{119}N_{15}O_{22}$ (exact monoisotopic mass 1485.8654): $[M+3H]^{3+}$ calcd. 496.2957, found 496.2962, mass accuracy -0.9 ppm.

RP-HPLC (linear gradient from 0-50% eluent B in 30 min at 25 °C): t_r= 16.1 min. Determined purity: 99%.

Gal(1,3,5)-5-ODS(2,4), **6c**

Compound **6c** was obtained in a yield of 50% after purification by preparative RP-HPLC.

^{1}H-NMR (300 MHz, D_2O): δ(ppm) = 7.92-7.86 (m, 3H, Ar-H), 4.65 (t, ^3J= 5.0 Hz, 6H, -OCH**$_2$**C**H**$_2$N- (side chain)), 4.37 (d, ^3J= 7.8, 3H, Gal-H), 4.33–4.24 (m, 3H, -OC**H$_2$**CH$_2$N- (side chain)), 4.14–4.04 (m, 3H, -OC**H$_2$**CH$_2$N- (side chain)), 3.91 (d, ^3J= 3.3 Hz, 3H, Gal-H), 3.78–3.59 (m, 12H, Gal-H), 3.53–3.29 (m, 17H, -C(O)NHC**H**$_2$C**H**$_2$N- (TDS), Gal-H), 3.13 (t, ^3J= 6.8 Hz, 8H, -NHC**H$_2$**(CH$_2$)$_6$C**H**$_2$NH- (ODS)), 3.03-2.96 (m, 6H, -NC(O)CH$_2$C**H**$_2$- (side chain)), 2.79 (t, ^3J= 7.1 Hz, 6H, -NC(O)C**H**$_2$CH$_2$- (side chain)), 2.57–2.42 (m, 20H, -C(O)C**H**$_2$C**H**$_2$C(O)-), 1.94+1.92 (2s, 3H, -C(O)CH$_3$), 1.50-1.40 (m, 8H, -NHCH$_2$C**H$_2$**(CH$_2$)$_4$C**H**$_2$CH$_2$NH- (ODS)), 1.31–1.20 (m, 16H, -NH(CH$_2$)$_2$(C**H**$_2$)$_4$(CH$_2$)$_2$NH- (ODS)).

MALDI-TOF-MS for $C_{89}H_{151}N_{23}O_{32}$: $[M+Na]^+$ calcd. 2077.1, found 2077.1, $[M+K]^+$ calcd. 2093.1, found 2093.1.

HR-ESI-MS for $C_{89}H_{151}N_{23}O_{32}$ (exact monoisotopic mass 2054.0895): $[M+3H]^{3+}$ calcd. 685.7038, found 685.7040, mass accuracy -0.3 ppm.

RP-HPLC (linear gradient from 0-50% eluent B in 30 min at 25 °C): t_r= 14.6 min. Determined purity: 98%.

Gal(1,3,5)-5-EDS(4)-AR(2), **6d**

Compound **6d** was obtained in a yield of 12% after purification by preparative RP-HPLC. For the acetyl group on the N-terminal end two singlets with a 1:1 ratio were observed that we assign to two rotational isomers in equal amounts.

^{1}H-NMR (600 MHz, D_2O): δ(ppm) = 7.91–7.85 (m, 2H, Ar-H (triazole)), 7.78 (s, 0.5 H, Ar-H (triazole)), 7.67-7.59 (m, 2.5H, Ar-H (AR), Ar-H (triazole)), 7.53-7.25 (m, 2H, Ar-H, (AR)), 4.66-4.57 (m, 4H, -OCH$_2$C**H**$_2$N- (side chain)), 4.52-4.48 (m, 4H, -OCH$_2$C**H**$_2$N- (side chain)), 4.42 (t, ^3J= 2.8 Hz, 2H, -NHCH$_2$- (AR)), 4.38-4.31 (m, 3H, Gal-H), 4.31–3.19 (m, 3H, -OC**H**$_2$CH$_2$N- (side chain)), 3.12–3.97 (m, 3H, -OC**H**$_2$CH$_2$N- (side chain)), 3.92-3.88 (m, 3H, Gal-H), 3.78-3.70 (m, 6H, Gal-H), 3.68–3.27 (m, 47H, -OC**H**$_2$C**H**$_2$O- (EDS), -NHC**H**$_2$C**H**$_2$O- (EDS), Gal-H, -NH$_2$CH$_2$C**H**$_2$NH- (EDA), -C(O)NHC**H**$_2$C**H**$_2$N- (TDS)), 3.14 (t, ^3J= 5.9 Hz, 2H, -NH$_2$C**H**$_2$CH$_2$NH- (EDA)), 3.02–2.87 (m, 6H, -NC(O)CH$_2$C**H**$_2$- (side chain)), 2.81–2.72 (m, 6H, -NC(O)C**H**$_2$CH$_2$- (side chain)), 2.61–2.42 (m, 16H, -C(O)C**H**$_2$C**H**$_2$C(O)-), 1.93+1.91 (2s, 3H, -C(O)CH$_3$).

MALDI-TOF-MS for $C_{85}H_{137}N_{23}O_{33}$ $[M+Na]^+$ calcd. 2031.0, found 2031.0, $[M+K]^+$ calcd. 2047.0, found 2046.9.

HR-ESI-MS for $C_{85}H_{137}N_{23}O_{33}$ (exact monoisotopic mass 2007.9749): $[M+3H]^{3+}$ calcd. 670.3322, found 670.3311, mass accuracy -1.7 ppm.

RP-HPLC (linear gradient from 0-50% eluent B in 30 min at 25 °C): t_r= 10.0 min. Determined purity: 90%.

Gal(1,3,5)-5-AR(2,4), **6e**

Compound **6e** was obtained in a yield of 31% after purification by preparative RP-HPLC. For the acetyl group on the N-terminal end two singlets with a 1:1 ratio were observed that we assign to two rotational isomers in equal amounts.

^{1}H-NMR (600 MHz, D_2O): δ(ppm) = 7.84 (d, ^3J= 2.8 Hz, 1H, Ar-H (triazole)), 7.77-7.73 (m, 1 H, Ar-H (triazole)), 7.65-7.56 (m, 5H, Ar-H (AR), Ar-H (triazole)), 7.38-7.28 (m, 4H, Ar-H, (AR)), 4.60 (dt, $^{3,4}J$= 10.6, 5.1 Hz, 2H, -OCH$_2$C**H**$_2$N- (side chain)), 4.52-4.44 (m, 4H, -OCH$_2$C**H**$_2$N- (side chain)), 4.42-4.36 (m, 4H, -NHCH$_2$- (AR)), 4.35-4.28 (m, 3H, Gal-H), 4.28–4.16 (m, 3H, -OC**H**$_2$CH$_2$N- (side chain)), 4.09–3.94 (m, 3H, -OC**H**$_2$CH$_2$N- (side chain)), 3.91-3.87 (m, 3H, Gal-H), 3.78-3.69 (m, 6H, Gal-H), 3.66–3.25 (m, 35H, Gal-H, -NH$_2$CH$_2$C**H**$_2$NH- (EDA), -C(O)NHC**H**$_2$C**H**$_2$N- (TDS)), 3.14 (t, ^3J= 5.9 Hz, 2H, -NH$_2$C**H**$_2$CH$_2$NH-

(EDA)), 2.98–2.84 (m, 6H, -NC(O)CH$_2$C**H**$_2$- (side chain)), 2.79–2.69 (m, 6H, -NC(O)C**H**$_2$CH$_2$- (side chain)), 2.62–2.46 (m, 12H, -C(O)C**H**$_2$C**H**$_2$C(O)-), 1.92+1.89 (2s, 3H, -C(O)CH$_3$).

MALDI-TOF-MS for $C_{83}H_{126}N_{22}O_{30}$: $[M+Na]^+$ calcd. 1933.9, found 1934.0, $[M+K]^+$ calcd. 1949.9, found 1949.9.

HR-ESI-MS for $C_{83}H_{126}N_{22}O_{30}$ (exact monoisotopic mass 1910.9010): $[M+3H]^{3+}$ calcd. 637.9743, found 637.9738, mass accuracy -0.7 ppm.

RP-HPLC (linear gradient from 0-50% eluent B in 30 min at 25 °C): t_r= 10.4 min. Determined purity: 95%.

5.4.3.2 SPPoS of Thiolated Glycomacromolecules

All listed precision glycomacromolecules were synthesized on solid support by stepwise assembly of different building blocks according to general coupling protocol and Fmoc cleavage protocol.[121] As building blocks, functional building block bearing an alkyne group, termed TDS, and spacer building blocks with either hydrophilic ethylene glycol units (EDS) or hydrophobic aliphatic (ODS) were employed. In addition, natural amino acid L-cysteine was employed. In case of the hydrophobic spacer building block, ODS, a 0.4 M solution of LiCl in DCM/DMF (1/1, *v/v*) was used as coupling solution instead of pure DMF. All other steps were proceeded as described previously.

After successful assembly of the desired number of building blocks, capping of the N-terminal primary amine group was performed employing acetic anhydride.[121] The subsequent conjugation of the azide functionalized carbohydrates proceeded by general CuAAC protocol.[121] As last step, the product was cleaved from solid support using 30% TFA and 1% TIPS in DCM and was precipitated in diethyl ether. Subsequently, the product was redissolved in MeOH and carbohydrate deprotection was performed in solution using 0.1 M NaOMe in MeOH. After 2h shaking the solution was neutralized with Amberlite IR-120 (hydrogen form) and the resin was filtered off. After solvent evaporation the product was isolated by lyophilization.

All glycomacromolecules were purified by preparative RP-HPLC.

For the more hydrophilic structures **7** and **9** commercially available H-Gly-2-chlorotrityl PS resin was used for solid phase synthesis. For the more hydrophobic structure 8 commercially available Fmoc-Gly-Trt Tentagel resin was used. The batch sizes for synthesizing the glycomacromolecules were 0.1 mmol for structures **7** and **9** and 0.05 mmol for **8**.

Man(4)-5-Gly(1)-EDS(2,3)-Cys(5), **7**

Compound **7** was obtained in a yield of 78% after purification by prep-RP-HPLC. The anomeric proton of mannose could not be examined in ^{1}H-NMR due to the overlaying signal of the residual solvent.

^{1}H-NMR (600 MHz, D_2O): δ(ppm) = 8.27 (s, -N-H), 7.88 (s, 1H, Ar-H), 4.66–4.62 (m, 2H, -OCH$_2$CH$_2$N- (side chain)), 4.46 (t, ^3J=6.2 Hz, 1H, -C(O)CH(CH$_2$SH)NH- (Cys)), 4.12–4.06 (m, 1H, -OCH$_2$CH$_2$N- (side

chain)), 3.95–3.90 (m, 3H, -OCH_2CH_2N- (side chain), -$C(O)CH_2NH$- (Gly)), 3.88–3.85 (m, 1H, Man-H), 3.77–3.72 (m, 1H, Man-H), 3.70–3.58 (m, 19H, -OCH_2CH_2O- (EDS), -$NHCH_2CH_2O$- (EDS), Man-H), 3.51–3.32 (m, 16H, -$C(O)NHCH_2CH_2N$- (TDS), -$NHCH_2CH_2O$- (EDS)), 3.06–2.98 (m, 3H, Man-H, -$NC(O)CH_2CH_2$- (side chain)), 2.91 (d, ^3J=5.9 Hz, 2H, -$C(O)CH(CH_2SH)NH$- (Cys)), 2.80 (t, ^3J= 7.3 Hz, 2H, -$NC(O)CH_2CH_2$- (side chain)), 2.60–2.46 (m, 12H, -$C(O)CH_2CH_2C(O)$-), 2.07 (s, 3H, -$C(O)CH_3$).

MALDI-TOF-MS for $C_{48}H_{82}N_{12}O_{21}S$: $[M+Na]^+$ calcd. 1217.53, found 1217.62, $[disulfide+Na]^+$ calcd. 2410.06, found 2410.22.

HR-ESI-MS for $C_{48}H_{82}N_{12}O_{21}S$ (exact monoisotopic mass 1194.5438): $[M+2H]^{2+}$ calcd. 598.2792, found 598.2792, mass accuracy ±0.0 ppm.

RP-HPLC (linear gradient from 0-50% eluent B in 30 min at 25 °C): t_r= 10.6 min. Determined purity: 95%.

Man(4)-5-Gly(1)-ODS(2,3)-Cys(5), **8**

Compound **8** was obtained in a yield of 11% after purification by prep-RP-HPLC. The anomeric proton of mannose could not be examined in ^{1}H-NMR due to the overlaying signal of the residual solvent.

^{1}H-NMR (600 MHz, D_2O): δ(ppm) = 8.40 (s, -N-H), 7.88 (s, 1H, Ar-H), 4.66–4.62 (m, 2H, -OCH_2CH_2N- (side chain)), 4.41 (t, ^3J=6.3 Hz, 1H, -$C(O)CH(CH_2SH)NH$- (Cys)), 4.12–4.06 (m, 1H, -OCH_2CH_2N- (side chain)), 3.95–3.90 (m, 1H, -OCH_2CH_2N- (side chain)), 3.88–3.85 (m, 1H, Man-H), 3.83–3.79 (m, 2H, -$C(O)CH_2NH$- (Gly)), 3.77–3.71 (m, 1H, Man-H), 3.70- 3.58 (m, 3H Man-H), 3.51–3.31 (m, 8H, -$C(O)NHCH_2CH_2N$- (TDS)), 3.28-3.10 (m, 4H, -$NHCH_2(CH_2)_6CH_2NH$- (ODS)), 3.07–2.97 (m, 3H, Man-H, -$NC(O)CH_2CH_2$- (side chain)), 2.89 (dd, $^{3,4}J$=1.8, 6.3 Hz, 2H, -$C(O)CH(CH_2SH)NH$- (Cys)), 2.80 (t, ^3J= 7.2 Hz, 2H, -$NC(O)CH_2CH_2$- (side chain)), 2.61–2.44 (m, 12H, -$C(O)CH_2CH_2C(O)$-), 2.07 (s, 3H, -$C(O)CH_3$), 1.53–1.43 (m, 8H, -$NHCH_2CH_2(CH_2)_4CH_2CH_2NH$- (ODS)), 1.33–1.22 (m, 16H, -$NH(CH_2)_2(CH_2)_4(CH_2)_2NH$- (ODS)).

MALDI-TOF-MS for $C_{52}H_{90}N_{12}O_{17}S$: $[M+Na]^+$ calcd. 1209.62, found 1209.60, $[disulfide+Na]^+$ calcd. 2394.23, found 2396.3.

HR-ESI-MS for $C_{52}H_{90}N_{12}O_{17}S$ (exact monoisotopic mass 1186.6268): $[M+2H]^{2+}$ calcd. 594.3207, found 594.3202, mass accuracy +0.8 ppm.

RP-HPLC (linear gradient from 0-50% eluent B in 30 min at 25 °C): t_r= 17.6 min. Determined purity: 89% (8% thioether side product).

Man(2,4,6,8,10)-11-Gly(1)-EDS(3,5,7,9)-Cys(11), **9**

Compound **9** was obtained in a yield of 34% after purification by prep-RP-HPLC. The anomeric proton of mannose could not be examined in ^{1}H-NMR due to the overlaying signal of the residual solvent. For

the acetyl group on the N-terminal end two singlets with a 1:1 ratio were observed that we assign to two rotational isomers in equal amounts.

^{1}H-NMR (600 MHz, D_2O): δ(ppm) = 8.32 (s, -N-H), 7.89-7.86 (m, 5H, Ar-H), 4.66–4.62 (m, 10H, -OCH_2CH_2N- (side chain)), 4.45-4.40 (m, 1H, -C(O)$CH(CH_2SH)$NH- (Cys)), 4.12–4.06 (m, 5H, -OCH_2CH_2N- (side chain)), 3.94–3.84 (m, 12H, -OCH_2CH_2N- (side chain), -C(O)CH_2NH- (Gly), Man-H), 3.76–3.72 (m, 5H, Man-H), 3.70–3.57 (m, 47H, -OCH_2CH_2O- (EDS), -$NHCH_2CH_2O$- (EDS), Man-H), 3.52–3.29 (m, 56H, -C(O)$NHCH_2CH_2N$- (TDS), -$NHCH_2CH_2O$- (EDS)), 3.06–2.96 (m, 15H, Man-H, -NC(O)CH_2CH_2- (side chain)), 2.90-2.83 (m, 2H, -C(O)$CH(CH_2SH)$NH- (Cys)), 2.80 (t, ^3J= 7.1 Hz, 10H, -NC(O)CH_2CH_2- (side chain)), 2.60–2.44 (m, 36H, -C(O)$CH_2CH_2C(O)$-), 2.06+2.04 (2s, 3H, -C(O)CH_3).

MALDI-TOF-MS for $C_{152}H_{254}N_{40}O_{65}S$: $[M+Na]^+$ calcd. 3734.74, found 3734.79.

HR-ESI-MS for $C_{152}H_{254}N_{40}O_{65}S$ (exact monoisotopic mass 3711.7520): $[M+4H]^{4+}$ calcd. 928.9453, found 928.9450, mass accuracy +0.3 ppm.

RP-HPLC (linear gradient from 0-50% eluent B in 30 min at 25 °C): t_r= 11.9 min. Determined purity: 95%.

5.4.3.3 Capping of Glycomacromolecule-Thiol Functionalities with N-ethylmaleimid

For capping of the thiol functionalities, the respective glycomacromolecule was dissolved in degassed buffer (10 mM Hepes, pH 7) in a concentration of 5 mM. 10 eq. of TCEP were added under nitrogen stream. The reaction mixture was shaken for 48 h. Then 15 eq. of *N*-ethylmaleimide were added under nitrogen stream and the reaction was shaken for further 12 h at RT.
Glacomacromolecules were purified by preparative RP-HPLC.

Man(4)-5-Gly(1)-EDS(2,3)-Cys(5)-*N*-ethylmaleimide, **7a**

Compound **7a** was obtained in a yield of 73% after preparative HPLC after purification by prep-RP-HPLC. The anomeric proton of mannose could not be examined in ^{1}H-NMR due to the overlaying signal of the residual solvent. For the acetyl group on the N-terminal end two singlets with a 1:1 ratio were observed in ^{1}H-NMR that we assign to two rotational isomers in equal amounts.

^{1}H-NMR (300 MHz, D_2O): δ(ppm) = 8.28 (s, -N-H), 7.88 (s, 1H, Ar-H), 4.67–4.61 (m, 2H, -OCH_2**C**H_2N- (side chain)), 4.61-4.53 (m, 1H, -C(O)C**H**(CH_2S)NH- (Cys)), 4.14–4.01 (m, 2H, -OC**H**$_2CH_2$N- (side chain), -C(O)$CH(CH_2SC$**H**)NH- (*N*-ethylmaleimide)), 3.97–3.83 (m, 4H, -OC**H**$_2CH_2$N- (side chain), -C(O)C**H**$_2$NH- (Gly), Man-H), 3.78–3.24 (m, 38H, -OC**H**$_2$C**H**$_2$O- (EDS), -$NHCH_2$C**H**$_2$O- (EDS), Man-H, -C(O)NHC**H**$_2$C**H**$_2$N- (TDS), -NHC**H**$_2CH_2O$- (EDS), -NC**H**$_2CH_3$ (*N*-ethylmaleimide)), 3.17 (d, ^3J=6.7 Hz, 1H, -C(O)$CH($C**H**$_2$S)NH- (Cys)), 3.08–2.96 (m, 3H, Man-H, -NC(O)CH_2C**H**$_2$- (side chain)), 2.80 (t, ^3J= 7.2 Hz, 2H, -NC(O)C**H**$_2CH_2$- (side chain)), 2.72 (t, ^3J= 4.1 Hz, 1H, -SCHC**H**$_2$- (*N*-ethylmaleimide)), 2.65 (t,

^{3}J= 4.1 Hz, 1H, -SCHC**H**$_2$- (*N*-ethylmaleimide)), 2.63–2.44 (m, 12H, -C(O)C**H**$_2$C**H**$_2$C(O)-), 2.07+2.06 (2s, 3H, -C(O)CH$_3$), 1.13 (t, ^{3}J= 7.3 Hz, 3H, NCH$_2$C**H**$_3$ (*N*-ethylmaleimide)).

MALDI-TOF-MS for $C_{54}H_{89}N_{13}O_{23}S$: $[M+Na]^+$ calcd. 1342.58, found 1342.63.

HR-ESI-MS for $C_{54}H_{89}N_{13}O_{23}S$ (exact monoisotopic mass 1319.5915): $[M+2H]^{2+}$ calcd. 660.8030, found 660.8024, mass accuracy +0.9 ppm.

RP-HPLC (linear gradient from 0-50% eluent B in 30 min at 25 °C): t_r= 12.0 min. Determined purity: 97%.

Man(2,4,6,8,10)-11-Gly(1)-EDS(3,5,7,9)-Cys(11)-*N*-ethylmaleimide, **9a**

Compound **9a** was obtained in 44% yield after purification by prep-RP-HPLC. The anomeric proton of mannose could not be examined in ^{1}H-NMR due to the overlaying signal of the residual solvent. For the acetyl group on the N-terminal end two singlets with a 1:1 ratio were observed that we assign to two rotational isomers in equal amounts.

^{1}H-NMR (300 MHz, D_2O): δ(ppm) = 7.88 (s, 5H, Ar-H), 4.67–4.60 (m, 10H, -OCH$_2$C**H**$_2$N- (side chain)), 4.58-4.49 (m, 1H, -C(O)C**H**(CH$_2$SCH)NH- (Cys)), 4.14–4.04 (m, 5H, -OC**H**$_2$CH$_2$N- (side chain)), 4.04-3.98 (m, 1H, -C(O)CH(CH$_2$SC**H**)NH- (*N*-ethylmaleimide)), 3.97–3.84 (m, 12H, -OC**H**$_2$CH$_2$N- (side chain), -C(O)C**H**$_2$NH- (Gly), Man-H), 3.78–3.71 (m, 5H, Man-H), 3.70–3.55 (m, 47H, -OC**H**$_2$C**H**$_2$O- (EDS), -NHCH$_2$C**H**$_2$O- (EDS), Man-H), 3.52–3.30 (m, 58H, -C(O)NHC**H**$_2$C**H**$_2$N- (TDS), -NHC**H**$_2$CH$_2$O- (EDS), -NC**H**$_2$CH$_3$ (*N*-ethylmaleimide)), 3.17-3.09 (m, 2H, -C(O)CH(C**H**$_2$S)NH- (Cys)), 3.07–2.95 (m, 15H, Man-H, -NC(O)CH$_2$C**H**$_2$- (side chain)), 2.80 (t, ^{3}J= 7.2 Hz, 10H, -NC(O)C**H**$_2$CH$_2$- (side chain)), 2.72-2.60 (m, 2H, -SCHC**H**$_2$- (*N*-ethylmaleimide)) 2.55–2.42 (m, 36H, -C(O)C**H**$_2$C**H**$_2$C(O)-), 2.06+2.04 (2s, 3H, -C(O)CH$_3$), 1.11 (td, ^{3}J= 1.6, 7.3 Hz, 3H, NCH$_2$C**H**$_3$ (*N*-ethylmaleimide)).

MALDI-TOF-MS for $C_{158}H_{261}N_{41}O_{67}S$: $[M+Na]^+$ calcd. 3859.79, found 3859.65.

HR-ESI-MS for $C_{158}H_{261}N_{41}O_{67}S$ (exact monoisotopic mass 3836.7997): $[M+4H]^{4+}$ calcd. 960.2072, found 960.2065, mass accuracy +0.7 ppm.

RP-HPLC (linear gradient from 0-50% eluent B in 30 min at 25 °C): t_r= 12.5 min. Determined purity: 95%.

5.4.3.4 SPPoS of Glycomacromolecules for HIP/PAP Targeting

All listed precision glycomacromolecules were synthesized on solid support by stepwise assembly of different building blocks according to general coupling protocol and Fmoc cleavage protocol.[121] As building blocks, functional building block bearing an alkyne group, termed TDS, and spacer building blocks with either hydrophilic ethylene glycol units (EDS) or hydrophobic aliphatic (ODS) or aromatic (AR) properties were employed. In addition, natural amino acid L-cysteine was employed. In case of

the hydrophobic spacer building block, ODS, a 0.4 M solution of LiCl in DCM/DMF (1/1, *v/v*) was used as coupling solution instead of pure DMF. All other steps were proceeded as described previously. After successful assembly of the desired number of building blocks, the Fmoc protection group of the last building block was not removed and the resin was separated into three batches of 0.1 mmol each.

For batch 1: Deprotection of the last Fmoc group with 25% piperidine in DMF was performed followed by capping of the N-terminal primary amine group with acetic anhydride.[121] The subsequent conjugation of the azide functionalized carbohydrates proceeded by general CuAAC protocol.[121] Then, the sugar moieties were deprotected by the use of a 0.1 M solution of sodium methoxide in methanol and as last step the product was cleaved from solid support with 95% TFA and 1% TIPS in DCM. After cleavage trifluoracetic acid (TFA) residues were removed by the use of a strong anion exchange resin AG1-X8 (550 mg, quarternary ammonium, 100-200 mesh, acetate form, BioRad) as described by Roux and coworkers.[137] The procedure was repeated to ensure complete anion exchange from TF-acetate to acetate. As a last step the glycomacromolecule with end group **a** was isolated by freeze-drying.

For batch 2: Deprotection of the last Fmoc group with 25% piperidine in DMF was performed and the N-terminal site was coupled to succinic anhydride. Therefore, 5 eq. of succinic anhydride were dissolved in 4 mL DMF. After addition of 10 eq. of DIPEA the reaction mixture was loaded into the syringe reactor and shaken for 1 h followed by 10 washes with DMF. The subsequent conjugation of the azide functionalized carbohydrates proceeded by general CuAAC protocol.[121] Then, the sugar moieties were deprotected by the use of a 0.1 M solution of sodium methoxide in methanol and as last step the product was cleaved from solid support with 95% TFA and 1% TIPS in DCM. After cleavage trifluoracetic acid (TFA) residues were removed by the use of a strong anion exchange resin AG1-X8 (550 mg, quarternary ammonium, 100-200 mesh, acetate form, BioRad) as described by Roux and coworkers.[137] The procedure was repeated to ensure complete anion exchange from TF-acetate to acetate. As a last step the glycomacromolecule with end group **b** was isolated by freeze-drying.

For batch 3: The Fmoc protection group initially remained on the last building block and conjugation of the azide functionalized carbohydrates proceeded by general CuAAC protocol.[121] Then, Fmoc deprotection was performed with a solution of 25% piperidine in DMF followed by sugar deprotection using a 0.1 M solution of sodium methoxide in methanol. As next step coupling to the fluorescence dye FITC was performed. Therefore, a mixture of 3 eq. FITC (114 mg) and 10 eq. DIPEA (0.2 mL) was dissolved in 2 mL DMF, added to the resin and shaken for at least 24 h. Subsequently, the resin was washed 10 times with DMF, methanol and DCM. As last step the product was cleaved from solid support with 95% TFA and 1% TIPS in DCM. After cleavage trifluoracetic acid (TFA) residues were removed by the use of a strong anion exchange resin AG1-X8 (550 mg, quarternary ammonium, 100-200 mesh, acetate form, BioRad) as described by Roux and coworkers.[137] The procedure was repeated

to ensure complete anion exchange from TF-acetate to acetate. As a last step the glycomacromolecule with end group **c** was isolated by freeze-drying.

All glycomacromolecules were purified by preparative RP-HPLC.
For all structures commercially available Tentagel® SRam resin was used as resin for solid phase synthesis. The batch sizes for synthesizing the glycomacromolecules were 0.3 mmol.

Lac(6)-6-Cys(1)-EDS(2,3,4,5)-acetyl end group, **13a**

Compound **13a** was obtained in 31% yield after purification by prep-RP-HPLC. For the acetyl group on the N-terminal end two singlets with a 1:1 ratio were observed that we assign to two rotational isomers in equal amounts.

^{1}H-NMR (600 MHz, D_2O): δ(ppm) = 8.37 (s, -N-H), 8.07-8.02 (m, 1H, Ar-H), 5.75 (d, ^3J= 9.24 Hz, 1H, Lac-H), 4.54–4.48 (m, 2H, Lac-H, -C(O)C**H**(CH_2SH)NH- (Cys)), 4.05 (t, ^3J= 8.9 Hz, 1H, Lac-H) 3.99–3.74 (m, 9H, Lac-H), 3.71–3.57 (m, 34H, Lac-H, -OC**H**$_2$C**H**$_2$O- (EDS), -NHCH_2C**H**$_2$O- (EDS)), 3.51–3.30 (m, 24H, -C(O)NHC**H**$_2$C**H**$_2$N- (TDS), -NHC**H**$_2$CH_2O- (EDS)), 3.05 (t, ^3J= 7.1 Hz, 2H, -NC(O)CH_2C**H**$_2$- (side chain)), 2.98-2.89 (m, 2H, -C(O)CH(C**H**$_2$S)NH- (Cys)), 2.82 (q, ^3J= 7.1 Hz, 2H, -NC(O)C**H**$_2$CH_2- (side chain)), 2.68–2.45 (m, 20H, -C(O)C**H**$_2$C**H**$_2$C(O)-), 1.94+1.92 (2s, 3H, -C(O)CH_3).

MALDI-TOF-MS for $C_{70}H_{122}N_{16}O_{31}S$: $[M+Na]^+$ calcd. 1737.8, found 1737.8, $[M+K]^+$ calcd. 1753.8, found 1753.8, $[disulfide+Na]^+$ calcd. 3450.6, found 3450.6.

HR-ESI-MS for $C_{70}H_{124}N_{16}O_{31}S$ (exact monoisotopic mass 1714.8183): $[M+2H]^{2+}$ calcd. 858.4164, found 858.4145, mass accuracy -2.2 ppm.

RP-HPLC (linear gradient from 0-50% eluent B in 30 min at 25 °C): t_r= 11.6 min. Determined purity: 95%.

Lac(6)-6-Cys(1)-EDS(2,3,4,5)-succinyl end group, **13b**

Compound **13b** was obtained in 36% yield after purification by prep-RP-HPLC.

^{1}H-NMR (600 MHz, D_2O): δ(ppm) = 8.39 (s, -N-H), 8.07-8.03 (m, 1H, Ar-H), 5.75 (d, ^3J= 9.21 Hz, 1H, Lac-H), 4.54–4.48 (m, 2H, Lac-H, -C(O)C**H**(CH_2SH)NH- (Cys)), 4.05 (t, ^3J= 9.08 Hz, 1H, Lac-H) 3.99–3.75 (m, 9H, Lac-H), 3.72–3.57 (m, 34H, Lac-H, -OC**H**$_2$C**H**$_2$O- (EDS), -NHCH_2C**H**$_2$O- (EDS)), 3.51–3.32 (m, 24H, -C(O)NHC**H**$_2$C**H**$_2$N- (TDS), -NHC**H**$_2$CH_2O- (EDS)), 3.05 (t, ^3J= 7.1 Hz, 2H, -NC(O)CH_2C**H**$_2$- (side chain)), 2.98-2.89 (m, 2H, -C(O)CH(C**H**$_2$S)NH- (Cys)), 2.82 (q, ^3J= 7.2 Hz, 2H, -NC(O)C**H**$_2$CH_2- (side chain)), 2.67–2.45 (m, 24H, -C(O)C**H**$_2$C**H**$_2$C(O)-).

MALDI-TOF-MS for $C_{72}H_{124}N_{16}O_{33}S$: $[M+Na]^+$ calcd. 1795.8, found 1795.8, $[M+K]^+$ calcd. 1812.8, found 1812.8.

HR-ESI-MS for $C_{72}H_{126}N_{16}O_{33}S$ (exact monoisotopic mass 1772.8237): $[M+2H]^{2+}$ calcd. 887.4191, found 887.4188, mass accuracy -0.4 ppm.

RP-HPLC (linear gradient from 0-50% eluent B in 30 min at 25 °C): t_r= 11.6 min. Determined purity: 95%.

Lac(6)-6-Cys(1)-EDS(2,3,4,5)-FITC end group, **13c**

Compound **13c** was obtained in 14% yield after purification by prep-RP-HPLC.

^{1}H-NMR (600 MHz, D_2O): δ(ppm) = 8.02-7.87 (m, 1H, Ar-H), 7.63-7.47 (m, 1H, FITC-H), 7.12-7.01 (m, 1H, FITC-H), 6.93-6.43 (m, 7H, FITC-H), 5.70-5.59 (m, 1H, Lac-H), 4.52–4.43 (m, 2H, Lac-H, -C(O)C**H**(CH_2SH)NH- (Cys)), 4.03–3.16 (m, 67H, Lac-H, -OC**H**$_2$C**H**$_2$O- (EDS), -NHCH_2C**H**$_2$O- (EDS)), -NHC**H**$_2$CH_2O- (EDS), -C(O)NHC**H**$_2$C**H**$_2$N- (TDS)), 3.03-2.72 (m, 6H, -NC(O)CH_2C**H**$_2$- (side chain), -C(O)CH(C**H**$_2$S)NH- (Cys), -NC(O)C**H**$_2$CH_2- (side chain)), 2.66–2.37 (m, 20H, -C(O)C**H**$_2$C**H**$_2$C(O)-).

MALDI-TOF-MS for $C_{89}H_{131}N_{17}O_{35}S_2$: $[M+Na]^+$ calcd. 2084.8, found 2084.9, $[M+K]^+$ calcd. 2100.8, found 2100.8.

HR-ESI-MS for $C_{89}H_{134}N_{17}O_{35}S_2$ (exact monoisotopic mass 2061.8435): $[M+3H]^{3+}$ calcd. 688.2884, found 688.2890, mass accuracy +0.8 ppm.

RP-HPLC (linear gradient from 0-50% eluent B in 30 min at 25 °C): t_r= 17.6 min. Determined purity: 89% (4% disulphide).

Lac(6)-6-Cys(1)-EDS(2,3,4)-ODS(5)-acetyl end group, **14a**

Compound **14a** was obtained in 29% yield after purification by prep-RP-HPLC. For the acetyl group on the N-terminal end two singlets with a 1:1 ratio were observed that we assign to two rotational isomers in equal amounts.

^{1}H-NMR (600 MHz, D_2O): δ(ppm) = 8.45 (s, -N-H), 8.06-8.03 (m, 1H, Ar-H), 5.75 (d, ^3J= 9.23 Hz, 1H, Lac-H), 4.54–4.48 (m, 2H, Lac-H, -C(O)C**H**(CH_2SH)NH- (Cys)), 4.05 (t, ^3J= 9.1 Hz, 1H, Lac-H) 3.99–3.75 (m, 9H, Lac-H), 3.72–3.60 (m, 26H, Lac-H, -OC**H**$_2$C**H**$_2$O- (EDS), -NHCH_2C**H**$_2$O- (EDS)), 3.50–3.31 (m, 20H, -C(O)NHC**H**$_2$C**H**$_2$N- (TDS), -NHC**H**$_2$CH_2O- (EDS)), 3.17-3.13 (m, 4H, -NHC**H**$_2$(CH_2)$_6$C**H**$_2$NH- (ODS)), 3.07-3.02 (m, 2H, -NC(O)CH_2C**H**$_2$- (side chain)), 2.97-2.89 (m, 2H, -C(O)CH(C**H**$_2$S)NH- (Cys)), 2.82 (q, ^3J= 7.3 Hz, 2H, -NC(O)C**H**$_2$CH_2- (side chain)), 2.67–2.45 (m, 20H, -C(O)C**H**$_2$C**H**$_2$C(O)-), 1.94+1.92 (2s, 3H, -C(O)CH_3), 1.51-1.43 (m, 4H, -NHCH_2C**H**$_2$(CH_2)$_4$C**H**$_2$CH_2NH- (ODS)), 1.31-1.25 (m, 8H, -NH(CH_2)$_2$(C**H**$_2$)$_4$(CH_2)$_2$NH- (ODS)).

MALDI-TOF-MS for $C_{72}H_{126}N_{16}O_{29}S$: $[M+Na]^+$ calcd. 1733.9, found 1733.9, $[M+K]^+$ calcd. 1750.9, found 1750.8, [disulfide+Na]$^+$ calcd. 3442.7, found 3442.2.

HR-ESI-MS for $C_{72}H_{128}N_{16}O_{29}S$ (exact monoisotopic mass 1710.8597): $[M+2H]^{2+}$ calcd. 856.4371, found 856.4365, mass accuracy -0.8 ppm.

RP-HPLC (linear gradient from 0-50% eluent B in 30 min at 25 °C): t_r= 14.3 min. Determined purity: 88% (6% disulphide).

Lac(6)-6-Cys(1)-EDS(2,3,4)-ODS(5)-succinyl end group, **14b**

Compound **14b** was obtained in 29% yield after purification by prep-RP-HPLC.

^{1}H-NMR (600 MHz, D_2O): δ(ppm) = 8.36 (s, -N-H), 8.05 (s, 1H, Ar-H), 5.75 (d, ^3J= 9.2 Hz, 1H, Lac-H), 4.54–4.48 (m, 2H, Lac-H, -C(O)C**H**(CH_2SH)NH- (Cys)), 4.05 (t, ^3J= 9.1 Hz, 1H, Lac-H) 3.98–3.74 (m, 9H, Lac-H), 3.71–3.59 (m, 26H, Lac-H, -OC**H**$_2$C**H**$_2$O- (EDS), -NHCH_2C**H**$_2$O- (EDS)), 3.49–3.32 (m, 20H, -C(O)NHC**H**$_2$C**H**$_2$N- (TDS), -NHC**H**$_2$CH_2O- (EDS)), 3.17-3.12 (m, 4H, -NHC**H**$_2$(CH_2)$_6$C**H**$_2$NH- (ODS)), 3.05 (t, ^3J= 7.1 Hz, 2H, -NC(O)CH_2C**H**$_2$- (side chain)), 2.98-2.89 (m, 2H, -C(O)CH(C**H**$_2$S)NH- (Cys)), 2.82 (q, ^3J= 7.2 Hz, 2H, -NC(O)C**H**$_2$CH_2- (side chain)), 2.67–2.45 (m, 24H, -C(O)C**H**$_2$C**H**$_2$C(O)-), 1.50-1.43 (m, 4H, -NHCH_2C**H**$_2$(CH_2)$_4$C**H**$_2$CH_2NH- (ODS)), 1.31-1.25 (m, 8H, -NH(CH_2)$_2$(C**H**$_2$)$_4$(CH_2)$_2$NH- (ODS)).

MALDI-TOF-MS for $C_{74}H_{128}N_{16}O_{31}S$: $[M+Na]^+$ calcd. 1791.9, found 1791.9, $[M+K]^+$ calcd. 1807.9, found 1807.9.

HR-ESI-MS for $C_{74}H_{130}N_{16}O_{31}S$ (exact monoisotopic mass 1768.8652): $[M+2H]^{2+}$ calcd. 885.4399, found 885.4389, mass accuracy -1.2 ppm.

RP-HPLC (linear gradient from 0-50% eluent B in 30 min at 25 °C): t_r= 14.3 min. Determined purity: 88% (5% disulphide).

Lac(6)-6-Cys(1)-EDS(2,3,4)-ODS(5)-FITC end group, **14c**

Compound **14c** was obtained in 12% yield after purification by prep-RP-HPLC.

^{1}H-NMR (600 MHz, D_2O): δ(ppm) = 8.41 (s, -N-H), 8.07-7.92 (m, 1H, Ar-H), 7.63-7.51 (m, 1H, FITC-H), 7.00-6.87 (m, 1H, FITC-H), 6.79-6.35 (m, 7H, FITC-H), 5.73-5.61 (m, 1H, Lac-H), 4.54–4.44 (m, 2H, Lac-H, -C(O)C**H**(CH_2SH)NH- (Cys)), 4.05–3.25 (m, 55H, Lac-H, -OC**H**$_2$C**H**$_2$O- (EDS), -NHCH_2C**H**$_2$O- (EDS)), -NHC**H**$_2$CH_2O- (EDS), -C(O)NHC**H**$_2$C**H**$_2$N- (TDS)), 3.08-2.79 (m, 10H, -NHC**H**$_2$(CH_2)$_6$C**H**$_2$NH- (ODS), -NC(O)CH_2C**H**$_2$- (side chain), -C(O)CH(C**H**$_2$S)NH- (Cys), -NC(O)C**H**$_2$CH_2- (side chain)), 2.65–2.31 (m, 20H, -C(O)C**H**$_2$C**H**$_2$C(O)-), 1.32-1.16 (m, 4H, -NHCH_2C**H**$_2$(CH_2)$_4$C**H**$_2$CH_2NH- (ODS)), 1.10-0.86 (m, 8H, -NH(CH_2)$_2$(C**H**$_2$)$_4$(CH_2)$_2$NH- (ODS)).

MALDI-TOF-MS for $C_{91}H_{135}N_{17}O_{33}S_2$: $[M+Na]^+$ calcd. 2080.9, found 2080.9, $[M+K]^+$ calcd. 2096.9, found 2096.9.

HR-ESI-MS for $C_{91}H_{138}N_{17}O_{33}S_2$ (exact monoisotopic mass 2057.8850): $[M+3H]^{3+}$ calcd. 686.9689, found 686.9691, mass accuracy +0.2 ppm.

RP-HPLC (linear gradient from 0-50% eluent B in 30 min at 25 °C): t_r= 19.4 min. Determined purity: 84% (10% disulphide).

Lac(6)-6-Cys(1)-EDS(2,3,4)-AR(5)-acetyl end group, **15a**

Compound **15a** was obtained in 35% yield after purification by prep-RP-HPLC. For the acetyl group on the N-terminal end two singlets with a 1:1 ratio were observed that we assign to two rotational isomers in equal amounts.

^{1}H-NMR (600 MHz, D_2O): δ(ppm) = 8.44 (s, -N-H), 8.03-7.99 (m, 1H, Ar-H), 7.77-7.73 (m, 2H, Ar-H (AR)), 7.42-7.38 (m, 2H, Ar-H (AR)), 5.71 (dd, $^{3,4}J$= 9.3 Hz, 10.7 Hz, 1H, Lac-H), 4.52–4.47 (m, 2H, Lac-H, -C(O)C**H**(CH_2SH)NH- (Cys)), 4.42 (br. s, 2H, -NHC**H**$_2$- (AR)), 4.05-4.00 (m, 1H, Lac-H) 3.96–3.57 (m, 35H, Lac-H, -OC**H**$_2$C**H**$_2$O- (EDS), -NHCH_2C**H**$_2$O- (EDS)), 3.45–3.23 (m, 20H, -C(O)NHC**H**$_2$C**H**$_2$N- (TDS), -NHC**H**$_2$CH_2O- (EDS)), 3.02-2.98 (m, 2H, -NC(O)CH_2C**H**$_2$- (side chain)), 2.97-2.83 (m, 2H, -C(O)CH(C**H**$_2$S)NH- (Cys)), 2.80-2.72 (m, 2H, -NC(O)C**H**$_2$CH_2- (side chain)), 2.65–2.47 (m, 16H, -C(O)C**H**$_2$C**H**$_2$C(O)-), 1.93+1.90 (2s, 3H, -C(O)CH_3).

MALDI-TOF-MS for $C_{68}H_{111}N_{15}O_{28}S$: $[M+Na]^+$ calcd. 1640.7, found 1640.7, $[M+K]^+$ calcd. 1656.7, found 1656.7, [disulphide+Na]$^+$ calcd. 3256.5, found 3256.4.

HR-ESI-MS for $C_{68}H_{113}N_{15}O_{28}S$ (exact monoisotopic mass 1617.7444): $[M+2H]^{2+}$ calcd. 809.8795, found 809.8791, mass accuracy -0.4 ppm.

RP-HPLC (linear gradient from 0-50% eluent B in 30 min at 25 °C): t_r= 12.3 min. Determined purity: 92% (4% disulphide).

Lac(6)-6-Cys(1)-EDS(2,3,4)-AR(5)-succinyl end group, **15b**

Compound **15b** was obtained in 31% yield after purification by prep-RP-HPLC.

^{1}H-NMR (600 MHz, D_2O): δ(ppm) = 8.30 (s, -N-H), 7.94-7.91 (m, 1H, Ar-H), 7.68-7.64 (m, 2H, Ar-H (AR)), 7.33-7.29 (m, 2H, Ar-H (AR)), 5.62 (dd, ^3J= 9.3 Hz, 11.5 Hz, 1H, Lac-H), 4.43–4.39 (m, 2H, Lac-H, -C(O)C**H**(CH_2SH)NH- (Cys)), 4.33 (br. s, 2H, -NHC**H**$_2$- (AR)), 3.96-3.91 (m, 1H, Lac-H) 3.88–3.47 (m, 35H, Lac-H, -OC**H**$_2$C**H**$_2$O- (EDS), -NHCH_2C**H**$_2$O- (EDS)), 3.36–3.19 (m, 20H, -C(O)NHC**H**$_2$C**H**$_2$N- (TDS), -NHC**H**$_2$CH_2O- (EDS)), 2.94-2.90 (m, 2H, -NC(O)CH_2C**H**$_2$- (side chain)), 2.87-2.80 (m, 2H, -C(O)CH(C**H**$_2$S)NH- (Cys)), 2.70-2.65 (m, 2H, -NC(O)C**H**$_2$CH_2- (side chain)), 2.57–2.33 (m, 20H, -C(O)C**H**$_2$C**H**$_2$C(O)-).

MALDI-TOF-MS for $C_{70}H_{113}N_{15}O_{30}S$: $[M+Na]^+$ calcd. 1698.7, found 1698.8, $[M+K]^+$ calcd. 1714.7, found 1714.7, [disulphide+Na]$^+$ calcd. 3372.5, found 3372.4.

HR-ESI-MS for $C_{70}H_{115}N_{15}O_{30}S$ (exact monoisotopic mass 1675.7498): $[M+2H]^{2+}$ calcd. 838.8822, found 838.8825, mass accuracy +0.3 ppm.

RP-HPLC (linear gradient from 0-50% eluent B in 30 min at 25 °C): t_r= 12.4 min. Determined purity: 91% (3% disulphide).

Lac(6)-6-Cys(1)-EDS(2,3,4)-ARS(5)-FITC end group, **15c**

Compound **15c** was obtained in 15% yield after purification by prep-RP-HPLC.

^{1}H-NMR (600 MHz, D_2O): δ(ppm) = 8.43 (s, -N-H), 7.99-7.87 (m, 1H, Ar-H), 7.63-7.57 (m, 3H, FITC-H, Ar-H (AR)), 7.26-7.20 (m, 3H, FITC-H, Ar-H (AR)), 7.08-6.26 (m, 7H, FITC-H), 5.68-5.58 (m, 1H, Lac-H), 4.49–4.42 (m, 2H, Lac-H, -C(O)C**H**(CH_2SH)NH- (Cys)), 4.33–4.21 (m, 2H, -NHC**H**$_2$- (AR)), 4.03-3.15 (m, 56H, Lac-H, -OC**H**$_2$C**H**$_2$O- (EDS), -NHCH_2C**H**$_2$O- (EDS)), -NHC**H**$_2$CH_2O- (EDS), -C(O)NHC**H**$_2$C**H**$_2$N- (TDS)), 2.98-2.71 (m, 6H, -NC(O)CH_2C**H**$_2$- (side chain), -C(O)CH(C**H**$_2$S)NH- (Cys), -NC(O)C**H**$_2$CH_2- (side chain)), 2.63–2.34 (m, 16H, -C(O)C**H**$_2$C**H**$_2$C(O)-).

MALDI-TOF-MS for $C_{87}H_{120}N_{16}O_{32}S_2$: $[M+Na]^+$ calcd. 1987.8, found 1987.8.

HR-ESI-MS for $C_{87}H_{122}N_{16}O_{32}S_2$ (exact monoisotopic mass 1964.7696): $[M+2H]^{2+}$ calcd. 983.3921, found 983.3912, mass accuracy -0.9 ppm.

RP-HPLC (linear gradient from 0-50% eluent B in 30 min at 25 °C): t_r= 18.2 min. Determined purity: 78% (10% disulphide).

Lac(6,8,10)-10-Cys(1)-EDS(2,3,4,5,7,9)-acetyl end group, **16a**

Compound **16a** was obtained in 21% yield after purification by prep-RP-HPLC. For the acetyl group on the N-terminal end two singlets with a 1:1 ratio were observed that we assign to two rotational isomers in equal amounts.

^{1}H-NMR (600 MHz, D_2O): δ(ppm) = 8.41 (s, -N-H), 8.07-8.03 (m, 3H, Ar-H), 5.75 (d, ^3J= 9.2 Hz, 3H, Lac-H), 4.54–4.48 (m, 4H, Lac-H, -C(O)C**H**(CH_2SH)NH- (Cys)), 4.05 (t, ^3J= 9.0 Hz, 3H, Lac-H) 4.00–3.74 (m, 27H, Lac-H), 3.72–3.55 (m, 54H, Lac-H, -OC**H**$_2$C**H**$_2$O- (EDS), -NHCH_2C**H**$_2$O- (EDS)), 3.51–3.29 (m, 48H, -C(O)NHC**H**$_2$C**H**$_2$N- (TDS), -NHC**H**$_2$CH_2O- (EDS)), 3.04 (t, ^3J= 6.9 Hz, 6H, -NC(O)CH_2C**H**$_2$- (side chain)), 2.98-2.89 (m, 2H, -C(O)CH(C**H**$_2$S)NH- (Cys)), 2.85-2.78 (m, 6H, -NC(O)C**H**$_2$CH_2- (side chain)), 2.66–2.44 (m, 36H, -C(O)C**H**$_2$C**H**$_2$C(O)-), 1.93+1.91 (2s, 3H, -C(O)CH_3).

MALDI-TOF-MS for $C_{140}H_{238}N_{32}O_{65}S$: $[M+Na]^+$ calcd. 3462.6, found 3462.5, $[M+K]^+$ calcd. 3478.6, found 3478.5.

HR-ESI-MS for $C_{140}H_{242}N_{32}O_{65}S$ (exact monoisotopic mass 3439.6022): $[M+4H]^{4+}$ calcd. 860.9078, found 860.9073, mass accuracy -0.7 ppm.

RP-HPLC (linear gradient from 0-50% eluent B in 30 min at 25 °C): t_r= 12.0 min. Determined purity: 87% (9% disulphide).

Lac(6,8,10)-10-Cys(1)-EDS(2,3,4,5,7,9)-succinyl end group, **16b**

Compound **16b** was obtained in 22% yield after purification by prep-RP-HPLC.

^{1}H-NMR (600 MHz, D_2O): δ(ppm) = 8.37 (s, -N-H), 8.07-8.03 (m, 3H, Ar-H), 5.75 (d, ^3J= 9.2 Hz, 3H, Lac-H), 4.55–4.48 (m, 4H, Lac-H, -C(O)C**H**(CH_2SH)NH- (Cys)), 4.05 (t, ^3J= 9.1 Hz, 1H, Lac-H) 3.99–3.74 (m, 27H, Lac-H), 3.72–3.57 (m, 54H, Lac-H, -OC**H**$_2$C**H**$_2$O- (EDS), -NHCH_2C**H**$_2$O- (EDS)), 3.49–3.30 (m, 48H, -C(O)NHC**H**$_2$C**H**$_2$N- (TDS), -NHC**H**$_2$CH_2O- (EDS)), 3.04 (t, ^3J= 6.9 Hz, 6H, -NC(O)CH_2C**H**$_2$- (side chain)), 2.97-2.89 (m, 2H, -C(O)CH(C**H**$_2$S)NH- (Cys)), 2.81 (t, ^3J= 7.1 Hz, 6H, -NC(O)C**H**$_2$CH_2- (side chain)), 2.66–2.43 (m, 40H, -C(O)C**H**$_2$C**H**$_2$C(O)-).

MALDI-TOF-MS for $C_{142}H_{240}N_{32}O_{67}S$: $[M+Na]^+$ calcd. 3520.6, found 3520.5, $[M+K]^+$ calcd. 3536.6, found 3536.5.

HR-ESI-MS for $C_{142}H_{244}N_{32}O_{67}S$ (exact monoisotopic mass 1772.8237): $[M+4H]^{4+}$ calcd. 875.4092, found 875.4081, mass accuracy -1.3 ppm.

RP-HPLC (linear gradient from 0-50% eluent B in 30 min at 25 °C): t_r= 12.1 min. Determined purity: 91% (5% disulphide).

Lac(6,8,10)-10-Cys(1)-EDS(2,3,4,5,7,9)-FITC end group, **16c**

Compound **16c** was obtained in 4% yield after purification by prep-RP-HPLC.

^{1}H-NMR (600 MHz, D_2O): δ(ppm) = 8.45 (s, -NH), 8.05-7.81 (m, 4H, Ar-H, FITC-H), 7.62-7.45 (m, 1H, FITC-H), 7.23-7.03 (m, 3H, FITC-H), 6.82-6.62 (m, 4H, FITC-H), 5.75-5.60 (m, 3H, Lac-H), 4.54–4.44 (m, 4H, Lac-H, -C(O)C**H**(CH_2SH)NH- (Cys)), 4.06–3.256 (m, 129H, Lac-H, -OC**H**$_2$C**H**$_2$O- (EDS), -NHCH_2C**H**$_2$O- (EDS)), -NHC**H**$_2$CH_2O- (EDS), -C(O)NHC**H**$_2$C**H**$_2$N- (TDS)), 3.04-2.87 (m, 8H, -NC(O)CH_2C**H**$_2$- (side chain), -C(O)CH(C**H**$_2$S)NH- (Cys)), 2.83-2.72 (m, 6H, -NC(O)C**H**$_2$CH_2- (side chain)), 2.66–2.38 (m, 36H, -C(O)C**H**$_2$C**H**$_2$C(O)-).

MALDI-TOF-MS for $C_{159}H_{247}N_{33}O_{69}S_2$: $[M+Na]^+$ calcd. 3809.6, found 3809.2, [disulphide+Na]$^+$ calcd. 7594.2, found 7594.2.

HR-ESI-MS for $C_{159}H_{251}N_{33}O_{69}S_2$ (exact monoisotopic mass 3786.6275): $[M+4H]^{4+}$ calcd. 947.6641, found 947.6624, mass accuracy -1.9 ppm.

RP-HPLC (linear gradient from 0-50% eluent B in 30 min at 25 °C): t_r= 16.4 min. Determined purity: 73% (22% disulphide).

Lac(6,8,10)-10-Cys(1)-EDS(2,3,4)-ODS(5,7,9)-acetyl end group, **17a**

Compound **17a** was obtained in 26% yield after purification by prep-RP-HPLC. For the acetyl group on the N-terminal end two singlets with a 1:1 ratio were observed that we assign to two rotational isomers in equal amounts.

^{1}H-NMR (600 MHz, D_2O): δ(ppm) = 8.44 (s, -N-H), 8.07-8.03 (m, 3H, Ar-H), 5.77-5.72 (m, 3H, Lac-H), 4.55–4.47 (m, 4H, Lac-H, -C(O)C**H**(CH_2SH)NH- (Cys)), 4.04 (t, ^3J= 9.2 Hz, 1H, Lac-H) 3.98–3.74 (m, 27H, Lac-H), 3.71–3.57 (m, 30H, Lac-H, -OC**H**$_2$C**H**$_2$O- (EDS), -NHCH_2C**H**$_2$O- (EDS)), 3.49–3.29 (m, 36H, -C(O)NHC**H**$_2$C**H**$_2$N- (TDS), -NHC**H**$_2$CH_2O- (EDS)), 3.17-3.10 (m, 12H, -NHC**H**$_2$(CH_2)$_6$C**H**$_2$NH- (ODS)), 3.04 (t, ^3J= 7.0 Hz, 6H, -NC(O)CH_2C**H**$_2$- (side chain)), 2.98-2.89 (m, 2H, -C(O)CH(C**H**$_2$S)NH- (Cys)), 2.81 (t, ^3J= 6.9 Hz, 6H, -NC(O)C**H**$_2$CH_2- (side chain)), 2.67–2.42 (m, 36H, -C(O)C**H**$_2$C**H**$_2$C(O)-), 1.94+1.92 (2s, 3H, -C(O)CH_3), 1.50-1.41 (m, 12H, -NHCH_2C**H**$_2$(CH_2)$_4$C**H**$_2$CH_2NH- (ODS)), 1.32-1.22 (m, 24H, -NH(CH_2)$_2$(C**H**$_2$)$_4$(CH_2)$_2$NH- (ODS)).

MALDI-TOF-MS for $C_{146}H_{250}N_{32}O_{59}S$: $[M+Na]^+$ calcd. 3450.7, found 3450.6, $[M+K]^+$ calcd. 3466.7, found 3466.6.

HR-ESI-MS for $C_{146}H_{254}N_{32}O_{59}S$ (exact monoisotopic mass 3427.7267): $[M+4H]^{4+}$ calcd. 857.9389, found 857.9399, mass accuracy +1.2 ppm.

RP-HPLC (linear gradient from 0-50% eluent B in 30 min at 25 °C): t_r= 16.8 min. Determined purity: 86% (12% disulphide).

Lac(6,8,10)-10-Cys(1)-EDS(2,3,4)-ODS(5,7,9)-succinyl end group, **17b**

Compound **17b** was obtained in 24% yield after purification by prep-RP-HPLC.

^{1}H-NMR (600 MHz, D_2O): δ(ppm) = 8.39 (s, -N-H), 8.08-8.02 (m, 3H, Ar-H), 5.74 (d, ^3J= 9.2 Hz, 3H, Lac-H), 4.55–4.47 (m, 4H, Lac-H, -C(O)C**H**(CH_2SH)NH- (Cys)), 4.04 (t, ^3J= 9.2 Hz, 3H, Lac-H) 3.98–3.74 (m, 27H, Lac-H), 3.71–3.57 (m, 30H, Lac-H, -OC**H**$_2$C**H**$_2$O- (EDS), -NHCH_2C**H**$_2$O- (EDS)), 3.49–3.30 (m, 36H, -C(O)NHC**H**$_2$C**H**$_2$N- (TDS), -NHC**H**$_2$CH_2O- (EDS)), 3.16-3.10 (m, 12H, -NHC**H**$_2$(CH_2)$_6$C**H**$_2$NH- (ODS)), 3.03 (t, ^3J= 7.0 Hz, 6H, -NC(O)CH_2C**H**$_2$- (side chain)), 2.97-2.89 (m, 2H, -C(O)CH(C**H**$_2$S)NH- (Cys)), 2.81 (t,

^{3}J= 7.1 Hz, 6H, -NC(O)C**H**$_2$CH$_2$- (side chain)), 2.66–2.42 (m, 40H, -C(O)C**H**$_2$C**H**$_2$C(O)-), 1.50-1.41 (m, 12H, -NHCH$_2$C**H**$_2$(CH$_2$)$_4$C**H**$_2$CH$_2$NH- (ODS)), 1.31-1.21 (m, 24H, -NH(CH$_2$)$_2$(C**H**$_2$)$_4$(CH$_2$)$_2$NH- (ODS)).

MALDI-TOF-MS for $C_{148}H_{252}N_{32}O_{61}S$: $[M+Na]^+$ calcd. 3508.7, found 3508.6, $[M+K]^+$ calcd. 3524.7, found 3524.5.

HR-ESI-MS for $C_{148}H_{256}N_{32}O_{61}S$ (exact monoisotopic mass 3485.7321): $[M+4H]^{4+}$ calcd. 872.4403, found 872.4413, mass accuracy +1.1 ppm.

RP-HPLC (linear gradient from 0-50% eluent B in 30 min at 25 °C): t_r= 16.8 min. Determined purity: 97% (2% disulphide).

Lac(6,8,10)-10-Cys(1)-EDS(2,3,4)-ODS(5,7,9)-FITC end group, **17c**

Compound **17c** was obtained in 5% yield after purification by prep-RP-HPLC.

^{1}H-NMR (600 MHz, D_2O): δ(ppm) = 8.06-7.96 (m, 3H, Ar-H), 7.73-7.62 (m, 1H, FITC-H), 7.03-6.93 (m, 1H, FITC-H), 6.76-6.47 (m, 7H, FITC-H), 5.77-5.64 (m, 3H, Lac-H), 4.56–4.45 (m, 4H, Lac-H, -C(O)C**H**(CH$_2$SH)NH- (Cys)), 4.08–3.20 (m, 96H, Lac-H, -OC**H**$_2$C**H**$_2$O- (EDS), -NHCH$_2$C**H**$_2$O- (EDS)), -NHC**H**$_2$CH$_2$O- (EDS), -C(O)NHC**H**$_2$C**H**$_2$N- (TDS)), 3.11-2.87 (m, 20H, -NHC**H**$_2$(CH$_2$)$_6$C**H**$_2$NH- (ODS), -NC(O)CH$_2$C**H**$_2$- (side chain), -C(O)CH(C**H**$_2$S)NH- (Cys)), 2.83-2.35 (m, 6H, -NC(O)C**H**$_2$CH$_2$- (side chain)), 2.65–2.35 (m, 36H, -C(O)C**H**$_2$C**H**$_2$C(O)-), 1.41-0.91 (m, 36H, -NHCH$_2$C**H**$_2$(CH$_2$)$_4$C**H**$_2$CH$_2$NH- (ODS), -NH(CH$_2$)$_2$(C**H**$_2$)$_4$(CH$_2$)$_2$NH- (ODS)).

MALDI-TOF-MS for $C_{165}H_{259}N_{33}O_{63}S_2$: $[M+Na]^+$ calcd. 3797.8, found 3797.5, [disulphide+Na]$^+$ calcd. 7570.8, found 7070.4.

HR-ESI-MS for $C_{165}H_{263}N_{33}O_{63}S_2$ (exact monoisotopic mass 3774.7519): $[M+4H]^{4+}$ calcd. 944.6952, found 944.6937, mass accuracy -1.7 ppm.

RP-HPLC (linear gradient from 0-50% eluent B in 30 min at 25 °C): t_r= 19.5 min. Determined purity: 77% (18% disulphide).

Lac(6,8,10)-10-Cys(1)-EDS(2,3,4)-AR(5,7,9)-acetyl end group, **18a**

Compound **18a** was obtained in 27% yield after purification by prep-RP-HPLC. For the acetyl group on the N-terminal end two singlets with a 1:1 ratio were observed that we assign to two rotational isomers in equal amounts.

^{1}H-NMR (600 MHz, D_2O): δ(ppm) = 8.44 (s, -N-H), 8.01-7.98 (m, 1H, Ar-H), 7.96-7.93 (m, 1H, Ar-H), 7.85-7.82 (m, 1H, Ar-H), 7.73-7.57 (m, 6H, Ar-H (AR)), 7.38-7.27 (m, 6H, Ar-H (AR)), 5.74-5.62 (m, 3H, Lac-H), 4.53–4.45 (m, 4H, Lac-H, -C(O)C**H**(CH$_2$SH)NH- (Cys)), 4.40-4.32 (m, 6H, -NHC**H**$_2$- (AR)), 4.05-3.23 (m,

96H, Lac-H, -OC**H**$_2$C**H**$_2$O- (EDS), -NHCH$_2$C**H**$_2$O- (EDS), -C(O)NHC**H**$_2$C**H**$_2$N- (TDS), -NHC**H**$_2$CH$_2$O- (EDS)), 3.03-2.83 (m, 8H, -NC(O)CH$_2$C**H**$_2$- (side chain), -C(O)CH(C**H**$_2$S)NH- (Cys)), 2.78-2.66 (m, 6H, -NC(O)C**H**$_2$CH$_2$- (side chain)), 2.66–2.41 (m, 24H, -C(O)C**H**$_2$C**H**$_2$C(O)-), 1.91+1.88 (2s, 3H, -C(O)CH$_3$).

MALDI-TOF-MS for $C_{134}H_{205}N_{29}O_{56}S$: $[M+Na]^+$ calcd. 3171.4, found 3171.3, $[M+K]^+$ calcd. 3187.4, found 3187.3.

HR-ESI-MS for $C_{134}H_{208}N_{29}O_{56}S$ (exact monoisotopic mass 3148.3806): $[M+3H]^{3+}$ calcd. 1050.4675, found 1050.4667, mass accuracy -0.8 ppm.

RP-HPLC (linear gradient from 0-50% eluent B in 30 min at 25 °C): t_r= 13.4 min. Determined purity: 88% (8% disulphide).

Lac(6,8,10)-10-Cys(1)-EDS(2,3,4)-AR(5,7,9)-succinyl end group, **18b**

Compound **18b** was obtained in 27% yield after purification by prep-RP-HPLC.

^{1}H-NMR (600 MHz, D$_2$O): δ(ppm) = 8.39 (s, -N-H), 8.02-7.98 (m, 1H, Ar-H), 7.96-7.92 (m, 1H, Ar-H), 7.86-7.82 (m, 1H, Ar-H), 7.72-7.56 (m, 6H, Ar-H (AR)), 7.37-7.25 (m, 6H, Ar-H (AR)), 5.73-5.62 (m, 3H, Lac-H), 4.53–4.46 (m, 4H, Lac-H, -C(O)C**H**(CH$_2$SH)NH- (Cys)), 4.40-4.32 (m, 6H, -NHC**H**$_2$- (AR)), 4.05-3.26 (m, 96H, Lac-H, -OC**H**$_2$C**H**$_2$O- (EDS), -NHCH$_2$C**H**$_2$O- (EDS), -C(O)NHC**H**$_2$C**H**$_2$N- (TDS), -NHC**H**$_2$CH$_2$O- (EDS)), 3.00-2.82 (m, 8H, -NC(O)CH$_2$C**H**$_2$- (side chain), -C(O)CH(C**H**$_2$S)NH- (Cys)), 2.77-2.67 (m, 6H, -NC(O)C**H**$_2$CH$_2$- (side chain)), 2.66–2.38 (m, 28H, -C(O)C**H**$_2$C**H**$_2$C(O)-).

MALDI-TOF-MS for $C_{136}H_{207}N_{29}O_{58}S$: $[M+Na]^+$ calcd. 3229.4, found 3229.3, $[M+K]^+$ calcd. 3245.4, found 3245.3.

HR-ESI-MS for $C_{136}H_{210}N_{29}O_{58}S$ (exact monoisotopic mass 3206.3860): $[M+3H]^{3+}$ calcd. 1069.8026, found 1069.8028, mass accuracy +0.2 ppm.

RP-HPLC (linear gradient from 0-50% eluent B in 30 min at 25 °C): t_r= 13.4 min. Determined purity: 87% (10% disulphide).

Lac(6,8,10)-10-Cys(1)-EDS(2,3,4)-AR(5,7,9)-FITC end group, **18c**

Compound **15c** was obtained in 6% yield after purification by prep-RP-HPLC.

^{1}H-NMR (600 MHz, D$_2$O): δ(ppm) = 8.41 (s, -N-H), 7.97-7.81 (m, 3H, Ar-H), 7.66-7.46 (m, 7H, FITC-H, Ar-H (AR)), 7.27-7.10 (m, 6H, Ar-H (AR)), 6.90-6.82 (m, 1H, FITC-H), 6.70-6.36 (m, 7H, FITC-H), 5.68-5.58 (m, 3H, Lac-H), 4.53–4.43 (m, 4H, Lac-H, -C(O)C**H**(CH$_2$SH)NH- (Cys)), 4.34–4.14 (m, 6H, -NHC**H**$_2$- (AR)), 4.03-3.15 (m, 96H, Lac-H, -OC**H**$_2$C**H**$_2$O- (EDS), -NHCH$_2$C**H**$_2$O- (EDS)), -NHC**H**$_2$CH$_2$O-

(EDS), -C(O)NHC**H**$_2$C**H**$_2$N- (TDS)), 2.94-2.77 (m, 8H, -NC(O)CH$_2$C**H**$_2$- (side chain), -C(O)CH(C**H**$_2$S)NH- (Cys)), 2.70–2.31 (m, 30H, -NC(O)C**H**$_2$CH$_2$- (side chain), -C(O)C**H**$_2$C**H**$_2$C(O)-).

MALDI-TOF-MS for $C_{153}H_{214}N_{30}O_{60}S_2$: $[M+Na]^+$ calcd. 3518.4, found 3518.9, [disulphide+Na]$^+$ calcd. 7011.8, found 7011.8.

HR-ESI-MS for $C_{153}H_{218}N_{30}O_{60}S_2$ (exact monoisotopic mass 3495.4058): $[M+4H]^{4+}$ calcd. 874.8587, found 874.8591, mass accuracy +0.4 ppm.

RP-HPLC (linear gradient from 0-50% eluent B in 30 min at 25 °C): t_r= 17.1 min. Determined purity: 79% (13% disulphide).

Man(6)-6-Cys(1)-EDS(2,3,4,5)-acetyl end group, **19a**

Compound **19a** was obtained in a yield of 29% after purification by prep-RP-HPLC. The anomeric proton of mannose could not be examined in ^{1}H-NMR due to the overlaying signal of the residual solvent. For the acetyl group on the N-terminal end two singlets with a 1:1 ratio were observed that we assign to two rotational isomers in equal amounts.

^{1}H-NMR (600 MHz, D_2O): δ(ppm) = 8.37 (s, -N-H), 7.89-7.86 (m, 1H, Ar-H), 4.67–4.62 (m, 2H, -OCH$_2$C**H**$_2$N- (side chain)), 4.50 (dd, ^3J=5.2 Hz, 7.3 Hz , 1H, -C(O)C**H**(CH$_2$SH)NH- (Cys)), 4.12–4.06 (m, 1H, -OC**H**$_2$CH$_2$N- (side chain)), 3.95–3.90 (m, 1H, -OC**H**$_2$CH$_2$N- (side chain)), 3.87–3.85 (m, 1H, Man-H), 3.76–3.72 (m, 1H, Man-H), 3.70–3.60 (m, 35H, -OC**H**$_2$C**H**$_2$O- (EDS), -NHCH$_2$C**H**$_2$O- (EDS), Man-H), 3.51–3.31 (m, 24H, -C(O)NHC**H**$_2$C**H**$_2$N- (TDS), -NHC**H**$_2$CH$_2$O- (EDS)), 3.06–2.98 (m, 3H, Man-H, -NC(O)CH$_2$C**H**$_2$- (side chain)), 2.98-2.86 (m, 2H, -C(O)CH(C**H**$_2$SH)NH- (Cys)), 2.84-2.77 (m, 2H, -NC(O)C**H**$_2$CH$_2$- (side chain)), 2.67–2.46 (m, 20H, -C(O)C**H**$_2$C**H**$_2$C(O)-), 1.94+1.93 (2s, 3H, -C(O)CH$_3$).

MALDI-TOF-MS for $C_{66}H_{116}N_{16}O_{27}S$: $[M+Na]^+$ calcd. 1619.8, found 1619.8, $[M+K]^+$ calcd. 1635.8, found 1636.4, [disulfide+Na]$^+$ calcd. 3214.6, found 3214.5.

HR-ESI-MS for $C_{66}H_{118}N_{16}O_{27}S$ (exact monoisotopic mass 1596.7917): $[M+2H]^{2+}$ calcd. 799.4031, found 799.4028, mass accuracy -0.4 ppm.

RP-HPLC (linear gradient from 0-50% eluent B in 30 min at 25 °C): t_r= 12.0 min. Determined purity: 93% (3% disulphide).

Man(6)-6-Cys(1)-EDS(2,3,4,5)-succinyl end group, **19b**

Compound **19b** was obtained in a yield of 38% after purification by prep-RP-HPLC. The anomeric proton of mannose could not be examined in ^{1}H-NMR due to the overlaying signal of the residual solvent.

^{1}H-NMR (600 MHz, D_2O): δ(ppm) = 8.32 (s, -N-H), 7.91-7.83 (m, 1H, Ar-H), 4.67–4.60 (m, 2H, -OCH$_2$C**H**$_2$N- (side chain)), 4.50 (dd, ^3J=5.1 Hz, 6.9 Hz , 1H, -C(O)C**H**(CH$_2$SH)NH- (Cys)), 4.11–4.06 (m, 1H, -OC**H**$_2$CH$_2$N- (side chain)), 3.95–3.90 (m, 1H, -OC**H**$_2$CH$_2$N- (side chain)), 3.87–3.85 (m, 1H, Man-H), 3.76–3.72 (m, 1H, Man-H), 3.71–3.58 (m, 35H, -OC**H**$_2$C**H**$_2$O- (EDS), -NHCH$_2$C**H**$_2$O- (EDS), Man-H), 3.50–3.33 (m, 24H, -C(O)NHC**H**$_2$C**H**$_2$N- (TDS), -NHC**H**$_2$CH$_2$O- (EDS)), 3.06–2.99 (m, 3H, Man-H, -NC(O)CH$_2$C**H**$_2$- (side chain)), 2.97-2.89 (m, 2H, -C(O)CH(C**H**$_2$SH)NH- (Cys)), 2.80 (t, ^3J=7.3 Hz, 2H, -NC(O)C**H**$_2$CH$_2$- (side chain)), 2.66–2.47 (m, 24H, -C(O)C**H**$_2$C**H**$_2$C(O)-).

MALDI-TOF-MS for $C_{68}H_{118}N_{16}O_{29}S$: $[M+Na]^+$ calcd. 1677.8, found 1677.8, $[M+K]^+$ calcd. 1693.8, found 1693.7, $[disulfide+Na]^+$ calcd. 3330.6, found 3330.5.

HR-ESI-MS for $C_{68}H_{120}N_{16}O_{29}S$ (exact monoisotopic mass 1654.7971): $[M+2H]^{2+}$ calcd. 828.4058, found 828.4053, mass accuracy -0.7 ppm.

RP-HPLC (linear gradient from 0-50% eluent B in 30 min at 25 °C): t_r= 12.0 min. Determined purity: 93% (3% disulphide).

Man(6)-6-Cys(1)-EDS(2,3,4,5)-FITC end group, **19c**

Compound **19c** was obtained in a yield of 14% after purification by prep-RP-HPLC.

^{1}H-NMR (600 MHz, D_2O): δ(ppm) = 8.25 (s, -N-H), 8.12-7.92 (m, 1H, Ar-H), 7.76-7.66 (m, 1H, FITC-H), 7.64-7.49 (m, 1H, FITC-H), 7.02-6.42 (m, 7H, FITC-H), 4.73-4.70 (m, 1H, Man-H, overlapped by HDO), 4.53–4.37 (m, 3H, -OCH$_2$C**H**$_2$N- (side chain), -C(O)C**H**(CH$_2$SH)NH- (Cys)), 4.01–3.94 (m, 1H, -OC**H**$_2$CH$_2$N- (side chain)), 3.83–3.27 (m, 62H, -OC**H**$_2$CH$_2$N- (side chain), Man-H, -OC**H**$_2$C**H**$_2$O- (EDS), -NHCH$_2$C**H**$_2$O- (EDS), -C(O)NHC**H**$_2$C**H**$_2$N- (TDS), -NHC**H**$_2$CH$_2$O- (EDS)), 3.06–2.68 (m, 7H, Man-H, -NC(O)CH$_2$C**H**$_2$- (side chain), -C(O)CH(C**H**$_2$SH)NH- (Cys), -NC(O)C**H**$_2$CH$_2$- (side chain)), 2.66–2.42 (m, 20H, -C(O)C**H**$_2$C**H**$_2$C(O)-).

MALDI-TOF-MS for $C_{85}H_{125}N_{17}O_{31}S_2$: $[M+Na]^+$ calcd. 1966.8, found 1966.8.

HR-ESI-MS for $C_{85}H_{128}N_{17}O_{31}S_2$ (exact monoisotopic mass 1943.8169): $[M+3H]^{3+}$ calcd. 648.9462, found 648.9468, mass accuracy +0.8 ppm.

RP-HPLC (linear gradient from 0-50% eluent B in 30 min at 25 °C): t_r= 18.1 min. Determined purity: 85% (1% disulphide).

Alkyne(6)-6-Cys(1)-EDS(2,3,4,5)-acetyl end group, **20a**

Compound **20a** was obtained in a yield of 36% after purification by prep-RP-HPLC. For the acetyl group on the N-terminal end two singlets with a 1:1 ratio were observed that we assign to two rotational isomers in equal amounts.

^{1}H-NMR (600 MHz, D_2O): δ(ppm) = 4.50 (dd, ^3J=5.1 Hz, 7.0 Hz , 1H, -C(O)C**H**(CH_2SH)NH- (Cys)), 3.71–3.67 (s, 16H, -OC**H**$_2$C**H**$_2$O- (EDS)), 3.63 (t, ^3J=5.4 Hz, 16H, -NHCH_2C**H**$_2$O- (EDS)), 3.56–3.48 (m, 4H, -C(O)NHCH_2C**H**$_2$N- (TDS)), 3.44-3.35 (m, 20H, -NHC**H**$_2$CH_2O- (EDS), -C(O)NHC**H**$_2$CH_2N- (TDS)), 2.98-2.89 (m, 2H, -C(O)CH(C**H**$_2$SH)NH- (Cys)), 2.69-2.62 (m, 4H, -NC(O)C**H**$_2$C**H**$_2$CCH- (side chain)), 2.61–2.47 (m, 20H, -C(O)C**H**$_2$C**H**$_2$C(O)-), 2.36 (t, ^3J=2.5 Hz, 1H, -NC(O)CH_2CH_2CC**H**- (side chain)), 2.0+1.96 (2s, 3H, -C(O)CH_3).

MALDI-TOF-MS for $C_{58}H_{101}N_{13}O_{21}S$: $[M+Na]^+$ calcd. 1370.7, found 1370.7, $[M+K]^+$ calcd. 1386.7, found 1386.7, $[disulfide+Na]^+$ calcd. 2716.4, found 2716.4.

HR-ESI-MS for $C_{58}H_{103}N_{13}O_{21}S$ (exact monoisotopic mass 1347.6956): $[M+2H]^{2+}$ calcd. 674.8551, found 674.8549, mass accuracy -0.3 ppm.

RP-HPLC (linear gradient from 0-50% eluent B in 30 min at 25 °C): t_r= 13.2 min. Determined purity: 90% (8% disulphide).

<u>Alkyne(6)-6-Cys(1)-EDS(2,3,4,5)-succinyl end group, **20b**</u>

Compound **20b** was obtained in a yield of 26% after purification by prep-RP-HPLC.

^{1}H-NMR (600 MHz, D_2O): δ(ppm) = 4.50 (dd, ^3J=5.2 Hz, 7.1 Hz , 1H, -C(O)C**H**(CH_2SH)NH- (Cys)), 3.71–3.67 (s, 16H, -OC**H**$_2$C**H**$_2$O- (EDS)), 3.63 (t, ^3J=5.4 Hz, 16H, -NHCH_2C**H**$_2$O- (EDS)), 3.55–3.49 (m, 4H, -C(O)NHCH_2C**H**$_2$N- (TDS)), 3.44-3.37 (m, 20H, -NHC**H**$_2$CH_2O- (EDS), -C(O)NHC**H**$_2$CH_2N- (TDS)), 2.98-2.89 (m, 2H, -C(O)CH(C**H**$_2$SH)NH- (Cys)), 2.67-2.57 (m, 4H, -NC(O)C**H**$_2$C**H**$_2$CCH- (side chain)), 2.57–2.47 (m, 24H, -C(O)C**H**$_2$C**H**$_2$C(O)-), 2.36 (t, ^3J=2.6 Hz, 1H, -NC(O)CH_2CH_2CC**H**- (side chain)).

MALDI-TOF-MS for $C_{60}H_{103}N_{13}O_{23}S$: $[M+Na]^+$ calcd. 1428.7, found 1428.7, $[M+K]^+$ calcd. 1444.7, found 1444.7, $[disulfide+Na]^+$ calcd. 2832.4, found 2832.4.

HR-ESI-MS for $C_{60}H_{105}N_{13}O_{23}S$ (exact monoisotopic mass 1405.7010): $[M+2H]^{2+}$ calcd. 703.8578, found 703.8576, mass accuracy -0.2 ppm.

RP-HPLC (linear gradient from 0-50% eluent B in 30 min at 25 °C): t_r= 13.2 min. Determined purity: 88% (7% disulphide).

<u>Alkyne(6)-6-Cys(1)-EDS(2,3,4,5)-FITC end group, **20c**</u>

Compound **20c** was obtained in a yield of 17% after purification by prep-RP-HPLC.

^{1}H-NMR (600 MHz, D_2O): δ(ppm) = 8.39 (s, -N-H), 8.07-7.96 (m, 1H, FITC-H), 7.64-7.53 (m, 1H, FITC-H), 7.00-6.42 (m, 7H, FITC-H), 4.48 (t, ^3J=6.1 Hz , 1H, -C(O)C**H**(CH_2SH)NH- (Cys)), 3.73–3.20 (s, 56H, -OC**H**$_2$C**H**$_2$O- (EDS), -NHCH_2C**H**$_2$O- (EDS), -C(O)NHC**H**$_2$C**H**$_2$N- (TDS), -NHC**H**$_2$CH_2O- (EDS)), 2.93-2.86

(m, 2H, -C(O)CH(C**H**$_2$SH)NH- (Cys)), 2.68-2.33 (m, 24H, -NC(O)C**H**$_2$C**H**$_2$CCH- (side chain), -C(O)C**H**$_2$C**H**$_2$C(O)-), 2.26-2.21 (m, 1H, -NC(O)CH$_2$CH$_2$CC**H**- (side chain)).

MALDI-TOF-MS for $C_{77}H_{110}N_{14}O_{25}S_2$: $[M+Na]^+$ calcd. 1717.7, found 1717.7, $[M+K]^+$ calcd. 1733.7, found 1733.7.

HR-ESI-MS for $C_{77}H_{112}N_{14}O_{25}S_2$ (exact monoisotopic mass 1694.7208): $[M+2H]^{2+}$ calcd. 848.3677, found 848.3677, mass accuracy ±0.0 ppm.

RP-HPLC (linear gradient from 0-50% eluent B in 30 min at 25 °C): t_r= 20.6 min. Determined purity: 93% (6% disulphide).

FITC(6)-6-Cys(1)-EDS(2,3,4,5,6), **21**

Compound **21** was obtained in a yield of 27% after purification by prep-RP-HPLC.

^{1}H-NMR (600 MHz, D_2O): δ(ppm) = 8.12-8.01 (m, 1H, FITC-H), 7.69-7.53 (m, 1H, FITC-H), 7.01-6.87 (m, 1H, FITC-H), 6.74-6.40 (m, 6H, FITC-H), 4.48 (dd, ^3J=5.4 Hz, 7.2 Hz , 1H, -C(O)C**H**(CH$_2$SH)NH- (Cys)), 3.78–3.20 (m, 60H, -OC**H**$_2$C**H**$_2$O- (EDS), -NHCH$_2$C**H**$_2$O- (EDS), -NHC**H**$_2$CH$_2$O- (EDS)), 2.95-2.85 (m, 2H, -C(O)CH(C**H**$_2$SH)NH- (Cys)), 2.67-2.36 (m, 20H, -C(O)C**H**$_2$C**H**$_2$C(O)-).

MALDI-TOF-MS for $C_{74}H_{109}N_{13}O_{26}S_2$: $[M+Na]^+$ calcd. 1682.7, found 1682.7, [disulphide+Na]$^+$ calcd. 3340.4, found 3340.3.

HR-ESI-MS for $C_{74}H_{111}N_{13}O_{26}S_2$ (exact monoisotopic mass 1659.7048): $[M+2H]^{2+}$ calcd. 830.8597, found 830.8597, mass accuracy ±0.0 ppm.

RP-HPLC (linear gradient from 0-50% eluent B in 30 min at 25 °C): t_r= 20.1 min. Determined purity: 98% (1% disulphide).

6-Cys(1)-EDS(2,3,4,5,6), **22**

Compound **22** was obtained in a yield of 50% after purification by prep-RP-HPLC.

^{1}H-NMR (600 MHz, D_2O): δ(ppm) = 4.50 (dd, ^3J=5.1 Hz, 7.1 Hz , 1H, -C(O)C**H**(CH$_2$SH)NH- (Cys)), 3.69 (s, 20H, -OC**H**$_2$C**H**$_2$O- (EDS)), 3.63 (t, ^3J= 5.4 Hz, 20H, -NHCH$_2$C**H**$_2$O- (EDS)), 3.39 (t, ^3J= 5.4 Hz, 20H, -NHC**H**$_2$CH$_2$O- (EDS)), 2.98-2.89 (m, 2H, -C(O)CH(C**H**$_2$SH)NH- (Cys)), 2.67-2.53 (m, 20H, -C(O)C**H**$_2$C**H**$_2$C(O)-), 2.01 (s, 3H, -C(O)CH$_3$).

MALDI-TOF-MS for $C_{55}H_{100}N_{12}O_{22}S$: $[M+Na]^+$ calcd. 1335.7, found 1335.7, $[M+K]^+$ calcd. 1351.7, found 1351.7, [disulphide+Na]$^+$ calcd. 2646.3, found 2646.3.

HR-ESI-MS for $C_{55}H_{102}N_{12}O_{22}S$ (exact monoisotopic mass 1312.6796): $[M+2H]^{2+}$ calcd. 657.3471, found 657.3465, mass accuracy -0.9 ppm.

RP-HPLC (linear gradient from 0-50% eluent B in 30 min at 25 °C): t_r= 12.5 min. Determined purity: 96%.

5.4.3.5 SPPoS of Glycomacromolecules for Dynamic Combinatorial Libraries

SPPoS of Glycomacromolecules for Disulphide Formation

All listed precision glycomacromolecules were synthesized on solid support by stepwise assembly of different building blocks according to general coupling protocol and Fmoc cleavage protocol.[121] As building blocks, functional building block bearing an alkyne group, termed TDS, and spacer building blocks with either hydrophilic ethylene glycol units (EDS) or hydrophobic aliphatic (ODS) were employed. In addition, natural amino acid L-cysteine was employed. In case of the hydrophobic spacer building block, ODS, a 0.4 M solution of LiCl in DCM/DMF (1/1, *v/v*) was used as coupling solution instead of pure DMF. All other steps were proceeded as described previously.

After successful assembly of the desired number of building blocks, capping of the N-terminal primary amine group was performed employing acetic anhydride.[121] The subsequent conjugation of the azide functionalized carbohydrates proceeded by general CuAAC protocol.[121] Then, the sugar moieties were deprotected by the use of a 0.1 M solution of sodium methoxide in methanol and as last step the product was cleaved from solid support with 95% TFA and 1% TIPS in DCM. After cleavage trifluoracetic acid (TFA) residues were removed by the use of a strong anion exchange resin AG1-X8 (550 mg, quarternary ammonium, 100-200 mesh, acetate form, BioRad) as described by Roux and coworkers.[137] The procedure was repeated to ensure complete anion exchange from TF-acetate to acetate. As a last step the glycomacromolecule was isolated by freeze-drying.

For all structures commercially available Tentagel® SRam resin was used as resin for solid phase synthesis. The batch sizes for synthesizing the glycomacromolecules were 0.2 mmol.

Man(2,4,6)-7-Cys(1,7)-EDS(3,5), **23**

Compound **23** was obtained in a yield of 65%. The anomeric proton of mannose could not be examined in ^{1}H-NMR due to the overlaying signal of the residual solvent. For the acetyl group on the N-terminal end two singlets with a 1:1 ratio were observed that we assign to two rotational isomers in equal amounts. Integration of EDS protons in the range of 3.76 to 3.58 ppm is higher than expected (32H instead of 28H). Glycomacromolecule **23** was not purified by preparative RP-HPLC as all previously presented glycomacromolecules so that this integral size might be explained by PEG residues from Tentagel® resin after cleavage that could not be removed by precipitation in diethylether. The singlet signal at 2.08 ppm can be assigned to the acetate group present as counter ion after ligand exchange.

^{1}H-NMR (600 MHz, D_2O): δ(ppm) = 7.90-7.84 (m, 3H, Ar-H), 4.66–4.61 (m, 6H, -$OCH_2C\mathbf{H}_2$N- (side chain)), 4.48 (dd, ^3J=5.2 Hz, 7.2 Hz , 1H, -C(O)C**H**(CH_2SH)NH- (Cys)), 4.45-4.41 (m, 1H, -C(O)C**H**(CH_2SH)NH- (Cys)), 4.11–4.06 (m, 3H, -$OC\mathbf{H}_2CH_2$N- (side chain)), 3.95–3.89 (m, 3H, -$OC\mathbf{H}_2CH_2$N- (side chain)), 3.88–3.45 (m, 3H, Man-H), 3.76–3.58 (m, 36H, -$OC\mathbf{H}_2C\mathbf{H}_2$O- (EDS), -$NHCH_2C\mathbf{H}_2$O- (EDS), Man-H), 3.52–3.31 (m, 32H, -C(O)NH$C\mathbf{H}_2C\mathbf{H}_2$N- (TDS), -$NHC\mathbf{H}_2CH_2$O- (EDS)), 3.06–2.97 (m, 9H, Man-H, -$NC(O)CH_2C\mathbf{H}_2$- (side chain)), 2.96-2.83 (m, 4H, -C(O)CH($C\mathbf{H}_2$SH)NH- (Cys)), 2.80 (t, ^3J=6.9 Hz, 6H, -$NC(O)C\mathbf{H}_2CH_2$- (side chain)), 2.62–2.45 (m, 20H, -$C(O)C\mathbf{H}_2C\mathbf{H}_2C(O)$-), 2.06+2.04 (2s, 3H, -$C(O)CH_3$).

MALDI-TOF-MS for $C_{91}H_{153}N_{25}O_{38}S_2$: [disulphide ring+Na]$^+$ calcd. 2289.0, found 2289.0, [disulphide ring+K]$^+$ calcd. 2305.0, found 2305.0.

RP-HPLC (linear gradient from 0-50% eluent B in 30 min at 25 °C): t_r= 9.8 min. Determined purity: 94%.

Man(2,4,6)-7-Cys(1,7)-ODS(3,5), **24**

Compound **24** was obtained in a yield of 71%. The anomeric proton of mannose could not be examined in ^{1}H-NMR due to the overlaying signal of the residual solvent. For the acetyl group on the N-terminal end two singlets with a 1:1 ratio were observed that we assign to two rotational isomers in equal amounts. Integration of mannopyranoside protons in the range of 3.76 to 3.58 ppm is higher than expected (20H instead of 12H). Glycomacromolecule **24** was not purified by preparative RP-HPLC as all previously presented glycomacromolecules so that this integral size might be explained by PEG residues from Tentagel® resin after cleavage that could not be removed by precipitation in diethylether. The singlet signal at 2.05 ppm can be assigned to the acetate group present as counter ion after ligand exchange.

^{1}H-NMR (600 MHz, D_2O): δ(ppm) = 7.90-7.84 (m, 3H, Ar-H), 4.66–4.60 (m, 6H, -$OCH_2C\mathbf{H}_2$N- (side chain)), 4.48 (dd, ^3J=5.3 Hz, 7.7 Hz , 1H, -C(O)C**H**(CH_2SH)NH- (Cys)), 4.45-4.40 (m, 1H, -C(O)C**H**(CH_2SH)NH- (Cys)), 4.12–4.06 (m, 3H, -$OC\mathbf{H}_2CH_2$N- (side chain)), 3.95–3.89 (m, 3H, -$OC\mathbf{H}_2CH_2$N- (side chain)), 3.88–3.84 (m, 3H, Man-H), 3.76–3.58 (m, 20H, Man-H), 3.51–3.32 (m, 24H, -C(O)NH$C\mathbf{H}_2C\mathbf{H}_2$N- (TDS)), 3.13 (t, ^3J= 5.9 Hz, 8H, -$NH(C\mathbf{H}_2)_2(CH_2)_4(C\mathbf{H}_2)_2$NH- (ODS)), 3.08–2.97 (m, 9H, Man-H, -$NC(O)CH_2C\mathbf{H}_2$- (side chain)), 2.96-2.83 (m, 4H, -C(O)CH($C\mathbf{H}_2$SH)NH- (Cys)), 2.80 (t, ^3J= 7.1 Hz, 6H, -$NC(O)C\mathbf{H}_2CH_2$- (side chain)), 2.62–2.44 (m, 20H, -$C(O)C\mathbf{H}_2C\mathbf{H}_2C(O)$-), 2.06+2.04 (2s, 3H, -$C(O)CH_3$), 1.49-1.39 (m, 8H, -$NHCH_2C\mathbf{H}_2(CH_2)_4C\mathbf{H}_2CH_2$NH- (ODS)), 1.35-1.18 (m, 16H, -$NH(CH_2)_2(C\mathbf{H}_2)_4(CH_2)_2$NH- (ODS)).

MALDI-TOF-MS for $C_{95}H_{161}N_{25}O_{34}S_2$: [disulphide ring+Na]$^+$ calcd. 2281.3, found 2281.1, [disulphide ring+K]$^+$ calcd. 2297.1, found 2297.1.

RP-HPLC (linear gradient from 0-50% eluent B in 30 min at 25 °C): t_r= 14.5 min. Determined purity: 94% (4% linear disulphide).

SPPoS of Glycomacromolecules for Imine Bond Formation

All listed precision glycomacromolecules were synthesized on solid support by stepwise assembly of different building blocks according to general coupling protocol and Fmoc cleavage protocol.[121] As building blocks, functional building blocks bearing an alkyne group, termed TDS, and commercially available aldehyde building block AL were employed. As spacer building block the hydrophilic ethylene glycol unit bearing EDS was employed. Moreover, the azide functionalized carbohydrate was deprotected in solution before use on solid support.[292] Therefore, 1.1 g of the protected mannose azide derivative was dissolved in 12 mL methanol and 12 mL 0.2 M NaOMe in MeOH was added. After 2 h the solution was neutralized with Amberlite IR-120 (hydrogen form) and the resin was filtered off. The product was isolated by solvent evaporation.

After successful assembly of the desired number of building blocks conjugation of the azide functionalized carbohydrate was proceeded by general CuAAC protocol.[121] Subsequently, the product was cleaved from solid support with 10% TFA in DCM. After cleavage trifluoracetic acid (TFA) residues were removed by the use of a strong anion exchange resin AG1-X8 (550 mg, quarternary ammonium, 100-200 mesh, acetate form, BioRad) as described by Roux and coworkers.[137] The procedure was repeated to ensure complete anion exchange from TF-acetate to acetate. As a last step the glycomacromolecule was isolated by freeze-drying.

For all structures commercially available Tentagel® chlorotrityl resin modified with ethylene diamine was used as resin for solid phase synthesis.[95] The batch sizes for synthesizing the glycomacromolecules were 0.2 mmol.

Man(3)-5-EDA(1)-EDS(2,4)-AL(5), **25**

Compound **25** was obtained in a yield of 67%. The anomeric proton of mannose could not be examined in ^{1}H-NMR due to the overlaying signal of the residual solvent. Integration of EDS protons in the range of 3.78 to 3.55 ppm is higher than expected (23H instead of 19H). Glycomacromolecule **25** was not purified by preparative RP-HPLC as all previously presented glycomacromolecules so that this integral size might be explained by PEG residues from Tentagel® resin after cleavage that could not be removed by precipitation in diethylether. The singlet signal at 1.93 ppm can be assigned to the acetate group present as counter ion after ligand exchange. Due to the formation of different DCL components in solution sharpness of NMR signals is lost. In addition to the signal for the aldehyde proton the signal for the imine proton can be found.

^{1}H-NMR (600 MHz, D_2O): δ(ppm) = 10.03-9.96 (m, 0.5H, -C**H**(O)- (AL)), 8.05-7.76 (m, 5H, Ar-H, Ar-H (AL)), 7.63-7.53 (m, 0.5H, -C**H**(N)- (imine)), 4.67–4.60 (m, 2H, -$OCH_2C\mathbf{H}_2$N- (side chain)), 4.10–4.04 (m, 1H, -$OC\mathbf{H}_2CH_2$N- (side chain)), 4.02–3.95 (m, 1H, -$OC\mathbf{H}_2CH_2$N- (side chain)), 3.93–3.88 (m, 1H, Man-H), 3.87-3.83 (m, 1H, Man-H), 3.78–3.55 (m, 23H, -$OC\mathbf{H}_2C\mathbf{H}_2$O- (EDS), -$NHCH_2C\mathbf{H}_2$O- (EDS), Man-H), 3.52–

3.48 (m, 2H, $NH_2CH_2C\mathbf{H}_2NH$- (EDA)), 3.47-3.41 (m, 4H, C(O)NHC$\mathbf{H}_2CH_2$N- (TDS)), 3.41-3.28 (m, 12H, -C(O)NHC$\mathbf{H}_2C\mathbf{H}_2$N- (TDS), -NHC$\mathbf{H}_2CH_2$O- (EDS)), 3.15 (t, ^3J= 5.6 Hz, 2H, $NH_2C\mathbf{H}_2CH_2NH$- (EDA)), 3.06–2.95 (m, 3H, Man-H, -NC(O)$CH_2C\mathbf{H}_2$- (side chain)), 2.78 (td, ^3J=1.4 Hz, 7.3 Hz, 2H, -NC(O)C$\mathbf{H}_2CH_2$- (side chain)), 2.57–2.37 (m, 12H, -C(O)C$\mathbf{H}_2C\mathbf{H}_2$C(O)-).

MALDI-TOF-MS for $C_{51}H_{82}N_{12}O_{19}$: $[M+Na]^+$ calcd. 1189.6, found 1189.7, [imine ring+Na]$^+$ calcd. 1171.6, found 1171.6, $[M_2+Na]^+$ calcd. 2338.2, found 2338.3, $[M_3+Na]^+$ calcd. 3486.7, found 3486.9.

RP-HPLC (linear gradient from 0-50% eluent B in 30 min at 25 °C): t_r= 10.1 min.

Man(7)-13-EDA(1)-EDS(2,3,4,5,6,8,9,10,11,12)-AL(13), **26**

Compound **26** was obtained in a yield of 45%. The anomeric proton of mannose could not be examined in ^{1}H-NMR due to the overlaying signal of the residual solvent. Integration of EDS protons in the range of 3.79 to 3.57 ppm is higher than expected (97H instead of 84H). Glycomacromolecule **26** was not purified by preparative RP-HPLC as all previously presented glycomacromolecules so that this integral size might be explained by PEG residues from Tentagel® resin after cleavage that could not be removed by precipitation in diethylether. The singlet signal at 1.94 ppm can be assigned to the acetate group present as counter ion after ligand exchange. Due to the formation of different DCL components in solution sharpness of NMR signals is lost. In addition to the signal for the aldehyde proton the signal for the imine proton can be found.

^{1}H-NMR (600 MHz, D_2O): δ(ppm) = 10.03 (s, 0.8H, -C$\mathbf{H}$(O)- (AL)), 8.10-7.79 (m, 5H, Ar-H, Ar-H (AL)), 7.64-7.59 (m, 0.2H, -C$\mathbf{H}$(N)- (imine)), 4.66–4.61 (m, 2H, -$OCH_2C\mathbf{H}_2$N- (side chain)), 4.12–4.05 (m, 1H, -OC$\mathbf{H}_2CH_2$N- (side chain)), 3.95–3.89 (m, 1H, -OC$\mathbf{H}_2CH_2$N- (side chain)), 3.87-3.84 (m, 1H, Man-H), 3.79–3.57 (m, 97H, -OC$\mathbf{H}_2C\mathbf{H}_2$O- (EDS), -NHC$H_2C\mathbf{H}_2$O- (EDS), Man-H), 3.53–3.44 (m, 6H, $NH_2CH_2C\mathbf{H}_2NH$- (EDA)), -C(O)NHC$\mathbf{H}_2CH_2$N- (TDS)), 3.42-3.31 (m, 44H, -C(O)NHC$\mathbf{H}_2C\mathbf{H}_2$N- (TDS), -NHC$\mathbf{H}_2CH_2$O- (EDS)), 3.15 (t, ^3J= 5.9 Hz, 2H, $NH_2C\mathbf{H}_2CH_2NH$- (EDA)), 3.06–2.97 (m, 3H, Man-H, -NC(O)$CH_2C\mathbf{H}_2$- (side chain)), 2.80 (t, ^3J= 7.3 Hz, 2H, -NC(O)C$\mathbf{H}_2CH_2$- (side chain)), 2.59–2.45 (m, 44H, -C(O)C$\mathbf{H}_2C\mathbf{H}_2$C(O)-).

MALDI-TOF-MS for $C_{131}H_{226}N_{28}O_{51}$: $[M+Na]^+$ calcd. 3030.6, found 3030.8.

RP-HPLC (linear gradient from 0-50% eluent B in 30 min at 25 °C): t_r= 14.1 min.

Man(2,8,14)-15-EDA(1)-EDS(3,4,5,6,7, 9,10,11,12,13)-AL(14), **27**

Compound **27** was obtained in a yield of 26%. The anomeric proton of mannose could not be examined in ^{1}H-NMR due to the overlaying signal of the residual solvent. Integration of EDS protons in the range of 3.76 to 3.59 ppm is higher than expected (152H instead of 89H). Glycomacromolecule **27** was not purified by preparative RP-HPLC as all previously presented glycomacromolecules so that this integral

size might be explained by PEG residues from Tentagel® resin after cleavage that could not be removed by precipitation in diethylether. The singlet signal at 1.95 ppm can be assigned to the acetate group present as counter ion after ligand exchange. Due to the formation of different DCL components in solution sharpness of NMR signals is lost. In addition to the signal for the aldehyde proton the signal for the imine proton can be found.

^{1}H-NMR (600 MHz, D_2O): δ(ppm) = 10.04 (s, 0.5H, -C**H**(O)- (AL)), 8.07-7.63 (m, 7H, Ar-H, Ar-H (AL)), 7.62-7.49 (m, 0.5H, -C**H**(N)- (imine)), 4.65–4.62 (m, 6H, -OCH_2C**H**$_2$N- (side chain)), 4.12–4.06 (m, 3H, -OC**H**$_2CH_2$N- (side chain)), 3.95–3.89 (m, 3H, -OC**H**$_2CH_2$N- (side chain)), 3.87-3.81 (m, 6H, Man-H), 3.76–3.59 (m, 152H, -OC**H**$_2C$**H**$_2$O- (EDS), -$NHCH_2C$**H**$_2$O- (EDS), Man-H), 3.51–3.44 (m, 14H, NH_2CH_2C**H**$_2$NH- (EDA)), -C(O)NHC**H**$_2CH_2$N- (TDS)), 3.41-3.36 (m, 52H, -C(O)NHC**H**$_2C$**H**$_2$N- (TDS), -NHC**H**$_2CH_2$O- (EDS)), 3.15 (t, ^3J= 5.9 Hz, 2H, NH_2C**H**$_2CH_2$NH- (EDA)), 3.06–2.98 (m, 9H, Man-H, -$NC(O)CH_2C$**H**$_2$- (side chain)), 2.82-2.78 (m, 6H, -$NC(O)C$**H**$_2CH_2$- (side chain)), 2.57–2.46 (m, 52H, -$C(O)C$**H**$_2C$**H**$_2$C(O)-).

MALDI-TOF-MS for $C_{173}H_{294}N_{40}O_{69}$: $[M+Na]^+$ calcd. 4059.1, found 4059.3.

RP-HPLC (linear gradient from 0-50% eluent B in 30 min at 25 °C): t_r= 13.4 min.

6. Appendix

6.1 List of Abbreviations

General Abbreviations

Abbreviation	*Definition*
AuNP	gold nanoparticle
cAuNP	citrate stabilized gold nanoparticle
calcd.	calculated
Cer	ceamide
CMC	critical micelle concentration
CRD	carbohydrate recognition domain
DCC	dynamic combinatorial chemistry
DCL	dynamic combinatorial library
DLVO	Derjaguin, Landau, Verwey, Overbeek
DNA	deoxyribonucleic acid
e.g.	exempli gratia (for example)
EPR	enhanced permeation and retention
ER	endoplasmatic reticulum
et al.	et alii (and others)
glyco-AuNP	glyco-gold nanoparticle
NP	nanoparticle
rAuNP	rod shaped gold nanoparticle
rel.	relative
RU	resonance unit
UV	ultraviolet
vs.	versus

Chemicals and Lectins

Abbreviation	*Trivial or IUPAC name*
$AgNO_3$	silver nitrate
Alloc	allyloxycarbonyl
Au or Au^0	gold
Au^{3+}	gold(III)
$AuCl_4^-$	gold tetrachloride
Boc	tert-butyloxycarbonyl
BOP	benzotriazol-1-yl-oxy-tris-(dimethylamino)-phosphonium hexafluorophosphate
BSA	bovine serum albumin
CA	carbonic anhydrase
Ca^{2+}	calcium (II)
$CaCl_2$	calcium chloride
$CDCl_3$	deuterated chloroform
ChlorH	chlorpromazine hydrochloride
$CHCl_3$	chloroform
CO_2	carbon dioxide
ConA	Concanavalin A

CTAB	cetyl trimethylammonium bromide
Cu	copper
$CuSO_4$	copper sulfate
CytoD	cytochalasin D
D_2O	deuterium oxide
DCC	*N,N'*-dicyclohexylcarbodiimide
DBF	dibenzofulvene
DCM	dichloromethane
DIPEA	*N,N*-diisopropylethylamine
DMF	dimethylformamide
DMSO	dimethyl sulfoxide
DMSO-d_6	deuterated dimethyl sulfoxide
DTT	dithiothreitol
DVB	divinylbenzene
E. coli	*Escherichia coli*
EDA	ethylene diamine
EDC	1-ethyl-3-(3-dimethylaminopropyl)carbodiimide
EMEM	Eagle's Minimum Essential Medium
Et_2O	diethylether
EtOH	ethanol
FBS	fetal bovine serum
FITC	fluoresceineisothiocyanate
Fmoc(-Cl)	9-fluorenylmethyloxycarbonyl-(chloride)
HATU	2-(1H-7-azabenzotriazol-1-yl)-1,1,3,3-tetramethyl uronium hexafluorophosphate
$HAuCl_4$	chloroauric acid
HCl	hydrochloric acid
HEPES	4-(2-hydroxyethyl)-1-piperazineethanesulfonic acid
HF	hydrofluoric acid
HIP/PAP or Reg3A	hepatocarcinoma-intestine-pancreas/ pancreatitis-associated protein
HNO_3	nitric acid
H_2O	water
H_2SO_4	sulphuric acid
HMPA	hexamethylphosphoric triamide
HOBt	*N*-hydroxybenzotriazole
KCl	potassium chloride
K_2CO_3	potassium carbonate
LBB	lectin binding buffer
LiCl	lithium chloride
MeCN	acetonitrile
MeOH	methanol
Mn^{2+}	manganese (II)
$MnCl_2$	manganese (II) chloride
Na_2SO_4	sodium sulfate
$NaBH_4$	sodium borohydride
$NaBH_3CN$	sodium cyanoborohydride
NaCl	sodium chloride
NaH_2PO_4	sodium dihydrogen phosphate
$NaHCO_3$	sodium hydrogen carbonate
NaN_3	sodium azide

NaOH	sodium hydroxide
NEt_3	triethylamine
NHS	*N*-hydroxysuccinimide
NMP	*N*-methyl-2-pyrrolidon
MβCD	methyl-β-cyclodextrin
OMe	methoxy group
PAA	poly(amidoamine)
PBS	phosphate buffered saline
PEG	polyethylene glycol
Pen/Strep	penicillin/streptomycin
PNA	peanut agglutinin
PF_6^-	hexafluorophosphate anion
PS	polystyrene
PyBOP	benzotriazol-1-yl-oxytripyrrolidinophosphonium hexafluorophosphate
RCA_{120}	ricinus communis agglutinin
TBO	toluidine blue O
TCEP	tris(2-carboxyethyl)phosphine hydrochloride
TFA	trifluoroacetic acid
THF	tetrahydrofuran
TIPS	triisopropylsilane
TOAB	tetraoctylammonium bromide
Trt-(Cl)	trityl-(chloride)
UPEC	uropathogenic *Escherichia coli*

Building Blocks

Abbreviation	*Definition*
ADS	Alloc – Diethylenetriamine – Succinic acid
AL	4-formylbenzoic acid
AR	4-(Fmoc-aminomethyl)benzoic acid
BADS	Benzyl Azide – Diethylenetriamine – Succinic acid
BDS	Boc – Diethylenetriamine – Succinic acid
CDS	Cystamine – Diamine – Succinic acid
DDS	Double bond − Diethylenetriamine − Succinic acid
EDS	Ethylene glycol – Diamine – Succinic acid
HDS	Hexyl – Diamine – Succinic acid
MDS	Methyl succinyl – Diethylenetriamine − Succinic acid
ODS	Octyl – Diamine – Succinic acid
SDS	Short – Diamine – Succinic acid
TDS	Triple bond − Diethylenetriamine − Succinic acid

Monosaccharides

Abbreviation	*Trivial Name*
Man	α-D-mannose
MeMan	methyl-α-D-mannose
Fuc	α-L-fucose

Gal	D-galactose
GalNAc	D-*N*-acetylgalactose
Glc	D-glucose
GlcNAc	D-*N*-acetylglucose
Lac	β-D-lactose
NeuAc	sialic acid
pNMan	p-nitrophenyl α-D-mannose

Amino Acids

Abbreviation	*Trivial Name*
Asn	L-asparagine
Cys	L-cysteine
Gly	L-glycine
Ser	L-serine
Thr	L-threonine
Tyr	L-tyrosine

Methods and Instruments

Abbreviation	*Definition*
ATRP	atom transfer radical polymerization
^{13}C	carbon with 13 atomic mass units
^{19}F	fluor with 19 atomic mass units
^{1}H	hydrogen with 1 atomic mass unit
CuAAC	copper(I)-catalyzed azide-alkyne cycloaddition
DLS	dynamic light scattering
ELLA	enzyme-linked lectin assay
ESI-MS	electrospray ionization mass spectrometry
FACS	fluorescence-activated cell sorting
HPCL	high-performance liquid chromatography
HR-ESI-MS	high resolution – electrospray ionization – mass spectrometry
ICP-MS	inductively coupled plasma – mass spectrometry
ITC	isothermal titration calorimetry
LSPR	localized surface plasmon resonance
MALDI-TOF-MS	matrix-assisted laser desorption ionization – time of flight mass spectrometry
NMR	nuclear magnetic resonace spectroscopy
NMRP	nitroxide-mediated radical polymerization
PET	positron emission tomography
PSA	phenol sulphuric acid method
PTT	photothermal therapy
Q-TOF	quadrupole – time of flight
RAFT	reversible addition fragmentation chain transfer
ROMP	ring-opening metathesis polymerization
RP-HPLC	reverse phase-high pressure liquid chromatography
SPS	solid phase synthesis
SPPS	solid phase peptide synthesis
SPPoS	solid phase polymer synthesis
SPR	surface plasmon resonance

TEM	transmission electron microscopy
TLC	thin layer chromatography
UV-Vis	ultraviolet/visible
VWD	variable wavelength detector

Units and Symbols

Abbreviation	*Definition*
%	percent
β	enhancement factor for multivalent binding
°C	degree Celsius (centigrade)
Δδ	chemical shift change
δ	chemical shift
µL	microliter(s)
µM	micromolar
µm	micrometer
µmol	micromole
Å	ångström (10-10 meter)
c	concentration
cm	centimetre
d	doublet
Da	dalton
dd	doublet of doublets
eq	equivalents
FV	functional valency
ΔG	Gibbs free energy change
g	gram(s)
g/mol	gram per mole(s)
ΔH	molar enthalpy change
h	hour
Hz	hertz
IC_{50}	half maximum inhibitory concentration
J	coupling constant
K_A	binding constant
K_D	dissociation constant
$K_{D,app}$	apparent dissociation constant
kDA	kilodalton
ln	natural logarithm
M	molarity (mole(s) per liter)
m	multiplet
mAu	milliabsorption units
mbar	millibar
MCK	multi cycle kinetic
mg	milligram(s)
mg/mL	milligram(s) per milliliter(s)
MHz	Megahertz
min	minute(s)
mL	milliliter(s)
mL/min	milliliter(s) per minute(s)
mM	millimolar
mmol	millimole(s)

mmol/g	millimole(s) per gram
mV	millivolt
m/z	mass-to-charge ratio
n	stochiometry in carbohydrate lectin complexes
nM	nanomolar
nm	nanometer(s)
pH	potentia hydrogenii
ppb	parts per billion
ppm	parts per million
rcf	relative centrifugal force
R	general gas constant
R_H	hydrodynamic radius
RIP	relative inhibitory potency
RIP_{vc}	valency corrected relative inhibitory potency
R_{max}	maximal response
rpm	rounds per minute
RT	room temperature
s (NMR)	singlet
s (time interval)	second
SV	structural valency
ΔT	temperature difference
T	temperature
t (NMR)	triplet
t	time
t_R	retention time (RP-HPLC/LC-MS)
vol%	volume percent
SCK	single cycle kinetic
ΔS	entropy change
ΔS_{config}	entropy of configuration
ΔS_{rot}	entropy of rotation
ΔS_{solv}	entropy of solvation
ΔS_{trans}	entropy of translation

6.2 List of Figures

Figure 1: Schematic overview of the different parts of this thesis. XVI
Figure 2: Schematic representation of the cell surface presented as cross-section through the membrane. The different glycosylation pathways within the cell are also schematically outlined (Adapted from [6]. Reprinted with permission from AAAS). 2
Figure 3: Examples of crystal structures and schematic representation of representatives of different legume lectin families (Protein Database codes: 1jbc, 3zl2, 4lbq, 4mth). 6
Figure 4: Schematic representation of mannose binding in the ConA binding site. Green arrows indicate hydrogen bonding. The hydroxyl group not involved in hydrogen bonding is highlighted with a grey circle (adapted from [] with permission from Elsevier)..... 8
Figure 5: Schematic representation of galactose binding in the human Galectin-1 binding site. Green arrows indicate hydrogen bonding. The hydrophobic B face of galactose is highlighted with the grey oval. It is involved in C-H/π-interaction with the central tryptophan residue indicated by black dashed lines (adapted from [57] with permission from Elsevier)..... 9
Figure 6: Schematic representation of mannose binding a C-type serum lectin and the involvement of the metal ion (yellow sphere) in carbohydrate binding. Green arrows represent hydrogen bonding and yellow dashed lines coordinative bonds (adapted from [57] with permission from Elsevier)..... 11
Figure 7: Multivalent binding modes discussed for enhancing multivalent binding avidity: chelation, receptor clustering, binding and sliding, steric shielding and subsite association. 13
Figure 8: Ligand and receptor based approaches for glycomimetic design and schematic representatives for polymeric, spherical and defined glycomimetic scaffolds. 17
Figure 9: Schematic representation of the solid phase beads and different resin types, the Merrifield PS resin and the Tentagel® resin. 19
Figure 10: Schematic illustration of the principle of solid phase peptide synthesis (SPPS) together with exemplary illustrations of the linker group, protecting groups and activation reagents. The deprotection scheme for Fmoc and the activation scheme for BOP/PyBOP is also shown..... 20
Figure 11: Overview of the solid phase polymer synthesis of precision glycomacromolecules. Exemplary structures for functional (left) and spacer (right) building blocks are listed below. For functional building blocks the structures for TDS[95], DDS[97], ADS[96], MDS[99], BADS[101] and BDS[96] are shown. For spacer building blocks the structures for EDS[95], HDS[], SDS[104] and CDS[104] are shown..... 23
Figure 12: Overview of the four parts of the results and discussion section..... 26
Figure 13: Schematic overview of glycomimetic design. By changing spacing, architecture, valency and hydrophobicity the perfect match for the lectin binding site is obtained. 28

Figure 14: Overview of structural design features varied in the first part of this work: Carbohydrate Spacing with constant molecular weight (left), carbohydrate arrangement along the scaffold from symmetric to asymmetric (middle) and backbone hydrophobicity (right). 31
Figure 15: Overview of building blocks employed in SPPoS in this work. 33
Figure 16: ^{19}F-NMR (300 MHz, D_2O) before (left) and after (right) HCl treatment and freeze drying in three cycles. The red circles highlight the signal reduction in the NMR spectrum. 36
Figure 17: ^{1}H-NMR (300 MHz, D_2O) before (bottom) and after (top) HCl treatment. The red cycles highlight the impurities resulted from HCl treatment. 37
Figure 18: Overview of glycomacromolecule structures of series 1 to 3. The glycomacromolecules presented, vary in different structural features. In series 1 the carbohydrate spacing is varied (**1**-**1c**). In series 2 the carbohydrate arrangement is varied (**2**-**2a**). For both series 1 and 2, carbohydrate valency and the molecular weight are kept constant. In series 3 the carbohydrate valency and backbone hydrophobicity are varied (**3**-**5b**). In addition, glycomacromolecules bearing β-D-galactopyranoside moieties are presented that function as negative controls. Glycomacromolecules **3a**, **4a** and **4b** were previously presented but no TFA removal was performed for these structures so that their synthesis was repeated in this work.[132] Glycomacromolecules **4** and **5** were also presented previously and were included in this work for comparability.[120] Glycomacromolecules **2**, **2a** and **6b** were provided by members of the Hartmann group[139,] [adapted from [188] with permission from John Wiley and Sons]. 38
Figure 19: Comparison of ^{1}H-NMR (600 MHz, D_2O) spectra of trivalent glycomacromolecules (**4**, **4b**, **4d**) with EDS, ODS or AR spacer. Spacer protons are highlighted in red. 42
Figure 20: Exemplary MALDI-TOF-MS (left) and HR-ESI (right) spectrum of glycomacromolecule **4**. ... 43
Figure 21: RP-HPLC chromatogram (95/5 H_2O/MeCN with 0.1% formic acid (A) and 5/95 H_2O/MeCN with 0.1% formic acid (B); 100% A to 50% A in 30 min) determined at 214 nm for glycomacromolecules (A) **4**, **4a**, **4b**, **4c**, **4d** and (B) **1**, **1a**, **1b**, **1c** [adapted from [188] with permission from John Wiley and Sons]. 43
Figure 22: (A) Experimental setup of ITC ([]), (B) ITC thermogram and binding isotherm of compound **5a** binding to dimeric ConA at 25 °C. 45
Figure 23: (A) Experimental setup of SPR, (B) Exemplary SPR sensorgram of glycomacromolecule **5a** binding to immobilized ConA at various concentrations at 25 °C, (C) K_D evaluation where the equilibrium response values are plotted against glycomacromolecule concentration [adapted from [] - Published by The Royal Society of Chemistry]. 47
Figure 24: K_D values derived from ITC and SPR, A: Trivalent glycomacromolecules differing in carbohydrate spacing, B: Trivalent glycomacromolecules varying in backbone hydrophobicity. Structures $\mathbf{x_1}$ and $\mathbf{x_2}$ with thiahexyl- and phenyl- linker were presented previously.[120] ITC results of

these structures are included for comparison [adapted from [188] with permission from John Wiley and Sons]. 52
Figure 25: Exemplary chemical shift changes of glycomacromolecule **5a** at varying phenol concentrations. Chemical shift changes for linker and spacer protons are significant (left) while chemical shift changes for the mannopyranoside unit are small or non-existent (right) [adapted from [188] with permission from John Wiley and Sons]. 54
Figure 26: ^{1}H-NMR chemical shift changes ($\Delta\delta$(ppb)= $\delta_{phenol} - \delta_{phenol\text{-}free}$) of glycomacromolecules **5**, **5a** and **5b** with 16 mM phenol in D_2O represented by circle size and color. The aromatic region of ^{1}H-NMR spectra for 5 mM glycomacromolecule solutions is exemplary shown for the triazole proton of the linker (c) without (black) and with (grey) phenol in D_2O [adapted from [188] with permission from John Wiley and Sons]. 55
Figure 27: Schematic presentation of the bacterial adhesion inhibition assay with E. coli FimH receptor and glycomacromolecule **4a** as inhibitor. Exemplary IC_{50} curves determined for **4a** in comparison to references methyl α-D-mannose and p-nitrophenyl α-D-mannose are also shown [adapted from [188] with permission from John Wiley and Sons]. 58
Figure 28: Advantageous properties of glyco-AuNPs resulting from metallic core and the glyco-coating [adapted from [216] with permission from Beilstein Journal of Organic Chemistry]. 61
Figure 29: The two commonly employed approaches for AuNP synthesis. A: Brust method and B: Turkevich method.[218,219] 62
Figure 30: Overview of structural design features varied in the second part of this work. Glycomacromolecules are varied in backbone hydrophobicity and valency and installed on AuNP surface. 65
Figure 31: Overview of building blocks and natural amino acids employed in SPPoS (left) and overview of glycomacromolecule structures for AuNP functionalization (right).[100] 66
Figure 32: A. RP-HPLC chromatogram of glycomacromolecule **8** displaying the product, thioether and disulphide peaks. B: MALDI-TOF-MS of glycomacromolecule **8** with m/z peaks for the product, thioether and disulphide. C: Mechanism of thioether formation suggested in literature.[100,233] 68
Figure 33: Exemplary ^{1}H-NMR (600 MHz, D_2O) of glycomacromolecule **7**. Protons of natural amino acids L-cysteine and L-glycine are highlighted in red. 69
Figure 34: Exemplary ^{1}H-NMR (600 MHz, D_2O) and MALDI-TOF spectra of glycomacromolecule **7a**. Protons of natural amino acids L-cysteine and L-glycine as well as protons of N-ethylmaleimide are highlighted in red. 70
Figure 35: A: TEM image of citrate stabilized AuNPs (cAuNPs). Inset: Sketch of citrate stabilized AuNP, B: TEM derived histogram of citrate stabilized AuNPs with derived diameter of 14.1±1.2 nm, C: Ligand

exchange reaction of citrate stabilized cAuNPs with glacomacromolecules **7**-**9** resulting in glyco-AuNPs **10**-**12**.[100] 71
Figure 36: A: UV-Vis spectra of cAuNPs in comparison to glyco-AuNPs **10**-**12**. B: Autocorrelation function and Cumulant plot determined by DLS of cAuNPs in comparison to glyco-AuNPs **10**-**12**.[100] 72
Figure 37: A: UV-Vis spectrum recorded after PSA treatment of glyco-AuNP **10** and cAuNPs demonstrating the background signal at 490 nm. B: Reaction Scheme for PSA. C: Schematic illustration of TBO interaction. 74
Figure 38: UV-Vis absorbance spectra of cAuNP and glyco-AuNPs **10**-**12** testing for sodium chloride stability after 24 h incubation time.[100] 75
Figure 39: Aggregation behaviour of glyco-AuNPs in presence of increasing ConA concentration: A: Normalized absorbance (normalized to absorbance at 400 nm) at 700 nm plotted against ConA concentration, different scenarios of glyco-AuNP ConA binding are presented schematically; B: Photograph of 96-well plate (background removed); UV-Vis absorbance spectra in presence of increasing ConA concentration for glyco-AuNP C: **10**, E: **11**, F: **12**; D: UV-Vis absorbance spectra in presence of increasing ConA concentration of glyco-AuNP **10** after addition of excess of MeMan.[100] 77
Figure 40: Kinetic analysis of glyco-AuNP interaction with ConA by A: UV-Vis absorbance at 700 nm and B: Representative evolutions of the hydrodynamic radii obtained from time-dependent DLS measurements at $K_{D,app}$ concentrations of ConA (for all curves see Appendix 269).[100] 80
Figure 41: Exemplary SPR sensorgram for solutions of 100 nM ConA incubated with serial dilutions of A: glyco-AuNP **12** and B: N-ethylmaleimide capped glycomacromolecule **9a**; C: resulting IC_{50} curve fitted to Hill1 function for glyco-AuNP **12** and N-ethylmaleimide capped glycomacromolecule **9a** (for all curves see Appendix 270-273).[100] 82
Figure 42: UV-Vis absorbance spectra of spherical and rod shaped AuNPs. The absorbance maximum for spherical AuNPs lies in the range of 520 nm so that green laser light can be used for PTT. The higher absorption cross section for rod shaped AuNPs lies in Near-IR (NIR) region so that laser light in this wavelength range can be used for effective PTT. 85
Figure 43: Illustration of the enhanced permeation and retention (EPR) effect of PEG functionalized AuNPs in malignant tissue (adapted from []). 86
Figure 44: Overview of building blocks employed in SPPoS. 88
Figure 45: Overview of macromolecular structures obtained after SPPoS. 89
Figure 46: Comparison of ^{1}H-NMR (600 MHz, D_2O) spectra of trivalent glycomacromolecule **16** with the three different end groups **a**, **b** and **c**. End group protons are highlighted in red. 90
Figure 47: A: RP-HPLC chromatogram (95/5 H_2O/MeCN with 0.1% formic acid (A) and 5/95 H_2O/MeCN with 0.1% formic acid (B); 100% A to 50% A in 30 min) determined at 214 nm for glycomacromolecules

16a, **b** and **c**, B: Exemplary MALDI-TOF-MS of glycomacromolecule **16b**, C: Exemplary HR-ESI of glycomacromolecule **16b**. 92
Figure 48: A: TEM image of citrate stabilized AuNPs (cAuNPs). The inset shows the sketch of a citrate stabilized AuNP. B: TEM derived histogram of citrate stabilized AuNPs with derived diameter of 13.7 ± 1.4 nm. C: Ligand exchange reaction of citrate stabilized AuNPs with a 1/9 ratio of dye functionalized macromolecule 21 or no dye carrying macromolecule 22 and a lactose carrying glycomacromolecule with varying backbone and end group fragments. 93
Figure 49: A: Exemplary UV-Vis spectra of cAuNPs in comparison to glyco-AuNPs-**13a**. B: Exemplary autocorrelation function determined by DLS of cAuNPs in comparison to glyco-AuNPs-**13a**, C: Exemplary UV-Vis absorbance spectra of glyco-AuNP-**13a** in MilliQ water, PBS buffer and EMEM medium after 48 h in comparison to UV-Vis spectrum of the same glyco-AuNP in MilliQ water at time 0 (for all spectra see Appendix 274-281)..... 94
Figure 50: TEM image of CTAB stabilized rod shaped AuNPs (rAuNPs). B: UV-Vis absorbance spectrum of CTAB stabilized rAuNPs. The inset shows the sketch of a CTAB stabilized rAuNP. C: TEM derived histogram of CTAB stabilized rAuNPs with derived diameter of 16.6 ± 0.8 nm. D: TEM derived histogram of CTAB stabilized rAuNPs with derived length of 73.3 ± 10.2 nm. 97
Figure 51: Schematic illustration of different approaches used for the ligand exchange reaction with all reactions resulting in insufficient stability and accumulation of rAuNPs observed by UV-Vis spectroscopy..... 98
Figure 52: Mean fluorescence obtained for different incubation times (10 nM concentration) (left) and different incubation concentrations (48 h incubation time) (right) for the two glyco-AuNPs **13a-FITC** and **19a-FITC** in RKO cell line in flow cytometry measurement. 100
Figure 53: Percentual cell viability of T3M4, RKO and SK-BR-3 cell lines in presence of 10 nM glyco-AuNP after 48 h incubation at 37 °C and 5% CO_2. Cell viability of unstained cells was set to 100%. MilliQ water was used as vehicle control..... 101
Figure 54: A: Comparison of cell uptake in PBS buffer and full growth medium of glyco-AuNP-**13a-FITC** and -**19a-FITC** in RKO cancer cell line after 24 h incubation at 10 nM concentration. Fluorescence of the unstained control was set to 1, B: Comparison of cell uptake at 37 °C and 4 °C of glyco-AuNP-**13a-FITC** and -**19a-FITC** in RKO cancer cell line after 24 h incubation at 10 nM concentration. Relative and fluorescence corrected values are presented. Fluorescence of the unstained control was set to 1, C: Sketch of glyco-AuNP labelling demonstrating why fluorescence correction is necessary. 103
Figure 55: Obtained (left) and corrected (right) mean fluorescence values in flow cytometry measurements of all glyco-AuNP-FITC in the three different cell lines after 24 h incubation at 37 °C and 5% CO_2 with 10 nM glyco-AuNP-FITC concentration. Fluorescence of the unstained control was set to

1. The dashed black line shows the threshold for the uptake of negative control structures glyco-AuNP-**19-FITC** and AuNP-**20-FITC**. 105
Figure 56: Obtained (left) and corrected (right) mean fluorescence values in repeated flow cytometry measurements of monovalent glyco-AuNP-FITC compounds in the three different cell lines after 24 h incubation at 37 °C and 5% CO_2 with 10 nM glyco-AuNP-FITC concentration. The dashed black line shows the threshold for the uptake of negative control structure AuNP-**20b-FITC**. 106
Figure 57: A: Comparison of cell uptake after 3 and 24 h incubation time, B: Comparison of cell uptake at 2 and 20 µM glycomacromolecule concentration, C: Comparison of cell uptake of 2 µM glycomacromolecule concentration after 24 h incubation time at 4 °C and 37 °C, D: Percentage of cell viability of RKO cell line in presence of 2 and 20 µM glycomacromolecule concentration after 48 h incubation at 37 °C and 5% CO_2. Cell viability of unstained cells was set to 100%. MilliQ water was used as vehicle control. 108
Figure 58: A: Corrected mean fluorescence values in flow cytometry measurement of all glyco-AuNP-FITC in RKO cell line after 24 h incubation at 37 °C and 5% CO_2 with 10 nM glyco-AuNP-FITC concentration. B: ICP-MS results obtained for all glyco-AuNP-FITC in RKO cell line after 24 h incubation at 37 °C and 5% CO_2 with 10 nM glyco-AuNP-FITC concentration. ICP-MS was performed in two different sets of experiments with triplicate determination per experiment. 110
Figure 59: A: Relative mean fluorescence obtained in flow cytometry measurements for the incubation of RKO and SK-BR-3 cells with 10 nM glyco-AuNP-**15b-FITC**, glyco-AuNP-**13b-FITC** and AuNP-**20b-FITC** alone and together with competitors D-lactose and anti-Reg3A-antibody after total incubation of 25 h. Fluorescence for cells treated with glyco-AuNP-**15b-FITC**, glyco-AuNP-**13b-FITC** and AuNP-**20b-FITC**, respectively, was set to 100%, B: ICP-MS results obtained for incubation of RKO cells with 10 nM glyco-AuNP-**15b-FITC** alone and together with anti-Reg3A-antibody as competitor after total incubation of 24 h at 37 °C and 5% CO_2. Wells that were only containing cells and AuNPs were included in the study as control. 111
Figure 60: A: RKO cell viability test with trypan blue for unstained cells and in prescence of endocytosis pathway inhibitors chlorpromazine hydrochloride (ChlorH), methyl-β-cyclodextrin (MβCD) and cytochalasin D (CytoD) after 0, 1 and 4 h, B: Relative mean fluorescence values obtained in flow cytometry measurements for incubation of RKO cells with 20 nM glyco-AuNP-**15b-FITC** and AuNP-**20b-FITC** alone and together with the endocytosis pathway inhibitors chlorpromazine hydrochloride (ChlorH), methyl-β-cyclodextrin (MβCD) and cytochalasin D (CytoD) after total incubation of 4 h. Fluorescence for cells treated with glyco-AuNP-**15b-FITC** and AuNP-**20b-FITC**, respectively, was set to 100%. 114
Figure 61: Schematic illustration of the concept of a dynamic combinatorial library. 116

Figure 62: Overview of structural design features varied in the two different DCL approaches: Backbone hydrophobicity in thiol-disulphide exchange (left) and carbohydrate spacing in imine formation approach (right). 117
Figure 63: Overview of chemical and schematic glycomacromolecule structures for use in DCL. 118
Figure 64: Exemplary ^{1}H-NMR (600 MHz, D2O), RP-HPLC chromatogram (95/5 H_2O/MeCN with 0.1% formic acid (A) and 5/95 H_2O/MeCN with 0.1% formic acid (B); 100% A to 50% A in 30 min) and MALDI-TOF-MS spectrum of glycomacromolecule **23**. Protons of natural amino acid L-cysteine are highlighted in red. 119
Figure 65: A: Color development in the reaction of thiol groups with Elman´s reagent. Development of the amount of thiol groups in solution under atmospheric oxygen over a time period of two weeks for B: glycomacromolecule **23** and C: glycomacromolecule **24**. 120
Figure 66: Exemplary RP-HPLC chromatogram (95/5 H_2O/MeCN with 0.1% formic acid (A) and 5/95 H_2O/MeCN with 0.1% formic acid (B); 100% A to 5% A in 17 min)of compound **23** at 10 mM concentration and pH 8 after two weeks of equilibration under atmospheric oxygen. Broad peaks at time ranges from 4 to 5 and 12 to 13 minutes belong to the blank. The inset shows the magnification of the chromatogram area of interest. 122
Figure 67: RP-HPLC chromatograms (95/5 H_2O/MeCN with 0.1% formic acid (A) and 5/95 H_2O/MeCN with 0.1% formic acid (B); 100% A to 5% A in 17 min) of A: **23**, B: 24 and C: 23 and 24. Broad peaks at time ranges from 4 to 5 and 12 to 13 minutes belong to the blank. 123
Figure 68: Overview of glycomacromolecule structures for use in DCL. 124
Figure 69: A: Schematic Overview of synthetic routes employed to test for optimal coupling of AL building block, B: RP-HPLC chromatogram (95/5 H_2O/MeCN with 0.1% formic acid (A) and 5/95 H_2O/MeCN with 0.1% formic acid(B); 100% A to 5% A in 17 min) of the product obtained by the first route, C: RP-HPLC chromatogram (95/5 H_2O/MeCN with 0.1% formic acid (A) and 5/95 H_2O/MeCN with 0.1% formic acid(B); 100% A to 5% A in 17 min) of the product obtained by route 4. Broad peaks at time ranges from 4 to 5 and 12 to 13 minutes belong to the blank. 125
Figure 70: Exemplary ^{1}H-NMR (600 MHz, D_2O), RP-HPLC chromatogram (95/5 H_2O/MeCN with 0.1% formic acid (A) and 5/95 H_2O/MeCN with 0.1% formic acid (B); 100% A to 50% A in 30 min) and MALDI-TOF-MS spectrum of glycomacromolecule **25**. Protons of EDA and AL moiety as well as of the formed imine bond are highlighted in red. 126
Figure 71: A: Exemplary RP-HPLC chromatogram (95/5 H_2O/MeCN with 0.1% formic acid (A) and 5/95 H_2O/MeCN with 0.1% formic acid (B); 100% A to 5% A in 17 min) of compound **25** at 20 mM concentration and pH 7.4 after 0, 1, 2, 3, 7 and 28 days of equilibration. Broad peaks at time ranges from 4 to 5 and 12 to 13 minutes belong to the blank. B: Evolution of the signal intensity of the

respective DCL compounds as determined by integration of RP-HPLC chromatogram peaks after 0, 1, 2, 3, 7 and 28 days of equilibration. 127
Figure 72: RP-HPLC chromatogram (95/5 H_2O/MeCN with 0.1% formic acid (A) and 5/95 H_2O/MeCN with 0.1% formic acid (B); 100% A to 5% A in 17 min) of compound A: **25**, B: **26**, C: **27** at 0.9 mM concentration and pH 7.4 after one week of equilibration in absence (grey line) and presence (black line) of ConA. Evolution of the signal intensity of the respective DCL compounds as determined by integration of RP-HPLC chromatogram peaks of compound D: **25**, E: **26**, F: **27**. 129
Figure 73: A: RP-HPLC chromatogram (95/5 H_2O/MeCN with 0.1% formic acid (A) and 5/95 H_2O/MeCN with 0.1% formic acid (B); 100% A to 5% A in 17 min) of compounds **25**, **26**, **27** at 0.9 mM concentration and pH 7.4 after one week of equilibration in absence (grey line) and presence (black line) of ConA. B: Evolution of the signal intensity of the respective DCL compounds as determined by integration of RP-HPLC chromatogram peaks. 130
Figure 74: Schematic overview of the results obtained in the different part of this thesis. 136

6.3 List of Schemes

Scheme 1: SPPoS of precision glycomacromolecules varying in backbone composition and ligand distribution 35

Scheme 2: Exchange of TF-acetate by acetate employing a strong anion exchange resin. 37

6.4 List of Tables

Table 1: Coupling efficiency determined by UV absorption at 290 nm for ODS and AR building block. Standard conditions for SPPoS are compared to conditions varied in regard to amount of building block, reaction time, coupling reagent and coupling solvent. Coupling efficiency is reported relative to the coupling efficiency determined for the amino acid valine under the same conditions set to 100% coupling efficiency [reprinted from [188] with permission from John Wiley and Sons].[100] 40

Table 2: ITC-derived thermodynamic parameters of glycomacromolecules varying in carbohydrate spacing and arrangement or backbone hydrophobicity binding to dimeric ConA (acetate buffer pH 5.20±0.01, 25 °C). SPR derived K_D values of glycomacromolecules binding to immobilized dimeric ConA (acetate buffer pH 5.20±0.01, 25 °C) are also included [reprinted from [188] with permission from John Wiley and Sons].[] 49

Table 3: RIP and valency corrected RIP_{VC} values of glycomacromolecules varying in carbohydrate spacing and backbone hydrophobicity determined in bacterial-adhesion inhibition studies with the bacterial lectin FimH. MeMan was set as reference with RIP=1[adapted from [188] with permission from John Wiley and Sons]..... 59

Table 4: DLS derived hydrodynamic radii (R_H) in MilliQ water and degree of glycomacromolecule (GM) functionalization as determined by two methods: phenol sulfuric acid method (PSA) and Toluidine Blue O-titration (TBO). The degree of carbohydrate (C) functionalization and average of occupied surface area were calculated and are also listed.[100] 74

Table 5: $K_{D,app}$ values obtained for glyco-AuNPs **10**-**12** and $K_{D,app}$ values normalized on the number of glycomacromolecules (GM) and carbohydrates (C) presented on one AuNP.[100] 78

Table 6: DLS derived hydrodynamic radii (R_H) for glyco-AuNPs in buffer medium as well as the determined R_H upon exposure to $K_{D,app}$ concentration of Con A after 30 min and after subsequent addition of αMeMan. The values for the absorbance at wavelengths of 700 nm (normalized to absorbance at 400 nm) are an indirect measure for the particle aggregation. Error values for kinetic measurements refer to the root mean square deviation from at least three repetitive experiments.[100] 80

Table 7: IC_{50} and RIP values as measured for glyco-AuNPs **10**–**12** and N-ethylmaleimide capped glycomacromolecules **7a** and **9a** by SPR and derived RIP values corrected for glycomacromolecule (GM) and carbohydrate (C) number.[100] 83

Table 8: DLS derived hydrodynamic radii (R_H) in MilliQ water and relative degree of glycomacromolecule functionalization determined by TBO titration for glyco-AuNP with and without fluorescent properties..... 95

6.5 Analytics

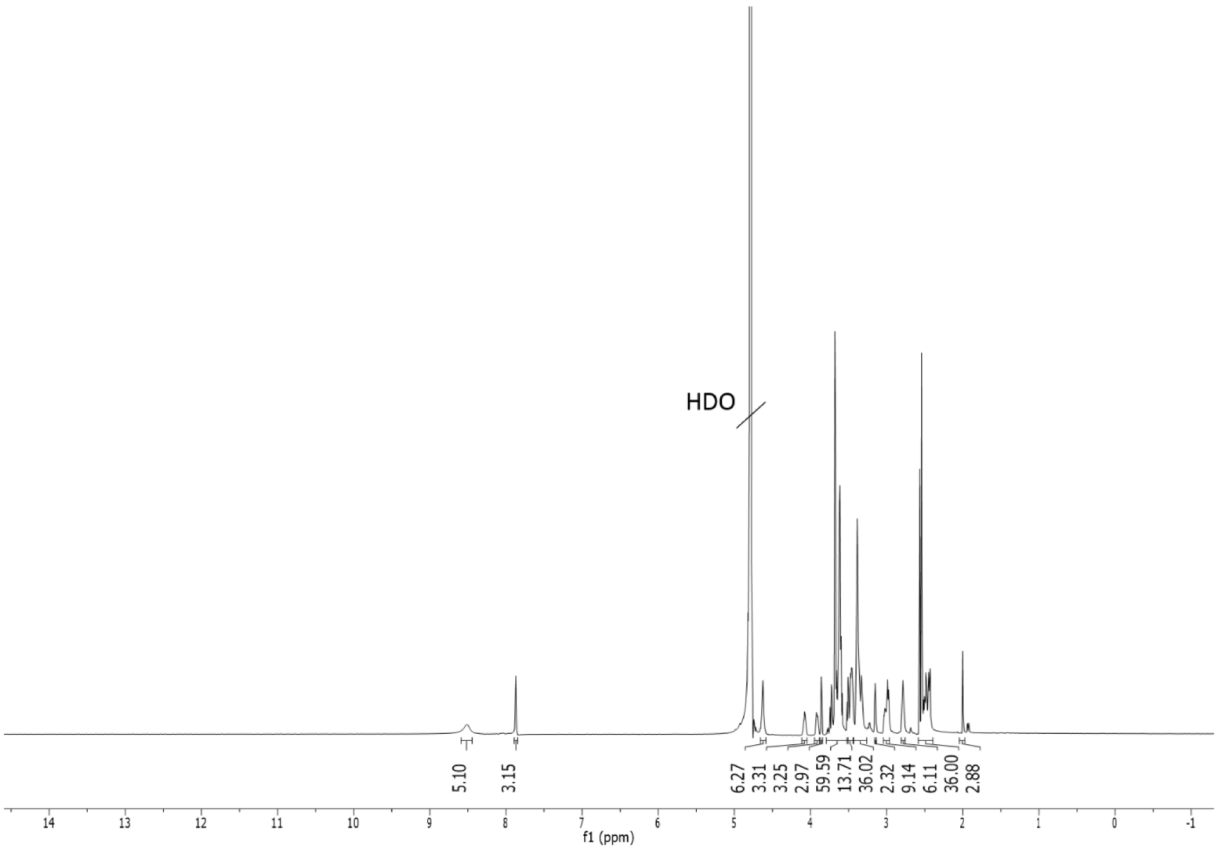

*Appendix 1: ^{1}H-NMR spectrum of **1** (600 MHz, D_2O).*

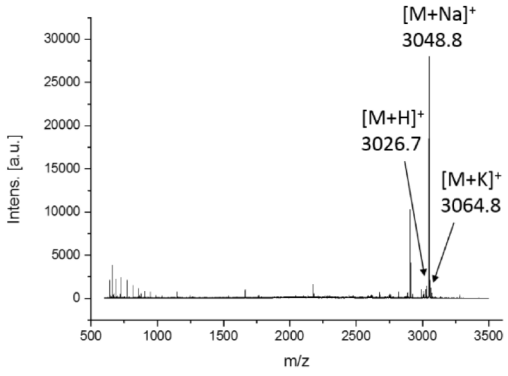

*Appendix 2: MALDI-TOF-MS spectrum of **1**. One further signal with the mass-to-charge ratio of 2906.7 can be found in the spectrum but cannot be assigned to potential by-products.*

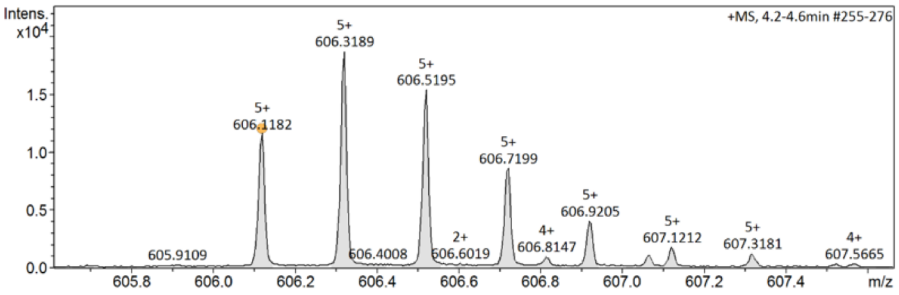

*Appendix 3: HR-MS (ESI⁺ Q-TOF) of compound **1**.*

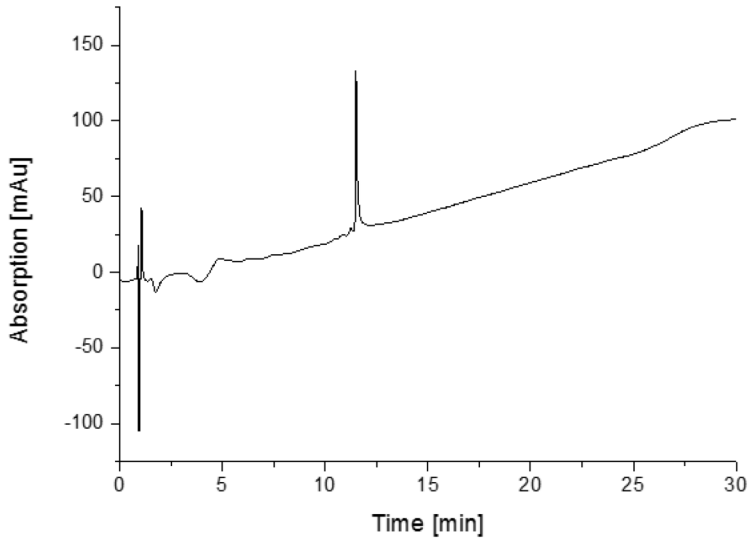

*Appendix 4: RP-HPLC chromatogram (linear gradient from 0-50% eluent B in 30 min at 25 °C) of compound **1**.*

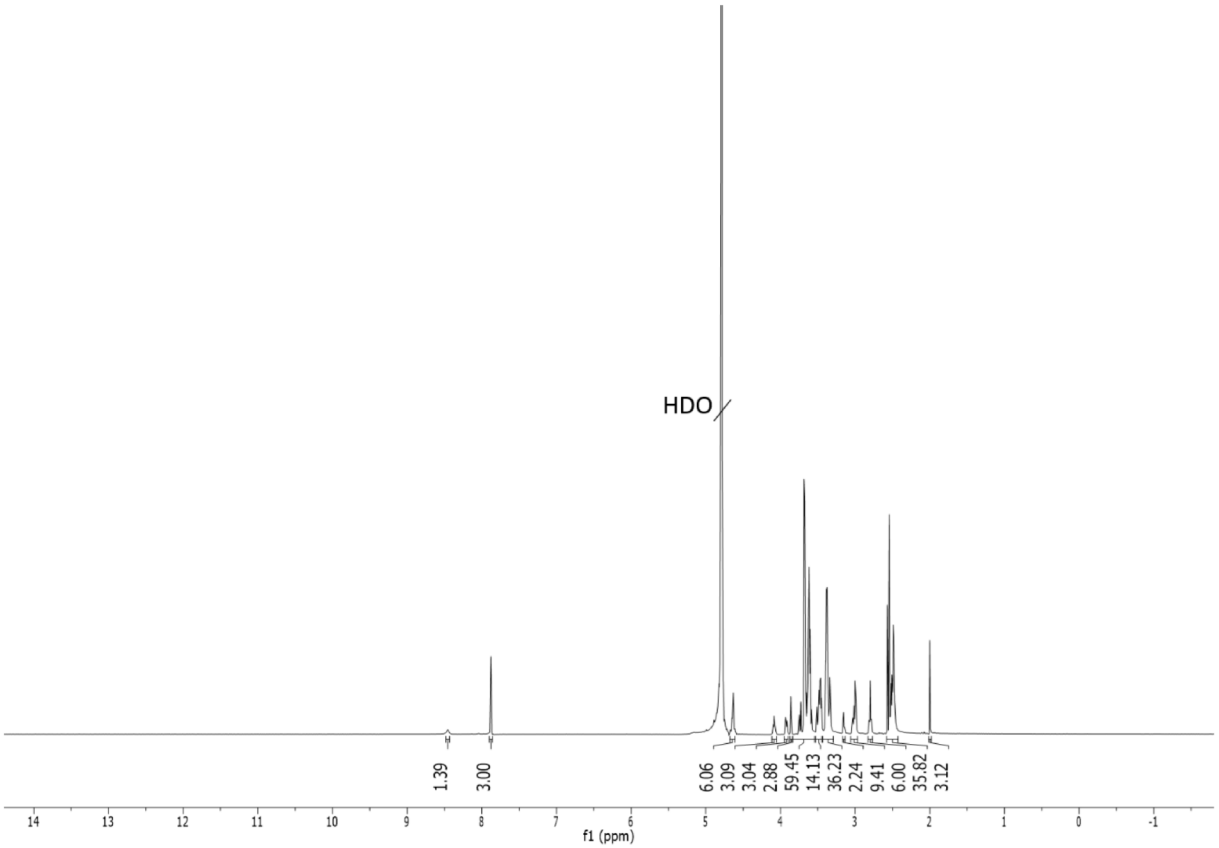

*Appendix 5: ^{1}H-NMR spectrum of **1a** (600 MHz, D_2O).*

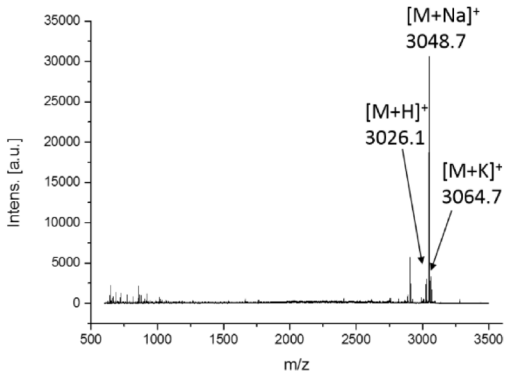

*Appendix 6: MALDI-TOF-MS spectrum of **1a**. One further signal with the mass-to-charge ratio of 2906.6 can be found in the spectrum but cannot be assigned to potential by-products.*

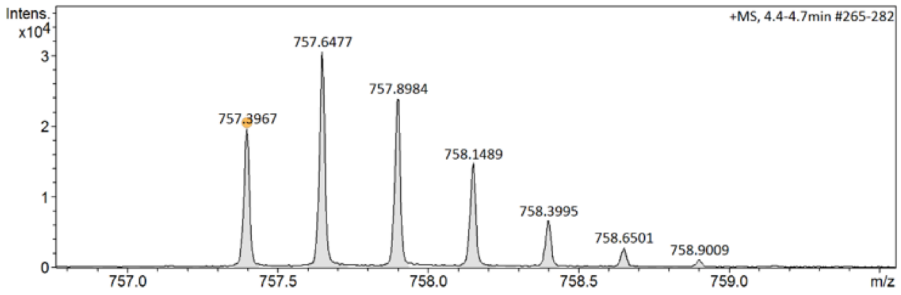

*Appendix 7: HR-MS (ESI⁺ Q-TOF) of compound **1a**.*

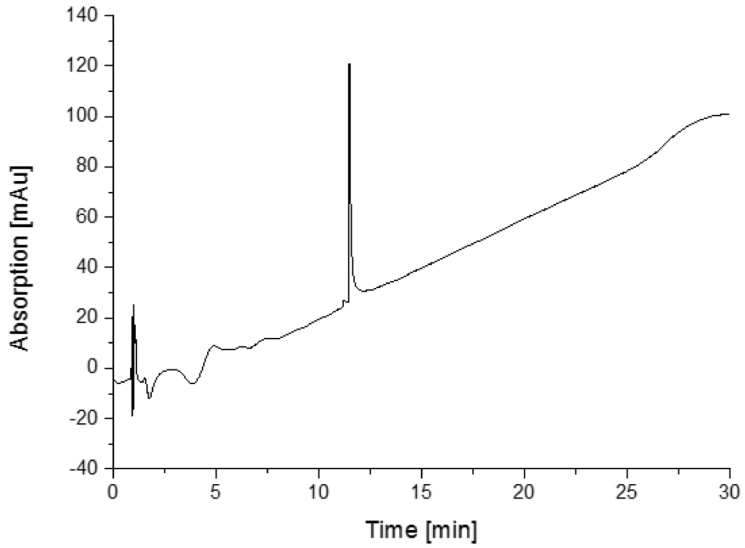

*Appendix 8: RP-HPLC chromatogram (linear gradient from 0-50% eluent B in 30 min at 25 °C) of compound **1a**.*

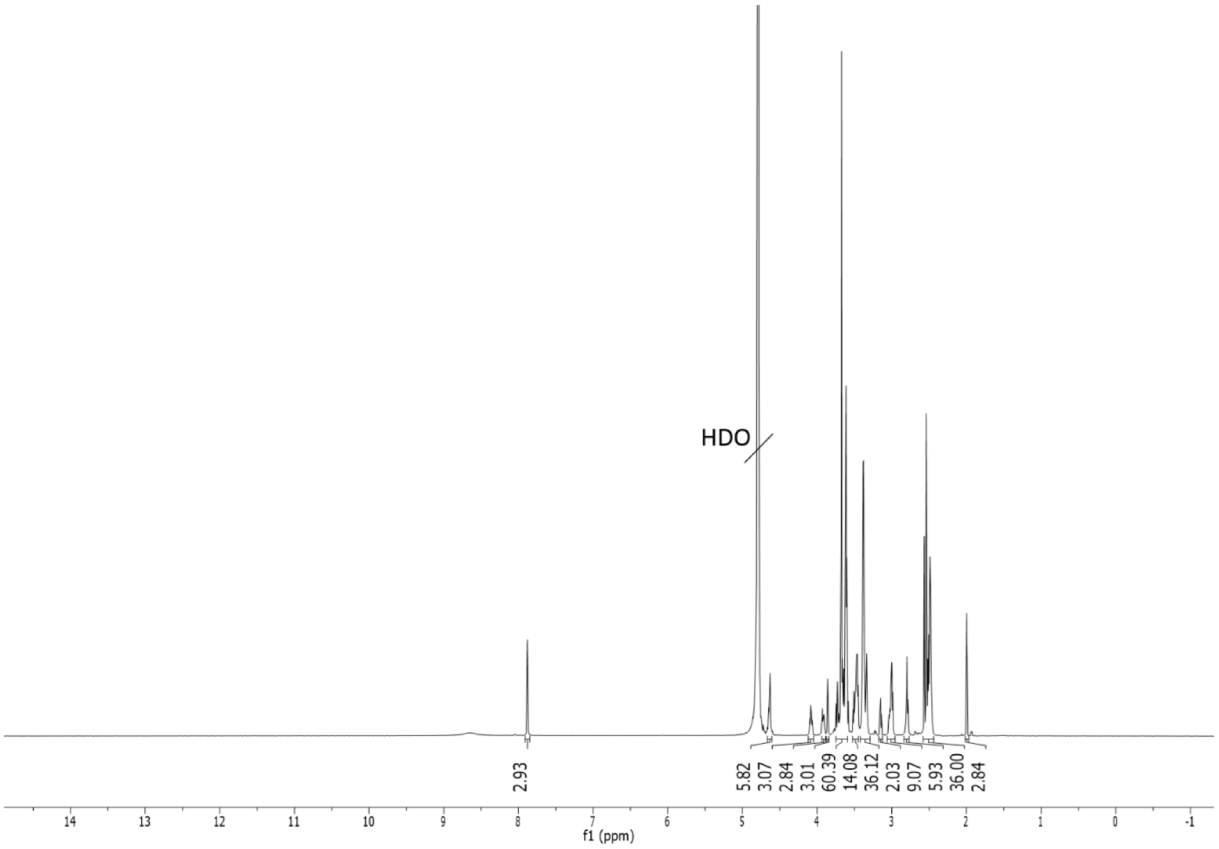

*Appendix 9: ^{1}H-NMR spectrum of **1b** (600 MHz, D_2O).*

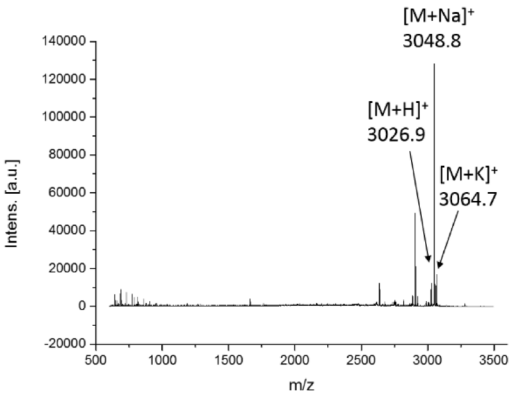

*Appendix 10: MALDI-TOF-MS spectrum of **1b**. One further signal with the mass-to-charge ratio of 2906.6 can be found in the spectrum but cannot be assigned to potential by-products.*

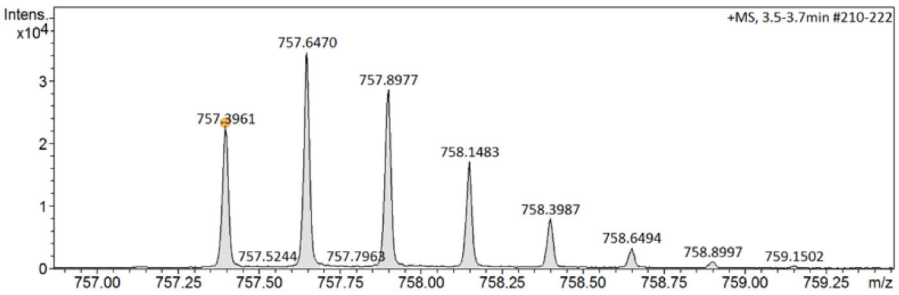

*Appendix 11: HR-MS (ESI⁺ Q-TOF) of compound **1b**.*

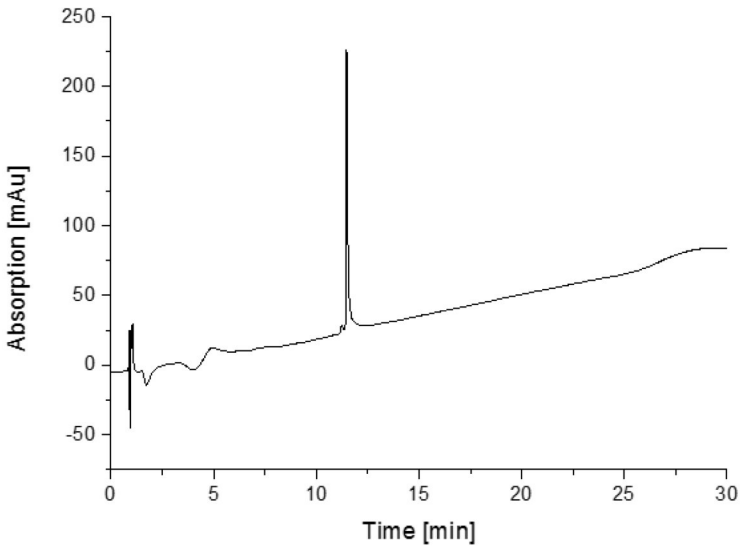

*Appendix 12: RP-HPLC chromatogram (linear gradient from 0-50% eluent B in 30 min at 25 °C) of compound **1b**.*

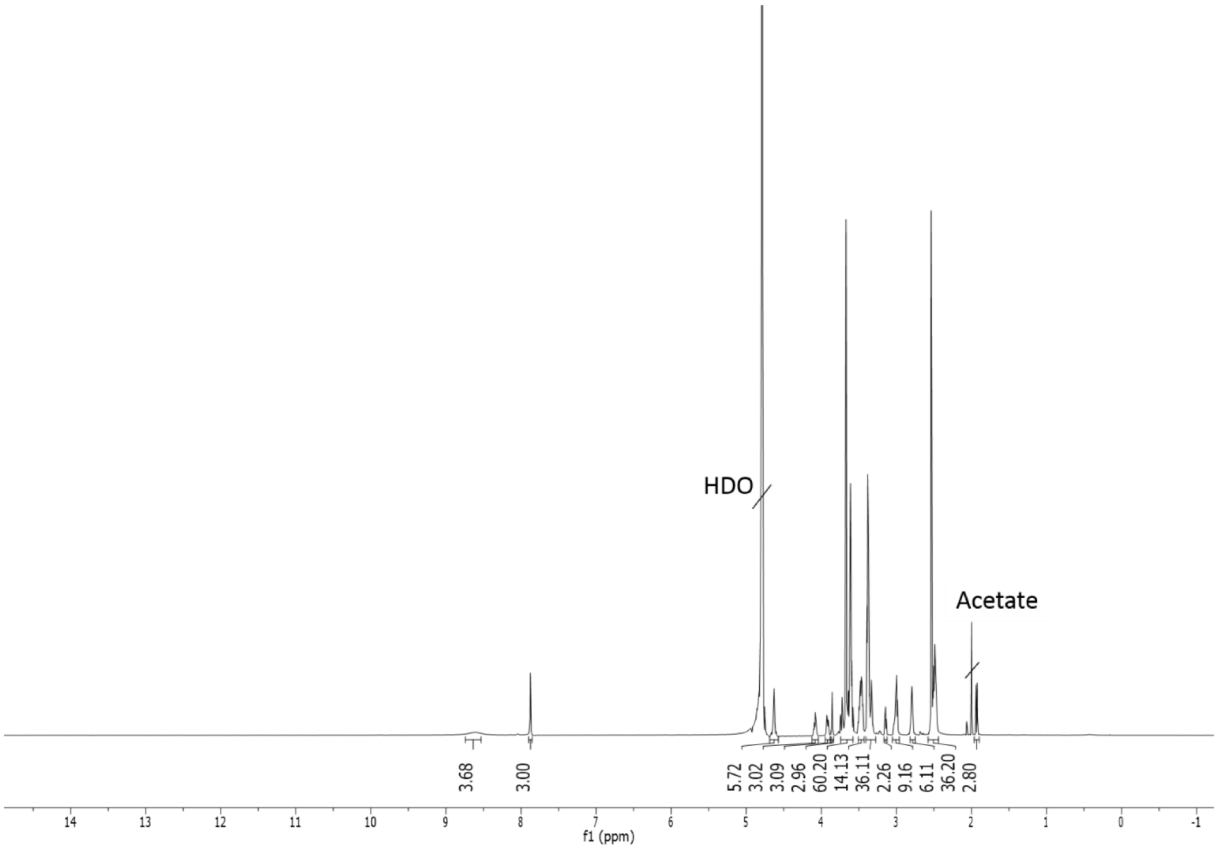

*Appendix 13: ^{1}H-NMR spectrum of **1c** (600 MHz, D_2O). The singlet signal at a chemical shift of 2.00 ppm can be assigned to the acetate counter ion present after ion exchange.*

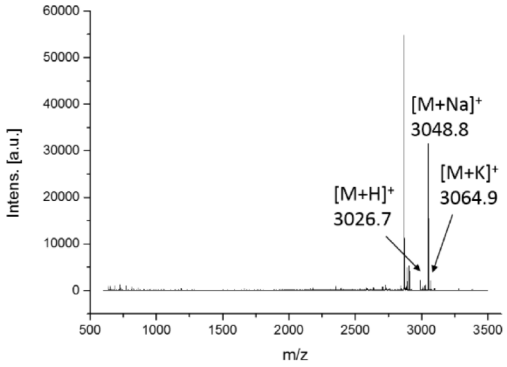

*Appendix 14: MALDI-TOF-MS spectrum of **1c**. One further signal with the mass-to-charge ratio of 2866.7 can be found in the spectrum but cannot be assigned to potential by-products.*

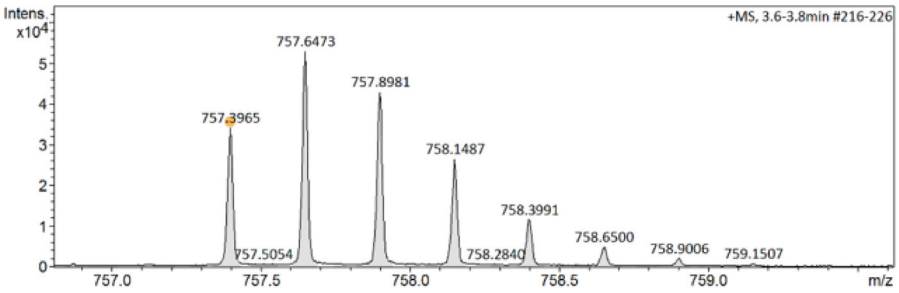

*Appendix 15: HR-MS (ESI⁺ Q-TOF) of compound **1c**.*

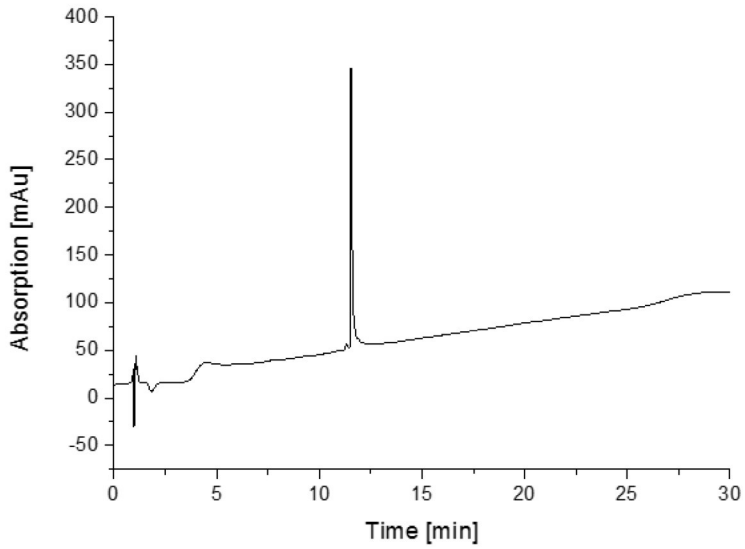

*Appendix 16: RP-HPLC chromatogram (linear gradient from 0-50% eluent B in 30 min at 25 °C) of compound **1c**.*

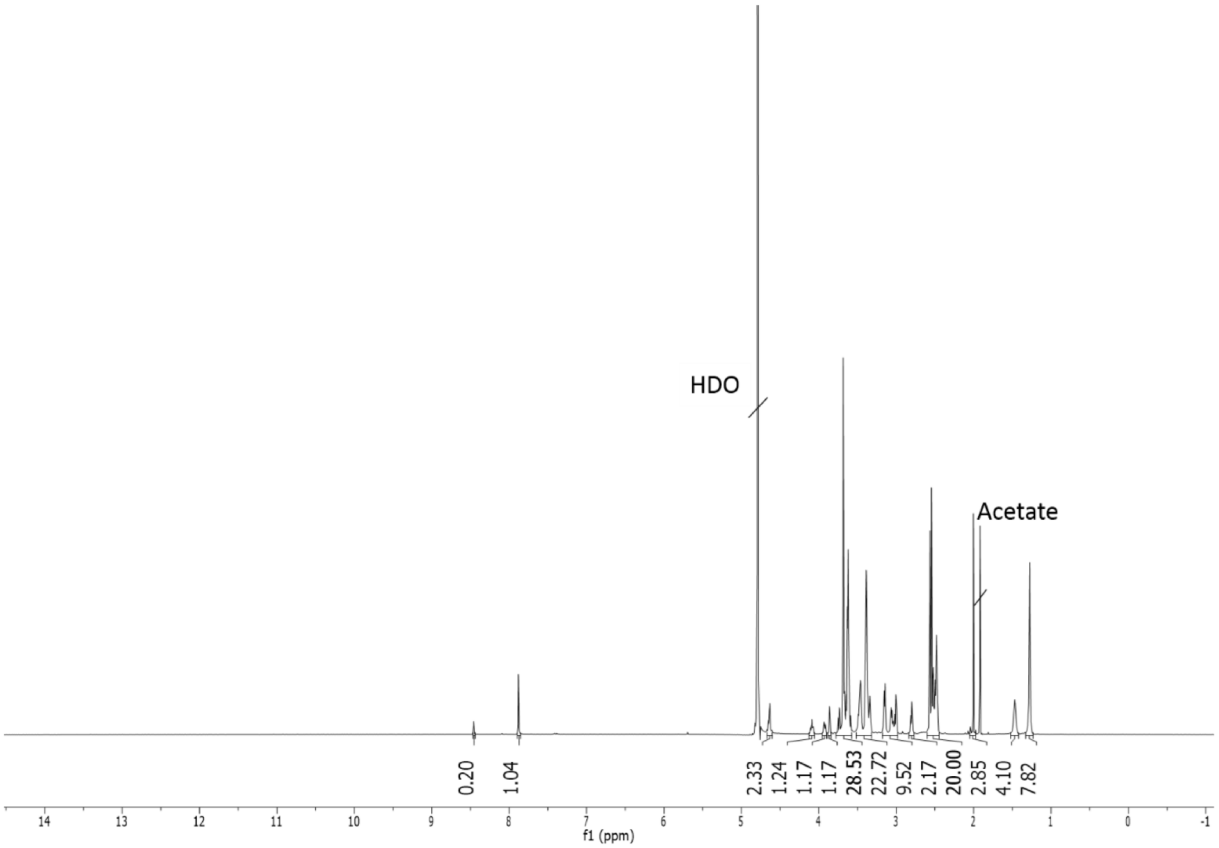

*Appendix 17: ^{1}H-NMR spectrum of **3** (600 MHz, D_2O). The singlet signal at a chemical shift of 1.92 ppm can be assigned to the acetate counter ion present after ion exchange.*

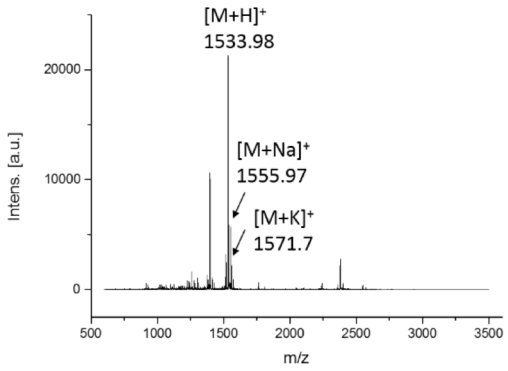

*Appendix 18: MALDI-TOF-MS spectrum of **3**. Two further signal with the mass-to-charge ratio of 1397.0 and 2378.4 can be found in the spectrum but cannot be assigned to potential by-products.*

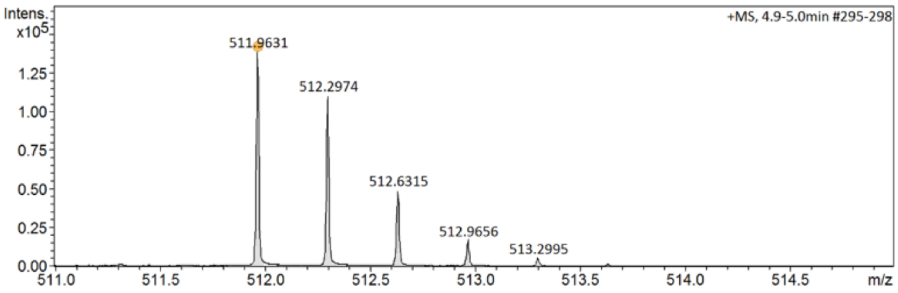

*Appendix 19: HR-MS (ESI$^+$ Q-TOF) of compound **3**.*

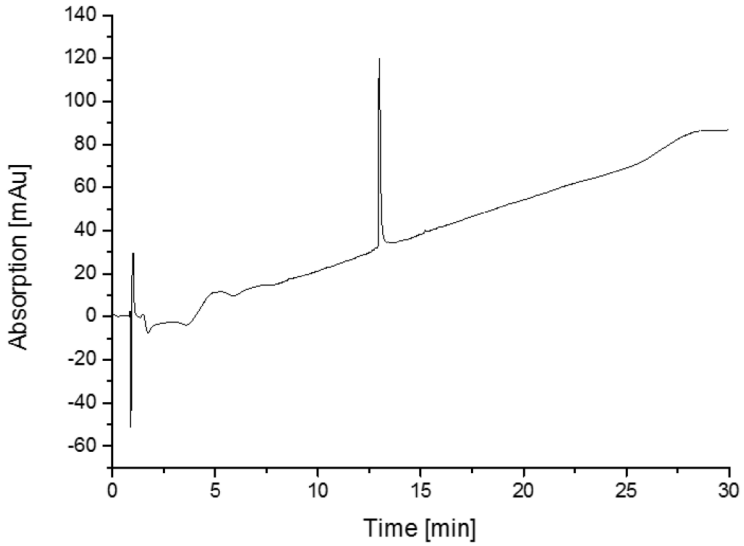

*Appendix 20: RP-HPLC chromatogram (linear gradient from 0-50% eluent B in 30 min at 25 °C) of compound **3**.*

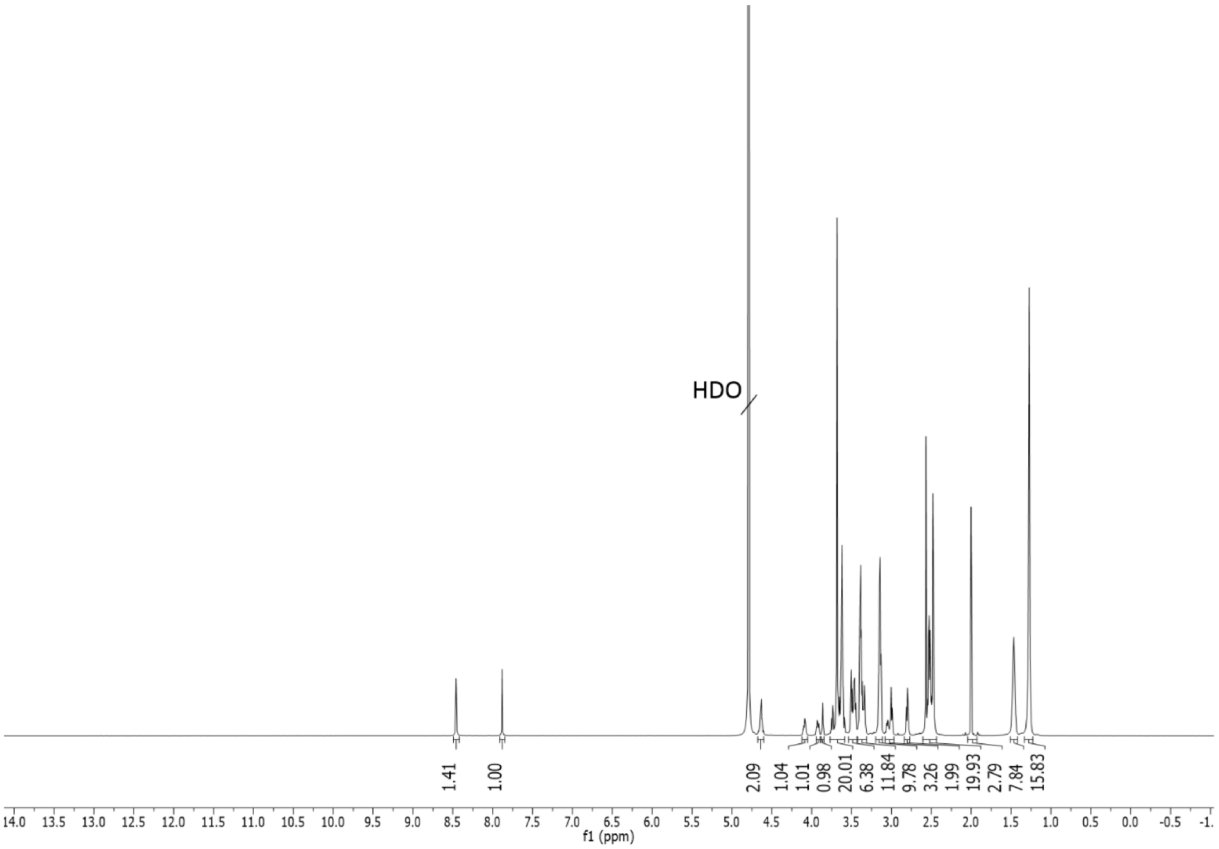

*Appendix 21: ^{1}H-NMR spectrum of **3a** (600 MHz, D_2O).*

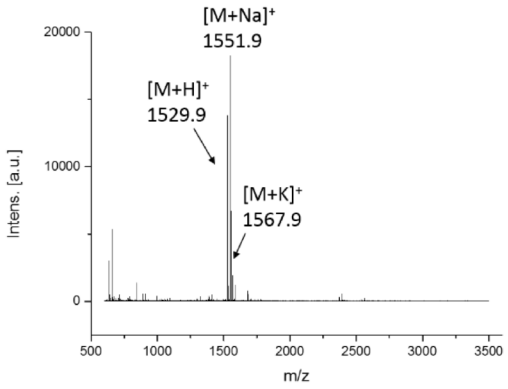

*Appendix 22: MALDI-TOF-MS spectrum of **3a**. One further signal with the mass-to-charge ratio of 659.3 can be found in the spectrum but cannot be assigned to potential by-products.*

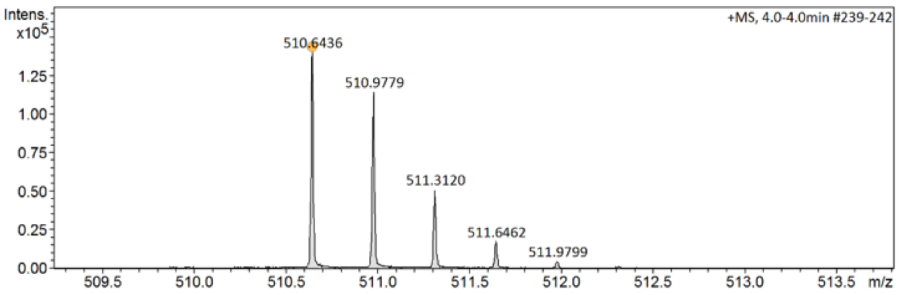

*Appendix 23: HR-MS (ESI⁺ Q-TOF) of compound **3a**.*

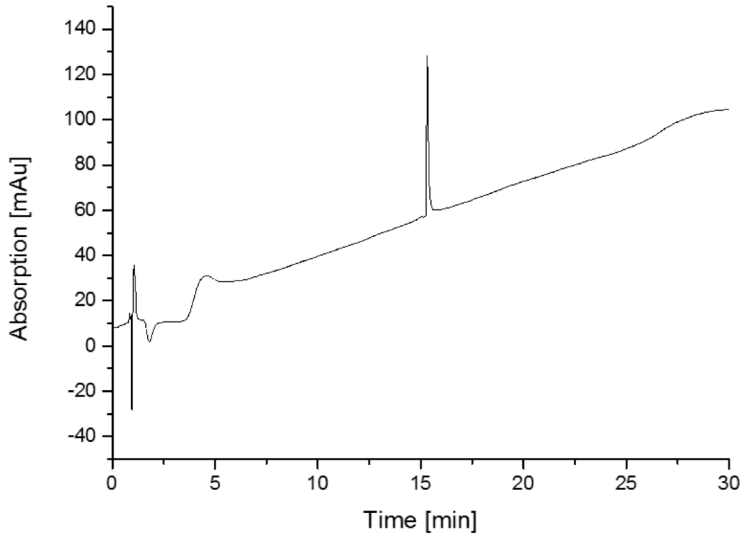

*Appendix 24: RP-HPLC chromatogram (linear gradient from 0-50% eluent B in 30 min at 25 °C) of compound **3a**.*

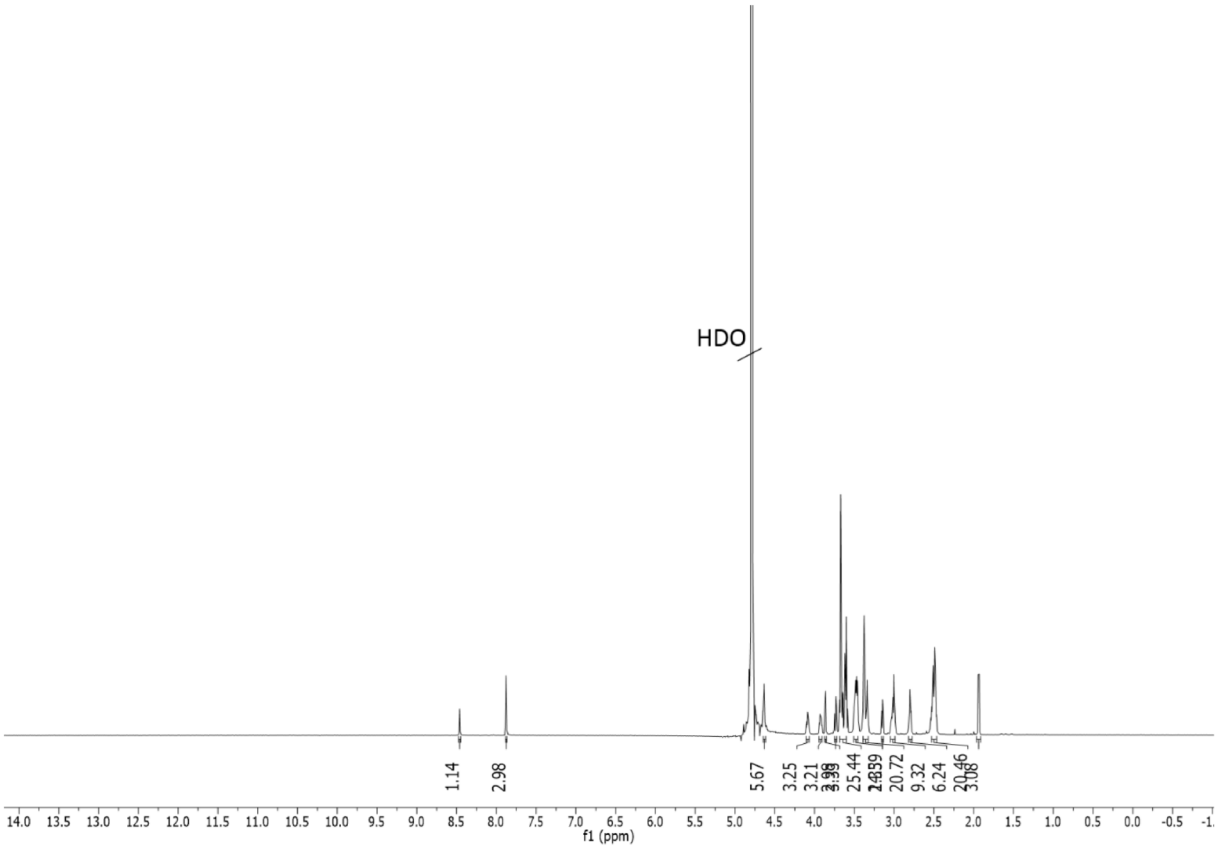

*Appendix 25: ^{1}H-NMR spectrum of **4** (600 MHz, D_2O).*

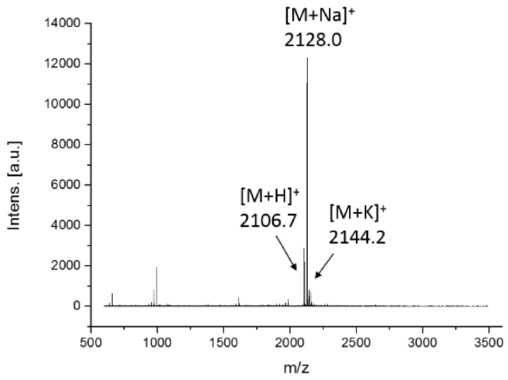

*Appendix 26: MALDI-TOF-MS spectrum of **4**. One further signal with the mass-to-charge ratio of 994.5 can be found in the spectrum but cannot be assigned to potential by-products.*

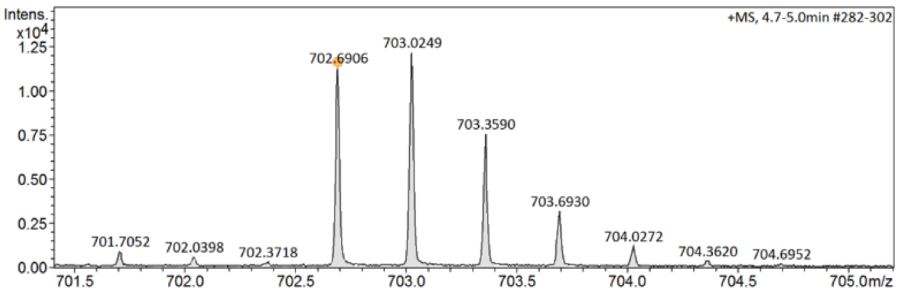

*Appendix 27: HR-MS (ESI$^+$ Q-TOF) of compound **4**.*

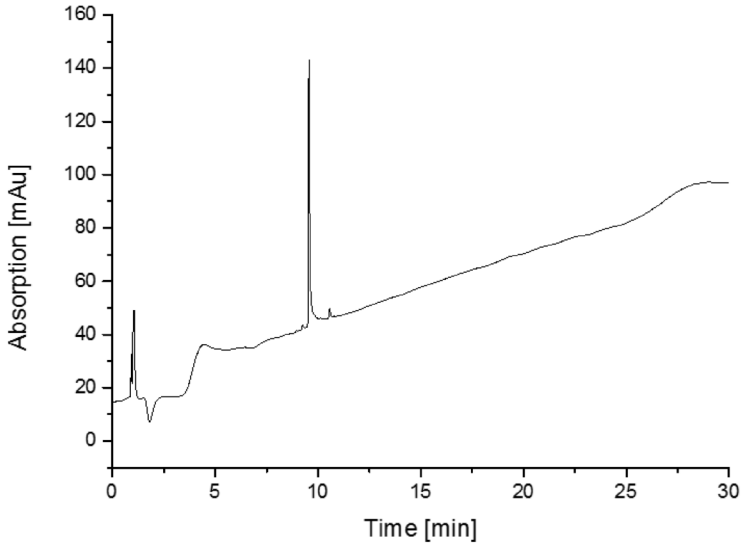

*Appendix 28: RP-HPLC chromatogram (linear gradient from 0-50% eluent B in 30 min at 25 °C) of compound **4**.*

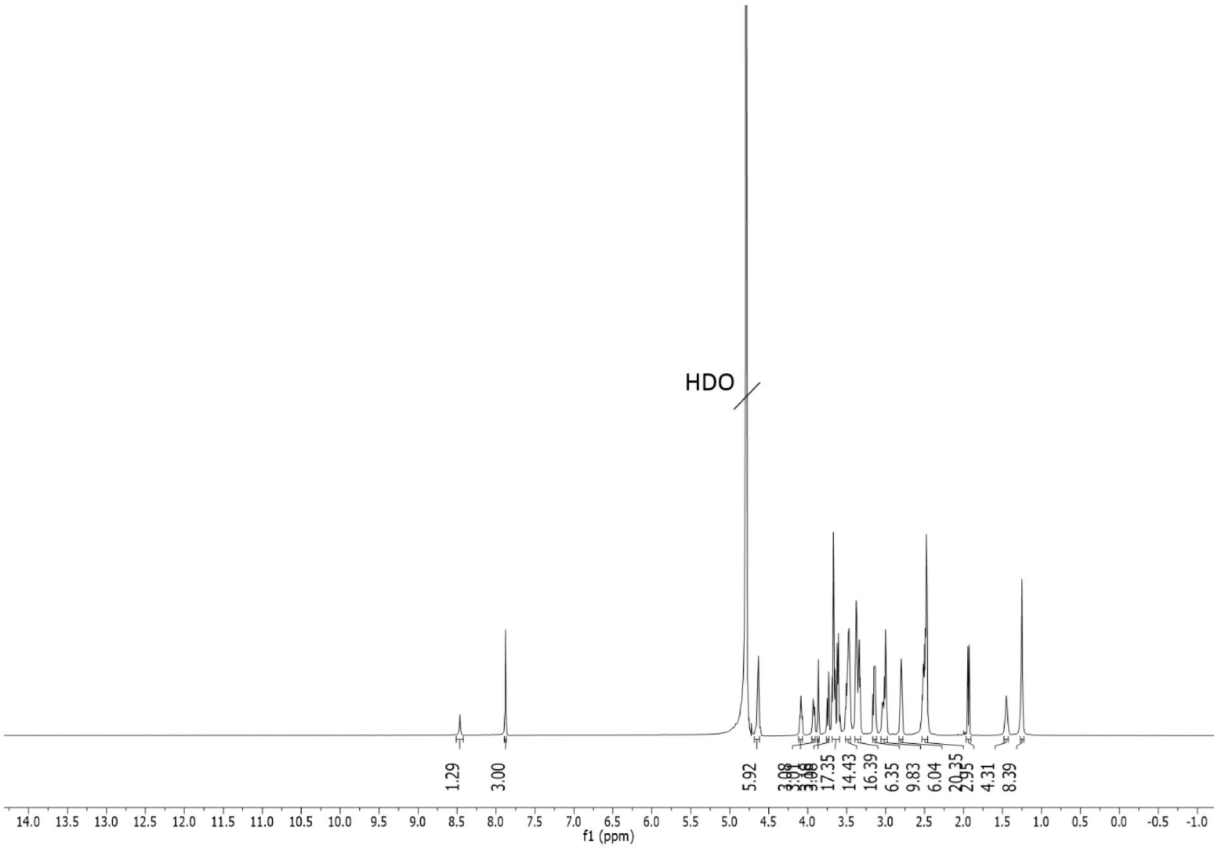

*Appendix 29: ^{1}H-NMR spectrum of **4a** (600 MHz, D_2O).*

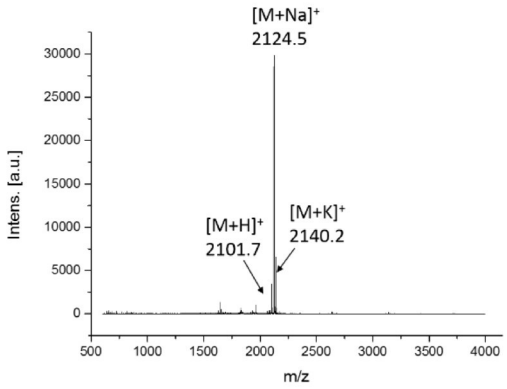

*Appendix 30: MALDI-TOF-MS spectrum of **4a**.*

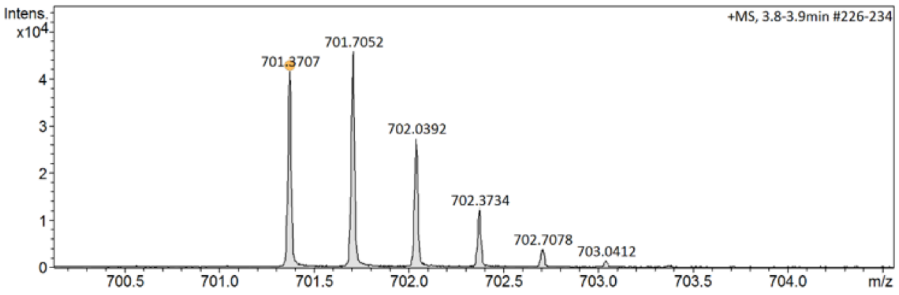

*Appendix 31: HR-MS (ESI⁺ Q-TOF) of compound **4a**.*

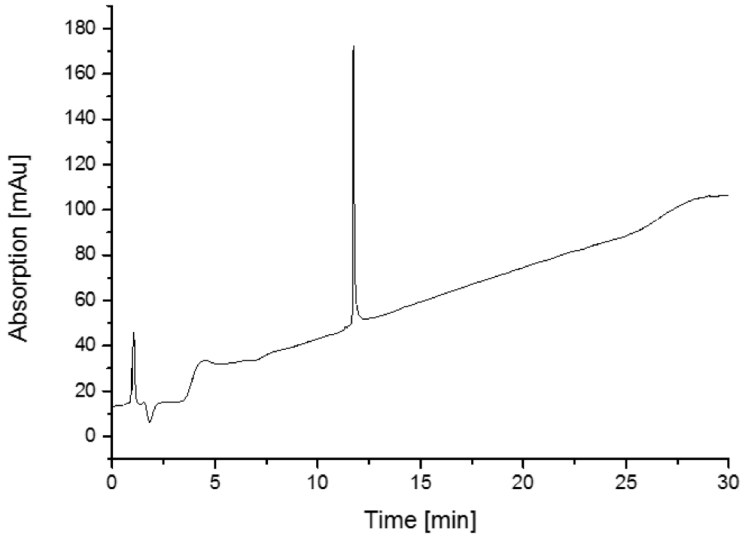

*Appendix 32: RP-HPLC chromatogram (linear gradient from 0-50% eluent B in 30 min at 25 °C) of compound **4a**.*

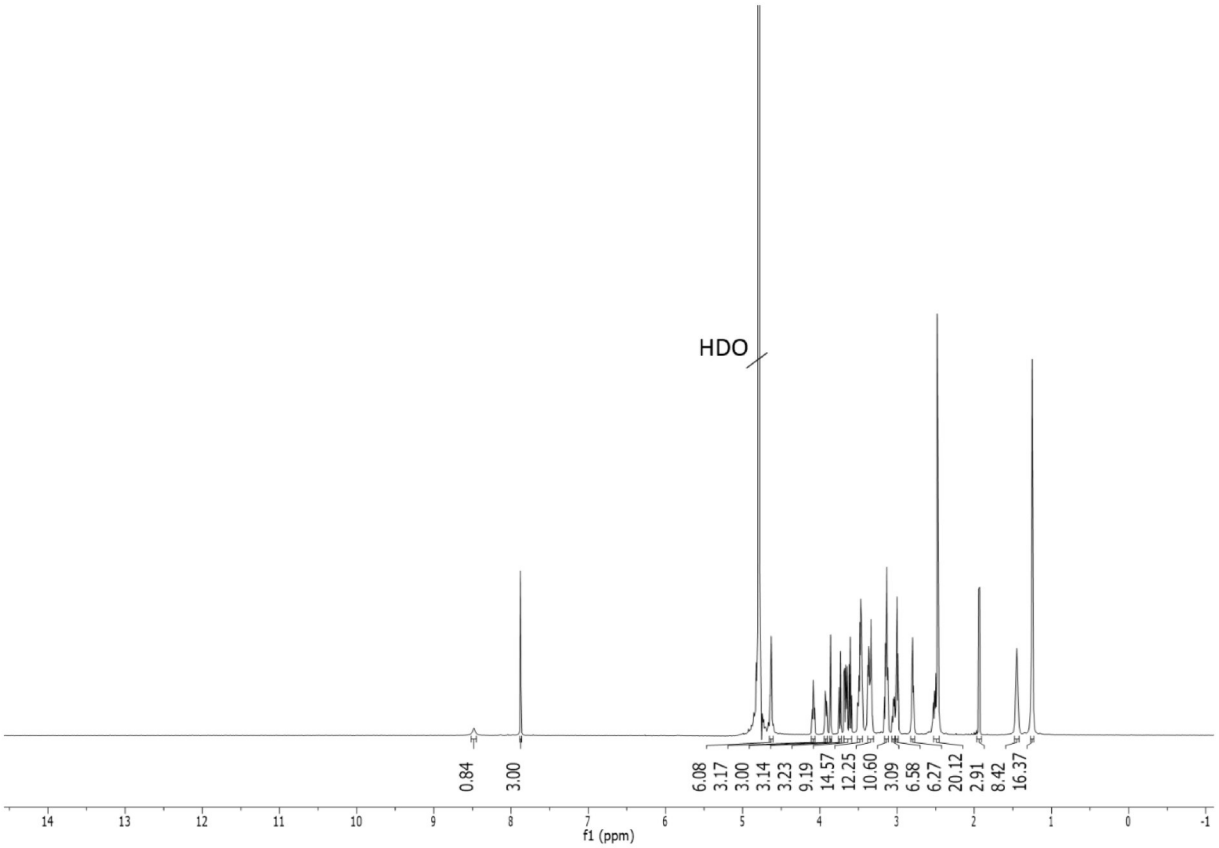

*Appendix 33: ^{1}H-NMR spectrum of **4b** (600 MHz, D_2O).*

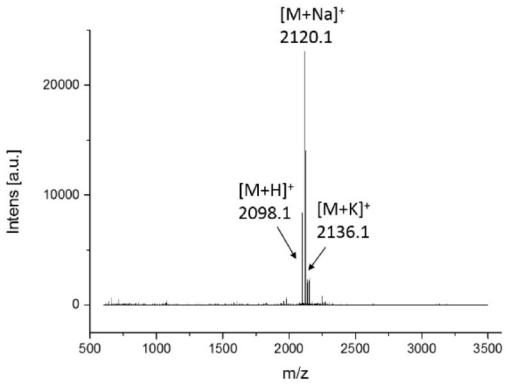

*Appendix 34: MALDI-TOF-MS spectrum of **4b**.*

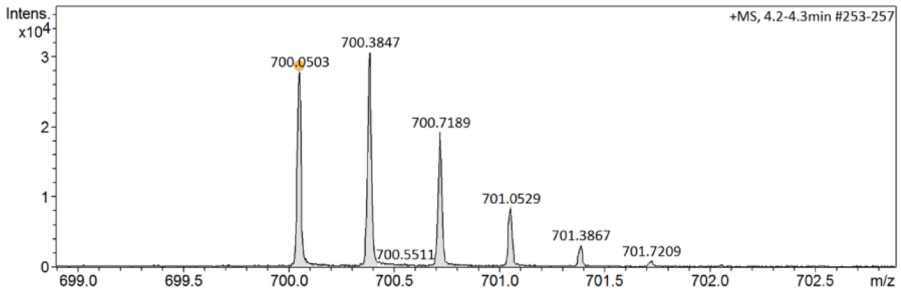

*Appendix 35: HR-MS (ESI⁺ Q-TOF) of compound **4b**.*

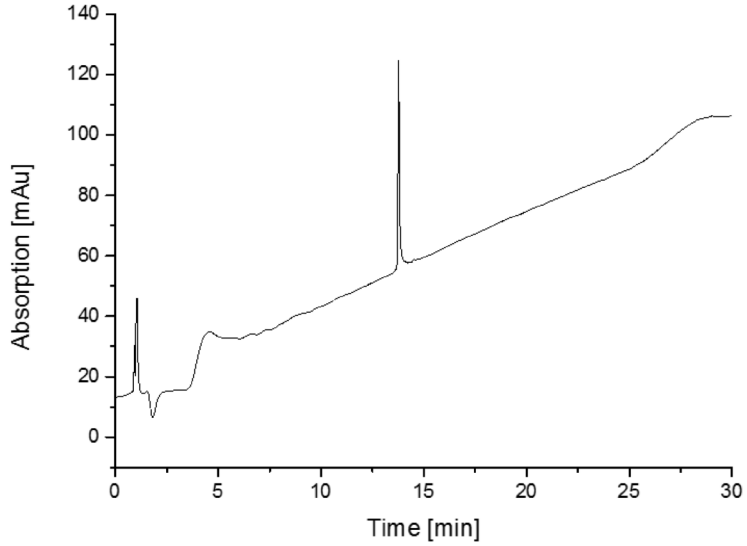

*Appendix 36: RP-HPLC chromatogram (linear gradient from 0-50% eluent B in 30 min at 25 °C) of compound **4b**.*

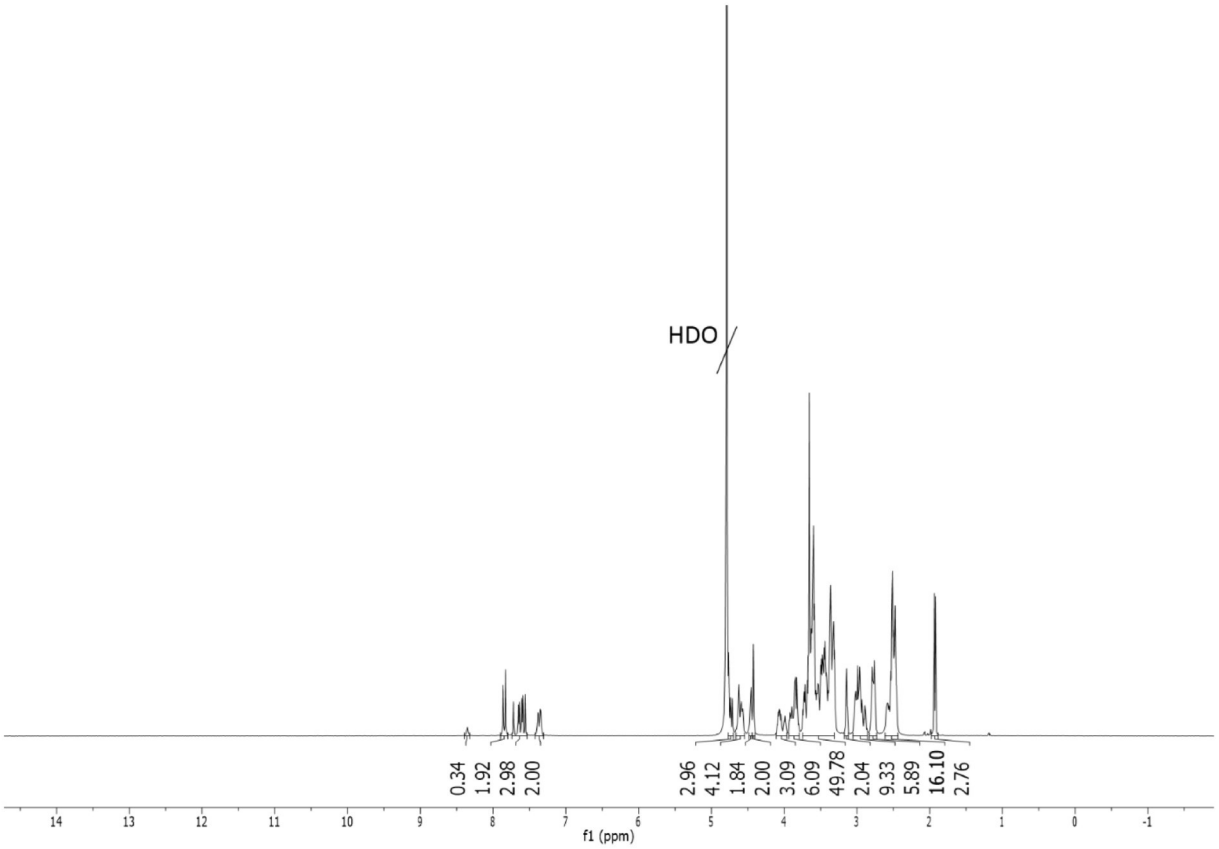

*Appendix 37: ^{1}H-NMR spectrum of **4c** (600 MHz, D_2O).*

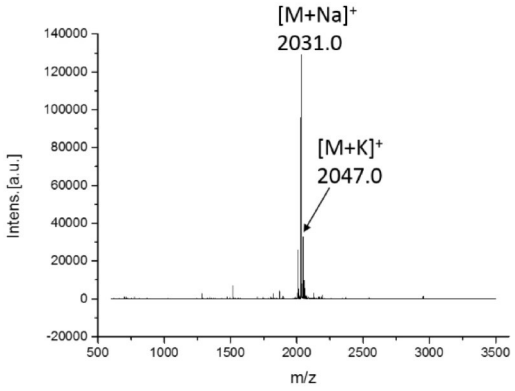

*Appendix 38: MALDI-TOF-MS spectrum of **4c**.*

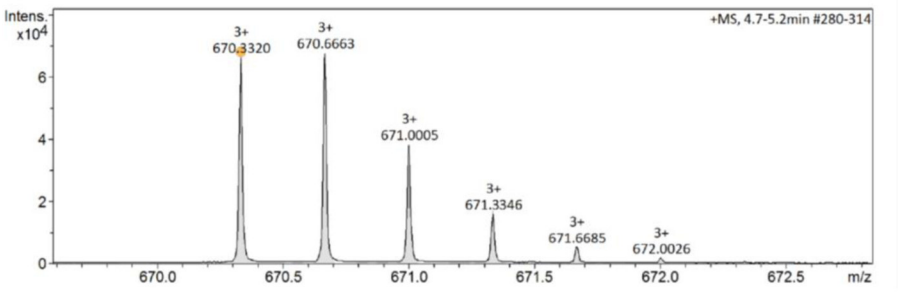

*Appendix 39: HR-MS (ESI⁺ Q-TOF) of compound **4c**.*

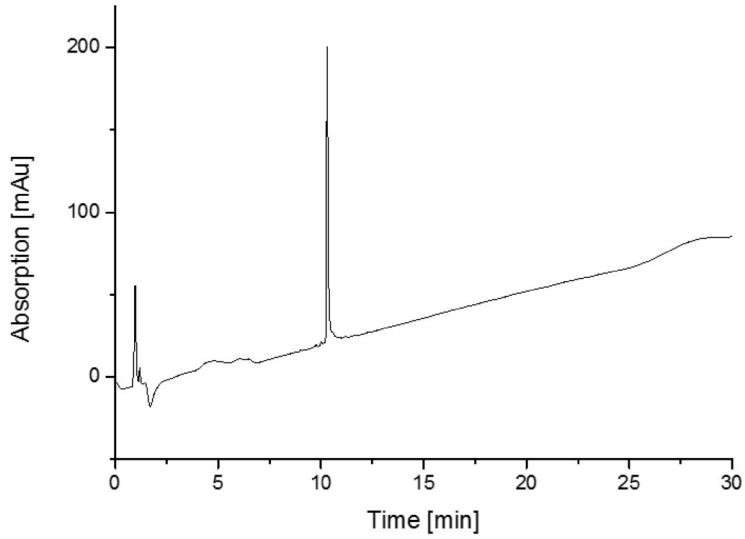

*Appendix 40: RP-HPLC chromatogram (linear gradient from 0-50% eluent B in 30 min at 25 °C) of compound **4c**.*

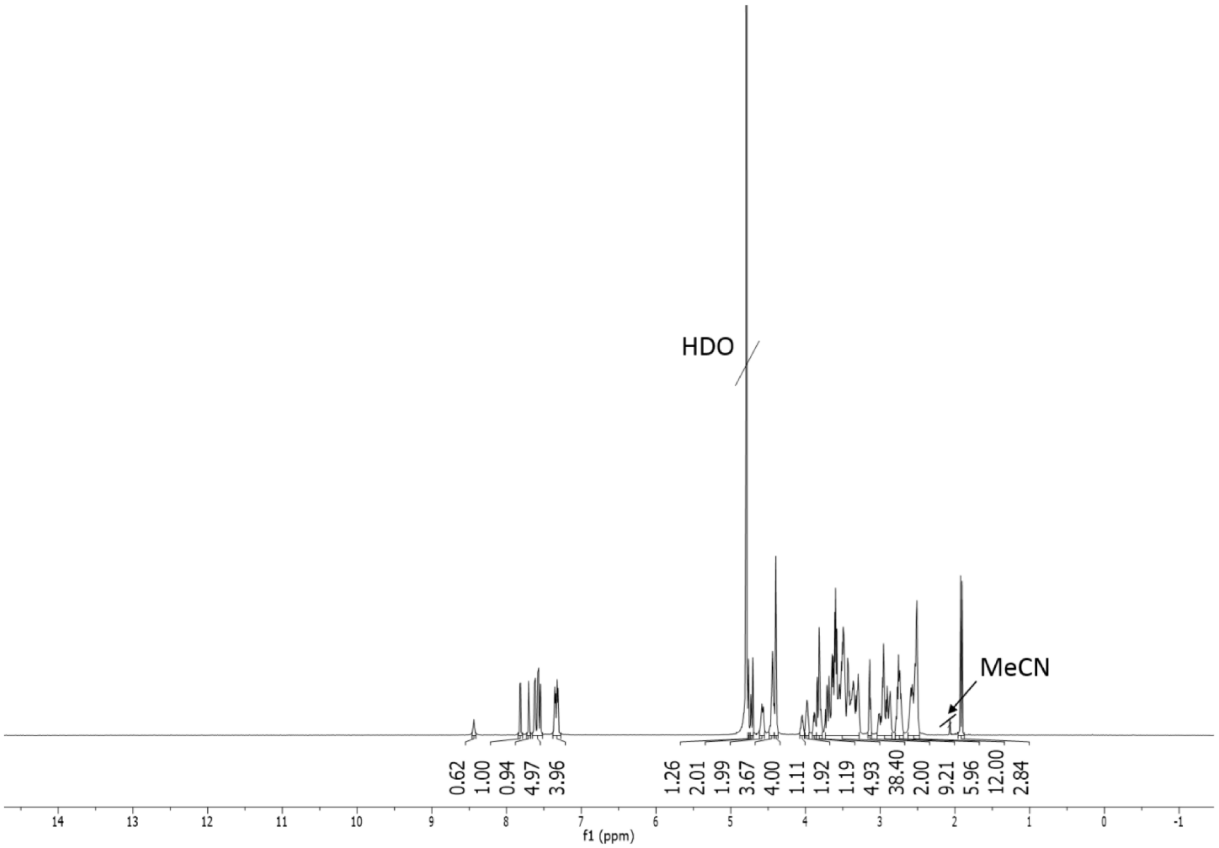

*Appendix 41: ^{1}H-NMR spectrum of **4d** (600 MHz, D_2O). The singlet signal at a chemical shift of 2.07 ppm can be assigned to residues of acetonitrile (MeCN).*

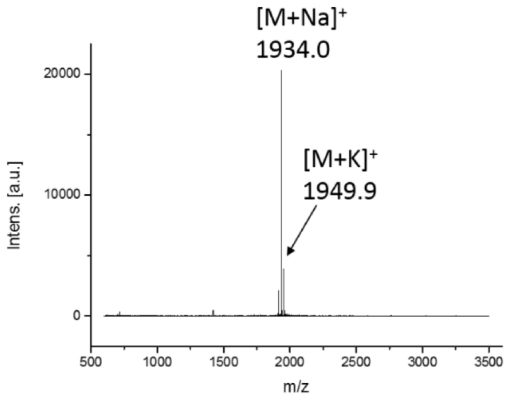

*Appendix 42: MALDI-TOF-MS spectrum of **4d**.*

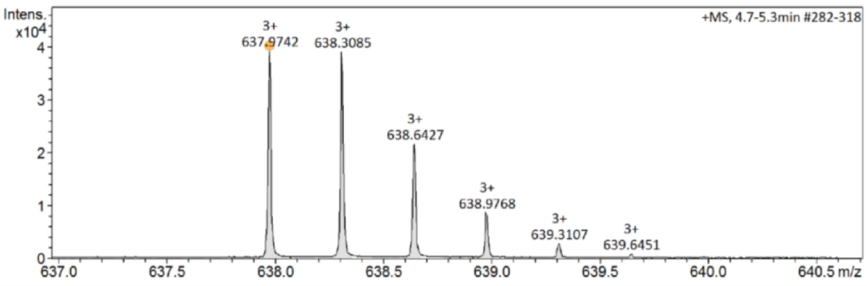

*Appendix 43: HR-MS (ESI⁺ Q-TOF) of compound **4d**.*

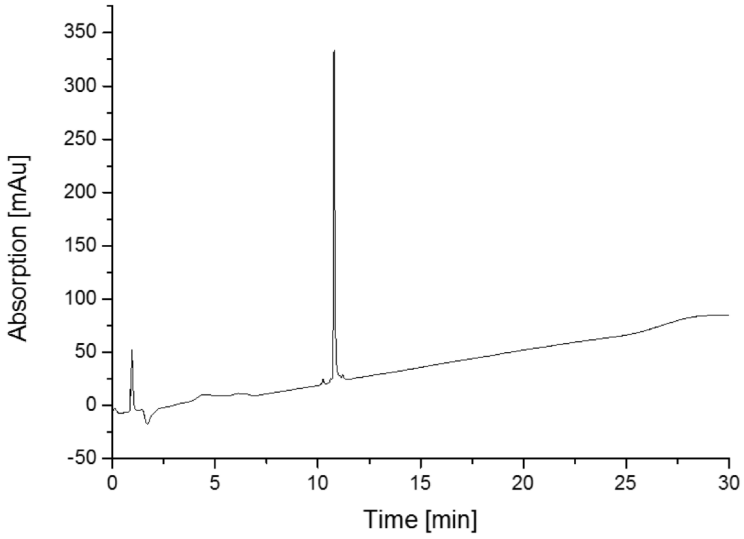

*Appendix 44: RP-HPLC chromatogram (linear gradient from 0-50% eluent B in 30 min at 25 °C) of compound **4d**.*

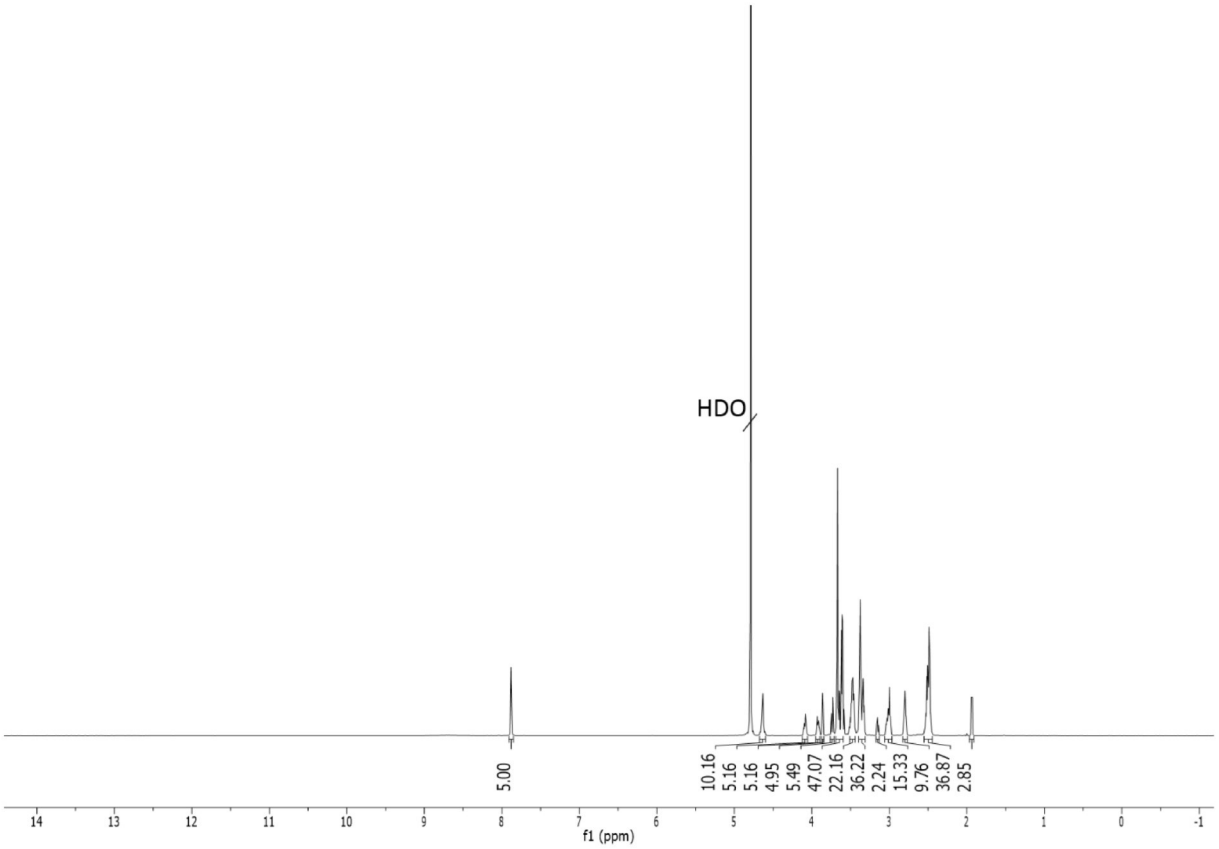

*Appendix 45: ^{1}H-NMR spectrum of **5** (600 MHz, D_2O).*

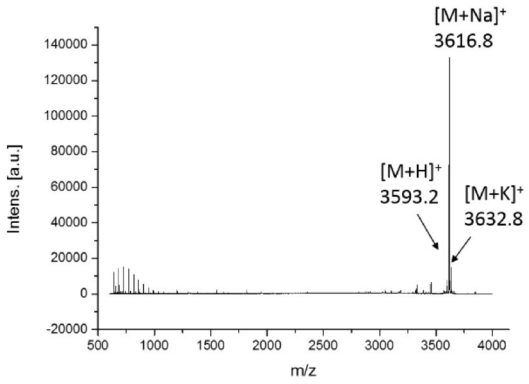

*Appendix 46: MALDI-TOF-MS spectrum of **5**.*

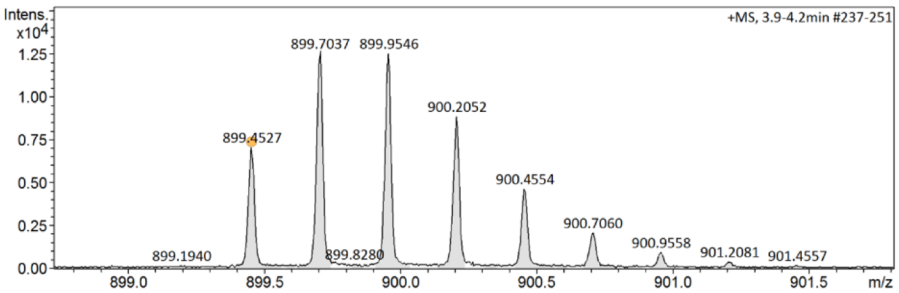

*Appendix 47: HR-MS (ESI⁺ Q-TOF) of compound **5**.*

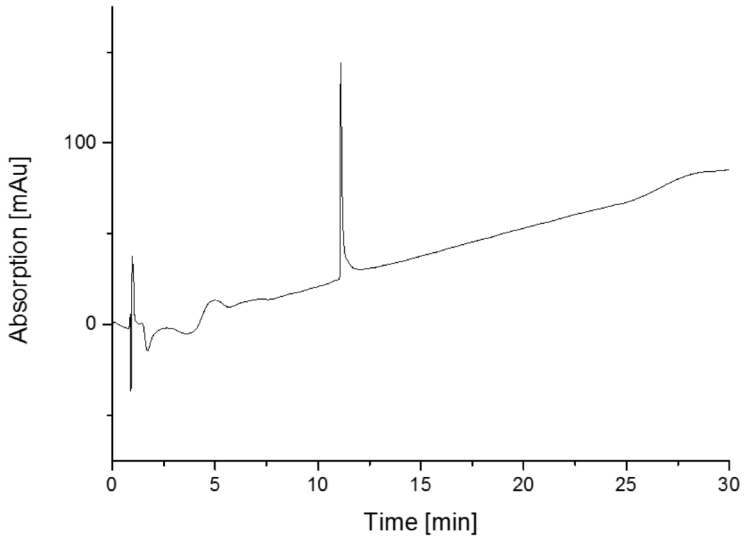

*Appendix 48: RP-HPLC chromatogram (linear gradient from 0-50% eluent B in 30 min at 25 °C) of compound **5**.*

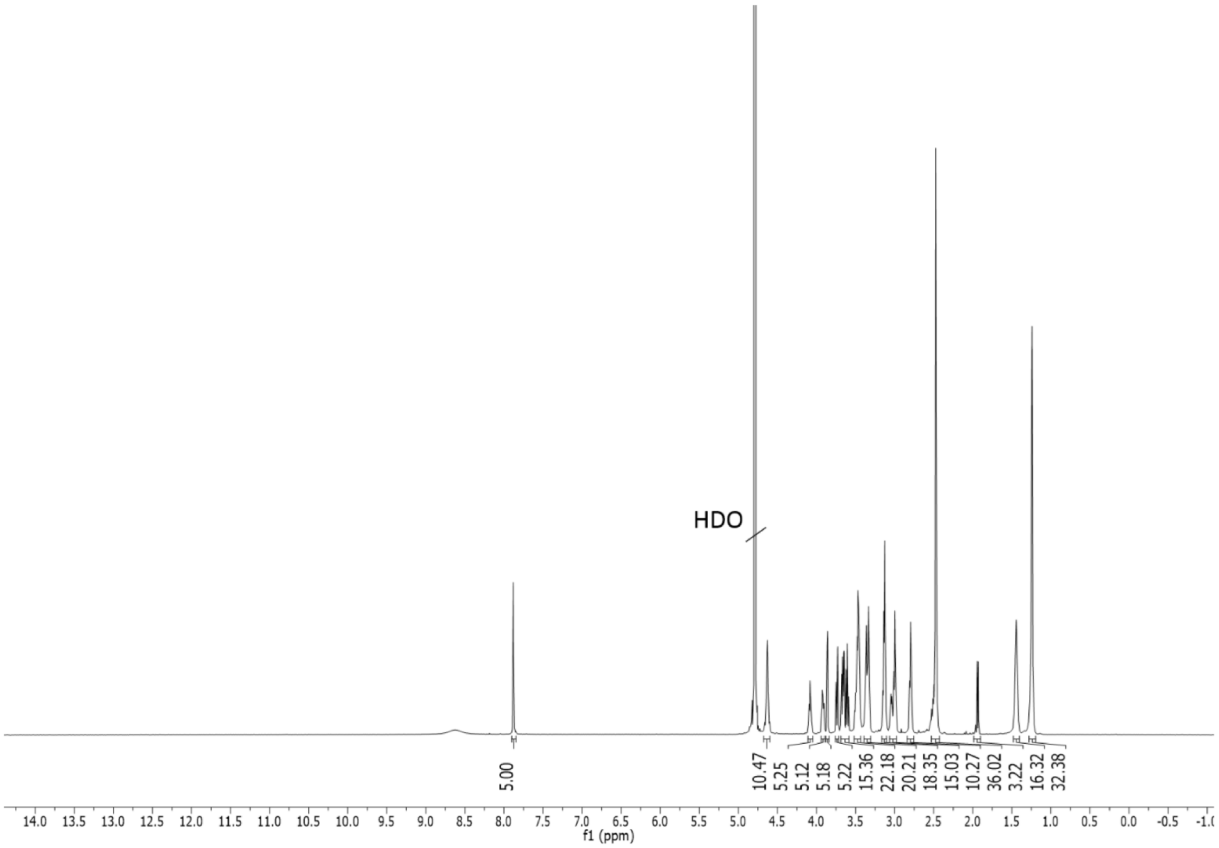

*Appendix 49: ^{1}H-NMR spectrum of **5a** (600 MHz, D_2O).*

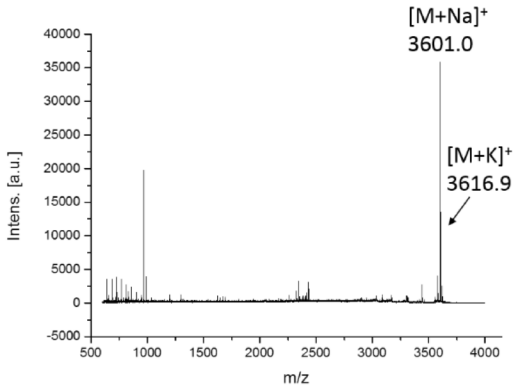

*Appendix 50: MALDI-TOF-MS spectrum of **5a**. One further signal with the mass-to-charge ratio of 968.6 can be found in the spectrum but cannot be assigned to potential by-products.*

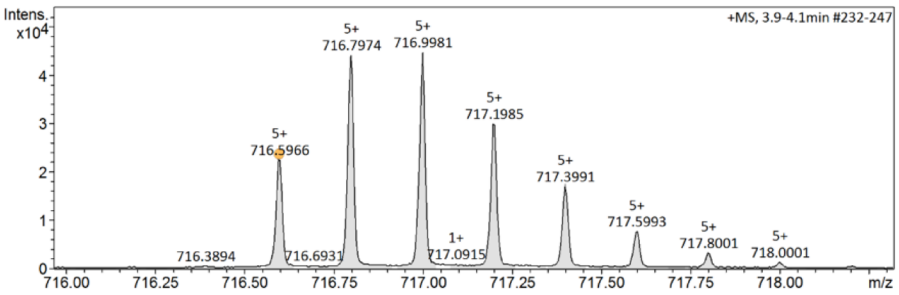

*Appendix 51: HR-MS (ESI⁺ Q-TOF) of compound **5a**.*

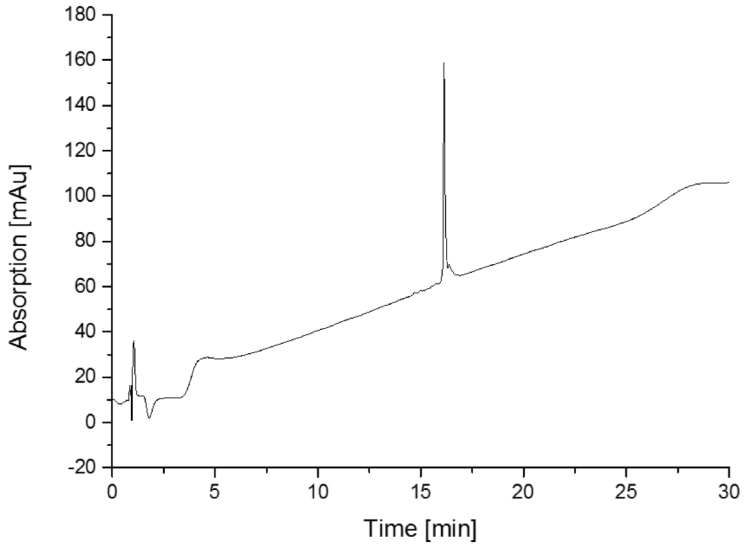

*Appendix 52: RP-HPLC chromatogram (linear gradient from 0-50% eluent B in 30 min at 25 °C) of compound **5a**.*

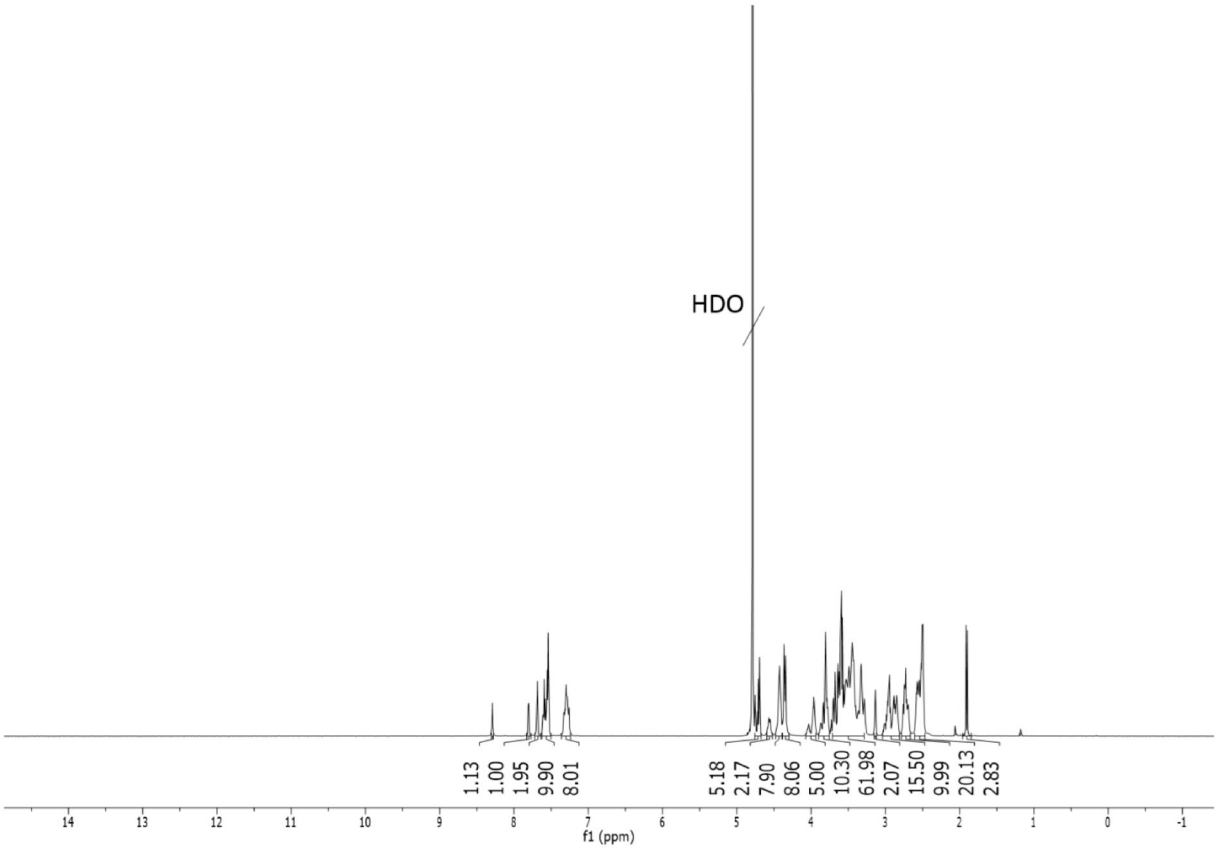

*Appendix 53: ^{1}H-NMR spectrum of **5b** (600 MHz, D_2O).*

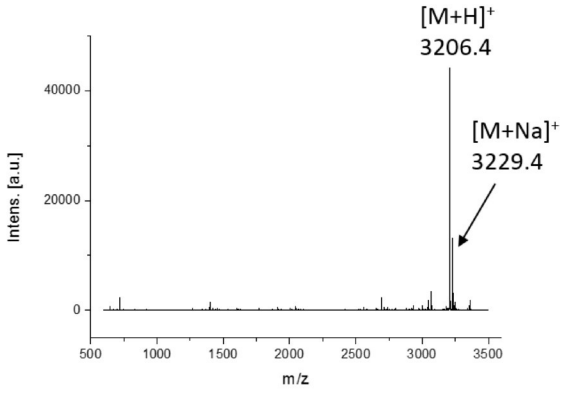

*Appendix 54: MALDI-TOF-MS spectrum of **5b**.*

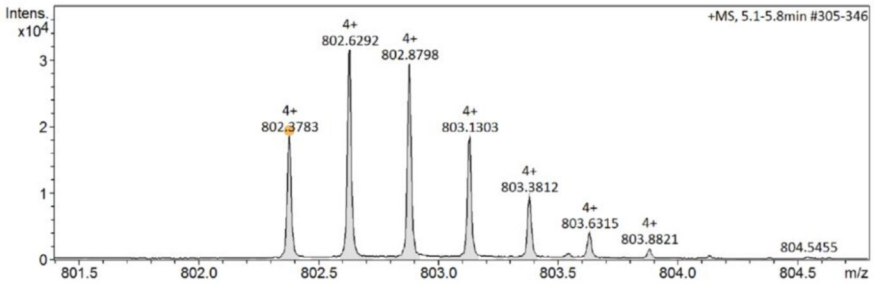

*Appendix 55: HR-MS (ESI⁺ Q-TOF) of compound **5b**.*

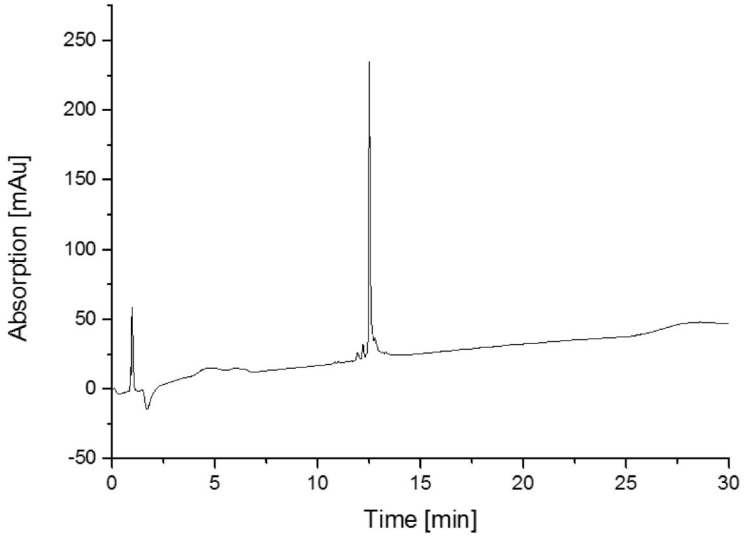

*Appendix 56: RP-HPLC chromatogram (linear gradient from 0-50% eluent B in 30 min at 25 °C) of compound **5b**.*

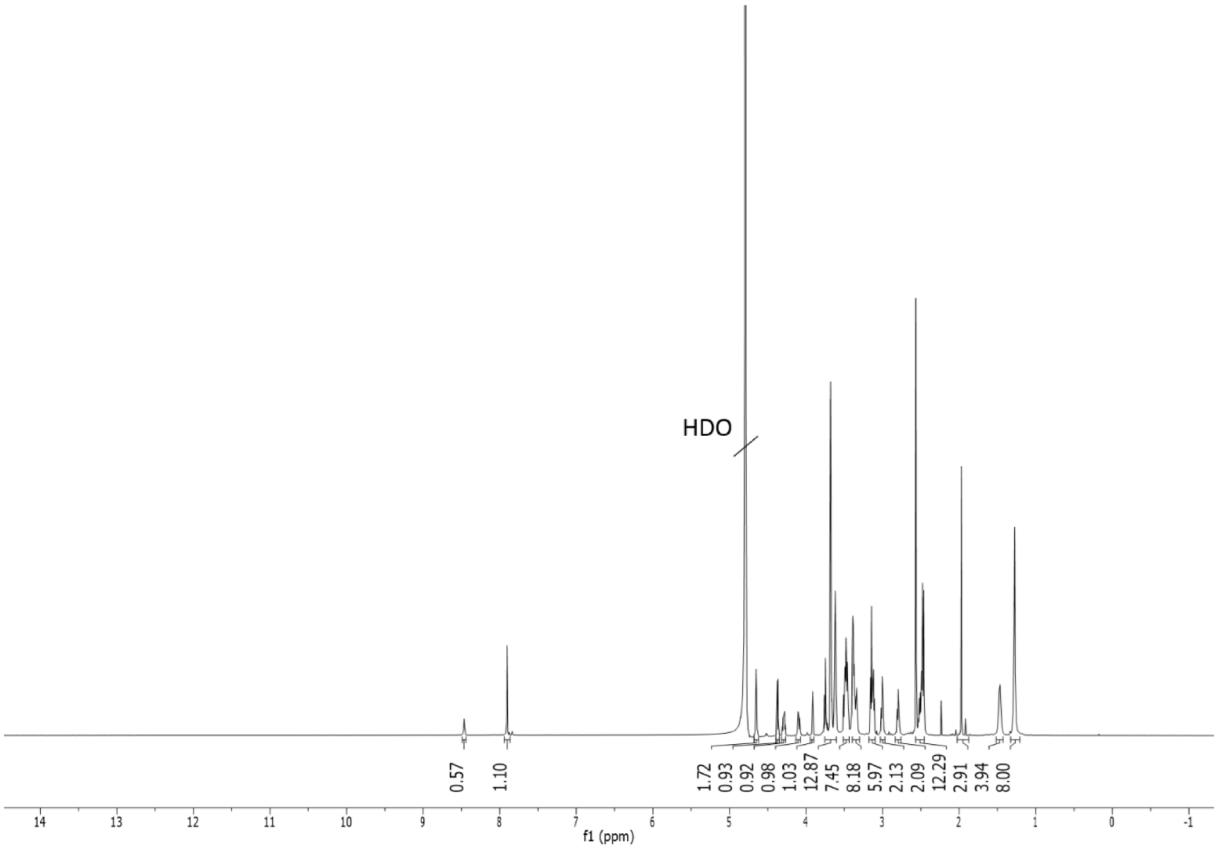

*Appendix 57: ^{1}H-NMR spectrum of **6** (600 MHz, D_2O).*

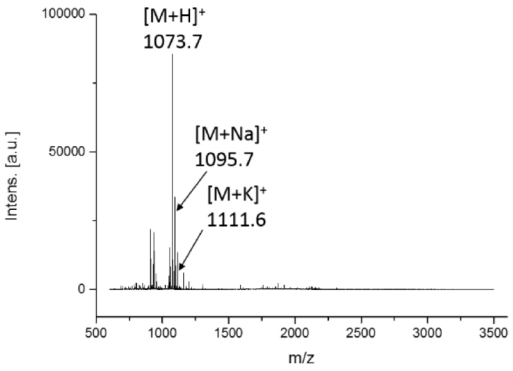

*Appendix 58: MALDI-TOF-MS spectrum of **6**. Two further signals with the mass-to-charge ratio of 912.6 and 938.6 can be found in the spectrum but cannot be assigned to potential by-products.*

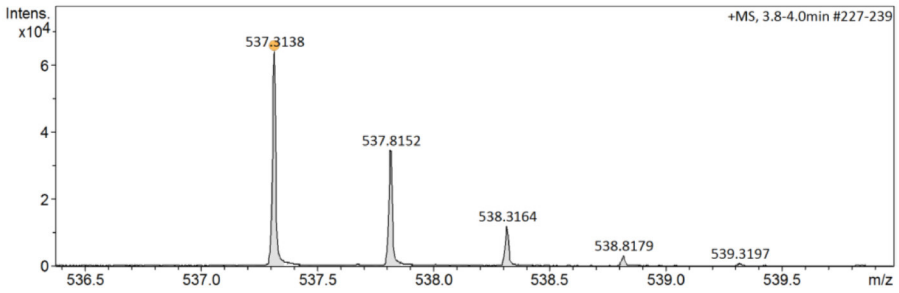

*Appendix 59: HR-MS (ESI⁺ Q-TOF) of compound **6**.*

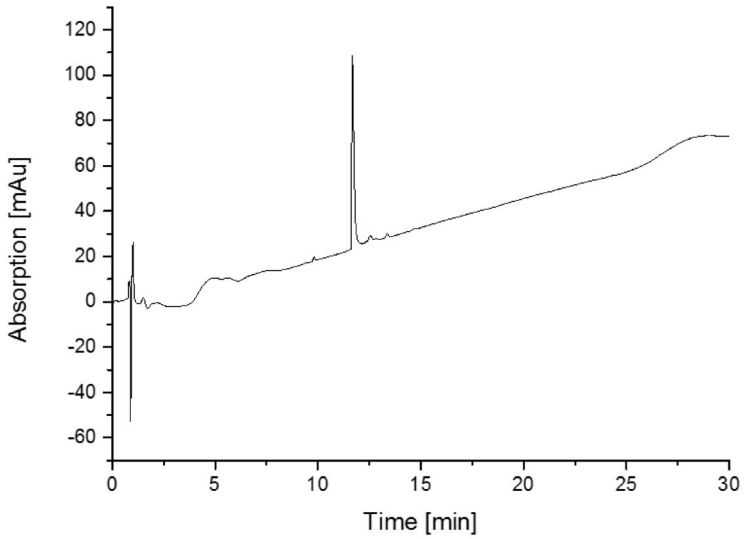

*Appendix 60: RP-HPLC chromatogram (linear gradient from 0-50% eluent B in 30 min at 25 °C) of compound **6**.*

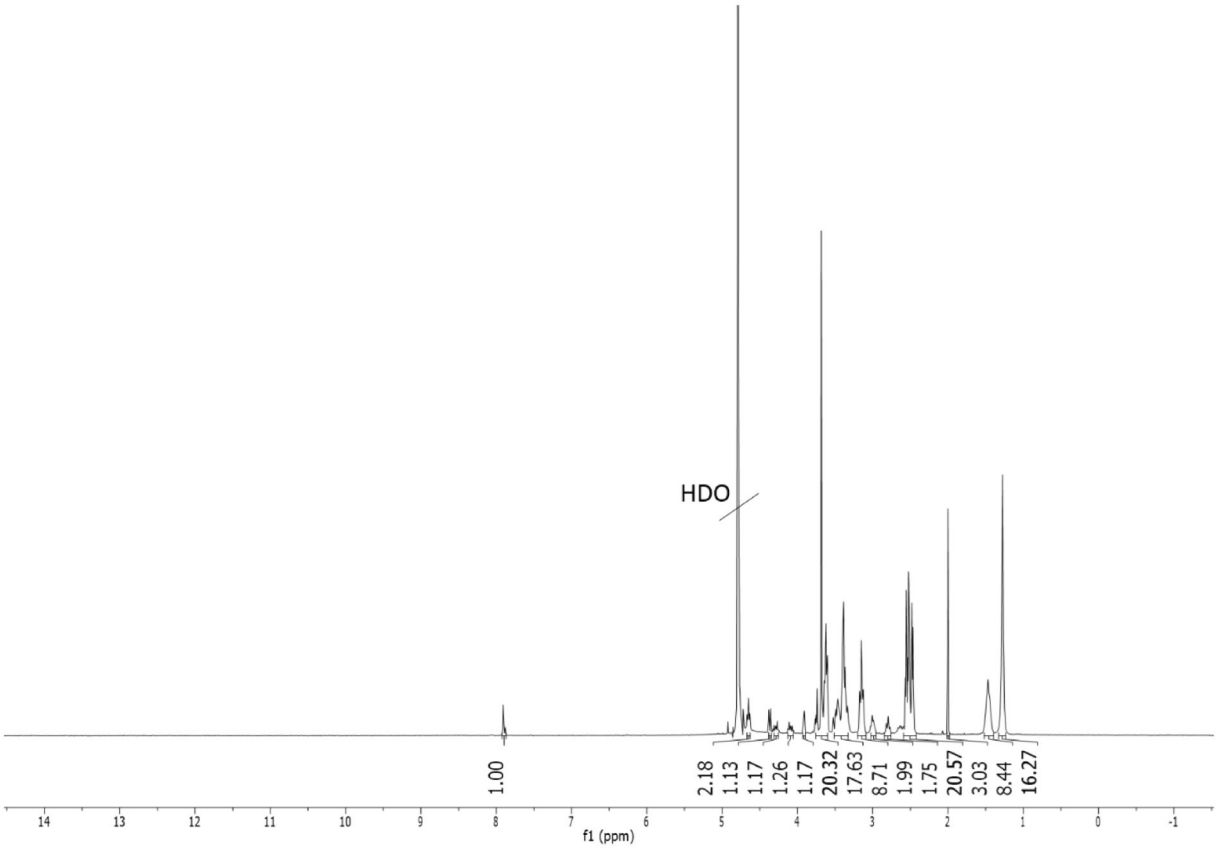

*Appendix 61: ^{1}H-NMR spectrum of **6a** (600 MHz, D_2O).*

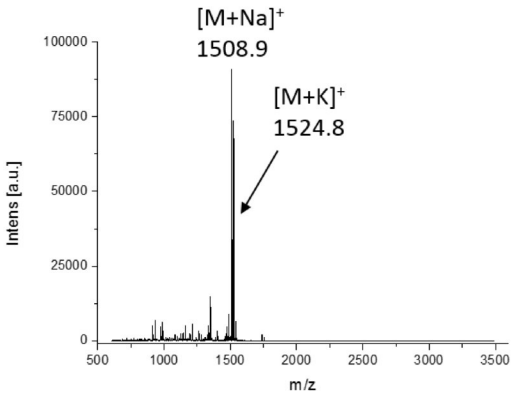

*Appendix 62: MALDI-TOF-MS spectrum of **6a**.*

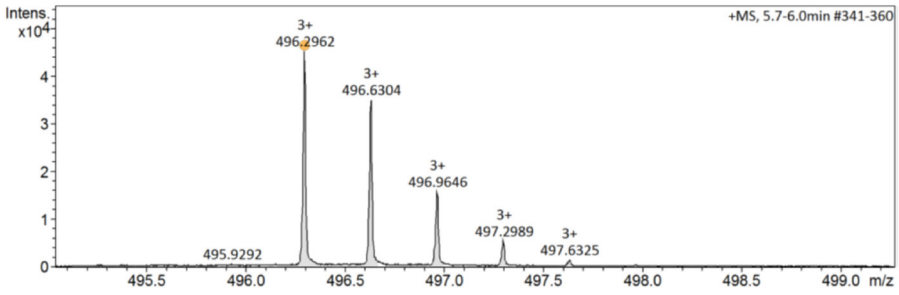

*Appendix 63: HR-MS (ESI⁺ Q-TOF) of compound **6a**.*

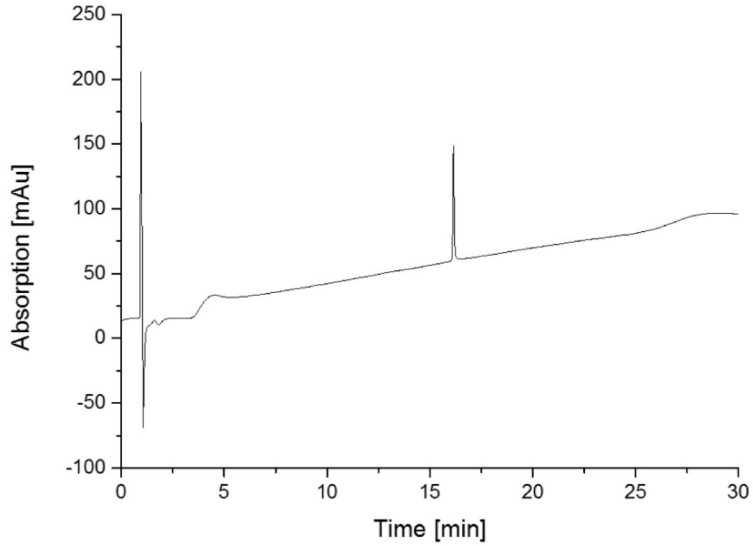

*Appendix 64: RP-HPLC chromatogram (linear gradient from 0-50% eluent B in 30 min at 25 °C) of compound **6a**.*

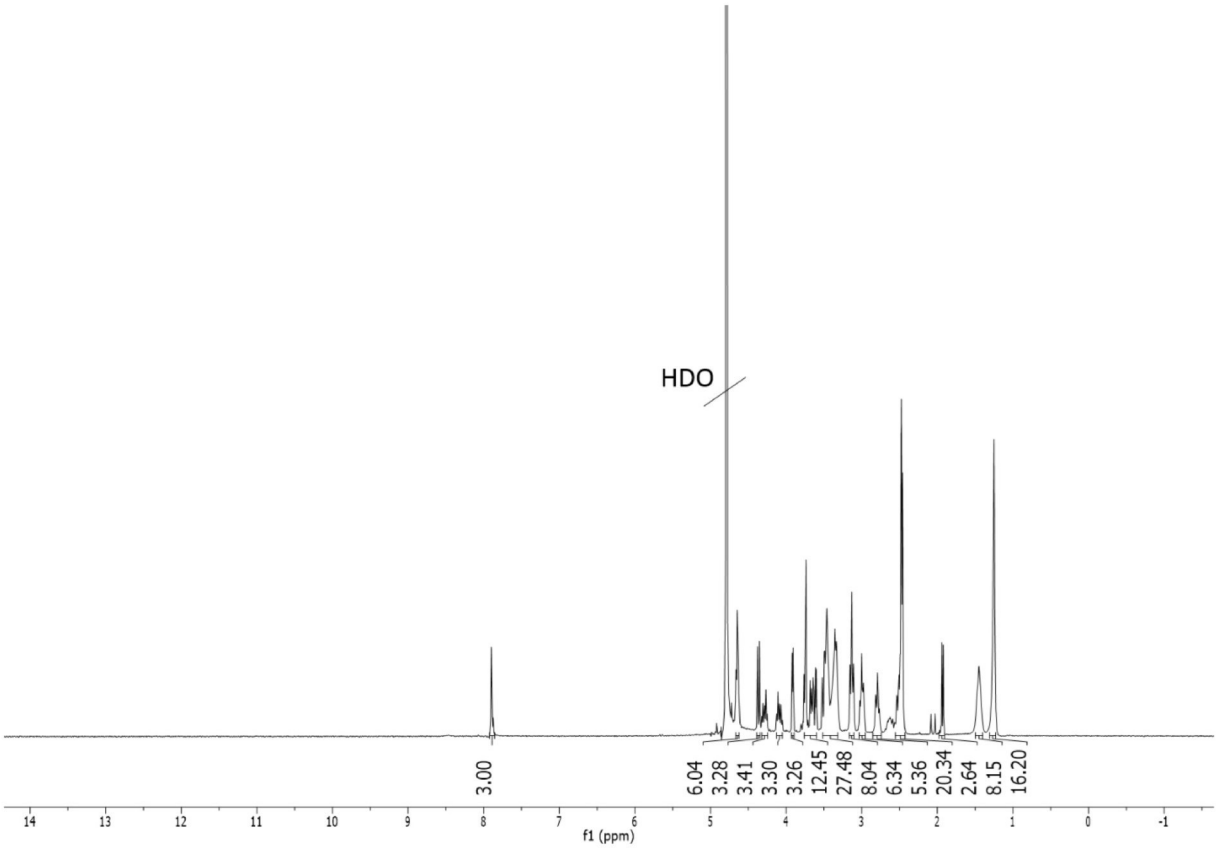

*Appendix 65: ^{1}H-NMR spectrum of **6c** (600 MHz, D_2O).*

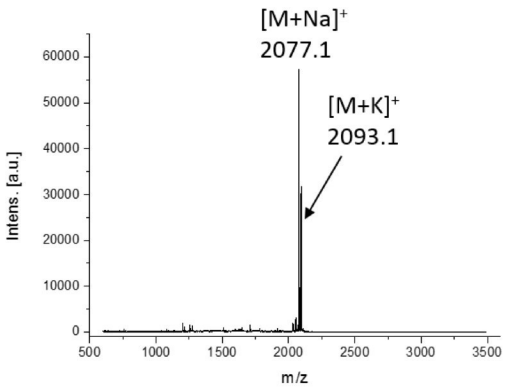

*Appendix 66: MALDI-TOF-MS spectrum of **6c**.*

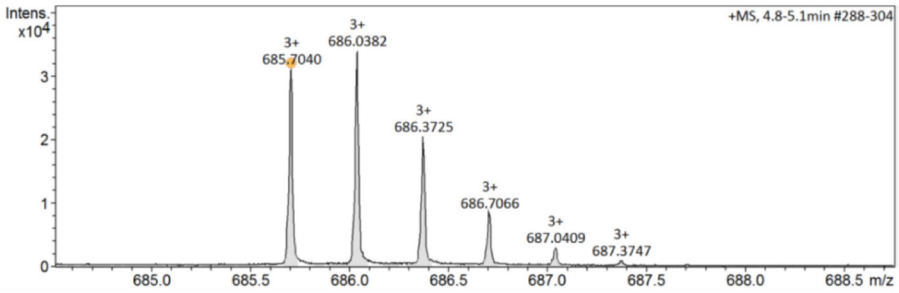

*Appendix 67: HR-MS (ESI$^+$ Q-TOF) of compound **6c**.*

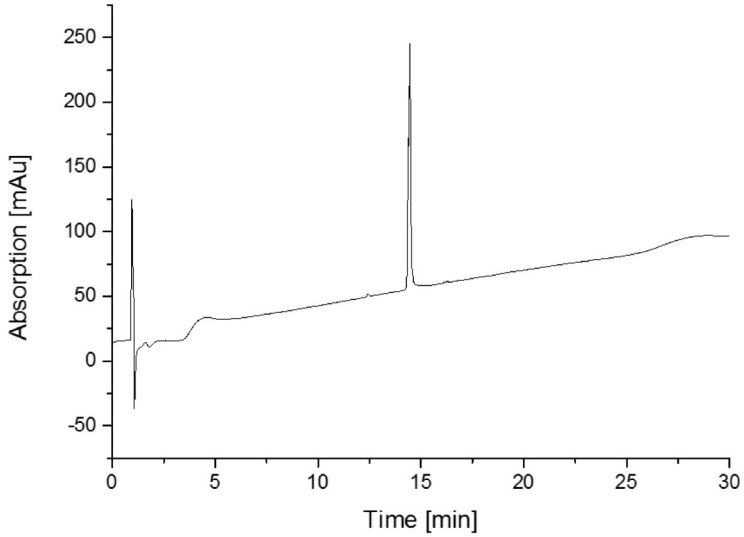

*Appendix 68: RP-HPLC chromatogram (linear gradient from 0-50% eluent B in 30 min at 25 °C) of compound **6c**.*

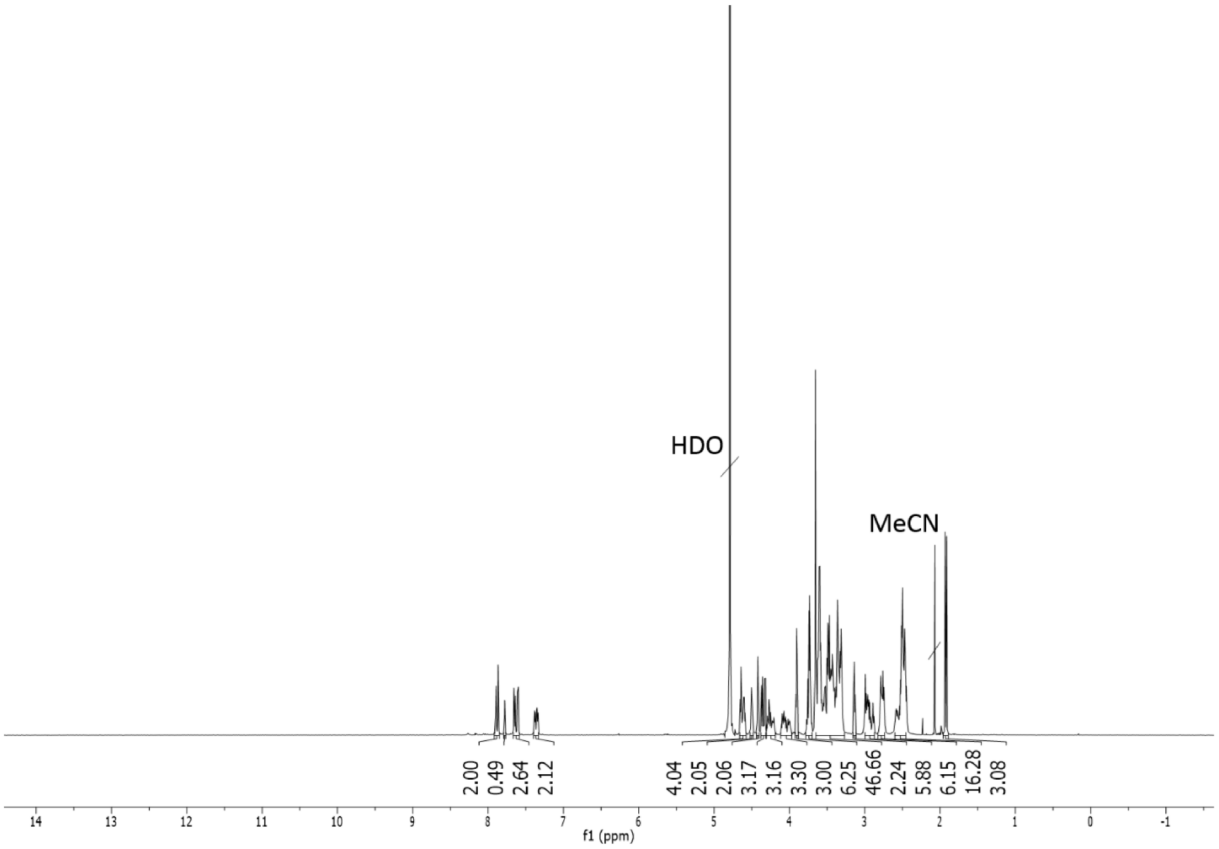

*Appendix 69: ^{1}H-NMR spectrum of **6d** (600 MHz, D_2O). The singlet signal at a chemical shift of 2.07 ppm can be assigned to residues of the solvent acetonitrile (MeCN).*

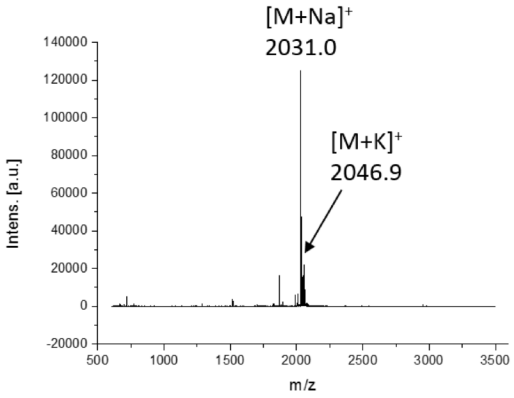

*Appendix 70: MALDI-TOF-MS spectrum of **6d**.*

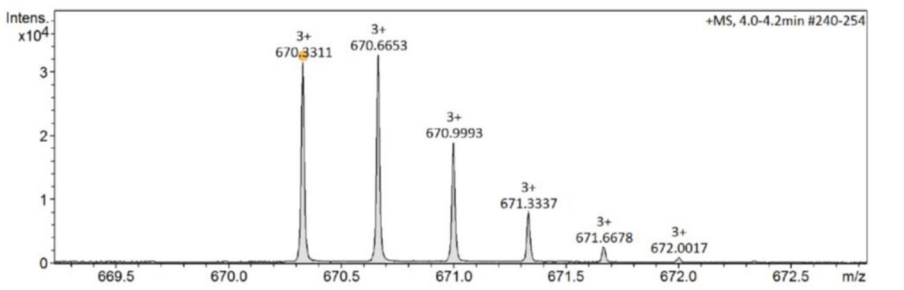

*Appendix 71: HR-MS (ESI$^+$ Q-TOF) of compound **6d**.*

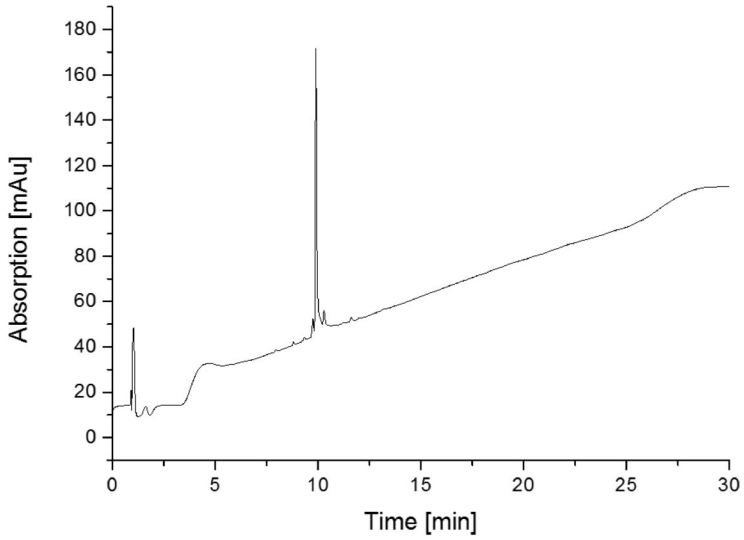

*Appendix 72: RP-HPLC chromatogram (linear gradient from 0-50% eluent B in 30 min at 25 °C) of compound **6d**.*

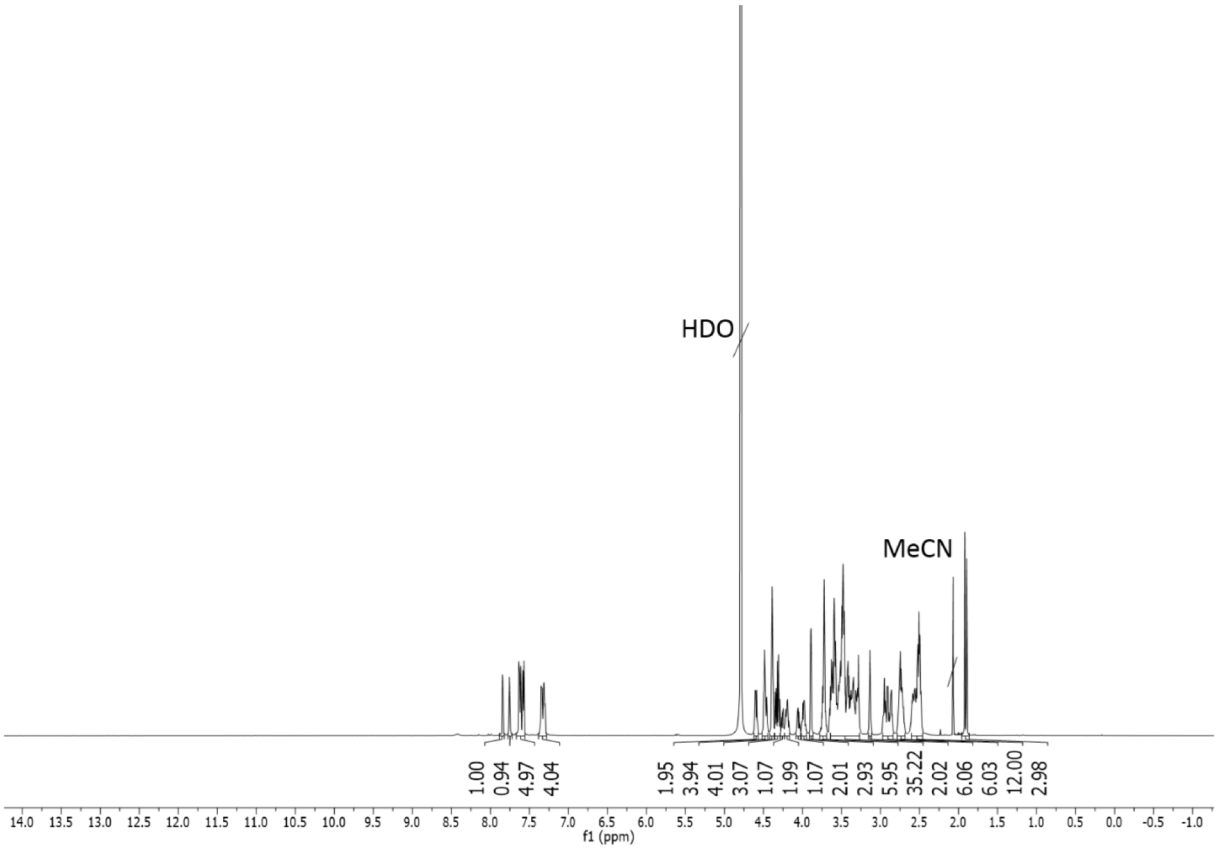

*Appendix 73: ^{1}H-NMR spectrum of **6e** (600 MHz, D_2O). The singlet signal at a chemical shift of 2.07 ppm can be assigned to residues of the solvent acetonitrile (MeCN).*

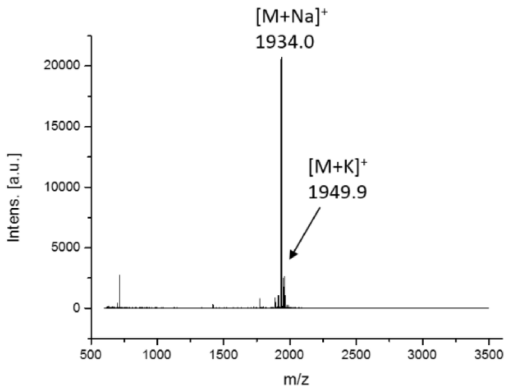

*Appendix 74: MALDI-TOF-MS spectrum of **6e**.*

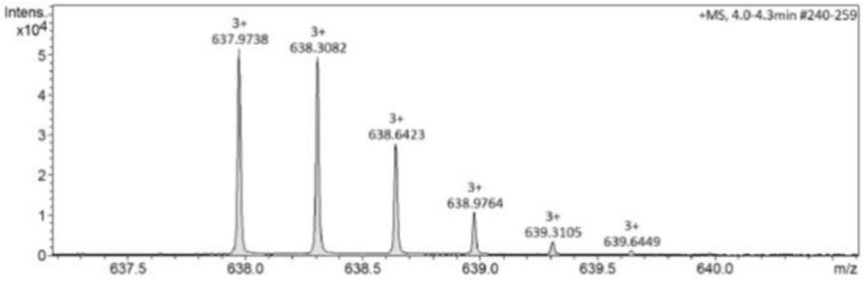

*Appendix 75: HR-MS (ESI$^+$ Q-TOF) of compound **6e**.*

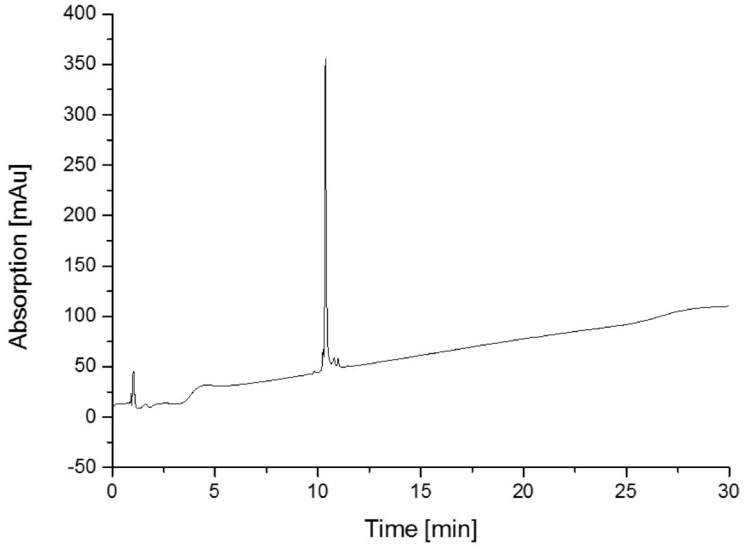

*Appendix 76: RP-HPLC chromatogram (linear gradient from 0-50% eluent B in 30 min at 25 °C) of compound **6e**.*

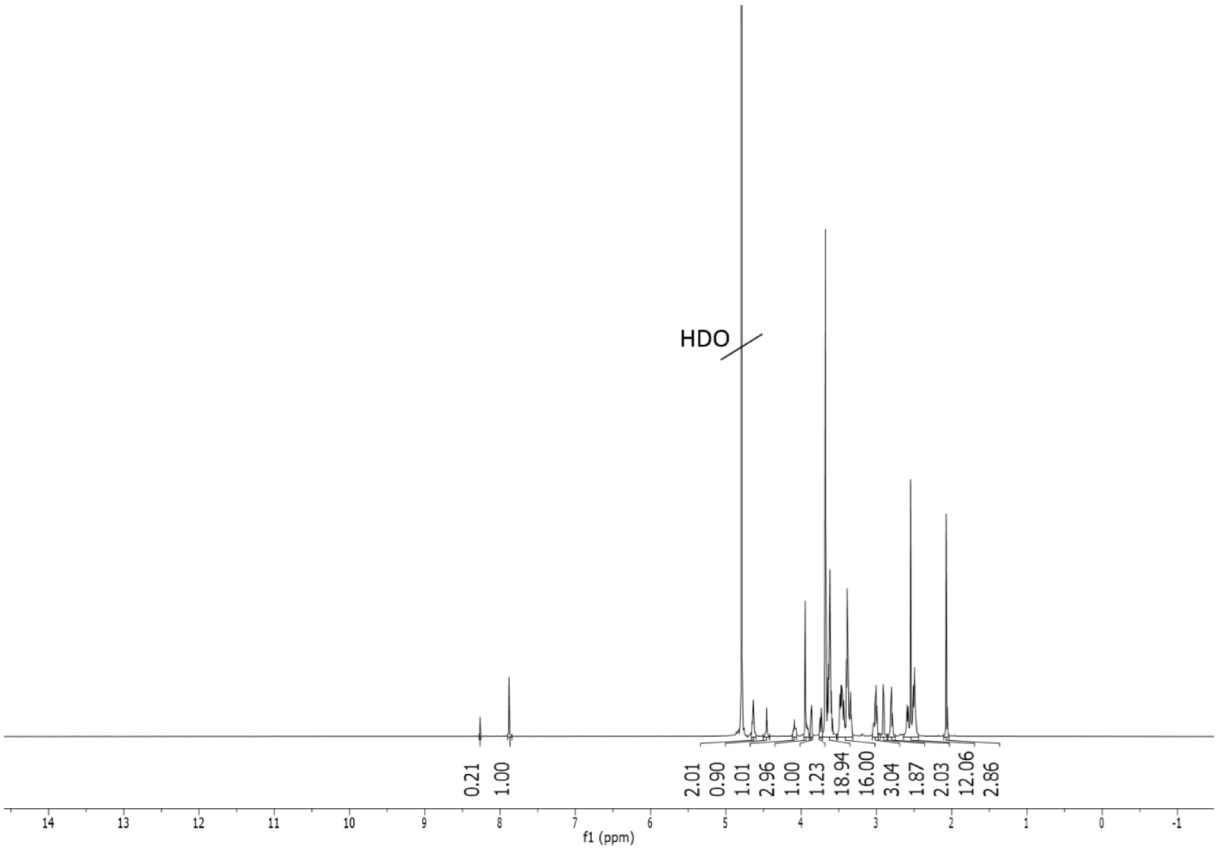

*Appendix 77: ^{1}H-NMR spectrum of **7** (600 MHz, D_2O).*

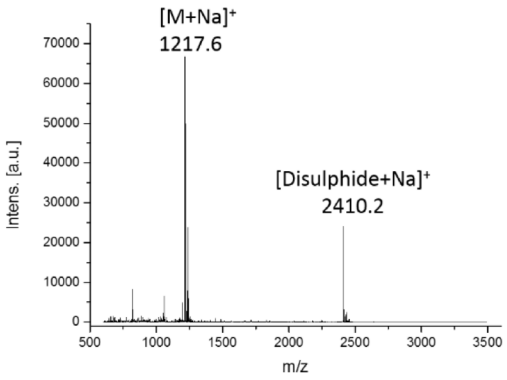

*Appendix 78: MALDI-TOF-MS spectrum of **7**. The signal with the mass to charge ratio of 2410.2 can be assigned to the disulphide.*

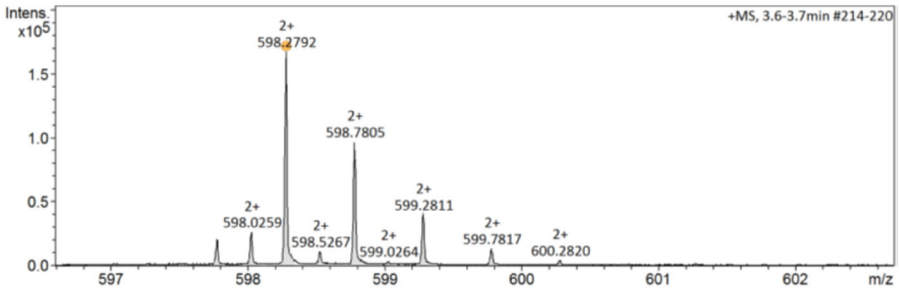

*Appendix 79: HR-MS (ESI⁺ Q-TOF) of compound **7**.*

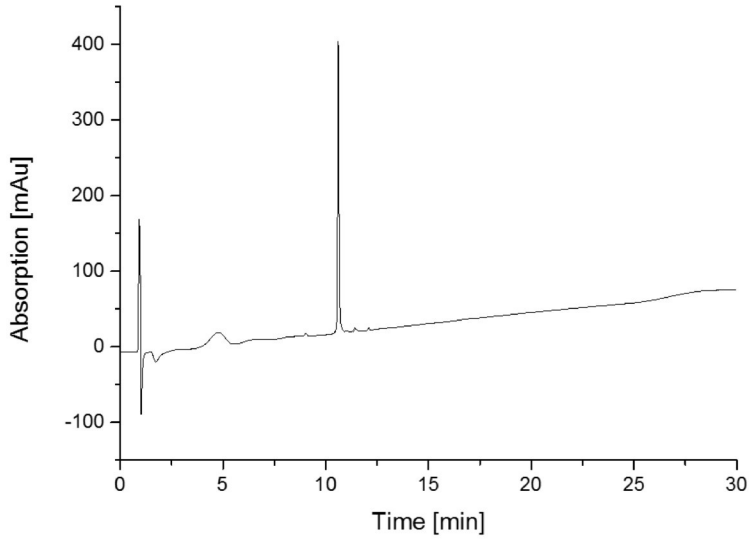

*Appendix 80: RP-HPLC chromatogram (linear gradient from 0-50% eluent B in 30 min at 25 °C) of compound **7**.*

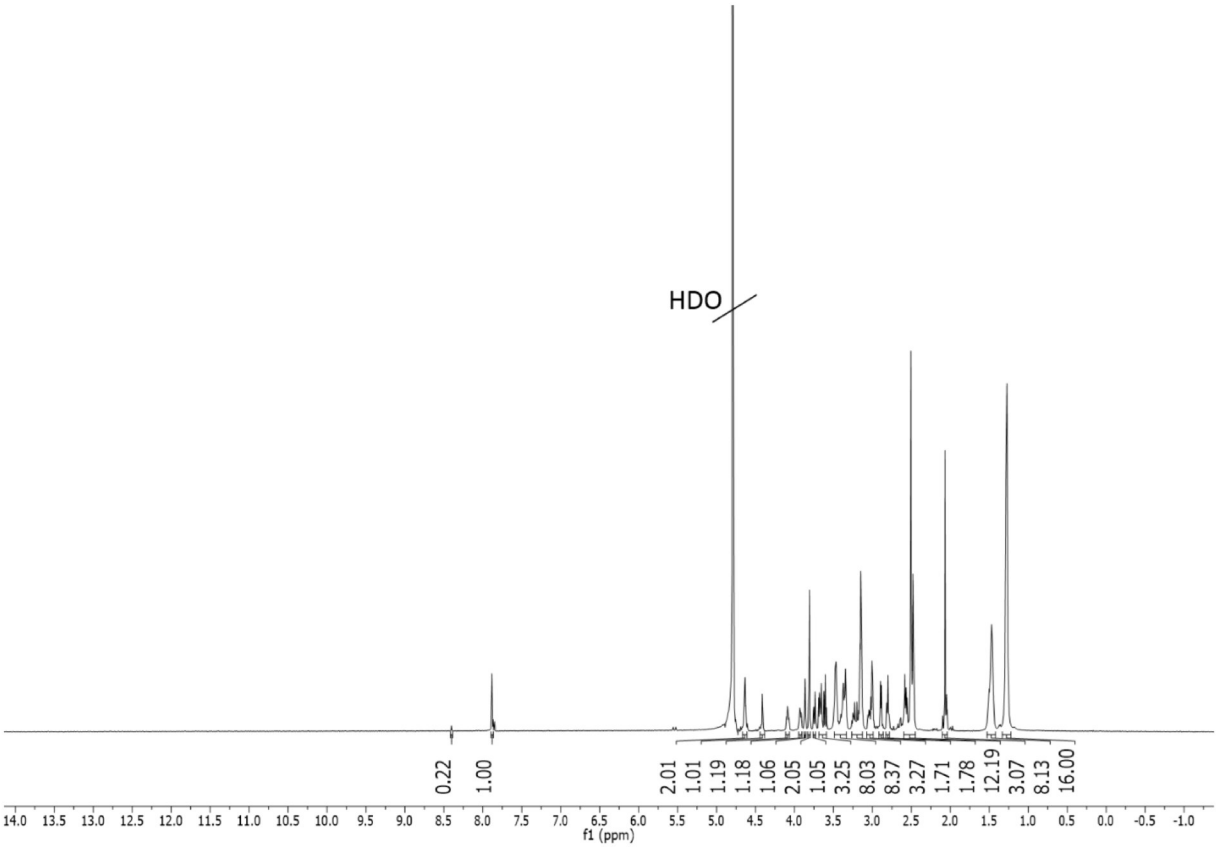

*Appendix 81: ^{1}H-NMR spectrum of **8** (600 MHz, D_2O).*

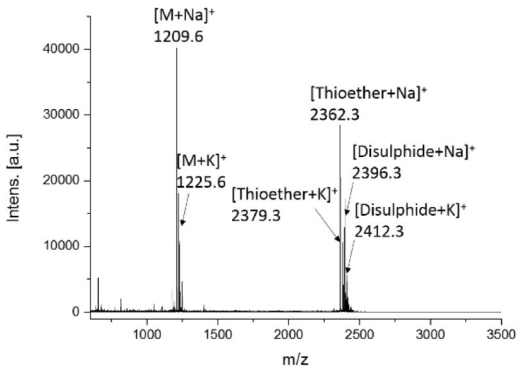

*Appendix 82: MALDI-TOF-MS spectrum of **8**. The signal with the mass to charge ratio of 2396.3 can be assigned to the disulphide. Besides the product peak furher signals with the mass-to-charge ratio of 2379.3 and 2362.3 can be found in the spectrum that can be assigned to a thioether side product.*

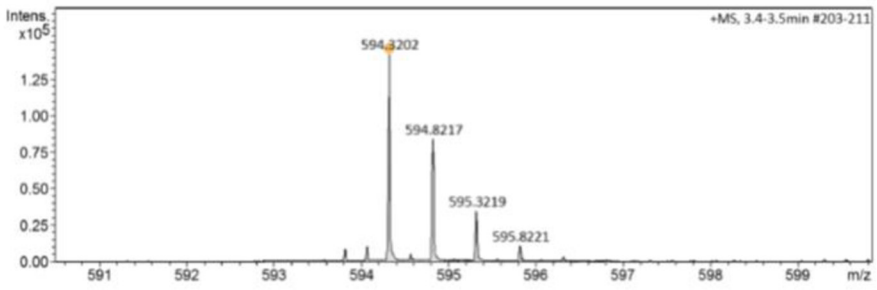

*Appendix 83: HR-MS (ESI⁺ Q-TOF) of compound **8**.*

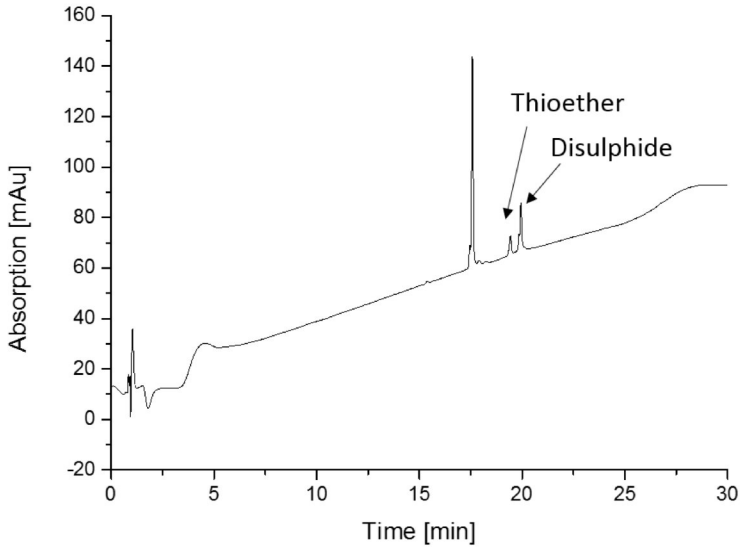

*Appendix 84: RP-HPLC chromatogram (linear gradient from 0-50% eluent B in 30 min at 25 °C) of compound **8**. The peaks at 19.4 and 19.9 min can be assigned to the disulphide and thioether side prduct.*

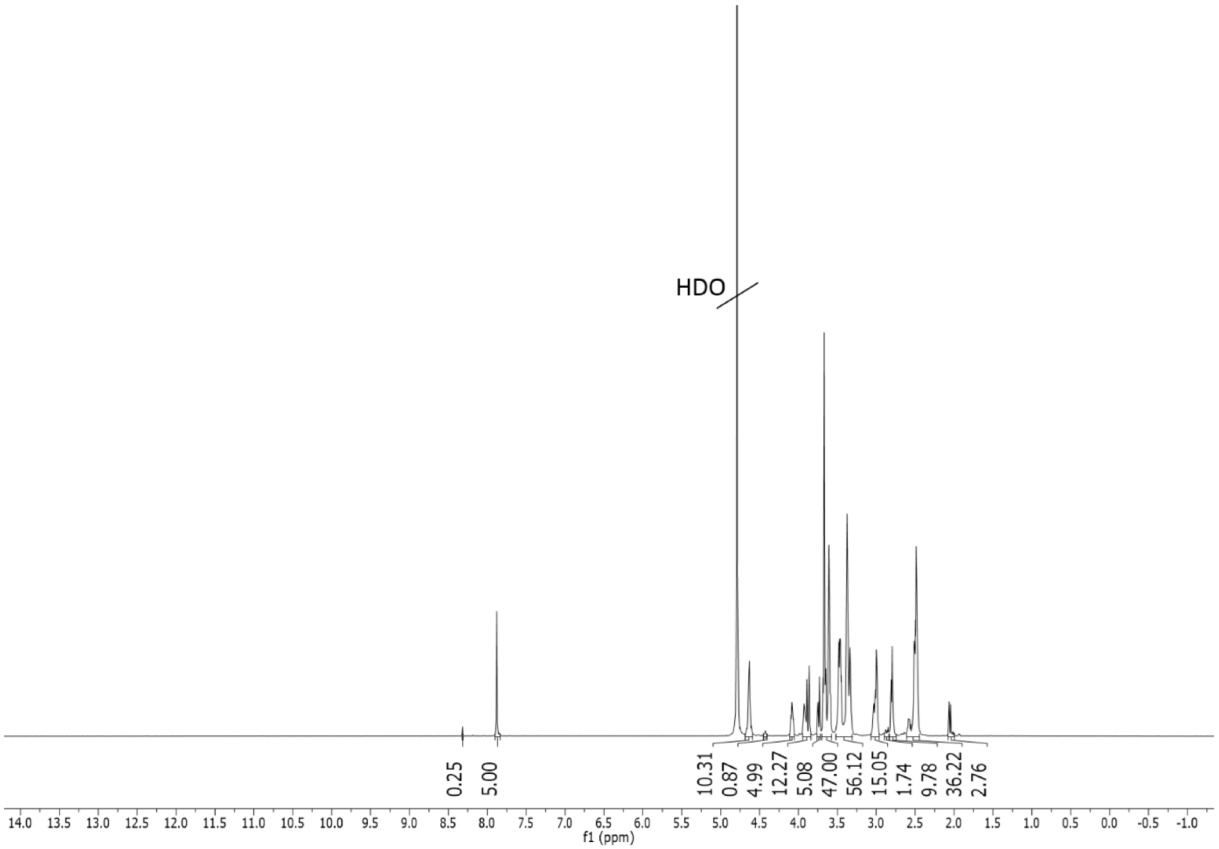

*Appendix 85: ^{1}H-NMR spectrum of **9** (600 MHz, D_2O).*

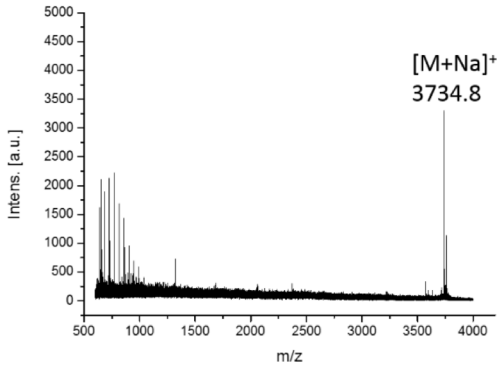

*Appendix 86: MALDI-TOF-MS spectrum of **9**. Further signals with the mass-to-charge ratio of 727.5, 859.6, 903.6 and 947.6 can be found in the spectrum but cannot be assigned to potential by-products.*

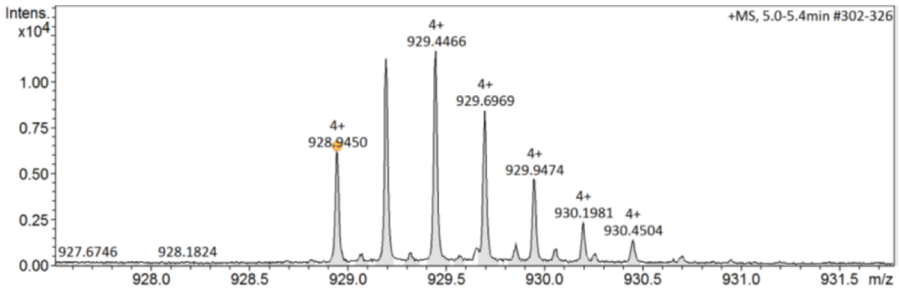

*Appendix 87: HR-MS (ESI$^+$ Q-TOF) of compound **9**.*

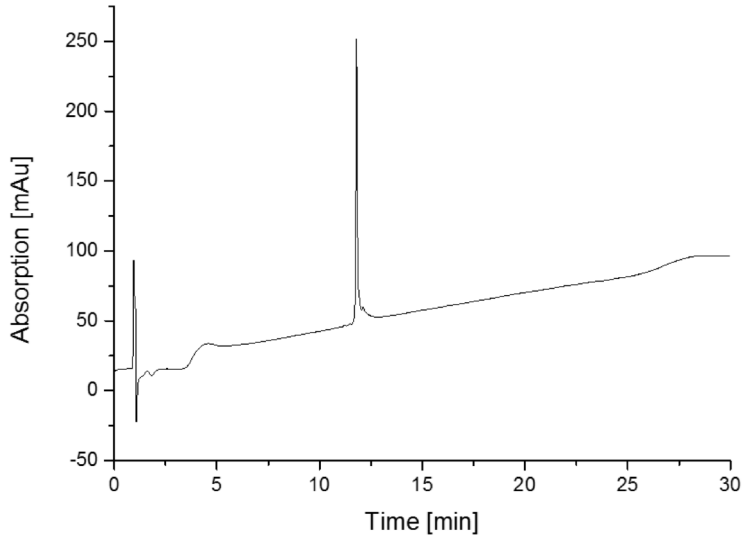

*Appendix 88: RP-HPLC chromatogram (linear gradient from 0-50% eluent B in 30 min at 25 °C) of compound **9**.*

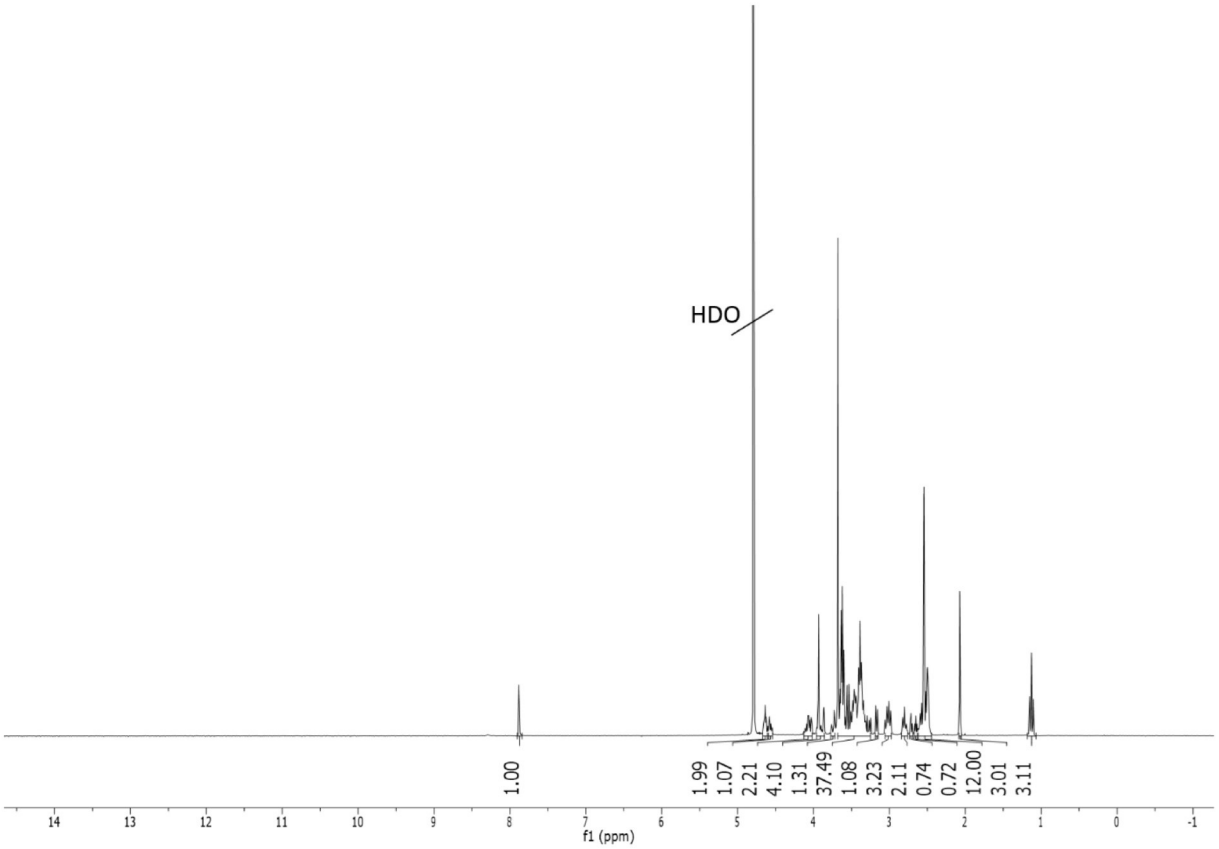

*Appendix 89: ^{1}H-NMR spectrum of **7a** (600 MHz, D_2O).*

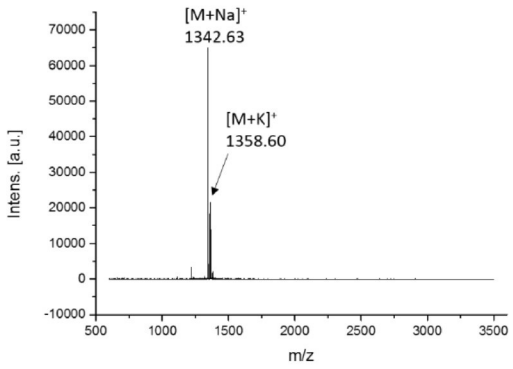

*Appendix 90: MALDI-TOF-MS spectrum of **7a**.*

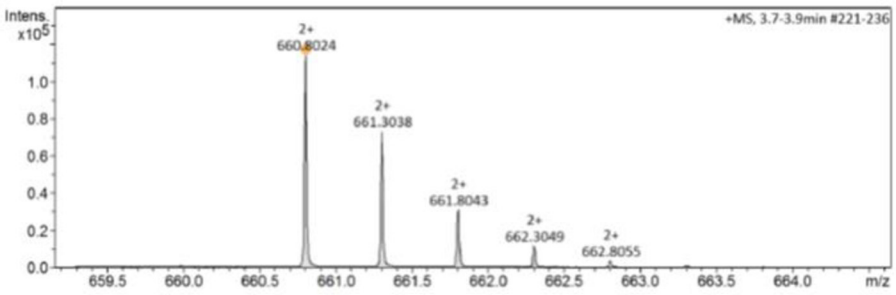

*Appendix 91: HR-MS (ESI⁺ Q-TOF) of compound **7a**.*

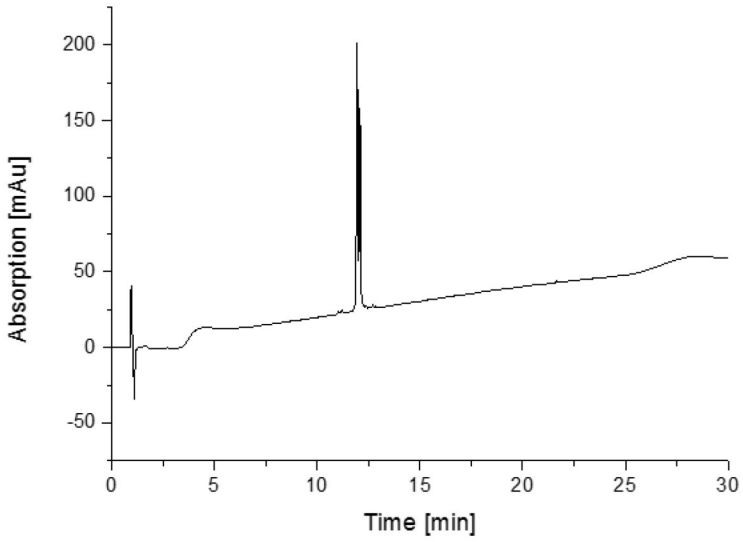

*Appendix 92: RP-HPLC chromatogram (linear gradient from 0-50% eluent B in 30 min at 25 °C) of compound **7a**.*

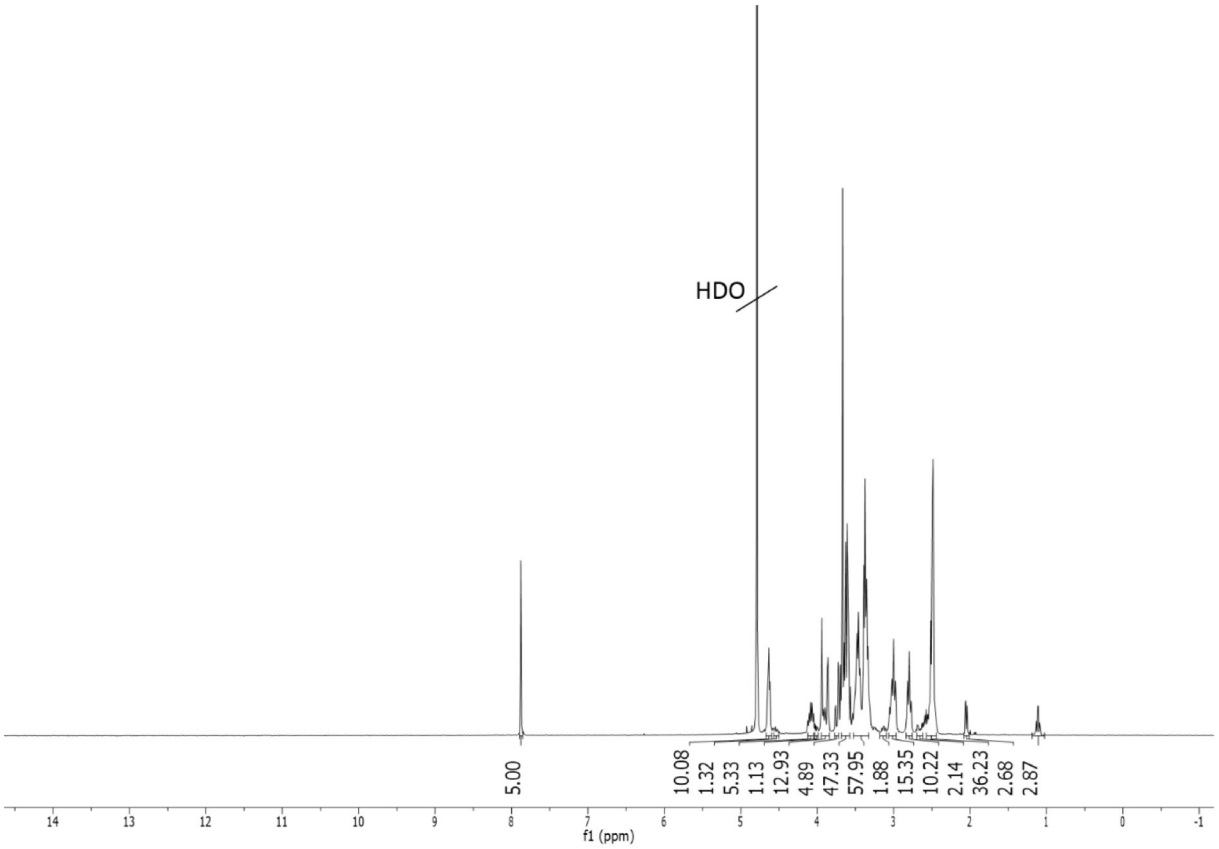

*Appendix 93: ^{1}H-NMR spectrum of **9a** (600 MHz, D_2O).*

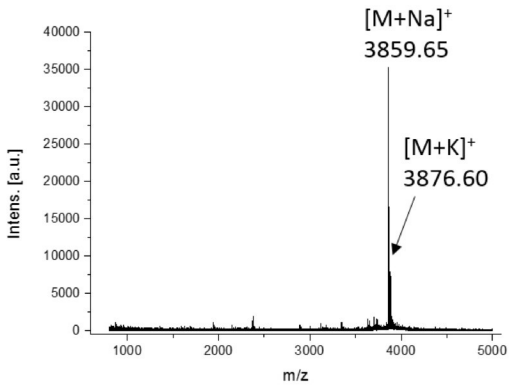

*Appendix 94: MALDI-TOF-MS spectrum of **9a**.*

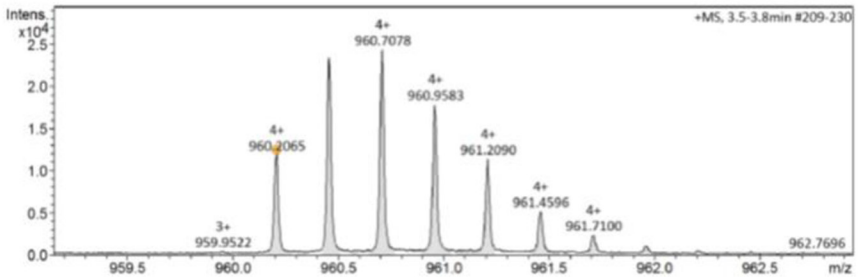

*Appendix 95: HR-MS (ESI⁺ Q-TOF) of compound **9a**.*

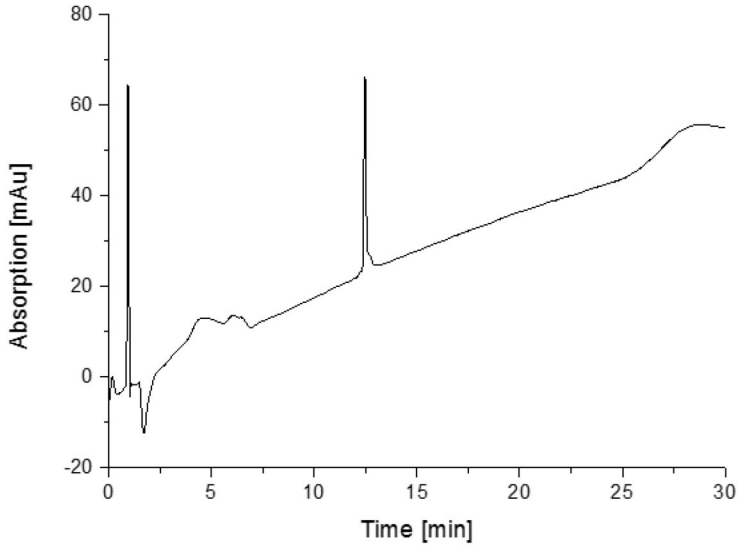

*Appendix 96: RP-HPLC chromatogram (linear gradient from 0-50% eluent B in 30 min at 25 °C) of compound **9a**.*

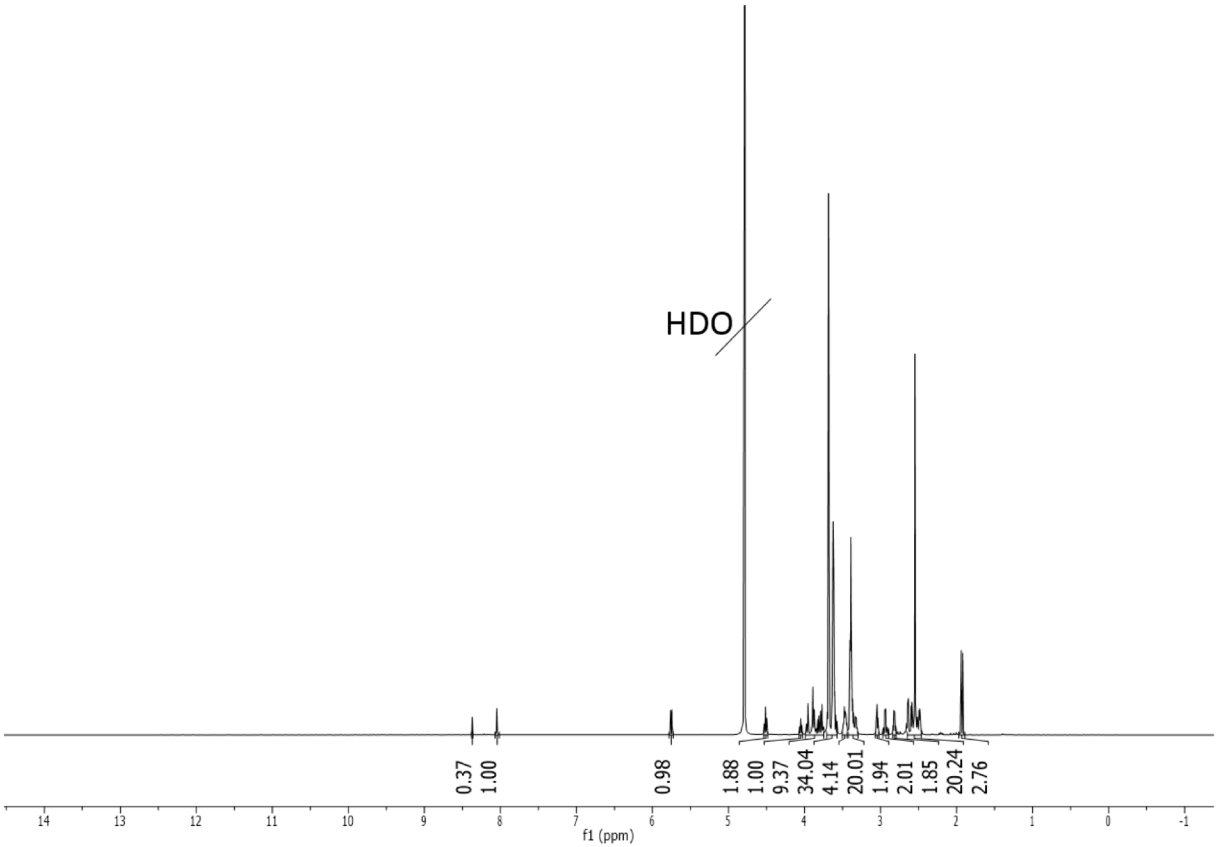

*Appendix 97: ^{1}H-NMR spectrum of **13a** (600 MHz, D_2O).*

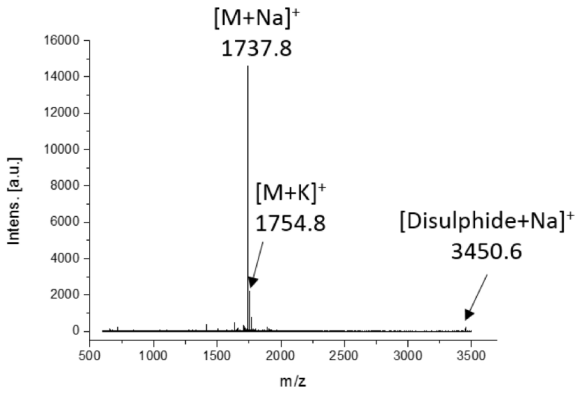

*Appendix 98: MALDI-TOF-MS spectrum of **13a**. The signal with the mass to charge ratio of 3450.6 can be assigned to the disulphide.*

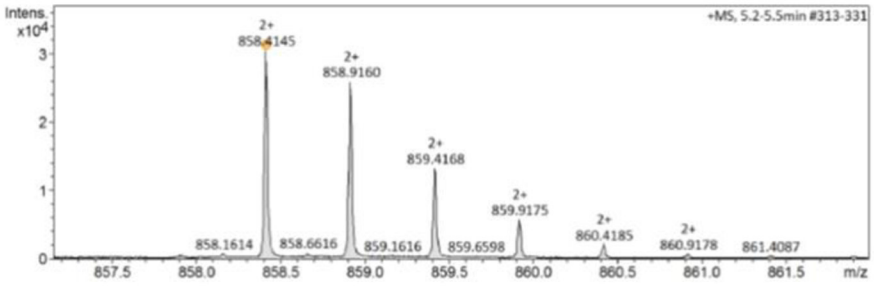

*Appendix 99: HR-MS (ESI⁺ Q-TOF) of compound **13a**.*

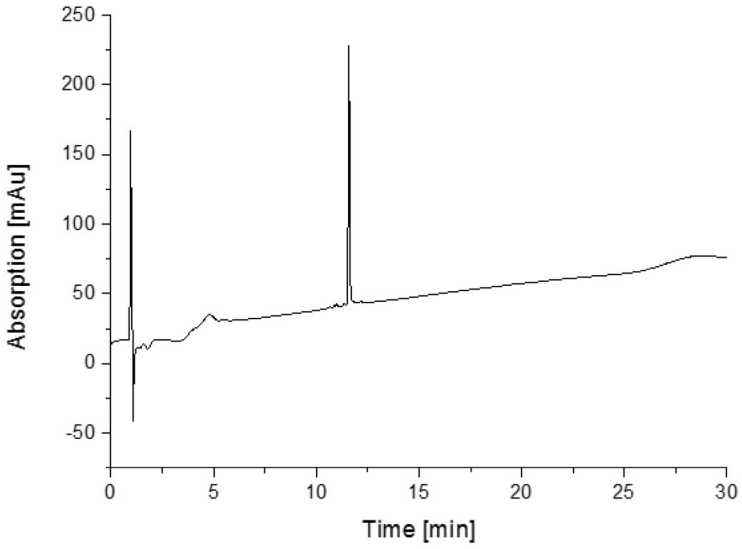

*Appendix 100: RP-HPLC chromatogram (linear gradient from 0-50% eluent B in 30 min at 25 °C) of compound **13a**.*

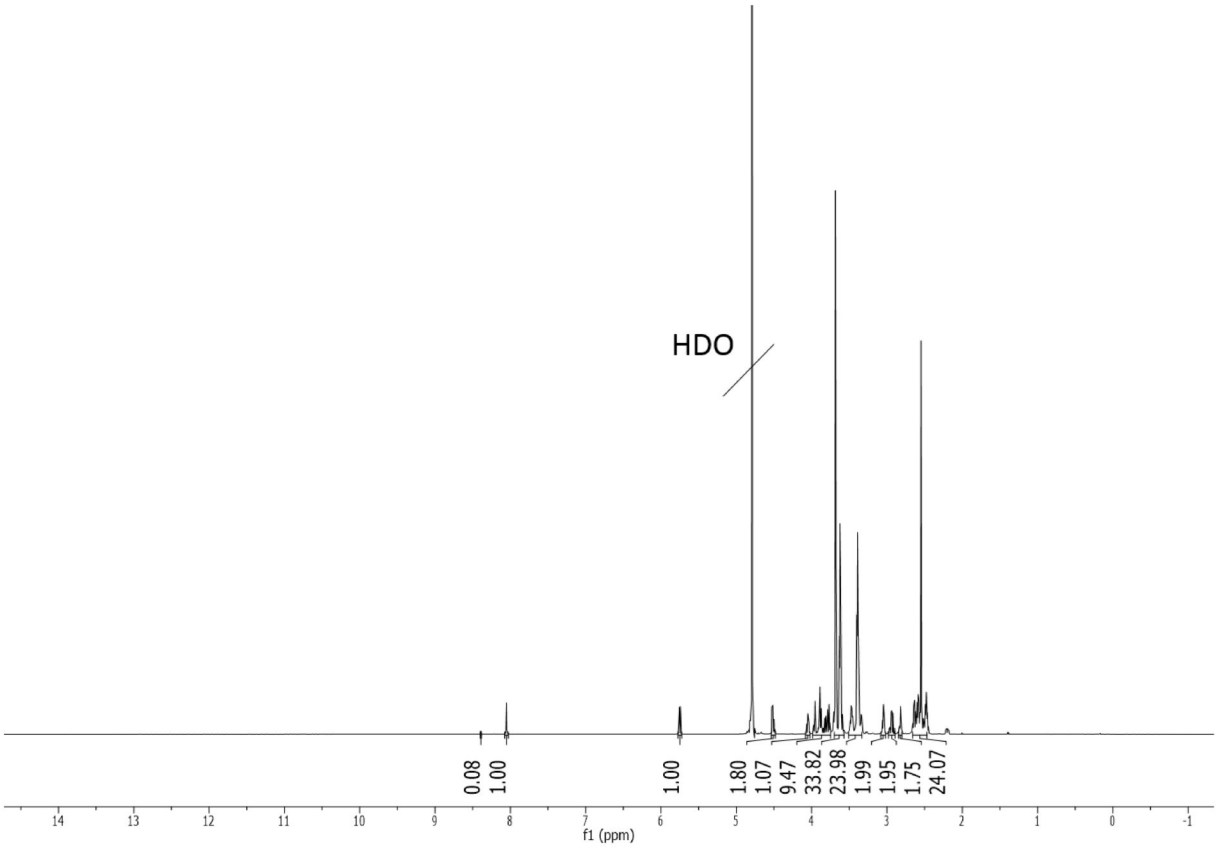

*Appendix 101: ^{1}H-NMR spectrum of **13b** (600 MHz, D_2O).*

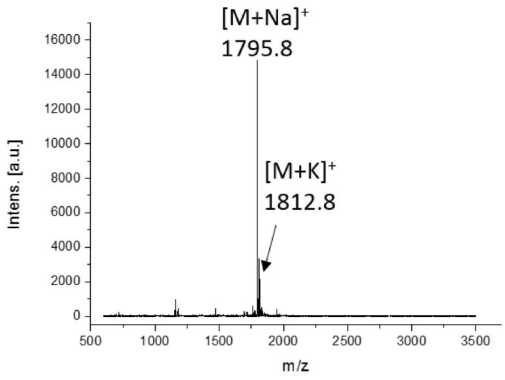

*Appendix 102: MALDI-TOF-MS spectrum of **13b**.*

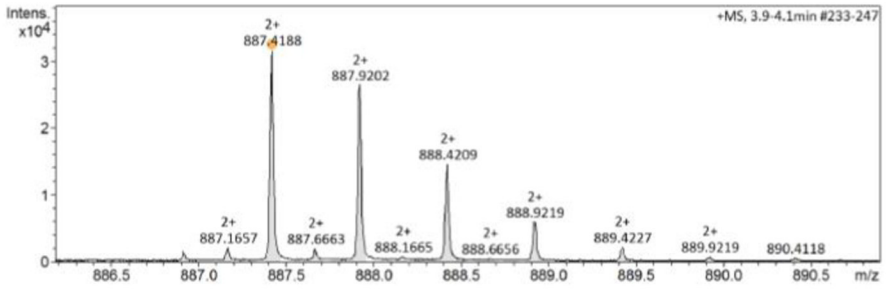

*Appendix 103: HR-MS (ESI⁺ Q-TOF) of compound **13b**.*

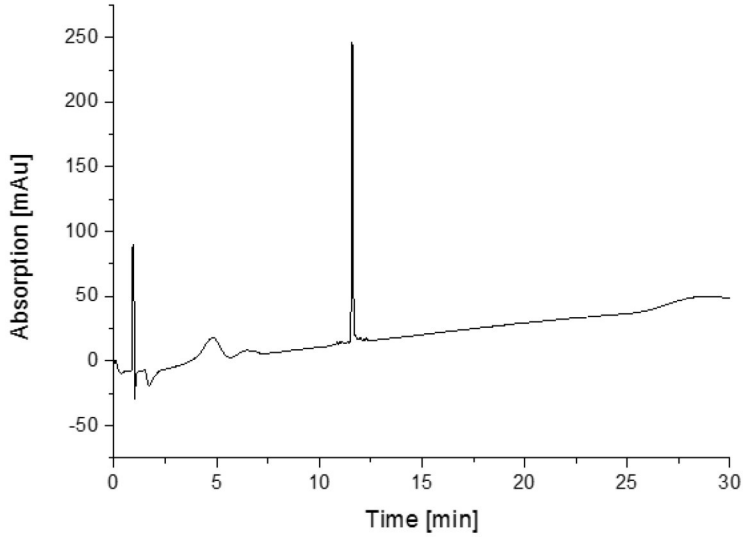

*Appendix 104: RP-HPLC chromatogram (linear gradient from 0-50% eluent B in 30 min at 25 °C) of compound **13b**.*

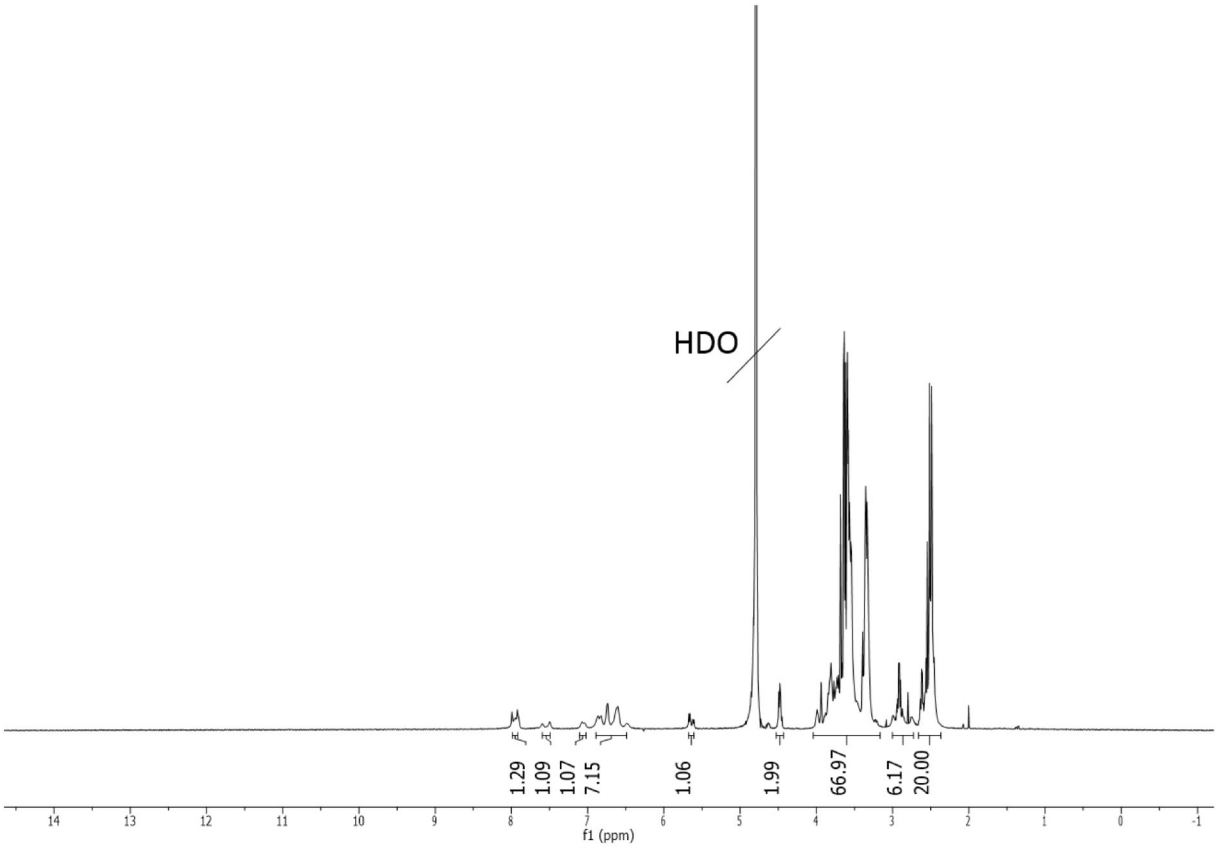

*Appendix 105: ^{1}H-NMR spectrum of **13c** (600 MHz, D_2O).*

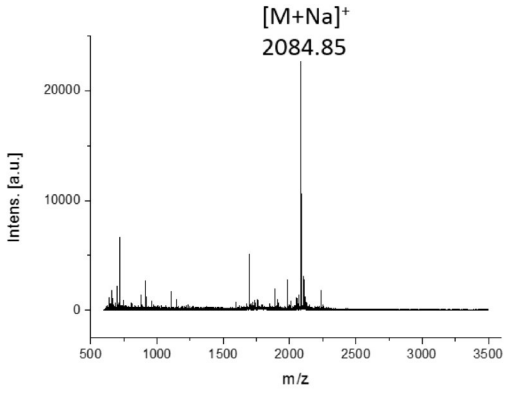

*Appendix 106: MALDI-TOF-MS spectrum of **13c**. One further signal with the mass-to-charge ratio of 1695.8 can be found in the spectrum and can be assigned to the product peak that is unconjugated. Further signals with the mass-to-charge ratio of 715.4, 915.4 and 1105.6 can be found in the spectrum but cannot be assigned to potential by-products.*

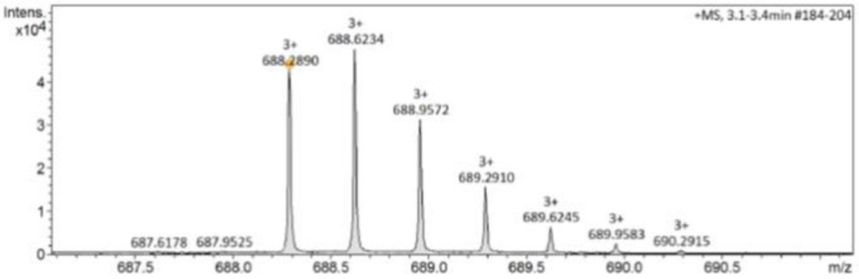

*Appendix 107: HR-MS (ESI⁺ Q-TOF) of compound **13c**.*

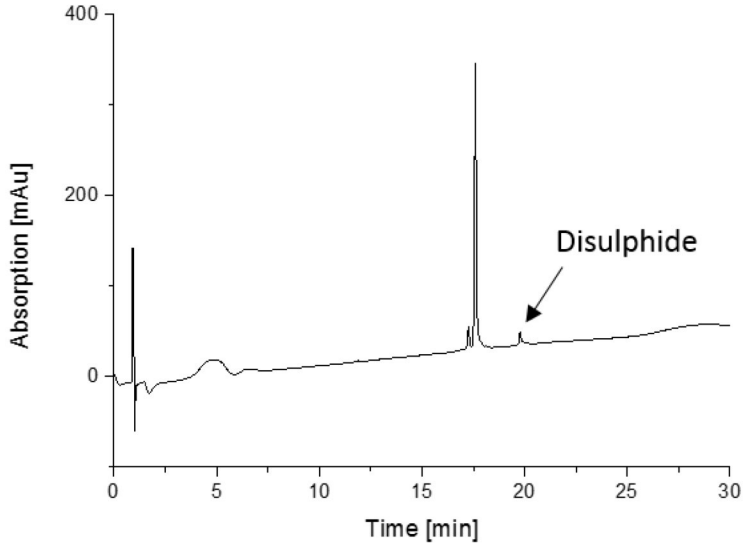

*Appendix 108: RP-HPLC chromatogram (linear gradient from 0-50% eluent B in 30 min at 25 °C) of compound **13c**. The peaks at 17.2 and 19.7 min can be assigned to the side product in which FITC is conjugated to the thiol functionality and the disulphide.*

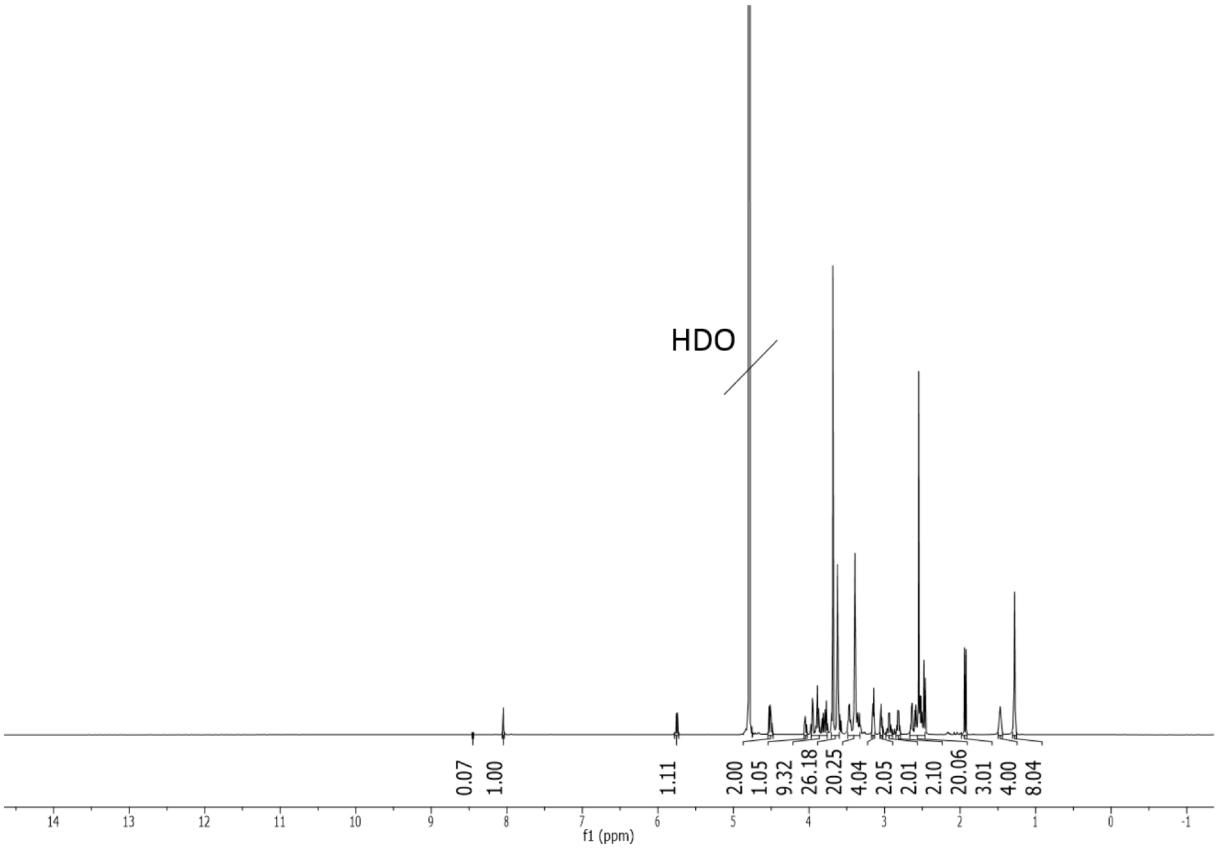

*Appendix 109: ^{1}H-NMR spectrum of **14a** (600 MHz, D_2O).*

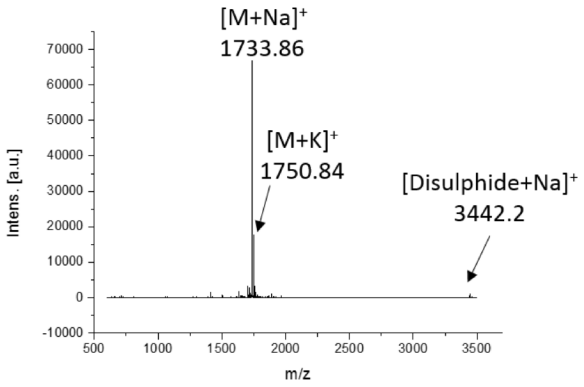

*Appendix 110: MALDI-TOF-MS spectrum of **14a**. The signal with the mass to charge ratio of 3442.2 can be assigned to the disulphide.*

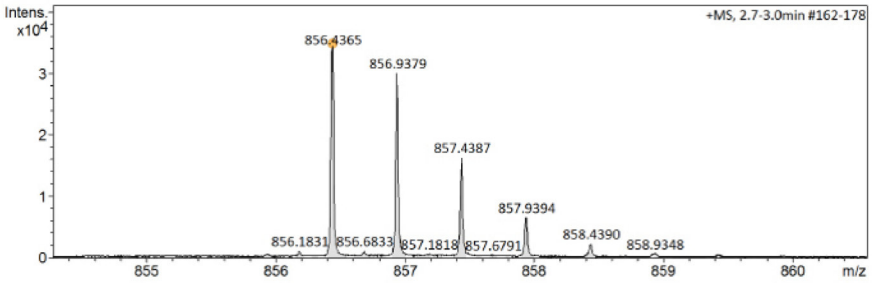

*Appendix 111: HR-MS (ESI⁺ Q-TOF) of compound **14a**.*

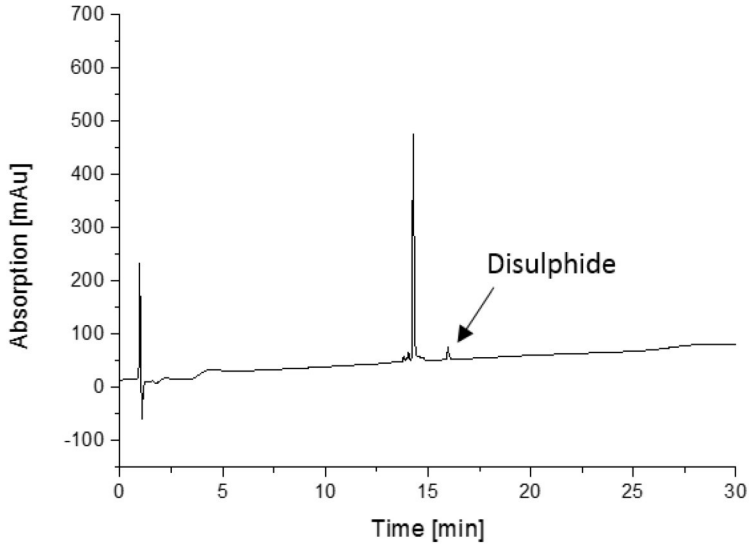

*Appendix 112: RP-HPLC chromatogram (linear gradient from 0-50% eluent B in 30 min at 25 °C) of compound **14a**. The peak at 15.9 min can be assigned the disulphide.*

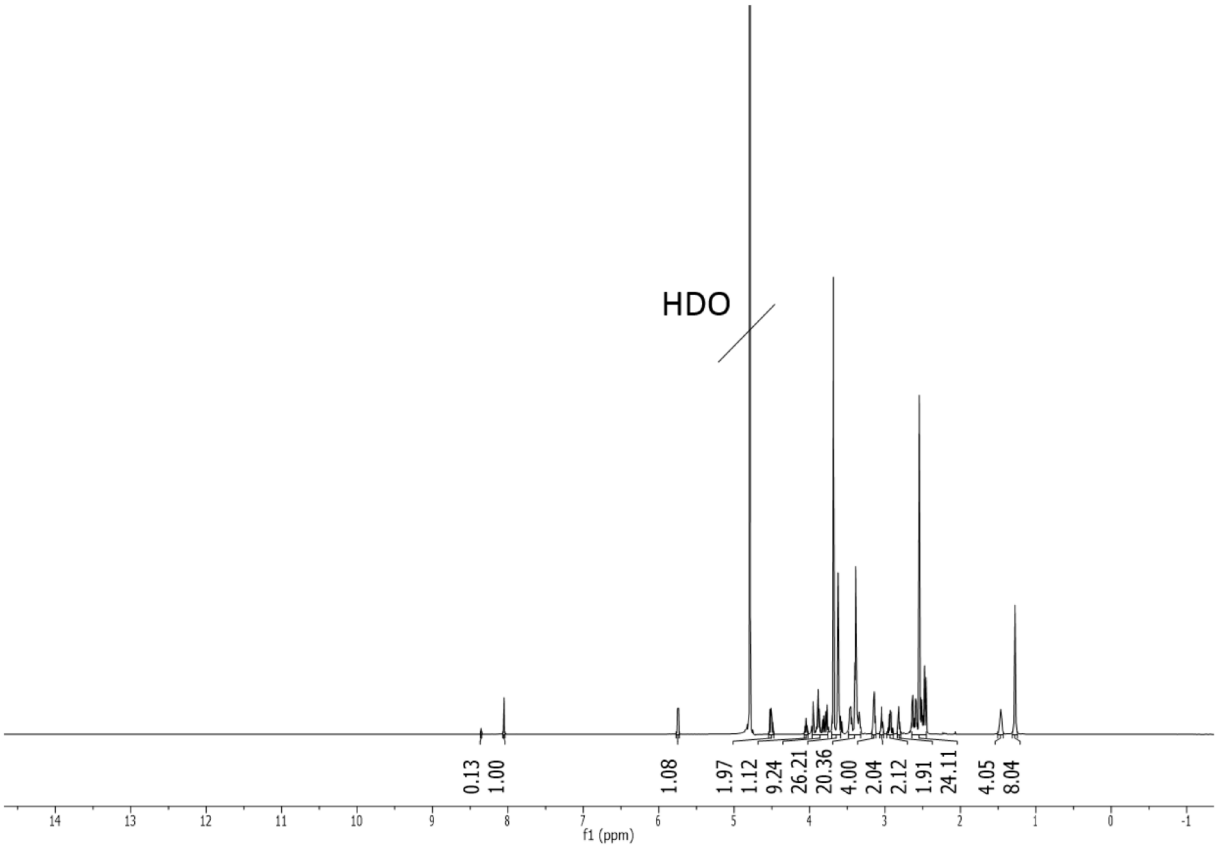

*Appendix 113: ^{1}H-NMR spectrum of **14b** (600 MHz, D_2O).*

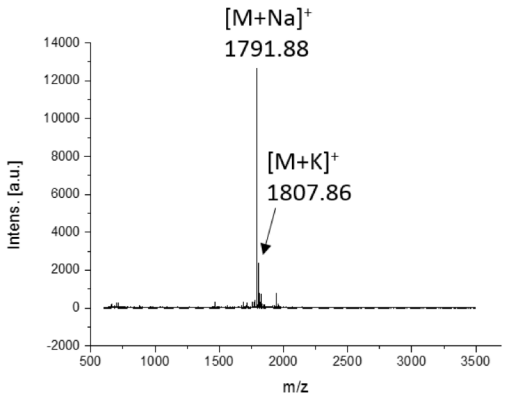

*Appendix 114: MALDI-TOF-MS spectrum of **14b**.*

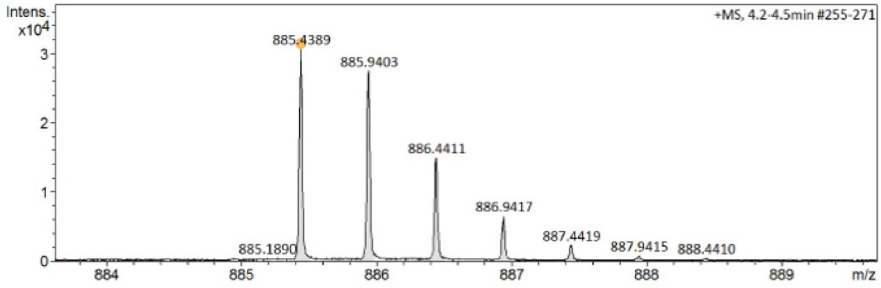

*Appendix 115: HR-MS (ESI⁺ Q-TOF) of compound **14b**.*

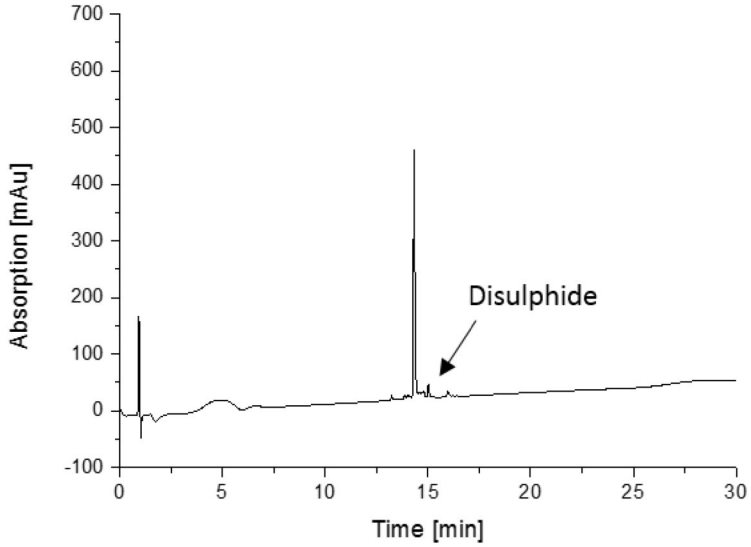

*Appendix 116: RP-HPLC chromatogram (linear gradient from 0-50% eluent B in 30 min at 25 °C) of compound **14b**. The peak at 15.1 min can be assigned to the disulphide.*

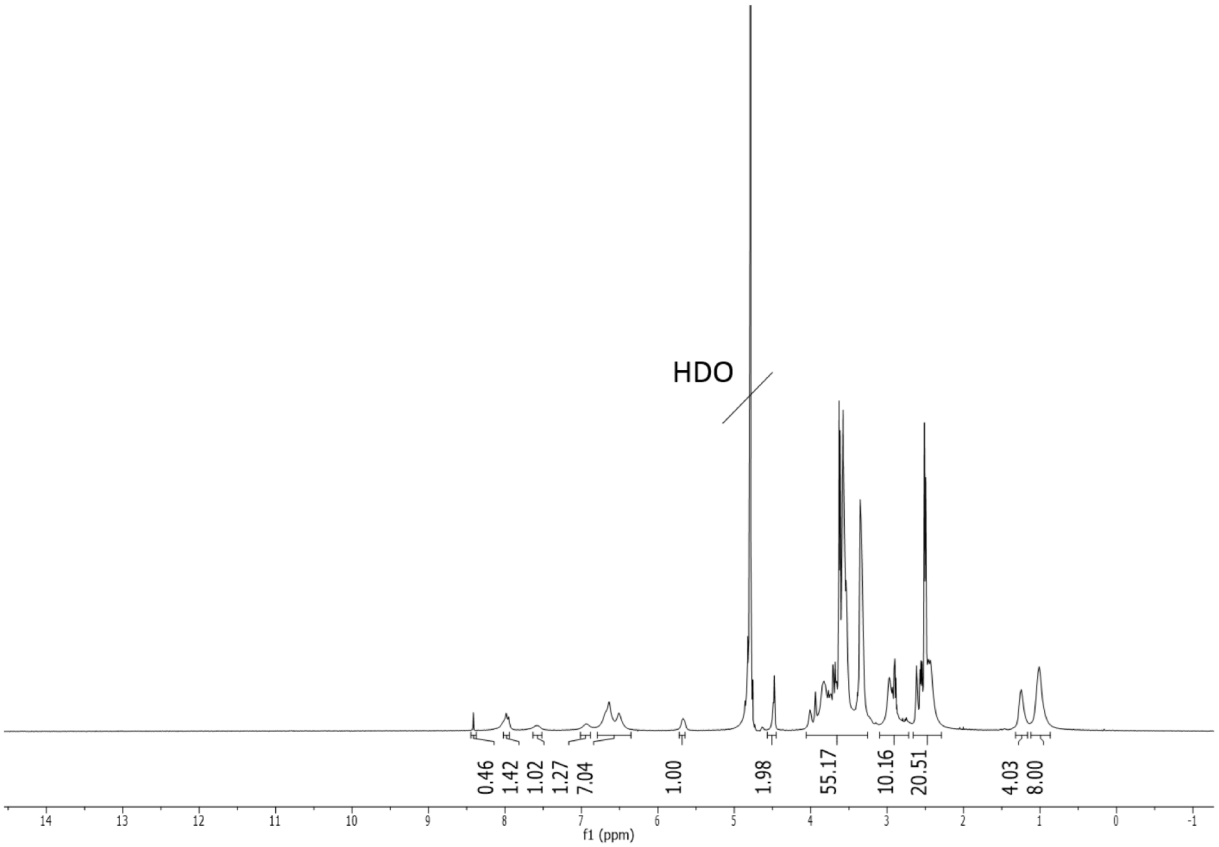

*Appendix 117: ^{1}H-NMR spectrum of **14c** (600 MHz, D_2O).*

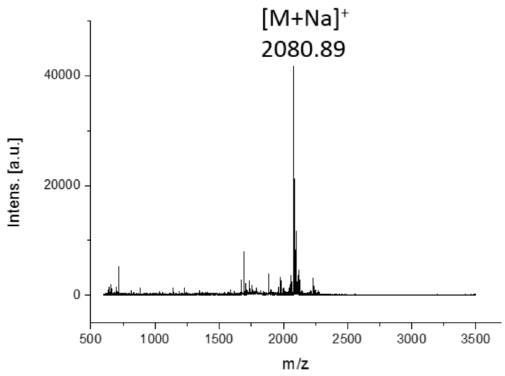

*Appendix 118: MALDI-TOF-MS spectrum of **14c**. One further signal with the mass-to-charge ratio of 1691.9 can be found in the spectrum and can be assigned to the product peak that is unconjugated.*

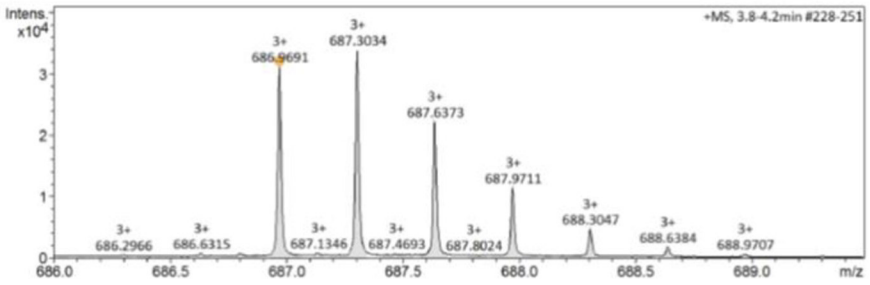

*Appendix 119: HR-MS (ESI⁺ Q-TOF) of compound **14c**.*

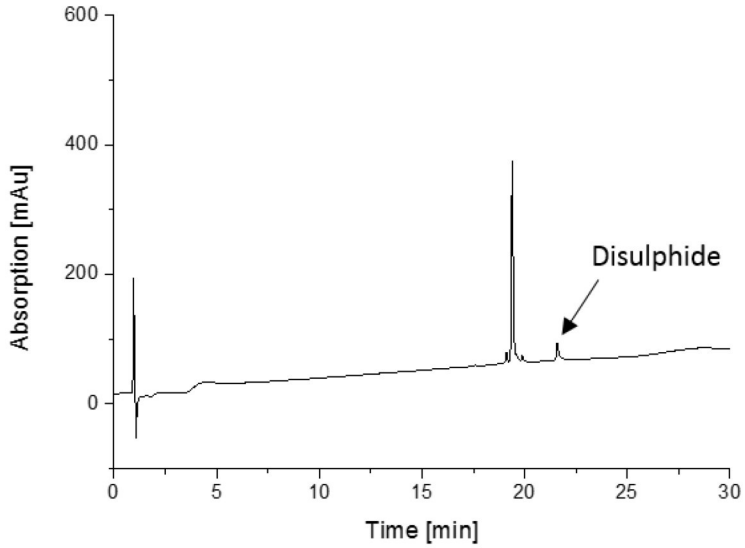

*Appendix 120: RP-HPLC chromatogram (linear gradient from 0-50% eluent B in 30 min at 25 °C) of compound **14c**. The peak at 21.6 min can be assigned to the disulphide.*

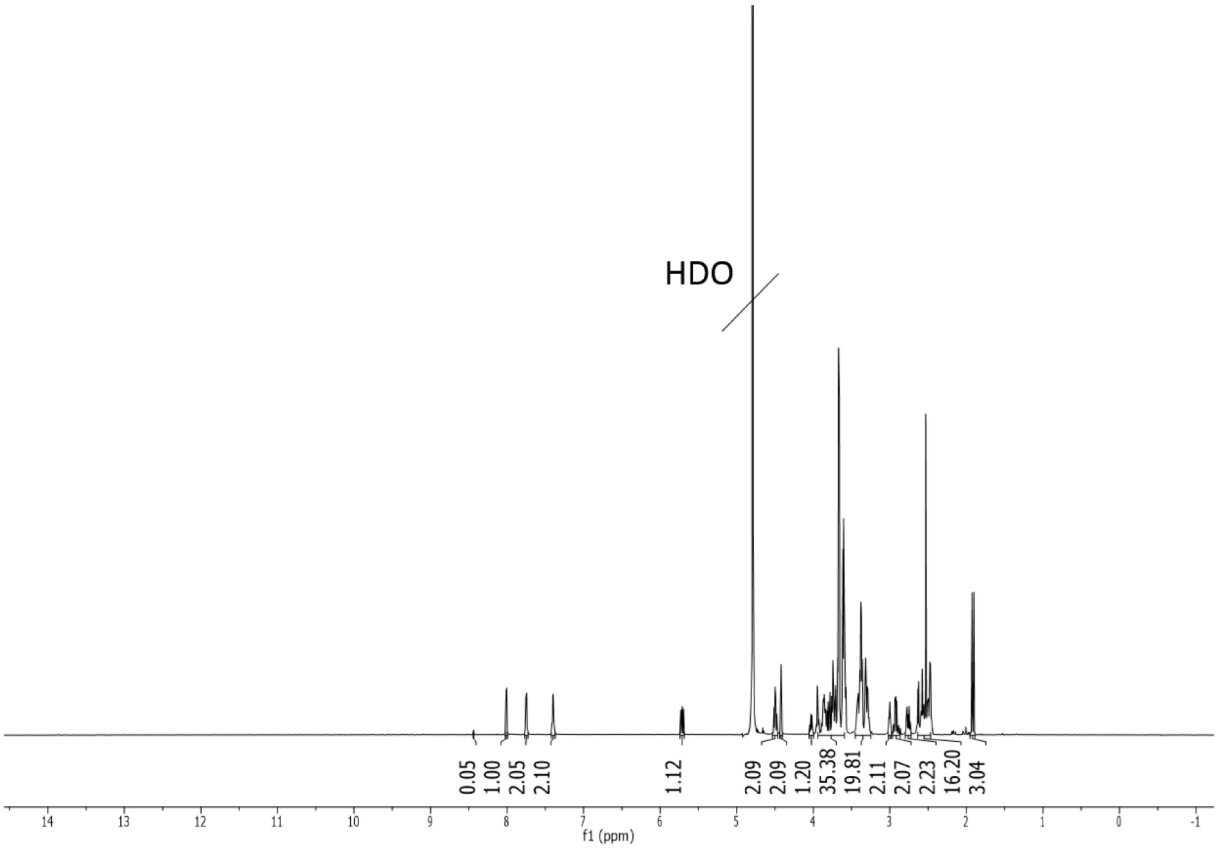

*Appendix 121: ^{1}H-NMR spectrum of **15a** (600 MHz, D_2O).*

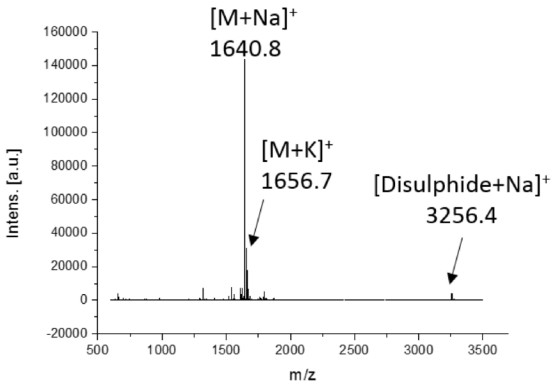

*Appendix 122: MALDI-TOF-MS spectrum of **15a**. The signal with the mass to charge ratio of 3256.4 can be assigned to the disulphide.*

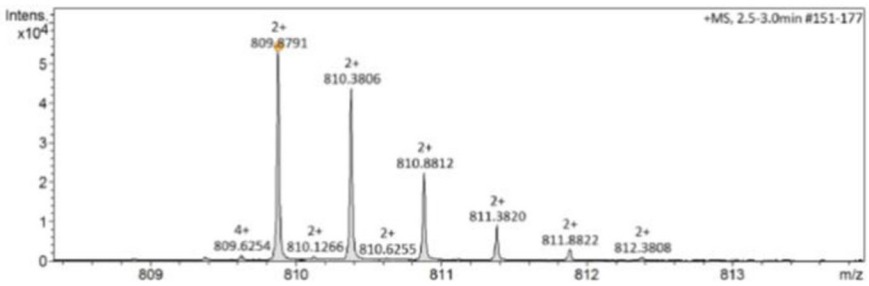

*Appendix 123: HR-MS (ESI⁺ Q-TOF) of compound **15a**.*

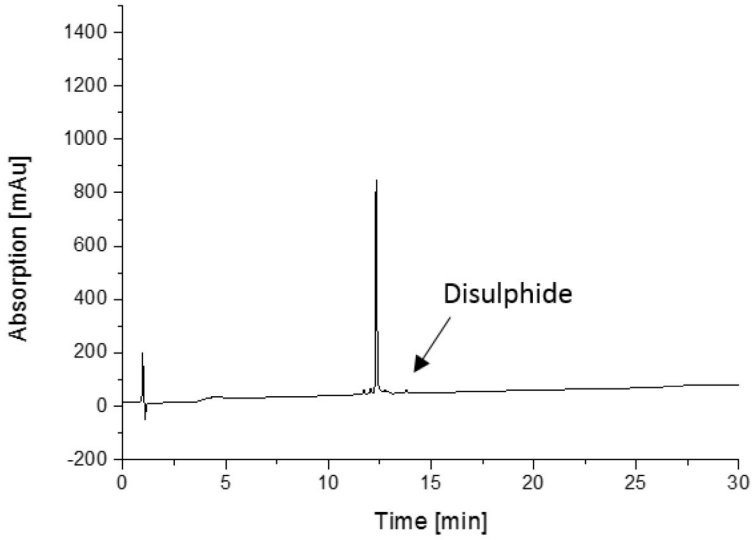

*Appendix 124: RP-HPLC chromatogram (linear gradient from 0-50% eluent B in 30 min at 25 °C) of compound **15a**. The peak at 13.8 min can be assigned to the disulphide.*

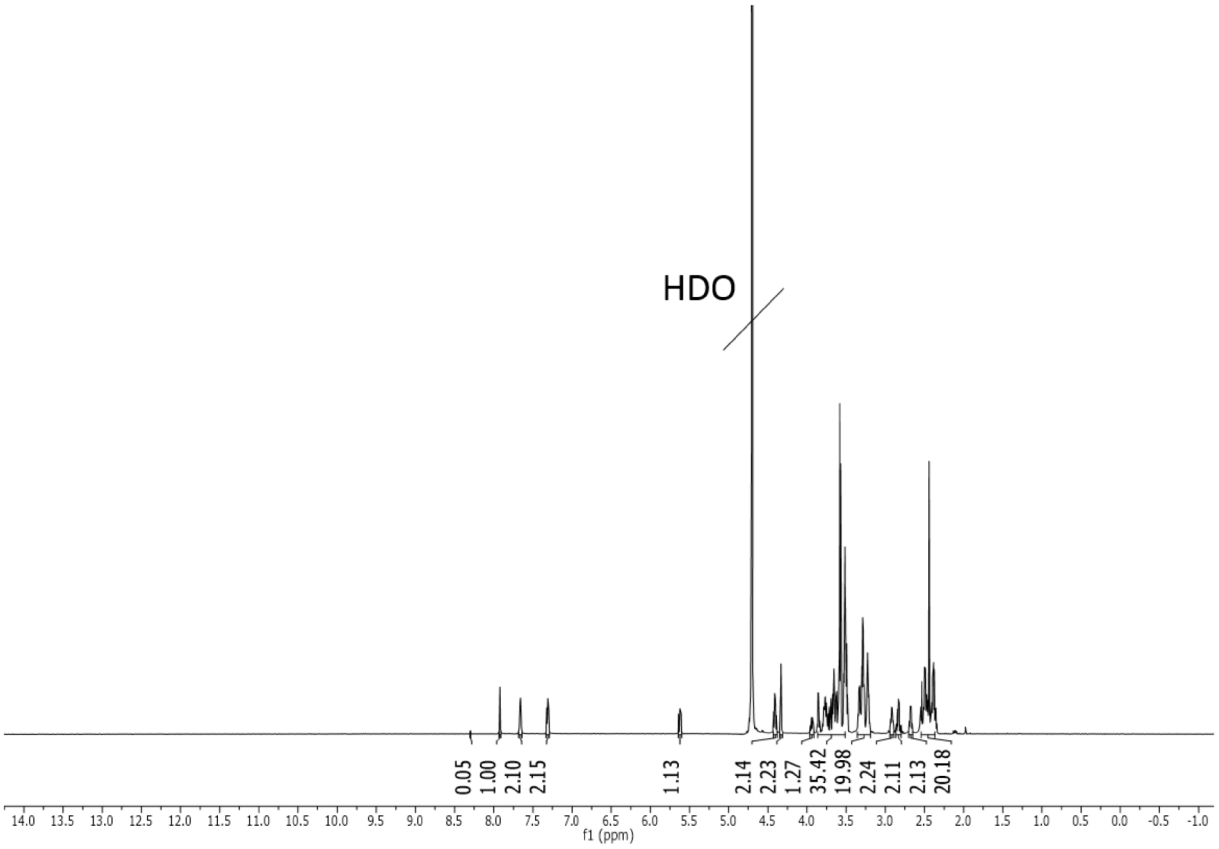

*Appendix 125: ^{1}H-NMR spectrum of **15b** (600 MHz, D_2O).*

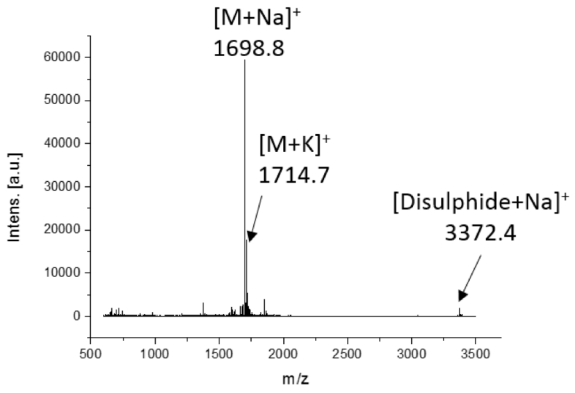

*Appendix 126: MALDI-TOF-MS spectrum of **15b**. The signal with the mass to charge ratio of 3372.4 can be assigned to the disulphide.*

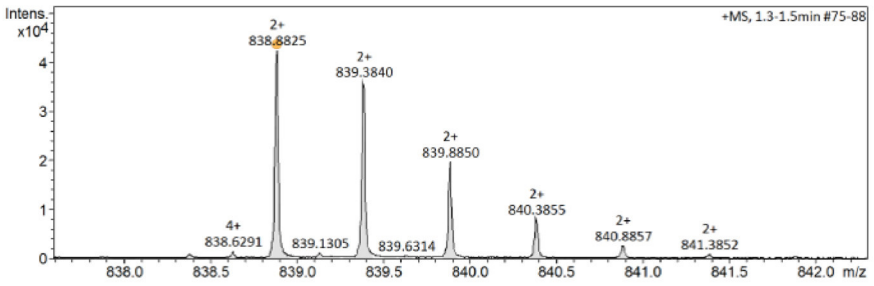

*Appendix 127: HR-MS (ESI⁺ Q-TOF) of compound **15b**.*

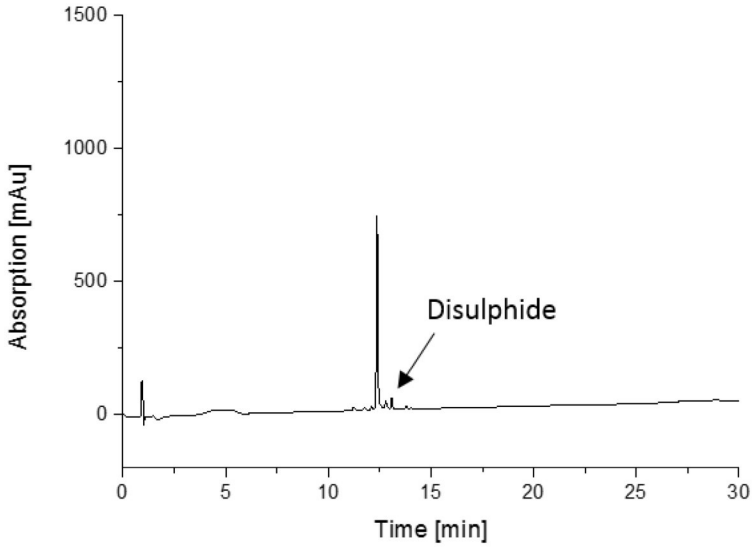

*Appendix 128: RP-HPLC chromatogram (linear gradient from 0-50% eluent B in 30 min at 25 °C) of compound **15b**. The peak at 13.1 min can be assigned to the disulphide.*

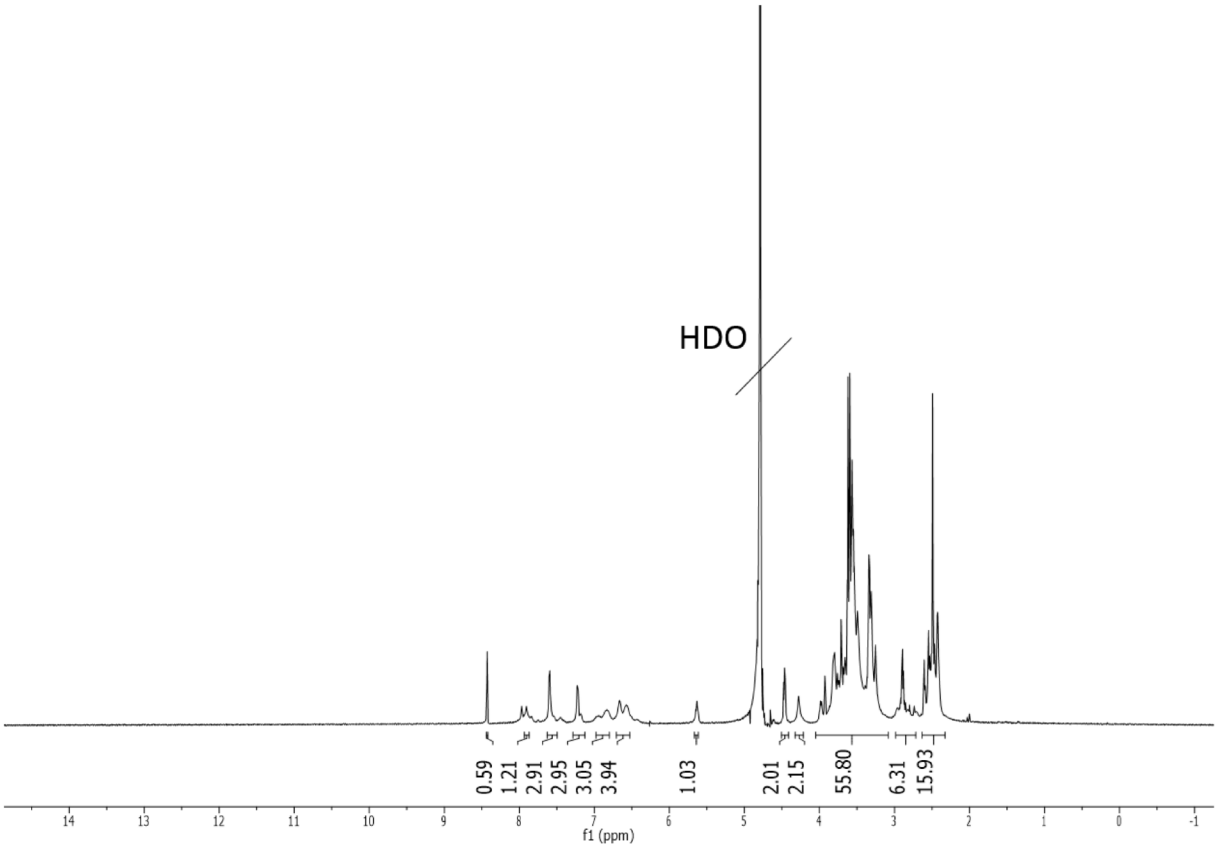

*Appendix 129: ^{1}H-NMR spectrum of **15c** (600 MHz, D_2O).*

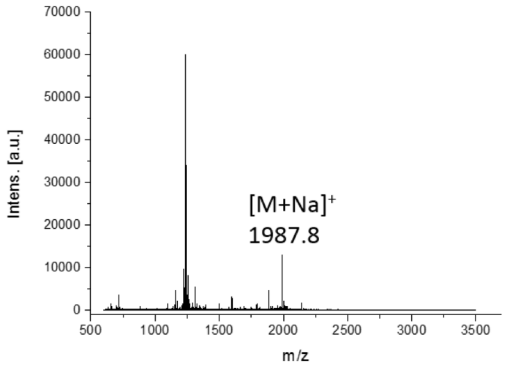

*Appendix 130: MALDI-TOF-MS spectrum of **15c**. One further signal with the mass-to-charge ratio of 1239.5 can be found in the spectrum but cannot be assigned to potential by-products.*

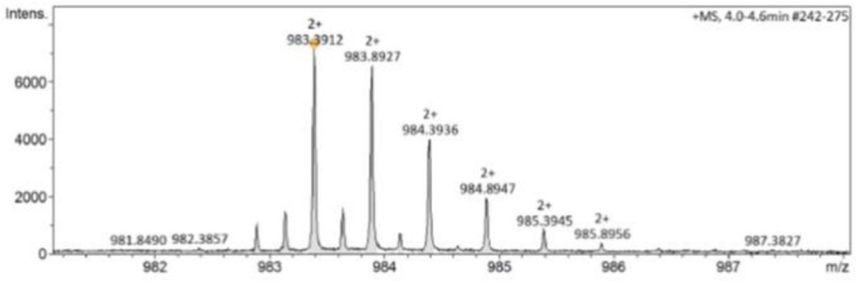

*Appendix 131: HR-MS (ESI⁺ Q-TOF) of compound **15c**.*

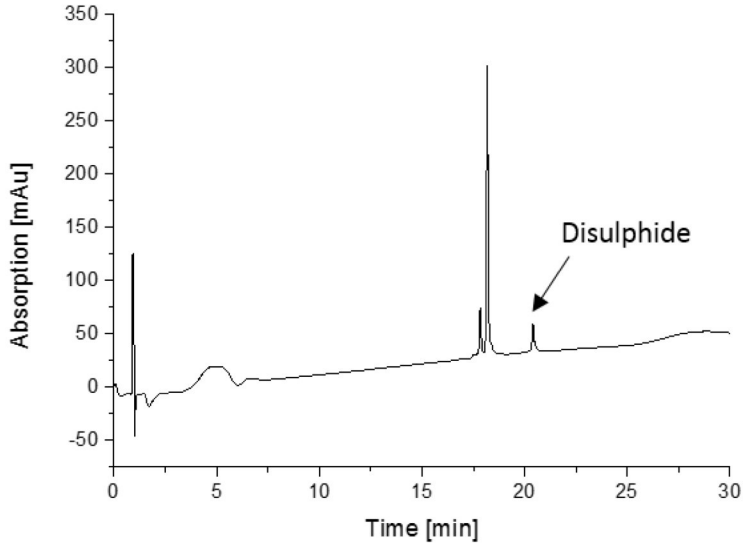

*Appendix 132: RP-HPLC chromatogram (linear gradient from 0-50% eluent B in 30 min at 25 °C) of compound **15c**. The peaks at 17.8 and 20.4 min can be assigned to the side product in which FITC is conjugated to the thiol functionality and the disulphide.*

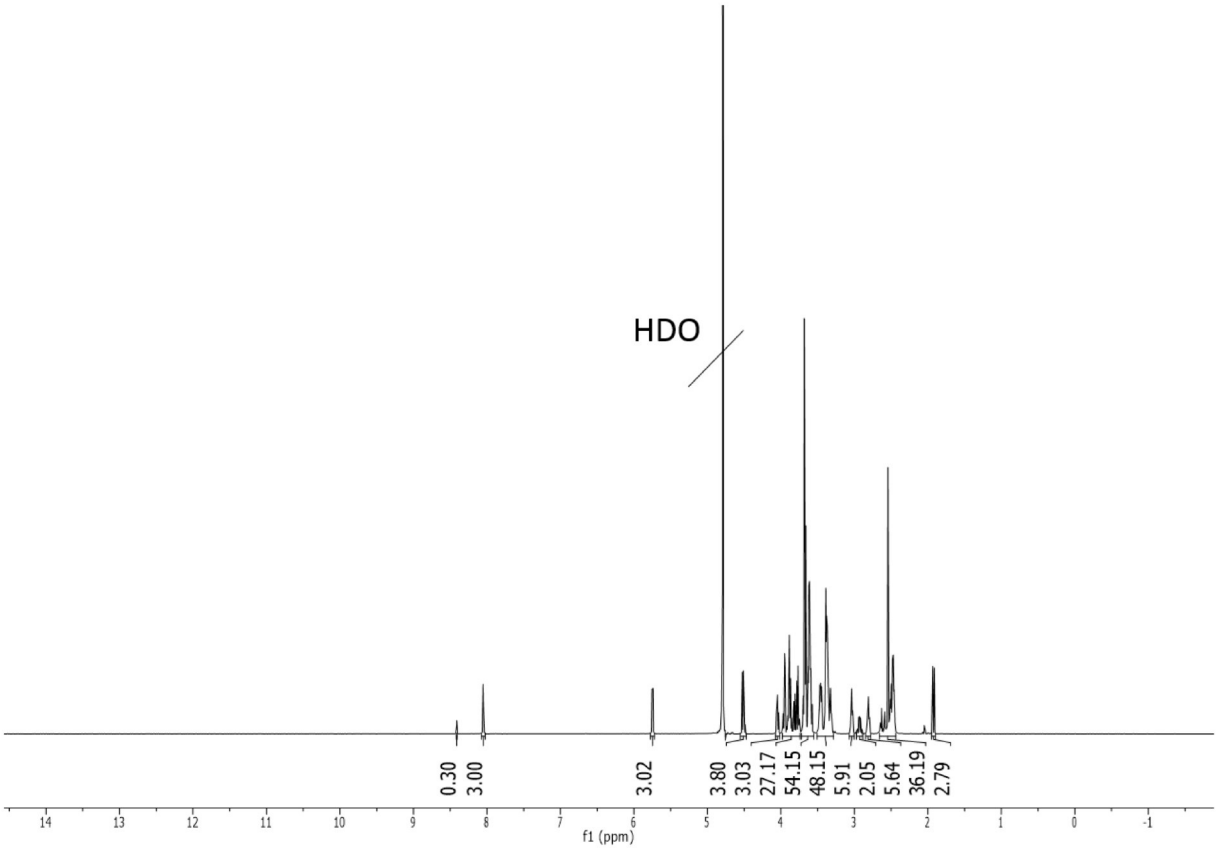

*Appendix 133: ^{1}H-NMR spectrum of **16a** (600 MHz, D_2O).*

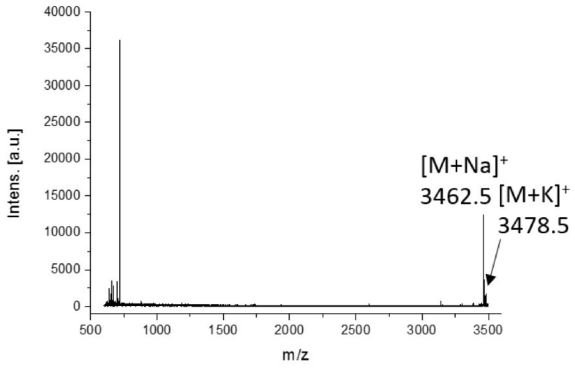

*Appendix 134: MALDI-TOF-MS spectrum of **16a**. One further signal with the mass-to-charge ratio of 716.4 can be found in the spectrum but cannot be assigned to potential by-products.*

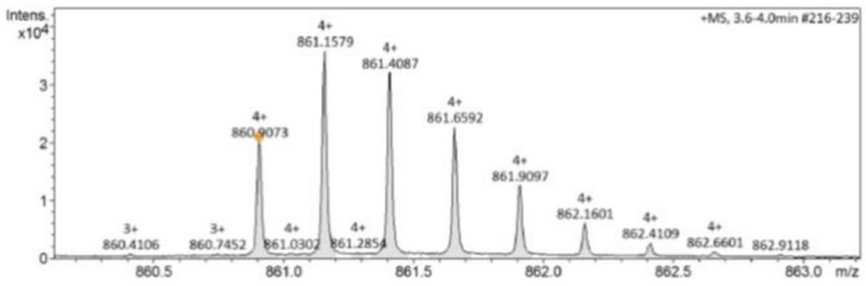

*Appendix 135: HR-MS (ESI⁺ Q-TOF) of compound **16a**.*

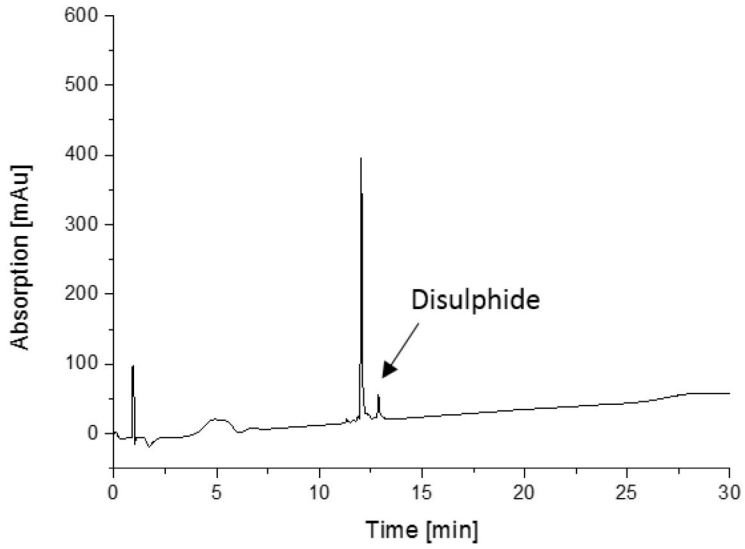

*Appendix 136: RP-HPLC chromatogram (linear gradient from 0-50% eluent B in 30 min at 25 °C) of compound **16a**. The peak at 12.9 min can be assigned to the disulphide.*

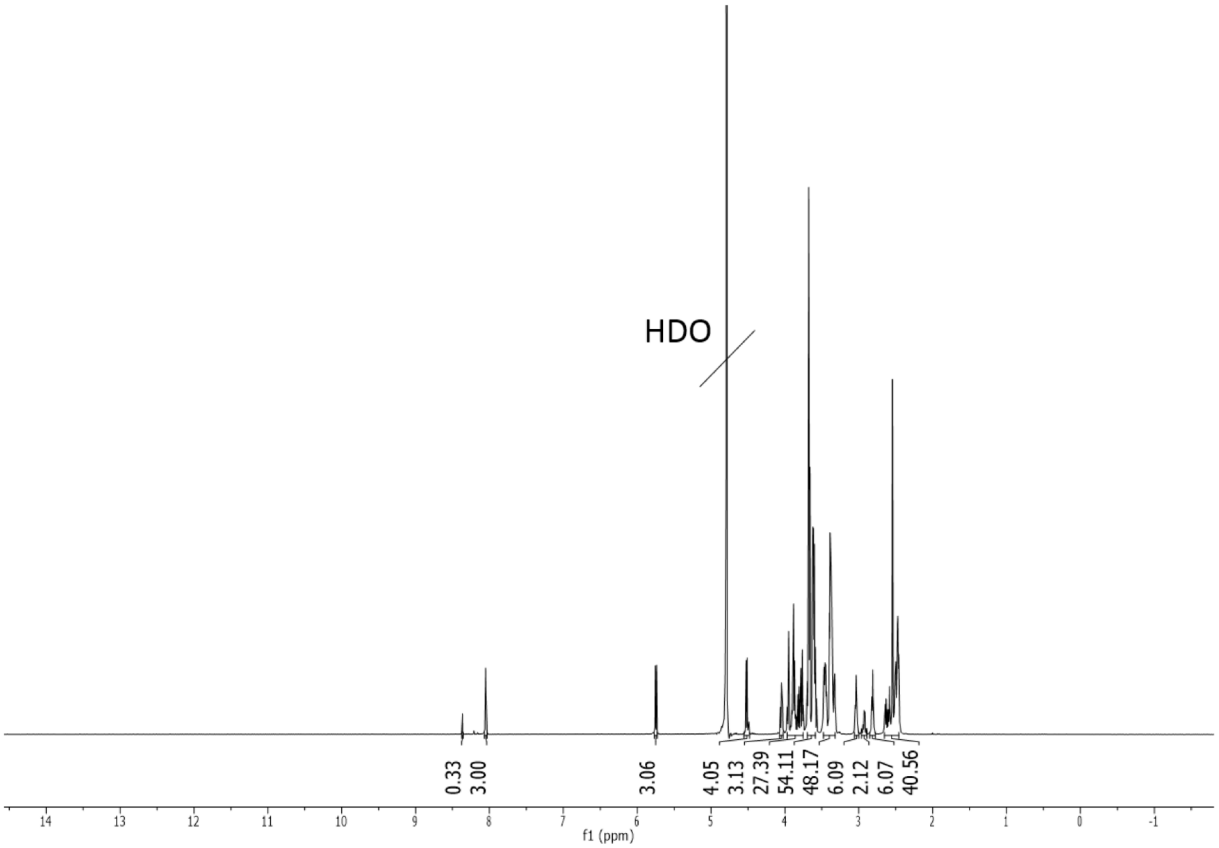

*Appendix 137: ^{1}H-NMR spectrum of **16b** (600 MHz, D_2O).*

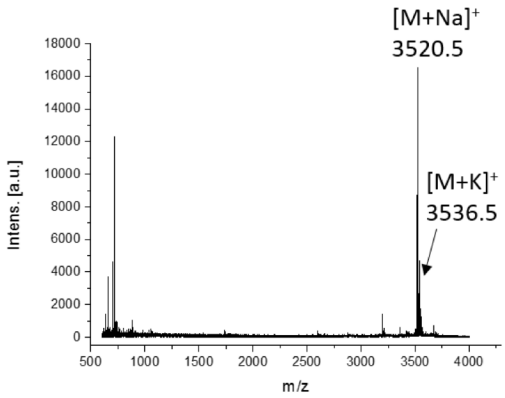

*Appendix 138: MALDI-TOF-MS spectrum of **16b**. One further signal with the mass-to-charge ratio of 715.4 can be found in the spectrum but cannot be assigned to potential by-products.*

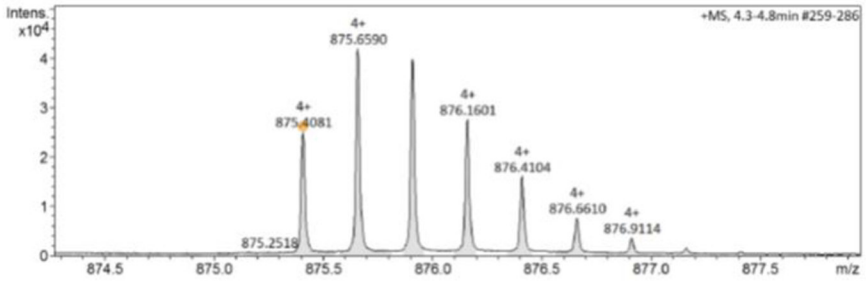

*Appendix 139: HR-MS (ESI⁺ Q-TOF) of compound **16b**.*

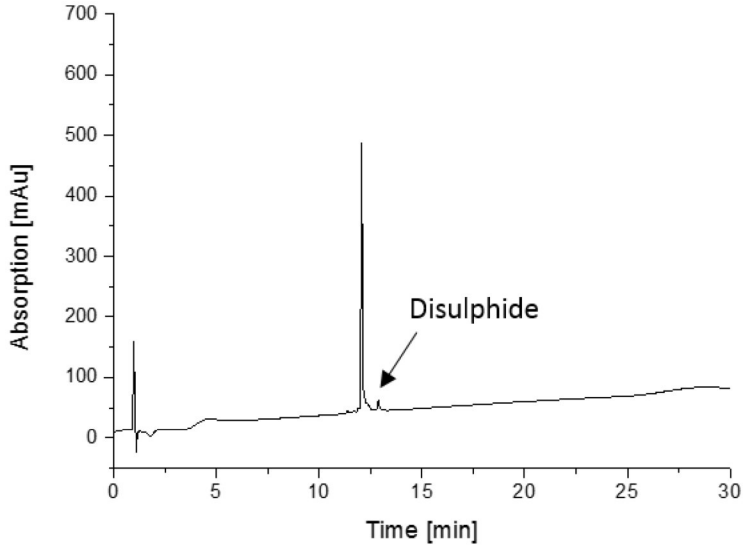

*Appendix 140: RP-HPLC chromatogram (linear gradient from 0-50% eluent B in 30 min at 25 °C) of compound **16b**. The peak at 12.9 min can be assigned to the disulphide.*

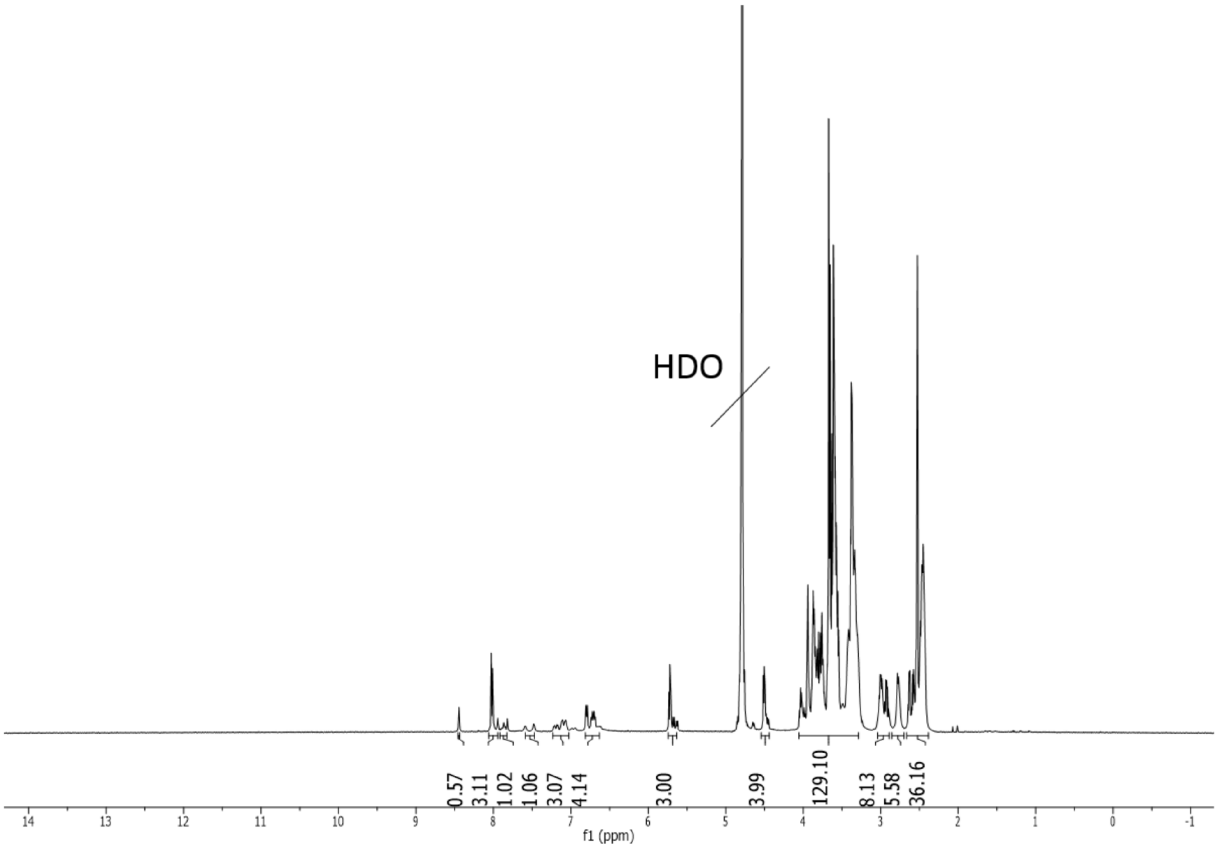

*Appendix 141: ^{1}H-NMR spectrum of **16c** (600 MHz, D_2O).*

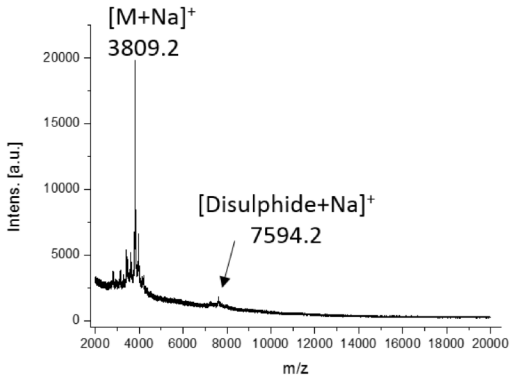

*Appendix 142: MALDI-TOF-MS spectrum of **16c**. The signal with the mass to charge ratio of 7594.2 can be assigned to the disulphide.*

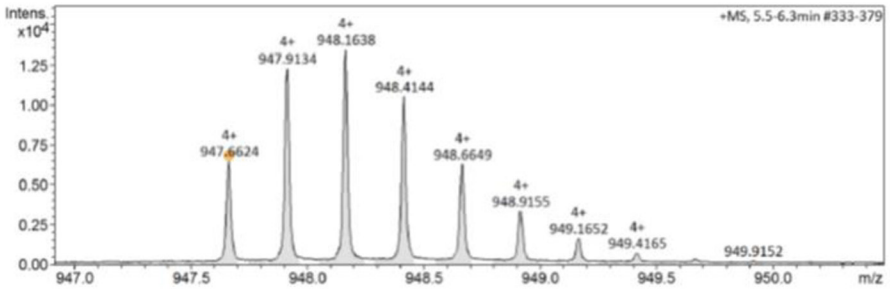

*Appendix 143: HR-MS (ESI⁺ Q-TOF) of compound **16c**.*

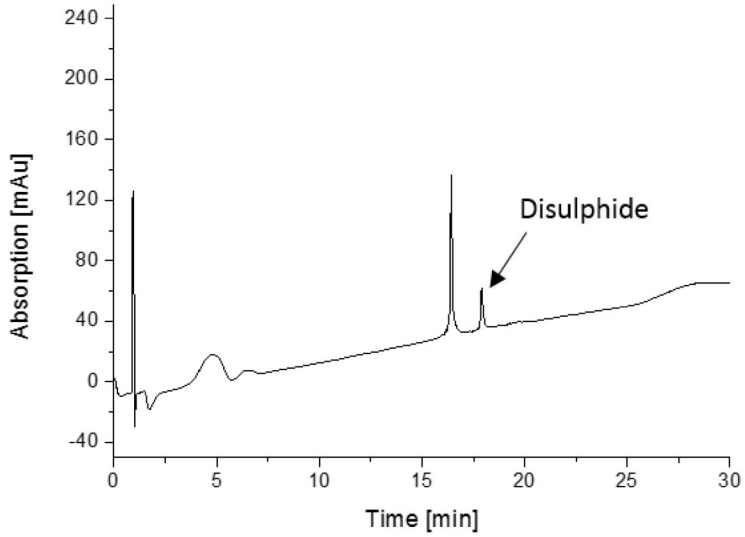

*Appendix 144: RP-HPLC chromatogram (linear gradient from 0-50% eluent B in 30 min at 25 °C) of compound **16c**. The further peak at 17.9 min can be assigned to the disulphide.*

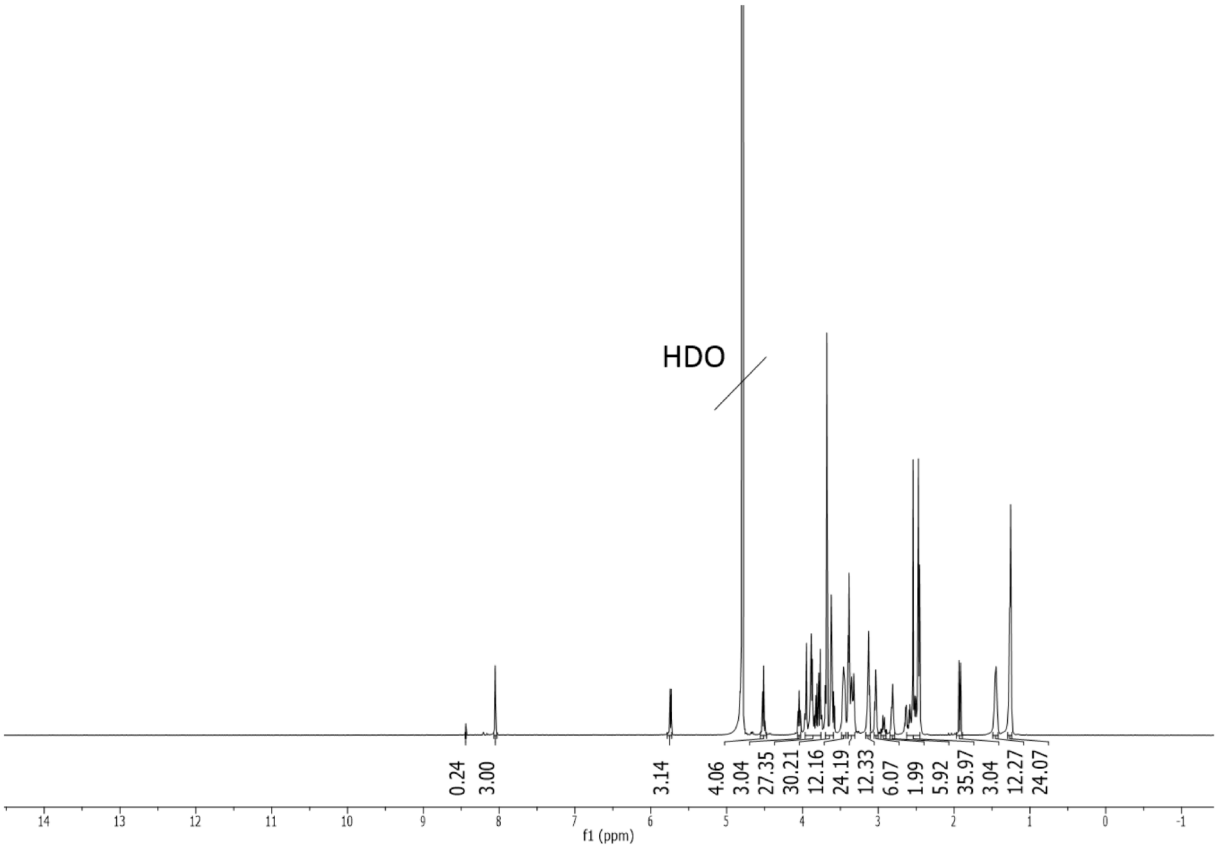

*Appendix 145: ^{1}H-NMR spectrum of **17a** (600 MHz, D_2O).*

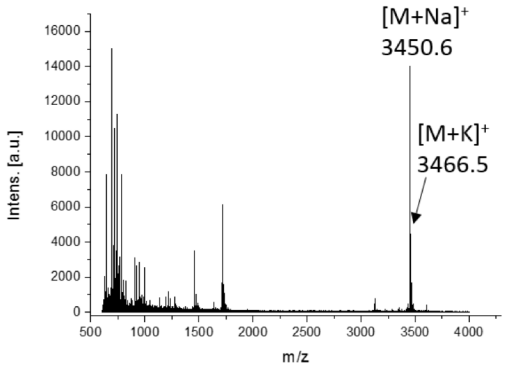

*Appendix 146: MALDI-TOF-MS spectrum of **17a**. Further signals with the mass-to-charge ratio of 695.3, 783.4, 906.4, 1453.7 and 1714.8 can be found in the spectrum but cannot be assigned to potential by-products.*

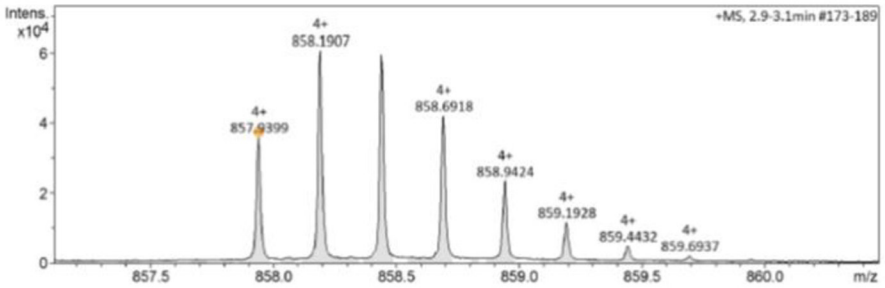

*Appendix 147: HR-MS (ESI⁺ Q-TOF) of compound **17a**.*

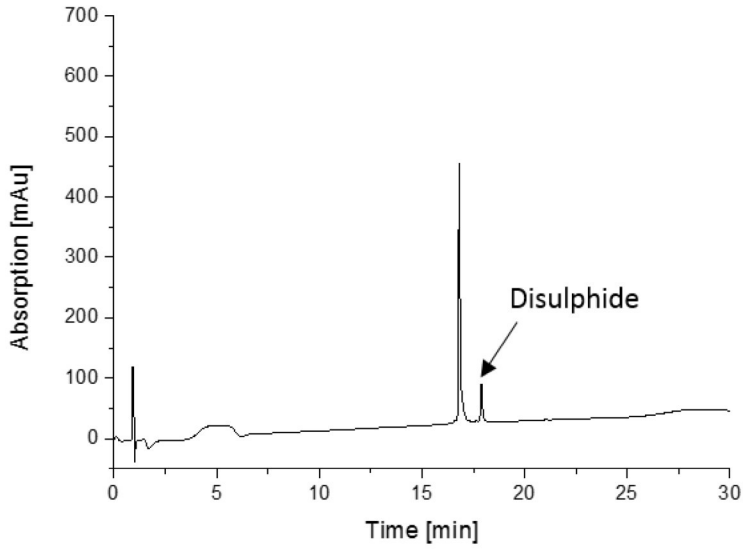

*Appendix 148: RP-HPLC chromatogram (linear gradient from 0-50% eluent B in 30 min at 25 °C) of compound **17a**. The peak at 17.9 min can be assigned to the disulphide.*

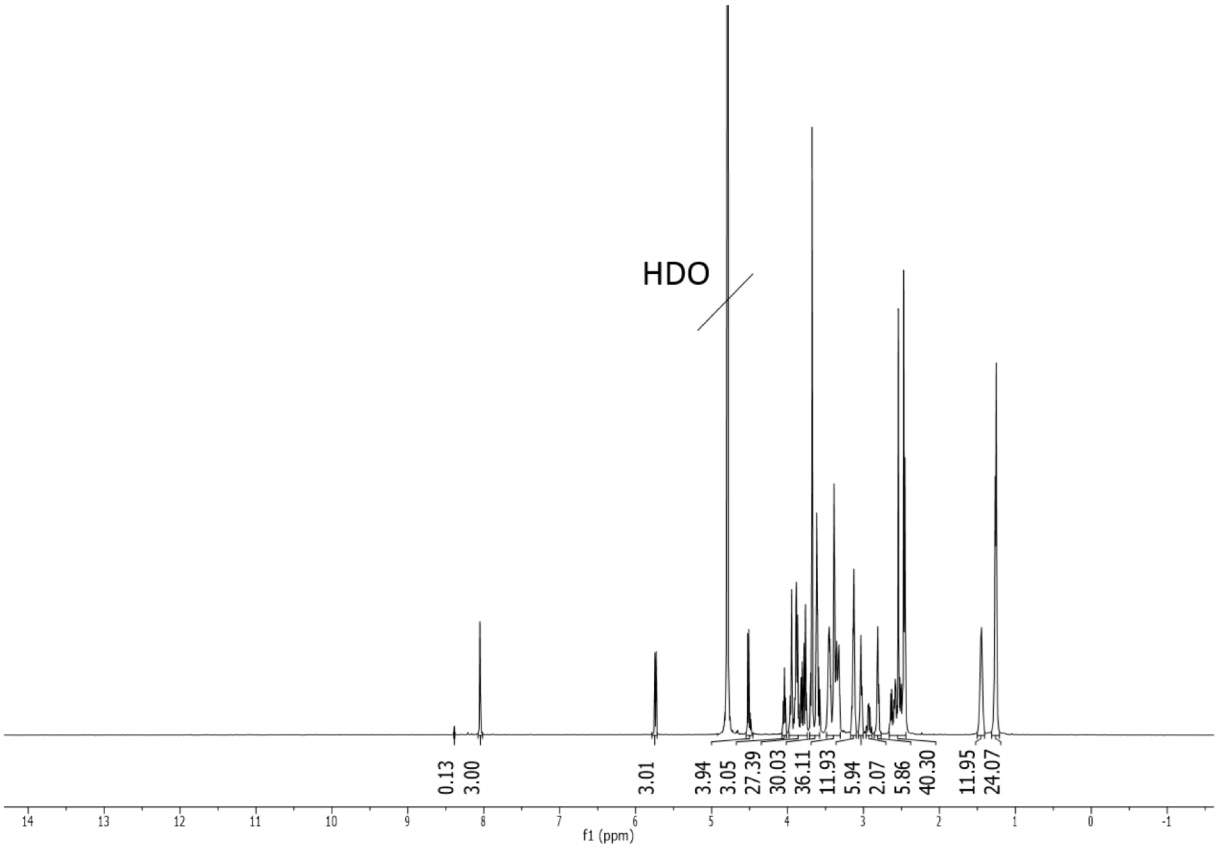

*Appendix 149: ^{1}H-NMR spectrum of **17b** (600 MHz, D_2O).*

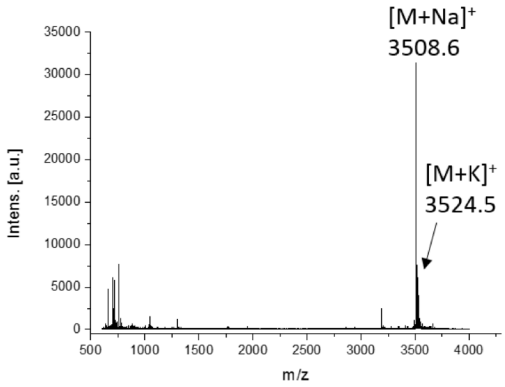

*Appendix 150: MALDI-TOF-MS spectrum of **17b**. Further signals with the mass-to-charge ratio of 757.4 and 3184.5 can be found in the spectrum but cannot be assigned to potential by-products.*

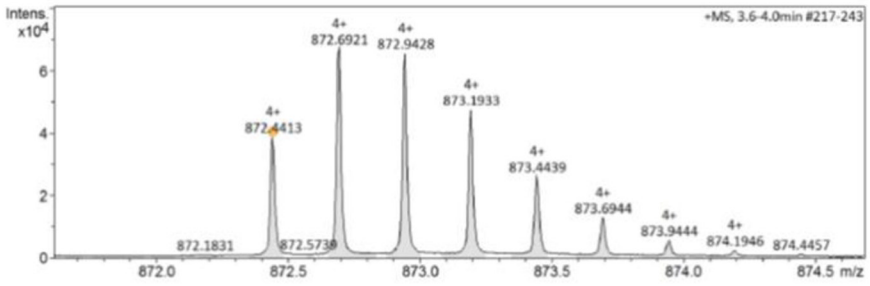

*Appendix 151: HR-MS (ESI⁺ Q-TOF) of compound **17b**.*

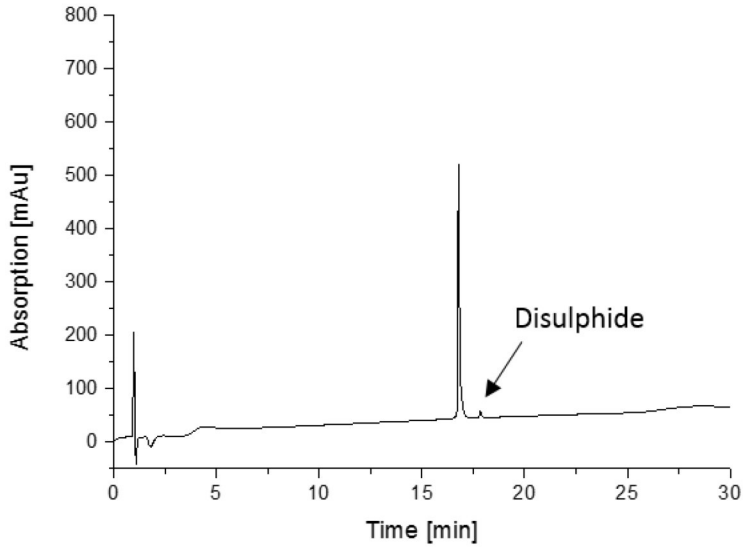

*Appendix 152: RP-HPLC chromatogram (linear gradient from 0-50% eluent B in 30 min at 25 °C) of compound **17b**. The peak at 17.8 min can be assigned to the disulphide.*

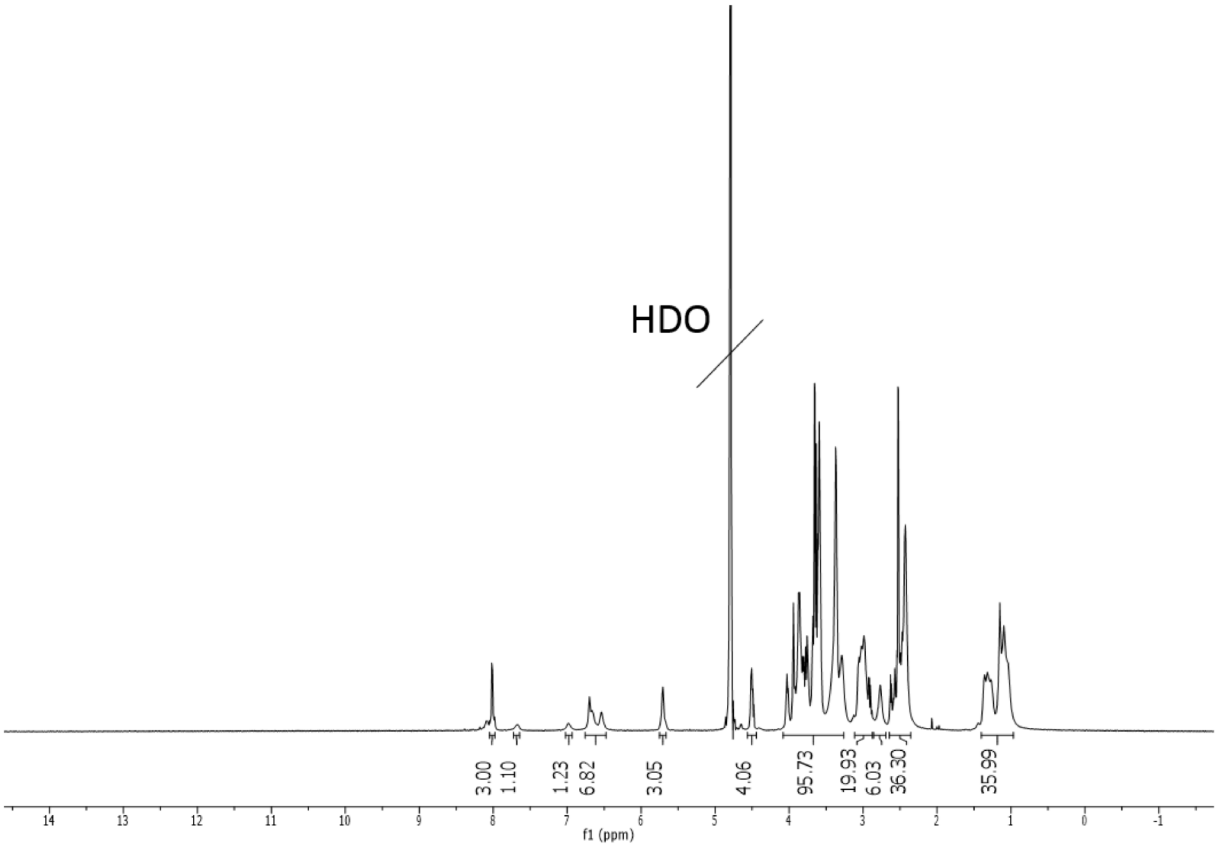

*Appendix 153: ^{1}H-NMR spectrum of **17c** (600 MHz, D_2O).*

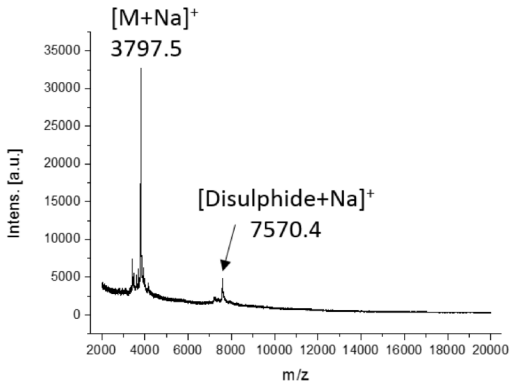

*Appendix 154: MALDI-TOF-MS spectrum of **17c**. The signal with the mass to charge ratio of 7570.4 can be assigned to the disulphide.*

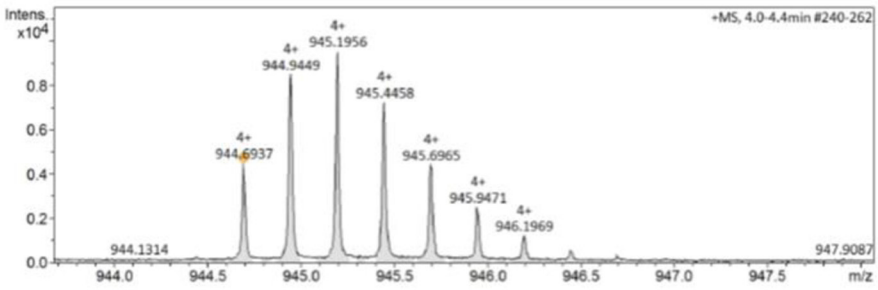

*Appendix 155: HR-MS (ESI⁺ Q-TOF) of compound **17c**.*

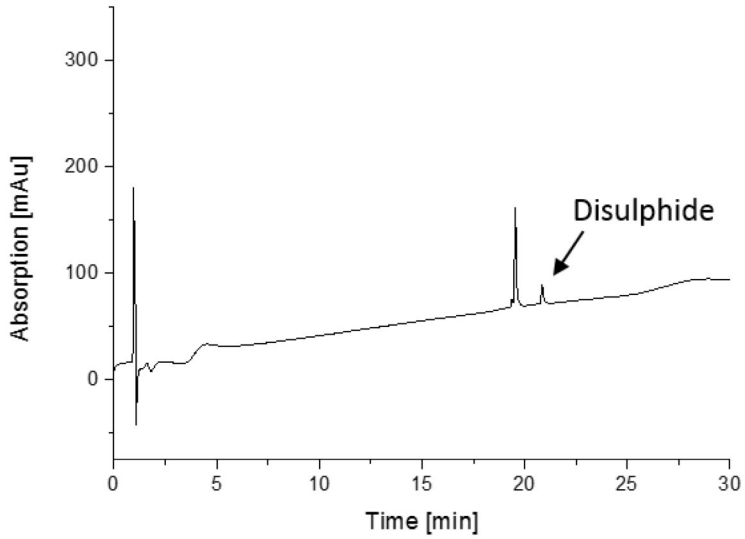

*Appendix 156: RP-HPLC chromatogram (linear gradient from 0-50% eluent B in 30 min at 25 °C) of compound **17c**. The peak at 20.9 min can be assigned to the disulphide.*

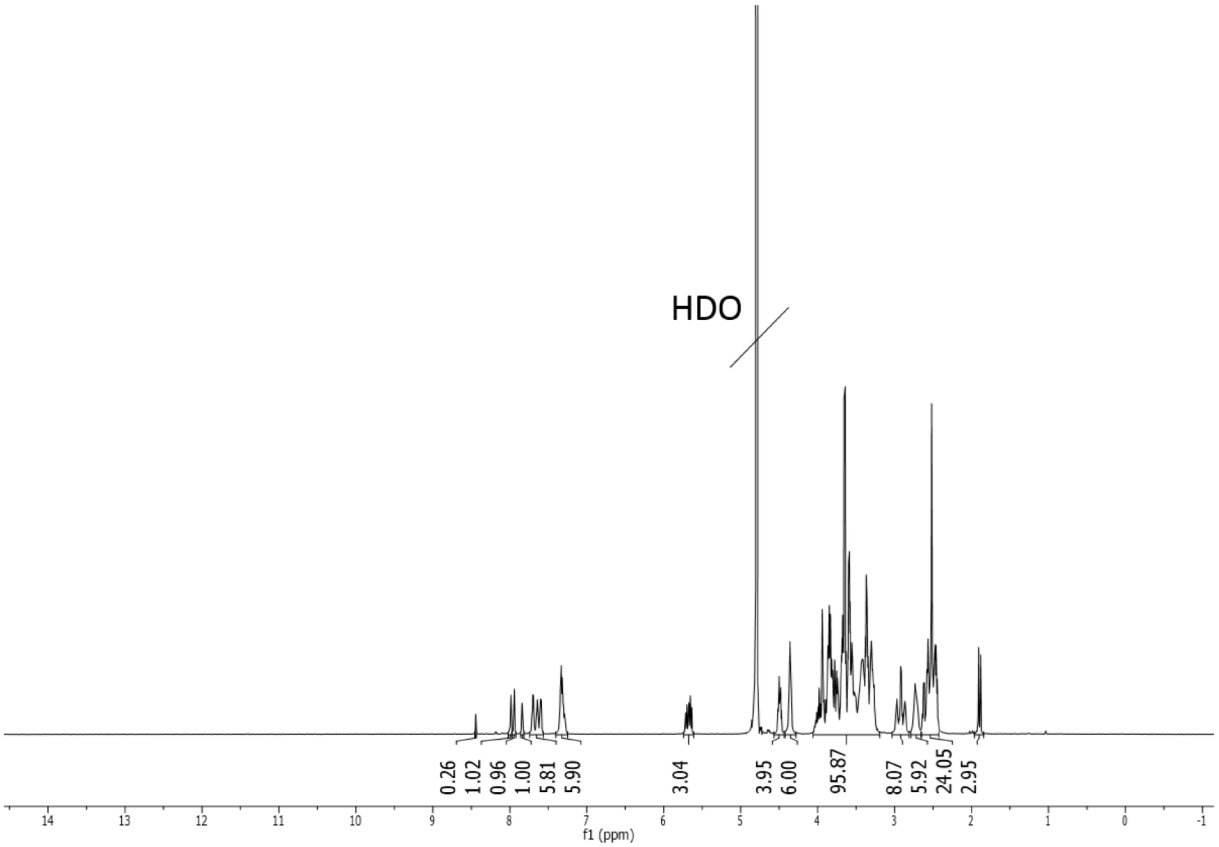

*Appendix 157: ^{1}H-NMR spectrum of **18a** (600 MHz, D_2O).*

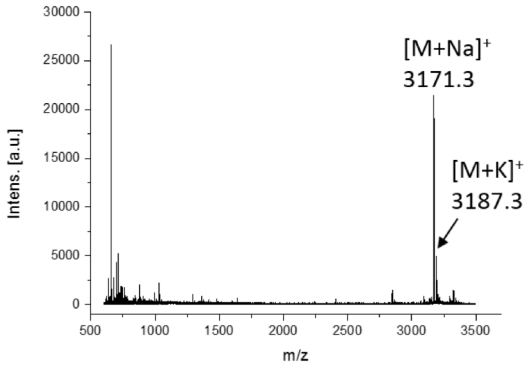

*Appendix 158: MALDI-TOF-MS spectrum of **18a**. Further signals with the mass-to-charge ratio of 715.3 and 759.9 can be found in the spectrum but cannot be assigned to potential by-products.*

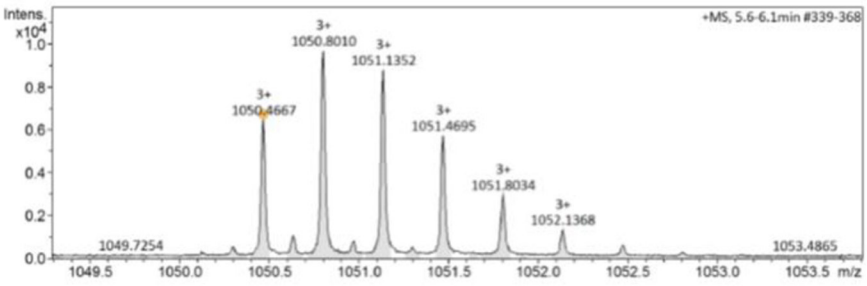

*Appendix 159: HR-MS (ESI⁺ Q-TOF) of compound **18a**.*

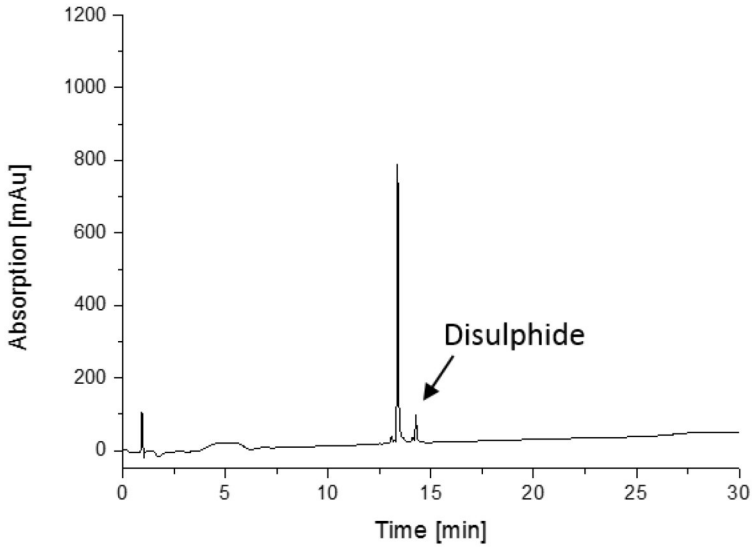

*Appendix 160: RP-HPLC chromatogram (linear gradient from 0-50% eluent B in 30 min at 25 °C) of compound **18a**. The peak at 14.2 min can be assigned to the disulphide.*

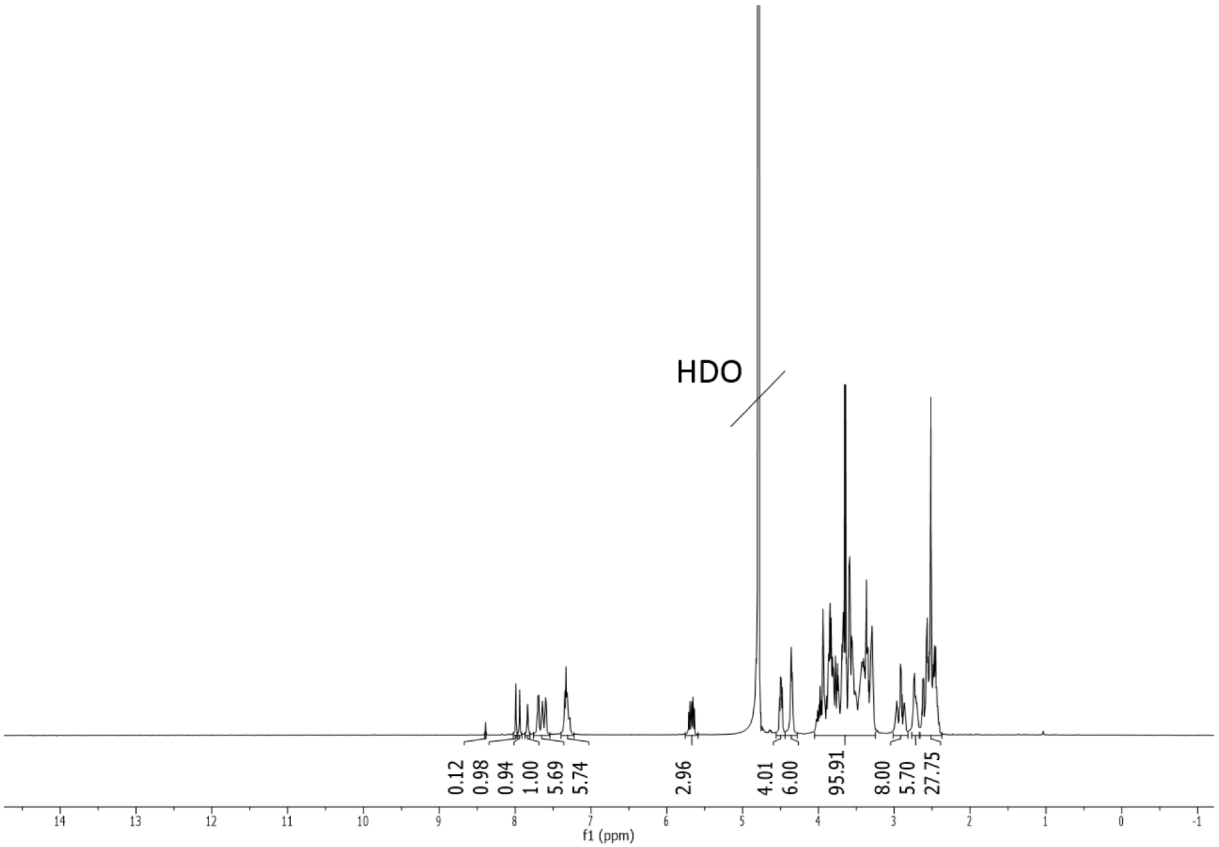

*Appendix 161: ^{1}H-NMR spectrum of **18b** (600 MHz, D_2O).*

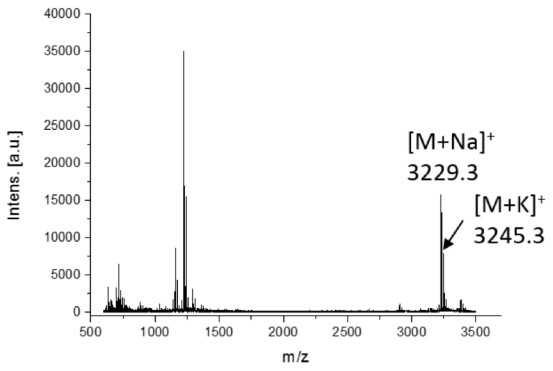

*Appendix 162: MALDI-TOF-MS spectrum of **18b**. Further signals with the mass-to-charge ratio of 715.3, 1139.3 and 1225.4 can be found in the spectrum but cannot be assigned to potential by-products.*

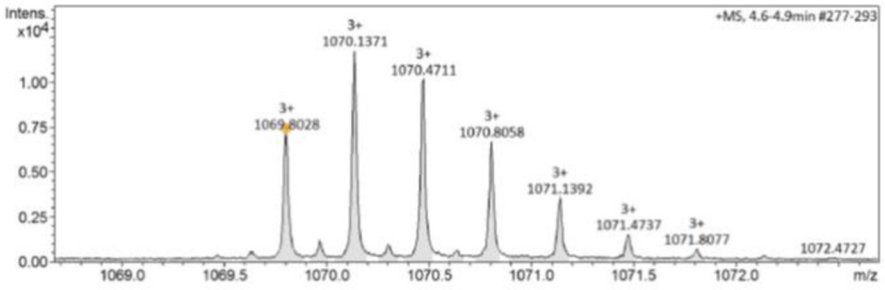

*Appendix 163: HR-MS (ESI⁺ Q-TOF) of compound **18b**.*

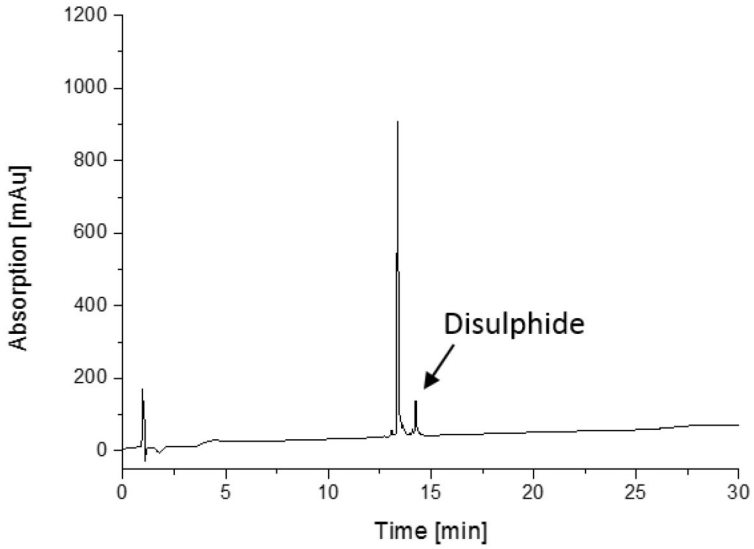

*Appendix 164: RP-HPLC chromatogram (linear gradient from 0-50% eluent B in 30 min at 25 °C) of compound **18b**. The peak at 14.3 min can be assigned to the disulphide.*

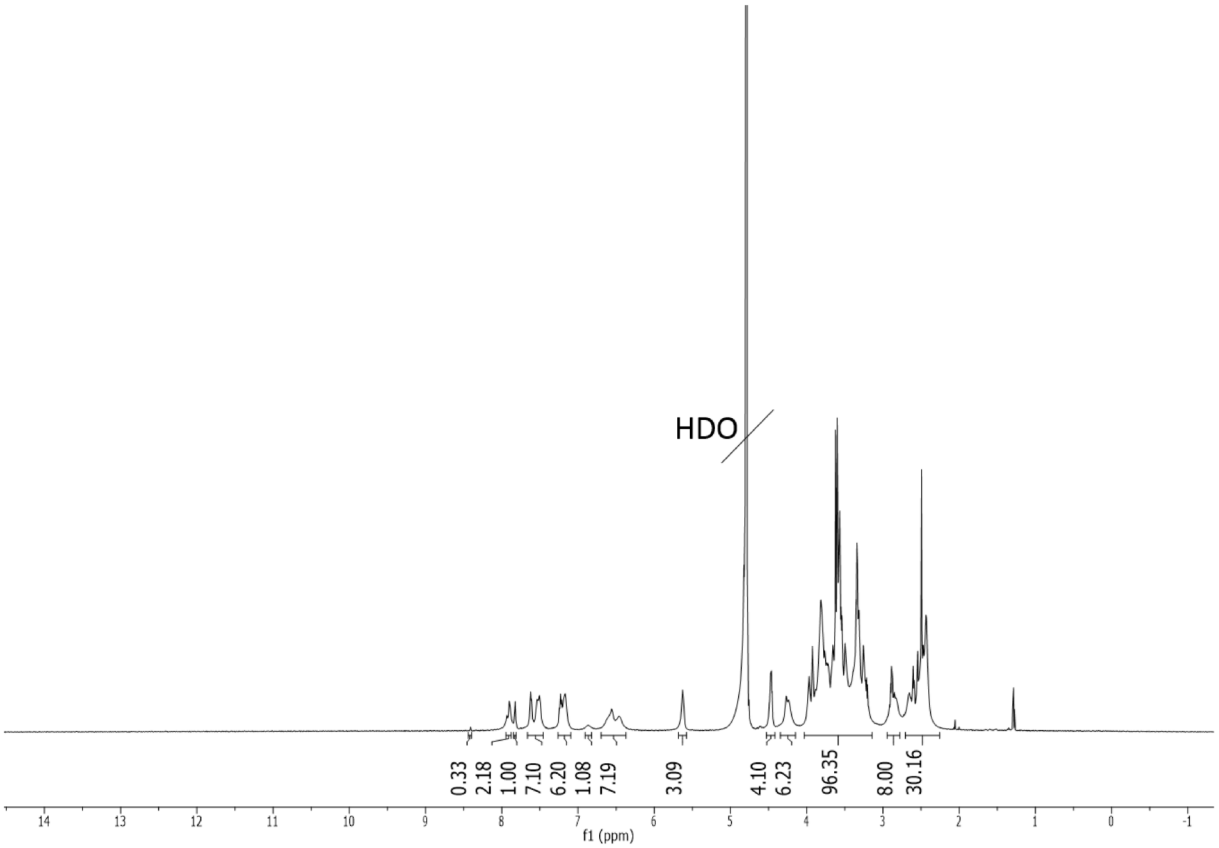

*Appendix 165: ^{1}H-NMR spectrum of **18c** (600 MHz, D_2O).*

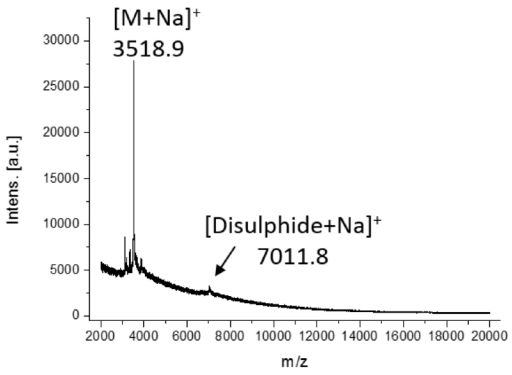

*Appendix 166: MALDI-TOF-MS spectrum of **18c**. The signal with the mass to charge ratio of 7011.8 can be assigned to the disulphide.*

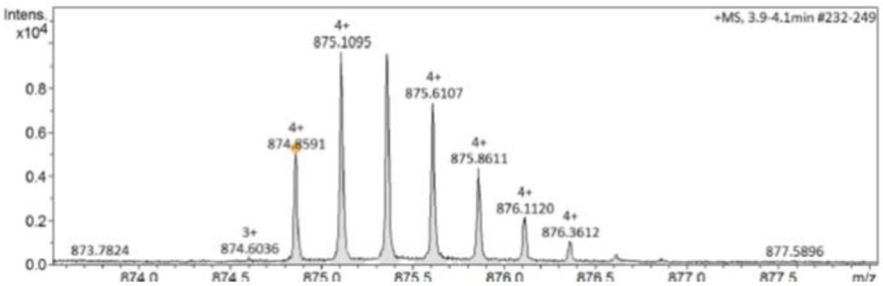

*Appendix 167: HR-MS (ESI⁺ Q-TOF) of compound **18c**.*

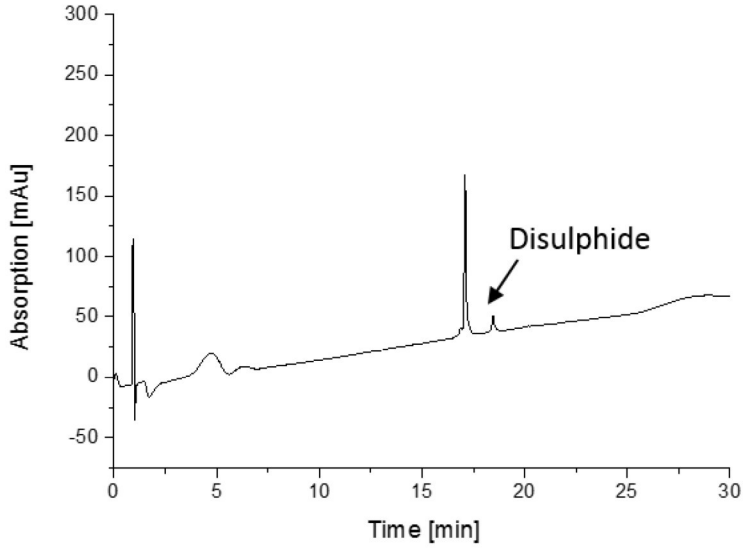

*Appendix 168: RP-HPLC chromatogram (linear gradient from 0-50% eluent B in 30 min at 25 °C) of compound **18b**. The peak at 18.5 min can be assigned to the disulphide.*

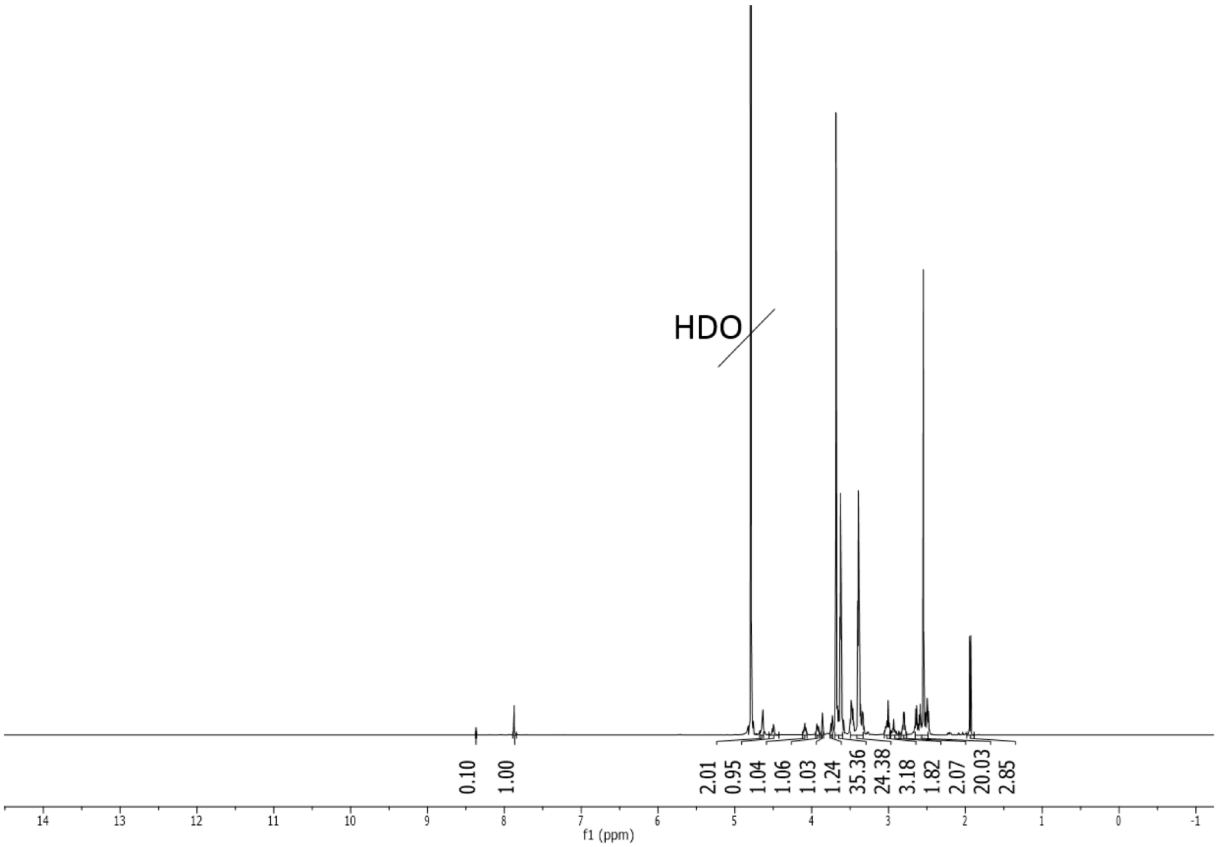

*Appendix 169: ^{1}H-NMR spectrum of **19a** (600 MHz, D_2O).*

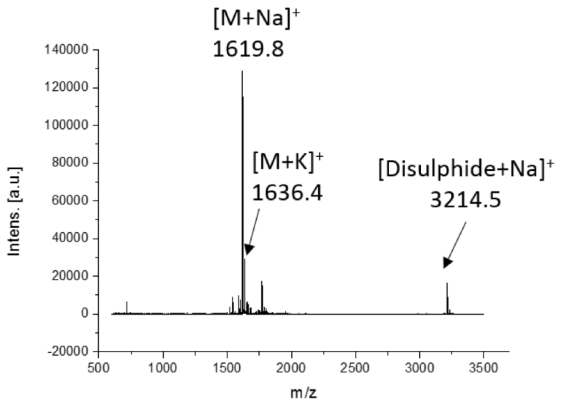

*Appendix 170: MALDI-TOF-MS spectrum of **19a**. The signal with the mass to charge ratio of 3214.5 can be assigned to the disulphide.*

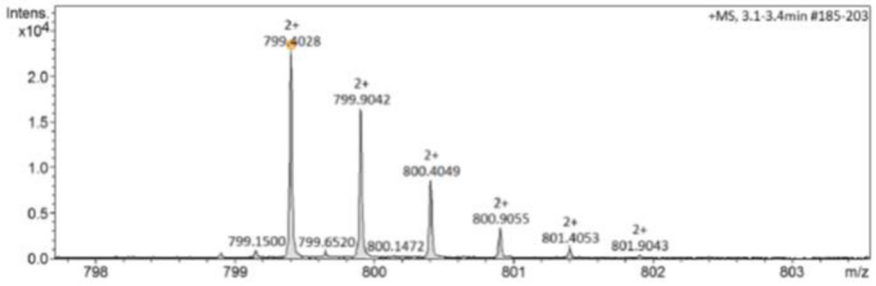

*Appendix 171: HR-MS (ESI⁺ Q-TOF) of compound **19a**.*

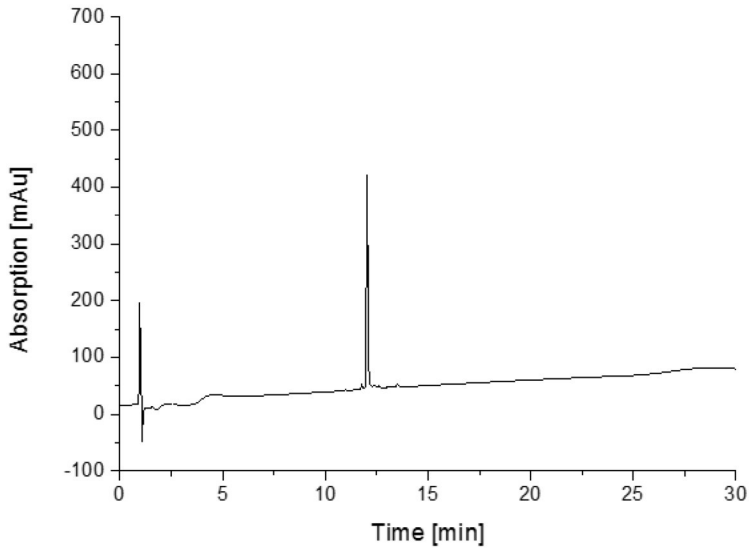

*Appendix 172: RP-HPLC chromatogram (linear gradient from 0-50% eluent B in 30 min at 25 °C) of compound **19a**.*

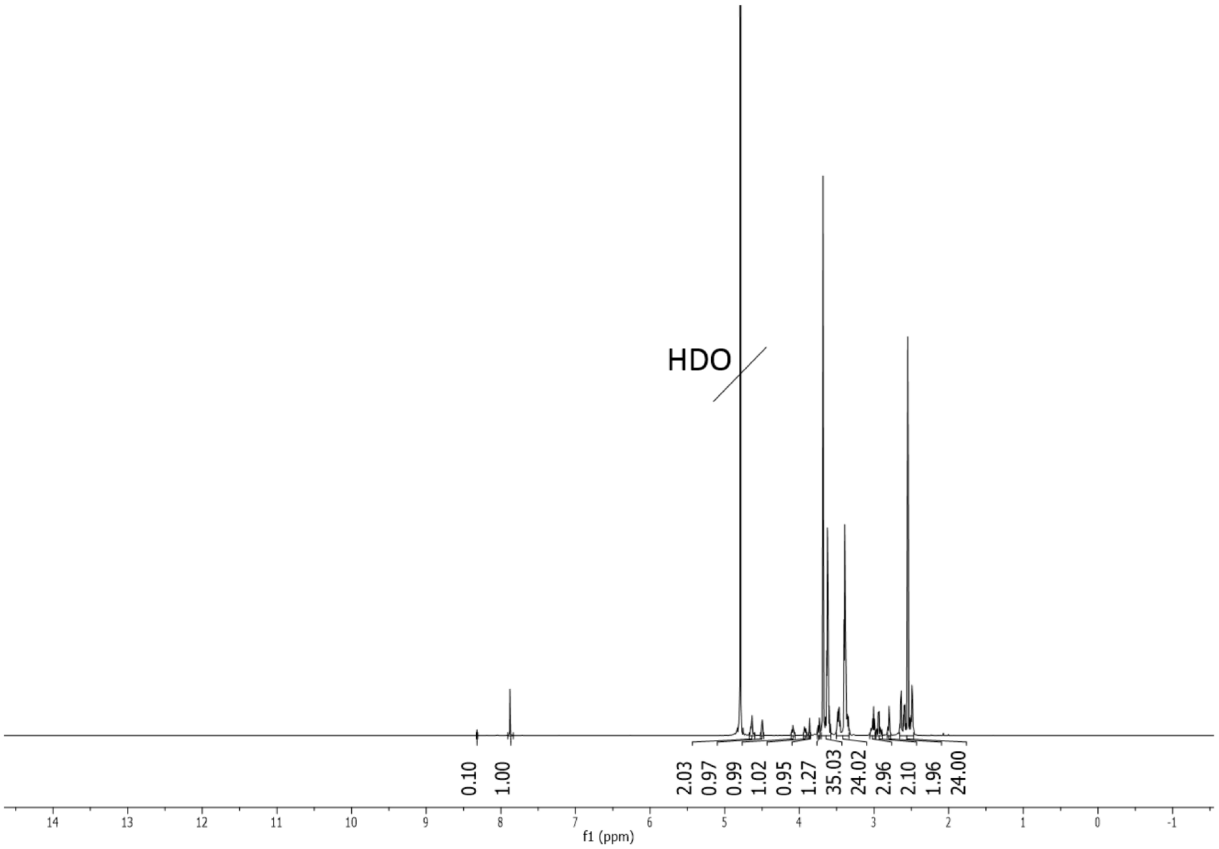

*Appendix 173: ^{1}H-NMR spectrum of **19b** (600 MHz, D_2O).*

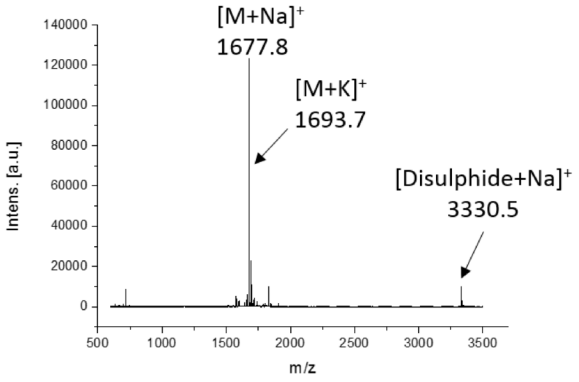

*Appendix 174: MALDI-TOF-MS spectrum of **19b**. The signal with the mass to charge ratio of 3330.5 can be assigned to the disulphide.*

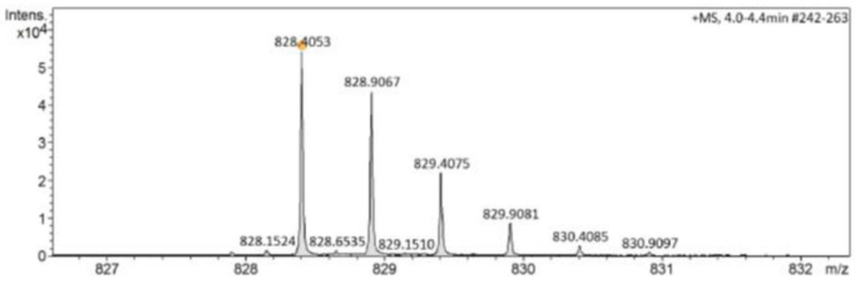

*Appendix 175: HR-MS (ESI⁺ Q-TOF) of compound **19b**.*

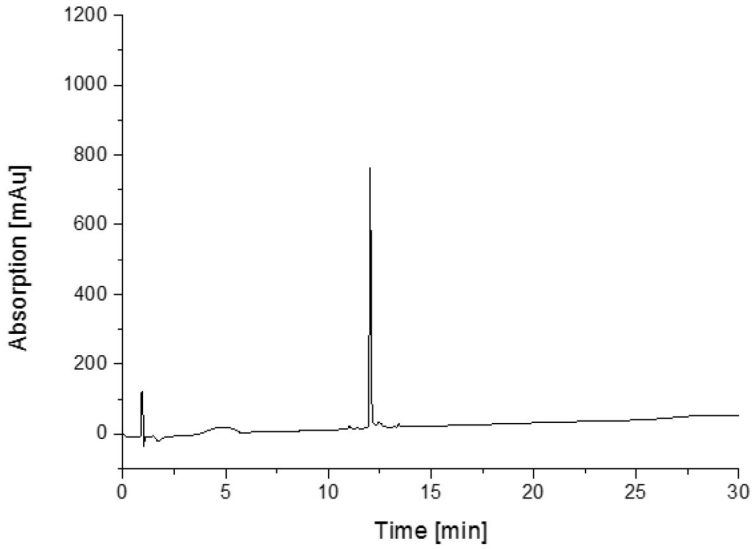

*Appendix 176: RP-HPLC chromatogram (linear gradient from 0-50% eluent B in 30 min at 25 °C) of compound **19b**.*

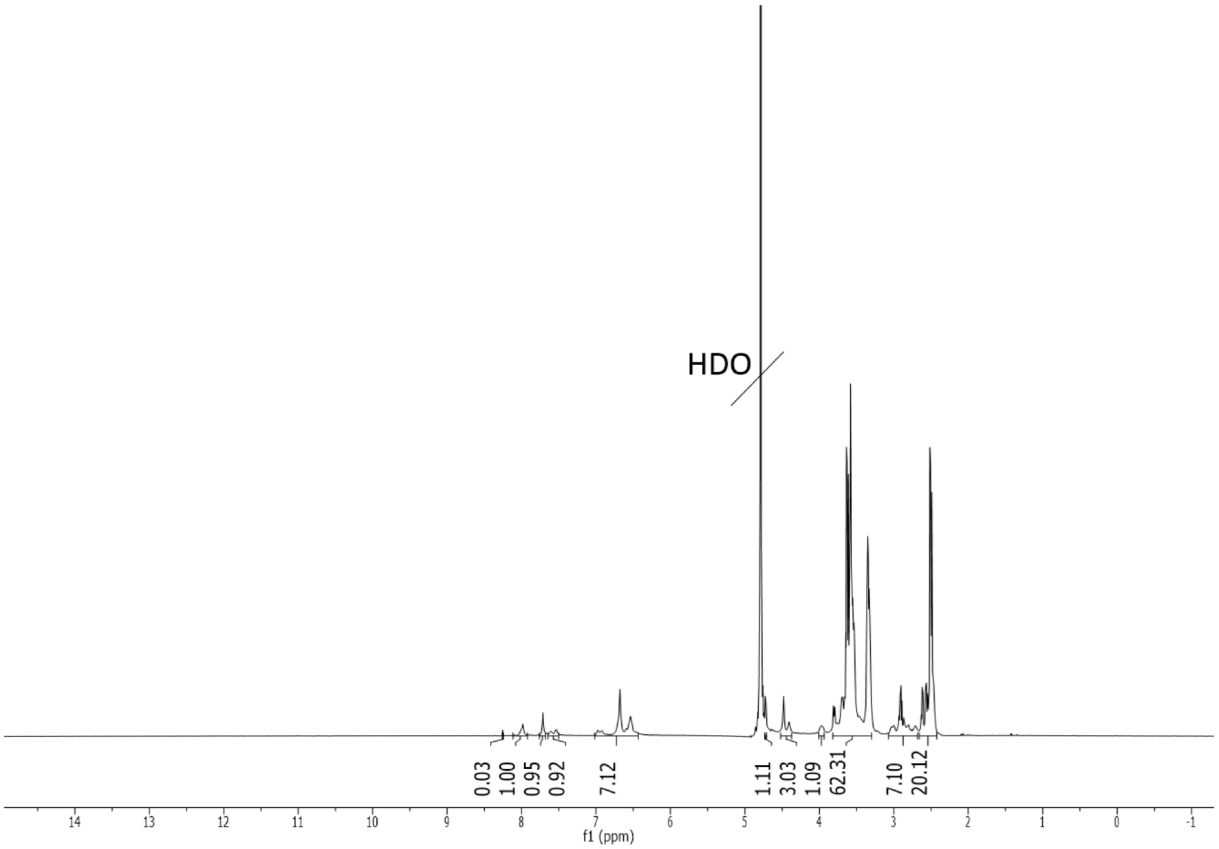

*Appendix 177: ^{1}H-NMR spectrum of **19c** (600 MHz, D_2O).*

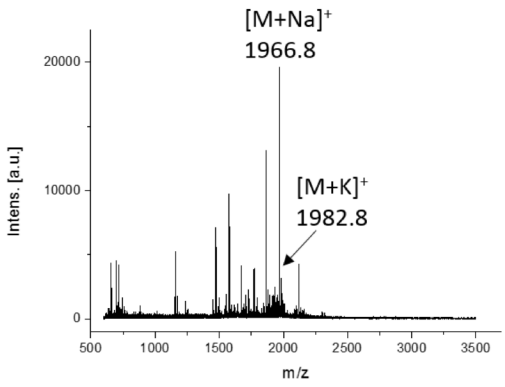

*Appendix 178: MALDI-TOF-MS spectrum of **19c**. The signal with the mass to charge ratio of 1577.8 can be assigned to the unconjugated glycomacromolecule. Two further peaks with a mass to charge ratio of 1474.8 and 1863.8 can be assigned to a deletion sequence without cysteine building block in unconjugated and conjugated form. Further signals with the mass-to-charge ratio of 715.4, 1157.4 and 2118.8 can be found in the spectrum but cannot be assigned to potential by-products.*

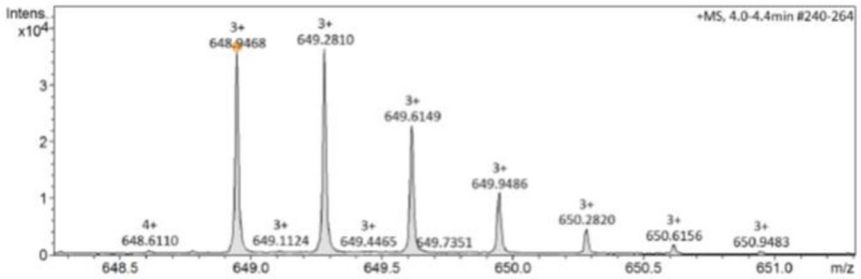

*Appendix 179: HR-MS (ESI⁺ Q-TOF) of compound **19c**.*

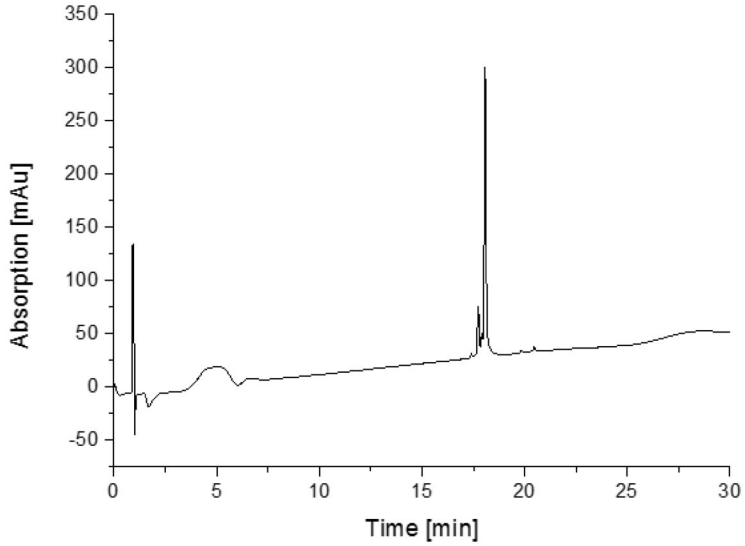

*Appendix 180: RP-HPLC chromatogram (linear gradient from 0-50% eluent B in 30 min at 25 °C) of compound **19c**. The peak at 17.7 min can be assigned to the side product in which FITC is conjugated to the thiol functionality.*

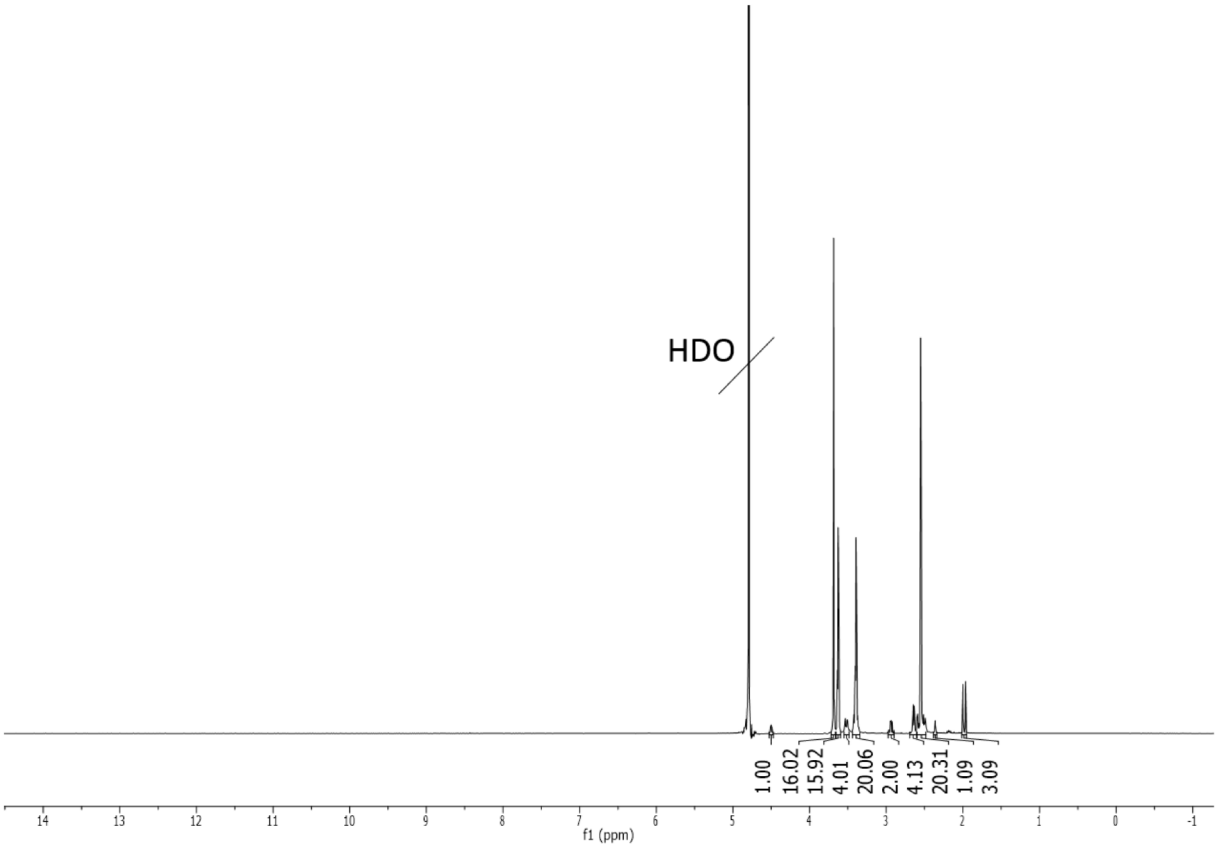

*Appendix 181: ^{1}H-NMR spectrum of **20a** (600 MHz, D_2O).*

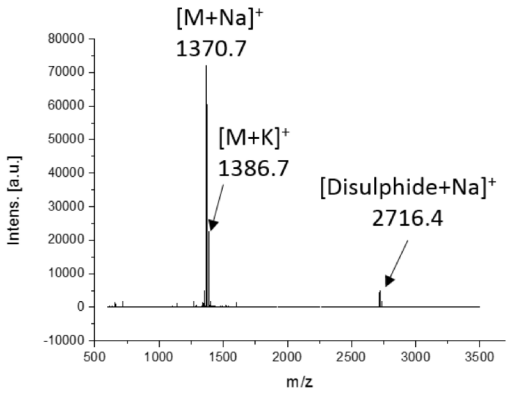

*Appendix 182: MALDI-TOF-MS spectrum of **20a**. The signal with the mass to charge ratio of 2716.4 can be assigned to the disulphide.*

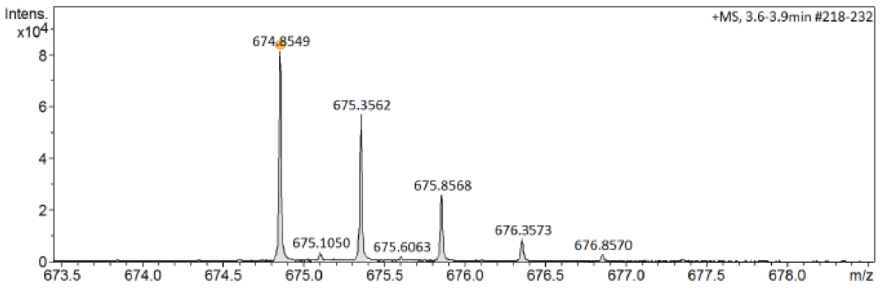

*Appendix 183: HR-MS (ESI⁺ Q-TOF) of compound **20a**.*

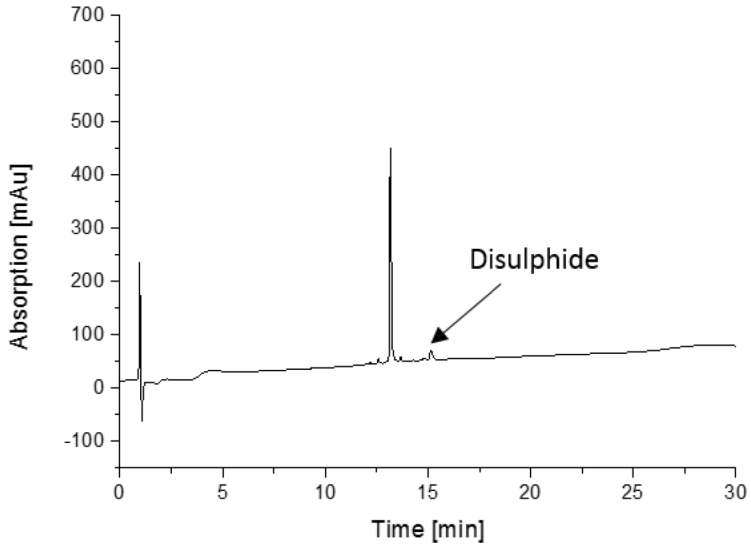

*Appendix 184: RP-HPLC chromatogram (linear gradient from 0-50% eluent B in 30 min at 25 °C) of compound **20a**. The peak at 15.2 min can be assigned to the disulphide.*

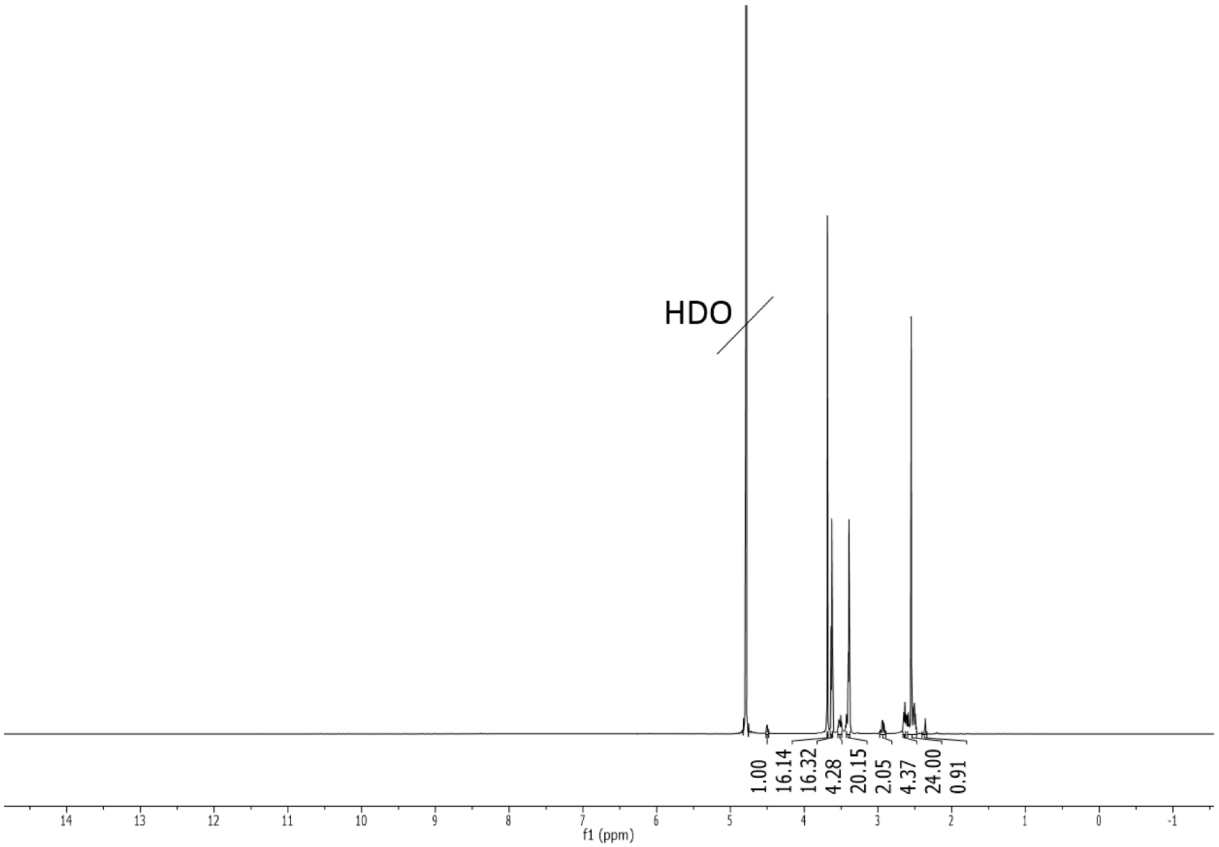

*Appendix 185: ^{1}H-NMR spectrum of **20b** (600 MHz, D_2O).*

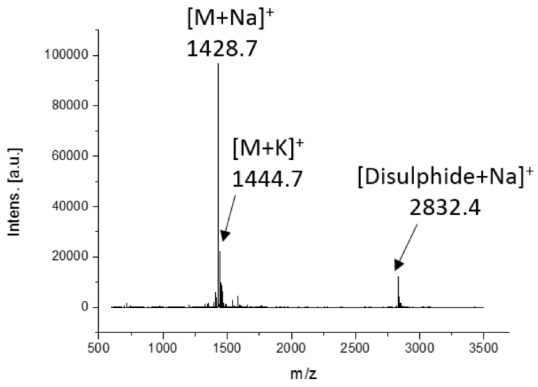

*Appendix 186: MALDI-TOF-MS spectrum of **20b**. The signal with the mass to charge ratio of 2832.4 can be assigned to the disulphide.*

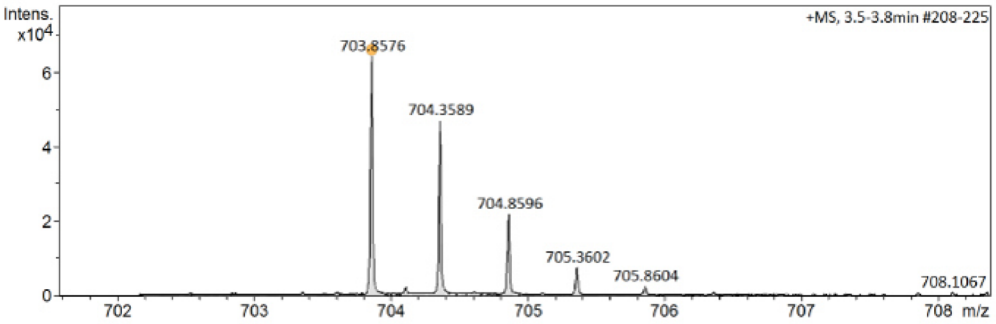

*Appendix 187: HR-MS (ESI⁺ Q-TOF) of compound **20b**.*

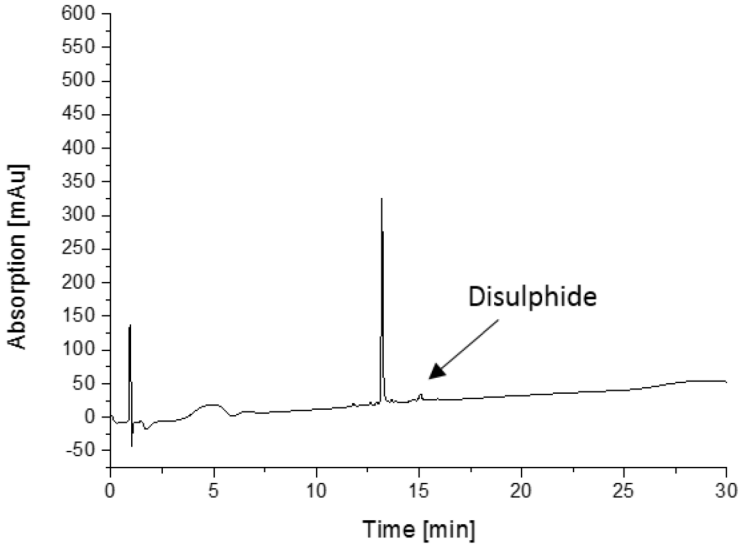

*Appendix 188: RP-HPLC chromatogram (linear gradient from 0-50% eluent B in 30 min at 25 °C) of compound **20b**. The peak at 15.1 min can be assigned to the disulphide.*

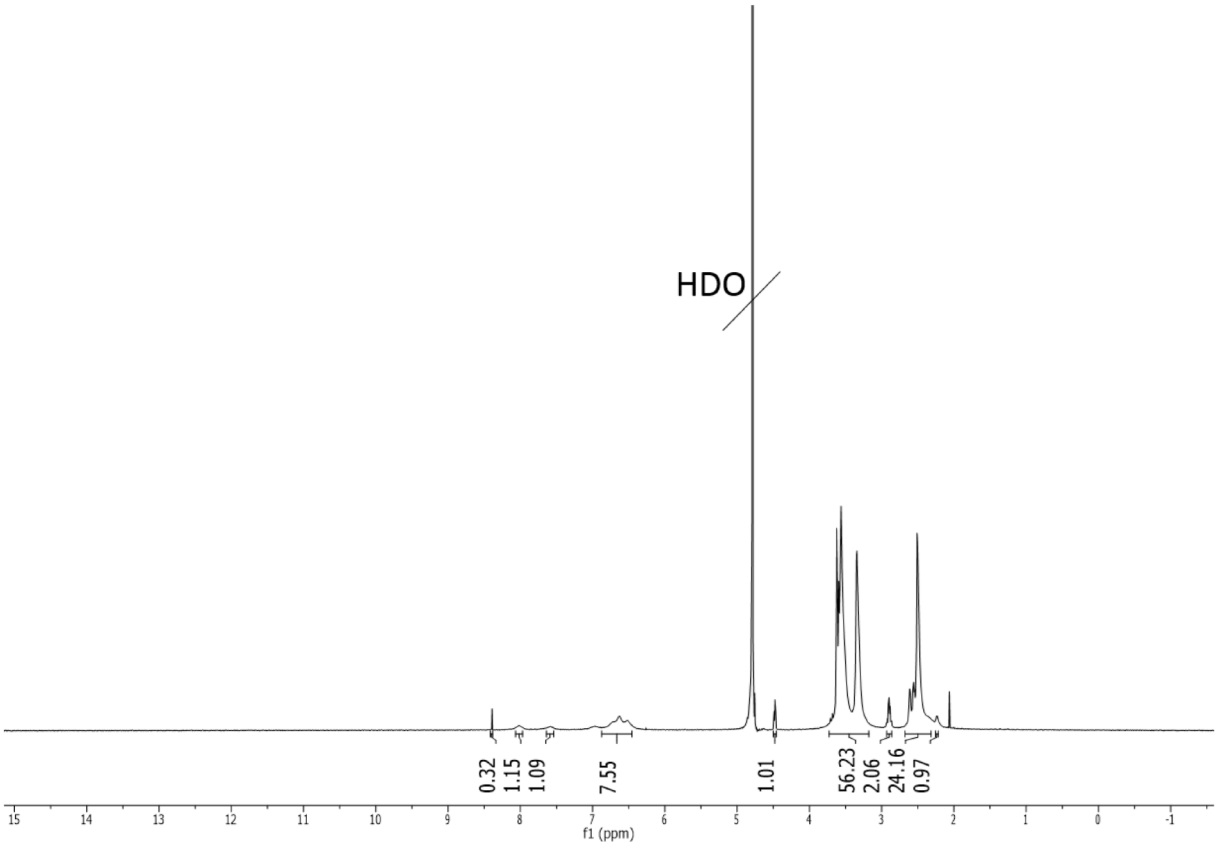

*Appendix 189: ^{1}H-NMR spectrum of **20c** (600 MHz, D_2O).*

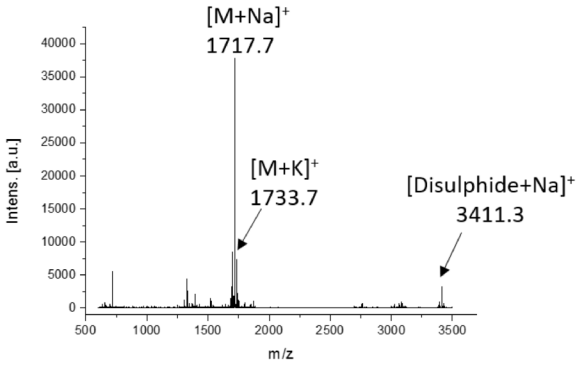

*Appendix 190: MALDI-TOF-MS spectrum of **20c**. The signal with the mass to charge ratio of 3411.3 can be assigned to the disulphide.*

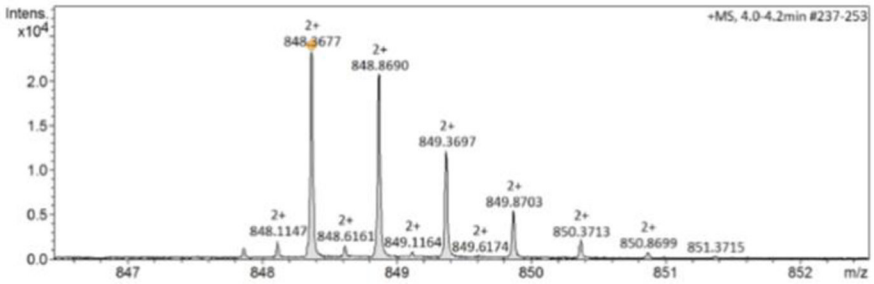

*Appendix 191: HR-MS (ESI⁺ Q-TOF) of compound **20c**.*

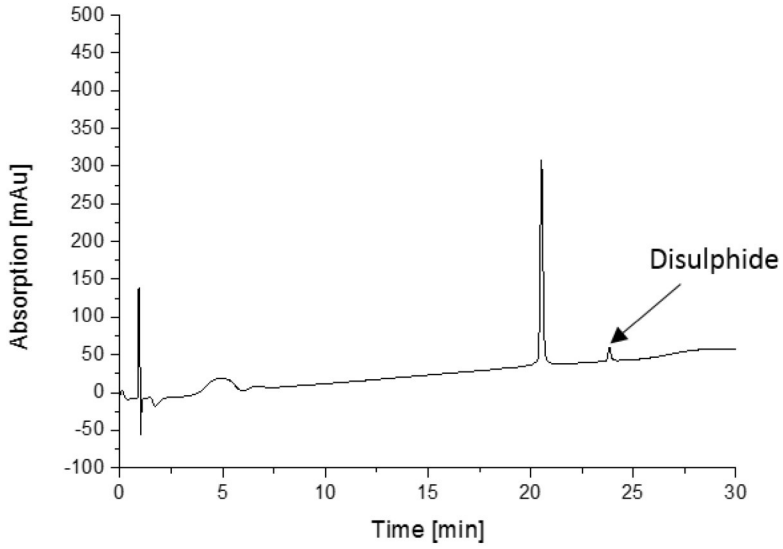

*Appendix 192: RP-HPLC chromatogram (linear gradient from 0-50% eluent B in 30 min at 25 °C) of compound **20c**. The peak at 23.9 min can be assigned to the disulphide.*

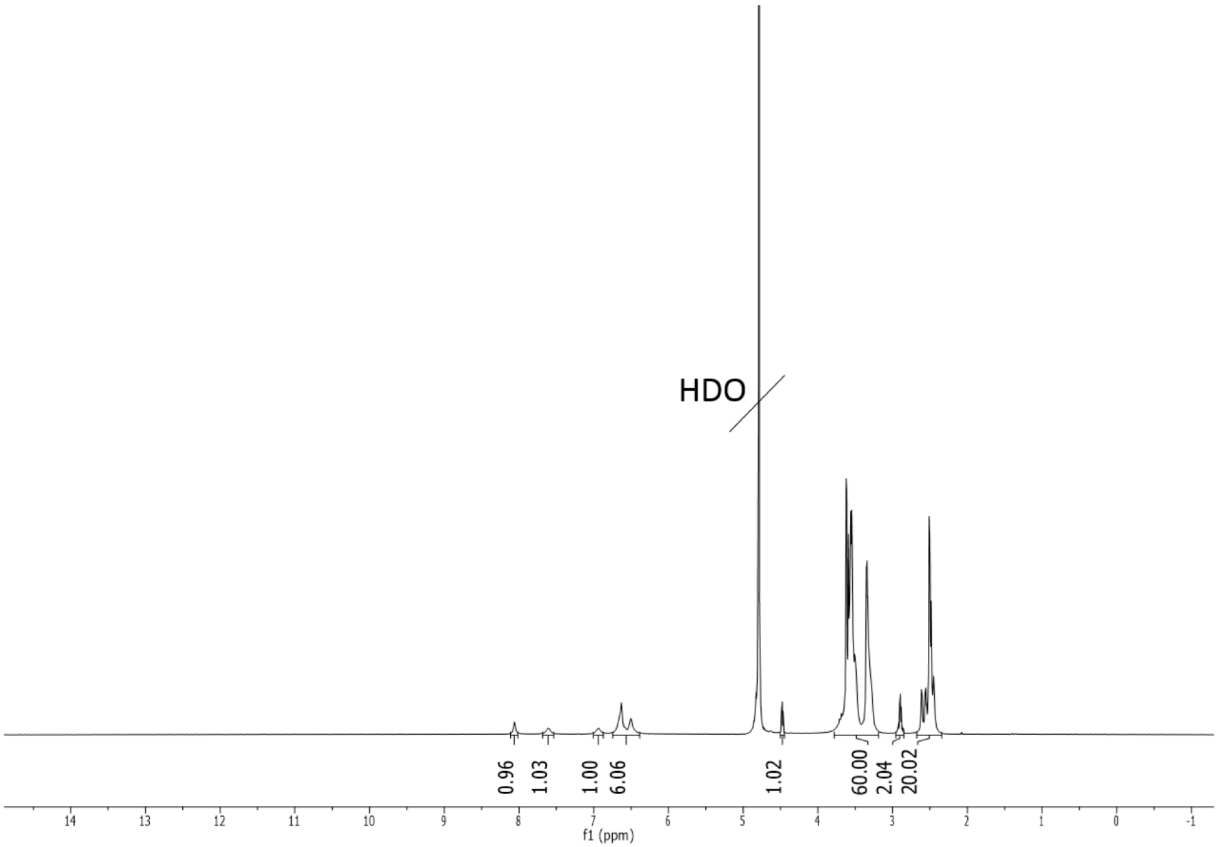

*Appendix 193: ^{1}H-NMR spectrum of **21** (600 MHz, D_2O).*

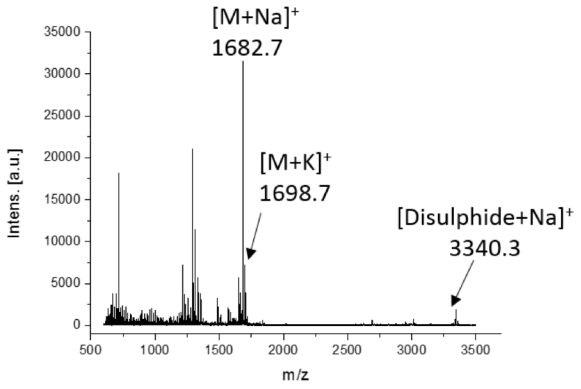

*Appendix 194: MALDI-TOF-MS spectrum of **21**. The signal with the mass to charge ratio of 1293.7 can be assigned to the unconjugated glycomacromolecule. The peak with a mass to charge ratio of 3340.3 can be assigned to the disulphide. One further signal with the mass-to-charge ratio of 715.4 can be found in the spectrum but cannot be assigned to potential by-products.*

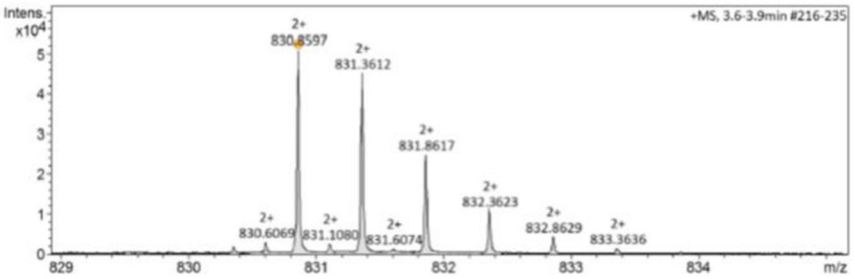

*Appendix 195: HR-MS (ESI⁺ Q-TOF) of compound **21**.*

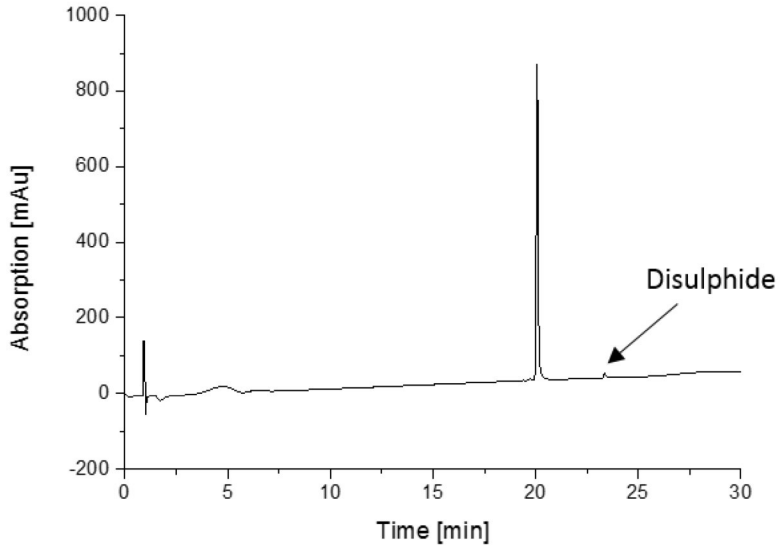

*Appendix 196: RP-HPLC chromatogram (linear gradient from 0-50% eluent B in 30 min at 25 °C) of compound **21**. The peak at 23.4 min can be assigned to the disulphide.*

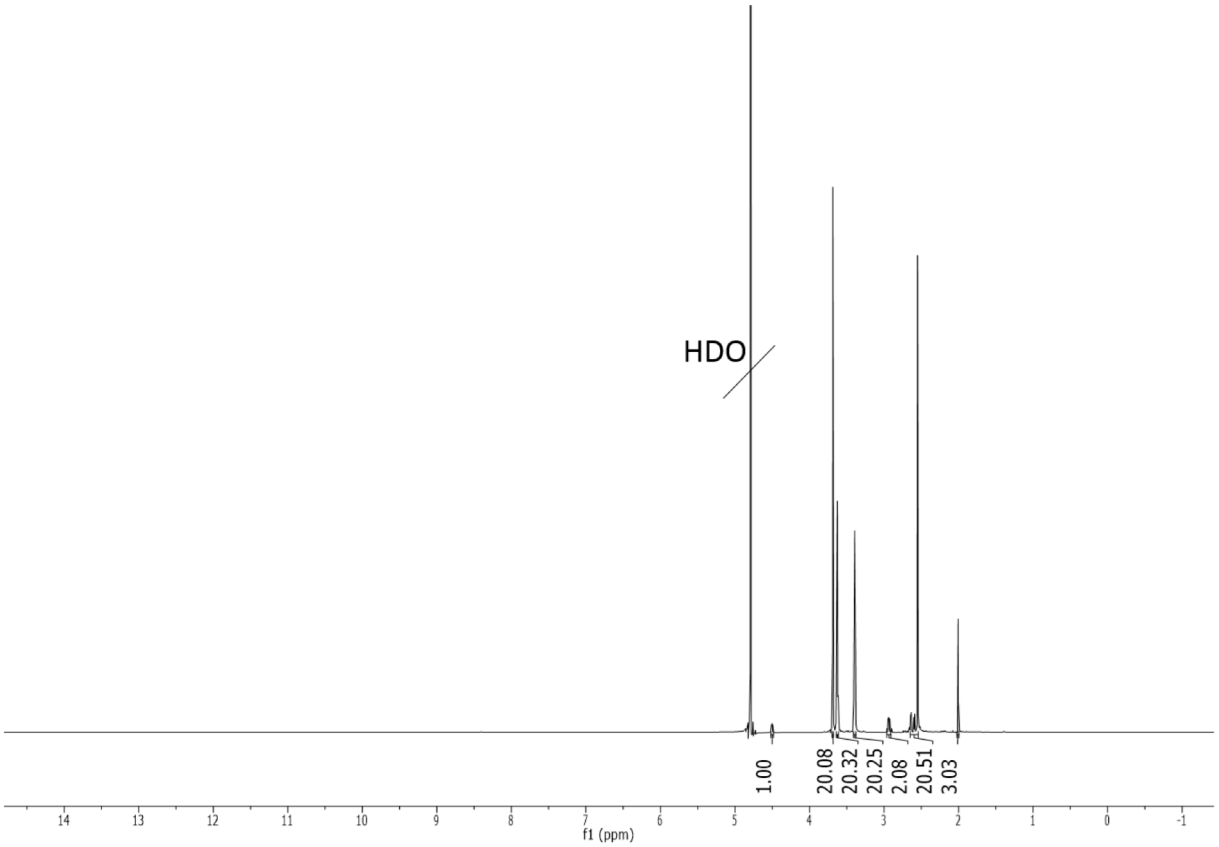

*Appendix 197: ^{1}H-NMR spectrum of **22** (600 MHz, D_2O).*

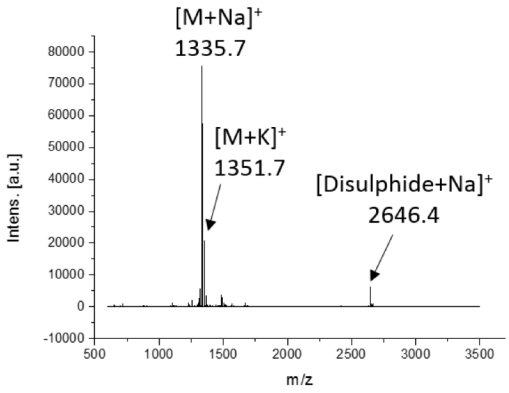

*Appendix 198: MALDI-TOF-MS spectrum of **22**. The signal with the mass to charge ratio of 2646.4 can be assigned to the disulphide.*

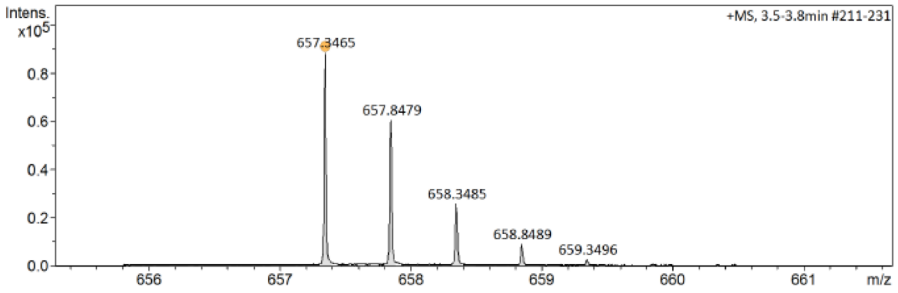

*Appendix 199: HR-MS (ESI⁺ Q-TOF) of compound **22**.*

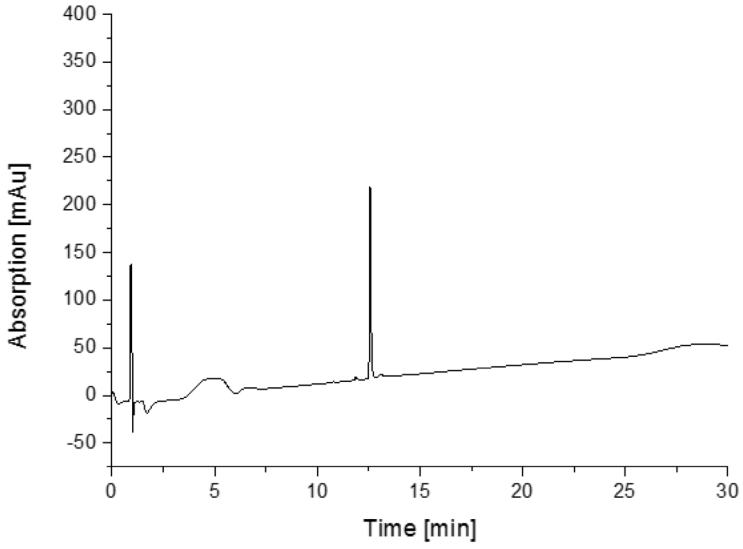

*Appendix 200: RP-HPLC chromatogram (linear gradient from 0-50% eluent B in 30 min at 25 °C) of compound **22**.*

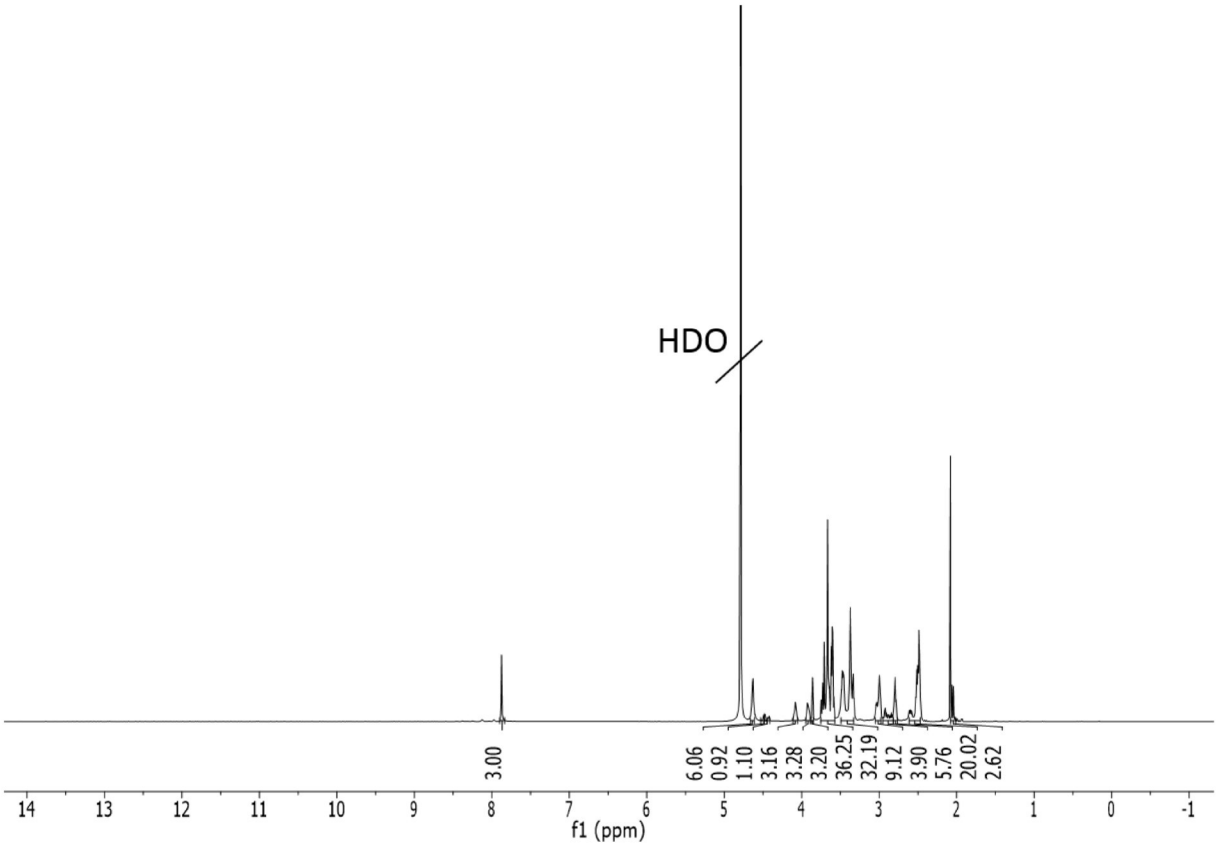

*Appendix 201: ^{1}H-NMR spectrum of **23** (600 MHz, D_2O).*

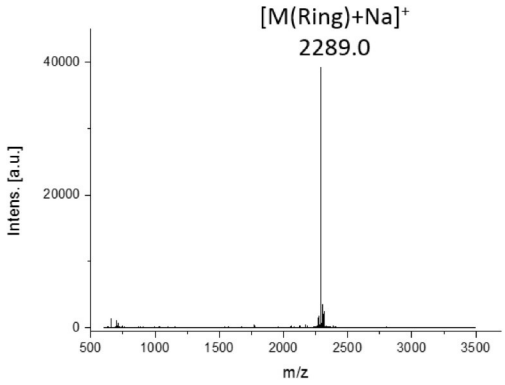

*Appendix 202: MALDI-TOF-MS spectrum of **23**.*

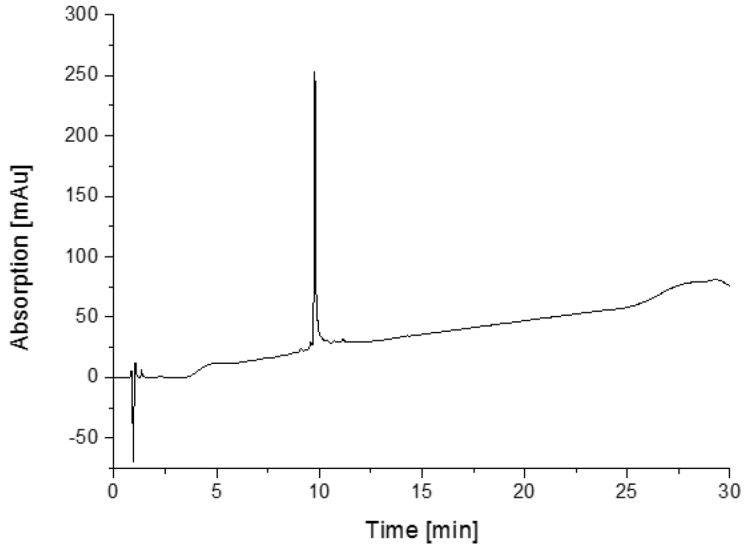

*Appendix 203: RP-HPLC chromatogram (linear gradient from 0-50% eluent B in 30 min at 25 °C) of compound **23**.*

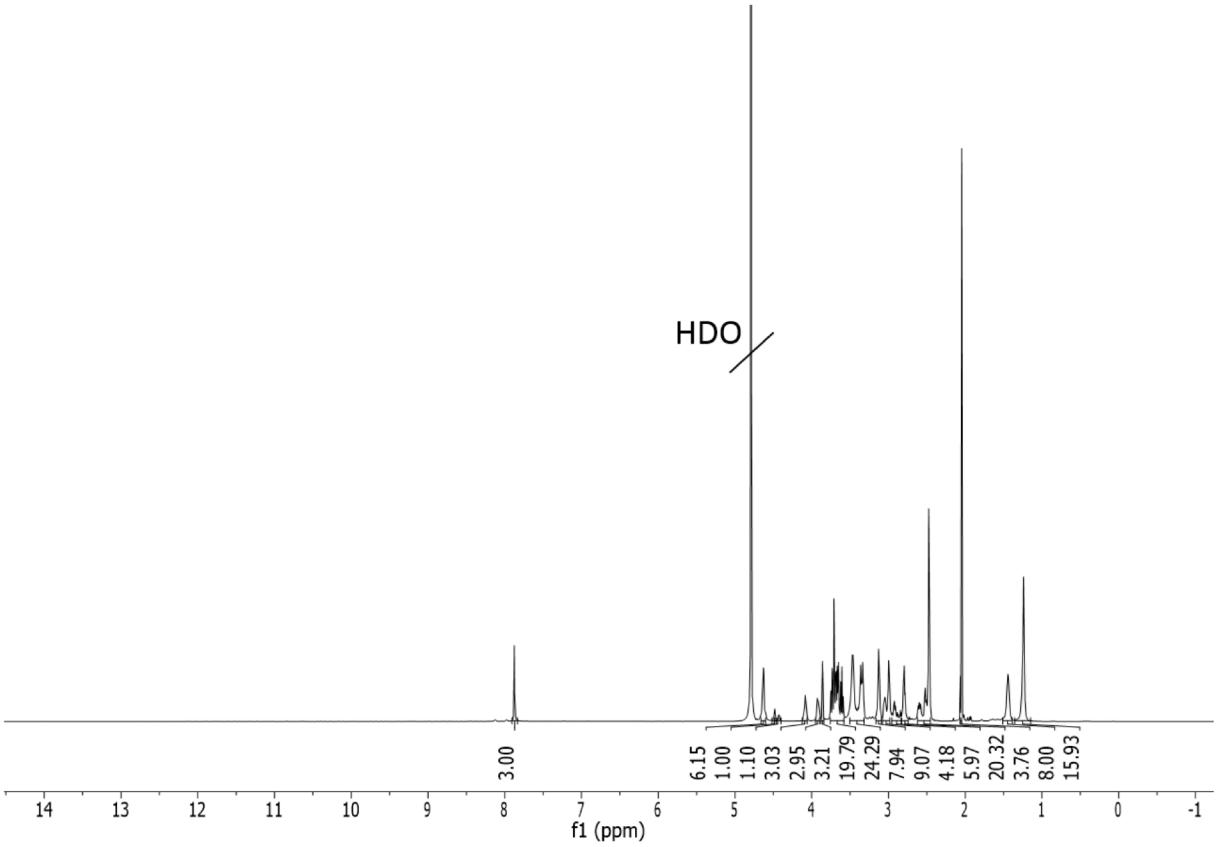

*Appendix 204: ^{1}H-NMR spectrum of **24** (600 MHz, D_2O).*

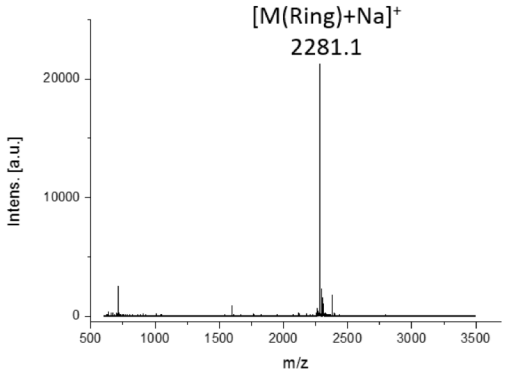

*Appendix 205: MALDI-TOF-MS spectrum of **24**.*

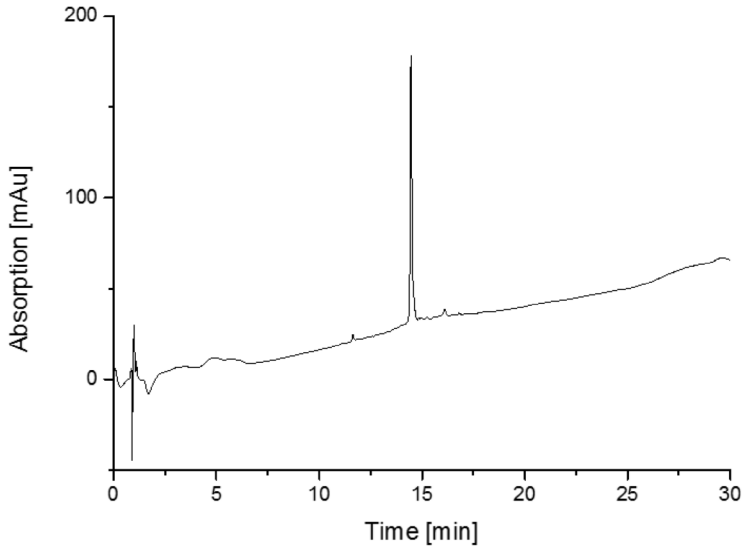

*Appendix 206: RP-HPLC chromatogram (linear gradient from 0-50% eluent B in 30 min at 25 °C) of compound **24**.*

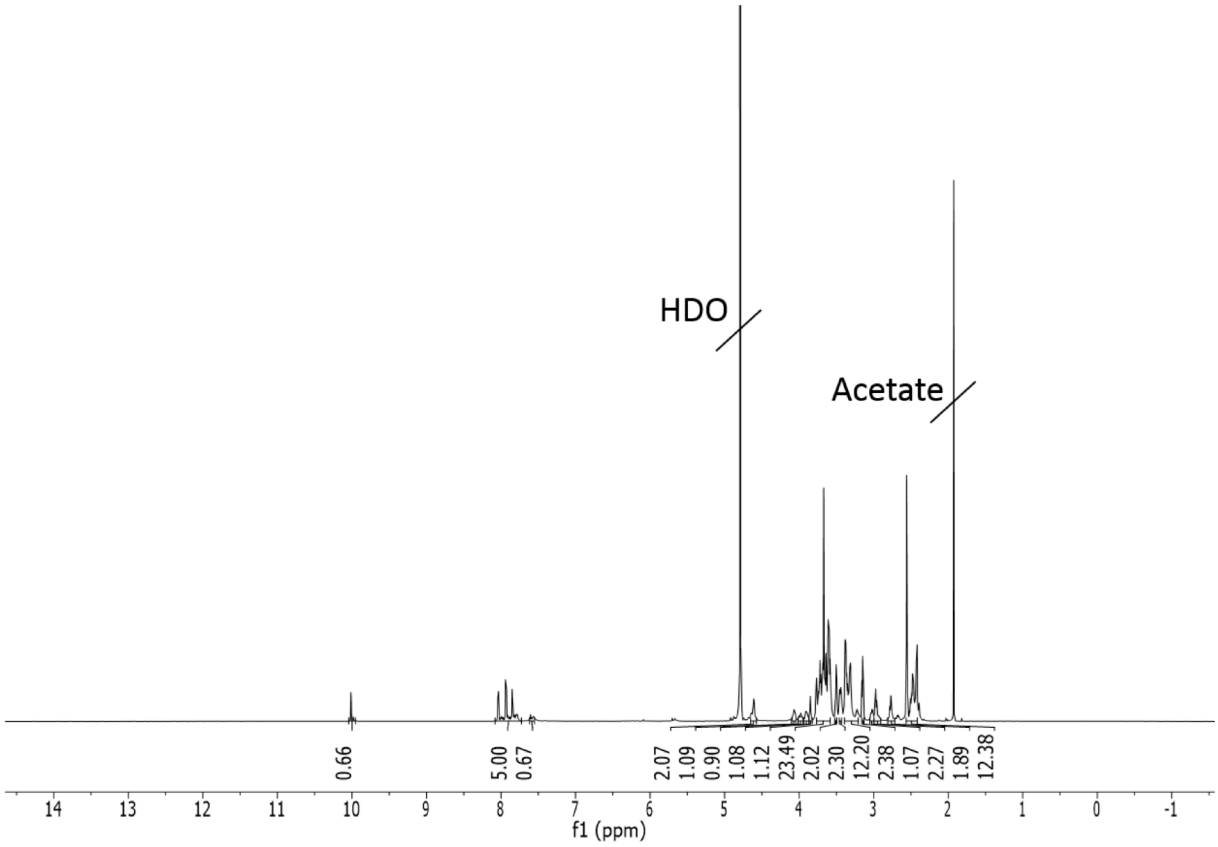

*Appendix 207: ^{1}H-NMR spectrum of **25** (600 MHz, D_2O).*

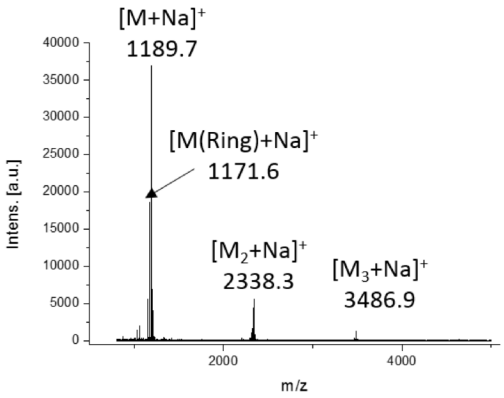

*Appendix 208: MALDI-TOF-MS spectrum of **25**. Further signals with the mass to charge ratios of 1171.6, 2338.3 and 3486.9 can be assigned to imines formed in solution.*

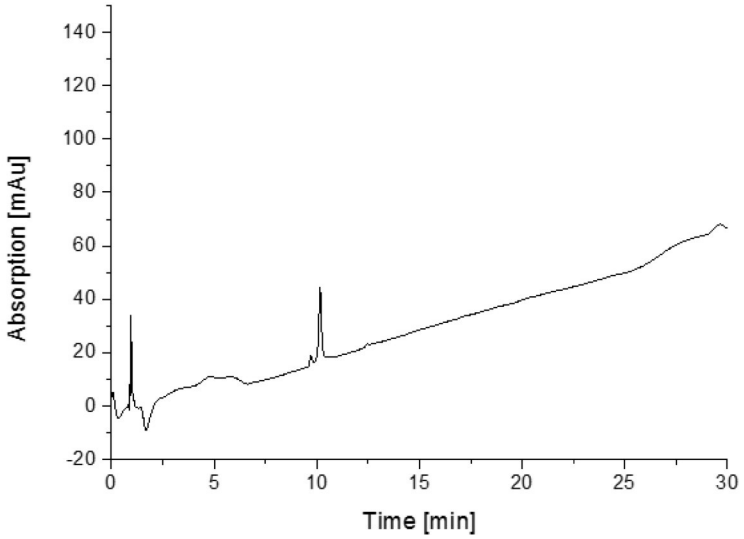

*Appendix 209: RP-HPLC chromatogram (linear gradient from 0-50% eluent B in 30 min at 25 °C) of compound **25**.*

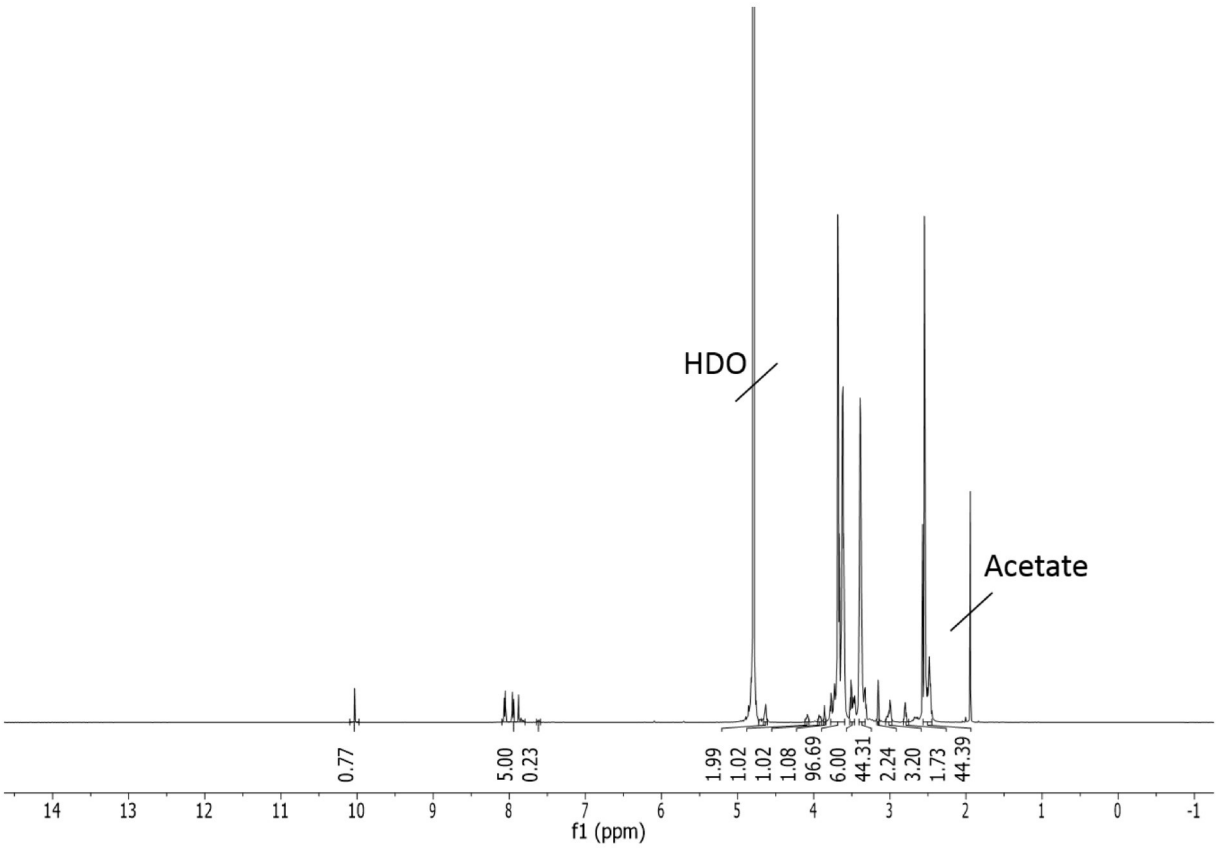

*Appendix 210: ^{1}H-NMR spectrum of **26** (600 MHz, D_2O).*

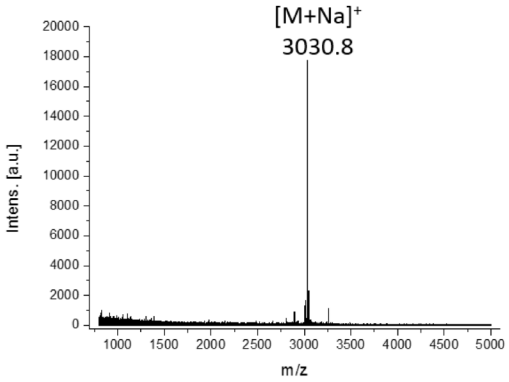

*Appendix 211: MALDI-TOF-MS spectrum of **26**.*

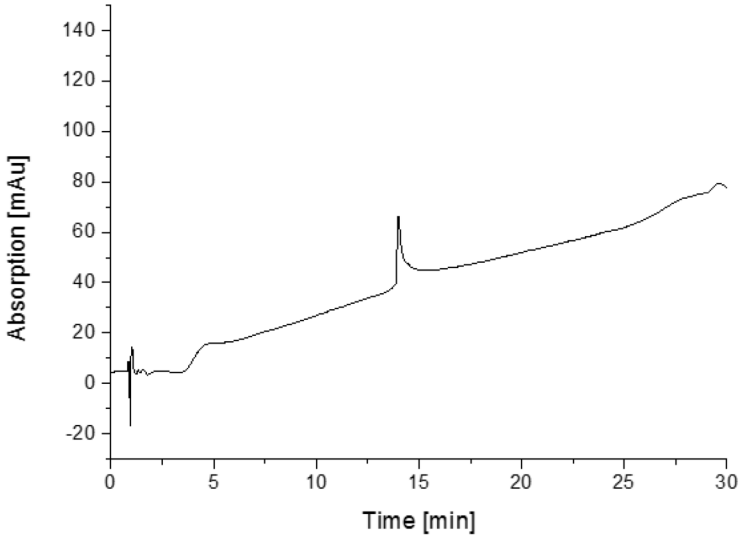

*Appendix 212: RP-HPLC chromatogram (linear gradient from 0-50% eluent B in 30 min at 25 °C) of compound **26**.*

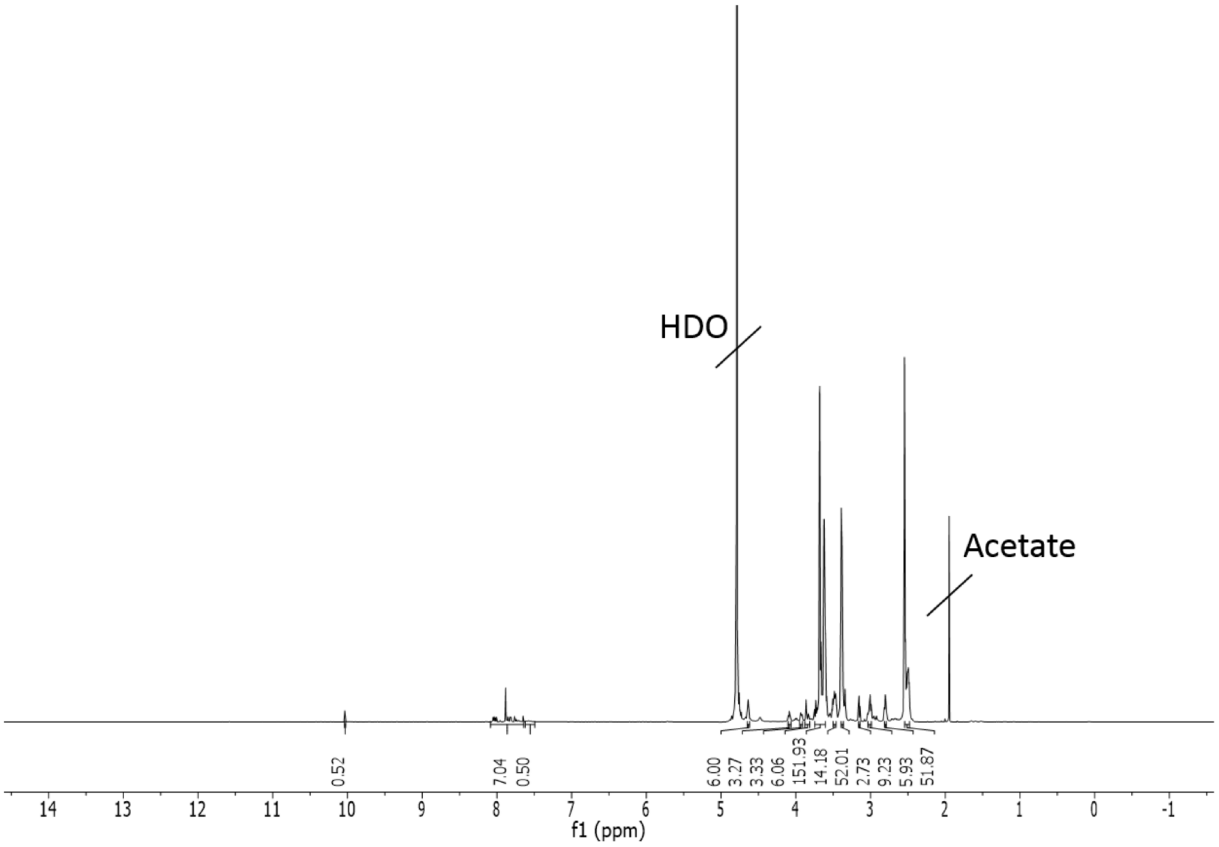

*Appendix 213: ^{1}H-NMR spectrum of **27** (600 MHz, D_2O).*

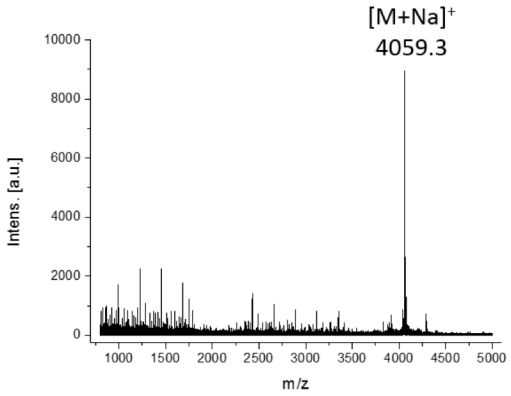

*Appendix 214: MALDI-TOF-MS spectrum of **27**. Further peaks with the mass-to-charge ratio of 994.6, 1224.7, 1454.9, 1685.1, 2429.4, 2661.6, 2889.7, 3120.9, 3352.0 and 4292.4 can be found in the spectrum but cannot be assigned to potential by-products.*

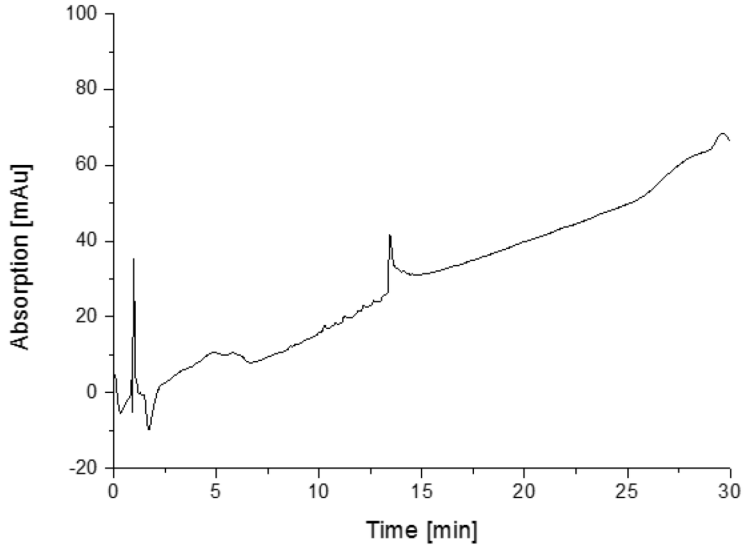

*Appendix 215: RP-HPLC chromatogram (linear gradient from 0-50% eluent B in 30 min at 25 °C) of compound **27**.*

6.6 Additional Information

6.6.1 TFA Removal

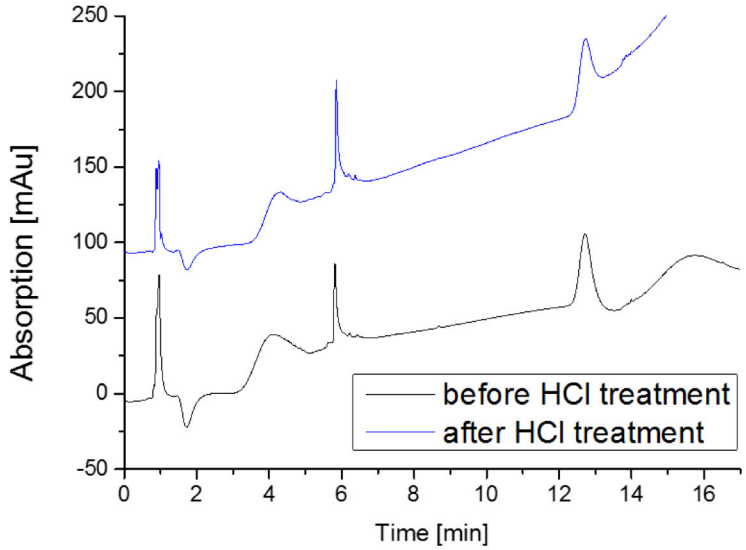

Appendix 216: Exemplary RP-HPLC chromatogram (95/5 H_2O/MeCN with 0.1% formic acid (A) and 5/95 H_2O/MeCN with 0.1% formic acid (B); 100% A to 5% A in 17 min) of a glycomacromolecule before and after HCl treatment. Relative purity before treatment was determined to be 90% and after treatment to be 64%. Broad peaks at time ranges from 4 to 5 and 12 to 13 minutes belong to the blank.

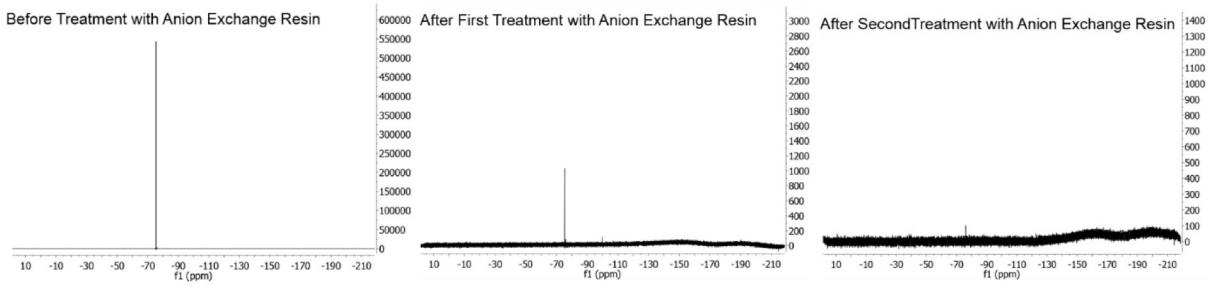

Appendix 217: ^{19}F-NMR (300 MHz, D_2O) before (left), after the first treatment (middle) and after the second treatment (right) with strong anion exchange resin.

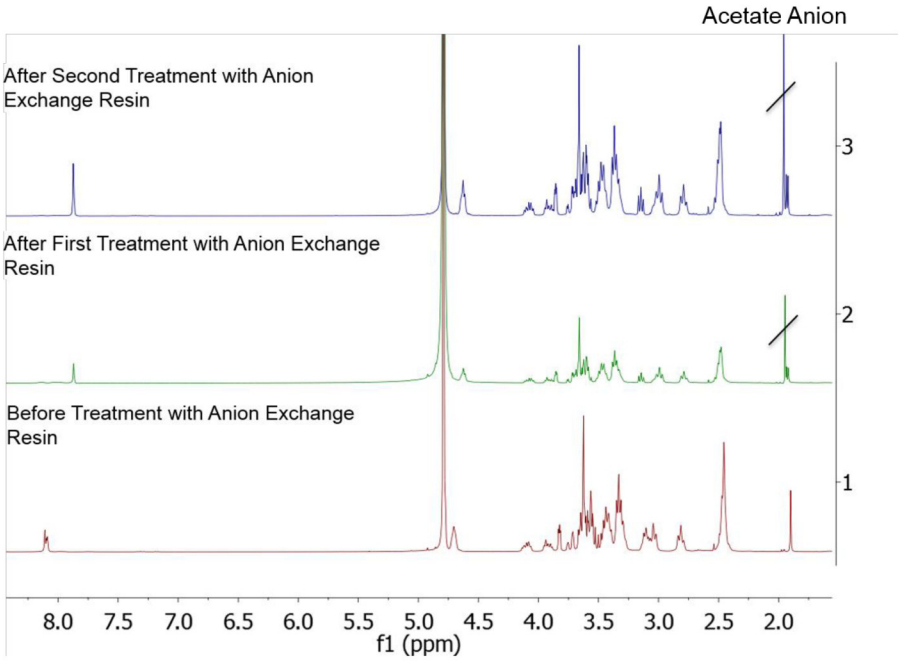

Appendix 218: ^{1}H-NMR (300 MHz, D_2O) before (bottom), after the first treatment (middle) and after the second treatment (top) with stron anion exchange resin. After treatment the signal for the acetate counter ion appears in the spectrum.

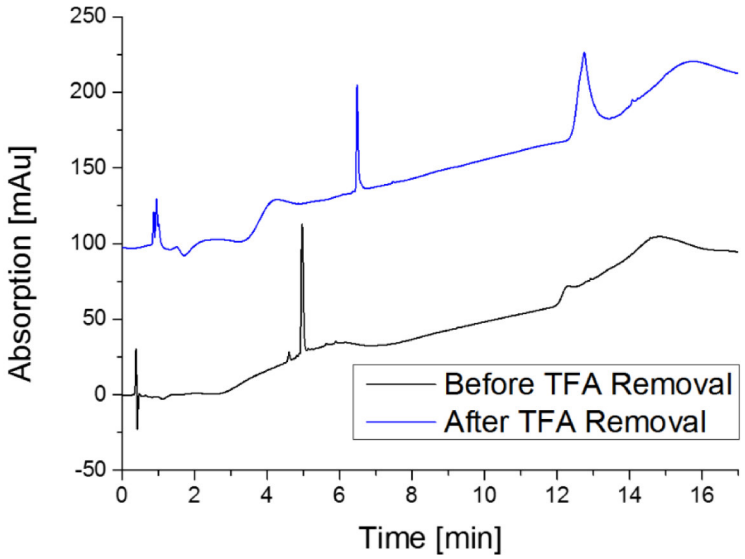

Appendix 219: Exemplary RP-HPLC chromatogram (95/5 H_2O/MeCN with 0.1% formic acid (A) and 5/95 H_2O/MeCN with 0.1% formic acid (B); 100% A to 5% A in 17 min) of a glycomacromolecule before and after TFA removal with strong anion exchange resin. Relative purity before treatment was determined to be 92% and after treatment to be 96%. Broad peaks at time ranges from 4 to 5 and 12 to 13 minutes belong to the blank.

6.6.2 Binding Studies with Glycomacromolecules by ITC

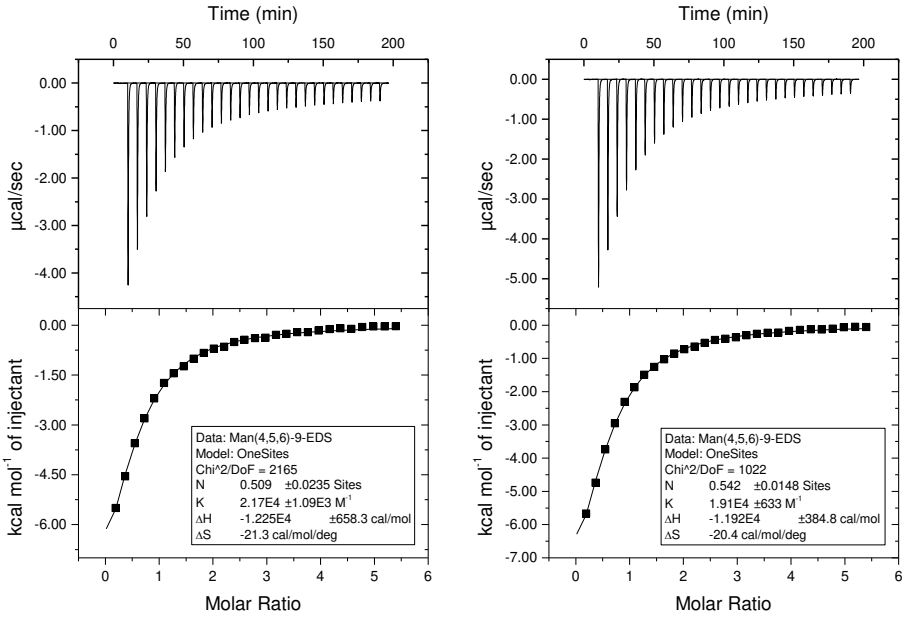

*Appendix 220: Experimental ITC heat pulses (top) and titration curves (bottom) for two independent measurements of glycomacromolecule **1** in acetate buffer (pH 5.2) at 25 °C.*

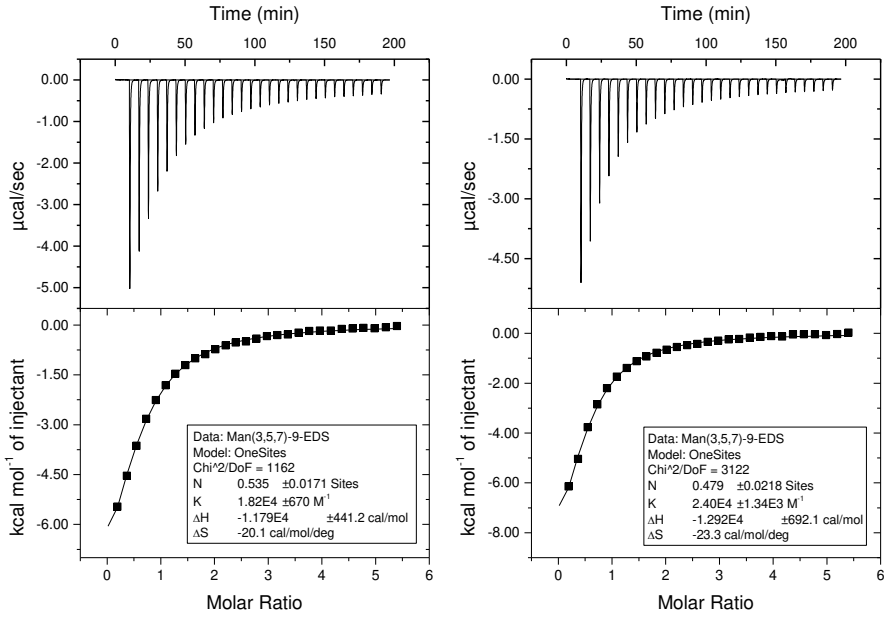

*Appendix 221: Experimental ITC heat pulses (top) and titration curves (bottom) for two independent measurements of glycomacromolecule **1a** in acetate buffer (pH 5.2) at 25 °C.*

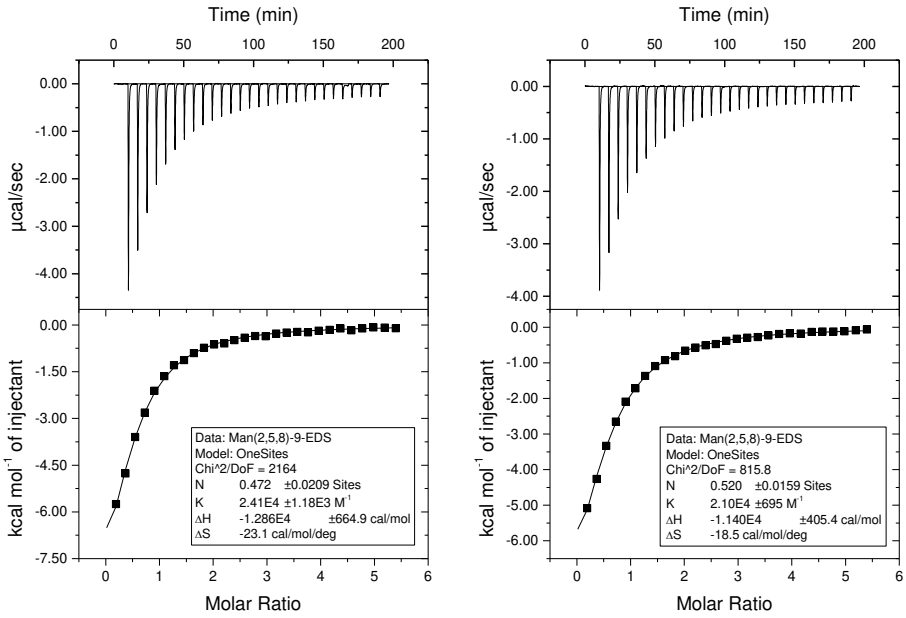

*Appendix 222: Experimental ITC heat pulses (top) and titration curves (bottom) for two independent measurements of glycomacromolecule **1b** in acetate buffer (pH 5.2) at 25 °C.*

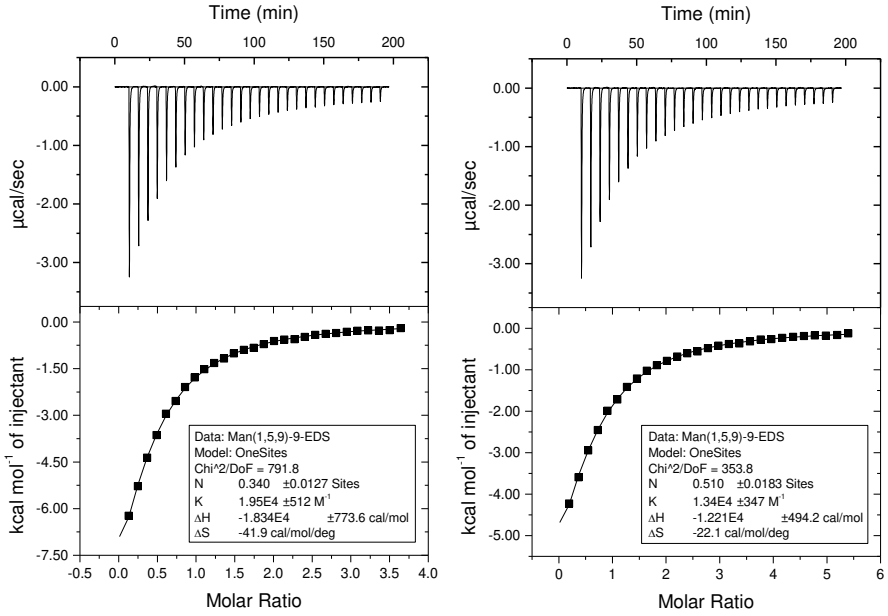

*Appendix 223: Experimental ITC heat pulses (top) and titration curves (bottom) for two independent measurements of glycomacromolecule **1c** in acetate buffer (pH 5.2) at 25 °C.*

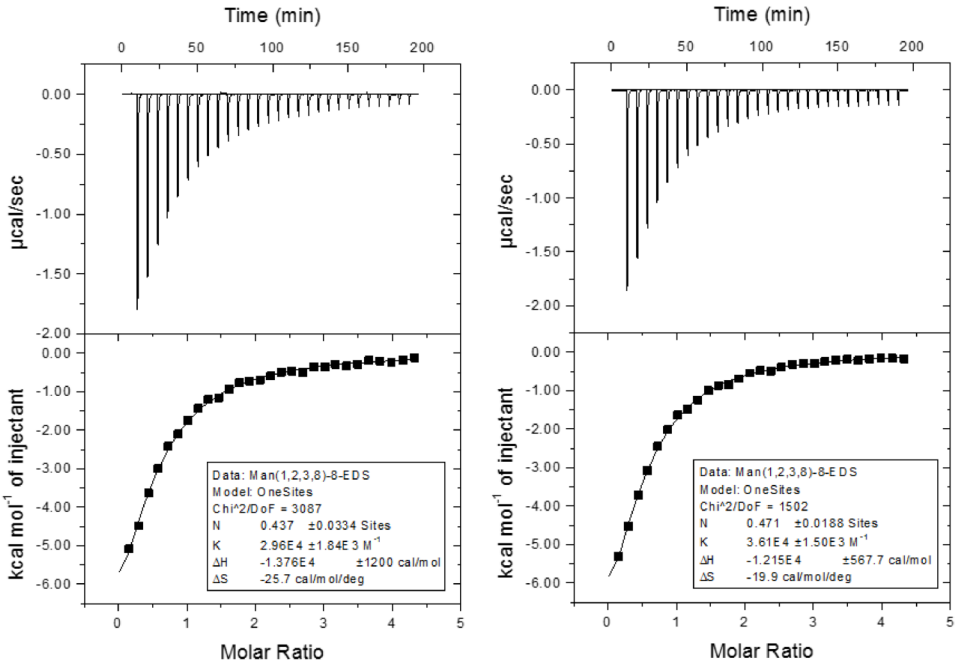

*Appendix 224: Experimental ITC heat pulses (top) and titration curves (bottom) for two independent measurements of glycomacromolecule **2** in acetate buffer (pH 5.2) at 25 °C.*

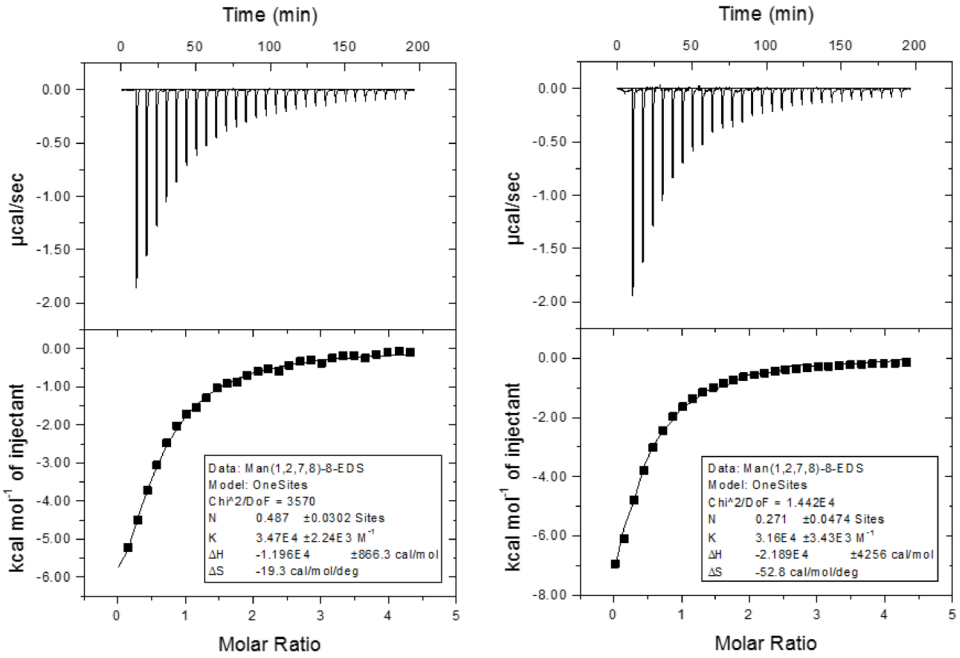

*Appendix 225: Experimental ITC heat pulses (top) and titration curves (bottom) for two independent measurements of glycomacromolecule **2a** in acetate buffer (pH 5.2) at 25 °C.*

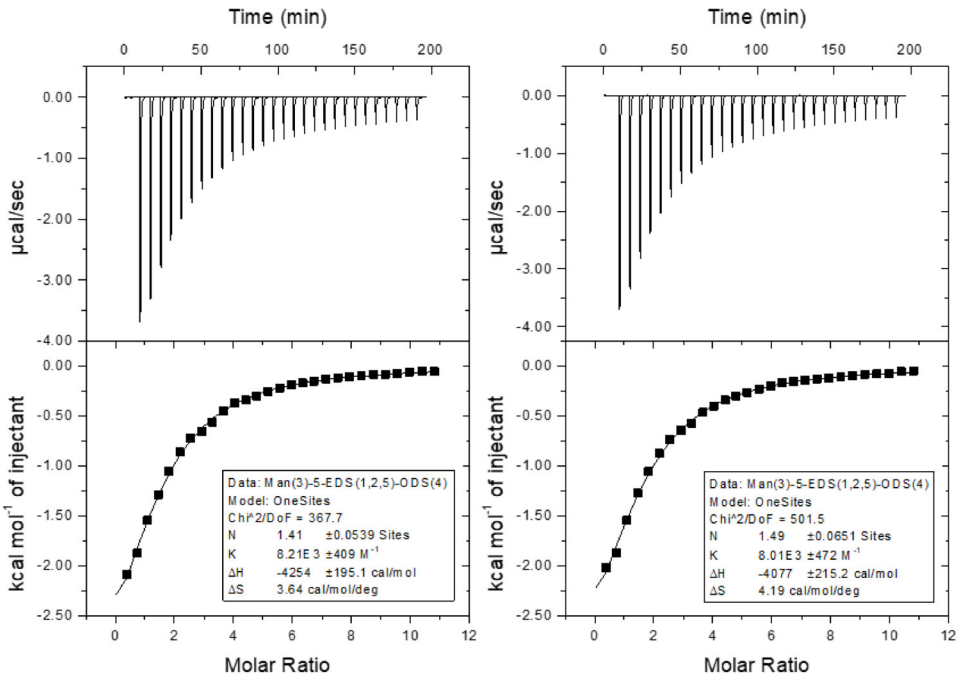

*Appendix 226: Experimental ITC heat pulses (top) and titration curves (bottom) for two independent measurements of glycomacromolecule **3** in acetate buffer (pH 5.2) at 25 °C.*

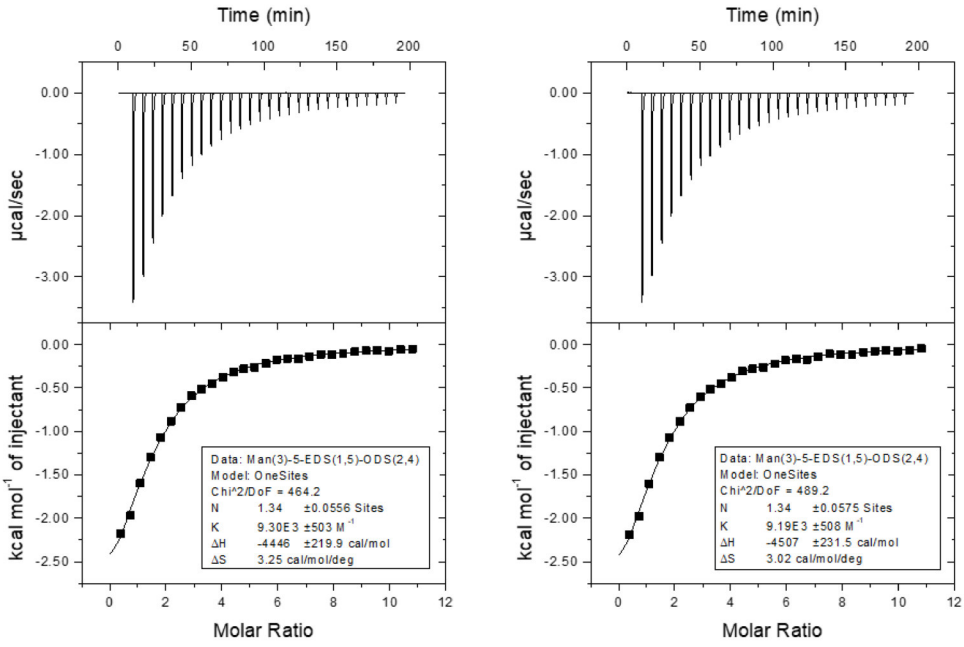

*Appendix 227: Experimental ITC heat pulses (top) and titration curves (bottom) for two independent measurements of glycomacromolecule **3a** in acetate buffer (pH 5.2) at 25 °C.*

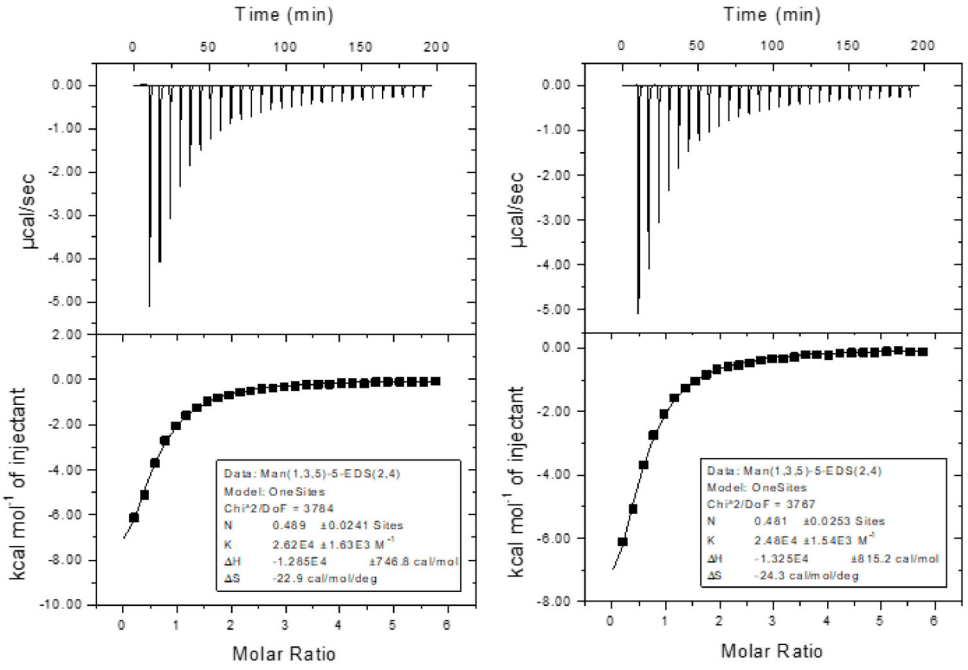

*Appendix 228: Experimental ITC heat pulses (top) and titration curves (bottom) for two independent measurements of glycomacromolecule **4** in acetate buffer (pH 5.2) at 25 °C.*

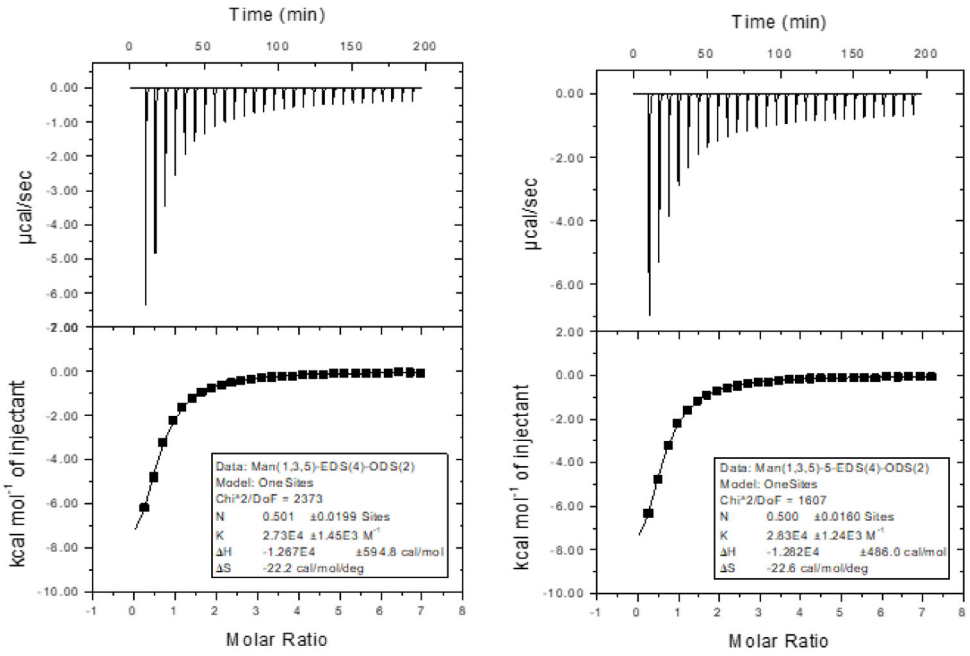

*Appendix 229: Experimental ITC heat pulses (top) and titration curves (bottom) for two independent measurements of glycomacromolecule **4a** in acetate buffer (pH 5.2) at 25 °C.*

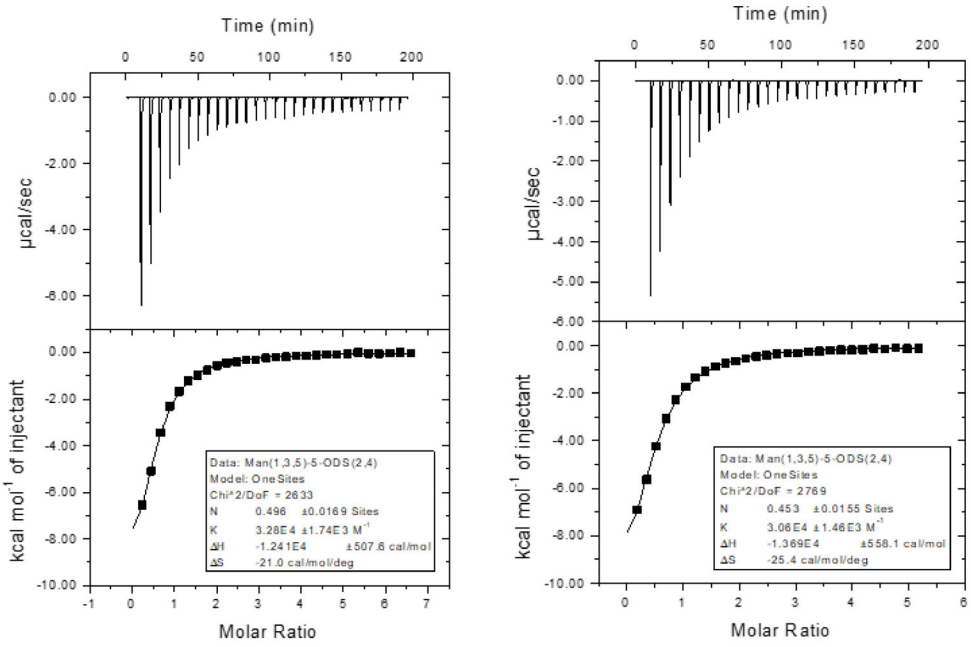

*Appendix 230: Experimental ITC heat pulses (top) and titration curves (bottom) for two independent measurements of glycomacromolecule **4b** in acetate buffer (pH 5.2) at 25 °C.*

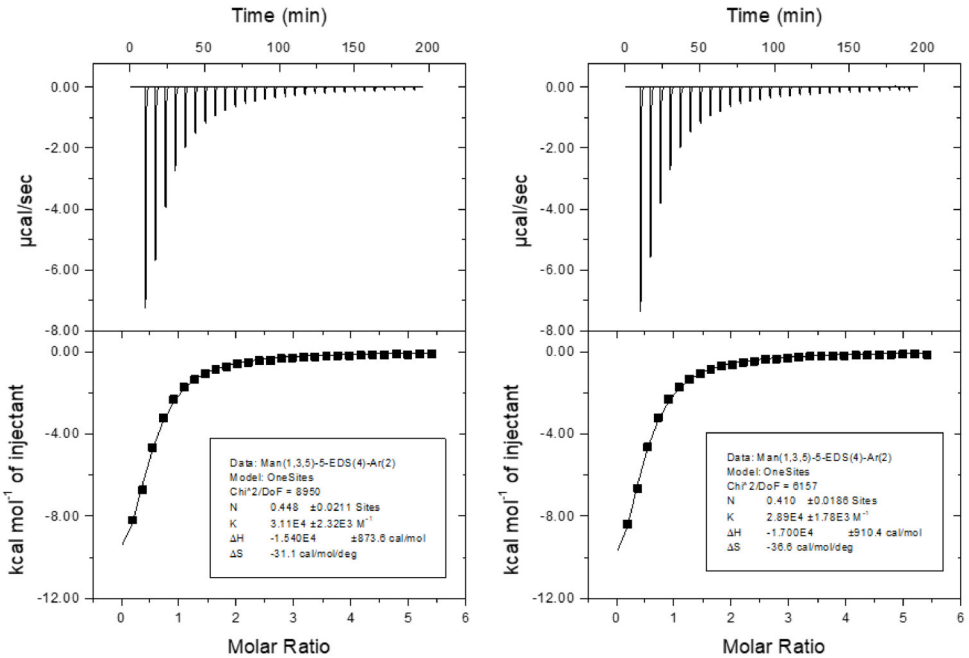

*Appendix 231: Experimental ITC heat pulses (top) and titration curves (bottom) for two independent measurements of glycomacromolecule **4c** in acetate buffer (pH 5.2) at 25 °C.*

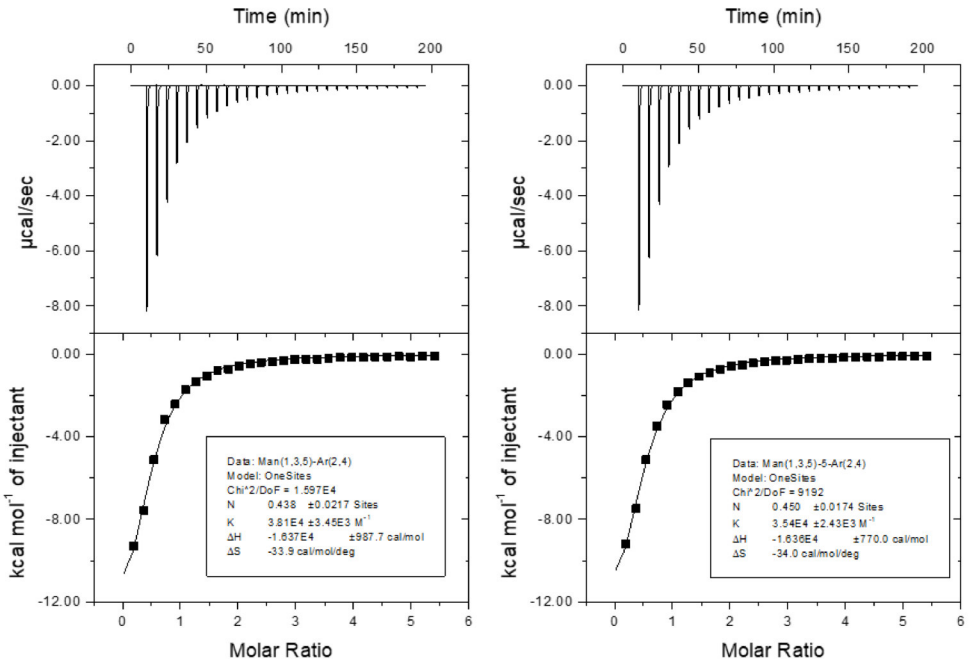

*Appendix 232: Experimental ITC heat pulses (top) and titration curves (bottom) for two independent measurements of glycomacromolecule **4d** in acetate buffer (pH 5.2) at 25 °C.*

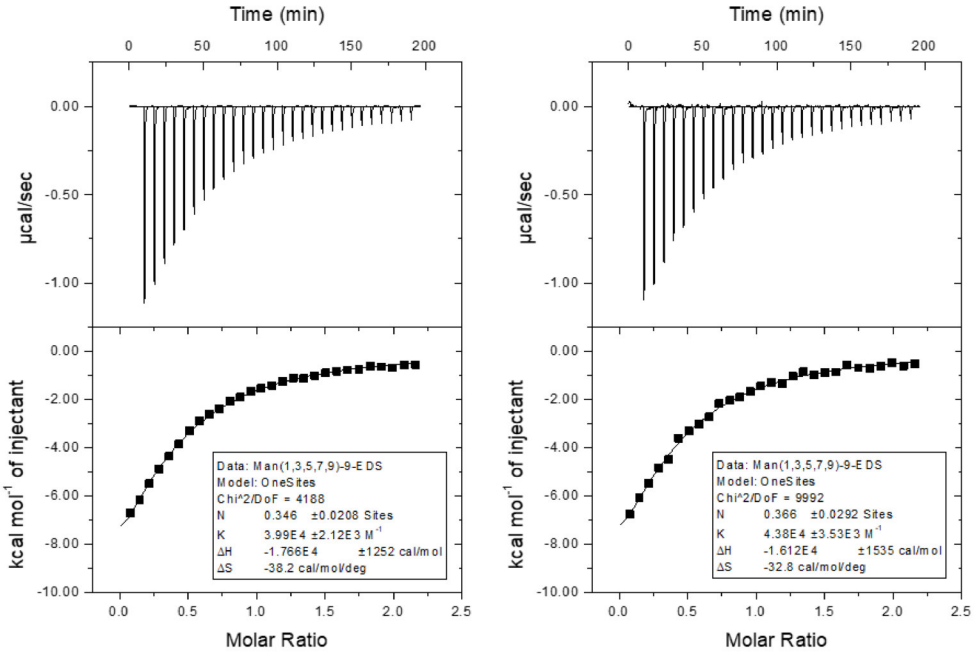

*Appendix 233: Experimental ITC heat pulses (top) and titration curves (bottom) for two independent measurements of glycomacromolecule **5** in acetate buffer (pH 5.2) at 25 °C.*

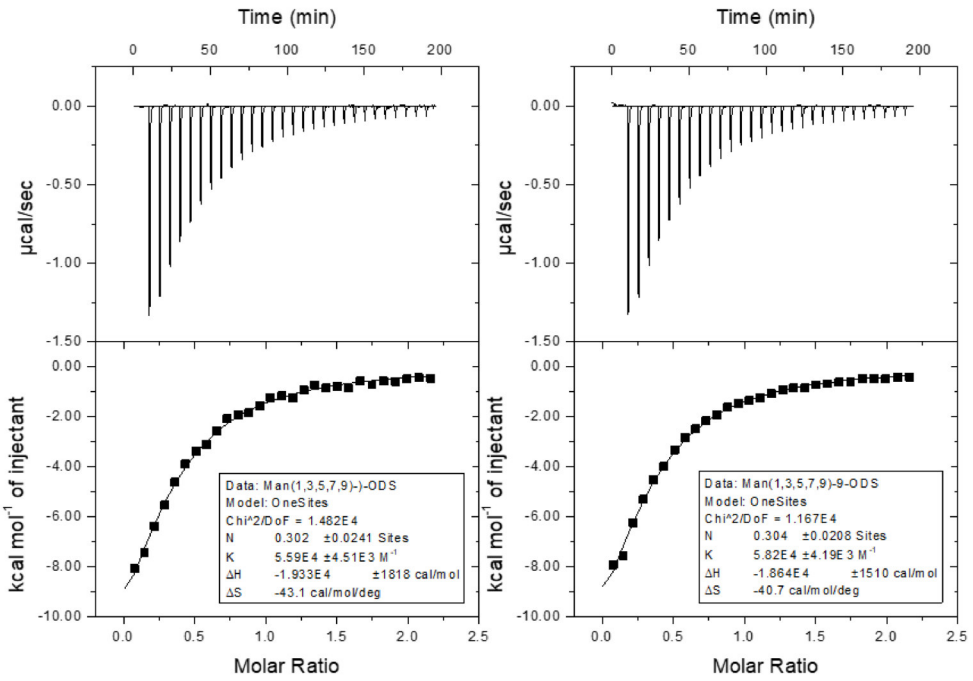

*Appendix 234: Experimental ITC heat pulses (top) and titration curves (bottom) for two independent measurements of glycomacromolecule **5a** in acetate buffer (pH 5.2) at 25 °C.*

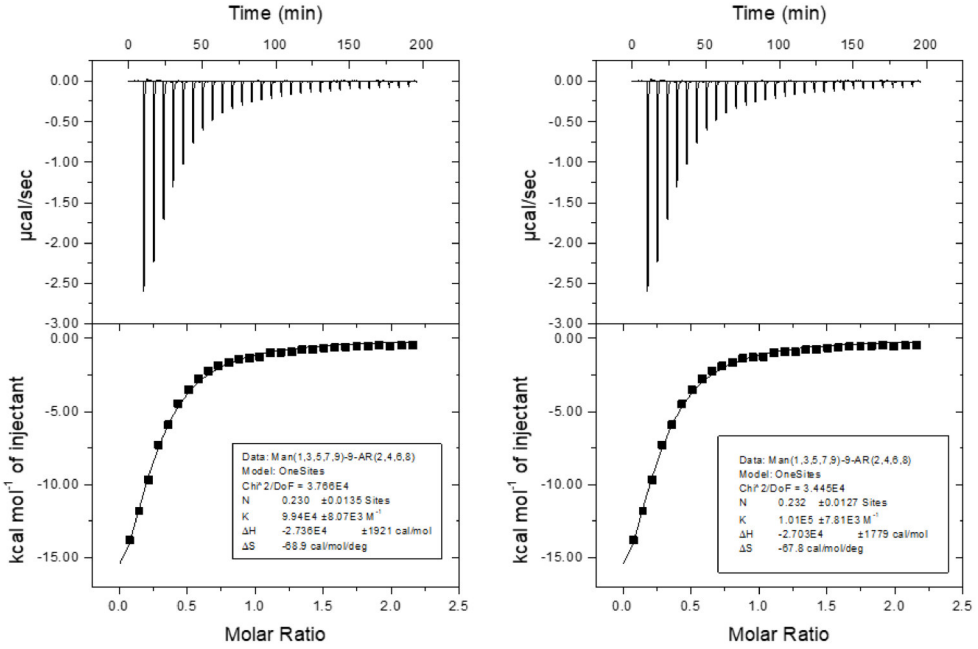

*Appendix 235: Experimental ITC heat pulses (top) and titration curves (bottom) for two independent measurements of glycomacromolecule **5b** in acetate buffer (pH 5.2) at 25 °C.*

6.6.3 Binding Studies with Glycomacromolecules by SPR

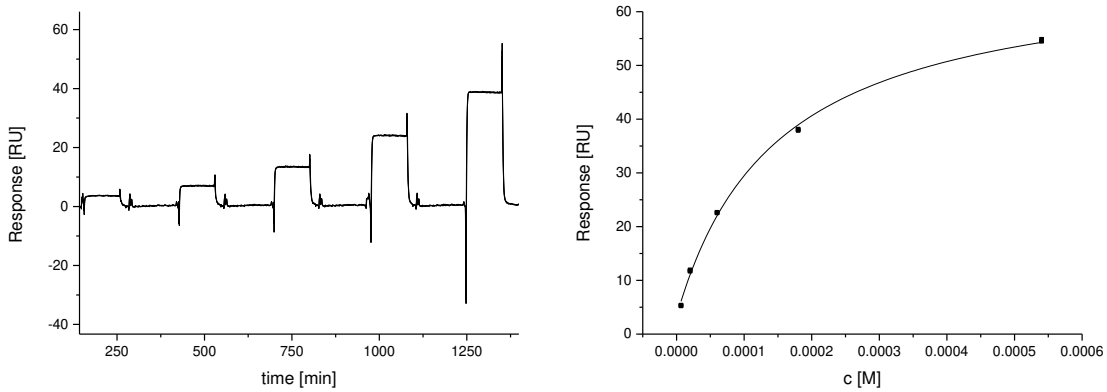

*Appendix 236: Representative sensorgrams and the equilibrium response as a function of concentration from glycomacromolecule **1** plotted using a steady state model. Experimental data from three consecutive measurements are shown.*

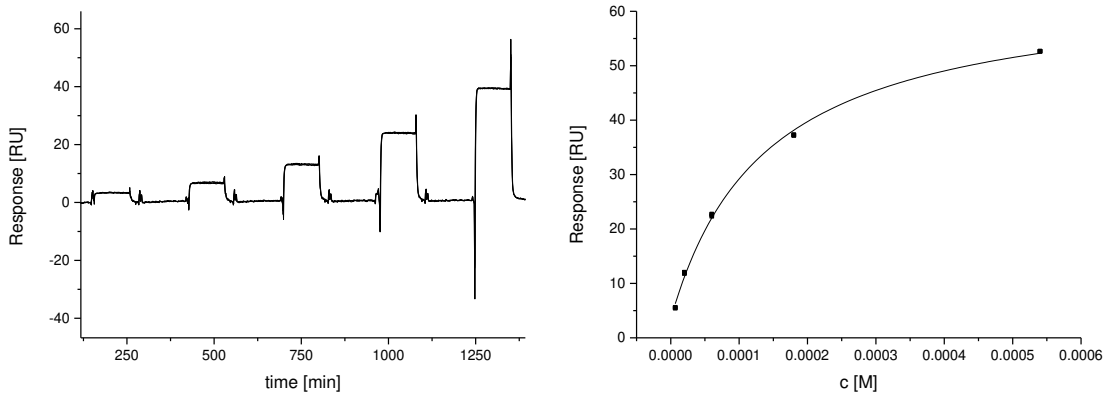

*Appendix 237: Representative sensorgrams and the equilibrium response as a function of concentration from glycomacromolecule **1a** plotted using a steady state model. Experimental data from three consecutive measurements are shown.*

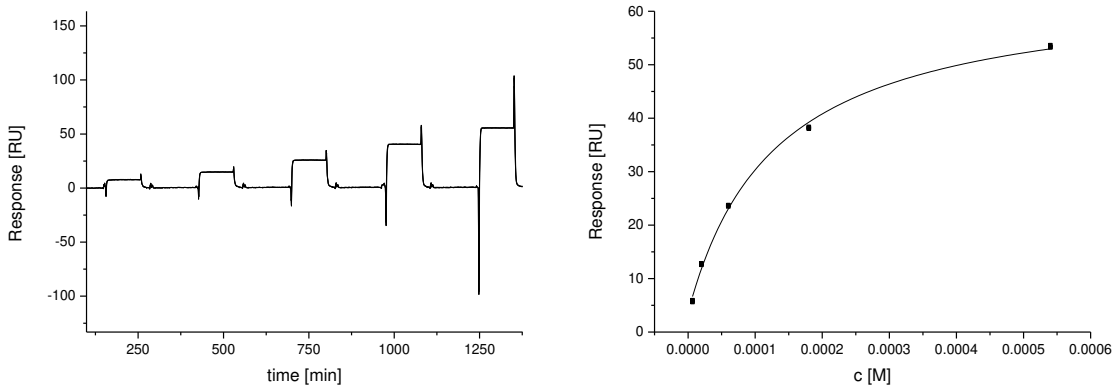

*Appendix 238: Representative sensorgrams and the equilibrium response as a function of concentration from glycomacromolecule **1b** plotted using a steady state model. Experimental data from three consecutive measurements are shown.*

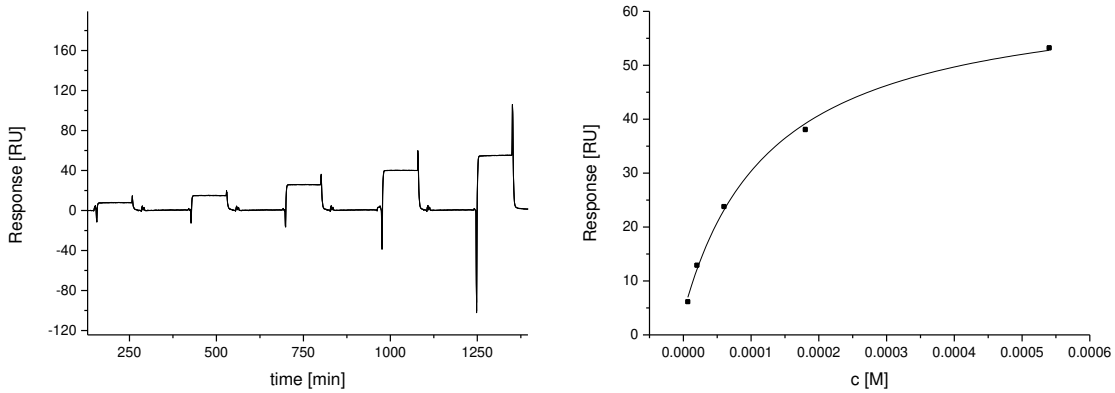

*Appendix 239: Representative sensorgrams and the equilibrium response as a function of concentration from glycomacromolecule **1c** plotted using a steady state model. Experimental data from three consecutive measurements are shown.*

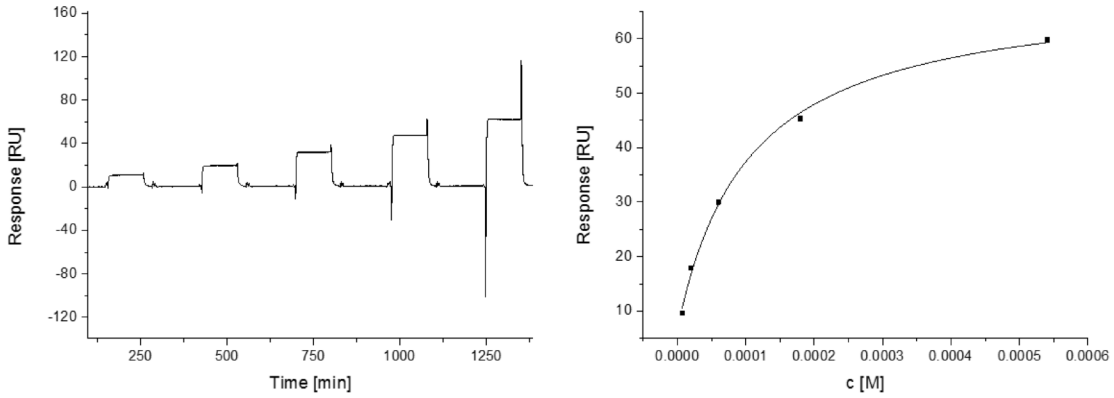

*Appendix 240: Representative sensorgrams and the equilibrium response as a function of concentration from glycomacromolecule **2** plotted using a steady state model. Experimental data from three consecutive measurements are shown.*

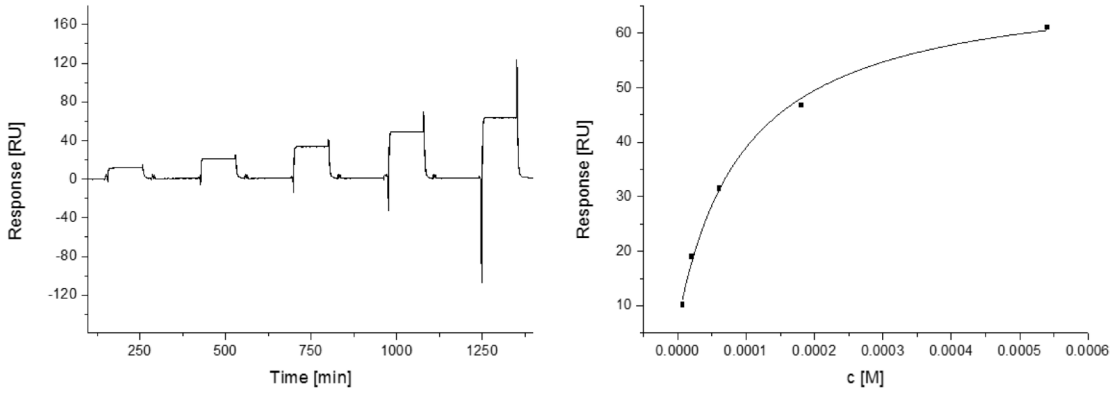

*Appendix 241: Representative sensorgrams and the equilibrium response as a function of concentration from glycomacromolecule **2a** plotted using a steady state model. Experimental data from three consecutive measurements are shown.*

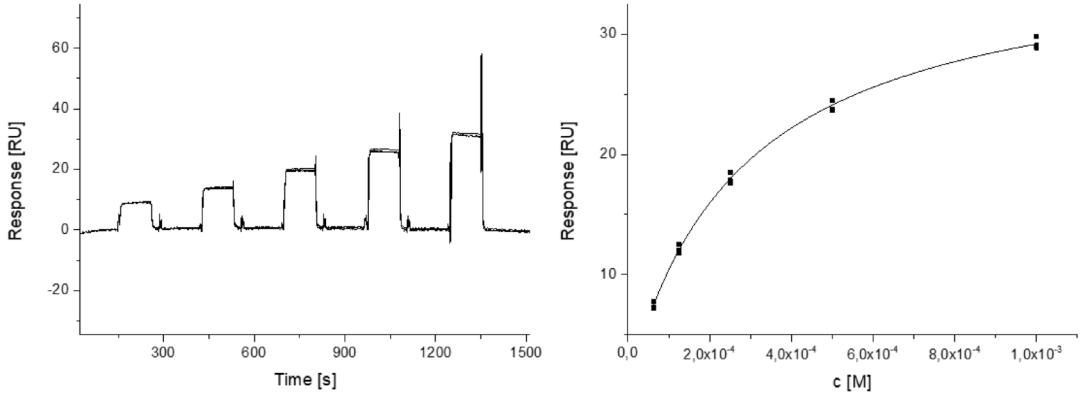

*Appendix 242: Representative sensorgrams and the equilibrium response as a function of concentration from glycomacromolecule **3** plotted using a steady state model. Experimental data from three consecutive measurements are shown.*

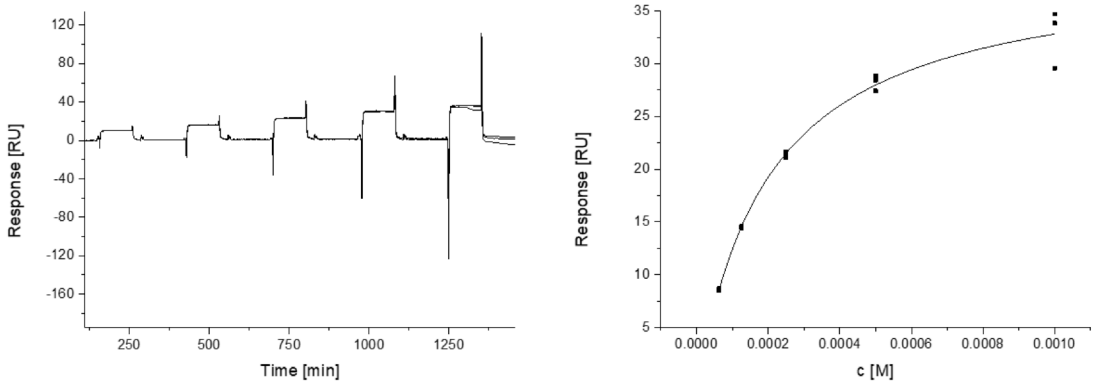

*Appendix 243: Representative sensorgrams and the equilibrium response as a function of concentration from glycomacromolecule **3a** plotted using a steady state model. Experimental data from three consecutive measurements are shown.*

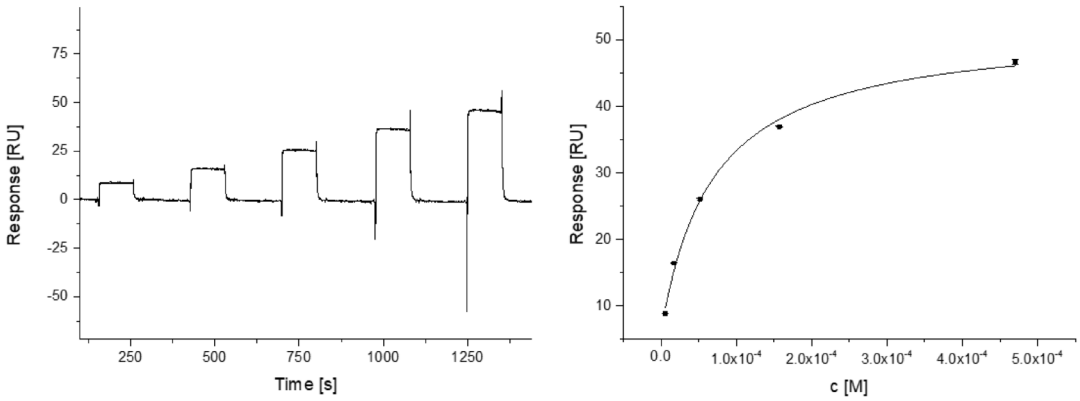

*Appendix 244: Representative sensorgrams and the equilibrium response as a function of concentration from glycomacromolecule **4** plotted using a steady state model. Experimental data from three consecutive measurements are shown.*

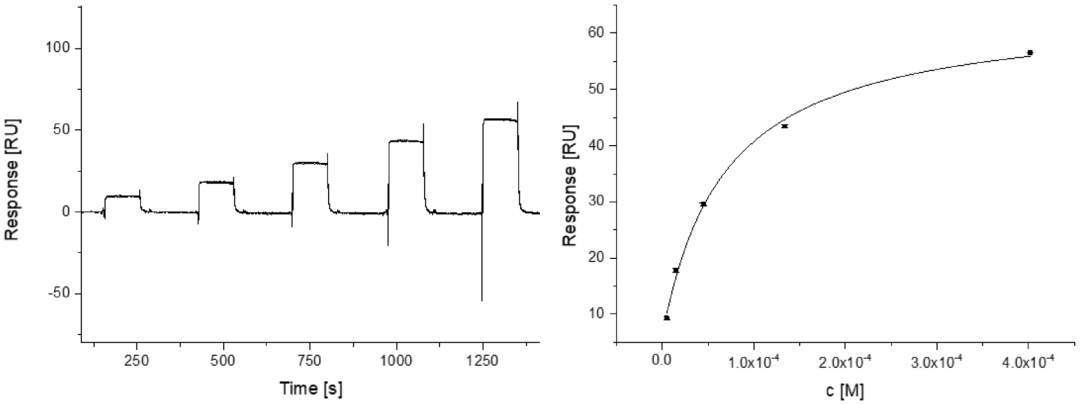

*Appendix 245: Representative sensorgrams and the equilibrium response as a function of concentration from glycomacromolecule **4a** plotted using a steady state model. Experimental data from three consecutive measurements are shown.*

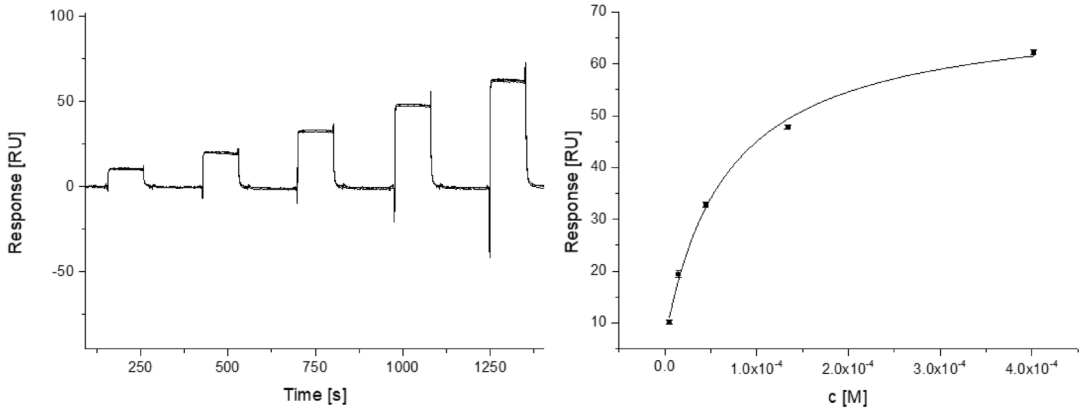

*Appendix 246: Representative sensorgrams and the equilibrium response as a function of concentration from glycomacromolecule **4b** plotted using a steady state model. Experimental data from three consecutive measurements are shown.*

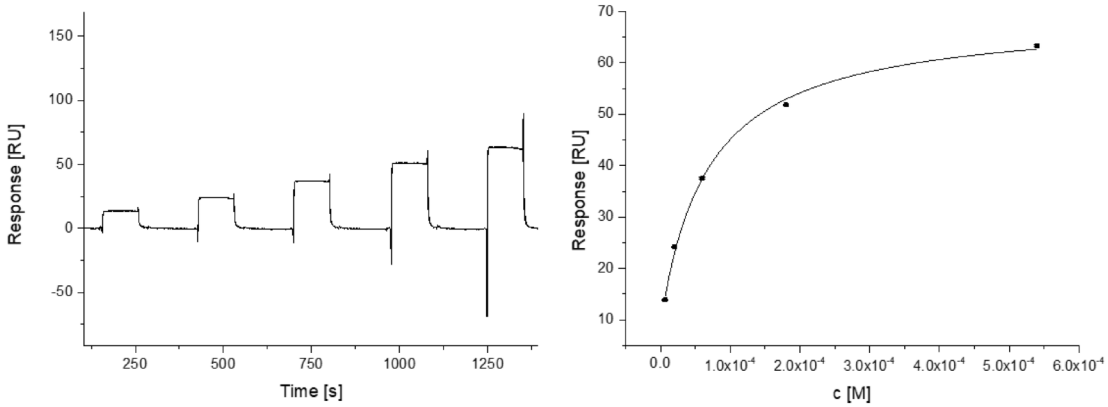

*Appendix 247: Representative sensorgrams and the equilibrium response as a function of concentration from glycomacromolecule **4c** plotted using a steady state model. Experimental data from three consecutive measurements are shown.*

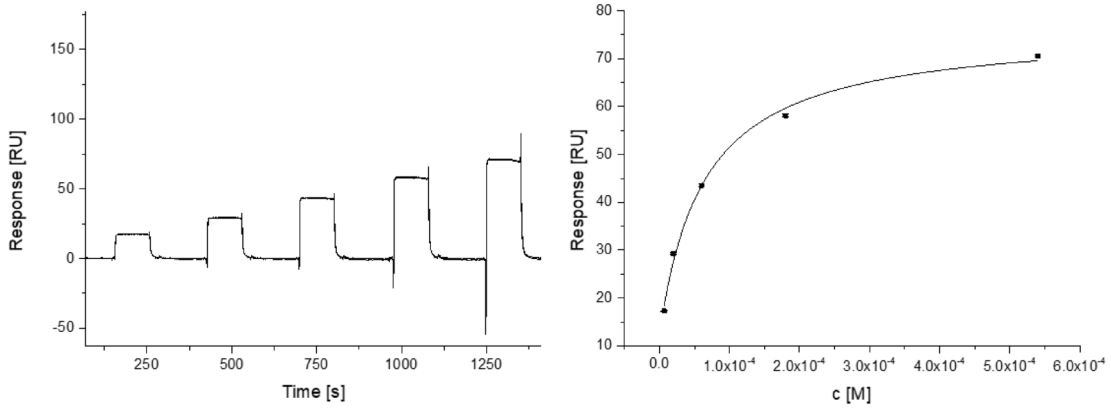

*Appendix 248: Representative sensorgrams and the equilibrium response as a function of concentration from glycomacromolecule **4d** plotted using a steady state model. Experimental data from three consecutive measurements are shown.*

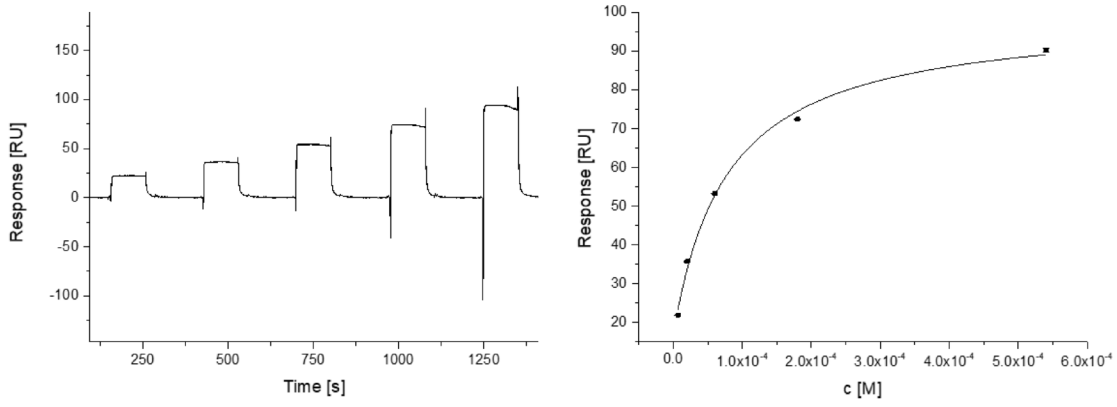

*Appendix 249: Representative sensorgrams and the equilibrium response as a function of concentration from glycomacromolecule **5** plotted using a steady state model. Experimental data from three consecutive measurements are shown.*

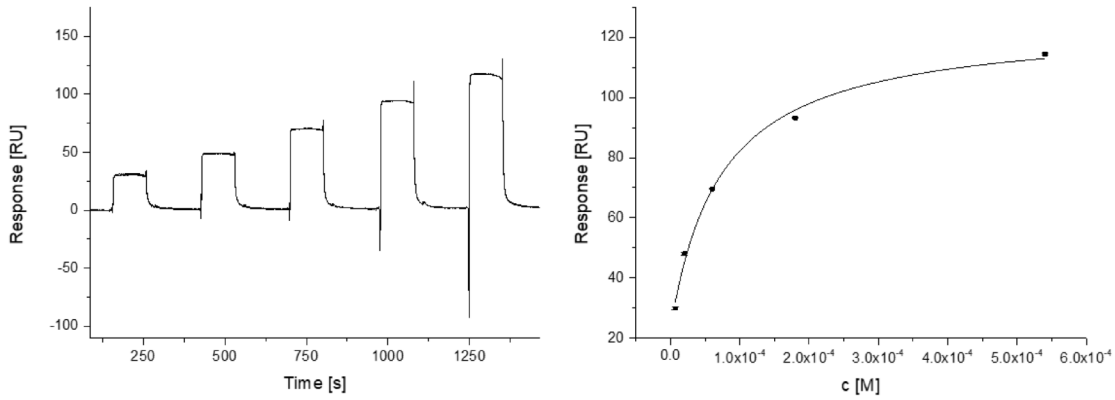

*Appendix 250: Representative sensorgrams and the equilibrium response as a function of concentration from glycomacromolecule **5a** plotted using a steady state model. Experimental data from three consecutive measurements are shown.*

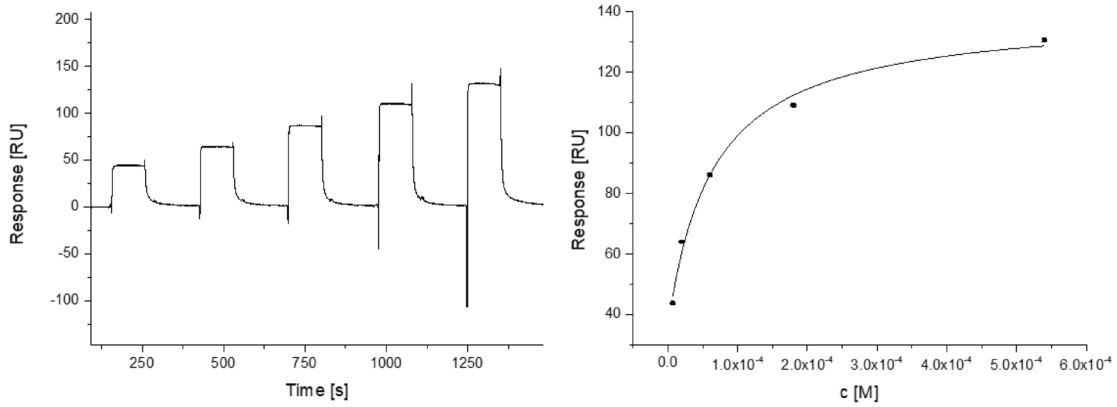

*Appendix 251: Representative sensorgrams and the equilibrium response as a function of concentration from glycomacromolecule **5b** plotted using a steady state model. Experimental data from three consecutive measurements are shown.*

6.6.4 NMR Study

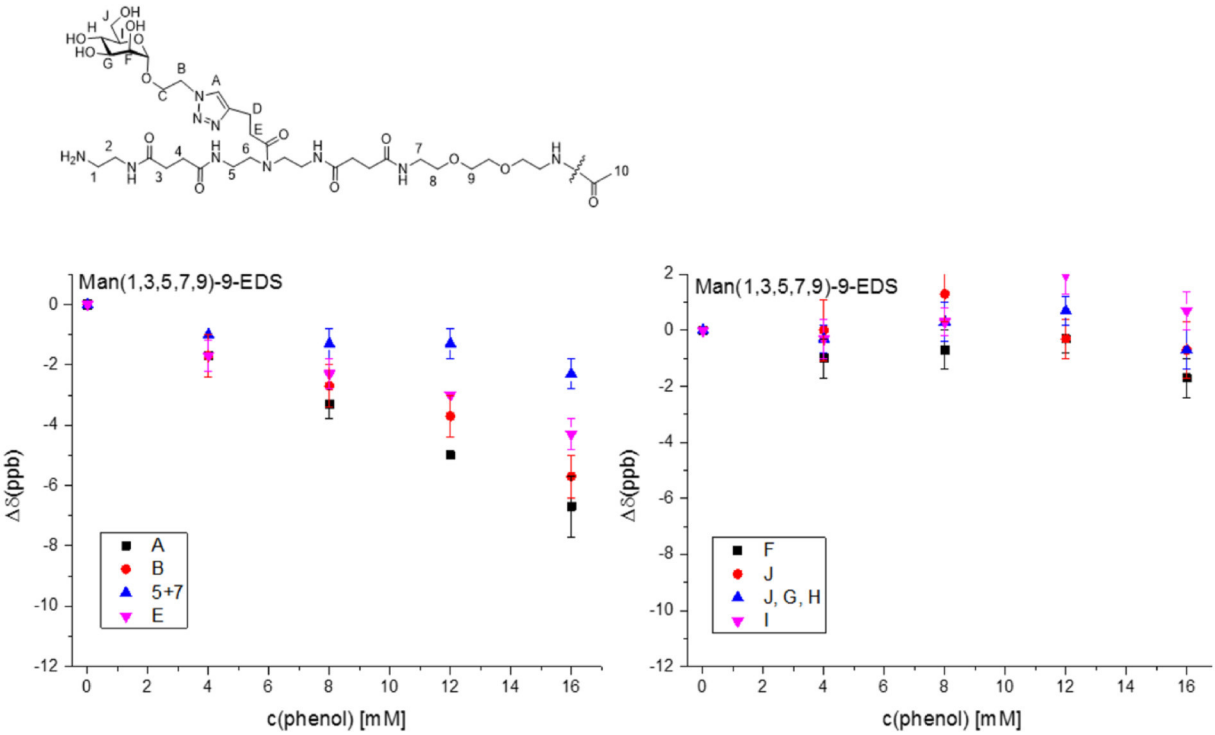

*Appendix 252: Chemical shift change of exemplary glycomacromolecule **5** C-H protons at varying phenol concentrations in D_2O.*

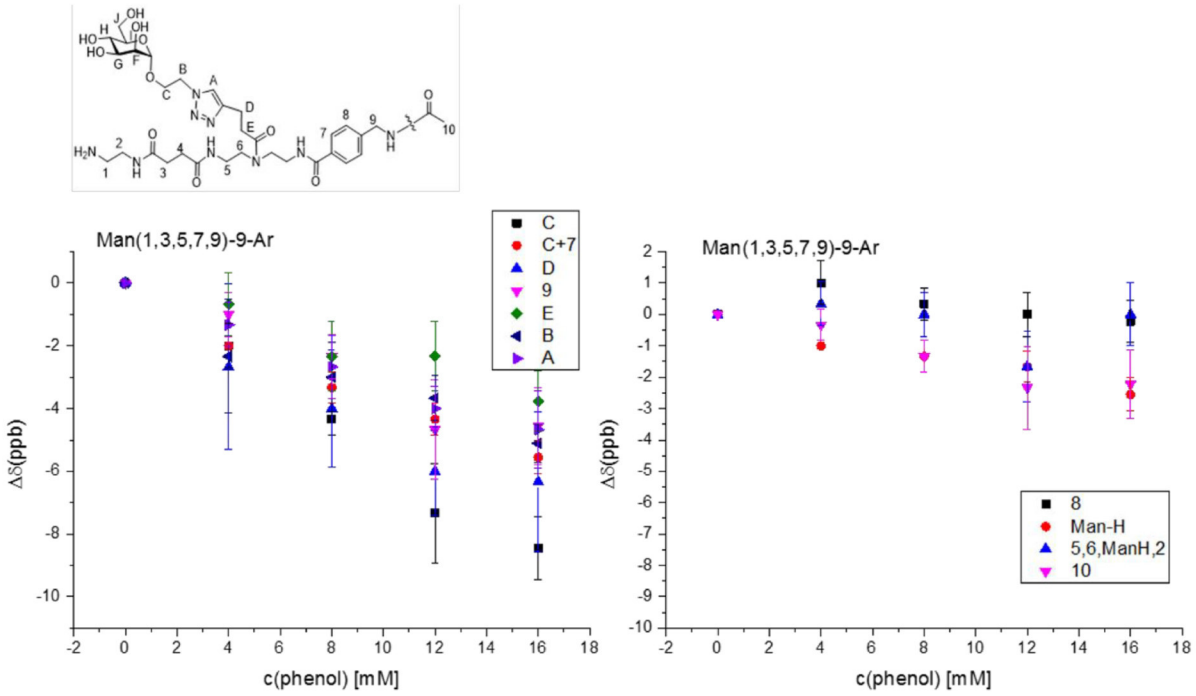

*Appendix 253: Chemical shift change of exemplary glycomacromolecule **5b** C-H protons at varying phenol concentrations in D_2O.*

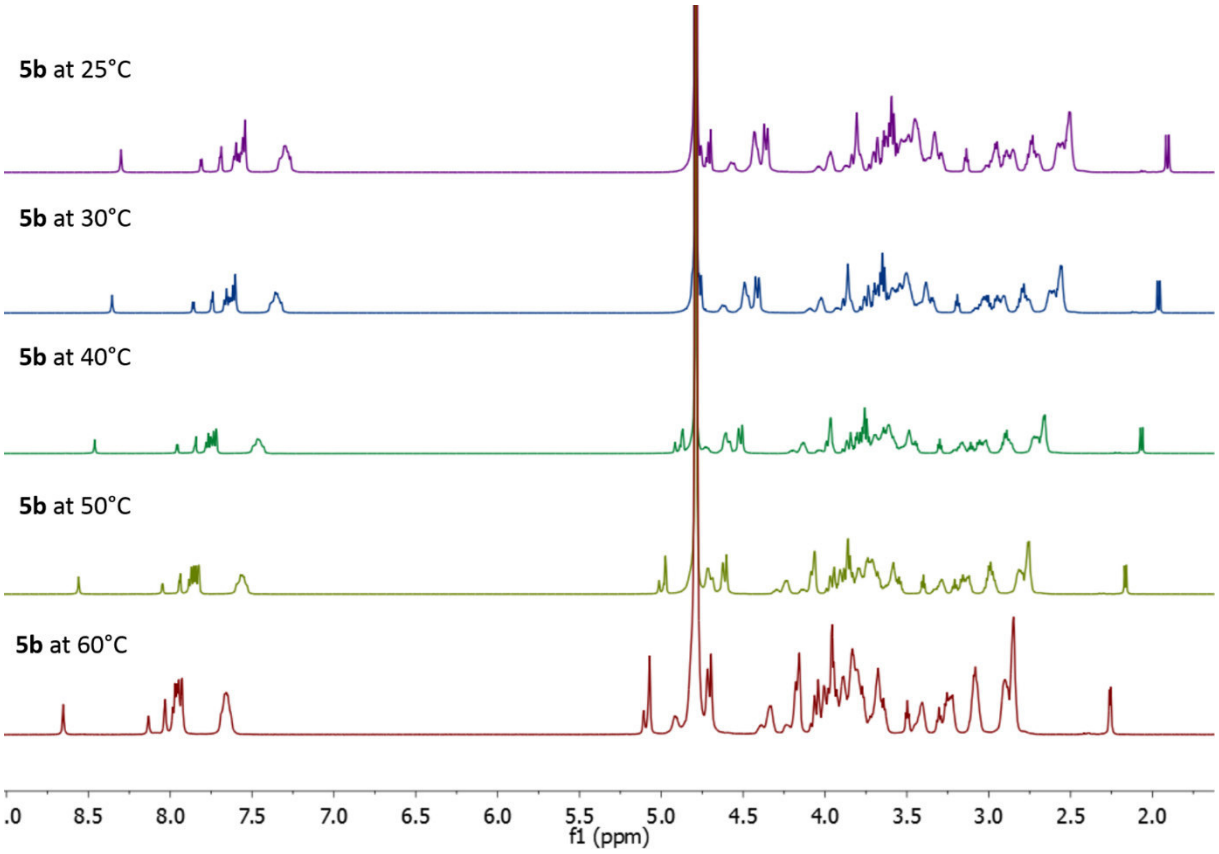

*Appendix 254: ^{1}H-NMR (300 MHz, D_2O) of **5b** at different temperatures.*

6.6.5 Bacterial Inhibition-Adhesion Studies

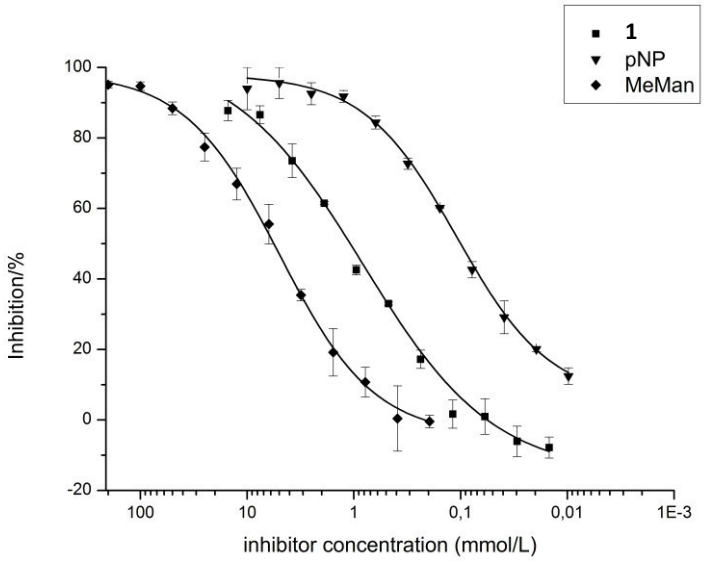

*Appendix 255: Representative inhibition curves obtained in testing of compound **1**. The curves result from one experiment and the depicted standard deviations from triplicate determinations on one plate.*

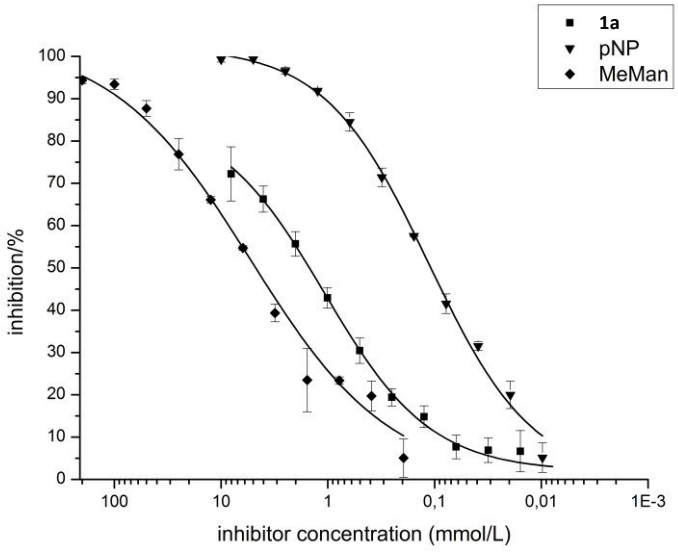

*Appendix 256: Representative inhibition curves obtained in testing of compound **1a**. The curves result from one experiment and the depicted standard deviations from triplicate determinations on one plate.*

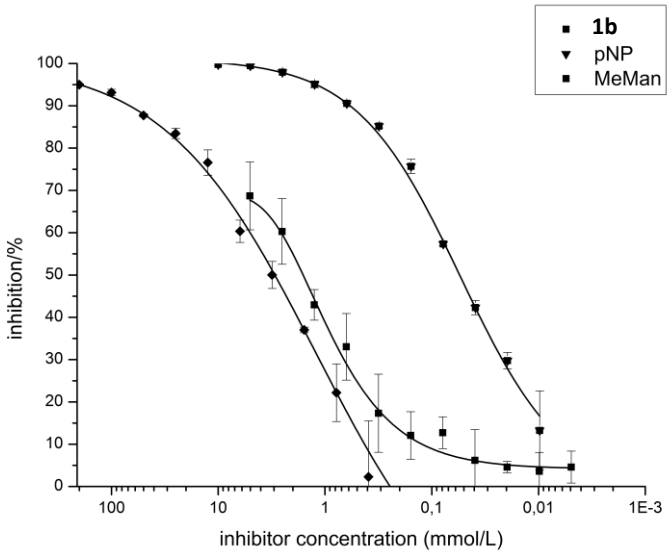

*Appendix 257: Representative inhibition curves obtained in testing of compound **1b**. The curves result from one experiment and the depicted standard deviations from triplicate determinations on one plate.*

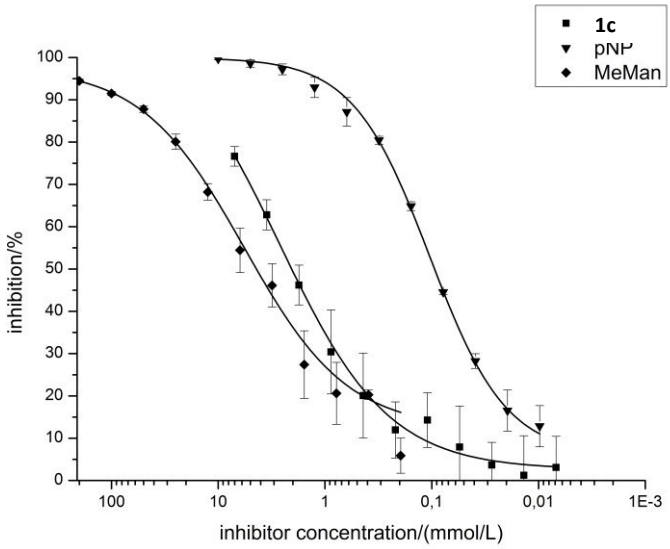

*Appendix 258: Representative inhibition curves obtained in testing of compound **1c**. The curves result from one experiment and the depicted standard deviations from triplicate determinations on one plate.*

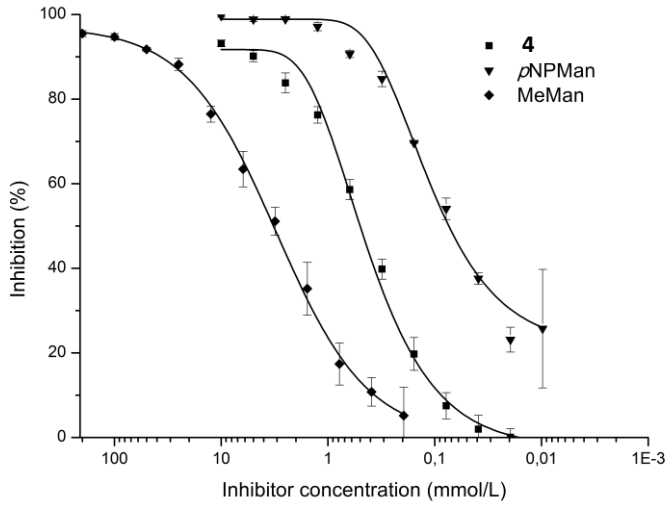

*Appendix 259: Representative inhibition curves obtained in testing of compound **4**. The curves result from one experiment and the depicted standard deviations from triplicate determinations on one plate.*

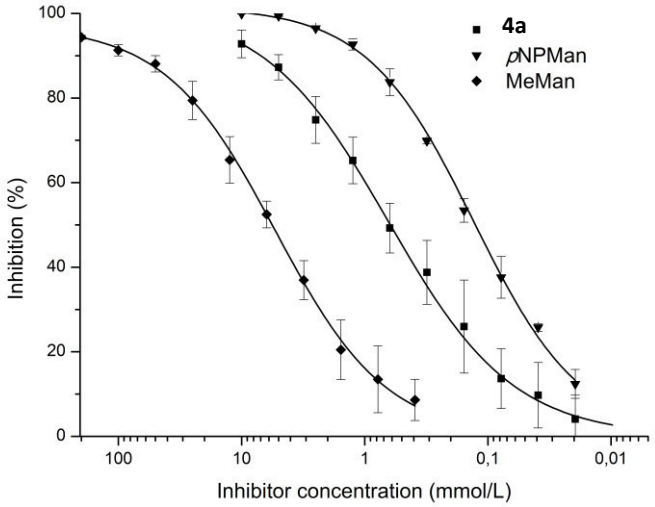

*Appendix 260: Representative inhibition curves obtained in testing of compound **4a**. The curves result from one experiment and the depicted standard deviations from triplicate determinations on one plate.*

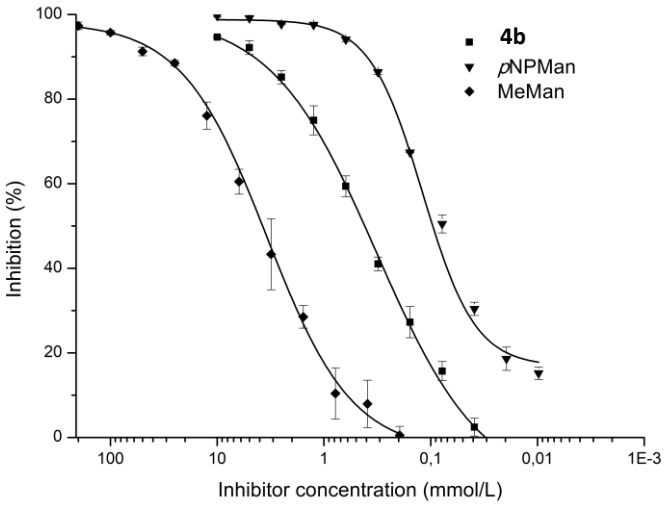

*Appendix 261: Representative inhibition curves obtained in testing of compound **4b**. The curves result from one experiment and the depicted standard deviations from triplicate determinations on one plate.*

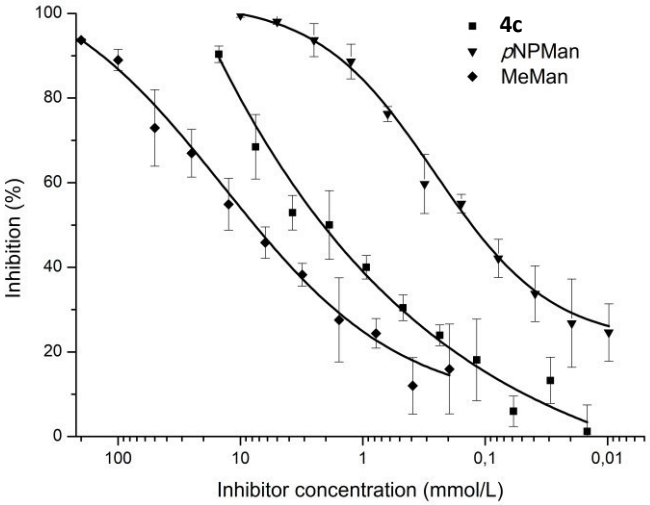

*Appendix 262: Representative inhibition curves obtained in testing of compound **4c**. The curves result from one experiment and the depicted standard deviations from triplicate determinations on one plate.*

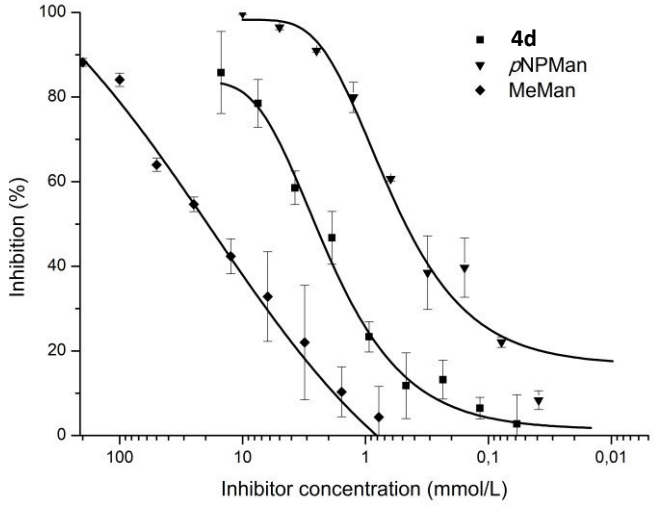

*Appendix 263: Representative inhibition curves obtained in testing of compound **4d**. The curves result from one experiment and the depicted standard deviations from triplicate determinations on one plate.*

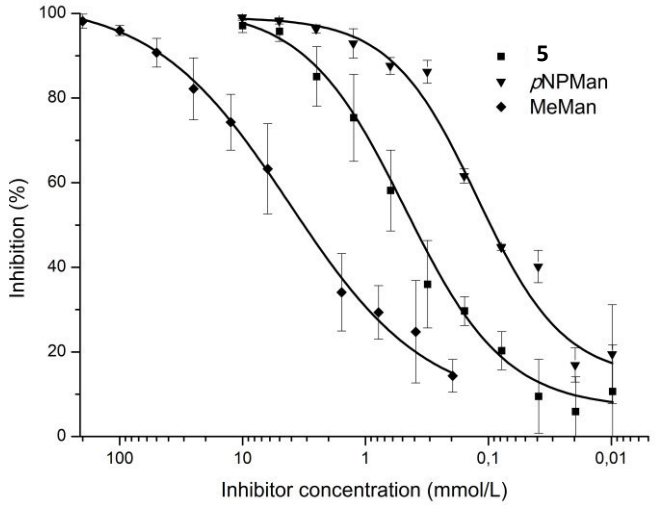

*Appendix 264: Representative inhibition curves obtained in testing of compound **5**. The curves result from one experiment and the depicted standard deviations from triplicate determinations on one plate.*

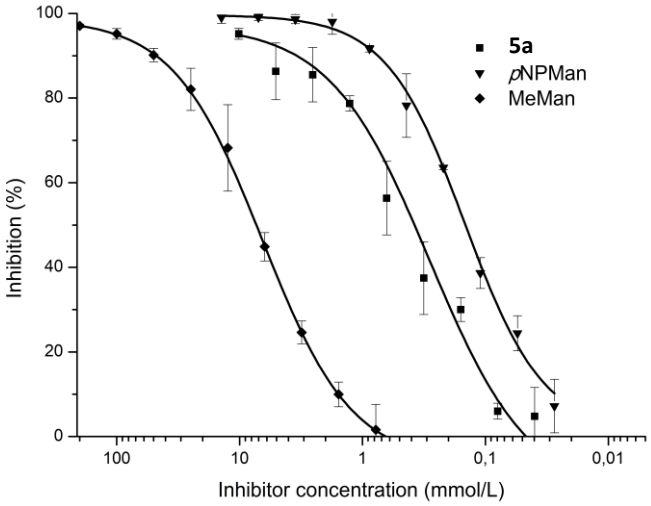

*Appendix 265: Representative inhibition curves obtained in testing of compound **5a**. The curves result from one experiment and the depicted standard deviations from triplicate determinations on one plate.*

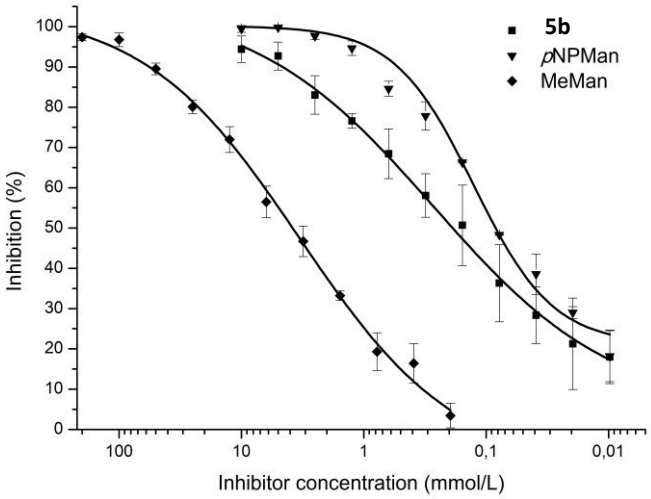

*Appendix 266: Representative inhibition curves obtained in testing of compound **5b**. The curves result from one experiment and the depicted standard deviations from triplicate determinations on one plate.*

6.6.6 Glyco-Gold Nanoparticles

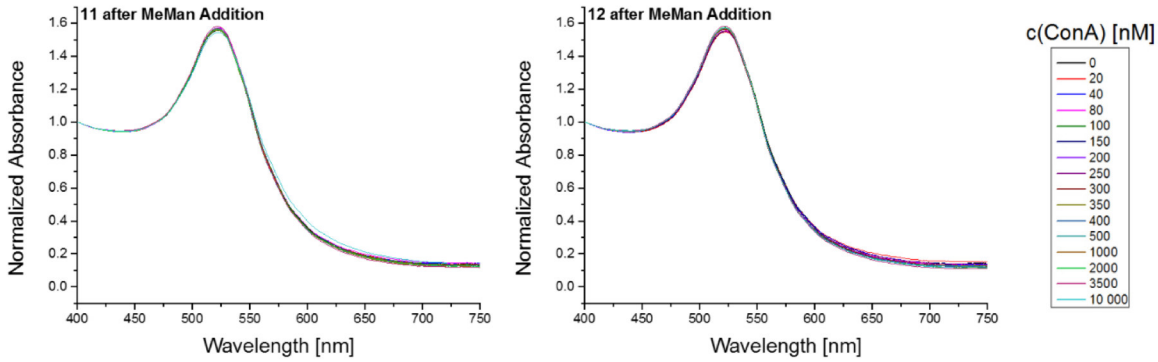

*Appendix 267: UV-Vis absorbance spectra of glyco-AuNPs **11** and **12** at serial dilutions of Con A after addition of MeMan in final concentration of 60 mM.*

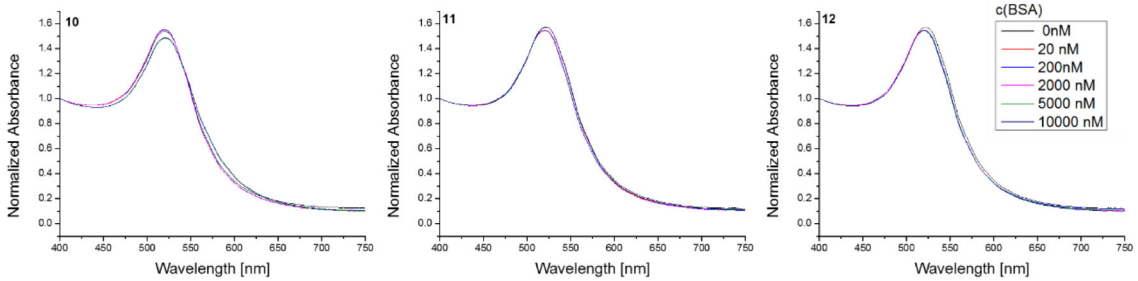

*Appendix 268: UV-Vis absorbance spectra of glyco-AuNPs **10**-**12** at serial dilutions of BSA.*

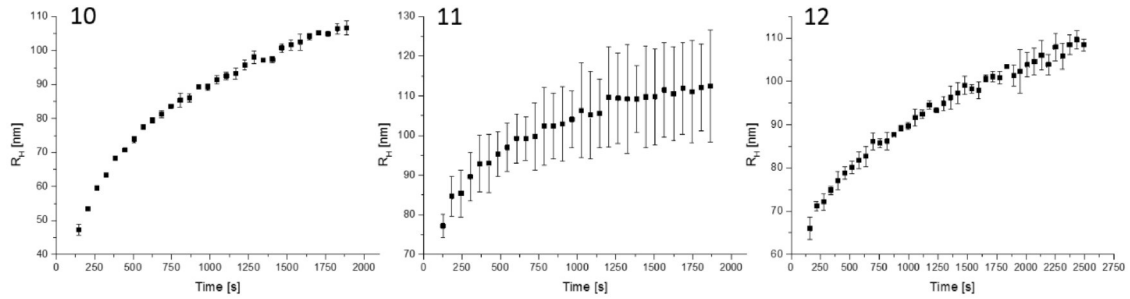

*Appendix 269: Kinetic analysis of glyco-AuNP interaction with Con A by DLS measurements at $K_{D,app}$ concentration of Con A for glyco-AuNP **10**, **11** and **12**. The average of three independent measurements is shown and the error bars correspond to the standard deviation in R_H. The error bars of the time are in the range of the symbol size.*

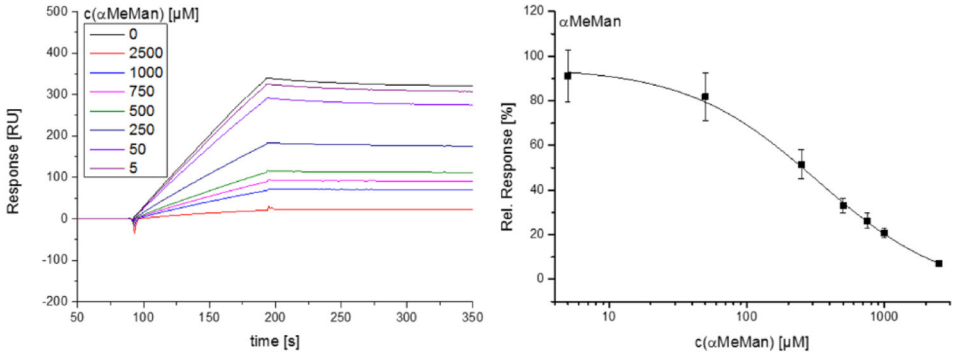

Appendix 270: Exemplary SPR sensorgram for solutions of 100 nM Con A incubated with serial dilutions of MeMan and the resulting IC_{50} curve fitted to Hill1 function.

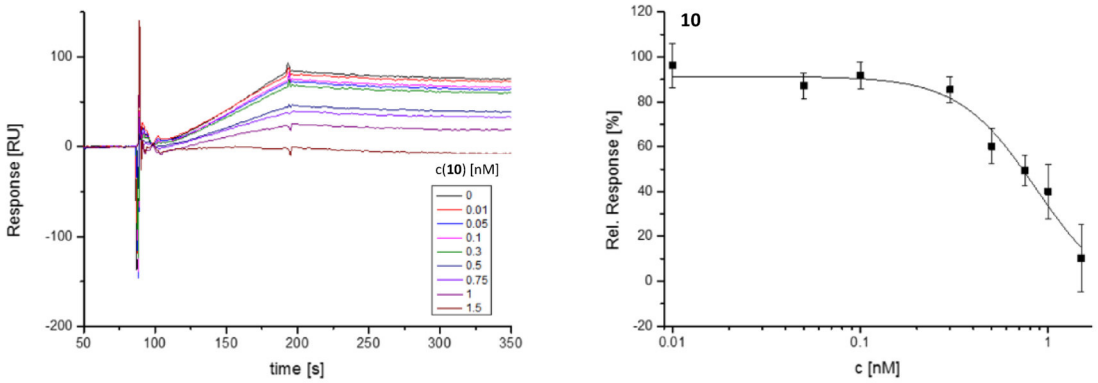

*Appendix 271: Exemplary SPR sensorgram for solutions of 100 nM Con A incubated with serial dilutions of glyco-AuNP **10** and the resulting IC_{50} curve fitted to Hill1 function.*

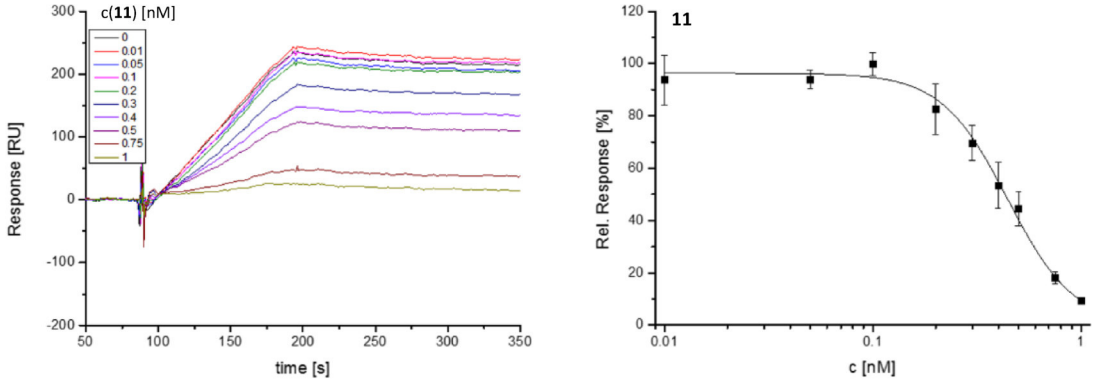

*Appendix 272: Exemplary SPR sensorgram for solutions of 100 nM Con A incubated with serial dilutions of glyco-AuNP **11** and the resulting IC_{50} curve fitted to Hill1 function.*

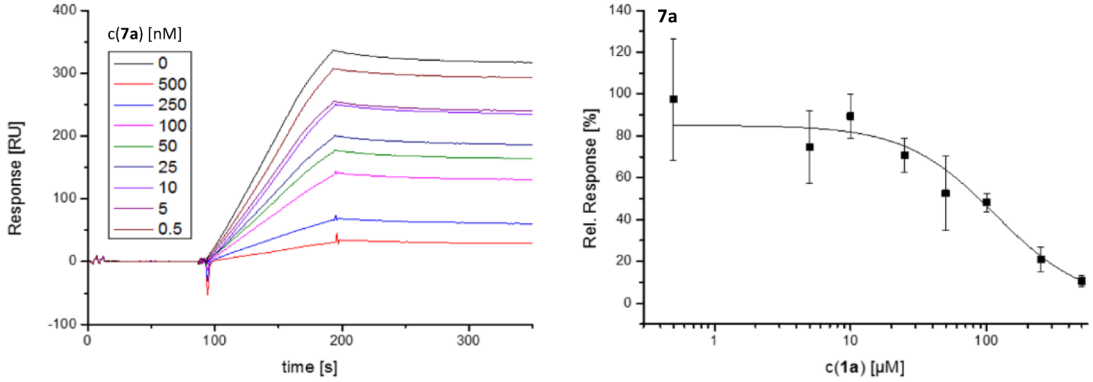

Appendix 273: *Exemplary SPR sensorgram for solutions of 100 nM Con A incubated with serial dilutions of N-ethylmaleimide capped glycomacromolecule* ***7a*** *and the resulting* IC_{50} *curve fitted to Hill1 function.*

6.6.7 Glyco-Gold Nanoparticles for HIP/PAP Targeting

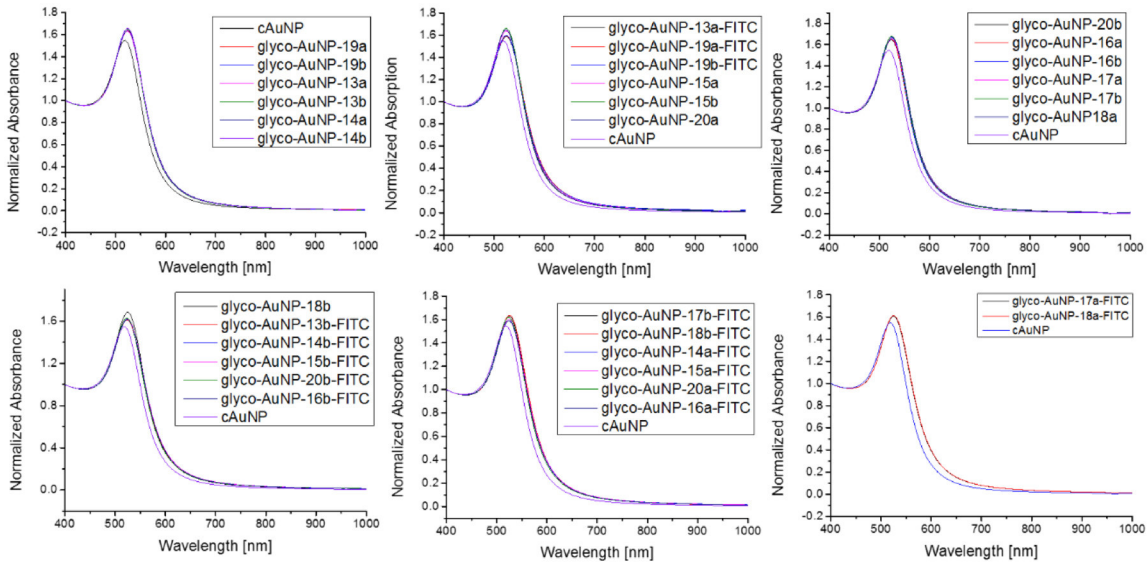

Appendix 274: UV-Vis spectra of cAuNPs in comparison to glyco-AuNPs.

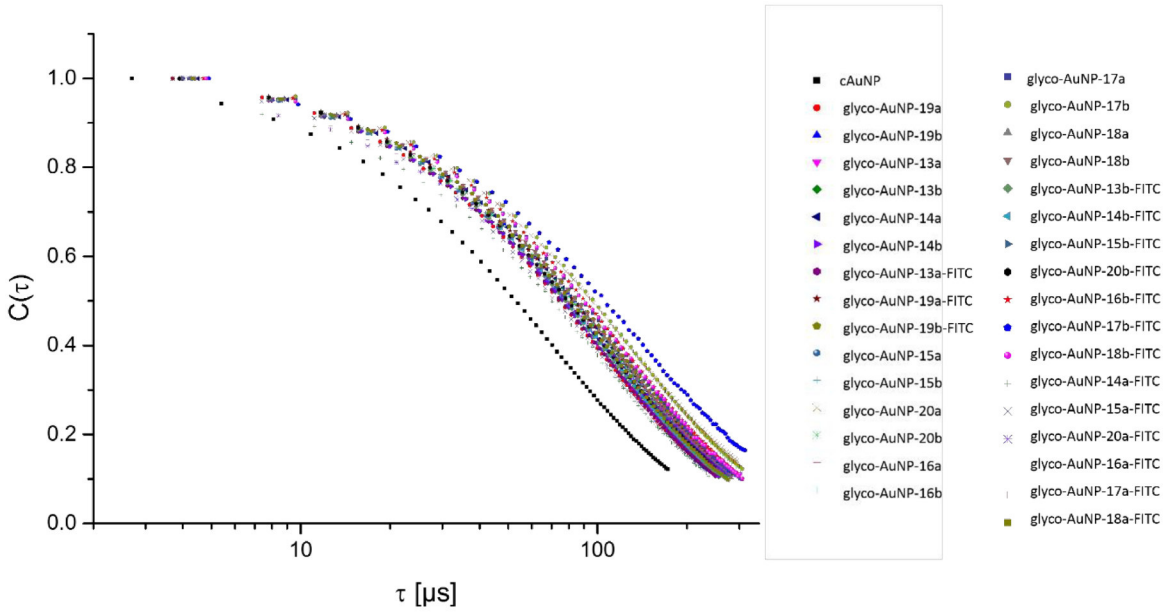

Appendix 275: Autocorrelation function determined by DLS of cAuNPs in comparison to glyco-AuNPs.

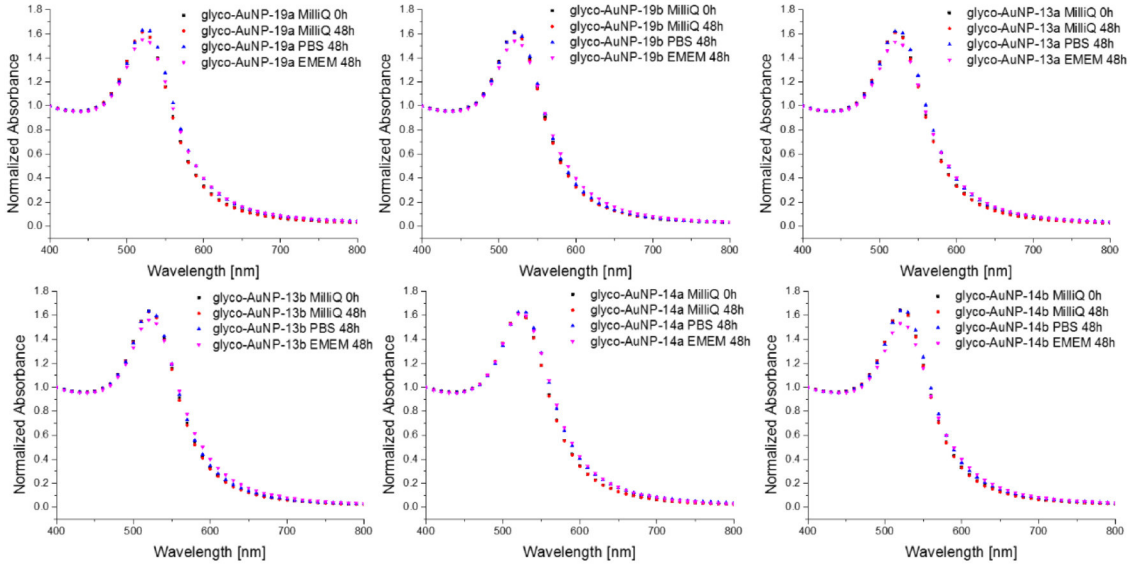

*Appendix 276: UV-Vis absorbance spectra of glyco-AuNP-**19a**, -**19b**, -**13a**, -**13b**, -**14a** and -**14b** in MilliQ water, PBS buffer and EMEM medium after 48 h in comparison to UV-Vis spectrum of the same glyco-AuNP in MilliQ water at time 0.*

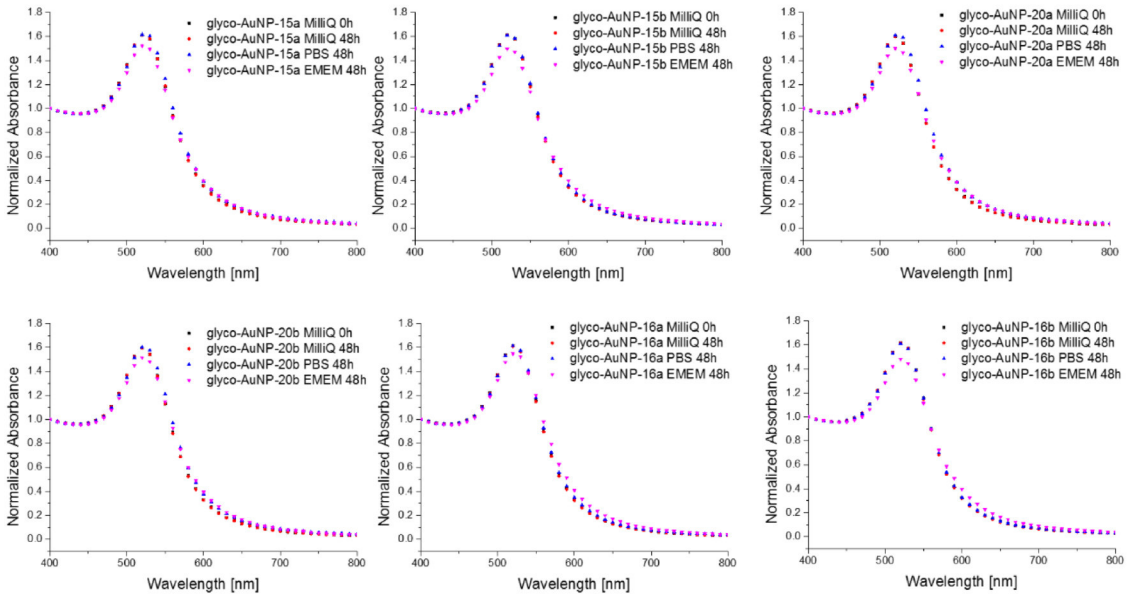

*Appendix 277: UV-Vis absorbance spectra of glyco-AuNP-**15a**, -**15b**, -**20a**, -**20b**, -**16a** and -**16b** in MilliQ water, PBS buffer and EMEM medium after 48 h in comparison to UV-Vis spectrum of the same glyco-AuNP in MilliQ water at time 0.*

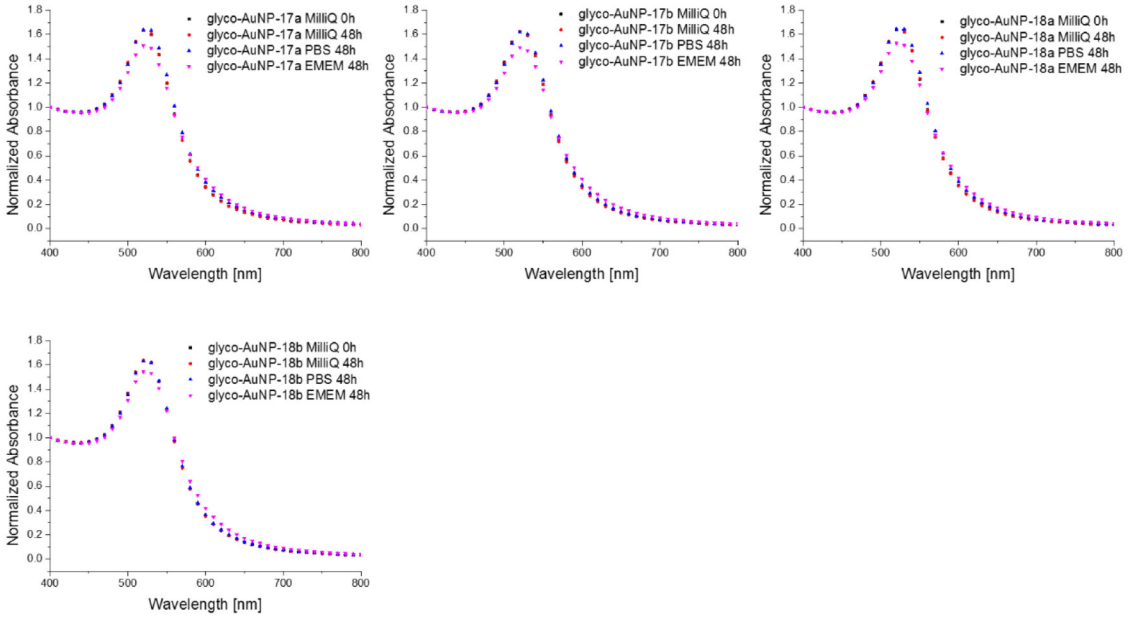

*Appendix 278: UV-Vis absorbance spectra of glyco-AuNP-**17a**, -**17b**, -**18a**, and -**18b** in MilliQ water, PBS buffer and EMEM medium after 48 h in comparison to UV-Vis spectrum of the same glyco-AuNP in MilliQ water at time 0.*

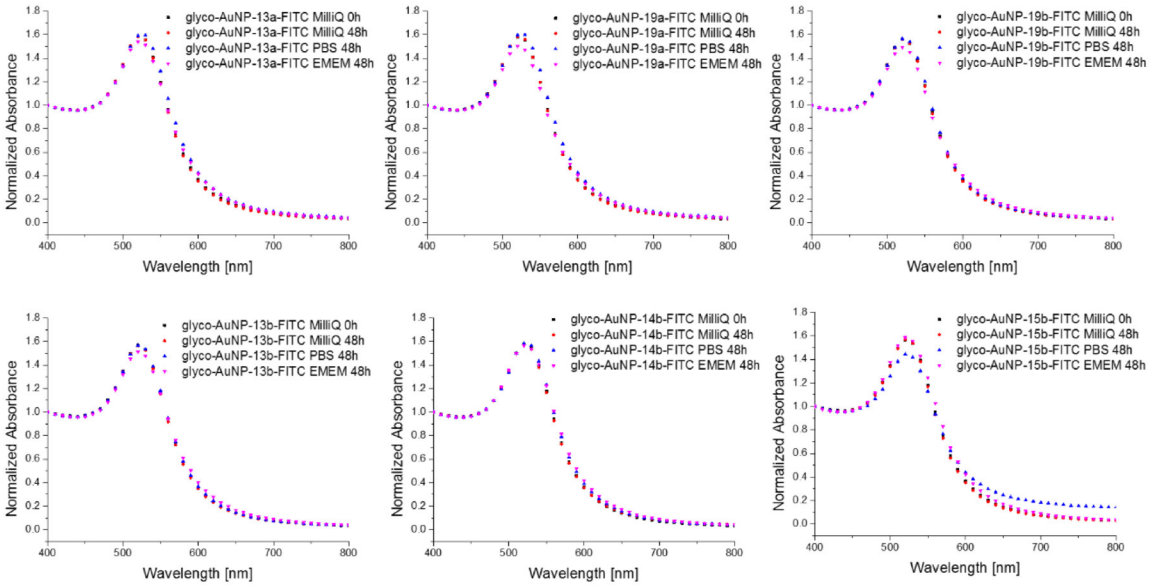

*Appendix 279: UV-Vis absorbance spectra of glyco-AuNP-**13a-**, -**19a-**, -**19b-**, -**13b-**, -**14b-** and -**15b-FITC** in MilliQ water, PBS buffer and EMEM medium after 48 h in comparison to UV-Vis spectrum of the same glyco-AuNP in MilliQ water at time 0.*

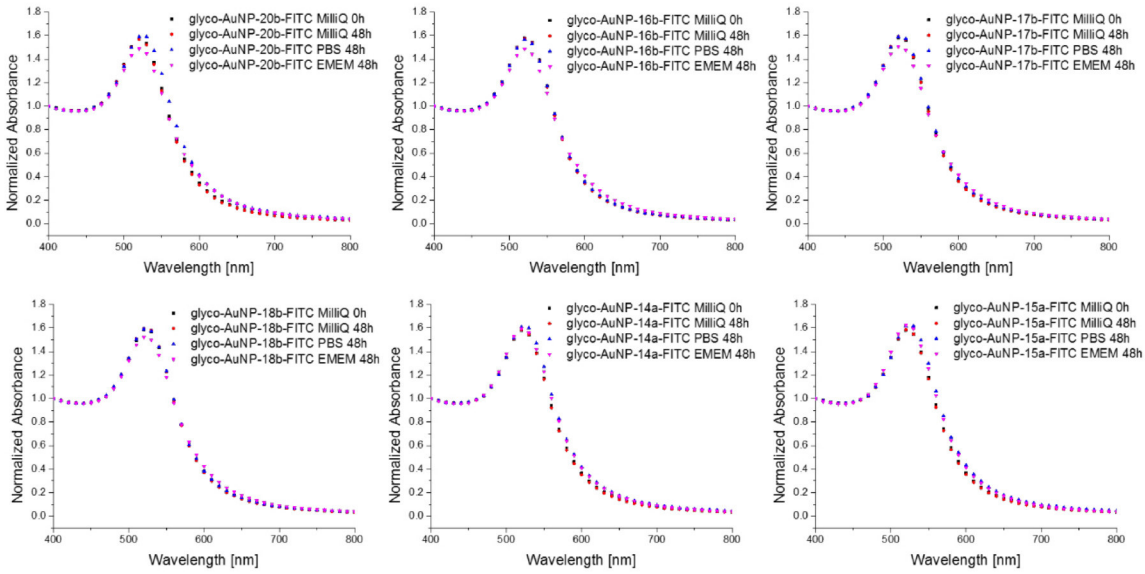

*Appendix 280: UV-Vis absorbance spectra of glyco-AuNP-**20b-**, -**16b-**, -**17b-**, -**18b-**, -**14a-** and **-15a-FITC** in MilliQ water, PBS buffer and EMEM medium after 48 h in comparison to UV-Vis spectrum of the same glyco-AuNP in MilliQ water at time 0.*

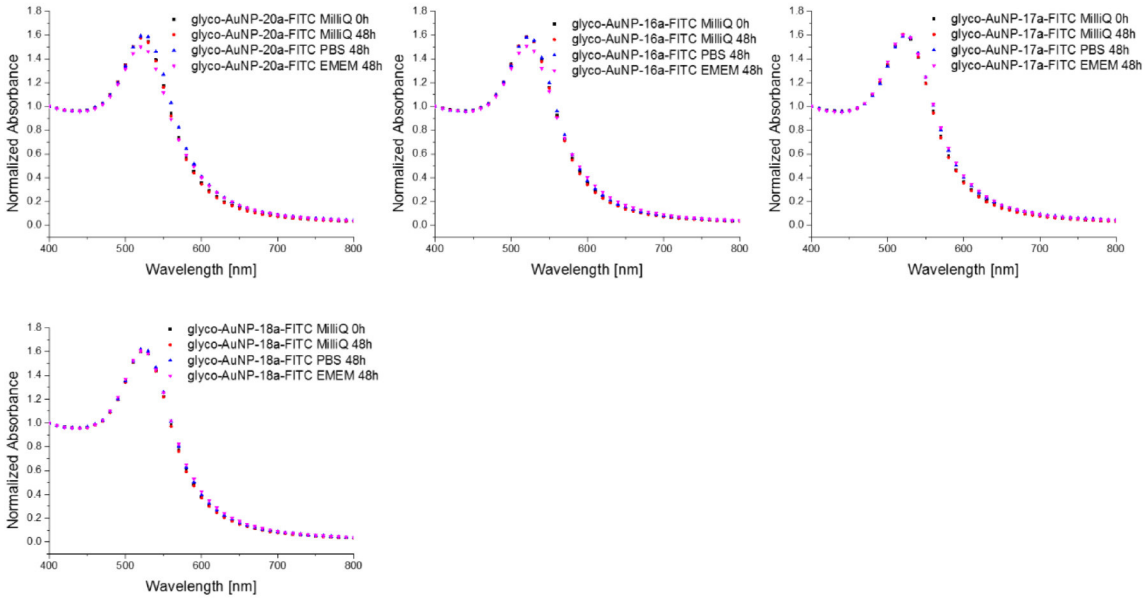

*Appendix 281: UV-Vis absorbance spectra of glyco-AuNP-**20a-**, -**16a-**, -**17a-**, and **-18a-FITC** in MilliQ water, PBS buffer and EMEM medium after 48 h in comparison to UV-Vis spectrum of the same glyco-AuNP in MilliQ water at time 0.*

6.6.8 Dynamic Combinatorial Libraries

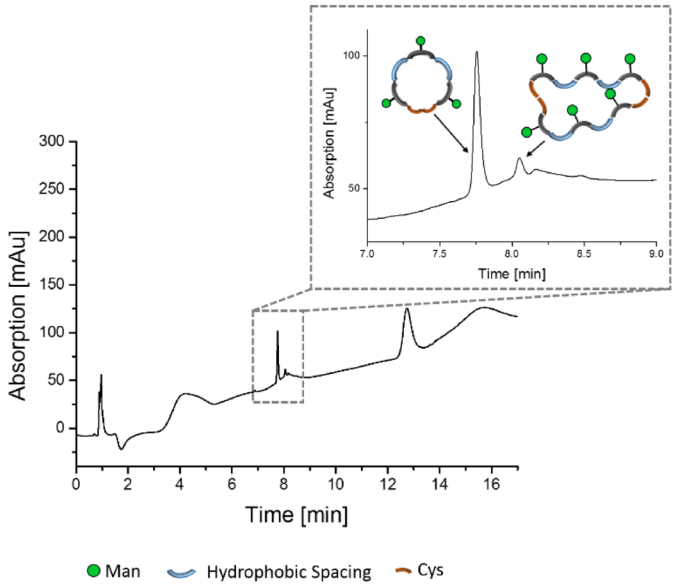

*Appendix 282: Exemplary RP-HPLC chromatogram (95/5 H_2O/MeCN with 0.1% formic acid (A) and 5/95 H_2O/MeCN with 0.1% formic acid (B); 100% A to 5% A in 17 min) of compound **24** at 10 mM concentration and pH 8 after two weeks of equilibration under atmospheric oxygen. Broad peaks at time ranges from 4 to 5 and 12 to 13 minutes belong to the blank. The inset shows the magnification of the chromatogram area of interest.*

7. References

[1] N. R. Krishnaswamy, *Resonance* **2011**, *16*, 620-639.

[2] D. B. Werz, P. H. Seeberger, *Chem. Eur. J.* **2005**, *11*, 3194-3206.

[3] H. S. Bennett, J. Histochem. Cytochem. 1963, 11, 14-23.

[4] B. Ernst, J. L. Magnani, *Nat. Rev. Drug Discov.* **2009**, *8*, 661-667.

[5] A. Imberty, A. Varrot, *Curr. Opin. Struct. Biol.* **2008**, *18*, 567-576.

[6] C. R. Bertozzi, L. L. Kiessling, *Science* **2001**, *291*, 2357-2364.

[7] G. Opdenakker, P. M. Rudd, C. P. Ponting, R. A. Dwek, *FASEB J.* **1993**, *7*, 1330-1337.

[8] A. Kobata*, Acc. Chem. Res.* **1993**, *26*, 319-324.

[9] E. Köttgen, W. Reutter, R. Tauber, *Med. Klin.* **2003**, *98*, 717-738.

[10] R. A. Dwek, *Chem. Rev.* **1996**, *96*, 683-720.

[11] M. H. Caruthers, *Science* **1985**, *230*, 281–285.

[12] M. H. Caruthers, *Acc. Chem. Res.* **1991**, *24*, 278–284.

[13] E. Atherton, R. C. Sheppard, Solid-Phase Peptide Synthesis: A Practical Approach, Oxford University Press, Oxford, 1989.

[14] S. J. Danishefsky, M. T. Bilodeau, *Angew. Chem. Int. Ed. Engl.* **1996**, *35*, 1380–1419.

[15] C.-H. Wong, Pure Appl. Chem. 1995, 67, 1609–1616.

[16] O. J. Plante, E. R. Palmacci, P. H. Seeberger, *Science* **2001**, *291*, 1523–1527.

[17] K.-A. Karlsson, *TiPS* **1991**, *12*, 265-272.

[18] D. D. Leonidas, B. L. Elbert, Z. Zhou, H. Leffler, S. J. Ackerman, K. R. Acharya, *Structure* **1995**, *3*, 1379-1393.

[19] M. Ambrosi, N. R. Cameron, B. G. Davis, *Org. Biomol. Chem.* **2005**, *3*, 1593-1608.

[20] D. C. Kilpatrick, *Biochim. Biophys. Acta* **2002**, *1572*, 187-197.

[21] S. Flexner, H. Noguchi, *J. Exp. Med.* **1902**, *6*, 277– 301.

[22] N. Sharon, H. Lis, *Glycobiology* **2004**, *14*, 53R-62R.

[23] W. J. Peumans, E. J. M. van Damme, *Plant. Physiol.* **1995**, *109*, 347-352.

[24] J. B. Sumner, *J. Biol. Chem.* **1919**, *37*, 137-142.

[25] J. B. Sumner and S. F. Howell, *J. Bacteriol.* **1936**, 32, 227-237.

[26] W. T. J. Morgan, W. M. Watkins, *Br. J. Exp. Pathol.* **1953**, *34*, 94-103.

[27] W. C. Boyd, E. Shapleigh, *Science* **1954**, *119*, 419.

[28] P. C. Nowell, *Cancer Res.* **1960**, *20*, 462-466.

[29] J. C. Aub, C. Tieslau, A. Lankester, *Proc. Nat. Acad. Sci.* **1963**, *50*, 613-618.

[30] J. C. Aub, B. H. Sanford, M. N. Core, *Proc. Nat. Acad. Sci.* **1965**, *54*, 396-399.

[31] G. M. Edelman, B. A. Cunningham, G. N. Reeke, J. W. Becker, M. J. Waxdal, J. L. Wang, *Proc. Natl. Acad. Sci. USA* **1972**, *69*, 2580– 2584.

[32] K. D. Hardman, C. F. Ainsworth, *Biochemistry* **1972**, *11*, 4910– 4919.

[33] R. J. Stockert, A. G. Morell, I. H.Scheinberg, *Science* **1974**, 186, 365–366.

[34] K. Drickamer, *J. Biol. Chem.* **1988**, *263*, 9557-9560.

[35] M. Inbar and L. Sachs, *Nature* **1969**, *223*, 710-712.

[36] R. Loris*, Biochim. Biophys. Acta* **2002**, *1572*, 198-208.

[37] R. Loris, T. Hamelryck, J. Bouckaert, L. Wyns, *Biochim. Biophys. Acta* **1998**, *1383*, 9 – 36.

[38] R. J. Pieters, *Org. Biomol. Chem.* **2009**, *7*, 2013-2025.

[39] A. M. Hirsch, *Curr. Opin. Plant Biol.* **1999**, *2*, 320-326.

[40] M.J. Chrispeels, N.V. Raikhel, *Plant Cell* **1991**, 3, 1-9.

[41] W. Weis, R. Kahn, R. Fourme, K. Drickamer, W. A. Hendrickson, *Science* **1991**, *254*, 1608-1615.

[42] S. Yao, Y. Luo, Z. Zhang, G. Hu, Z. Zhu, F. Li, *Oncotarget* **2017**, *8*, 75162-75173.

[43] J. L. Iovanna, J.-C. Dagorn, *Biochim. Biophys. Acta* **2005**, *1723*, 8-18.

[44] C. Lasserre, M.-T. Simon, H. Ishikawa, S. Diriong, V. C. Nguyen, L. Christa, P. Vernier, C. Brechot, *Eur. J. Biochem.* **1994**, *224*, 29-38.

[45] R.-Y. Yang, G. A. Rabinovich, F.-T. Liu, *Expert. Rev. Mol. Med.* **2008**, *10*, e17.

[46] H. Leffler, S. Carlsson, M. Hedlund, Y. Qian, F. Poirier, *Glycoconj. J.* **2004**, *19*, 433-440.

[47] S. Cecioni, A. Imberty, S. Vidal, *Chem. Rev.* **2015**, *115*, 525-561.

[48] J. J. Martinez, M. A. Mulvey, J. D. Schilling, J. S. Pinkner, S. J. Hultgren, *EMBO J.* **2000**, *19*, 2803-2812.

[49] S. Knight, J. Bouckaert, *Top. Curr. Chem.* **2009**, *288*, 67-107.

[50] C. S. Hung, J. Bouckaert, D. Hung, J. Pinkner, C. Widberg, A. DeFusco, C. G. Auguste, R. Strouse, S. Langermann, G. Waksman, S. J. Hultgren, *Mol. Microbiol.* **2002**, *44*, 903-915.

[51] N. Sharon, *Biochim. Biophys. Acta* **2006**, *1760*, 527-537.

[52] M. G. Blango, M. A. Mulvey, *Antimicrob. Agents Chemother.* **2010**, *54*, 1855-1863.

[53] I. Ofek, D. L. Hasty, N. Sharon, *FEMS Immunol. Med. Microbiol.* **2003**, *38*, 181-190.

[54] L. L. Kiessling, T. Young, T. D. Gruber, K. H. Mortell, *Glycoscience*, B. Fraser-Reid, K. Tatsuta, J. Thiem (eds), Springer Verlag, Berlin, **2008**, 2483-2523.

[55] R. Loris, P. P. Stas, L. Wyns, *J. Biol. Chem.* **1994**, *269*, 26722-26733.

[56] W. I. Weis, K. Drickamer, *Annu. Rev. Biochem.* **1996**, *65*, 441-473.

[57] H.-J. Gabius, S. André, J. Jiménez-Barbero, A. Romero, D. Solís, *Trends Biochem. Sci.* **2011**, *36*, 298-313.

[58] E. J. Toone, *Curr. Opin. Struct. Biol.* **1994**, *4*, 719-728.

[59] B. G. Davis, *J. Chem. Soc., Perkin Trans. 1*, **1999**, 3215-3237.

[60] N. K. Vyas, *Curr. Opin. Struct. Biol.* **1991**, *1*, 732-740.

[61] R. D. Brown, C. F. Brewer, S. H. Koenig, *Biochemistry* **1977**, 16, 3883-3896.

[62] R. U. Lemieux, *Acc. Chem. Res.* **1996**, *29*, 373-380.

[63] M. C. Chervenak, E. J. Toone, *J. Am. Chem. Soc.* **1994**, *116*, 10533-10539.

[64] C. B. Carlson, P. Mowery, R. M. Owen, E. C. Dykhuizen, L. L. Kiessling, *ACS Chem. Biol.* **2007**, *2*, 119-127.

[65] R. Alon, D. A. Hammer, T. A. Springer, *Nature* **1995**, *374*, 539-542.

[66] C. W. Cairo, J. E. Gestwicki, M. Kanai, L. L. Kiessling, *J. Am. Chem. Soc.* **2002**, *124*, 1615-1619.

[67] J. J. Lundquist, E. J. Toone, *Chem. Rev.* **2002**, *102*, 555–578.

[68] G. Ashwell, A. G. Morell, *Adv. Enzymol.* **1974**, *41*, 99-128.

[69] R. T. Lee, Y. C. Lee, *Glycoconj. J.* **2000**, *17*, 543-551.

[70] G. Schwarzenbach, *Helv. Chim. Acta* **1952**, *35*, 2344-2359.

[71] M. I. Page, W. P. Jencks, *Proc. Nat. Acad. Sci.* **1971**, *68*, 1678-1683.

[72] M. Mammen, S.-K- Choi, G. M. Whitesides, *Angew. Chem. Int. Ed.* **1998**, *37*, 2754-2794.

[73] M. Mammen, G. Dahmann, G. M. Whitesides, *J. Med. Chem.* **1995**, *38*, 4179-4190.

[74] P. Sears, C.-H. Wong, *Angew. Chem. Int. Ed.* **1999**, *38*, 2300-2324.

[75] M. Okada, *Prog. Polym. Sci.* **2001**, *26*, 67-104.

[76] V. Ladmiral, E. Melia, D. M. Haddleton, *Eur. Polym. J.* **2004**, *40*, 431-449.

[77] B. Voit, D. Appelhans, *Macromol. Chem. Phys.* **2010**, *211*, 727-735.

[78] J.-F. Lutz, *Polym. Chem.* **2010**, *1*, 55-62.

[79] L. L. Kiessling, J. E. Gestwicki, L. E. Strong, *Angew. Chem. Int. Ed.* **2006**, *45*, 2348-2368.

[80] S. Toraskar, M. Gade, S. Sangabathuni, H. V. Thulasiram, R. Kikkeri, *ChemMedChem* **2017**, *12*, 1116-1124.

[81] E. Fischer, E Fourneau, Über einige Derivale des Glykolls, In: Untersuchungen über Aminosäuren, Polypeptide und Proteine, **1906**, Springer, Berlin, Heidelberg, 279-289.

[82] M. Bergmann, L. Zervas, *Eur. J. Inorg. Chem.* **1932**, *65*, 1192-1201

[83] R. B. Merrifield, *Angew. Chem. Int. Ed. Engl.* **1985**, *24*, 799-892.

[84] R. B. Merrifield*, J. Am. Chem. Soc.* **1963**, *85*, 2149-2154.

[85] J. A. Moss, *Curr. Protoc. Protein Sci.* **2005**, *40*, 18.7.1-18.7.19.

[86] L. Carpino, *Acc. Chem. Res.* **1987**, *20*, 401-407.

[87] B. F. Lundt, N. L. Johansen, A. Vølund, J. Markussen, *Int. J. Peptide Protein Res.* **1978**, *12*, 258-268.

[88] B. M. Trost, T. J. Fullerton, *J. Am. Chem. Soc.* **1973**, *95*, 292-294.

[89] B. M. Trost, P. E. Strege, *J. Am. Chem. Soc.* **1977**, *99*, 1649-1651.

[90] C. A. G. N. Montalbetti, V. Falque, *Tetrahedron* **2005**, *61*, 10827-10852.

[91] B. Castro, J. R. Dormoy, G. Evin, C. Selve, *Tetrahedron Lett.* **1975**, *14*, 1219-1222.

[92] R. L. Letsinger, V. Mahadevan, *J. Am. Chem. Soc.* **1965**, *87*, 3526-3527.

[93] J. M. Frechet, C. Schuerch, *J. Am. Chem. Soc.* **1971**, *93*, 492-496.

[94] L. Hartmann, E. Krause, M. Antonietti, H.G. Börner, *Biomacromolecules* **2006**, *7*, 1239-1244.

[95] D. Ponader, F. Wojcik, F. Beceren-Braun, J. Dernedde, L. Hartmann, *Biomacromolecules* **2012**, *13*, 1845-1852.

[96] F. Wojcik, S. Mosca, L. Hartmann, *J. Org. Chem.* **2012**, *77*, 4226-4234.

[97] F. Wojcik, A. G. O´Brien, S. Götze, P. H. Seeberger, L. Hartmann, *Chem. Eur. J.* **2013**, *19*, 3090-3098.

[98] D. Ponader, S. Igde, M. Wehle, K. Märker, M. Santer, D. Bléger, L. Hartmann, *Beilstein J. Org. Chem.* **2014**, *10*, 1603-1612.

[99] T. Freichel, S. Eierhoff, N. L. Snyder, L. Hartmann, *J. Org. Chem.* **2017**, *82*, 9400-9409.

[100] S. Boden, K. G. Wagner, M. Karg, L. Hartmann, *Polymers* **2017**, *9*, 716.

[101] M. Baier, M. Giesler, L. Hartmann, *Chem Eur. J.* **2018**, *24*, 1619-1630.

[102] C. Gerke, F. Jacobi, L. E. Goodwin, F. pieper, S. Schmidt, L. Hartmann, *Macromolecules* **2018**, *51*, 5608-5619.

[103] K. S. Bücher, P. B. Konietzny, N. L. Snyder, L. Hartmann, *Chem. Eur. J.* **2019**, *25*, 1-10.

[104] D. Ponader, *Synthesis of Sequence-defined Glycooligomers for Studying Multivalent Interactions*, PhD Thesis, Freie Universität Berlin, **2014**.

[105] R. Huisgen, G. Szeimies, L. Möbius, *Chem. Ber.* **1967**, *100*, 2494-2507.

[106] V. D. Bock, H. Hiemstra, J. H. van Maarseveen, *Eur. J. Org. Chem.* **2006**, *1*, 51-68.

[107] H. C. Kolb, M. G. Finn, K. B. Sharpless, *Angew. Chem.* **2001**, *113*, 2056-2075.

[108] A. Munoz-Bonilla, V. Brdegé, O. León, R. Cuervo-Rodríguez, M.Sánchez-Chaves, *Eur. Polym. J.* **2012**, *48*, 963-973.

[109] Y. Chen, M. S. Lord, A. Piloni, M. H. Stenzel, *Macromol.* **2015**, *48*, 346-357.

[110] O. León, V. Bordegé, A. Munoz-Bonilla, M. Sánchez-Chaves, M. Fernández-García, *J. Polym. Sci. A Polym. Chem.* **2010**, *48*, 3623-3631.

[111] A. Patel, T. K. Lindhorst, *Carbohydr. Res.* **2006**, *341*, 1657-1668.

[112] W. Jiang, K. Nawosinski, N. L. Löw, E. V.Dzyuba, F. Klautzsch, A. Schäfer, J. Huuskonen, K. Rissanen, C. A. Schalley, *J. Am. Chem. Soc.* **2012**, *134*, 1860-1868.

[113] X.-L. Meng, Y. Fang, L.-S. Wan, X.-J. Huang, Z.-K. Xu, *Langmuir* **2012**, *28*, 13616-13623.

[114] J. E. Gestwicki, C. W. Cairo, L. E. Strong, K. A. Oetjen, L. L. Kiessling, *J. Am. Chem. Soc*. **2002**, *124*, 14922-14933.

[115] X. Yan, A. Sivignon, N. Barnich, S. G. Gouin, J. Bouckaert, E. Fleury, J. Bernard, *Polym. Chem.* **2016**, *7*, 2674-2683.

[116] M. W. Jones, L. Otten, S.-J. Richards, R. Lowery, D. J. Philips, D. M. Haddleton, M. I. Gibson, *Chem. Sci.* **2014**, *5*, 1611-1616.

[117] A. Munoz-Bonilla, O. León, V. Bordegé, M. Sánchez-Chaves, M. Fernández- García, *J. Polym. Sci. A Polym. Chem.* **2013**, *51*, 1337-1347.

[118] T. Hasegawa, S. Kondoh, K. Matsuura, K. Kobayashi, *Macromol.* **1999**, *32*, 6595-6603.

[119] M. C. Schuster, K. H. Mortell, A. D. Hegeman, l. L. Kiessling, *J. Mol. Catal. A Chem.* **1997**, *116*, 209-216.

[120] S. Igde, S. Röblitz, A. Müller, K. Kolbe, S. Boden, C. Fessele, T. K. Lindhorst, M. Weber, L. Hartmann, Macromol. Biosci. 2017, 17, 1700198.

[121] C. Gerke, M. F. Ebbesen, D. Jansen, S. Boden, T. Freichel, L. Hartmann, *Biomacromolecules* **2017**, *18*, 787-796.

[122] R. D. Poretz, I. J. Goldstein, *Arch. Biochem. Biophys.* **1968**, *125*, 1034-1036.

[123] D. Loganathan, S. E. Osborne, G. D. Glick, I. J. Goldstein, *Arch. Biochem. Biophys.* **1992**, *299*, 268-274.

[124] R. D. Poretz, I. J. Goldstein, *Biochem. Pharmacol.* **1971**, *20*, 2727-2739.

[125] G. M. Edelman, J. L. Wang, *J. Biol. Chem.* **1978**, *253*, 3016-3022.

[126] G. R. Munske, H. Krakauer, J. A. Magnuson, *Arch. Biochem. Biophys.* **1984**, *233*, 582-587.

[127] K. T. Welch, T. A. Turner, C. E. Preast, *Bioorg. Med. Chem. Lett.* **2008**, *18*, 6573-6575.

[128] S. S. Komath, M. Kavitha, M.-J. Swamy, *Org. Biomol. Chem.* **2006**, *4*, 973-988.

[129] D. Pagé, D. Zanini, R. Roy, *Bioorg. Med. Chem.* **1996**, *4*, 1949-1961.

[130] W. Hayes, H. M. Osborn, S. D. Osborne, R. A. Rastall, B. Romagnoli, *Tetrahedron* **2003**, *59*, 7983-7996.

[131] M. F. Ebbesen, C. Gerke, P. Hartwig, L. Hartmann, *Polym. Chem.* **2016**, *7*, 7086-7093.

[132] S. Boden, *Linear and Cyclic Hydrophobic Glycomacromolecules Based on an Octyl Spacer Building Block*, Master Thesis, Heinrich-Heine-Universität Düsseldorf, **2015**.

[133] C.-L. Shen, M. C. Fitzgerald, R. M. Murphy, *Biophys. J.* **1994**, *67*, 1238-1246

[134] A. Ahmad, K. P. Madhusudanan, V. Bhakuni, *Biochim. Biophys. Acta* **2000**, *1480*, 201-210.

[135] J. Cornish, K. E. Callon, C. Q.-X. Lin, C. L. Xiao, T. B. Mulvey, G. J. S. Cooper, I. R. Freid, *Am. J. Physiol. Endocrinol. Metab.* **1999**, *277*, E779.E783.

[136] V. V. Andruschenko, H. J. Vogel, E. J. Prenner, *J. Pept. Sci.* **2007**, *13*, 37-43.

[137] S. Roux, E. Zékri, B. Rousseau, M. Paternostre, J.-C. Cintrat, N. Fay, *J. Pept. Sci.* **2008**, *14*, 354-359.

[138] T. Freichel, D. Laaf, V. Heine, E.E. Mackintosh, S. Sarafova, L. Elling, L. Hartmann, N.L. Snyder, "Sequence-defined Heteroglycomacromolecules Delay Wound Healing of a Galectin-3 Positive Tumor Cell Line." in preparation for the Journal of the American Chemical Society

[139] J. Kania, *Festphasensynthese von Glycooligomeren mit unregelmäßig angeordneten Mannose Liganden*, Bachelor Thesis, Heinrich-Heine-Universität Düsseldorf, **2016**.

[140] J. T. Varkey, V. N. R. Pillai, *J. Peptide Sci.* **1999**, *5*, 577-581.

[141] K. J. Jensen, P. Tofteng Shelton, S. L. Pedersen, Linkers, resins, and general procedures for solid-phase peptide synthesis, Springer, *Peptide Synthesis and Applications* **2013**, 23-41

[142] F. Hofmeister, *Arch. Exp. Pathol. Pharmkol.* **1888**, *24*, 247-260.

[143] Y. Zhang, P. S. Cremer, *Curr.Opin. Chem. Biol.*, **2006**, *10*, 658-663.

[144] F. García-Martin, M. Quintanar-Audelo, Y. García-Ramos, L. J. Cruz, C .Gravel, R. Furic, S. Coté, J. Tulla-Puche, F. Albericio, *J. Comb. Chem.*, **2006**, *8*, 213-220.

[145] C. F. Brewer, R. D. I. Brown, S. H. Koenig, *J. Biomol. Struct. Dynam.*, **1983**, *1*, 961.

[146] B. Basca, K. Horváti, S. Bosze, F. Andreae, C. O. Kappe, *J. Am. Chem. Soc.*, **1963**, *85*, 2149-2154.

[147] D. K. Mandal, N. Kishore, C. F. Brewer, *Biochemistry*, **1994**, *33*, 1149-1156.

[148] R. A. Bryce, I. H. Hillier, J. H. Naismith, *Biophys. J.*, **2001**, *81*, 1373-1388.

[149] C. Shalley, F. P. Schmidtchen, *Analytical Methods in Supramolecular Chemistry*, Wiley VCH Verlag GmbH & Co. KGaA, **2007**, Weinheim.

[150] O. Sulak, E. Lameignère, M. Wimmerova, A. Imberty, *Carbohydr. Chem.* **2009**, *35*, 356-371.

[151] T. K. Dam, C. F. Brewer, *Chem. Rev.* **2002**, *102*, 387-430.

[152] T. K. Dam, R. Roy, D. Pagé, C. F. Brewer, *Biochemistry* **2002**, *41*, 1359-1363.

[153] X. Wang, E. Matei, A. M. Gronenborn, O. Ramström, M. Yan, *Anal. Chem.* **2012**, *84*, 4248-4252.

[154] M. J. Cliff, J. E. Landbury, *J. Mol. Recognit.* **2003**, *16*, 383-391.

[155] A. Ababou, J. E. Ladbury, J. Mol. Recognit. 2007, 20, 4-14.

[156] C. Song, S. Zhang, H. Huang, *Front. Microbiol.* **2015**, *6*, 1-18.

[157] T. K. Dam, R. Roy, S. K. Das, S. Oscarson, C. F. Brewer, *J. Biol. Chem.* **2000**, *275*, 14223-14230.

[158] R. S. Loka, M. S. McConnell, H. M. Nguyen, *Biomacromolecules* **2015**, *16*, 4013-4021.

[159] M. C. Chervenak, E.Toone, *J. Biochemistry* **1995**, *34*, 5685-5695.

[160] L. Baranauskiene, V. Petrikaite, J. Matuliene, D. Matulis, *Int. J. Mol. Sci.* **2009**, *10*, 2752-2762.

[161] M. De Rivera, F. Socorro, *J. Therm. Anal. Calorim.* **2005**, *80*, 769-773.

[162] L. D. Hansen, G. W. Fellingham, D. J. Russel, *Anal. Biochem.* **2011**, *409*, 220-229.

[163] F. Socorro, I. de la Nuez, L. Alvarez, M. De Rivera, *Thermochim. Acta* **2004**, *420*, 163-167.

[164] J. Tellinghuisen, *Anal. Biochem.* **2003**, *321*, 79-88.

[165] J. Tellinghuisen, *Methods Enzymol.* **2004**, *383*, 245-282.

[166] J. Tellinghuisen, *Anal. Biochem*. **2004**, *333*, 405-406.

[167] J. Tellinghuisen, *Anal. Biochem*. **2005**, *343*, 106-115.

[168] J. Tellinghuisen, J. D. Chodera, *Anal. Biochem.* **2011**, *414*, 297-299.

[169] M. Dubois, K. A. Gilles, J. K. Hamilton, P. A. Rebers, F. Smith, *Anal. Chem.* **1956**, *28*, 350-356.

[170] T. Wiseman, S. Williston, J. F. Brandts, L.-N. Lin, *Anal. Biochem.* **1989**, *179*, 131-137.

[171] W. B. Turnbull, A. H. Daranas, *J. Am. Chem. Soc.* **2003**, *125*, 14859-14866.

[172] J. Tellinghuisen, *Anal. Biochem.* **2008**, *373*, 395-397.

[173] J. R. Beasely, D. F. Doyle, L. Chen, D. S. Cohen, B. R. Fine, G. J. Pielak, *Proteins* **2002**, *49*, 398-402.

[174] A. Cooper, C. M. Johnson, J. H. Lakey, M. Nöllmann, *Biophys. Chem.* **2001**, *93*, 215-230.

[175] J. D. Dunitz, *Chem. Biol.* **2003**, *2*, 709-712.

[176] O. Exner, *Chem. Commun.* **2000**, *2000*, 1655-1656.

[177] D. M. Ford, *J. Am. Chem. Soc*. **2005**, *127*, 16167-16170.

[178] E. Gallicchio, M. M. Kubo, R. M. Levy, *J. Am. Chem. Soc*. **1998**, *120*, 4526-4527.

[179] R. R. Krug, W. G. Hungter, R. A. Grieger, *Nature* **1976**, *261*, 566-567.

[180] R. Lumry, S. Rajender, *Biopolymers* **1970**, *9*, 1125-1127.

[181] R. McGregor, B. Milicevic, *Nature* **1966**, *211*, 523-525.

[182] K. Sharp, *Protein Sci.* **2001**, *10*, 661-667.

[183] J. D. Chodera, D. L. Mobley, *Annual Review of Biophysics* **2013**, *42*, 121.

[184] B. Brogioni, F. Berti, *Med. Chem. Commun.* **2014**, *5*, 1058-1066.

[185] J. J. Lundquist, E. J. Toone. *Chem. Rev.* **2002**, *102*, 555-578.

[186] M. Ambrosi, N. R. Cameron, B. G. Davis, *Org. Biomol. Chem.* **2005**, *3*, 1593-1608.

[187] J. B. Corbell, J. J. Lundquist, E. J. Toone, *Tetrahedron: Asymmetry* **2000**, *11*, 95-111.

[188] S. Boden, F. Reise, J. Kania, T. K. Lindhorst, L. Hartmann, *Macromol. Biosci.* **2019**, 1800425.

[189] M. Reynolds, S. *C. R.* Pérez, *Chimie*, **2011**, *14*, 74-95.

[190] D. Ponader, P. Maffre, J. Aretz, D. Pussak, N. M. Ninnemann, S. Schmidt, P. H. Seeberger, C. Rademacher, G. U. Nienhaus, L. Hartmann, *J. Am. Chem. Soc.* **2014**, *136*, 2008-2016.

[191] M. Mammen, S.-K. Choi, G. M. Whitesides, *Angew. Chem. Int. Ed.* **1998**, *37*, 2754-2794.

[192] K. L. Hudson, G. J. Bartlett, R. C. Diehl, J. Agirre, T. Gallagher, L. L. Kiessling, D. N. Woolfson, *J. Am. Chem. Soc.* **2015**, *137*, 15152.

[193] P. N. Kanellopoulos, K. Pavlou, A. Perrakis, B. Agianian, C. E. Vorgias, C. Mavrommatis, M. Soufi, P. Tucker, S. J. Hamodrakas, *J. Struct. Biol.* **1996**, *116*, 345-355.

[194] M. Francois-Heude, A. Méndez-Ardoy, V. Cendret, P. Lafite, R. Daniellou, C. Ortiz Mellet, J. M. García Fernández, V. Moreau, F. Djedaini-Pilard *Chem. Eur. J.* **2015**, *21*, 1978-1991.

[195] E. K. Mulholland, R. A. Adegbola, *Engl. J. Med.* **2005**, *352*, 75-77.

[196] M. Hartmann, A. K. Horst, P. Klemm, T. K. Lindhorst, *Chem. Commun.* **2010**, *46*, 330-332.

[197] T. A. Oelschlaeger, U. Dobrindt, J. Hacker, *Curr. Opin. Urol.* **2002**, *12*, 33-38.

[198] M. Hartmann, T. K. lindhorst*, Eur. J. Org. Chem.* **2011**, *2011*, 3583-3609.

[199] L. Möckl, C. Fessele, G. Despras, C. Bräuchle, T. K. Lindhorst, *Biochim. Biophys. Acta Gen. Subj.* **2016**, *1860*, 2031-2036.

[200] M. Hartmann, H. Papavlassopoulos, V. Chandrasekaran, F. Beiroth, T. K. Lindhorst, C. Röhl, *FEBS Letters* **2012**, *586*, 1459-1465.

[201] T. K. Lindhorst, C. Kieburg, U. Krallmann-Wenzel, *Glycoconj. J.* **1998**, *15*, 605-613.

[202] C. Grabosch, M. Hartmann, J. Schmidt-Lassen, T. K. Lindhorst, *ChemBioChem* **2011**, *12*, 1066-1074.

[203] D. Choudhury, A. Thompson, V. Stojanoff, S. Langermann, J. Pinkner, S. J. Hultgren, S. D. Knight, *Science* **1999**, *285*, 1061-1066.

[204] C.-S. Hung, J. Bouckaert, D. Hung, J. Pinkner, C. Widberg, A. DeFusco, C. G. Auguste, R. Strouse, S. Langermann, G. Waksman, S. J. Hultgren, *Mol. Microbiol.* **2002**, *44*, 903-918.

[205] J. Bouckaert, J. Berglund, M. Schembri, E. De Genst, L. Cools, M. Wuhrer, C.-S. Hung, J. Pinkner, R. Slättegård, A. Zavialov, D. Choudhury, S. Langermann, S. J. Hultgren, L. Wyns, P. Klemm, S. Oscarson, S. D. Knight, H. De Greve, *Mol. Microbiol.* **2005**, *55*, 441-455.

[206] S. D. Knight, J. Bouckaert, *Structure, Function, and Assembly of Type 1 Fimbriae*. In: T. Lindhorst, S. Oscarson (eds), Glycoscience and Microbial Adhesion. *Top. Curr. Chem.* **2009**, *288*, pp. 67-107, Springer, Berlin, Heidelberg.

[207] O. Sperling, A. Fuchs, T. K. Lindhorst, *Org. Biomol. Chem.* **2006**, *4*, 3913-3922.

[208] B. Benaissa-Trouw, D. J. Lefeber, J. P. Kamerling, J. F. G. Vliegenthart, K. Kraaijeveld, H. Snippe, *Infect. Immun.* **2001**, *69*, 4698–4701.

[209] R. Roy, M.-G. Baek, *Rev. Mol. Biotechnol.* **2002**, *90*, 291–309.

[210] R. Narain, S. P. Armes, *Biomacromolecules* **2003**, *4*, 1746–1758.

[211] J.-F. Nierengarten, J. Iehl, V. Oerthel, M. Holler, B. M. Illescas, A. Muñoz, N. Martín, J. Rojo, M. Sánchez-Navarro, S. Cecioni, S. Vidal, K. Buffet, M. Durka, S. P. Vincent, *Chem. Commun.* **2010**, *46*, 3860–3862.

[212] L. Baldini, A. Casnati, F. Sansone, R. Ungaro, *Chem. Soc. Rev.* **2007**, *36*, 254–266.

[213] S. Y. Hong, G. Tobias, K. T. Al-jamal, B. Ballesteros, H. Ali-Boucetta, S. Lozano-Perez, P. D. Nellist, R. B. Sim, C. Finucane, S. J. Mather, M. L. H. Green, K. Kostarelos, B. G. Davis, *Nat. Mater.* **2010**, *9*, 485–490.

[214] A. Robinson, J.-M. Fang, P.-T. Chou, K.-W. Liao, R.-M. Chu, S.-J. Lee, *ChemBioChem* **2005**, *6*, 1899–1905.

[215] E. Katz, I. Willner, *Angew. Chem. Int. Ed.* **2004**, *43*, 6042–6108.

[216] F. Compostella, O. Pitirollo, A. Silvestri, L. Polito, *Beilstein J. Org. Chem.* **2017**, *13*, 1008-1021.

[217] S.-J. Richards, E. Fullam, G. S. Besra, M. I. Gibson, *J. Mater. Chem. B* **2014**, *2*, 1490-1498.

[218] M. Brust, M. Walker, D. Bethell, D. J. Schiffrin, R. Whyman, *J. Chem. Soc. Chem. Commun.* **1994**, 0, 801-802.

[219] J. Turkevich, P. C. Stevenson, J. Hillier, *Discuss. Faraday Soc.* **1951**, *11*, 55-75.

[220] M. Reynolds, M. Marradi, A. Imberty, S. Penadés, S. Pérez, *Chem. Eur. J.* **2012**, *18*, 4264-4273.

[221] L.-D. Huang, A. K. Adak, C.-C. Yu, W.-C. Hsiao, H.-J. Lin, M.-L. Chen, C.-C. Lin, *Chem. Eur. J.* **2015**, *21*, 3956-3967.

[222] H. Christenson, *J. Chem. Soc., Faraday Trans.* 1 **1984**, *80*, 1933.

[223] X. Yang, M. Yang, B. Pang, M. Vara, Y. Xia, *Chem. Rev.* **2015**, *115*, 10410-10488.

[224] S.-J. Richards, L. Otten, M. I. Gibson, *J. Mater. Chem. B* **2016**, *4*, 3046-3053.

[225] B. Arnáiz, O. Martínez-Ávila, J. M. Falcon-Perez, S. Penadés, *Bioconj. Chem.* **2012**, *23*, 814–825.

[226] A. L. Brown, A. M. Goforth, *Chem. Mater.* **2012**, *24*, 1599–1605.

[227] S.-J. Richards, M. I. Gibson, *ACS Macro Lett.* **2014**, *3*, 1004–1008.

[228] A. G. Barrientos, J. M. de la Fuente, T. C. Rojas, A. Fernández, S. Penadés, *Chem. Eur. J.* **2003**, *9*, 1909–1921.

[229] S. Sangabathuni, R. V. Murthy, P. M. Chaudhary, M. Surve, A. Banerjee, R. Kikkeri, *Nanoscale* **2016**, *8*, 12729–12735

[230] S. Toraskar, M. Gade, S. Sangabathuni, H. V. Thulasiram, R. Kikkeri, *ChemMedChem* **2017**, *12*, 1116–1124.

[231] C. L. Schofield, B. Mukhopadhyay, S. M. Hardy, M. B. McDonnell, R. A. Field, D. A. Russell, *Analyst* **2008**, *133*, 626-634.

[232] H. Tsutsumi, H. Ohkusa, H. Park, T. Takahashi, H. Yuasa, H. Mihara, *Bioorg. Med. Chem. Lett.* **2012**, *22*, 6825–6827.

[233] M. V. Trivedi, J. S. Laurence, T. J. Siahaan, *Curr. Protein Pept. Sci.* **2009**, *10*, 614-625.

[234] L. Valtola, A. Rahikkala, J. Raula, E. I. Kauppinen, H. Tenhu, S. Hietala, *Eur. Polym. J.* **2014**, *59*, 282-289.

[235] S. Schmidt, H. Wang, D. Pussak, S. Mosca, L. Hartmann, *Beilstein J. Org. Chem.* **2015**, *11*, 720–729.

[236] K. Rahme, L. Chen, R. G. Hobbs, M. A. Morris, C. O´Driscoll, J. D. Holmes, RSC Advances, 2017, 7, 8798-8799.

[237] S. Watanabe, K. Yoshida, K. Shinkawa, D. Kumagawa, H. Seguchi, *Colloids Surf. B Biointerfaces* **2010**, *81*, 570–577.

[238] C.-C. Lin, Y.-C. Yeh, C.-Y. Yang, G.-F. Chen, Y.-C. Chen, Y.-C. Wu, *Chem. Commun.* **2003**, 2920–2921.

[239] L. Dykman, N. Khlebtsov, *Chem. Soc. Rev.* **2012**, *41*, 2256–2282.

[240] S. R. S. Ting, G. Chen, M. H. Stenzel, *Polym. Chem.* **2010**, *1*, 1392–1412.

[241] R. L. Siegel, K. D. Miller, A. Jemal, *CA Cancer J. Clin.* **2019**, *69*, 7-34.

[242] X. Huang, M. A. El-Sayed, *Alexandria J. Med.* **2011**, *47*, 1-9.

[243] X. Huang, P. K. Jain, I. H. El-Sayed, M. A. El-Sayed, *Lasers Med. Sci.* **2008**, *23*, 217-238.

[244] W. R. Chen, R. L. Adams, E. Heaton, D. T. Dickey, K. E. Bartels, R. E. Nordquist, *Cancer Lett.* **1995**, *88*, 15-19

[245] G. Jori, L. Schindl, A. Schindl, L. Polo, *J. Photochem. Photobiol. A Chem.* **1996**, *102*, 101-107.

[246] G. Jori, J. D. Spikes, *J. Photochem. Photobiol. B Biol.* **1990**, *6*, 93-101.

[247] S. Link, M. A. El-Sayed, *J. Phys. Chem. B* **1999**, *103*, 8410-8426.

[248] C. J. Murphy, T. K. Sau, A. Gole, C. J. Orendorff, J. Gao, L. Gou, S. Hunyadi, T. Li, *J. Phys. Chem. B* **2005**, *109*, 13857-13870.

[249] R. Weissleder, *Nat. Biotechnol.* **2001**, *19*, 316-317.

[250] H. Maeda, *Adv. Enzyme Regul.* **2001**, *41*, 189-207.

[251] R. Weissleder, K. Kelly, E. Y. Sun, T. Shatland, L. Josephson, *Nat. Biotechnol*. **2005**, *23*, 1418-1423.

[252] I. Sur, D. Cam, M. Kahraman, A. Baysal, M. Culha, *Nanotechnology* **2010**, *21*, 175104.

[253] K. Stockhofe, J. M. Postema, H. Schieferstein, T. L. Ross, *Pharmaceuticals* **2014**, *7*, 392-418.

[254] S. Yao, Y. Luo, Z. Zhang, G. Hu, Z. Zhu, F. Li, *Oncotarget* **2017**, *8*, 75162-75173.

[255] L. Vigderman, E. R. Zubarev, *Chem. Mater.* **2013**, *25*, 1450−1457.

[256] N. Bogliotti, B. Oberleitner, A. Di-Cicco, F. Schmidt, J.-C. Florent, V. Semetey, *J. Colloid Interface Sci.* **2011**, *357*, 75-81.

[257] J. Li, B. Zhu, Z. Zhu, Y. Zhang, X. Yao, S. Tu, R. Liu, S. Jia, C. J. Yang, *Langmuir* **2015**, *31*, 7869-7876.

[258] A. Swarnapali, D. S. Indrasekara, R. C. Wadams, L. Fabris, *Part. Part. Syst. Charact.* **2014**, *31*, 819-838.

[259] C. Kinnear, H. Dietsch, M. J. D. Clift, C. Endes, B. Rothen-Rutishauser, A. Petri-Fink, *Angew. Chem. Int. Ed.* **2013**, *125*, 1988-1992.

[260] Y. Ye, L. Xiao, S.-J. Wang, W. Yue, Q.-S. Yin, M.-Y. Sun, W. Xia, Z.-Y. Shao, H. Zhang, *Oncotarget* **2016**, *7*, 3921-3933.

[261] L. Shang, K. Nienhaus*, J. Nanobiotechnology* **2014**, *12*, 5.

[262] J. Dausend, A. Musyanovych, M. Dass, P. Walther, H. Schrezenmeier, K. Landfester, V. Mailänder, *Macromol. Biosci.* **2008**, *8*, 1135-1143.

[263] D. A. Kuhn, D. Vanhecke, B. Michen, F. Blank, P. Gehr, A. Petri-Fink, B. Rothen-Rutishauser, *Beilstein J. Nanotechnol.* **2014**, *5*, 1625-1636.

[264] O. Ramström, J.-M. Lehn, *Nat. Rev. Drug Discov.* **2002**, *1*, 26-36.

[265] A. Herrmann, *Chem. Soc. Rev.* **2014**, *43*, 1899-1933.

[266] I. Huc, J.-M. Lehn, *Proc. Natl. Acad. Sci. USA* **1997**, *94*, 2106-2110.

[267] F. Aricó, T. Chang, S. J. Cantrill, S. I. Khan, J. F. Stoddart*, Chem. Eur. J.* **2005**, *11*, 4655-4666.

[268] Y. Liu, J.-M. Lehn, A. K. H. Hirsch, *Acc. Chem. Res.* **2017**, *50*, 376-386.

[269] O. Ramström, J.-M. Lehn, *ChemBioChem* **2000**, *1*, 41-48.

[270] B. Brisig, J. K. M. Sanders, S. Otto, *Angew. Chem. Int. Ed.* **2003**, *42*, 1270-1273.

[271] S. Otto, S. Kubik, *J. Am. Chem. Soc.* **2003**, *125*, 7804-7805.

[272] M. Pepels, I. Filot, B. Klumperman, H. Goossens, *Polym. Chem.* **2013**, *4*, 4955-4965.

[273] P. A. Fernandes, M. J. Ramos*, Chem. Eur. J.* **2004**, *10*, 257-266.

[274] S. Otto, R. L. E. Furlan, J. K. Sanders, *J. Am. Chem. Soc.* **2000**, *122*, 12063-12064.

[275] G. L. Ellman, *Arch. Biochem. Biophys.* **1959**, *82*, 70-77.

[276] A. Bernkop-Schnürch, V. Schwarz, S. Steininger, *Phar. Res.* **1999**, *16*, 876-881.

[277] C. Godoy-Alcántar, A. K. Yatsimirsky, J.-M. Lehn, *J. Phys. Org. Chem.* **2005**, *18*, 979-985.

[278] S. Ladame, *Org. Biomol. Chem.* **2008**, *6*, 219-226.

[279] T. Bunyapaiboonsri, O. Ramström, S. Lohmann, J.-M. Lehn, L. Peng, M. Goeldner, *ChemBioChem* **2001**, *2*, 438-444.

[280] O. Ramström, S. Lohmann, T. Bunyapaiboonsri, J.-M. Lehn, *Chem. Eur. J.* **2004**, *10*, 1711-1715.

[281] V. T. Bhat, A. M. Caniard, T. Luksch, R. Brenk, D. J. Campopiano, M. F. Greaney, *Nature Chemistry* **2010**, *2*, 490–497.

[282] T. Bunyapaiboonsri, O. Ramström, S. Lohmann, J.-M. Lehn, L. Peng, M. Goeldner, *ChemBioChem* **2001**, *2*, 438-444.

[283] O. Ramström, S. Lohmann, T. Bunyapaiboonsri, J.-M. Lehn, *Chem. Eur. J.* **2004**, *10*, 1711-1715.

[284] V. T. Bhat, A. M. Caniard, T. Luksch, R. Brenk, D. J. Campopiano, M. F. Greaney, *Nature Chemistry* **2010**, *2*, 490–497.

[285] D. Bonnet, C. Grandjean, P. Rousselot-Pailley, P. Joly, L. Bourel-Bonnet, V. Santraine, H. Gras-Masse, O. Melnyk, *J. Org. Chem.* **2003**, *68*, 7033-7040.

[286] X. Liu, M. Atwater, J. Wang, Q. Huo, *Colloids Surf. B Biointerfaces* **2007**, *58*, 3-7.

[287] L. Otten, D. Vlachou, S.-J. Richards, M. I. Gibson, *Analyst.* **2016**, *141*, 4305-4312.

[288] (a) A. Reisner, J. A. J. Haagensen, M. A. Schembri, E. L. Zechner, S. Molin, *Mol. Microbiol.* **2003**, *48*, 933-946; (b) The GFP-tagged strain pPKL1162 was constructed in the Klemm group by introduction of the plasmid pPKL174 into strain SAR18; pPKL174 contains the fim gene cluster, which is required for type 1 fimbriae assembly and expression. The chromosome of strain SAR18 from the Reisner group contains the GFP gene, controlled by a constitutive promoter.

[289] M. Hartmann, A. K. Horst, P. Klemm, Th. K. Lindhorst, *Chem. Commun.* **2010**, *46*, 330-332.

[290] W. Hayes, H. M. I. Osborn, S. D. Osborne, R. A. Rastall, B. Romagnoli, *Tetrahedron* **2003**, *59*, 7983-7996.

[291] L. Wu, N. S. Sampson, *ACS Chem. Biol.* **2014**, *9*, 468-475.

[292] J. Rieger, F. Stoffelbach, D. Cui, A. Imberty, E. Lameignere, J.-L. Putaux, R. Jérôme, C. Jérôme, R. Auzély-Velty, *Biomacromolecules* **2007**, *8*, 2717-2725.